AFRL-RY-WP-TR-2020-0128

FREQUENCY STABILITY IN A COMPACT, DEPLOYABLE OPTICAL ATOMIC CLOCK

Todd F. Sheerin
Charles Stark Draper Laboratory, Inc.

MAY 2020
Final Report

Approved for public release; distribution is unlimited.

See additional restrictions described on inside pages

STINFO COPY

AIR FORCE RESEARCH LABORATORY
SENSORS DIRECTORATE
WRIGHT-PATTERSON AIR FORCE BASE, OH 45433-7320
AIR FORCE MATERIEL COMMAND
UNITED STATES AIR FORCE

REPORT DOCUMENTATION PAGE

Form Approved
OMB No. 0704-0188

The public reporting burden for this collection of information is estimated to average 1 hour per response, including the time for reviewing instructions, searching existing data sources, gathering and maintaining the data needed, and completing and reviewing the collection of information. Send comments regarding this burden estimate or any other aspect of this collection of information, including suggestions for reducing this burden, to Department of Defense, Washington Headquarters Services, Directorate for Information Operations and Reports (0704-0188), 1215 Jefferson Davis Highway, Suite 1204, Arlington, VA 22202-4302. Respondents should be aware that notwithstanding any other provision of law, no person shall be subject to any penalty for failing to comply with a collection of information if it does not display a currently valid OMB control number. **PLEASE DO NOT RETURN YOUR FORM TO THE ABOVE ADDRESS**.

1. REPORT DATE *(DD-MM-YY)*	2. REPORT TYPE	3. DATES COVERED *(From - To)*
May 2020	Thesis	19 March 2020 –19 March 2020

4. TITLE AND SUBTITLE
FREQUENCY STABILITY IN A COMPACT, DEPLOYABLE OPTICAL ATOMIC CLOCK

5a. CONTRACT NUMBER
FA8650-15-C-7532

5b. GRANT NUMBER

5c. PROGRAM ELEMENT NUMBER
69199E

6. AUTHOR(S)
Todd F. Sheerin

5d. PROJECT NUMBER
DARPA

5e. TASK NUMBER
N/A

5f. WORK UNIT NUMBER
Y19D

7. PERFORMING ORGANIZATION NAME(S) AND ADDRESS(ES)

Decision Sciences Branch
Multi-Domain Sensing Autonomy Division (AFRL/RYWN)
Air Force Research Laboratory, Sensors Directorate
Wright-Patterson Air Force Base, OH 45433-7320
Air Force Materiel Command, United States Air Force

Charles Stark Draper Laboratory, Inc.

8. PERFORMING ORGANIZATION REPORT NUMBER

9. SPONSORING/MONITORING AGENCY NAME(S) AND ADDRESS(ES)

Air Force Research Laboratory
Sensors Directorate
Wright-Patterson Air Force Base, OH 45433-7320
Air Force Materiel Command
United States Air Force

10. SPONSORING/MONITORING AGENCY ACRONYM(S)
AFRL/RYWN

11. SPONSORING/MONITORING AGENCY REPORT NUMBER(S)
AFRL-RY-WP-TR-2020-0128

12. DISTRIBUTION/AVAILABILITY STATEMENT
Approved for public release; distribution is unlimited.

13. SUPPLEMENTARY NOTES
PAO case number 88ABW-2020-0924, Clearance Date 19 March 2020. ©2020 Todd F. Sheerin. To be Submitted to the Department of Aeronautics and Astronautics at the Massachusetts Institute of Technology in partial fulfillment of the requirements for the Degree of Doctor of Philosophy in Aeronautics and Astronautics. This work was funded in whole or in part by Department of the Air Force contract #. The U.S. Government has for itself and others acting on its behalf an unlimited, paid-up, nonexclusive, irrevocable worldwide license to use, modify, reproduce, release, perform, display, or disclose the work by or on behalf of the U. S. Government. Report contains color.

14. ABSTRACT

The advent of ultra-narrow lasers, ultra-fast lasers, and optical frequency combs in the last several decades have enabled a new generation of atomic clocks based on optical transitions as opposed to microwave transitions. While optical atomic clocks in the laboratory outperform microwave standards by orders of magnitude, their complexity, size, weight, and power have so far precluded their application to fielded, compact systems. Efforts described in this thesis to transfer optical atomic timekeeping technology from the laboratory to the field and to improve analytic tools for spectroscopy with ultra-narrow lasers are motivated by a need to support GPS-denied operations (a DARPA objective) and to enable a broad range of positioning, navigation, and timing applications in civil, commercial, and defense sectors. Existing theoretical frameworks describing coupling strength for atom-laser interactions in optical atomic systems implicitly assume broad laser linewidths. This thesis explores possible spectroscopic implications of ultra-narrow lasers interacting with atoms. Additionally, a simple optical atomic clock architecture based on thermal calcium Ramsey-Bordé (R-B) matter-wave interferometry is described. Experimental investigations in this thesis were carried out in two systems: a compact, deployable Ca Beam Optical Timekeeping (CaBOT) clock, and a second-generation laboratory clock at NIST (Ca-2). This thesis describes a performance evaluation of the CaBOT frequency reference exhibiting fractional frequency instability of 5.0x10-14 at one second. Measurement noise floor analyses revealed excess laser noise to be the dominant performance limitation. With modest improvements, instability is projected to reach the 10-15 decade. In the Ca-2 system, temperature fluctuations were observed to drive instability for time scales >100s, and a temperature-frequency correlation study indicated that temperature control at the mK level would enable 10-16 instability. A thermal enclosure limiting frequency reference temperature variations to 10s-mK enabled repeatable, sustained Ca-2 operations with ≤2x10-16 instability between 10s-1,000s. Finally, a thermal-fluid temperature control system was designed for the deployable CaBOT clock to dissipate ~220W and maintain mK level instability for the <0.09 m3 chassis with low added noise. Physical demonstration of sub-mK temperature control with a model liquid cooling circuit indicated the potential for excellent mid- to long-term stability of the CaBOT clock when fully integrated.

15. SUBJECT TERMS
atomic clock, GPS-denied navigation, optical reference

16. SECURITY CLASSIFICATION OF:			17. LIMITATION OF ABSTRACT:	18. NUMBER OF PAGES	19a. NAME OF RESPONSIBLE PERSON (Monitor)
a. REPORT	b. ABSTRACT	c. THIS PAGE			Thao Nguyen
Unclassified	Unclassified	Unclassified	SAR	294	19b. TELEPHONE NUMBER *(Include Area Code)* N/A

Frequency Stability in a Compact, Deployable Optical Atomic Clock

by
Todd F. Sheerin

A.B. Physics
Harvard College, 2012

S.M. Aeronautics and Astronautics
Massachusetts Institute of Technology, 2015

SUBMITTED TO THE DEPARTMENT OF AERONAUTICS AND ASTRONAUTICS IN PARTIAL FULFILLMENT OF THE REQUIREMENTS FOR THE DEGREE OF

DOCTOR OF PHILOSOPHY IN AERONAUTICS AND ASTRONAUTICS
AT THE
MASSACHUSETTS INSTITUTE OF TECHNOLOGY

JUNE 2019

©2019 Todd F. Sheerin. All rights reserved.

The author hereby grants to the Massachusetts Institute of Technology and to The Charles Stark Draper Laboratory, Inc. permission to reproduce and to distribute publicly paper and electronic copies of this thesis document in whole or in part in any medium now known or hereafter created.

Signature of Author ……...
Department of Aeronautics and Astronautics
May 23, 2019

Certified by ……...
Jeffrey A. Hoffman, Professor of the Practice of Aeronautics and Astronautics, MIT
Thesis Committee Chair

Certified by ……...
Richard E. Stoner, Laboratory Technical Staff, Draper
Thesis Advisor

Certified by ……...
Paulo Lozano, M. Alemán-Velasco Professor of Aeronautics and Astronautics, MIT
Thesis Committee Member

Certified by ……...
Vladan Vuletić, Lester Wolfe Professor of Physics, MIT
Thesis Committee Member

Accepted by ……...……...
Sertac Karaman, Aeronautics and Astronautics Graduate Committee Chair
Professor of Aeronautics and Astronautics, MIT

Approved for public release; distribution is unlimited

Frequency Stability in a Compact, Deployable Optical Atomic Clock

by
Todd F. Sheerin

Submitted to the Department of Aeronautics and Astronautics
on May 23, 2019 in Partial Fulfillment of the
Requirements for the Degree of Doctor of Philosophy in
Aeronautics and Astronautics

ABSTRACT

The advent of ultra-narrow lasers, ultra-fast lasers, and optical frequency combs in the last several decades have enabled a new generation of atomic clocks based on optical transitions as opposed to microwave transitions. While optical atomic clocks in the laboratory outperform microwave standards by orders of magnitude, their complexity, size, weight, and power have so far precluded their application to fielded, compact systems. Efforts described in this thesis to transfer optical atomic timekeeping technology from the laboratory to the field and to improve analytic tools for spectroscopy with ultra-narrow lasers are motivated by a need to support GPS-denied operations (a DARPA objective) and to enable a broad range of positioning, navigation, and timing applications in civil, commercial, and defense sectors.

Existing theoretical frameworks describing coupling strength for atom-laser interactions in optical atomic systems implicitly assume broad laser linewidths. This thesis explores possible spectroscopic implications of ultra-narrow lasers interacting with atoms. Additionally, a simple optical atomic clock architecture based on thermal calcium Ramsey-Bordé (R-B) matter-wave interferometry is described. Experimental investigations in this thesis were carried out in two systems: a compact, deployable Ca Beam Optical Timekeeping (CaBOT) clock, and a second-generation laboratory clock at NIST (Ca-2). This thesis describes a performance evaluation of the CaBOT frequency reference exhibiting fractional frequency instability of 5.0×10^{-14} at one second. Measurement noise floor analyses revealed excess laser noise to be the dominant performance limitation. With modest improvements, instability is projected to reach the 10^{-15} decade. In the Ca-2 system, temperature fluctuations were observed to drive instability for time scales >100s, and a temperature-frequency correlation study indicated that temperature control at the mK level would enable 10^{-16} instability. A thermal enclosure limiting frequency reference temperature variations to 10s-mK enabled repeatable, sustained Ca-2 operations with $\leq 2 \times 10^{-16}$ instability between 10s-1,000s. Finally, a thermal-fluid temperature control system was designed for the deployable CaBOT clock to dissipate ~220W and maintain mK level instability for the <0.09 m^3 chassis with low added noise. Physical demonstration of sub-mK temperature control with a model liquid cooling circuit indicated the potential for excellent mid- to long-term stability of the CaBOT clock when fully integrated.

Thesis Committee Chair
Jeffrey A. Hoffman, Professor of the Practice of Aeronautics and Astronautics, MIT

Thesis Advisor
Richard E. Stoner, Laboratory Technical Staff, Draper

Thesis Committee Member
Paulo Lozano, M. Alemán-Velasco Professor of Aeronautics and Astronautics, MIT

Thesis Committee Member
Vladan Vuletić, Lester Wolfe Professor of Physics, MIT

Approved for public release; distribution is unlimited

Acknowledgments

This research was conducted with Government support under and awarded by DoD, Air Force Office of Scientific Research, National Defense Science and Engineering Graduate (NDSEG) Fellowship, 32 CFR 168a. Additional support was provided by Draper through the Draper Fellow Program and by MIT through a Research Assistantship with the Space Systems Laboratory. I must also acknowledge the support provided by the DoD for the DARPA STOIC program award to Draper that provided motivation for my Ph.D. research.

Beyond the financial and institutional support that enabled my thesis research, I'd also like to acknowledge my collaborative partners among the Draper staff including my thesis advisor and mentor Richard Stoner for our countless discussions and fruitful interactions that have made my Ph.D. experience so valuable and transformative for me as a scientist and engineer, as well as Krish Kotru, John Hamilton, Jason Durant, Adam Kelsey, Matt Sinclair, Valerie Lowe, and Sungyung Lim at Draper for their technical support and insight. I've grown immeasurably as a researcher and an individual working alongside these incredibly bright and kind individuals, and I owe them my sincerest gratitude. I'd also like to acknowledge our collaborators at NIST in the Optical Frequency Measurements Group in Boulder, CO including Rich Fox, Judith Olson, Andrew Ludlow, and Chris Oates, as well as Tara Fortier. Conversations and experimental work with this group including extended discussions with my Ph.D. candidate counterpart at NIST, Judith Olson, proved invaluable to my research and to my experience investigating the stability of optical atomic clocks based on thermal Ca Ramsey-Bordé atom interferometry. The opportunity they generously afforded me to work in their group as a visiting scientist was an opportunity of a lifetime for a scientist and engineer, and one that I will not soon forget.

In addition to those already named, I wish to thank Prof. Hoffman for his steadfast support over the decade of our advisor-advisee interactions beginning with an undergraduate research experience that afforded me the opportunity to reach where I am today. I also need to thank the rest of my first aerospace engineering advisors and supervisors, including Pat Troutman, Phillip Cunio, and Bobby Cohanim who provided me with opportunities when I wasn't sure I deserved any.

Finally, I'd like to thank my family for their love and patience with me as I pursued degree after degree on the opposite side of the country. Without their unwavering support, guidance, and encouragement, I would never have been able to engender and pursue the passions that have brought me to where I am today. I feel incredibly lucky to have them in my life, providing a seemingly endless source of inspiration, emphathy, and warmth for which I will always be grateful.

Approved for public release; distribution is unlimited

Table of Contents

Approved for public release; distribution is unlimited

Approved for public release; distribution is unlimited

Approved for public release; distribution is unlimited

Approved for public release; distribution is unlimited

Abbreviations

AOM	Acousto-optical modulator
COTS	Commercial off the shelf
CaBOT	Calcium Based Optical Timekeeping (Draper)
Ca-2	Calcium-2 (NIST)
CTE	Coefficient of thermal expansion
DARPA	Defense Advanced Research Projects Agency
Draper	The Charles Stark Draper Laboratory, Inc.
FWHM	Full-width at half-maximum
GNSS	Global Navigation Satellite System
GPS	Global Positioning System
IR	Infrared
LIF	Light-induced fluorescence
MPPC	Multi-pixel photon counter
NEG	Non-evaporative getter
NIST	National Institute of Standards and Technology
PDH	Pound-Drever-Hall (laser frequency stabilization)
PNT	Positioning, navigation, and timing
PSD	Power spectral density
R-B	Ramsey-Bordé
RF	Radio frequency
RIN	Relative intensity noise
RMS	Root mean squared
RTD	Resistance temperature detector
SNR	Signal-to-noise ratio
SWaP	Size, weight, and power
ULE	Ultra-low expansion

Abbreviations are also defined in the text at point of first use.

Approved for public release; distribution is unlimited

Chapter 1

Introduction

1.1. Research motivation

1.1.1. GPS-denied positioning, navigation, and timing

Today there is a widespread dependence in public, private, and defense sectors on Global Positioning Services (GPS) and other global navigation satellite systems (GNSS) around the world. Figure 1-1 depicts the GPS constellation (a) and photographs corresponding to several applications that rely on the satellite network (b). Chief among these applications are land, sea, air, and space vehicles, as well as the tracking and communication systems that support these various forms of transport. In the space domain, for instance, NASA's Tracking and Data Relay Satellite (TDRS) constellation and the Deep Space Network (DSN) currently provide communications between ground stations and spacecraft near and far from Earth, respectively. Both of these networks rely on precise timing and positioning information aided by GPS/GNSS to determine orbit properties and to aid propulsive calculations for commanded maneuvers. In

(a) 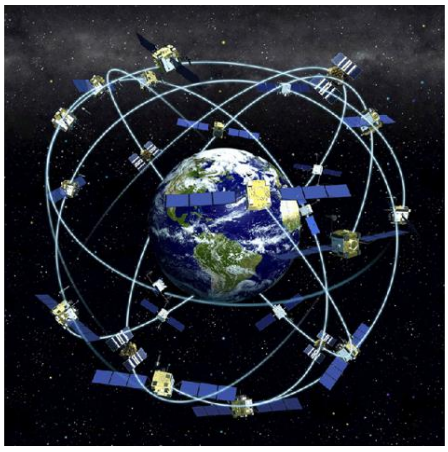 (b) 

Figure 1-1. Global Positioning System and applications: (a) graphic of GPS system, courtesy of NOAA; (b) collage of applications enabled by GPS, courtesy of Leveson 2015.

Approved for public release; distribution is unlimited

addition to supporting astrodynamics calculations, precision timing is also relied upon to maintain network synchronicity of spacecraft with network nodes and ground stations.

While a reliance on GPS/GNSS may be most visible in transportation and communication networks, a similar reliance extends into a broad range of industries critical to worldwide infrastructure and commerce. In 2015, the National Space-Based Positioning, Navigation and Timing Advisory Board reported that commercial applications of GPS accounted for approximately $68.7 billion of the annual United States Gross Domestic Product [Leveson 2015]. The broader impact around the globe for GNSS applications was reported in the European GNSS Agency's 2015 market report. Core and enabled markets including road, maritime, aviation, rail, location based services, agriculture, surveying, and timing and synchronization were found to account for an estimated core market size of €60B and an enabled market size of €230B in 2014, with 3.6 billion GNSS devices in use [European GNSS Agency 2015].

Despite the prevalence of GPS/GNSS in commerce and industry, the role that these satellite systems and the role that their timing signals play often go unnoticed. A 2008 assessment of GPS criticality found that "not all users are or were aware of the fact that their reference systems rely on GPS," and that disruptions to electric power and telecommunications networks were often caused by a loss of accurate timing [Carroll and Montgomery 2008]. The near-ubiquitous dependence on GPS/GNSS implies vulnerability. Tactical, civil, and commercial positioning, navigation, and timing (PNT) operations in regions with insecure GPS access risk service degradation or loss. In addition, there is an elevated risk posed by malicious actors that are capable of jamming or spoofing GPS signals in order to disrupt or corrupt the flow of GPS information to end-users.

One approach to reducing the dependence on GPS/GNSS is to use local timing and frequency references that can replace GPS/GNSS timing signals for extended periods of time for critical infrastructure and service operations including network synchronization. By coupling these local references with stationary beacons and stable time transfer protocols, positioning and navigation solutions may also be provided without GPS/GNSS. Unfortunately, there is no deployable frequency reference that is capable of providing GPS-level timing and frequency performance. While there are mature technologies including

Approved for public release; distribution is unlimited

cesium beam clocks and hydrogen masers that have been regularly used for a broad range of PNT related tasks in the field, their fractional frequency instability at short-term and mid-term time scales do not meet the challenge of supporting the most demanding GPS-denied operations.

A recent study by the Defense Advanced Research Projects Agency (DARPA) [DARPA 2014] identified a fractional frequency instability of 1×10^{-14} at one second and 1×10^{-16} at one month as a target performance for a low size, weight, and power (SWaP), deployable form factor for immediate application in the field to support GPS-denied operations. Among nascent technologies that hold promise to meet this objective, optical atomic timekeeping provides a viable path given the rapid advances in laboratory clocks in the last two decades, surpassing performance of even the most advanced microwave atomic clock technologies by several orders of magnitude [Poli *et al*. 2014]. Unfortunately, there have yet to be any optical clocks produced in a deployable and compact form factor comparable to currently available microwave standard. Instead, optical atomic clocks today are large, complex, and costly laboratory assemblies.

The research conducted in this thesis concerns the design and evaluation of a compact and simple optical atomic clock design based on Ramsey-Bordé (R-B) atom interferometry with a thermal beam of neutral calcium. Figure 1-2 depicts a qualitative comparison between the large size and complexity of state of the art laboratory optical atomic clocks such as the Ytterbium (Yb) optical lattice clock and the optical clock design described in this thesis. The Ca Beam Optical Timekeeping (CaBOT) clock depicted in Figure

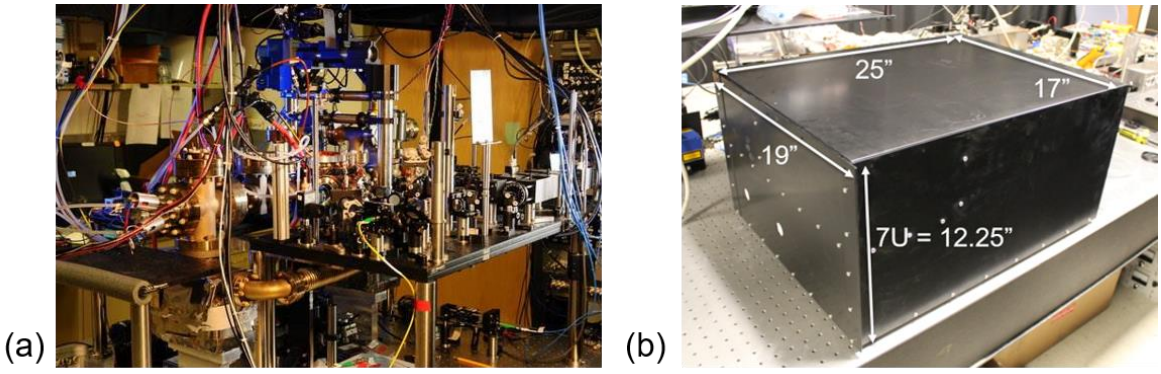

Figure 1-2. Optical atomic clocks: (a) Yb optical lattice clock at NIST [Hinkley *et al*. 2013]. (b) a compact, fieldable optical atomic clock chassis designed as part of this thesis research for the CaBOT clock.

Approved for public release; distribution is unlimited

1-2 relies on a single laser and thermal atomic beams, significantly reducing complexity, cost, and SWaP over contemporary optical atomic clocks involving many lasers and complex measurement schemes involving cooled and trapped atoms or ions. While the primary motivation for CaBOT is a fielded clock capable of meeting the DARPA objective for GPS-denied operations for critical services with small SWaP, CaBOT may also be applied to other precision timing applications. In addition to the CaBOT clock, this thesis involves research conducted with the second generation thermal Ca R-B frequency reference at NIST (Ca-2) [Olson *et al.* 2017, Olson *et al.* 2019]. While CaBOT was designed for compact, fielded application, Ca-2 was designed for laboratory evaluation of the limitations and ultimate performance objectives for a thermal Ca R-B architecture.

1.1.2. Other science and industry applications

In addition to enabling GPS-denied operations, a compact, deployable optical atomic clock would be widely applicable to Earth and space services and fundamental science investigations. The primary application of the NIST Ca-2 effort, for instance, involves laser frequency stabilization that may be readily applied to laboratory clocks at the forefront of timekeeping technology [Olson *et al.* 2019].

Uses of ultra-stable frequency references and precise timekeeping solutions include tests of relativity [Ashby, Parker, and Patla 2018, Georgescu 2017, Chou *et al.* 2010] and searches for gravity waves [Abott *et al.* 2016, Acernese *et al.* 2014, Graham *et al.* 2016], dark matter, and variation of fundamental constants [Stadnik and Flambaum 2016, Derevianko and Pospelov 2014, Safronova *et al.* 2018]. Quantum simulation and quantum control experiments including recent explorations of SU(n) interactions also require ultra-stable references [Zhang *et al.* 2014, Schmidt-Kaler *et al.* 2003]. Quantum manipulation methods relying on stable frequency references underlie the emerging industry of quantum computing, and so compact, fieldable, and cost-effective optical atomic clocks may prove useful in a wide range of future systems. Furthermore, the demonstration of stable transfer [Leopardi *et al.* 2017, Sinclair *et al.* 2018] across the electromagnetic spectrum indicates immediate applicability of optical atomic clocks to civil,

Approved for public release; distribution is unlimited

commercial, defense, and science operations including advanced positioning, navigation and timing, communication, and radar systems.

In addition, ultra-stable clocks would transform deep space exploration. Today, all deep space navigation relies on two-way communications with the Deep Space Network (DSN) on Earth, a process that is both slow and costly. With on-board stable local oscillators, deep space missions would need only one-way communication with the DSN for navigation, enabling a higher degree of autonomy for more flexible missions. Two-way communications with the DSN would still be necessary to exchange mission and telemetry data. Even so, relaxing navigation-related communications requirements would reduce deep space mission cost, risk, and complexity, and would enable the DSN to service more missions than currently possible. NASA's Deep Space Atomic Clock (DSAC) aims to enable this transformation [Prestage and Weaver 2007], though DSAC is based on a microwave transition in mercury ions and so further performance improvements would be possible with a design based on an optical transition. In addition to navigation, high precision on-board clocks would enable solar system relativity tests, gravimetry of planetary bodies, and radio occultation measurements.

1.2. Timing and frequency reference overview

1.2.1. Atom-based timekeeping background

All clocks are composed of two basic components: a frequency reference and a counter. Examples of a frequency reference include a swinging pendulum in a grandfather clock or a vibrating quartz crystal in a smartphone. The function of a clock's counter is to convert the frequency reference oscillations into the final, useable timing signal such as the movement of a second, minute, or hour hand in an analog clock or the digital readout of time in an electronic device. An atomic clock is no different. Instead of a quartz oscillator or pendulum, the frequency splitting of an atomic transition serves as the oscillating reference to be counted to generate a timing signal.

Approved for public release; distribution is unlimited

Unlike a classical pendulum or crystal oscillator that feature frequency drifts corresponding to the macroscopic nature of their composition, construction, and local environmental conditions, the basis of an atomic clock's signal is the physical structure of the atom itself, which remains well isolated from the environment and constant from atom to atom. In addition, electronic transitions in atoms occur at relatively high frequencies as compared with crystal oscillators or pendulums, a property that contributes to enhanced clock performance.

Spectroscopy provides a mechanism by which atomic energy levels are used as a clock's oscillator. By sweeping a coherent radiation source such as a laser or microwave generator across the resonant frequency of an atomic transition, a fluorescent feature is generated corresponding to the atomic resonance frequency. By locking to this fluorescent signal, the atom provides a frequency reference from which the clock timing signal is based. Even if the source frequency is subject to drift, the atomic resonance remains stable and so only perturbations to the atomic structure result in clock frequency drifts.

1.2.2. Accuracy, stability, and Allan deviations

There are two metrics by which a clock's performance may be evaluated: clock uncertainty, or accuracy, and clock instability, or precision. An accurate clock measures seconds with the correct length as defined by international standards. Evaluating the accuracy of an atomic clock amounts to measuring the absolute atomic frequency and comparing against catalogued values in the literature for the same transition. A precise or stable clock, on the other hand, may be said to measure seconds that are the same length, regardless of whether each second is the right length. A stable clock produces repeated frequency measurements that are clustered closely to one another.

The applications motivating this research prioritize clock stability over clock accuracy. In general, short-term stability enables reliable, repeatable, and quick measurements for dynamic and network applications and for pre-stabilization of other types of oscillators. Long-term stability enables maintenance

Approved for public release; distribution is unlimited

of network synchronicity and constant standards for time; thus, this type of performance is especially useful for distributed networks.

The standard method of characterizing frequency instability is the standard Allan deviation $\sigma_y(\tau)$ or the square root of the two-sample Allan variance. The two-sample Allan variance $\sigma_y^2(\tau)$ measured over N time intervals lasting τ seconds is defined to be [Allan 1966, Allan *et al.* 1997]:

$$\sigma_y^2(\tau) = \frac{1}{2(N-1)} \sum_{n=1}^{N-2} \left(\bar{y}_{n+1}(\tau) - \bar{y}_n(\tau) \right)^2$$
$$\bar{y}_n(\tau) = \frac{1}{\tau} \sum_{k=n}^{n+\frac{\tau}{\tau_s}} y_k \qquad (1.1)$$

Each $\bar{y}_n$ in equation (1.1) is the mean of τ/τ_s individual frequency measurements acquired at a rate $1/\tau_s$ beginning at the n^{th} interval, where τ_s is the sample interval. The factor of ½ is included so that the Allan variance is equal to the classical variance in which $\bar{y}_n$ values are random and uncorrelated. The same set of clock frequency error values may be separated into different sized bins according to different values of τ and assessed for instability at different averaging times. In order to provide a universal performance metric, the Allan deviation of fractional frequency measurements is usually reported in which each measured frequency is divided by the expected frequency. For clock Allan deviations, this expected frequency is the clock frequency.

A key feature of Allan deviations is that instability arising from noise processes is measured as opposed to an absolute frequency error measurement. A white noise process will produce an Allan deviation profile that trends as $1/\sqrt{\tau}$; a linear drift process results in an Allan deviation that trends as τ . In addition to the standard Allan deviation corresponding to the two-sample variance in equation (1.1), there are alternative types of Allan deviations that are sometimes used to analyze frequency data sets including the Total Allan deviation and the Modified Allan deviation (for further information, see [Allan *et al.* 1997]).

Approved for public release; distribution is unlimited

1.2.3. Atomic clock instability limit and ideal clocks

An atomic clock's fractional frequency instability and associated standard Allan deviation is theoretically limited by the quantum atom shot noise inherent to the transition and to the population utilized for measurement. Atom shot noise instability $\sigma_{\text{atom shot}}(\tau)$ over an averaging time τ is [Fox *et al.* 2012]:

$$\sigma_{\text{atom shot}}(\tau) = \frac{\delta\nu}{\nu_0}\sqrt{\frac{1}{\dot{N}\tau}} \tag{1.2}$$

In equation (1.2), $\delta\nu$ is the frequency width of the locking feature, ν_0 is the resonant atomic transition clock frequency, and $\dot{N}$ is the rate of atoms participating in the measurement, i.e. the number of atoms contributing to the fluorescence signal measurement per second assuming that each atom contributes at most one photon. The form of equation (1.2) illustrates the characteristics of an atomic clock that are most desirable. Reduced atom shot noise over a given measurement period is possible with high transition frequencies ν_0 narrow locking features $\delta\nu$ and high rates of atom contributions to the signal $\dot{N}$.

The ideal clock transition based on a quantum system occurs at the highest possible frequency (gamma radiation), and would be a delta-function in frequency space, corresponding to a vanishingly narrow natural linewidth and an infinite excitation lifetime. Because an infinite excitation lifetime implies zero signal, since there would be no spontaneous emission to measure, a means of cycling excited state atoms to a third, short-lived state would be desired. Additionally, an ideal quantum reference would be isolated to the greatest possible extent from the environment.

Given these criteria for the ideal clock, nuclear transitions might in principle be considered as the most desirable frequency references. Not only are nuclear transition frequencies many orders of magnitude higher than atomic transitions, but nuclei are also well shielded from the environment by electrons. However, nuclear clocks are not yet achievable given the lack of narrow linewidth coherent sources at gamma, x-ray, and ultra-violet regions of the spectrum. Until stable, narrow-linewidth lasers at these

Approved for public release; distribution is unlimited

frequencies and methods to stably convert these frequencies for distribution are developed, clocks based on electronic transitions will continue to provide the best candidates for quantum-based clocks.

Aside from the selection of a good candidate clock transition, efforts must be made to prepare or interrogate atoms such that perturbations to the relevant energy structure are minimized. For atomic clocks, common approaches include cooling or trapping atoms. These techniques rely on the fact that large Doppler effects are eliminated with slow- or non-moving atom samples. In addition to cooling and trapping approaches, Doppler-free spectroscopic approaches such as saturation spectroscopy are commonly employed for the same reasons. An ideal clock would feature atoms at zero absolute temperature in an equally cool environment involving no Doppler or blackbody effects, completely isolated from external fields. Atoms optically confined in vacuum come close to this ideal scenario, though perturbative effects of confinement can be mitigated but not totally eliminated.

1.2.4. Atomic clock technology trends

Until the turn of the 21st century, atomic clocks were limited to atomic transitions in the microwave (1-10 GHz) region of the electromagnetic spectrum. Despite the identification of optical frequency standards, there was no technology available to transform and distribute the high frequencies (100s of THz) associated with optical transitions into the radio frequency (RF) domain. Microwave based atomic clocks are well suited to conversion and distribution in the RF domain and have been improved over the decades with sophisticated methods to produce narrow-linewidth, high signal-to-noise spectroscopic signals as in the Cs fountain clocks developed and operated at NIST [Heavner *et al.* 2014].

Over the last few decades the landscape of precision timekeeping has changed dramatically with rapid advances in laser and laser-based technologies that enabled the application of optical frequency references to atomic clocks. Principal among enabling technologies were ultra-narrow lasers characterized by Hz-scale and sub-Hz linewidths at visible wavelengths [Salomon *et al.* 1988] and ultra-fast lasers capable of producing femtosecond-scale pulse durations [Morgner *et al.* 1999, Sutter *et al.* 1999]. A

Approved for public release; distribution is unlimited

combination of these technologies with a method for high resolution spectroscopy depending on fast (picosecond) lasers [Eckstein *et al.* 1978] resulted in the invention of the optical frequency comb technique that ultimately earned Glauber, Hall, and Hansch the 2005 Nobel Prize in Physics [Trabesinger 2005]. This technique generates a series of regularly spaced, sharply peaked comb "teeth" in frequency space. The most common optical frequency comb variety relies on a mode-locked ultrafast (femtosecond pulse) laser as described, for instance, in [Cundiff and Ye 2003]. The laser pulse repetition rate, ranging from tens of MHz to several GHz, determines the spacing of individual harmonics and the pulse duration determines the carrier envelope width within which comb teeth are observed. The inverse relationship between time and frequency domains enables femtosecond scale laser pulses to generate wide carrier envelopes spanning an optical frequency octave or more, with shorter pulses providing wider carrier envelope bandwidths.

By beating an optical frequency reference signal with a single tooth of an optical frequency comb, the reference signal can be transformed into microwave and ultimately RF frequencies while maintaining the stability inherent in the optical signal. With this innovation, optical frequency references characterized since the 1970s could be utilized as frequency references for atomic clocks. In addition to enabling the invention of the optical frequency comb technique, lasers with linewidths $< 1\,\mathrm{Hz}$ may function independently as highly stable flywheel oscillators at short time scales to be used to generate optical atomic resonance features and which underlie enhanced optical atomic clock performance.

Aside from a transition to optical transition frequencies, laboratory timekeeping efforts are increasingly employing cooling and trapping techniques for atoms and ions to narrow locking features and to eliminate environmental perturbations to the clock signal. These methods have resulted in record-breaking clock accuracies and instabilities e.g. Hinkley 2013, owing principally to the reduced fractional frequencies $\delta\nu/\nu_0$ achievable. The optical lattice is currently the best performing method used to prepare atoms for interrogation. Using a standing wave tuned to a so-called "magic" wavelength (i.e., a wavelength that perturbs the two states of the clock transition equally), multiple atoms can be individually trapped in potential wells of an electromagnetic field that preserve the clock transition frequency between ground and

Approved for public release; distribution is unlimited

excited states. Cold atoms loaded into the optical lattice experience a pristine and stable environment, thereby preserving to the greatest extent possible the atomic structure energy levels to reduce instabilities in the clock signal [Ludlow *et al.* 2015].

Unfortunately, the large number of lasers and the high degree of complexity and cost associated with these approaches, as well as the large SWaP involved, have precluded widespread deployment in the field and commercialization. Highly stable and compact laser oscillators are emerging in the marketplace, as are highly stable and compact optical frequency combs. What is lacking are highly stable and compact optical atomic frequency references that would be required in conjunction with lasers and combs to field optical atomic clocks.

In this thesis, a compact and deployable optical atomic clock based on thermal Ca Ramsey-Bordé atom interferometry is described, along with theoretical and experimental investigations concerning the clock's operational principals and performance. Unlike other approaches to field optical atomic clocks, the CaBOT clock does not require atom cooling or trapping, nor does it require multiple laser frequencies for atom signal generation and locking. Rather, it relies on only a single cavity stabilized, narrow linewidth laser and a fiber optic frequency comb. With this simple architecture, optical frequency standards may be deployed to the field to enable extended GPS-denied operations and other science and industry applications requiring ultra-stable timing references.

Approved for public release; distribution is unlimited

1.3. Research focus: thermal calcium Ramsey-Bordé atom interferometry

1.3.1. Calcium intercombination line

The optical clock transition used in this research is the $\left(4s^2\right)^1S_0 - \left(4s4p\right)^3P_1$ transition in neutral ^{40}Ca, often referred to as calcium's intercombination line. This transition features a narrow (374 Hz) natural linewidth at 657 nm [Degenhardt *et al.* 2005]. The relevant level structure is depicted in Figure 1-3.

This transition is semi-forbidden since the coupling involves a violation of the selection rule for spin conservation, but spin-orbit (L-S) coupling enables a weak coupling through an electric dipole transition. Specifically, the two valence electrons of neutral ^{40}Ca are excited from a ground singlet configuration in which the electrons have paired, opposing spins represented in ket notation as $\left(\left|\uparrow\downarrow\right\rangle - \left|\downarrow\uparrow\right\rangle\right)/\sqrt{2}$ to an excited state triplet configuration represented as $\left(\left|\uparrow\downarrow\right\rangle + \left|\downarrow\uparrow\right\rangle\right)/\sqrt{2}$ in ket notation. This transition involves linearly polarized light, and while the total spin changes from zero to one, the final, excited state spin projection quantum number is zero. A qualitative explanation for this semi-forbidden transition may be found by considering L-S coupling: the electrons' angular motion about the

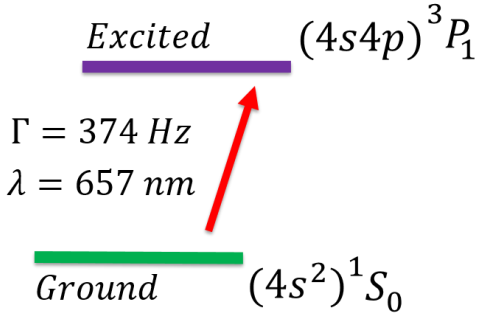

Figure 1-3. Energy level diagram for neutral calcium's intercombination line.

Approved for public release; distribution is unlimited

nucleus generates an additional, induced magnetic moment. This moment enables a non-classical spin transition mediated through weak coupling to resonant electromagnetic radiation to an excited triplet state.

By contrast, a more common (and not forbidden) electric dipole transition would involve ground state and excited state coupling in which the total spin angular momentum is conserved. In this case, a singlet ground state couples with a singlet excited state, or a triplet state couples with a triplet state. These transitions between strongly coupled states involve short natural lifetimes and wide natural linewidths since the atom may readily transition from one state to the other.

Given the myriad of spectroscopy techniques that may be employed to utilize the Ca intercombination line for a frequency reference, this thesis utilizes one of the oldest and simplest methods: a thermal atomic beam, as pioneered by early atomic clock efforts as reviewed in Holloway, *et al.* 1959. By utilizing a Ramsey-Bordé atom interferometry scheme involving four coherent atom-laser interaction sites, a Doppler free, narrow linewidth spectroscopy signal can be produced with a thermal atomic beam for stable timekeeping.

1.3.2. Thermal atomic beams

The geometry of a laser spectroscopy setup based on a Ca atomic beam is shown in Figure 1-4. A calcium oven at the left of the figure contains a crucible that vaporizes a Ca sample, and a nozzle at the right side of the oven allows a beam of atoms to exit moving from left to right along the $\hat{z}$ axis, intersecting with a laser oriented in the orthogonal $\hat{x}$ axis. An aperture downstream from the oven further collimates the atomic beam into an angle α in the $\hat{x}-\hat{z}$ plane. A detector is positioned beyond the atom-laser interaction site and beyond the collimating aperture in order to collect fluorescence from excited Ca atoms. In the figure, a parabolic reflector aids fluorescence detection by increasing the overall collection fraction that may be observed from the isotropic spontaneous emission of the excited Ca.

By sweeping the laser frequency across the clock transition frequency, a Doppler-broadened profile results with a full-width half maximum (FWHM) frequency width $\Delta\nu_{FWHM}$ given by [Foot 2005]:

Approved for public release; distribution is unlimited

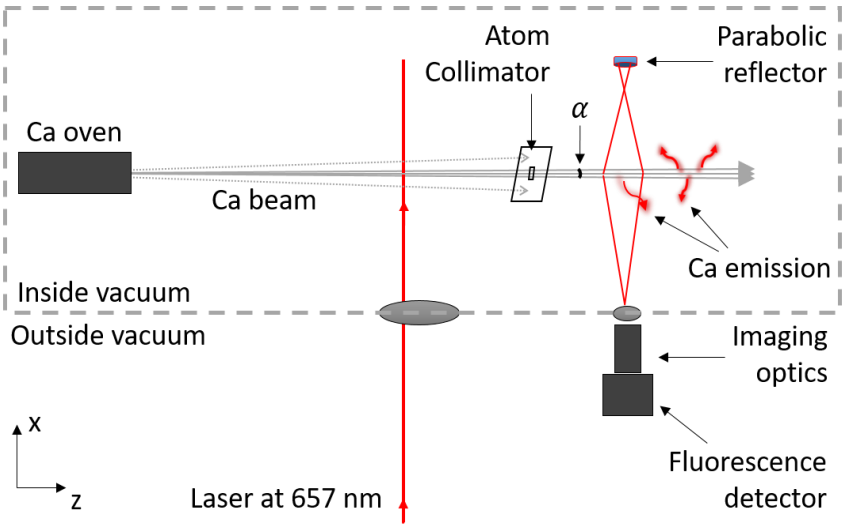

Figure 1-4. Laser spectroscopy of a collimated atomic beam.

$$\Delta\nu_{FWHM} \approx \frac{1.2}{1.7}\frac{\alpha\langle v\rangle}{\lambda} \tag{1.3}$$

In equation (1.3), λ is the clock transition wavelength and $\langle v\rangle$ is the most probable speed of the atoms. The most probable velocity $\langle v\rangle$ is determined from kinetic theory by the temperature of the atomic sample and the atomic mass. For a Ca oven mean temperature of $T = 625^{\circ}\mathrm{C}$, the most probable atomic velocity of $\langle v\rangle = \sqrt{3/2}\sqrt{2k_BT/M} = 748\ \mathrm{m/s}$ is calculated for the Maxwellian gas distribution that may be expected with an effusive oven [Ramsey 1956]. For an angle of $\alpha = 6.8\ \mathrm{mrad}$ and $\lambda = 657\ \mathrm{nm}$, a FWHM of $\Delta\nu_{FWHM} = 5.5\ \mathrm{MHz}$ is predicted. This may be compared with the Doppler width of a signal resulting from the same conditions, but without beam collimation, for instance for a thermal gas cell of Ca. In this case, the expected FWHM for the isotropic gas distribution would be $\Delta\nu_{FWHM} = 0.8\ \mathrm{GHz}$.

Even with collimation, the spectroscopy signal resulting from a single atom-laser interaction is many times wider than the natural linewidth of 374 Hz. In order to make use of the high atom fluxes possible with an atom beam, additional laser interactions may be employed to eliminate the first-order Doppler shift and otherwise produce a narrow spectroscopic signal to which a laser clock oscillator may be locked.

Approved for public release; distribution is unlimited

1.3.3. Doppler-free spectroscopy and R-B atom interferometry

Several examples of Doppler-free spectroscopy include saturated absorption spectroscopy, spectral hole burning and two-photon spectroscopy. Each of these techniques involves counter-propagating lasers. In the first two methods listed, only one photon scattering event is necessary to drive the transition: while one laser drives absorption, the second laser drives stimulated emission, producing a saturation dip, often referred to as a hole, in the resonant spectrum. By contrast, two-photon spectroscopy involves an atomic transition that requires resonant scattering of two photons to achieve the state transition; because the photons are arriving from opposite directions, the recoil associated with their absorption cancel.

These techniques are relevant to the current thesis only insofar as they represent alternate approaches to Doppler-free spectroscopy. For further information on these topics, please refer to resources such as [Foot 2005, Letokhov and Chebotaev 1977, Demtröder 1996, Corney 2000, or Meschede 2004]. For a description of spectral hole burning techniques, some recent research includes [Thorpe *et al.* 2011] and [Cook *et al.* 2015].

In the field of atom interferometry, there is one approach to Doppler-free spectroscopy that is particularly interesting as an applicable technology for compact optical timekeeping and which lies at the heart of this thesis: Ramsey-Bordé atom interferometry. This method is introduced in the seminal reference [Bordé *et al.* 1984]. This method eliminates leading Doppler shifts for a molecular beam with the use of four traveling wave lasers oriented in the manner depicted in Figure 1-5a. In general, this method may be described as an application of the Ramsey method as described in [Ramsey 1956]. The Ramsey method enables sub-Doppler width resolution of an atomic resonance feature through the use of separated oscillatory fields traveling in the same direction. To eliminate leading Doppler effects, Bordé *et al.* 1984 demonstrated the use of two successive Ramsey sequences oriented with traveling wave vectors in opposing directions from one sequence to the next.

Approved for public release; distribution is unlimited

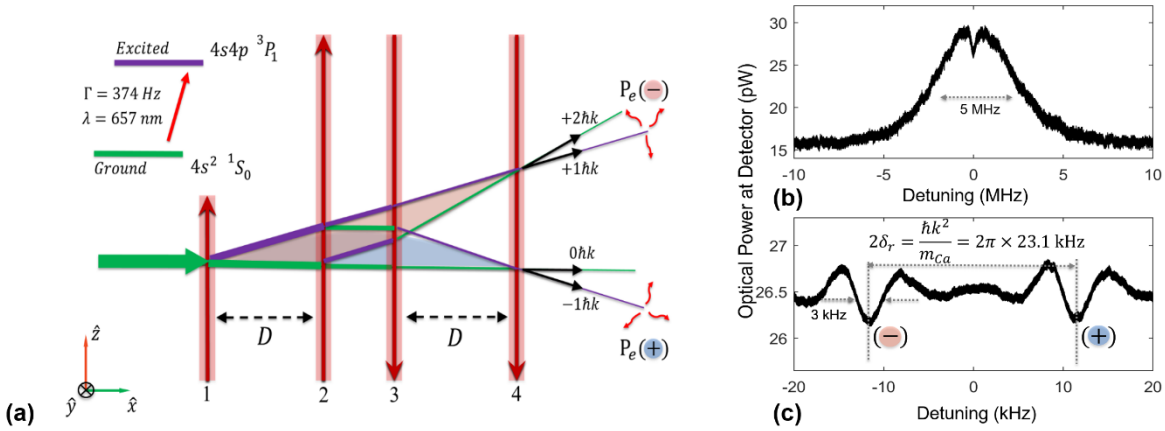

Figure 1-5. R-B atom interferometry with a thermal Ca beam. (a) Atoms pass through four mutually coherent laser beams, resulting in two output ports in which the atomic wavefunction exhibits interference. (b) Sweeping the laser frequency at the MHz scale produces a Doppler-broadened feature. (c) At the center of the Doppler feature, kHz-scale R-B fringes may be observed corresponding to the two output ports of the interferometer.

A Ca atomic beam crosses four mutually coherent laser beams from left to right in Figure 1-5a. At each atom-laser interaction site, there is a probability that the atom will undergo a change in internal energy and momentum states via photon absorption or stimulated emission. Internal states are denoted by color: green corresponding to the ground state and purple corresponding to the excited state. Momentum states separated by individual photon recoils are identified by the angle of atom trajectories traced through the interferometer. After all four optical laser beams, there are 2^4 possible final states for the atomic states, four of which are traced in the figure. The atomic wavefunction recombines in two distinct interferometer output ports, indicated by $P_e(+)$ and $P_e(-)$ with signs indicating a positive or negative recoil shift from the initial momentum state. The laser phase is imprinted on the atomic wavefunction throughout the interferometer such that the final atomic phase corresponds to the sum of the difference of laser pairs separated by distance "D" in Figure 1-5a.

By sweeping laser frequency across the intercombination resonance, a Doppler-broadened feature at the MHz scale is observed as depicted in Figure 1-5b, and Ramsey fringes are observed in the saturation dip of the Doppler profile, at the kHz scale as depicted in Figure 1-5c. Separation between fringes is

Approved for public release; distribution is unlimited

determined by the number of photon recoils separating the two ports (in this case, two recoils), and individual fringe widths are determined by atom time-of-flight between lasers 1-2 and 3-4.

Unlike previous efforts involving R-B with the intercombination line of Ca (e.g. Barger *et al.* 1979, Kisters 1994, Kersten 1999, Oates 2000, Degenhardt *et al.* 2005, McFerran and Luiten 2010, Fox 2012, Zhang 2016), this approach requires only a single laser in combination with a thermal atomic beam. This allows for an inherently simple, compact design. With a mean oven temperature of $T = 625^\circ\mathrm{C}$ and Ramsey laser pair separations of oven mean temperature of $D = 50\ \mathrm{mm}$, the CaBOT frequency reference generated fringes with widths of roughly 3 kHz, as depicted in experimental data shown in Figure 1-5c. In the final clock, these narrow features are to be used as a locking feature to stabilize the CaBOT laser, which is down converted to a useable timing signal in the radiofrequency domain by the optical frequency comb and associated electronics. The Ca-2 frequency reference has a larger beam separation of $D = 90\ \mathrm{mm}$ with a nominal R-B signal width of 1.6 kHz when atom ovens are operated at $T = 625^\circ\mathrm{C}$.

The primary advantage gained by using Ramsey-Bordé atom interferometry with a thermal beam of atoms is that a narrow resonant feature can be resolved with a large number of participating atom oscillators. The large signal-to-noise ratio arising from a large number of atom contributors labeled $\dot{N}$ in equation (1.2) coupled with the narrow fractional frequency resolvable with matter-wave interferometry together enable promising timekeeping performance with a simple architecture. In addition, this technique avails itself to frequency reference operation with only a single laser, further limiting the complexity and SWaP of an optical atomic clock based on R-B interferometry.

1.3.5. Precedents for thermal Ca R-B atom interferometry

Ca R-B efforts historically benefit from characterization of the Ca intercombination line as in [Barger *et al.* 1979]. Some of the initial efforts between 1994-2005 to apply R-B interferometry to the Ca intercombination line employed laser-cooled Ca [Kisters, *et al.* 1994, Oates, *et al.* 2000 and Degenhardt *et al.* 2005], while another effort used a thermal beam with the aim of constructing a transportable reference

Approved for public release; distribution is unlimited

[Kersten, *et al.* 1999]. In [Oates *et al.* 2000] and [Degenhardt *et al.* 2005], an R-B laser is used in conjunction with a blue laser for light-induced fluorescence (LIF) of the excited state atoms of the semi-stable excited state.

The trade to use blue LIF benefits from a higher possible signal-to-noise ratio at the cost of adding another laser. A higher excited state is coupled strongly to the excited Ca intercombination state, resulting in higher spontaneous emission rates than the lower clock transition. The result is that even with thermal atomic velocities, atoms exiting the R-B interferometer in the excited-state can be cycled repeatedly while still within the fluorescence detection region, releasing many blue photons for each excited state atom. The implication of course, is a larger available signal, especially when considering that in addition to many more photons being available for detection, the blue LIF frequency may be readily distinguished from the red clock transition frequency using in R-B interactions, reducing susceptibility to noise from scattered light.

Among efforts between 1994-2005, [Oates *et al.* 2000] achieved the best fractional frequency instability of 4×10^{-15} at once second of averaging time. [Kersten, *et al.* 1999] demonstrated a relative frequency uncertainty of 1.3×10^{-12} at one second for their reference aimed at transportability, though no further developments have been reported.

More recently, [McFerran and Luiten 2010] used a blue LIF laser and achieved a frequency stability of 9.2×10^{-14} at one second with a readout fluorescence shot noise of 7×10^{-15} at one second. This effort was not intended to be a transportable or fieldable package, but rather only a laboratory-based demonstration of a promising architecture for fielded technology. Another effort using blue LIF architecture was designed for transportability, achieving a fractional frequency stability of 1×10^{-13} at one second [Zhang *et al.* 2016]. No size, weight, or power specifications are reported for this effort, making it difficult to directly compare with the transportable clock described in this thesis. Finally, Hemingway *et al.* 2018 describes an effort to produce a compact thermal Ca R-B frequency reference also using blue LIF. This

Approved for public release; distribution is unlimited

effort did not measure a fractional frequency instability, but instead projects an instability of 5×10^{-13} based on observed fringes with a measured width of 15 kHz.

Though significant advantage is provided by blue LIF, a notable effort using only a single red laser demonstrated excellent short term instability for a thermal Ca R-B interferometer: at NIST, [Fox *et al.* 2012] demonstrated a fractional frequency stability of 5.5×10^{-15} at one second with a laboratory-based, single laser architecture. This represents more than 10x short-term stability improvement over the dual-laser [McFerran and Luiten 2010] approach, and served as the basis for CaBOT and Ca-2 design objectives.

While the design of the CaBOT frequency reference was largely based on the single-laser architecture of [Fox *et al.* 2012], design modifications were introduced to reduce overall clock SWaP and improve long term stability for a design capable of operating in a wide range of uncontrolled environmental conditions. Continued thermal Ca R-B efforts have been conducted at NIST with Ca-2, a second-generation thermal Ca apparatus following [Fox *et al.* 2012]. Ca-2 was designed with a blue LIF fluorescence capture system for improved performance at the cost of SWaP [Olson *et al.* 2017, Olson *et al.* 2019]. Communication between the NIST and Draper teams has been crucial for the mutual development of designs and strategies for frequency drift mitigation for both the CaBOT and Ca-2 efforts.

1.4. Context: optical atomic physics and modern timekeeping

1.4.1. Atom-beam interaction modeling for a single pulse

1.4.1.1. Rabi method and two level systems: the standard description

Atom-light interactions underlie the operations of optical atomic systems as well as the atomic molecular and optical physics field. In 1939, I. I. Rabi and colleagues [Rabi, *et al.* 1939] developed a method by which a nuclear magnetic spin transition frequency was measured using a molecular beam passing through a driving oscillating magnetic field. A static reference field was provided by external magnets. The magnetic moments of nuclear spins were aligned to the static reference field and driven in an oscillating

Approved for public release; distribution is unlimited

manner according to a Rabi rate $\Omega_B = \gamma\left|\vec{B}\right|$ where γ is the gyromagnetic ratio and $\vec{B}$ is the transverse, oscillatory magnetic field. While this treatment of a Rabi rate is expressed in the classical limit, i.e. without quantized spin, the concept is readily extended to a treatment of any quantized atomic system that may be driven with an external field.

For optical atomic systems relevant to optical timekeeping, the clock transition is usually an electric dipole transition in a two level system with a ground state $|g\rangle$ and excited state $|e\rangle$. For such a system, the so-called bare Rabi rate is given by

$$\Omega \equiv \frac{1}{\hbar}\langle e|\hat{\vec{r}}_{e-n}\cdot\vec{E}|g\rangle = \frac{eE}{\hbar}\langle e|\hat{\vec{r}}_{e-n}\cdot\hat{e}|g\rangle \tag{1.4}$$

where $\vec{E}$ is the electric field vector with amplitude $\left|\vec{E}_L\right| = E$ and where $\langle e|\hat{\vec{r}}_{e-n}\cdot\hat{e}|g\rangle$ is the matrix dipole element for the two level system. In equation (1.4), $\hat{e}$ is the electric field polarization, and $\hat{\vec{r}}_{e-n} = -e\hat{r}$ is the atom's electric dipole operator written in terms of the electron charge e and the dipole vector direction $\hat{r}$. For off-resonant driving, i.e. when there is some detuning $\delta = \omega - \omega_0$ of the driving field frequency ω as compared with the transition resonant frequency ω_0, then there is an extra source of oscillation contributing to Rabi fluctuations. The generalized Rabi rate in this case is expressed as $\Omega_g = \sqrt{\Omega^2 + \delta^2}$.

Assuming laser polarization along the atom's dipole moment, i.e. for $\hat{r} \parallel \hat{e}$, the probability of excitation from ground to excited state after an atom-field interaction time τ is given by:

$$P_{e,Rabi}(\tau) = \frac{\Omega^2}{\Omega_g{}^2}\sin^2\left(\frac{\Omega_g\tau}{2}\right) \tag{1.5}$$

It is clear from Equation (1.5) that the probability of transition is maximized when $\Omega_g\tau = \pi$, an interaction that is referred to as a π-pulse. For an interaction time $\tau = \pi/\left(2\Omega_g\right)$, referred to as a $\pi/2$-pulse, there is 50% probability that the atom remains in its initial state and 50% probability that a transition occurs.

Approved for public release; distribution is unlimited

After longer times, the atomic population oscillates between ground and excited states. By tuning the interaction time and driving oscillator strength, it is possible to manipulate atomic wavefunctions much like light is manipulated with common optics; for instance, a π-pulse serves for an atomic wavefunction as a mirror serves for an optical wavepacket; similarly, a $\pi/2$-pulse behaves as a beamsplitter for the atomic wavepacket.

In practice, optimization of an optical atomic interaction generally involves modulation of the driving radiation intensity until saturation is observed. The bare Rabi rate is related to the intensity of the resonant electromagnetic radiation I and the transition's natural linewidth Γ by the following relation (Foot 2005 Equation 7.86):

$$\frac{I}{I_{sat}} = \frac{2\Omega^2}{\Gamma^2} \tag{1.6}$$

where the saturation intensity I_{sat} is given by [Foot 2005 Equation 7.85]:

$$I_{sat} = \frac{\pi}{3}\frac{hc}{\lambda^3}\Gamma \tag{1.7}$$

In terms of the intensity of resonant light, then, the bare Rabi frequency is expressed as [Degenhardt *et al.* 2005 Equation 5b]:

$$\Omega = \sqrt{\frac{3c^2\Gamma I}{2\pi h\nu_0^{\,3}}} \tag{1.8}$$

where the relation $c = \lambda\nu_0$ is used and where $\nu_0 = \omega_0/2\pi$ is the clock transition frequency and λ is the transition wavelength.

1.4.1.2. Applied models for single pulse interactions: the Bordé *et al.* 1984 description

Equations (1.4)-(1.8) assume interaction between a perfectly homogeneous and isotropic driving field and a single atom. In practice, this will not be the case and instead the driving radiation will be non-uniform and atoms participating in the interaction will have some velocity distribution. A model for

Approved for public release; distribution is unlimited

experimental application must take into account the atom population's distribution and associated Doppler shifts to the radiation frequency in the atoms' frame relative to the inertial frame.

In [Bordé *et al.* 1984], a matter-wave interferometer was described in which the interaction between a molecule and driving radiation was treated in the molecular rest frame. In this frame, the electric field is written as $\vec{E}(\vec{r},t) = \mathrm{Re}\,\hat{e}^{\pm}E^{\pm}U^{\pm}\left(v_x\left(t-t_1\right)\right)\exp\left[i\left(\gamma\omega t \mp kv_z t \mp kz + \varphi^{\pm}\right)\right]$ where $\hat{e}$, E, U, k, and φ represent, respectively, the polarization vector, the amplitude, the transverse dependence, the wave number, and the phase of each wave. Molecular flow is along the $\hat{x}$ axis and the field is propagating along the $\hat{z}$ axis as in Figure 1-5a, and the second order Doppler is captured by the relativistic γ. When accounting for both energy and momenta in the description of the molecular states, each interaction results in both a change of the atom's internal state and a photon momentum exchange $\hbar\vec{k}$. The Schrödinger equation for the spinor corresponding to ground and excited states in the rotating frame, $\tilde{g}$ and $\tilde{e}$, can be written in terms of the Pauli spin matrices $\vec{\sigma}$ and the identity matrix σ_0 as:

$$\frac{\partial}{\partial t}\begin{bmatrix}\tilde{e}\\ \tilde{g}\end{bmatrix} = \frac{i}{2}\left[\vec{\Omega}_{Borde}\cdot\vec{\sigma} + \Omega_0\sigma_0\right]\begin{bmatrix}\tilde{e}\\ \tilde{g}\end{bmatrix} \tag{1.9}$$

where coupling rates are given by:

$$\vec{\Omega}_{Borde}\begin{cases}\Omega_1 = \Omega U^{\pm}\cos\varphi^{\pm}\\ \Omega_2 = \Omega U^{\pm}\sin\varphi^{\pm}\\ \Omega_3 = \left(\gamma\omega-\omega_0\right)\mp kv_z - \left[\left(m\pm1\right)^2 - m^2\right]\delta_r + i\left(\gamma_e-\gamma_g\right)/2\end{cases} \tag{1.10}$$
$$\Omega_0 = -\left[\left(m\pm1\right)^2 + m^2\right]\delta_r - \left(2m\pm1\right)kv_z + i\left(\gamma_e+\gamma_g\right)/2$$

In equation (1.10), m is the number of photon recoils corresponding to the interaction, where the initial ground state corresponds to $m=0$ and an excited state after a single interaction corresponds to $m=1$. Larger numbers of recoils correspond to multi-pulse interaction states. The recoil frequency is written as $\delta_r = \hbar k^2/2M$ where M is the mass of the molecule, and relaxation constants for the excited and ground

Approved for public release; distribution is unlimited

state are written as γ_e and γ_g, respectively. Positive or negative superscripts indicate interaction with a laser beam oriented along $\pm\hat{z}$ axis, and the magnitude of the coupling rate vector may be written simply as $\vec{\Omega}_{Borde}^2 = \Omega_{Borde}^2 = \Omega_3^2 + \Omega^2$. For the case where the electric field has no transverse dependence, i.e. for $U^{\pm} = 1$, the solution to the Schrödinger equation (1.9) may be evaluated to be:

$$\begin{bmatrix} \tilde{e}(t) \\ \tilde{g}(t) \end{bmatrix} = \exp\left[\frac{i}{2}\Omega_0\sigma_0\left(t-t_0\right)\right]\exp\left[\frac{i}{2}\vec{\Omega}_{Borde}\cdot\vec{\sigma}\left(t-t_0\right)\right]\begin{bmatrix} \tilde{e}(t_0) \\ \tilde{g}(t_0) \end{bmatrix} \tag{1.11}$$

which, when introducing the Pauli matrices and the coupling rate definition in equation (1.10), becomes:

$$\begin{bmatrix} \tilde{e}(t) \\ \tilde{g}(t) \end{bmatrix} = \begin{bmatrix} A\exp\left[\frac{i}{2}\Omega_0\left(t-t_0\right)\right] & B\exp\left[-i\varphi^{\pm}\right] \\ C\exp\left[i\varphi^{\pm}\right] & D\exp\left[\frac{i}{2}\Omega_0\left(t-t_0\right)\right] \end{bmatrix}\begin{bmatrix} \tilde{e}(t_0) \\ \tilde{g}(t_0) \end{bmatrix}$$

$$A = \cos\left[\frac{\Omega_{Borde}\left(t-t_0\right)}{2}\right] + i\frac{\Omega_3}{\Omega_{Borde}}\sin\left[\frac{\Omega_{Borde}\left(t-t_0\right)}{2}\right] \tag{1.12}$$

$$B = C = i\frac{\Omega}{\Omega_{Borde}}\sin\left[\frac{\Omega_{Borde}\left(t-t_0\right)}{2}\right]$$

$$D = \cos\left[\frac{\Omega_{Borde}\left(t-t_0\right)}{2}\right] - i\frac{\Omega_3}{\Omega_{Borde}}\sin\left[\frac{\Omega_{Borde}\left(t-t_0\right)}{2}\right]$$

After a single laser pulse interaction of duration t, the ground state and excited state probabilities $P_{g,Borde}(t)$ and $P_{e,Borde}(t)$ are calculated simply as:

$$\begin{aligned} P_{g,Borde}(t) &= \tilde{g}_{m=0}(t)\,\tilde{g}_{m=0}(t)^* \\ P_{e,Borde}(t) &= \tilde{e}_{m=1}(t)\,\tilde{e}_{m=0}(t)^* \end{aligned} \tag{1.13}$$

These probabilities may be used to estimate the total excitation fraction expected from an interaction with the laser field.

Approved for public release; distribution is unlimited

1.4.2. Limitations of the Bordé *et al.*1984 interaction model

The most prominent limitation of the treatment of the atom-laser interaction as described in [Bordé *et al.* 1984] and captured by equations (1.9)-(1.13) is the implicit assumption that all atomic velocity classes can interact with the laser, simply by selecting a laser wavelength detuned by a Doppler shift corresponding to the atom's velocity. While this may be an adequate description of atom-laser interactions with wide linewidth lasers, this treatment does not accurately capture conditions involving narrow-linewidth, near monochromatic lasers that are currently used in optical atomic experimental setups around the world, including the NIST test laser utilized in this thesis for CaBOT and Ca-2.

When considering a nearly monochromatic Gaussian laser, strict conservation of momentum would imply that atom-laser interactions are only allowed for each atom velocity class if a corresponding wave vector Doppler shifted to the proper frequency is present. The Gaussian laser beam waist therefore represents a critical experimental parameter for these scenarios since the dispersion of wave vectors $\vec{k}$ depends not only on the linewidth of the laser, but on the waist size according to usual Gaussian beam propagation. Historically, interaction rates for experimental setups involving narrow linewidth radiation sources driving atomic transitions have been optimized empirically with saturation studies in which the beam waist and driving radiation intensity are varied until saturation is observed or until spectroscopic contrast is maximized.

In order to supplement empirical methods, a theoretical framework can be developed that accounts for momentum conservation between a localized atomic wavepacket and a near-monochromatic Gaussian laser to calculate expected interaction strengths and transition probabilities as a function of experimental parameters. Chapters 2-3 of this thesis introduce such a theory that may be extended not only to multi-pulse interactions for thermal atomic systems like CaBOT and Ca-2, but also to cold atom experiments and a broad range of associated atomic molecular and optical physics experiments and applications involving narrow linewidth lasers.

Approved for public release; distribution is unlimited

1.4.3. Multi-pulse interactions: the standard description

1.4.3.1. Ramsey method and atom interferometry overview

A description of multiple atom-laser interactions is traditionally introduced with a standard approach following from the single-pulse description in Section 1.4.1.1. Rabi method and two level systems: the standard description. A two-pulse interaction was first established in seminal spectroscopy efforts by Norman Ramsey and colleagues in order to overcome the experimental limitations associated with the Rabi method, namely that the spectroscopy experiment precision relied on a long-duration characterized by a high degree of isotropy and homogeneity.

Ramsey proposed a method by which an atom or molecule interacts only briefly with two separated oscillatory fields with the same directionality as opposed to one large oscillatory field [Ramsey 1956]. If the intensity of radiation in the first of the oscillating field regions is tuned such that a $\pi/2$-pulse is delivered to an atom, then that atom's wavepacket is coherently split into equal probabilities of excited and ground state populations after the interaction. A second $\pi/2$-pulse following a dwell time T in a "dark" region, the atomic population is once again split and an interference pattern can be observed in the emission spectrum of the final excited state population. The final excitation probability at the end of the sequence is derived in several textbooks, e.g. [Ramsey 1956, pp.127-128], and may be expressed as:

$$P_{e,Ramsey}(\tau) = \frac{4\Omega^2}{{\Omega_g}^2}\sin^2\left(\frac{\Omega_g\tau}{2}\right)\left[\cos\left(\frac{\Omega_g\tau}{2}\right)\cos\left(\frac{\delta T}{2}\right) - \frac{\delta}{\Omega_g}\sin\left(\frac{\Omega_g\tau}{2}\right)\sin\left(\frac{\delta T}{2}\right)\right]^2 \quad (1.14)$$

Unlike the Rabi expression of equation (1.5), population inversion for the Ramsey method as described by equation (1.14) is maximized on resonance, i.e. for $\delta = 0$ when $\Omega_g\tau = \pi/2$, i.e. for two $\pi/2$-pulses as opposed to one π-pulse like the Rabi method. While the Rabi method's linewidth can be made narrower by reducing the driving oscillator power alone, the Ramsey method can be used to produce much narrower linewidths by increasing the free precession (dark) time T. When inhomogeneity is present in the driving

Approved for public release; distribution is unlimited

oscillator's radiation, it is therefore preferable to use the Ramsey method, since the Rabi method relies on averaging over an extended atom-oscillator interaction.

A key feature of the Ramsey method is that longer dark times T directly correspond to narrower resulting interference fringes. The power of the Ramsey method lies in the fact that in order to improve frequency resolution, it is not necessary to produce a perfectly homogenous driving radiation as in the Rabi method, elongating interaction times to enable extensive averaging. Instead, it is only necessary to lengthen the dark time between the two brief interactions that serve as the interferometer beamsplitter and combiner. Thus, the experimental effort does not require an extended, coherent driving oscillator, but only a sufficient vacuum to allow the participating atoms to remain in a coherent superposition state throughout the sequence.

A similar mechanism is used by an optical Mach-Zehnder interferometer: light is split between two pathways and the difference in the length of the pathway is revealed when observing the phase of the laser light when the two laser pathways are recombined. In the Mach-Zehnder optical interferometer, fringes are visible because the resulting optical phase at the end of each pathway is different. This may be caused by differing interferometer arm lengths or by some other phase-shifting effect that differs from one arm to the other.

In the Ramsey sequence as with any matter-wave interferometer, the same principles of interferometry apply. When passing through several interaction regions, an initially ground-state atomic wavepacket has a probability of resonant interaction and resulting excitation. If coherence is maintained, part of the atomic wavepacket may be excited at one pulse while another component is excited at the second pulse. Because the atomic phase precesses at a different rate when the atomic wavefunction is in the ground state as opposed to the excited state, an overlap of the two excited wavepackets results in an interference pattern in their internal atomic phase just as an overlap of two coherent laser beams traveling different distances reveal an interference in their relative phase when recombined in the Mach-Zehnder interferometer.

Approved for public release; distribution is unlimited

For matter-wave interferometry in the Ramsey sequence to occur, the displacement of the interfering wavepackets must be shorter than the coherence length L_{coh} of the atom. This coherence length is determined by the atom's momentum uncertainty Δp according to $L_{coh} = h/\Delta p$ [Sterr *et al.* 1992]. The largest displacement of the atomic wavepacket in this sequence is along the principal laser beam propagation axis $\hat{z}$, with a magnitude given by $\Delta z = T\hbar k_z / M$ where $\hbar k_z$ is the momentum component of the laser beam along the principal laser axis $\hat{z}$ and M is the mass of the atom. The implication is that while the Ramsey method may be readily applied to microwave transitions in thermal beams as originally implemented, optical transitions require vanishingly short separations T given their larger photon momentum transfers $\hbar k_z$. For instance, a thermal Ca beam with a temperature of $625\,^{\circ}\mathrm{C}$ has a momentum uncertainty of $\Delta p \approx m_{Ca}\left(700\ \mathrm{m/s}\right) = 4.7\times10^{-23}\ \mathrm{kg\cdot m/s}$ corresponding to a coherence length of $L_{coh} \approx 14\ \mathrm{pm}$. The coherence requirement $\Delta z < L_{coh}$ requires $T < 94\ \mathrm{ns}$, corresponding to a beam separation of $< 0.7\ \mu\mathrm{m}$. In order to see interference, either cold atoms need to be used, or atomic transitions featuring lower energy separations. By comparison, separations at the cm-scale and beyond are afforded for thermal beams involving microwave transitions as described in [Ramsey 1956].

1.4.3.2. Ramsey-Bordé atom interferometry

The challenge of performing matter-wave interferometry with optical transitions was addressed by the development of the Ramsey-Bordé method. An R-B atom interferometer is essentially composed of two Ramsey interferometers oriented such that the laser propagation vectors from one interferometer to the next are counter-propagating, resulting in a final wavepacket displacement along the laser beams of $\Delta z = 0$ regardless of how large the Ramsey separation T [Sterr *et al.* 1992]. Figure 1-6 depicts this configuration for a generalized Ca thermal beam architecture. The opposing geometry and parallelism of all four laser beam fields produces a Doppler-free spectroscopic signal to first order, since photon recoil effects of the first interferometer are counteracted by those of the second. In a physical apparatus, residual Doppler shifts

Approved for public release; distribution is unlimited

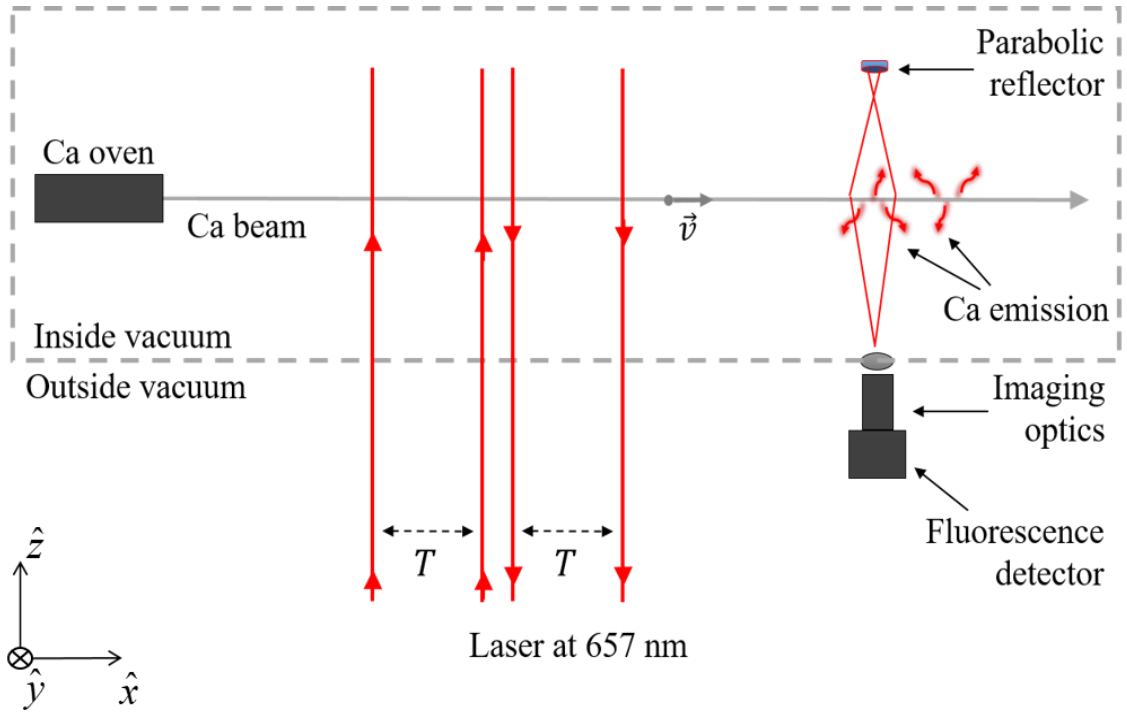

Figure 1-6. R-B configuration with a thermal Ca beam.

arising from imperfect geometry will arise, and second-order Doppler shifts corresponding to the atom's absolute speed are not avoidable.

[Bordé *et al.* 1984] or [Sterr *et al.* 1997] provide derivations for excitation probabilities in this configuration. In the latter reference, the interference term for both recoil components is expressed as:

$$P_{e,R-B} = A_1 \cos\left[2T\left(\delta + \frac{v_{atom}{}^2\omega_0}{2c^2} - \frac{\hbar k^2}{2m_{Ca}}\right) + \varphi_L\right] + A_2 \cos\left[2T\left(\delta + \frac{v_{atom}{}^2\omega_0}{2c^2} + \frac{\hbar k^2}{2m_{Ca}}\right) + \varphi_L\right] \quad (1.15)$$

where A_1 and A_2 are the recoil component amplitudes that depend on the Rabi frequency, v_{atom} is the magnitude of the atom velocity, and c is the speed of light. The phase difference between the laser beams is indicated by $\varphi_L = \varphi_2 - \varphi_1 + \varphi_4 - \varphi_3$, for laser phases φ.

Atom interferometers have broad applications beyond timekeeping along in atom-based inertial and environmental sensing, as well as fundamental science. The interested reader is encouraged to refer to [Cronin, Schmeidmayer, and Pritchard in 2009] for a review of the subject.

Approved for public release; distribution is unlimited

1.4.4. State of the art timekeeping

1.4.4.1. Current leaders in stable timekeeping

An overview of timekeeping stability leaders is depicted on an Allan deviation plot in Figure 1-7. Not shown in the figure are the smallest SWaP precision timekeeping devices including chip-based atomic clocks, oven controlled crystal oscillators, and rubidium cell atomic clocks. The reason these are not included is that these options generally do not offer instability performance capable of servicing GPS-denied operations or other ultra-stable timekeeping objectives. A proposed GPS-denied clock performance objective based on [DARPA 2014] is shown in blue with performance lying between currently fielded mid- to long-term timekeeping solutions and leading laboratory timekeeping options that operate predominantly at short time scales.

Fabry-Pérot cavities are leading solutions for stable local oscillators at short time scales as described, for instance, by [Barger 1973, Jiang 2011, Nicholson 2012, Kessler 2012, Cole 2013, Haefner

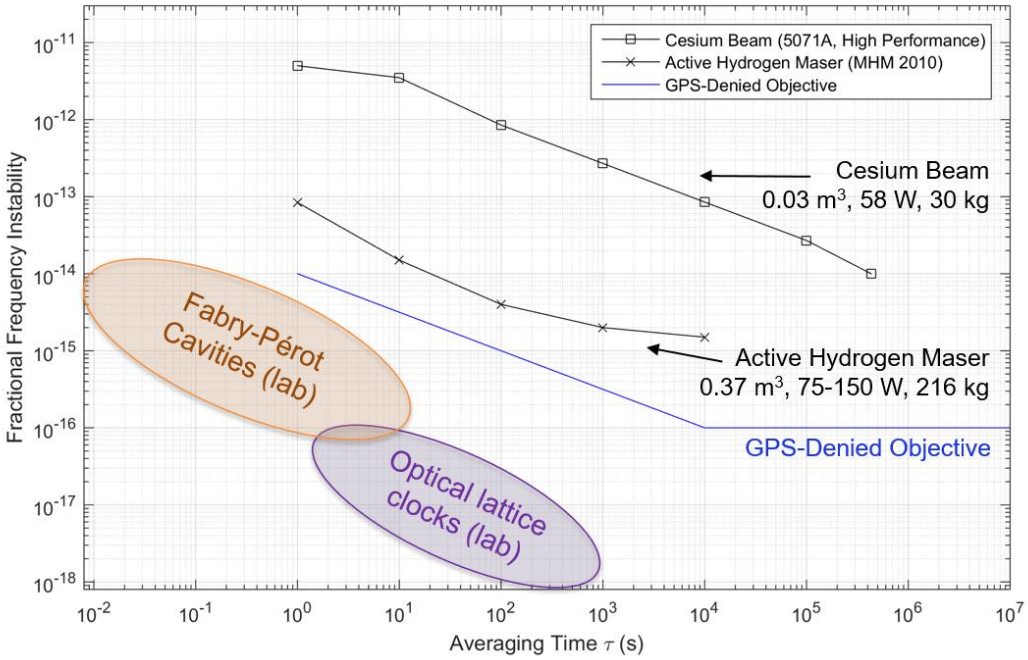

Figure 1-7. Fielded timekeeping and frequency reference instability comparison. Cesium beam and active hydrogen maser data from [Microsemi website, 5071A Cesium Clock Primary Frequency Standard and MHM 2010 Active Hydrogen Maser].

Approved for public release; distribution is unlimited

2015]. These cavities are used primarily for laser pre-stabilization, most notably for high-performance laboratory optical atomic clock lasers. The main limitation of these cavities is fluctuations to cavity length due to thermal effects; in order for these cavities to approach instabilities of 1×10^{-17} at one second, researchers are turning to cryogenic designs to reduce thermal fluctuations. However, cryogenics significantly increase the SWaP, cost, and complexity of these designs. Even with cryogenic temperatures, though, thermal fluctuations will always place a limit on the performance gains of future cavities, and so a search for alternatives becomes necessary for further short-term stability improvements.

An atom-based alternative is based on spectral hole burning techniques [Thorpe 2011, Cook 2015], though these methods are still costly and complex, and on-going approaches suffer from a small number of contributing atomic oscillators. A second path currently being explored is the Ca-2 thermal Ca Ramsey-Bordé atom interferometer at NIST, the collaborative effort to this thesis [Olson *et al.* 2017, Olson *et al.* 2019]. While the Draper CaBOT clock does not aim to compete with short-term stability leaders, efforts to identify long term frequency instability sources of the Ramsey-Bordé atom interferometer and to generate a compact and fieldable design for a clock based on this concept are directly transferable.

At mid to long averaging times, the leading fielded options are (for decades now) the compact and modest SWaP cesium beam clocks and the more complex and larger active hydrogen masers. These devices have representative Allan deviations of 1×10^{-11} at one second and 1×10^{-13} at one second, respectively, as depicted in Figure 1-7 for the "High Performance" version of the 5071A Cescium Clock Primary Frequency Standard and the MHM 2010 Active Hydrogen Maser, which are available commercially at Microsemi. While each device can reach instabilities in the 1×10^{-15} decade, long averaging times are needed to reach this low instability. Furthermore, both of these devices are mature technologies with little remaining scope for major improvements. SWaP values corresponding to these devices are noted next to their Allan deviations in Figure 1-7. An objective for the final CaBOT clock is to provide performance commensurate with or exceeding the active hydrogen maser with a SWaP nearer that of the Cs beam clock.

Approved for public release; distribution is unlimited

1.4.4.2. Efforts to field optical atomic clocks

There are currently no commercially available optical atomic clocks, though there have been several notable efforts to build and demonstrate transportable units. Before describing these examples further, it must be emphasized that these previous approaches involve SWaP, cost, and complexity far beyond the efforts described in this thesis. The comparison is equivalent to that between a multi-million-dollar facility re-creating the demonstrated laboratory performance of leading optical clocks for mainly scientific applications as compared with a more widely applicable and deployable system that trades some performance for drastic reductions in size, weight, power, cost, and complexity.

In broad terms, optical atomic clocks can be sorted into two categories: architectures involving cooling or trapping (for a thorough review of these clocks see [Ludlow *et al.* 2015]) and architectures that rely on thermal atoms. Figure 1-8, depicts the various optical atomic clocks and optical frequency references designed for transportability that have been demonstrated to-date in a Venn diagram constructed to provide context for this thesis research.

Koller *et al.* 2017 describes the demonstration of a transportable strontium (Sr) optical lattice clock installed inside an air-conditioned car trailer, which achieved a frequency uncertainty of 7.4×10^{-17} with a one-second instability of 1.3×10^{-15}. No routes for SWaP, cost, or complexity reduction are provided. Even so, the demonstrated capacity to perform optical atomic timekeeping measurements at two different locations with the same apparatus represents a critical and necessary step toward international frequency comparisons of leading optical atomic clocks. The European Space Agency has its own Sr optical lattice clock development as described in two arXiv preprints: Poli *et al.* 2014 and Bongs *et al.* 2015 for eventual deployment as a Space Optical Clock (SOC). With this effort as with Koller *et al.* 2017, the objective is a small enough SWaP for deployment in a physically mobile form factor, but at the high costs and complexities associated with a major scientific effort. As with Koller *et al.* 2017, ESA's SOC technology

Approved for public release; distribution is unlimited

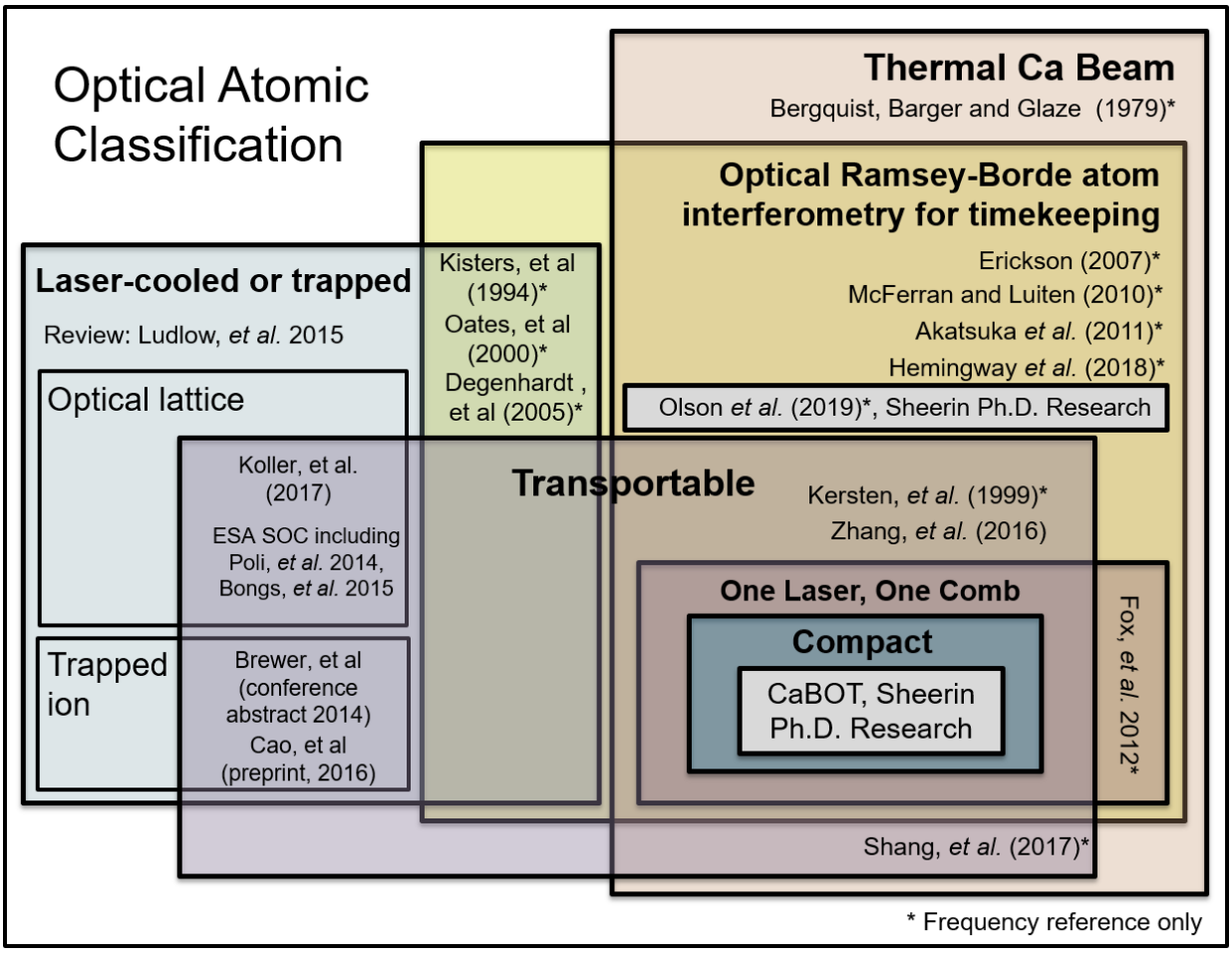

Figure 1-8. Optical atomic clock Venn diagram with selected references and research corresponding to this thesis "Sheerin Ph.D. Research" boxed in grey.

does not have broad applicability across industries and instead represents a multi-national, expensive effort to generate a new timekeeping standard for space science and possibly a future, optically-based GPS successor.

Transportable clock designs based on trapped ions are described by Brewer *et al.* 2014 (an IEEE conference talk, published as an abstract) and Cao *et al.* 2016 (arXiv preprint). The former reference appears to be an abandoned project to transfer aluminum quantum logic clock technology from the laboratory to the field. Neither performance nor SWaP figures are readily available for this approach. In general, efforts with aluminum quantum logic clocks largely fell off with the introduction of the optical lattice. For more information, the reader is referred to the review Ludlow *et al.* 2015.

Approved for public release; distribution is unlimited

By contrast, the latter ion reference (Cao *et al.* 2016), describes a demonstrated frequency reference based on singly-ionized Ca and seems to be promising in two regards: first, the entire frequency reference not including an optical frequency comb and associated electronics is designed to fit inside a box measuring 120 cm x 90 cm x 50 cm; second, the reference has a measured fractional frequency instability of 2.3×10^{-14} at one second with a measured fractional frequency uncertainty (inaccuracy) of 7.7×10^{-17}. The principal drawback of this approach is the high complexity and power necessary for operation: no fewer than five lasers are needed, as well as an RF source to drive the ion trapping mechanism. At the same time, the specified volume is some 6x larger than a usual rack-mountable electronics product, not to mention in a geometry prohibitive to installation on a standard rack. For these reasons, the Cao *et al.* 2016 clock may be best considered as a stand-alone facility that requires dedicated space and power much like an active hydrogen maser. No information is given about power consumption for this clock, which is a primary driver for the cost of operation should this design be fielded.

Considerably less complex than these cooled and trapped atom and ion examples are thermal architectures for optical atomic clocks. Among these, calcium Ramsey-Bordé atom interferometers are of particular interest given this thesis' focus on the same method. Precedents for Ca R-B interferometry are introduced in section 1.3.5. Precedents for thermal Ca R-B atom interferometry and shown in context with general architecture design choices in the Venn diagram of Figure 1-8. In addition to R-B approaches, another thermal Ca beam effort based on a fully sealed vacuum tube [Shang *et al.* 2017]. This effort does not utilize interferometry but instead relies on a two-laser saturation spectroscopy architecture and blue LIF for signal detection. A fractional frequency instability of 1.8×10^{-15} after 1600s of averaging is reported with a one second instability of 5.5×10^{-14} and a total volume, not including electronics, of $0.3\ \mathrm{m}^3$. With electronics volume projected to be $0.18\ \mathrm{m}^3$, the total clock volume would be $\sim 0.5\ \mathrm{m}^3$.

As a point of comparison, the CaBOT chassis of this thesis including all electronics measures $< 0.09\ \mathrm{m}^3$, with an external thermal control unit measuring $< 0.02\ \mathrm{m}^3$ involving only a single laser. The ultimate goal would be for the CaBOT clock to have similar size to a modern Cs beam clock, with

Approved for public release; distribution is unlimited

performance exceeding the most advanced hydrogen masers. In addition to designing and evaluating the frequency reference of CaBOT, this thesis research also includes the chassis design and thermal control architecture design and prototyping for CaBOT. Finally, this thesis research includes sensitivity studies and the design and operations of a temperature controlled thermal enclosure for the NIST Ca-2 thermal Ca R-B system with blue LIF [Olson *et al.* 2017, Olson *et al.* 2019].

1.5. Research contributions

1.5.1. Contributions as organized into thesis chapters

Novel contributions contained in this thesis pertaining to the optical atomic physics and timekeeping community include both theoretical results and experimental demonstrations. The introduction of ultra-narrow linewidth lasers in the last few decades motivates a reconsideration of the underlying theory concerning optical atomic interactions. Chapter 2 of this thesis introduces a theory that appears to be the first of its kind to describe the interaction of a Gaussian laser and a localized atomic wavepacket at the monochromatic limit of a narrow linewidth laser as well as the application of this new theory to the prediction of excitation probabilities for single atom-laser interactions. A comparison of this theory to a standard formulation of an atom-laser interaction model presented in [Bordé *et al.* 1984] illustrates a divergence in the theoretical predictions for optical saturation properties parameterized according to laser waist size and other experimental parameters.

Experimental objectives are described to supplement the limited experimental data currently available to further elucidate the merit and applicability of this new theory to optical atomic physics experiments and applications. As an immediate example of applicability, both the CaBOT and Ca-2 systems exhibited higher R-B fringe contrast with narrow laser beam waists that produced widely diverging beams at the atom-laser interaction regions despite the lower optical intensity present as compared with the case of a higher degree of laser collimation. It is hypothesized that the driving mechanism underlying this

Approved for public release; distribution is unlimited

observation may be described by the theory presented in this thesis when extended to a multi-beam interaction.

In addition to presenting a new theory for single atom-laser interactions and a specific application to thermal atomic beams, a path to application to cold atoms and multi-pulse matter-wave interferometry with thermal and cold atoms is presented, providing a new class of investigations that hold promise for improving experimental methods and optimization techniques for a broad range of applications involving ultra-narrow linewidth lasers.

Chapter 3 contains details relevant to contributions concerning the development of a first-of-its-kind optical atomic clock's frequency reference. The CaBOT thermal Ca R-B atom interferometer frequency reference was designed to meet and exceed currently fielded timekeeping options and to be one of the first optical atomic frequency references to transfer optical timekeeping technology from the laboratory to the field. The form factor is orders of magnitude smaller than any other transportable optical atomic clock currently in development and is designed to be operable in environmental temperatures ranging from $0-50^{0}\mathrm{C}$. Aside from frequency reference design activities, a noise characterization study is also included in Chapter 3 that identified the limiting sources of instability for the CaBOT system. Avenues for performance improvements are identified as well as the underlying mechanisms contributing to measured instability providing a roadmap for future CaBOT and thermal Ca R-B optical atomic clock development.

Chapter 4 describes contributions corresponding to chassis-related design considerations and sensitivity measurements for frequency reference signal instability obtained with the Ca-2 system. These sensitivity measurements were conducted to characterize the frequency reference response as a function of experimental parameters and environmental conditions including most notably the local temperature. Temperature control of a thermal enclosure for the NIST Ca-2 frequency reference was demonstrated and experimental instabilities $\leq 2\times10^{-16}$ were measured, representing an order of magnitude improvement over any previous thermal atomic architecture to date [Olson *et al.* 2019].

Approved for public release; distribution is unlimited

In addition to Ca-2 related research, Chapter 4 includes details corresponding to the designed, analysis, and experimental demonstration of a thermal-fluid control system for CaBOT. The engineering challenge was to remove a large heat load (~220 W) from a small volume (17" x 25" x 12.25" chassis) without the use of convective cooling in an environmental temperature $0-50^{0}\mathrm{C}$, and to otherwise isolate the frequency reference from environmental or other perturbations to ensure ultra-stable conditions to enable excellent short- and long-term instability performance of the CaBOT clock. This challenge was addressed with a full system design and a scaled prototype demonstration of system temperature maintenance with an instability at the mK level. Results from the engineering effort described show promise for the relatively inexpensive and simple approach to robust thermal control for the Draper CaBOT clock that may be applied to future fielded, compact optical atomic clocks that require exceptional temperature stability and environmental isolation.

1.5.2. Summary

CaBOT related research contained in this thesis resulted in a demonstrated optical atomic clock frequency reference and a thermal control architecture for a new atomic clock to outperform other options in the marketplace. The 7U (12.25" tall x 17" wide x 25" deep) chassis form factor makes CaBOT widely applicable, and the low power consumption corresponding to the simple design would make the costs of operation appreciably lower than any other transportable optical timekeeper concept to date. Ca-2 related research contained in this thesis contributed to a series of experimental instability measurements exceeding any other thermal atomic experimental result to date by an order of magnitude.

Theoretical investigations conducted for atom-beam interactions produced a new theory with broad potential application across the optical atomic physics and timekeeping community to improve methodology by providing researchers with a new tool to assess the impact of experimental parameters on the coupling strength that may be predicted for a given setup.

Approved for public release; distribution is unlimited

In summary, the clock of this thesis is a first-of-its-kind effort to produce a transportable, compact, optical atomic clock designed for extended autonomous operations with unprecedented instability. The simplified architecture of just one laser with a thermal atomic beam for Ramsey-Bordé atom interferometry marks a departure from all other transportable optical clock technologies, ushering in the possibility for accessible optical timekeeping technology across a broad range of science, industry, civil, and defense applications.

Approved for public release; distribution is unlimited

Chapter 2

Modeling atom beam interactions with a restricted Rabi rate theory

2.1. Motivation and theory overview

2.1.1. Momentum conservation with narrow linewidth lasers

Existing theoretical treatments for the interaction of atomic wavepackets and lasers including [Bordé *et al.* 1984, Sterr *et al.* 1992, and Sterr *et al.* 1994] account for energy and conservation but in doing so implicitly assume that all atomic velocity classes may interact with the laser beam. For an absorption event in which an atom in the ground state $|\mathrm{g}\rangle$ with momentum $\vec{p}$ absorbs a photon with momentum $\hbar\vec{k}$ and is raised to the excited state $|\mathrm{e}\rangle$, energy and momentum conservation is given by [Sterr *et al.* 1992]:

$$\frac{\vec{p}^{\,2}}{2m_{Ca}} + \hbar\omega_L = \frac{\left(\vec{p} + \hbar\vec{k}\right)^2}{2m_{Ca}} + \hbar\omega_0 \tag{2.1}$$

where ω_L is the laser photon angular frequency, ω_0 is the atomic transition frequency, and m_{Ca} is the mass of the atom. The subscript Ca is included to indicate the application of this conservation equation to calcium, though equation (2.1) applies to any atomic or molecular two level system. The wavevector $\vec{k}$ has a magnitude $\left|\vec{k}\right| = \omega_L / c$ where c is the speed of light, and a direction corresponding to the propagation direction and dispersion of the laser beam. Equation (2.1) can be simplified to:

$$\frac{\vec{k}\cdot\vec{p}}{m_{Ca}} = \delta - \frac{\hbar\vec{k}^{\,2}}{2m_{Ca}} \tag{2.2}$$

Approved for public release; distribution is unlimited

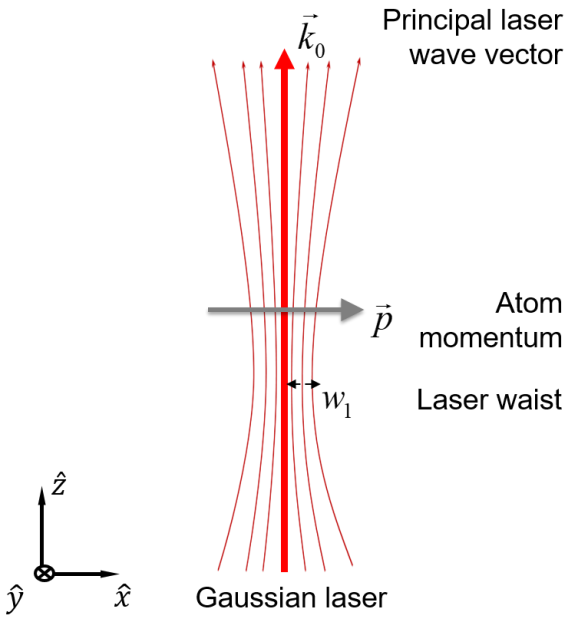

Figure 2-1. Interaction geometry for theoretical treatment of an atom beam and laser beam interaction.

where $\delta = \omega_L - \omega_0$ is the laser detuning and $\hbar\vec{k}^2/(2m_{Ca})$ is the single photon recoil frequency in angular units. This momentum condition stipulates that for detuning values $\delta \neq \hbar\vec{k}^2/(2m_{Ca})$, a laser wave vector component parallel to the atom momentum vector must be transferred to the atom with a magnitude equal to the first order Doppler shift given by $(\vec{k}\cdot\vec{p}_0)/m_{Ca}$. Equations (2.1)-(2.2) also apply to a stimulated emission event in which an atom in the excited state $|e\rangle$ with an initial momentum $\vec{p}+\hbar\vec{k}$ emits a photon with momentum $\hbar\vec{k}$ resulting in a final atomic momentum $\vec{p}$. In this case, the stimulated emission event can be illustrated by reading equation (2.1) from right to left.

For an atom-laser interaction geometry in which the atom propagates along the $\hat{x}$ axis, and the principal laser propagation axis lies in the $\hat{z}$ axis as depicted in Figure 2-1, the momentum conservation condition expressed by equation (2.2) stipulates that a photon momentum component $\hbar k_x$ is transferred to the atom in the case of absorption, or stimulated back into the radiation field in the case of stimulated emission. For absorption, this means that the resonant transfer would never occur for a perfectly collimated

Approved for public release; distribution is unlimited

laser when $\delta \neq \hbar\vec{k}^2/(2m_{Ca})$ since perfect collimation along $\hat{z}$ implies no dispersion of laser momenta components in $\hat{x}$. In practice, no laser is perfectly collimated. For Gaussian laser beam profiles, the angle of dispersion of laser momentum components is determined by the laser beam waist.

While Gaussian lasers have momentum component dispersion strictly determined by the beam waist size, a broad range of transverse momentum components $\hbar k_x$ may be accessed with a laser with a wide laser linewidth $\Delta\omega_L$ given the variability of wave vector magnitudes associated with this frequency width given by the dispersion relation $\Delta|\vec{k}| = \Delta\omega_L/c$. For a narrow linewidth laser with a nearly monochromatic frequency composition, it is not guaranteed that there exists a photon momentum component $\hbar k_x$ that satisfies the momentum condition expressed in equation (2.2) for a given atom momentum to produce a spectroscopic feature of interest.

Laser technology has rapidly advanced in recent decades, and ultra-narrow linewidths at optical frequencies are now common in atomic, molecular, optical physics laboratories and commercial applications around the world. There is great potential value in exploring the possible spectroscopic implications of ultra-narrow laser linewidths.

2.1.2. Theory overview

A theoretical framework is presented in this thesis that accounts for momentum conservation between a localized atomic wavepacket and a near-monochromatic Gaussian laser, deriving expected interaction strengths and transition probabilities as a function of experimental parameters. This theory may be extended not only to multi-pulse interactions for thermal atomic systems like CaBOT and Ca-2, but also to cold atom experiments and a broad range of associated atomic molecular and optical physics experiments and applications involving narrow linewidth lasers.

A standard approach is used in which an interaction Hamiltonian corresponding to an electric dipole transition is employed in a Schrödinger picture describing the time evolution of ground and excited state

Approved for public release; distribution is unlimited

atomic wavepackets. The method departs from extant theory in that the interaction Hamiltonian involves a Gaussian laser field composed of a superposition of wave vectors that are constrained to interaction with the atom assuming monochromaticity and strict momentum and energy conservation. Resulting equations of motion derived with the Schrödinger picture are solved with perturbation theory resulting in the derivation of momentum dependent Rabi rates as well as expressions for ground and excited state amplitudes that can be directly integrated over momentum space to derive transition probabilities. Derived Rabi rates and associated atomic state distributions are dependent on atom momenta and the atom-laser geometry, and feature the wave vector restriction corresponding to the assumption of a monochromatic laser beam. With appropriate initial and boundary conditions, a comparison can be made between the restricted Rabi rate theory, extant theory, and available experimental data to compare predictions and observables for single-pulse interactions under various experimental conditions.

2.2. Equations of motion for an atomic wavepacket illuminated by a Gaussian, narrow linewidth laser

2.2.1. Gaussian laser mode description

Consider a scalar field description of a Gaussian laser beam in terms of a superposition of plane waves. The electric field amplitude $E = \left|\vec{E}_L\right|$ of a Gaussian laser beam with a circular cross section characterized by a $1/e^2$ waist radius w_0 can be described in CGS units as:

$$E = E_o \frac{{w_0}^2}{4\pi} \int_{\vec{k}\cdot\hat{\vec{k}}_o \geq 0} d^3\vec{k} \cdot \delta\left(\left|\vec{k}\right| - k_o\right) \frac{\left(\vec{k}\cdot\hat{k}_o\right)}{k_o} \exp\left(-\frac{{w_0}^2}{4}\left|\vec{k}\times\hat{k}_0\right|^2\right) \exp\left(i\vec{k}\cdot\left(\hat{\vec{r}} - \vec{r}_w\right)\right) \qquad (2.3)$$

where the wave vector $\vec{k}$ spans a Gaussian spatial mode with a principal wave propagation vector $\vec{k}_o$ along the center of the beam. In equation (2.3), $\hat{\vec{r}}$ is the position operator, and $\vec{r}_w$ is the beam waist position. E_o is the electric field amplitude in units of statvolt/cm. An orthogonal basis can be defined in terms of $\vec{k}_o$ and

Approved for public release; distribution is unlimited

two vectors defining the beam's cross section geometry. For an elliptical beam shape, the semi-major axis can be defined as $\hat{e}_{w1}$ while the second component has a direction vector along $\hat{e}_{w2}$. For elliptical waists w_1 and w_2 decomposed along $\hat{e}_{w1}$ and $\hat{e}_{w2}$ respectively, equation (2.3) becomes:

$$E = E_o \frac{w_1 w_2}{4\pi} \int_{\vec{k}\cdot\vec{k}_o \geq 0} d^3\vec{k} \cdot \delta\left(\left|\vec{k}\right| - k_o\right) \frac{\left(\vec{k}\cdot\hat{k}_o\right)}{k_o} \exp\left(-\frac{1}{4}\left(w_1^{\,2}\left|\vec{k}\cdot\hat{e}_{w1}\right|^2 + w_2^{\,2}\left|\vec{k}\cdot\hat{e}_{w2}\right|^2\right)\right) \exp\left(i\vec{k}\cdot\left(\hat{\vec{r}} - \vec{r}_w\right)\right)$$

(2.4)

Equations (2.3) and (2.4) are used in the derivation of the interaction Hamiltonian to describe the equations of motion of atoms interacting with the Gaussian laser beam. These expressions for the electric field can be shown to match the description of a Gaussian beam provided by [Enderlein and Pamploni 2004] by replacing the position vector argument of equations (2.3)-(2.4) with the classical relative position vector $\left(\hat{\vec{r}} - \vec{r}_w\right) \rightarrow \vec{\rho}$. In addition, a Cartesian coordinate system is defined by the waist vector components and the central wave vector according to $k_x = \vec{k}\cdot\hat{e}_{w1}$, $k_y = \vec{k}\cdot\hat{e}_{w2}$ and $k_z = \vec{k}\cdot\hat{k}_o$, such that the expression for the classical electric field can be simplified to:

$$E = E_o \frac{w_1 w_2}{4\pi} \int_{\substack{k_x^{\,2}+k_y^{\,2}\leq k_o^{\,2} \\ \vec{k}\cdot\vec{k}_o>0}} dk_x dk_y \exp\left(-\frac{1}{4}\left(w_1^{\,2}k_x^{\,2} + w_2^{\,2}k_y^{\,2}\right)\right) \exp\left(\begin{matrix} ik_x\rho_x + ik_y\rho_y \\ +i\sqrt{k_o^{\,2} - k_x^{\,2} - k_y^{\,2}}\,\rho_z \end{matrix}\right) \qquad (2.5)$$

The restriction $k_x^{\,2} + k_y^{\,2} \leq k_o^{\,2}$ follows as a requirement that the wave vector remain real-valued, while the restriction $\vec{k}\cdot\vec{k}_o > 0$ establishes the direction of laser beam propagation. Equation (2.5) matches the form for a Gaussian laser profile as presented in [Enderlein and Pamploni 2004] and can be directly integrated to derive an expression for the electric field amplitude as well as the total optical laser power P_o.

At the peak intensity along the central axis of the laser where $\rho_x = \rho_y = 0$, the integral expression in equation (2.5) evaluates to $4\pi/\left(w_1 w_2\right)$. The total magnitude of the electric field at peak intensity is

Approved for public release; distribution is unlimited

therefore given by $E = E_o$. An expression for the optical power P_o of the beam is derived by integrating over wavevector components of (2.5) at $\rho_z = 0$:

$$P_o = \frac{c}{8\pi}\int |E|^2 \Big|_{\rho_z=0} dxdy = cE_o{}^2 \frac{w_1 w_2}{16} \tag{2.6}$$

Using equation (2.6), the electric field amplitude in equations (2.3)-(2.4) may be written in terms of the total optical laser power according to $E_o = \sqrt{16P_o/cw_1w_2}$. Next, these expressions for electric field amplitude are used to derive an interaction Hamiltonian and ultimately equations of motion for the ground and excited atomic wavepackets participating in atom-laser interactions.

2.2.2. Atom Hamiltonian in the laboratory frame

In the laboratory frame, the atomic state Hamiltonian for a two-level system driven by electromagnetic radiation is given by:

$$\hat{H}_{lab} = \frac{\hat{\vec{p}}^2}{2m_{Ca}} + \hat{H}_o + \hat{H}_1 \tag{2.7}$$

where the atom's kinetic energy contribution is given by the operator $\hat{\vec{p}}^2/(2m_{Ca})$ and where the atomic internal energy operator is given in bra-ket notation by $\hat{H}_o = \hbar\left(\omega_g |\mathrm{g}\rangle\langle \mathrm{g}| + \omega_e |e\rangle\langle e|\right)$ where the ground state is represented by $|\mathrm{g}\rangle$ and the excited state by $|e\rangle$, with their characteristic frequencies separated by the transition frequency $\omega_0 = \omega_e - \omega_g$. In a thermal atom system like CaBOT, the effect of gravity is negligible, and thus no gravity term is included in the Hamiltonian. For simplicity, we also do not attempt to account for photon spontaneous emission. The final term of the lab-frame Hamiltonian is the interaction Hamiltonian corresponding to an electric dipole transition: $\hat{H}_1 = e\hat{\vec{r}}_{e-n} \cdot E\hat{e}_L$. In this expression, $\hat{\vec{r}}$ is the position operator, $\hat{\vec{r}}_{e-n}$ is the relative electron-nucleus position operator, and $\hat{e}_L$ is the polarization vector of the laser electric field. The electric field amplitude is given by E, and e is the electron charge.

Approved for public release; distribution is unlimited

The interaction Hamiltonian H_1 for the case of the Gaussian laser beam described by equation (2.4) for an elliptical beam is written as:

$$\begin{aligned}\hat{H}_1 &= e\hat{\vec{r}}_{e-n}\cdot E\hat{e}_L \\ &= -\frac{eE_o}{2}\frac{w_1 w_2}{4\pi}\int\limits_{\substack{|\vec{k}|^2=k_o{}^2 \\ \vec{k}\cdot\vec{k}_o>0}} d^3\vec{k}\left[\begin{array}{l}\delta\left(|\vec{k}|-k_o\right)\dfrac{\left(\vec{k}\cdot\hat{k}_o\right)}{k_o}\exp\left(-\dfrac{1}{4}\left(w_1{}^2\left|\vec{k}\cdot\hat{e}_{w1}\right|^2+w_2{}^2\left|\vec{k}\cdot\hat{e}_{w2}\right|^2\right)\right) \\ \exp\left(i\vec{k}\cdot\left(\hat{\vec{r}}-\vec{r}_w\right)-ik_o ct\right)\end{array}\right]\hat{e}_L\cdot\hat{\vec{r}}_{e-n}+h.c.\end{aligned}$$

(2.8)

where *h.c.* represents the Hermitian conjugate term. For the case of an interaction of an atom with a monochromatic laser, conservation of energy and momentum must be preserved, and so equation (2.2) will be applied as a new constraint, restricting the action of the component field's modes to the atom's momenta. To do so, it is necessary to express the Hamiltonian as a superposition of momentum state functionals $\langle\vec{p}|$.

The lab-frame Hamiltonian given by equation (2.8) can be expressed in terms of the matrix coupling element $\langle e|\hat{e}_L\cdot\hat{\vec{r}}_{e-n}|\mathrm{g}\rangle$ and the coupled pair of states $\left\{|\mathrm{g}\rangle|\vec{p}\rangle,|\mathrm{e}\rangle\left|\vec{p}+\hbar\vec{k}\right\rangle\right\}$ by applying a product of internal and center-of-mass motion momentum space identity operators given by $\mathbf{1}_{\mathrm{int}}\equiv\left(|\mathrm{g}\rangle\langle\mathrm{g}|+|e\rangle\langle e|\right)$ and $\mathbf{1}_{c-m}\equiv\left(\int d^3\vec{p}\,|\vec{p}\rangle\langle\vec{p}|\right)$ respectively. Finally, with an application of the position operator $\hat{\vec{r}}$, physically allowed terms of the Hamiltonian may be written[1] as:

[1] See Appendix A.1. The atom-laser interaction Hamiltonian.

Approved for public release; distribution is unlimited

$$H_1 = \mathbf{1}_{c-m}\mathbf{1}_{\text{int}} \cdot H_1 \cdot \mathbf{1}_{\text{int}}$$

$$H_1 = \hbar \begin{pmatrix} -\frac{eE_o}{2\hbar}\langle e|\hat{e}_L \cdot \hat{\vec{r}}_{e-n}|\mathrm{g}\rangle \frac{w_1 w_2}{4\pi}\int d^3\vec{p} \int\limits_{\substack{|\vec{k}|^2=k_o^2;\ \vec{k}\cdot\vec{k}_o>0 \\ \frac{\vec{k}\cdot\vec{p}}{m_{Ca}}=\left(\delta-\frac{\hbar k_o^2}{2m_{Ca}}\right)}} d^3\vec{k} \left[\begin{array}{l} \delta\left(|\vec{k}|-k_o\right)\frac{\left(\vec{k}\cdot\hat{k}_o\right)}{k_o}\exp\left(-\frac{1}{4}\left(\begin{array}{l} w_1^{\,2}\left|\vec{k}\cdot\hat{e}_{w1}\right|^2 \\ +w_2^{\,2}\left|\vec{k}\cdot\hat{e}_{w2}\right|^2 \end{array}\right)\right) \\ \exp\left(-\left(i\vec{k}\cdot\vec{r}_w + ik_o ct\right)\right) \end{array} \right] |e\rangle\left|\vec{p}+\hbar\vec{k}\right\rangle\langle \mathrm{g}|\langle\vec{p}| \\ -\frac{eE_o}{2\hbar}\langle \mathrm{g}|\hat{e}_L \cdot \hat{\vec{r}}_{e-n}|e\rangle \frac{w_1 w_2}{4\pi}\int d^3\vec{p} \int\limits_{\substack{|\vec{k}|^2=k_o^2;\ \vec{k}\cdot\vec{k}_o>0 \\ \frac{\vec{k}\cdot\vec{p}}{m_{Ca}}=\left(\delta-\frac{\hbar k_o^2}{2m_{Ca}}\right)}} d^3\vec{k} \left[\begin{array}{l} \delta\left(|\vec{k}|-k_o\right)\frac{\left(\vec{k}\cdot\hat{k}_o\right)}{k_o}\exp\left(-\frac{1}{4}\left(\begin{array}{l} w_1^{\,2}\left|\vec{k}\cdot\hat{e}_{w1}\right|^2 \\ +w_2^{\,2}\left|\vec{k}\cdot\hat{e}_{w2}\right|^2 \end{array}\right)\right) \\ \exp\left(i\vec{k}\cdot\vec{r}_w + ik_o ct\right) \end{array} \right] |\mathrm{g}\rangle|\vec{p}\rangle\langle e|\left\langle\vec{p}+\hbar\vec{k}\right| \end{pmatrix}$$

(2.9)

The first term in equation (2.9) corresponds to a photon absorption event $|\mathrm{g}\rangle|\vec{p}\rangle \rightarrow |\mathrm{e}\rangle\left|\vec{p}+\hbar\vec{k}\right\rangle$, while the second term corresponds to a stimulated emission event $|\mathrm{e}\rangle\left|\vec{p}+\hbar\vec{k}\right\rangle \rightarrow |\mathrm{g}\rangle|\vec{p}\rangle$.

2.2.3. Atomic wavefunctions and the Schrödinger equation

The atom state Hamiltonian given by equation (2.7) is used to develop equations of motion for an atomic wavepacket $|\Psi(t)\rangle$ composed of a superposition of ground and excited state wave functions given by $|\Psi_g(t)\rangle$ and $|\Psi_e(t)\rangle$ respectively. The states may be expressed as expansions in momentum states $|\vec{p}\rangle$ in anticipation of applying the electromagnetic Hamiltonian (2.9). The following form is proposed for the atom state superposition coupled by the electromagnetic field:

$$\begin{aligned} |\Psi(t)\rangle &= |\Psi_g(t)\rangle + |\Psi_e(t)\rangle \\ |\Psi_g(t)\rangle &= |g\rangle\int d^3\vec{p}\cdot f_g(\vec{p},t)\exp\left(-i\omega_g t - i\frac{\vec{p}^{\,2}}{2m_{Ca}\hbar}t\right)|\vec{p}\rangle \\ |\Psi_e(t)\rangle &= |e\rangle\int d^3\vec{p}\, f_e(\vec{p},t)\exp\left(-i\omega_e t - i\frac{\vec{p}^{\,2}}{2m_{Ca}\hbar}t\right)|\vec{p}\rangle \end{aligned} \qquad (2.10)$$

Approved for public release; distribution is unlimited

In equation (2.10), the distribution functions $f_e\left(\vec{p},t\right)$ and $f_g\left(\vec{p},t\right)$ are yet to be determined, and the terms $\exp\left(-i\omega_e t - i\frac{\vec{p}^2}{2m_{Ca}\hbar}t\right)$ and $\exp\left(-i\omega_g t - i\frac{\vec{p}^2}{2m_{Ca}\hbar}t\right)$ are phase terms corresponding to freely propagating particles. The solution must be normalizable, i.e. $\left\langle\Psi\left(t\right)\middle|\Psi\left(t\right)\right\rangle = 1$. Applying this condition to equation (2.10) results in the probability conservation condition:

$$\int d^3\vec{p}'\left|f_g\left(\vec{p}',t\right)\right|^2 + \int d^3\vec{p}'\left|f_e\left(\vec{p}',t\right)\right|^2 = 1 \tag{2.11}$$

Equation (2.11) represents the sum of excited and ground state atom probabilities. Thus, we interpret the terms of the sum as

$$\begin{aligned} P_g\left(t\right) &= \int d^3\vec{p}'\left|f_g\left(\vec{p}',t\right)\right|^2 \\ P_e\left(t\right) &= \int d^3\vec{p}'\left|f_e\left(\vec{p}',t\right)\right|^2 \\ P_g\left(t\right) + P_e\left(t\right) &= 1 \end{aligned} \tag{2.12}$$

where both $P_g\left(t\right)$ and $P_e\left(t\right)$ are physical observables corresponding to whether the atom is in the ground or excited state internal state. Finally, the time-dependent Schrödinger equation for this atomic system may be expressed in terms of the wavefunction $\left|\Psi\left(t\right)\right\rangle$ and the laboratory-frame atomic Hamiltonian H_{lab} as:

$$i\hbar\frac{d}{dt}\left|\Psi\left(t\right)\right\rangle = H_{lab}\left|\Psi\left(t\right)\right\rangle \tag{2.13}$$

It can be shown[2] that when projecting ground and excited states into momentum space, the Schrödinger equation (2.13) reduces to a set of coupled equations given by:

[2] See Appendix A.2. Deriving equations of motion in the laboratory frame.

Approved for public release; distribution is unlimited

$$
\begin{aligned}
i\frac{d}{dt}f_e\left(\vec{p},t\right) &= -\frac{eE_o}{2\hbar}\left\langle e\left|\hat{e}_L\cdot\hat{\vec{r}}_{e-n}\right|\mathrm{g}\right\rangle\frac{w_1w_2}{4\pi}\int\limits_{\substack{\left|\vec{k}\right|^2=k_o{}^2;\ \vec{k}\cdot\vec{k}_o>0\\ \frac{\vec{k}\cdot\vec{p}}{m_{Ca}}=\left(\delta+\frac{\hbar\vec{k}_o{}^2}{2m_{Ca}}\right)}} d^3\vec{k}\,\delta\left(\left|\vec{k}\right|-k_o\right)\frac{\left(\vec{k}\cdot\hat{k}_o\right)}{k_o}\left[\begin{array}{l}\exp\left(-\frac{1}{4}\left(\begin{array}{l}w_1{}^2\left|\vec{k}\cdot\hat{e}_{w1}\right|^2\\ +w_2{}^2\left|\vec{k}\cdot\hat{e}_{w2}\right|^2\end{array}\right)\right)\\ \times\exp\left(-i\vec{k}\cdot\vec{r}_w\right)\end{array}\right]f_g\left(\left(\vec{p}-\hbar\vec{k}\right),t\right)\\
i\frac{d}{dt}f_g\left(\vec{p},t\right) &= -\frac{eE_o}{2\hbar}\left\langle \mathrm{g}\left|\hat{e}_L\cdot\hat{\vec{r}}_{e-n}\right|e\right\rangle\frac{w_1w_2}{4\pi}\int\limits_{\substack{\left|\vec{k}\right|^2=k_o{}^2;\ \vec{k}\cdot\vec{k}_o>0\\ \frac{\vec{k}\cdot\vec{p}}{m_{Ca}}=\left(\delta-\frac{\hbar\vec{k}_o{}^2}{2m_{Ca}}\right)}} d^3\vec{k}\,\delta\left(\left|\vec{k}\right|-k_o\right)\frac{\left(\vec{k}\cdot\hat{k}_o\right)}{k_o}\left[\begin{array}{l}\exp\left(-\frac{1}{4}\left(\begin{array}{l}w_1{}^2\left|\vec{k}\cdot\hat{e}_{w1}\right|^2\\ +w_2{}^2\left|\vec{k}\cdot\hat{e}_{w2}\right|^2\end{array}\right)\right)\\ \times\exp\left(i\vec{k}\cdot\vec{r}_w\right)\end{array}\right]f_e\left(\left(\vec{p}+\hbar\vec{k}\right),t\right)
\end{aligned}
$$

(2.14)

These equations of motion (EOMs) feature slightly different integral bounds and distribution function arguments. This is a consequence of the fact that the time dependence of an excited (ground) momentum state $\left|\vec{p}\right\rangle$ is driven by ground (excited) state $\left|\vec{p}\mp\hbar\vec{k}\right\rangle$ due to momentum imparted by the atom laser interaction. In other words, a single photon momentum couples the ground and excited state amplitudes. Stated in mathematical terms, in the case of the excited state distribution function time evolution, projection into the momentum state $\left|\vec{p}\right\rangle$ of the atomic state $\left|e\right\rangle\left|\vec{p}'+\hbar\vec{k}\right\rangle$ of equation (2.9) involves the dot product $\left\langle\vec{p}\left|\vec{p}'+\hbar\vec{k}\right.\right\rangle$. The resulting momentum projection shifts all momenta $\vec{p}'\rightarrow\vec{p}-\hbar\vec{k}$ in the first line of equation (2.14), affecting both the argument of the ground state distribution and the integral constraint. By using the relation $\left|\vec{k}\right|^2=k_o{}^2$, the shifted momentum condition is simplified as:

$$
\begin{aligned}
\frac{\vec{k}\cdot\left(\vec{p}-\hbar\vec{k}\right)}{m_{Ca}} &= \left(\delta-\frac{\hbar\vec{k}_o{}^2}{2m_{Ca}}\right)\\
\frac{\vec{k}\cdot\vec{p}}{m_{Ca}} &= \left(\delta+\frac{\hbar\vec{k}_o{}^2}{2m_{Ca}}\right)
\end{aligned}
\qquad (2.15)
$$

In the case of the ground state distribution time evolution, i.e. in the second line of equation (2.14), the dot product $\left\langle\vec{p}\left|\vec{p}'\right.\right\rangle$ selects momentum states $\vec{p}\,'=\vec{p}$, and so the momentum conservation constraint remains

Approved for public release; distribution is unlimited

as $\frac{\vec{k}\cdot\vec{p}}{m}=\left(\delta-\frac{\hbar\vec{k}_o^{\,2}}{2m}\right)$, and the argument of the excited state distribution function becomes $f_e\left(\vec{p}+\hbar\vec{k},t\right)$.

2.2.4. Comment on reference frames and equations of motion

While this treatment considers a derivation of the atom state Hamiltonian in the laboratory frame, an equivalent derivation could be performed in the atom rest frame. In this case, the frame co-moving with the atom must account for the time-dependent position of the atom and corresponding Doppler shifts resulting in the description of the Gaussian laser field. Resulting equations of motion would involve a transformation of distribution function arguments and momentum conditions for the wave vector integrals.

2.3. Initial conditions in momentum and position space

2.3.1. Comments on momentum distributions and initial conditions

For atom-laser interactions involving a thermal atomic beam, the momentum distribution boundary conditions are determined by the oven temperature, nozzle properties, and atom beam collimation as determined by apparatus geometry. No attempt is made here to carefully investigate initial atom states or to model a thermal atom source. However, simple examples of two classes of atom state descriptions are considered. One description of the atomic distribution function involves treating each atom as a wavepacket exhibiting the momentum spread of the entire atomic beam. A second approach models a statistical mixture of atomic wavepackets that together exhibit the momentum distribution of a thermal atomic beam.

In either case, boundary and initial conditions corresponding to ground and excited state distributions at $t=0$ must be provided to solve the coupled, first order differential equations of motion given by equation (2.14). The simplest selection is to consider the atomic distribution to begin in the ground

Approved for public release; distribution is unlimited

state, i.e. $\int d^3\vec{p}' \left| f_g\left(\vec{p}', t=0\right)\right|^2 = 1$, or equivalently, $P_g\left(t=0\right)=1$, though a superposition of ground and excited states could just as well be considered as long as probability is conserved as described in equations (2.11)-(2.12).

2.3.2. Accounting for a free particle initial position

It is desirable to obtain expressions for the coupled equations (2.14) that explicitly incorporate dependence on the initial atom state. The reason is that both boundary and initial conditions are required to solve the coupled first order time derivatives. An approach to assign a position dependent initial condition involves the introduction of free motion of the atomic wavepacket without any laser field interaction. The ground state wavefunction is considered first. Once a description of the initial state is derived, the equations of motion can be integrated to determine a transition probability after interaction with a laser field.

The spatial wave function for a free particle beginning in the ground state is derived by projecting equation (2.10) into position space with $\left\langle \vec{r}\right|$:

$$\begin{aligned}
\left\langle \vec{r}\left|\Psi_g\left(t\right)\right.\right\rangle &= \int d^3\vec{p}\cdot f_g\left(\vec{p},t\right)\exp\left(-i\omega_g t - i\frac{\vec{p}^2}{2m_{Ca}\hbar}t\right)\left\langle \vec{r}\left|\vec{p}\right.\right\rangle \\
\left\langle \vec{r}\left|\vec{p}\right.\right\rangle &= \left(\frac{1}{2\pi\hbar}\right)^{\frac{3}{2}}\exp\left(i\frac{\vec{p}\cdot\vec{r}}{\hbar}\right) \\
\left\langle \vec{r}\left|\Psi_g\left(t\right)\right.\right\rangle &= \left(\frac{1}{2\pi\hbar}\right)^{\frac{3}{2}}\int d^3\vec{p}\cdot f_g\left(\vec{p},t\right)\exp\left(-i\omega_g t - i\frac{\vec{p}^2}{2m_{Ca}\hbar}t\right)\exp\left(i\frac{\vec{p}\cdot\vec{r}}{\hbar}\right)
\end{aligned} \tag{2.16}$$

The initial momentum state corresponding to a free particle at position $\vec{r}_a$ at time $t=0$ is considered explicitly with a definition for the ground state distribution function:

$$f_g\left(\vec{p},t\right) \equiv f_g'\left(\vec{p},t\right)\exp\left(-i\frac{\vec{p}\cdot\vec{r}_a}{\hbar}\right) \tag{2.17}$$

Approved for public release; distribution is unlimited

When applying this definition to equation (2.16), it can be shown that stationary phase for the position space wavefunction's integration is near $\langle \vec{p}/m \rangle t - (\vec{r} - \vec{r}_a)$. Recalling that the position operator is represented in momentum space as $\hat{\vec{r}} = i\hbar \nabla_{\vec{p}}$, the expectation value of the position operator is given by:

$$\begin{aligned} \langle \vec{r} \rangle &= i\hbar \int d^3\vec{p} \cdot f_g(\vec{p},t)^* \left(\nabla_{\vec{p}} f_g(\vec{p},t) \right) \\ &= i\hbar \int d^3\vec{p} \cdot f_g{}'(\vec{p},t)^* \left(\nabla_{\vec{p}} \left(f_g{}'(\vec{p},t) \right) + f_g{}'(\vec{p},t) \left(-i \frac{\vec{r}_a}{\hbar} \right) \right) \\ &= \vec{r}_a + i\hbar \int d^3\vec{p} \cdot f_g{}'(\vec{p},t)^* \nabla_{\vec{p}} \left(f_g{}'(\vec{p},t) \right) \end{aligned} \tag{2.18}$$

The expression $i\hbar \int d^3\vec{p} \cdot f_g{}'(\vec{p},t)^* \nabla_{\vec{p}} \left(f_g{}'(\vec{p},t) \right)$ is real-valued for momentum distributions that vanish at infinity. The (*) symbol indicates the complex conjugate. If $f_g{}'(\vec{p},t)$ is real-valued, i.e. conjugate symmetric, then the integral must necessarily vanish, since in that case the integral must also be conjugate symmetric. Thus, if a momentum distribution of the form given by equation (2.17) is specified with a real-valued $f_g{}'(\vec{p},t)$, then the expectation value of particle position at $t = 0$ is $\vec{r}_a$.

By substituting equation (2.17) and an equivalent form for free particle motion of the excited state distribution function, i.e. $f_e(\vec{p},t) \equiv f_e{}'(\vec{p},t) \exp\left(-i \frac{\vec{p} \cdot \vec{r}_a}{\hbar} \right)$ the equations of motion given by equation (2.14) become:

Approved for public release; distribution is unlimited

$$i\frac{d}{dt}f_e\left(\vec{p},t\right)=-\frac{eE_o}{2\hbar}\left\langle e\left|\hat{e}_L\cdot\hat{\vec{r}}_{e-n}\right|\mathrm{g}\right\rangle\frac{w_1w_2}{4\pi}\int\limits_{\substack{|\vec{k}|^2=k_o^{\,2};\ \vec{k}\cdot\vec{k}_o>0\\ \frac{\vec{k}\cdot\vec{p}}{m_{Ca}}=\left(\delta+\frac{\hbar k_o^{\,2}}{2m_{Ca}}\right)}}d^3\vec{k}\,\delta\left(\left|\vec{k}\right|-k_o\right)\frac{\left(\vec{k}\cdot\hat{k}_o\right)}{k_o}\left[\begin{array}{l}\exp\left(-\frac{1}{4}\left(\begin{array}{l}w_1^{\,2}\left|\vec{k}\cdot\hat{e}_{w1}\right|^2\\ +w_2^{\,2}\left|\vec{k}\cdot\hat{e}_{w2}\right|^2\end{array}\right)\right)\\ \times\exp\left(i\vec{k}\cdot\left(\vec{r}_a-\vec{r}_w\right)\right)\end{array}\right]f_g\left(\left(\vec{p}-\hbar\vec{k}\right),t\right)$$

$$i\frac{d}{dt}f_g\left(\vec{p},t\right)=-\frac{eE_o}{2\hbar}\left\langle \mathrm{g}\left|\hat{e}_L\cdot\hat{\vec{r}}_{e-n}\right|e\right\rangle\frac{w_1w_2}{4\pi}\int\limits_{\substack{|\vec{k}|^2=k_o^{\,2};\ \vec{k}\cdot\vec{k}_o>0\\ \frac{\vec{k}\cdot\vec{p}}{m_{Ca}}=\left(\delta-\frac{\hbar k_o^{\,2}}{2m_{Ca}}\right)}}d^3\vec{k}\,\delta\left(\left|\vec{k}\right|-k_o\right)\frac{\left(\vec{k}\cdot\hat{k}_o\right)}{k_o}\left[\begin{array}{l}\exp\left(-\frac{1}{4}\left(\begin{array}{l}w_1^{\,2}\left|\vec{k}\cdot\hat{e}_{w1}\right|^2\\ +w_2^{\,2}\left|\vec{k}\cdot\hat{e}_{w2}\right|^2\end{array}\right)\right)\\ \times\exp\left(-i\vec{k}\cdot\left(\vec{r}_a-\vec{r}_w\right)\right)\end{array}\right]f_e\left(\left(\vec{p}+\hbar\vec{k}\right),t\right)$$

(2.19)

The transformed equations of motion now carry information about the initial atom location with respect to the initial position of the beam waist as quantified by $\left(\vec{r}_a-\vec{r}_w\right)$. The coordinate frame origin can by convention set $\vec{r}_a=0$. In that case, $\vec{r}_w$ is the vector displacement between the atom initial position and the initial position of the laser beam waist. These coupled integral equations are not separable. In order to address this challenge, a perturbation theory is devised.

2.4. Perturbation expansion of EOMs and atomic state solutions

2.4.1. Perturbation theory derivation and restricted Rabi rate definitions

The coupled equations given by (2.19) do not have an analytic solution in terms of elementary functions, given the convolution of the momentum distributions on the right hand sides of (2.19). However, a perturbation theory approach may be devised that allows for a hierarchy of simple solutions describing the state evolution of the ground and excited states. With this objective, an expansion is performed for both the ground and excited distributions $f_g\left(\vec{p}-\hbar\vec{k}\right)$ and $f_e\left(\vec{p}+\hbar\vec{k}\right)$, respectively, about the points $f_g\left(\vec{p}-\hbar\vec{k}_0,t\right)$ and $f_e\left(\vec{p}+\hbar\vec{k}_0,t\right)$. The ground state expansion results in:

Approved for public release; distribution is unlimited

$$
\begin{aligned}
f_g\left(\vec{p}-\hbar\vec{k}\right) &= f_g\left(\vec{p}-\hbar\vec{k}_0-\hbar\left(\vec{k}-\vec{k}_0\right)\right) \\
&\cong\left[f_g\left(\vec{p}-\hbar\vec{k}_0\right)\right]+\left[\nabla_p f_g\left(\vec{p}-\hbar\vec{k}_0\right)\cdot\left(-\hbar\left(\vec{k}-\vec{k}_0\right)\right)\right] \\
&+\left[\frac{1}{2}\left(-\hbar\left(\vec{k}-\vec{k}_0\right)\right)^T\cdot \mathrm{H} f_g\left(\vec{p}-\hbar\vec{k}_0\right)\cdot\left(-\hbar\left(\vec{k}-\vec{k}_0\right)\right)\right]+O\left(\left\|-\hbar\left(\vec{k}-\vec{k}_0\right)\right\|^3\right)
\end{aligned}
\tag{2.20}
$$

while the excited state expansion results in:

$$
\begin{aligned}
f_e\left(\vec{p}+\hbar\vec{k}\right) &= f_e\left(\vec{p}+\hbar\vec{k}_0+\hbar\left(\vec{k}-\vec{k}_0\right)\right) \\
&\cong\left[f_e\left(\vec{p}+\hbar\vec{k}_0\right)\right]+\left[\nabla_p f_e\left(\vec{p}+\hbar\vec{k}_0\right)\cdot\left(\hbar\left(\vec{k}-\vec{k}_0\right)\right)\right] \\
&+\left[\frac{1}{2}\left(\hbar\left(\vec{k}-\vec{k}_0\right)\right)^T\cdot \mathrm{H} f_e\left(\vec{p}+\hbar\vec{k}_0\right)\cdot\left(\hbar\left(\vec{k}-\vec{k}_0\right)\right)\right]+O\left(\left\|\hbar\left(\vec{k}-\vec{k}_0\right)\right\|^3\right)
\end{aligned}
\tag{2.21}
$$

In equations (2.20)-(2.21), H is an operator corresponding to a Hessian matrix for a second order momentum space derivative, and higher order terms are captured by $O\left(\left\|\hbar\left(\vec{k}-\vec{k}_0\right)\right\|^3\right)$. Substituting (2.21) into the coupled equations (2.19) results in:

Approved for public release; distribution is unlimited

$$\frac{d}{dt} f_e(\vec{p},t) = \left[i\frac{eE_o}{2\hbar}\langle e|\hat{e}_L\cdot\hat{\vec{r}}_{e-n}|g\rangle\frac{w_1 w_2}{4\pi}\cdot \right. \\ \left. \int\limits_{\substack{|\vec{k}|^2=k_o{}^2;\ \vec{k}\cdot\vec{k}_o>0 \\ \frac{\vec{k}\cdot\vec{p}}{m_{Ca}}=\left(\delta+\frac{\hbar\vec{k}_o{}^2}{2m_{Ca}}\right)}} d^3\vec{k} \left[\begin{array}{l} \delta\left(|\vec{k}|-k_o\right)\frac{\left(\vec{k}\cdot\hat{k}_o\right)}{k_o}\exp\left(-\frac{1}{4}\left(\begin{array}{l} w_1{}^2\left|\vec{k}\cdot\hat{e}_{w1}\right|^2 \\ +w_2{}^2\left|\vec{k}\cdot\hat{e}_{w2}\right|^2 \end{array}\right)\right)\exp\left(i\vec{k}\cdot\left(\vec{r}_a-\vec{r}_w\right)\right) \\ \left(\begin{array}{l} f_g\left(\vec{p}-\hbar\vec{k}_0\right)+\varepsilon\nabla_p f_g\left(\vec{p}-\hbar\vec{k}_0\right)\cdot\left(-\hbar\left(\vec{k}-\vec{k}_0\right)\right) \\ +\varepsilon^2\frac{1}{2}\left(-\hbar\left(\vec{k}-\vec{k}_0\right)\right)^T\cdot \mathrm{H}f_g\left(\vec{p}-\hbar\vec{k}_0\right)\cdot\left(-\hbar\left(\vec{k}-\vec{k}_0\right)\right) \\ +\varepsilon^3 O\left(\left\|-\hbar\left(\vec{k}-\vec{k}_0\right)\right\|^3\right) \end{array} \right) \end{array} \right] \right]$$

$$\frac{d}{dt} f_g(\vec{p},t) = \left[i\frac{eE_o}{2\hbar}\langle e|\hat{e}_L\cdot\hat{\vec{r}}_{e-n}|g\rangle\frac{w_1 w_2}{4\pi}\cdot \right. \\ \left. \int\limits_{\substack{|\vec{k}|^2=k_o{}^2;\ \vec{k}\cdot\vec{k}_o>0 \\ \frac{\vec{k}\cdot\vec{p}}{m_{Ca}}=\left(\delta-\frac{\hbar\vec{k}_o{}^2}{2m_{Ca}}\right)}} d^3\vec{k} \left[\begin{array}{l} \delta\left(|\vec{k}|-k_o\right)\frac{\left(\vec{k}\cdot\hat{k}_o\right)}{k_o}\exp\left(-\frac{1}{4}\left(\begin{array}{l} w_1{}^2\left|\vec{k}\cdot\hat{e}_{w1}\right|^2 \\ +w_2{}^2\left|\vec{k}\cdot\hat{e}_{w2}\right|^2 \end{array}\right)\right)\exp\left(-i\vec{k}\cdot\left(\vec{r}_a-\vec{r}_w\right)\right) \\ \left(\begin{array}{l} f_e\left(\vec{p}+\hbar\vec{k}_0\right)+\varepsilon\nabla_p f_e\left(\vec{p}+\hbar\vec{k}_0\right)\cdot\left(\hbar\left(\vec{k}-\vec{k}_0\right)\right) \\ +\varepsilon^2\frac{1}{2}\left(\hbar\left(\vec{k}-\vec{k}_0\right)\right)^T\cdot \mathrm{H}f_e\left(\vec{p}+\hbar\vec{k}_0\right)\cdot\left(\hbar\left(\vec{k}-\vec{k}_0\right)\right) \\ +\varepsilon^3 O\left(\left\|\hbar\left(\vec{k}-\vec{k}_0\right)\right\|^3\right) \end{array} \right) \end{array} \right] \right]$$

(2.22)

where the smallness parameter ε is exhibited to reflect the size order of terms in the gradient expansion. The ground and excited state distribution functions are assumed to have forms expressible in terms of an expansion of terms of decreasing size:

$$\begin{aligned} f_e(\vec{p},t) &= f_{e,0}(\vec{p},t)+\varepsilon f_{e,1}(\vec{p},t)+\varepsilon^2 f_{e,2}(\vec{p},t)+\cdots \\ f_g(\vec{p},t) &= f_{g,0}(\vec{p},t)+\varepsilon f_{g,1}(\vec{p},t)+\varepsilon^2 f_{g,2}(\vec{p},t)+\cdots \end{aligned} \tag{2.23}$$

Considering the first of equations (2.22) corresponding to the time evolution of the excited state distribution function, a substitution involving equation (2.23) is used to equate equal powers of the smallness parameter

Approved for public release; distribution is unlimited

and derive a hierarchical perturbation expansion of inhomogeneous equations, where higher order equations contain inhomogeneities depending on lower order solutions. Toward solving the coupled equations, the substitution $\vec{p} \to \vec{p} + \hbar\vec{k}_0$ is also made, resulting in the following expressions for the first two leading orders of the excited state time evolution:

$$\frac{d}{dt} f_{e,0}\left(\vec{p}+\hbar\vec{k}_0,t\right) = \left\{ i\frac{eE_o}{2\hbar}\left\langle e\middle|\hat{e}_L\cdot\hat{\vec{r}}_{e-n}\middle|\mathrm{g}\right\rangle\frac{w_1 w_2}{4\pi}\cdot \int\limits_{\substack{|\vec{k}|^2=k_o{}^2;\ \vec{k}\cdot\vec{k}_o>0 \\ \frac{\vec{k}\cdot\left(\vec{p}+\hbar\vec{k}_0\right)}{m_{Ca}}=\left(\delta+\frac{\hbar\vec{k}_o{}^2}{2m_{Ca}}\right)}} d^3\vec{k}\left[\delta\left(|\vec{k}|-k_o\right)\frac{\left(\vec{k}\cdot\hat{k}_o\right)}{k_o}\exp\left(-\frac{1}{4}\left(\begin{array}{l} w_1{}^2\left|\vec{k}\cdot\hat{e}_{w1}\right|^2 \\ +w_2{}^2\left|\vec{k}\cdot\hat{e}_{w2}\right|^2 \end{array}\right)\right)\exp\left(i\vec{k}\cdot\left(\vec{r}_a-\vec{r}_w\right)\right) f_{g,0}\left(\vec{p},t\right)\right] \right\}$$

$$\frac{d}{dt} f_{e,1}\left(\vec{p}+\hbar\vec{k}_0,t\right) = \left\{ i\frac{eE_o}{2\hbar}\left\langle e\middle|\hat{e}_L\cdot\hat{\vec{r}}_{e-n}\middle|\mathrm{g}\right\rangle\frac{w_1 w_2}{4\pi}\cdot \int\limits_{\substack{|\vec{k}|^2=k_o{}^2;\ \vec{k}\cdot\vec{k}_o>0 \\ \frac{\vec{k}\cdot\left(\vec{p}+\hbar\vec{k}_0\right)}{m_{Ca}}=\left(\delta+\frac{\hbar\vec{k}_o{}^2}{2m_{Ca}}\right)}} d^3\vec{k}\left[\delta\left(|\vec{k}|-k_o\right)\frac{\left(\vec{k}\cdot\hat{k}_o\right)}{k_o}\exp\left(-\frac{1}{4}\left(\begin{array}{l} w_1{}^2\left|\vec{k}\cdot\hat{e}_{w1}\right|^2 \\ +w_2{}^2\left|\vec{k}\cdot\hat{e}_{w2}\right|^2 \end{array}\right)\right)\exp\left(i\vec{k}\cdot\left(\vec{r}_a-\vec{r}_w\right)\right) \left(\begin{array}{l} f_{g,1}\left(\vec{p},t\right) \\ +\nabla_p f_{g,0}\left(\vec{p},t\right)\cdot\left(-\hbar\left(\vec{k}-\vec{k}_0\right)\right)\end{array}\right)\right] \right\}$$

(2.24)

At this stage of the derivation, the following momentum dependent frequencies are defined:

Approved for public release; distribution is unlimited

$$\Omega_{R,0}\left(\vec{p}\right)\equiv\left[\begin{array}{l}\frac{eE_o}{\hbar}\left\langle e\left|\hat{e}_L\cdot\hat{\vec{r}}_{e-n}\right|g\right\rangle\frac{w_1w_2}{4\pi}\cdot\\ \int\limits_{\substack{|\vec{k}|^2=k_o{}^2;\ \vec{k}\cdot\vec{k}_o>0\\ \frac{\vec{k}\cdot\vec{p}}{m_{Ca}}=\left(\delta-\frac{\hbar\vec{k}_o{}^2}{2m_{Ca}}\right)}} d^3\vec{k}\,\delta\left(\left|\vec{k}\right|-k_o\right)\frac{\left(\vec{k}\cdot\hat{k}_o\right)}{k_o}\exp\left(-\frac{1}{4}\left(\begin{array}{l}w_1{}^2\left|\vec{k}\cdot\hat{e}_{w1}\right|^2\\ +w_2{}^2\left|\vec{k}\cdot\hat{e}_{w2}\right|^2\end{array}\right)\right)\exp\left(i\vec{k}\cdot\left(\vec{r}_a-\vec{r}_w\right)\right)\end{array}\right]$$

$$\vec{\Omega}_{R,1}\left(\vec{p}\right)\equiv\left[\begin{array}{l}\frac{eE_o}{\hbar}\left\langle e\left|\hat{e}_L\cdot\hat{\vec{r}}_{e-n}\right|g\right\rangle\frac{w_1w_2}{4\pi}\cdot\\ \int\limits_{\substack{|\vec{k}|^2=k_o{}^2;\ \vec{k}\cdot\vec{k}_o>0\\ \frac{\vec{k}\cdot\vec{p}}{m_{Ca}}=\left(\delta-\frac{\hbar\vec{k}_o{}^2}{2m_{Ca}}\right)}} d^3\vec{k}\,\delta\left(\left|\vec{k}\right|-k_o\right)\frac{\left(\vec{k}\cdot\hat{k}_o\right)}{k_o}\exp\left(-\frac{1}{4}\left(\begin{array}{l}w_1{}^2\left|\vec{k}\cdot\hat{e}_{w1}\right|^2\\ +w_2{}^2\left|\vec{k}\cdot\hat{e}_{w2}\right|^2\end{array}\right)\right)\exp\left(i\vec{k}\cdot\left(\vec{r}_a-\vec{r}_w\right)\right)\frac{\left(\vec{k}-\vec{k}_0\right)}{k_o}\end{array}\right]$$

(2.25)

where the integral constraint $\frac{\vec{k}\cdot\left(\vec{p}+\hbar\vec{k}_0\right)}{m_{Ca}}=\left(\delta+\frac{\hbar\vec{k}_o{}^2}{2m_{Ca}}\right)$ from equation (2.24) is simplified to $\frac{\vec{k}\cdot\vec{p}}{m_{Ca}}=\left(\delta-\frac{\hbar\vec{k}_o{}^2}{2m_{Ca}}\right)$ in equation (2.25) with use of the identity $\left|\vec{k}\right|^2=k_o{}^2$. Using these rate definitions, the two leading orders describing the time evolution of the excited state distribution function, i.e. equation (2.24) can be written as:

$$\begin{aligned}\frac{d}{dt}f_{e,0}\left(\vec{p}+\hbar\vec{k}_0,t\right)&\cong\frac{i}{2}f_{g,0}\left(\vec{p},t\right)\Omega_{R,0}\left(\vec{p}\right)\\ \frac{d}{dt}f_{e,1}\left(\vec{p}+\hbar\vec{k}_0,t\right)&\cong\frac{i}{2}\left[f_{g,1}\left(\vec{p},t\right)\Omega_{R,0}\left(\vec{p}\right)-\hbar k_o\nabla_p f_{g,0}\left(\vec{p},t\right)\cdot\vec{\Omega}_{R,1}\left(\vec{p}\right)\right]\end{aligned}\tag{2.26}$$

Applying the same method to the ground state distribution function time evolution from equation (2.22) results in:

$$\begin{aligned}\frac{d}{dt}f_{g,0}\left(\vec{p},t\right)&\cong\frac{i}{2}f_{e,0}\left(\vec{p}+\hbar\vec{k}_0,t\right)\Omega_{R,0}\left(\vec{p}\right)^*\\ \frac{d}{dt}f_{g,1}\left(\vec{p},t\right)&\cong\frac{i}{2}\left[f_{e,1}\left(\vec{p}+\hbar\vec{k}_0,t\right)\Omega_{R,0}\left(\vec{p}\right)^*+\hbar k_0\nabla_p\left(f_{e,0}\left(\vec{p}+\hbar\vec{k}_0,t\right)\right)\cdot\vec{\Omega}_{R,1}\left(\vec{p}\right)^*\right]\end{aligned}\tag{2.27}$$

Approved for public release; distribution is unlimited

In equation (2.27), (*) denotes complex conjugate. Taking another time derivative and combining equations (2.26)-(2.27) results in isolated expressions for the excited state time evolution for the leading and first order perturbation expansion:

$$\frac{d^2}{dt^2} f_{e,0}\left(\vec{p}+\hbar\vec{k}_0,t\right)+\frac{1}{4}\left|\Omega_{R,0}\left(\vec{p}\right)\right|^2 f_{e,0}\left(\vec{p}+\hbar\vec{k}_0,t\right)\cong 0$$

$$\frac{d^2}{dt^2} f_{e,1}\left(\vec{p}+\hbar\vec{k}_0,t\right)+\frac{1}{4}\left|\Omega_{R,0}\left(\vec{p}\right)\right|^2 f_{e,1}\left(\vec{p}+\hbar\vec{k}_0,t\right)\cong \frac{1}{4}\begin{bmatrix} 2i\hbar k_o\left(\nabla_p\left(f_{e,0}\left(\vec{p}+\hbar\vec{k}_0,t\right)\right)\right)\cdot \mathrm{Im}\left(\Omega_{R,0}\left(\vec{p}\right)^*\vec{\Omega}_{R,1}\left(\vec{p}\right)\right) \\ +\hbar k_o f_{e,0}\left(\vec{p}+\hbar\vec{k}_0,t\right)\vec{\Omega}_{R,1}\left(\vec{p}\right)\cdot\nabla_p\left(\Omega_{R,0}\left(\vec{p}\right)^*\right)\end{bmatrix} \tag{2.28}$$

Similarly, the ground state evolution can be expressed as:

$$\frac{d^2}{dt^2} f_{g,0}\left(\vec{p},t\right)+\frac{1}{4}\left|\Omega_{R,0}\left(\vec{p}\right)\right|^2 f_{g,0}\left(\vec{p},t\right)\cong 0$$

$$\frac{d^2}{dt^2} f_{g,1}\left(\vec{p},t\right)+\frac{1}{4}\left|\Omega_{R,0}\left(\vec{p}\right)\right|^2 f_{g,1}\left(\vec{p},t\right)\cong \frac{1}{4}\begin{bmatrix} 2i\hbar k_o\left(\nabla_p f_{g,0}\left(\vec{p},t\right)\right)\cdot \mathrm{Im}\left(\Omega_{R,0}\left(\vec{p}\right)^*\vec{\Omega}_{R,1}\left(\vec{p}\right)\right) \\ -\hbar k_0 f_{g,0}\left(\vec{p},t\right)\vec{\Omega}_{R,1}\left(\vec{p}\right)^*\cdot\left(\nabla_p\Omega_{R,0}\left(\vec{p}\right)\right)\end{bmatrix} \tag{2.29}$$

Equations for both the excited and ground state distributions have the same overall form. The leading order perturbation expansions describe temporal harmonic oscillation and the first-order perturbative solutions correspond to driven harmonic oscillation where one of the drive terms is purely imaginary. To solve these equations, boundary and initial conditions must be assigned. The initial value of the distribution is assumed to be captured by the zeroth order solution, corresponding to the case that the first order solution is everywhere zero at the initial time. The general zeroth order solution is given by a superposition of sines and cosines:

$$\begin{aligned} f_{g,0}\left(\vec{p},t\right)\Big|_{general} &= a\left(\vec{p}\right)\cos\left(\frac{\left|\Omega_{R,0}\left(\vec{p}\right)\right|}{2}t\right)+b\left(\vec{p}\right)\sin\left(\frac{\left|\Omega_{R,0}\left(\vec{p}\right)\right|}{2}t\right) \\ f_{e,0}\left(\vec{p}+\hbar\vec{k}_0,t\right)\Big|_{general} &= c\left(\vec{p}\right)\cos\left(\frac{\left|\Omega_{R,0}\left(\vec{p}\right)\right|}{2}t\right)+d\left(\vec{p}\right)\sin\left(\frac{\left|\Omega_{R,0}\left(\vec{p}\right)\right|}{2}t\right) \end{aligned} \tag{2.30}$$

Approved for public release; distribution is unlimited

where the initial values $a(\vec{p})$, $b(\vec{p})$, $c(\vec{p})$, and $d(\vec{p})$ correspond to initial values of the distribution functions.

The form of equation (2.30) reveals the fact that $\Omega_{R,0}(\vec{p})$ behaves much like the standard Rabi rate Ω in an ideal interaction between a single atom and a resonant laser frequency. The difference, of course, is that the Rabi rates involved in equation (2.30) are momentum dependent and also involve an integration over wave vectors $\vec{k}$ that is restricted to a set of wave vector components that satisfy momentum and energy conservation for a monochromatic laser. Given the action of $\Omega_{R,0}(\vec{p})$, it is introduced as the leading order for the restricted Rabi rate, with $\vec{\Omega}_{R,1}(\vec{p})$ introduced as the first order perturbation to the restricted Rabi frequency.

2.4.2. Normalization conditions for the general zeroth order solution

General solutions for the ground and excited states presented in equation (2.30) may be considered in the context of persistence of normalization given by equations (2.11)-(2.12), i.e. for $P_g(t)+P_e(t)=1$, or equivalently, $\int d^3\vec{p}'\left|f_g(\vec{p}',t)\right|^2+\int d^3\vec{p}'\left|f_e(\vec{p}',t)\right|^2=1$. Conservation of probability requires that the general solution for the excited state is also represented in terms of the initial state distributions $a(\vec{p})$ and $b(\vec{p})$, and it can be shown that the relationships $c(\vec{p})=b(\vec{p})$ and $d(\vec{p})=a(\vec{p})$ enforce conservation of probability. With these substitutions, equation (2.30) becomes:

$$\begin{aligned} f_{g,0}(\vec{p},t)\big|_{general} &= a(\vec{p})\cos\left(\frac{\left|\Omega_{R,0}(\vec{p})\right|}{2}t\right)+b(\vec{p})\sin\left(\frac{\left|\Omega_{R,0}(\vec{p})\right|}{2}t\right) \\ f_{e,0}\left(\vec{p}+\hbar\vec{k}_0,t\right)\big|_{general} &= b(\vec{p})\cos\left(\frac{\left|\Omega_{R,0}(\vec{p})\right|}{2}t\right)+a(\vec{p})\sin\left(\frac{\left|\Omega_{R,0}(\vec{p})\right|}{2}t\right) \end{aligned} \tag{2.31}$$

The corresponding expression for the zeroth-order ground and excited state probabilities after interaction with a laser field for a duration of *t* seconds is given by:

Approved for public release; distribution is unlimited

$$P_{g,0}(t)=\int d^3\vec{p}\left(\begin{array}{l}\left|a(\vec{p})\right|^2\cos^2\left(\frac{\left|\Omega_{R,0}(\vec{p})\right|}{2}t\right)\\+\left|b(\vec{p})\right|^2\sin^2\left(\frac{\left|\Omega_{R,0}(\vec{p})\right|}{2}t\right)\\+\left(a(\vec{p})b(\vec{p})^*+a(\vec{p})^*b(\vec{p})\right)\cos\left(\frac{\left|\Omega_{R,0}(\vec{p})\right|}{2}t\right)\sin\left(\frac{\left|\Omega_{R,0}(\vec{p})\right|}{2}t\right)\end{array}\right)$$

$$P_{e,0}(t)=\int d^3\vec{p}\left(\begin{array}{l}\left|a(\vec{p})\right|^2\sin^2\left(\frac{\left|\Omega_{R,0}(\vec{p})\right|}{2}t\right)\\+\left|b(\vec{p})\right|^2\cos^2\left(\frac{\left|\Omega_{R,0}(\vec{p})\right|}{2}t\right)\\-\left(a(\vec{p})b(\vec{p})^*+a(\vec{p})^*b(\vec{p})\right)\cos\left(\frac{\left|\Omega_{R,0}(\vec{p})\right|}{2}t\right)\sin\left(\frac{\left|\Omega_{R,0}(\vec{p})\right|}{2}t\right)\end{array}\right) \quad (2.32)$$

Equation (2.32) permit the evaluation of the leading order time-dependent state probability for an atom or a statistical mixture of atoms when subjected to a light pulse with a narrow-linewidth Gaussian laser at the limit of monochromaticity.

The form of equations (2.32) provide a means to directly compare the zeroth order restricted Rabi rate $\Omega_{R,0}(\vec{p})$ to the standard Rabi rate treatment corresponding to an ideal interaction between an atom and laser without Doppler shift effects. Recall that for zero detuning $\delta=0$, the standard Rabi theory predicts an excitation probability of $P_{e,Rabi}(t)=\sin^2(\Omega t/2)$ for ground state atoms where the Rabi rate is defined to be $\Omega\equiv eE_o\left\langle e\left|\hat{\vec{r}}_{e-n}\cdot\hat{e}\right|g\right\rangle/\hbar$. For the equivalent case where atoms begin in the ground state in the restricted Rabi rate theory, $b(\vec{p})=0$ for all momentum classes and the excited state probability given by equation (2.32) reduces to $P_{e,0}(t)=\int d^3\vec{p}\left|a(\vec{p})\right|^2\sin^2\left(\left|\Omega_{R,0}(\vec{p})\right|t/2\right)$. The choice of the restricted Rabi rate definition in equation (2.25) was selected in part to enforce this close relationship between the function of the restricted Rabi rate and the standard Rabi rate when predicting atom transition probabilities.

Approved for public release; distribution is unlimited

2.4.3. Green's function integration for generalized ground and excited state solutions

While the zeroth order solution is simple to obtain, the first order can be derived, in general, as a sum of a homogeneous solution and a particular solution of the second order time differential equations given by equations (2.28) and (2.29). Use of a time domain Green function provides a mechanism to derive a particular solution. With a comparison to the standard driven harmonic oscillator, it can be shown[3] that a relevant Green's function $G(t,t')$ can be expressed as:

$$G(t,t') = \Theta(t-t')\frac{2}{|\Omega_{R,0}(\vec{p})|}\sin\left(\frac{|\Omega_{R,0}(\vec{p})|}{2}(t-t')\right) \tag{2.33}$$

where $\Theta(t-t')$ is the Heaviside step function. Using equation (2.29) and equation (2.33), the particular solution for the ground state distribution can be expressed as:

$$\begin{aligned} f_{g,1}(\vec{p},t)\big|_{particular} &= \int_{-\infty}^{\infty} dt' G(t,t')\frac{f(t')}{m} \\ &= \int_{-\infty}^{\infty} dt' \Theta(t-t')\frac{2}{|\Omega_{R,0}(\vec{p})|}\sin\left[\frac{|\Omega_{R,0}(\vec{p})|}{2}(t-t')\right]\frac{1}{4}\begin{bmatrix} 2i\hbar k_o\left(\nabla_p f_{g,0}(\vec{p},t')\right)\cdot \mathrm{Im}\left(\Omega_{R,0}(\vec{p})^*\,\vec{\Omega}_{R,1}(\vec{p})\right) \\ -\hbar k_0 f_{g,0}(\vec{p},t')\vec{\Omega}_{R,1}(\vec{p})^*\cdot\left(\nabla_p\Omega_{R,0}(\vec{p})\right) \end{bmatrix} \end{aligned} \tag{2.34}$$

An equivalent expression can be derived with equation (2.28) for the excited state distribution. It can be shown[4] that the particular solutions for the ground and excited state distributions are evaluated to be:

[3] See Appendix A.3.1. Green's function application to the driven harmonic oscillator.
[4] See Appendix A.3.2. Use of Green's function to derive state amplitude solutions.

Approved for public release; distribution is unlimited

$$
f_{g,1}(\vec{p},t)\Big|_{particular} = \left[\begin{array}{l} 2i\hbar k_o \dfrac{\mathrm{Im}\left(\Omega_{R,0}(\vec{p})^* \vec{\Omega}_{R,1}(\vec{p})\right)}{2\left|\Omega_{R,0}(\vec{p})\right|} \cdot \left[\begin{array}{l} a(\vec{p})\nabla_p\left(\dfrac{\left|\Omega_{R,0}(\vec{p})\right|}{2}\right)\left(\dfrac{t^2}{4}\cos\left(\dfrac{\left|\Omega_{R,0}(\vec{p})\right|}{2}t\right) - \dfrac{t}{2\left|\Omega_{R,0}(\vec{p})\right|}\sin\left(\dfrac{\left|\Omega_{R,0}(\vec{p})\right|}{2}t\right)\right) \\ +\nabla_p\left(a(\vec{p})\right)\left(\dfrac{t}{2}\sin\left(\dfrac{\left|\Omega_{R,0}(\vec{p})\right|}{2}t\right)\right) \\ +b(\vec{p})\nabla_p\left(\dfrac{\left|\Omega_{R,0}(\vec{p})\right|}{2}\right)\left(\dfrac{t^2}{4}\sin\left(\dfrac{\left|\Omega_{R,0}(\vec{p})\right|}{2}t\right) + \dfrac{t}{2\left|\Omega_{R,0}(\vec{p})\right|}\cos\left(\dfrac{\left|\Omega_{R,0}(\vec{p})\right|}{2}t\right) - \dfrac{1}{\left|\Omega_{R,0}(\vec{p})\right|^2}\sin\left(\dfrac{\left|\Omega_{R,0}(\vec{p})\right|}{2}t\right)\right) \\ +\nabla_p\left(b(\vec{p})\right)\left(\dfrac{-t}{2}\cos\left(\dfrac{\left|\Omega_{R,0}(\vec{p})\right|}{2}t\right) + \dfrac{1}{\left|\Omega_{R,0}(\vec{p})\right|}\sin\left(\dfrac{\left|\Omega_{R,0}(\vec{p})\right|}{2}t\right)\right) \end{array} \right] \\ -\hbar k_0 \dfrac{\vec{\Omega}_{R,1}(\vec{p})^* \cdot \left(\nabla_p \Omega_{R,0}(\vec{p})\right)}{2\left|\Omega_{R,0}(\vec{p})\right|} \left[\begin{array}{l} a(\vec{p})\left(\dfrac{t}{2}\sin\left(\dfrac{\left|\Omega_{R,0}(\vec{p})\right|}{2}t\right)\right) \\ +b(\vec{p})\left(\dfrac{-t}{2}\cos\left(\dfrac{\left|\Omega_{R,0}(\vec{p})\right|}{2}t\right) + \dfrac{1}{\left|\Omega_{R,0}(\vec{p})\right|}\sin\left(\dfrac{\left|\Omega_{R,0}(\vec{p})\right|}{2}t\right)\right) \end{array} \right] \end{array} \right]
$$

$$
f_{e,1}\left(\vec{p}+\hbar\vec{k}_0,t\right)\Big|_{particular} = \left[\begin{array}{l} 2i\hbar k_o \dfrac{\mathrm{Im}\left(\Omega_{R,0}(\vec{p})^* \vec{\Omega}_{R,1}(\vec{p})\right)}{2\left|\Omega_{R,0}(\vec{p})\right|} \cdot \left[\begin{array}{l} c(\vec{p})\nabla_p\left(\dfrac{\left|\Omega_{R,0}(\vec{p})\right|}{2}\right)\left(\dfrac{t^2}{4}\cos\left(\dfrac{\left|\Omega_{R,0}(\vec{p})\right|}{2}t\right) - \dfrac{t}{2\left|\Omega_{R,0}(\vec{p})\right|}\sin\left(\dfrac{\left|\Omega_{R,0}(\vec{p})\right|}{2}t\right)\right) \\ +\nabla_p\left(c(\vec{p})\right)\left(\dfrac{t}{2}\sin\left(\dfrac{\left|\Omega_{R,0}(\vec{p})\right|}{2}t\right)\right) \\ +d(\vec{p})\nabla_p\left(\dfrac{\left|\Omega_{R,0}(\vec{p})\right|}{2}\right)\left(\dfrac{t^2}{4}\sin\left(\dfrac{\left|\Omega_{R,0}(\vec{p})\right|}{2}t\right) + \dfrac{t}{2\left|\Omega_{R,0}(\vec{p})\right|}\cos\left(\dfrac{\left|\Omega_{R,0}(\vec{p})\right|}{2}t\right) - \dfrac{1}{\left|\Omega_{R,0}(\vec{p})\right|^2}\sin\left(\dfrac{\left|\Omega_{R,0}(\vec{p})\right|}{2}t\right)\right) \\ +\nabla_p\left(d(\vec{p})\right)\left(\dfrac{-t}{2}\cos\left(\dfrac{\left|\Omega_{R,0}(\vec{p})\right|}{2}t\right) + \dfrac{1}{\left|\Omega_{R,0}(\vec{p})\right|}\sin\left(\dfrac{\left|\Omega_{R,0}(\vec{p})\right|}{2}t\right)\right) \end{array} \right] \\ +\hbar k_o \dfrac{\vec{\Omega}_{R,1}(\vec{p}) \cdot \nabla_p\left(\Omega_{R,0}(\vec{p})^*\right)}{\left|\Omega_{R,0}(\vec{p})\right|} \left[\begin{array}{l} c(\vec{p})\left(\dfrac{t}{2}\sin\left(\dfrac{\left|\Omega_{R,0}(\vec{p})\right|}{2}t\right)\right) \\ +d(\vec{p})\left(\dfrac{-t}{2}\cos\left(\dfrac{\left|\Omega_{R,0}(\vec{p})\right|}{2}t\right) + \dfrac{1}{\left|\Omega_{R,0}(\vec{p})\right|}\sin\left(\dfrac{\left|\Omega_{R,0}(\vec{p})\right|}{2}t\right)\right) \end{array} \right] \end{array} \right]
$$

(2.35)

The perturbation theory solutions for atomic distributions as given by the leading (zeroth) order distribution functions in equation (2.31) and the first order distribution functions in equation (2.35) provide a means to describe the time evolution of the ground and excited state atomic wavefunction when subjected to a laser pulse with $P_g(t) = \int d^3\vec{p}' \left| f_g(\vec{p}',t) \right|^2$ and $P_e(t) = \int d^3\vec{p}' \left| f_e(\vec{p}',t) \right|^2$.

2.5. Numerical evaluation of restricted Rabi rate integrals

The perturbation theory results for atomic state distributions given by equations (2.31) and (2.35) are expressed in terms of the scalar Rabi rate $\Omega_{R,0}(\vec{p})$ and the vector Rabi rate $\vec{\Omega}_{R,1}(\vec{p})$ defined in

Approved for public release; distribution is unlimited

equation (2.25). The restricted Rabi rates $\Omega_{R,0}(\vec{p})$ and $\vec{\Omega}_{R,1}(\vec{p})$ must be compared against each other in order to validate the underlying assumption of the perturbation theory that the first order distributions $f_{g,1}(\vec{p}',t)$ and $f_{e,1}(\vec{p}',t)$ are in fact much smaller contributions to the overall distribution function as compared with the zeroth order distribution terms $f_{g,0}(\vec{p}',t)$ and $f_{e,0}(\vec{p}',t)$. This would be established for the case that $\left|\vec{\Omega}_{R,1}(\vec{p})\right| \ll \left|\Omega_{R,0}(\vec{p})\right|$.

Given the restriction on the wave vector integrals for each of these frequencies, these Rabi rates represent restricted Rabi rates corresponding to an atomic wavefunction's interaction with a narrow linewidth Gaussian laser pulse at the limit in which the laser wavelength is monochromatic. As such, these rates depart the standard treatments for interactions involving the ideal Rabi rate $\Omega \equiv eE_o \left\langle e\left|\hat{\vec{r}}_{e-n}\cdot\hat{e}\right|g\right\rangle/\hbar$ as introduced in [Rabi *et al.* 1939] and as applied to experimental atom distributions as in [Bordé *et al.* 1984, Sterr *et al.* 1992]. A quantitative comparison of the momentum dependent restricted Rabi rates with the standard treatment is required to assess where the theories depart and where they overlap in predictions for atom-laser interaction strength. In addition, because these restricted Rabi rates depend on the experimental parameters as defined by the atom momentum, laser collimation, and atom-laser geometry, a sensitivity study for $\Omega_{R,0}(\vec{p})$ and $\vec{\Omega}_{R,1}(\vec{p})$ on these experimental parameters is critical to identify implications for optical atomic experiment and system design. For reference, the two restricted Rabi rates from equation (2.25) are reprinted here:

Approved for public release; distribution is unlimited

$$\Omega_{R,0}\left(\vec{p}\right) \equiv \left[\begin{array}{l} \frac{eE_o}{\hbar}\left\langle e\left|\hat{e}_L \cdot \hat{\vec{r}}_{e-n}\right|\mathrm{g}\right\rangle \frac{w_1 w_2}{4\pi} \cdot \\ \int\limits_{\substack{\left|\vec{k}\right|^2 = {k_o}^2;\ \vec{k}\cdot\vec{k}_o > 0 \\ \frac{\vec{k}\cdot\vec{p}}{m_{Ca}} = \left(\delta - \frac{\hbar {\vec{k}_o}^2}{2m_{Ca}}\right)}} d^3\vec{k}\,\delta\left(\left|\vec{k}\right| - k_o\right) \frac{\left(\vec{k}\cdot\hat{k}_o\right)}{k_o} \exp\left(-\frac{1}{4}\left(\begin{array}{l} {w_1}^2 \left|\vec{k}\cdot\hat{e}_{w1}\right|^2 \\ +{w_2}^2 \left|\vec{k}\cdot\hat{e}_{w2}\right|^2 \end{array}\right)\right) \exp\left(i\vec{k}\cdot\left(\vec{r}_a - \vec{r}_w\right)\right) \end{array}\right]$$

$$\vec{\Omega}_{R,1}\left(\vec{p}\right) \equiv \left[\begin{array}{l} \frac{eE_o}{\hbar}\left\langle e\left|\hat{e}_L \cdot \hat{\vec{r}}_{e-n}\right|\mathrm{g}\right\rangle \frac{w_1 w_2}{4\pi} \cdot \\ \int\limits_{\substack{\left|\vec{k}\right|^2 = {k_o}^2;\ \vec{k}\cdot\vec{k}_o > 0 \\ \frac{\vec{k}\cdot\vec{p}}{m_{Ca}} = \left(\delta - \frac{\hbar {\vec{k}_o}^2}{2m_{Ca}}\right)}} d^3\vec{k}\,\delta\left(\left|\vec{k}\right| - k_o\right) \frac{\left(\vec{k}\cdot\hat{k}_o\right)}{k_o} \exp\left(-{w_o}^2 \frac{\left|\vec{k}\times\vec{k}_o\right|^2}{4{k_o}^2}\right) \exp\left(i\vec{k}\cdot\left(\vec{r}_a - \vec{r}_w\right)\right) \frac{\left(\vec{k} - \vec{k}_0\right)}{k_o} \end{array}\right]$$

Evaluation of these restricted Rabi rates reduces to an exercise in evaluating the wave vector integrals. This evaluation begins with a coordinate frame definition and the transformation of integral constraints to integrand terms in the relevant frame

2.5.1. Coordinate frame and integral constraints for restricted Rabi evaluation

A coordinate frame spanned by the basis vectors $\hat{e}_1$, $\hat{e}_2$, and $\hat{e}_3$ may be defined in terms of the atom momentum vector $\vec{p}$ and principal laser wave vector $\vec{k}_o$ according to:

$$\begin{aligned} \hat{e}_1 = \hat{e}_z &\equiv \frac{\hat{k}_o - \left(\hat{k}_o \cdot \hat{p}\right)\hat{p}}{\sqrt{1 - \left(\hat{k}_o \cdot \hat{p}\right)^2}} \\ \hat{e}_2 = \hat{e}_y &\equiv \hat{e}_3 \times \hat{e}_1 = \frac{\hat{p} \times \hat{k}_o}{\sqrt{1 - \left(\hat{k}_o \cdot \hat{p}\right)^2}} \\ \hat{e}_3 = \hat{e}_x &\equiv \frac{\vec{p}}{\left|\vec{p}\right|} = \hat{p} \end{aligned} \tag{2.36}$$

With this coordinate frame, an arbitrary wave vector $\vec{k}$ can be described in spherical coordinates as:

Approved for public release; distribution is unlimited

$$\vec{k} = k_o \begin{pmatrix} \hat{e}_1 \sin\theta_k \cos\phi_k + \hat{e}_2 \sin\theta_k \sin\phi_k \\ +\hat{e}_3 \cos\theta_k \end{pmatrix} \tag{2.37}$$

where θ_k is the polar angle and ϕ_k is the azimuthal angle describing the orientation of the $\vec{k}$ vector. An elliptical laser beam in this coordinate frame has an $1/e^2$ semi-major radius of w_1 and a semi-minor radius of w_2 in the plane orthogonal to $\hat{k}_o$. While the rotation of the beam is possible along this axis, the semi-major and semi-minor axes are taken to be oriented such that for an orthogonal $\hat{k}_o$ and $\hat{p}$, w_1 is oriented along the atom momentum vector $\hat{p}$ and w_2 is oriented vertical to the interaction plane, i.e. along $\hat{e}_2$. For simplicity, the case of a circular laser beam cross section is also considered in which the beam waist radius is given by $w_0 = w_1 = w_2$.

Concerning the three wave vector integral constraints, $\left|\vec{k}\right|^2 = k_o{}^2$ is already embedded in the definitions for restricted Rabi rates in the form of the delta function integrand $\delta\left(\left|\vec{k}\right| - k_o\right)$. The second condition $\vec{k} \cdot \vec{k}_o > 0$ requiring a single direction for laser propagation may be represented as a Heaviside step function $\Theta\left(\vec{k} \cdot \vec{k}_o\right)$. The energy and momentum conservation condition can be reduced to a restriction of the polar spherical angle by applying the geometric definition of the dot product according to:

$$\frac{\vec{k} \cdot \vec{p}}{m_{Ca}} = \left(\delta - \frac{\hbar \vec{k}_o{}^2}{2m_{Ca}}\right) \Rightarrow \cos\theta_k = \frac{m_{Ca}}{k_o \left|\vec{p}\right|}\left(\delta - \frac{\hbar \vec{k}_o{}^2}{2m_{Ca}}\right) \tag{2.38}$$

The application of this condition can be installed into the integration by including a delta function in the integrand of the form:

$$\delta\left(\cos\theta_k - \frac{m}{k_o \left|\vec{p}\right|}\left(\delta - \frac{\hbar \vec{k}_o{}^2}{2m_{Ca}}\right)\right) \tag{2.39}$$

Approved for public release; distribution is unlimited

When expressing the full integrand in spherical coordinates, the definition $u_p \equiv \cos\theta_k$, or equivalently, $u_p \equiv \frac{m}{k_o |\vec{p}|}\left(\delta - \frac{\hbar \vec{k}_o^{\,2}}{2m_{Ca}}\right)$ is used along with the Heaviside step function $\Theta_H\left(1-|u_p|\right)$ enforcing the requirement that $u_p \equiv \cos\theta_k$ cannot exceed unity. One subtlety that must be considered is that the delta function (2.39) concerns a dimensionless variable, and so a dimensionless scaling factor N_k must also be included in the integrand to account for the fact that (2.39) is only a constraint in direction and not in magnitude. The dimensionless scaling parameter N_k will be derived by correspondence to the single recoil detuning scenario in which $\delta = \hbar \vec{k}_o^{\,2} / \left(2m_{Ca}\right)$ and where the momentum condition of (2.39) vanishes. By evaluating the restricted integral at $\delta = \hbar \vec{k}_o^{\,2} / \left(2m_{Ca}\right)$, the integration result should match that of the unrestricted integration over the electric field of a Gaussian laser as captured by equation (2.5). With this evaluation, an expression for N_k can be derived.

In order to derive N_k and calculate quantitative results, the remaining integrands of $\Omega_{R,0}\left(\vec{p}\right)$ and $\vec{\Omega}_{R,1}\left(\vec{p}\right)$ can be transformed into the spherical coordinate frame and the integrals can be solved in terms of experimental parameters.

2.5.2. Scalar Rabi rate integral

For simplicity, a circular laser beam cross section is considered. An initial atom position placed at the origin $\vec{r}_a = 0$, the integral of $\Omega_{R,0}\left(\vec{p}\right)$ can be reduced to an expression involving an integration over a single variable. When substituting $u_p \equiv \cos\theta_k$ and $\sin\theta_k = \sqrt{1-u_p^{\,2}}$, it can be shown[5] that the integral can be expressed as:

[5] See Appendix B.1. Integrating restricted Rabi rate integrals for evaluation.

Approved for public release; distribution is unlimited

$$\int_{\substack{|\vec{k}|^2=k_o^2;\ \vec{k}\cdot\vec{k}_o>0 \\ \frac{\vec{k}\cdot\vec{p}}{m_{Ca}}=\left(\delta-\frac{\hbar k_o^2}{2m_{Ca}}\right)}} d^3\vec{k}\left[\begin{array}{l}\delta\left(|\vec{k}|-k_o\right)\dfrac{\left(\vec{k}\cdot\hat{k}_o\right)}{k_o}\exp\left(-w_o{}^2\dfrac{\left|\vec{k}\times\vec{k}_o\right|^2}{4k_o{}^2}\right) \\ \times\exp\left(-i\vec{k}\cdot\vec{r}_w\right)\end{array}\right]$$

$$= N_k\left(\begin{array}{l}\Theta_H\left(1-|u_p|\right)k_o{}^2 \\ \times\exp\left(-ik_o u_p\vec{r}_w\cdot\hat{e}_3\right)\end{array}\right)\int_0^{2\pi} d\phi_k\left[\begin{array}{l}\Theta_H\left(\begin{array}{l}\sqrt{1-u_p{}^2}\cos\phi_k\sqrt{1-\left(\hat{k}_o\cdot\hat{p}\right)^2} \\ +u_p\left(\hat{k}_o\cdot\hat{p}\right)\end{array}\right) \\ \times\left(\begin{array}{l}\sqrt{1-\left(\hat{k}_o\cdot\hat{p}\right)^2}\sqrt{1-u_p{}^2}\cos\phi_k \\ +\left(\hat{k}_o\cdot\hat{p}\right)u_p\end{array}\right)\end{array}\right]\left[\begin{array}{l}\exp\left(-\dfrac{w_o{}^2k_o{}^2}{4}\left(\begin{array}{l}\left|\hat{p}\times\hat{k}_o\right|^2\left(\left(\dfrac{-\left(\hat{k}_o\cdot\hat{p}\right)}{\sqrt{1-\left(\hat{k}_o\cdot\hat{p}\right)^2}}\right)\sqrt{1-u_p{}^2}\cos\phi_k\right)^2 \\ +u_p \\ +\left(\sqrt{1-u_p{}^2}\sin\phi_k\right)^2\end{array}\right)\right) \\ \times\exp\left(-ik_o\left(\begin{array}{l}\sqrt{1-u_p{}^2}\cos\phi_k\left(\vec{r}_w\cdot\hat{e}_1\right) \\ +\sqrt{1-u_p{}^2}\sin\phi_k\left(\vec{r}_w\cdot\hat{e}_2\right)\end{array}\right)\right)\end{array}\right]$$

(2.40)

This result comprises an integral with one degree of freedom, completely defined in terms of dot products of relevant system orientation and position vectors that can be readily integrated numerically. The two Heaviside step functions correspond to an application of the integral constraints described in section 2.5.1. Coordinate frame and integral constraints for restricted Rabi evaluation, and N_k is the dimensionless factor corresponding to the application of the momentum conservation delta function given by equation (2.39).

Equation (2.40) features integrands that are strongly suppressed everywhere except near $\phi_k = 0, 2\pi$, which corresponds to a situation where the wave vector of integration is along the $\hat{e}_1$ axis as defined in equation (2.36). This wave vector must lie nearly parallel to the central laser wave vector $\vec{k}_o$ for any appreciable coupling to occur.

This integral can be numerically evaluated with an appropriate Riemann sum. Alternatively, an analytical solution can be derived by expanding the integral about $\phi_k = 0, 2\pi$ involving an expansion of cosine and sine terms to leading orders in ϕ_k. The result of analytical integration for the circular cross section laser beam profile can be expressed as[6]:

[6] See Appendix B.1. Integrating restricted Rabi rate integrals for evaluation.

Approved for public release; distribution is unlimited

$$\int\limits_{\substack{|\vec{k}|^2=k_o^{\,2};\ \vec{k}\cdot\vec{k}_o>0 \\ \frac{\vec{k}\cdot\vec{p}}{m_{Cs}}=\left(\delta-\frac{\hbar k_o^{\,2}}{2m_{Cs}}\right)}} d^3\vec{k}\left[\begin{array}{l}\delta\left(|\vec{k}|-k_o\right)\dfrac{\left(\vec{k}\cdot\hat{k}_o\right)}{k_o}\exp\left(-w_o^{\,2}\dfrac{\left|\vec{k}\times\vec{k}_o\right|^2}{4k_o^{\,2}}\right) \\ \times\exp\left(i\vec{k}\cdot\left(-\vec{r}_w\right)\right)\end{array}\right]$$

$$\cong N_k\left(\begin{array}{l}\Theta_H\left(1-|u_p|\right)k_o^{\,2} \\ \times\exp\left(ik_o u_p\left(-\vec{r}_w\right)\cdot\hat{e}_3\right) \\ \times\exp\left(ik_o\sqrt{1-u_p^{\,2}}\left(-\vec{r}_w\right)\cdot\hat{e}_1\right) \\ \times\left(\begin{array}{l}\sqrt{1-\left(\hat{k}_o\cdot\hat{p}\right)^2}\sqrt{1-u_p^{\,2}} \\ +\left(\hat{k}_o\cdot\hat{p}\right)u_p\end{array}\right) \\ \times\Theta_H\left(\begin{array}{l}\sqrt{1-\left(\hat{k}_o\cdot\hat{p}\right)^2}\sqrt{1-u_p^{\,2}} \\ +\left(\hat{k}_o\cdot\hat{p}\right)u_p\end{array}\right) \\ \times\exp\left(-\dfrac{w_o^{\,2}k_o^{\,2}}{4}\left(\left|\hat{p}\times\hat{k}_o\right|^2\left(\left(\dfrac{\left(\hat{k}_o\cdot\hat{p}\right)}{\sqrt{1-\left(\hat{k}_o\cdot\hat{p}\right)^2}}\right)\sqrt{1-u_p^{\,2}}-u_p\right)^2\right)\right)\end{array}\right)\left(\begin{array}{l}\dfrac{\sqrt{\pi}}{\sqrt{\dfrac{w_o^{\,2}k_o^{\,2}}{4}\left(\left(1-u_p^{\,2}\right)-\left[\begin{array}{l}\left|\hat{p}\times\hat{k}_o\right|^2\dfrac{\left(\hat{k}_o\cdot\hat{p}\right)\sqrt{1-u_p^{\,2}}}{\sqrt{1-\left(\hat{k}_o\cdot\hat{p}\right)^2}} \\ \times\left(\dfrac{\left(\hat{k}_o\cdot\hat{p}\right)}{\sqrt{1-\left(\hat{k}_o\cdot\hat{p}\right)^2}}\sqrt{1-u_p^{\,2}}-u_p\right)\end{array}\right]\right)}+ik_o\left(\dfrac{1}{2}\sqrt{1-u_p^{\,2}}\left(-\vec{r}_w\right)\cdot\hat{e}_1\right)} \\ \times\exp\left(\dfrac{\left(k_o\sqrt{1-u_p^{\,2}}\left(-\vec{r}_w\right)\cdot\hat{e}_2\right)^2\left[\begin{array}{l}w_o^{\,2}k_o^{\,2}\left(\left(1-u_p^{\,2}\right)-\left[\begin{array}{l}\left|\hat{p}\times\hat{k}_o\right|^2\dfrac{\left(\hat{k}_o\cdot\hat{p}\right)\sqrt{1-u_p^{\,2}}}{\sqrt{1-\left(\hat{k}_o\cdot\hat{p}\right)^2}} \\ \times\left(\dfrac{\left(\hat{k}_o\cdot\hat{p}\right)}{\sqrt{1-\left(\hat{k}_o\cdot\hat{p}\right)^2}}\sqrt{1-u_p^{\,2}}-u_p\right)\end{array}\right]\right) \\ -2ik_o\sqrt{1-u_p^{\,2}}\left(-\vec{r}_w\right)\cdot\hat{e}_1\end{array}\right]}{\left[\begin{array}{l}w_o^{\,2}k_o^{\,2}\left(\left(1-u_p^{\,2}\right)-\left[\begin{array}{l}\left|\hat{p}\times\hat{k}_o\right|^2\dfrac{\left(\hat{k}_o\cdot\hat{p}\right)\sqrt{1-u_p^{\,2}}}{\sqrt{1-\left(\hat{k}_o\cdot\hat{p}\right)^2}} \\ \times\left(\dfrac{\left(\hat{k}_o\cdot\hat{p}\right)}{\sqrt{1-\left(\hat{k}_o\cdot\hat{p}\right)^2}}\sqrt{1-u_p^{\,2}}-u_p\right)\end{array}\right]\right)^2 \\ +\left(2k_o\sqrt{1-u_p^{\,2}}\left(-\vec{r}_w\right)\cdot\hat{e}_1\right)^2\end{array}\right]}\right)\end{array}\right)$$

(2.41)

The accuracy of analytical expression (2.41) was verified with numerical integration of equation (2.40) for various experimental parameters. Given the computational speed of using the analytical expressions, this verification is critical for further use of equation (2.41) as the restricted integral for computation of the leading order Rabi rate $\Omega_{R,0}\left(\vec{p}\right)$ in further theoretical investigations.

2.5.3. Vector Rabi rate in first order perturbation theory result

A necessary condition for validity of the perturbation expansion is that $\left|\vec{\Omega}_{R,1}\left(\vec{p}\right)\right| \ll \left|\Omega_{R,0}\left(\vec{p}\right)\right|$. The integral of the first-order perturbative vector Rabi rate $\vec{\Omega}_{R,1}\left(\vec{p}\right)$ differs from the integral in $\Omega_{R,0}\left(\vec{p}\right)$

Approved for public release; distribution is unlimited

in the inclusion of the vector $\left(\vec{k}-\vec{k}_0\right)/k_o$ as a multiplicative factor in the integrand of $\vec{\Omega}_{R,1}\left(\vec{p}\right)$. The evaluation of $\vec{\Omega}_{R,1}\left(\vec{p}\right)$ can proceed by returning to equation (2.40) and by multiplying the integrand by $\left(\vec{k}-\vec{k}_0\right)/k_o$.

When evaluating the integral equations $\vec{\Omega}_{R,1}\left(\vec{p}\right)$ numerically, it is observed that $\left|\vec{\Omega}_{R,1}\left(\vec{p}\right)\right| \ll \left|\Omega_{R,0}\left(\vec{p}\right)\right|$, a fact that may be intuitively understood by considering that near $\phi_k = 0, 2\pi$ where the integral is not strongly suppressed, the vector difference $\left(\vec{k}-\vec{k}_0\right)/k_o$ is very small. It can be shown[7] that the magnitude of the vector Rabi rate $\left|\vec{\Omega}_{R,1}\left(\vec{p}\right)\right|$ is at least two to three orders of magnitude smaller than the magnitude of the scalar Rabi rate $\left|\Omega_{R,0}\left(\vec{p}\right)\right|$ for a thermal calcium atom with a velocity between 600-800 m/s. For this reason, the remaining discussion focuses on $\Omega_{R,0}\left(\vec{p}\right)$ as the principal driver of interactions in the context of a thermal atomic beam as in the CaBOT and Ca-2 R-B atom interferometers.

2.5.4. Normalization of the restricted Rabi rate integral

In the integral evaluations presented, the dimensionless scaling factor N_k was introduced along with the application of the integral constraint corresponding to the conservation of momentum given by the delta function in equation (2.39). By evaluating the restricted integral corresponding to the scalar Rabi $\Omega_{R,0}\left(\vec{p}\right)$ at $\delta = \hbar\vec{k}_o^{\,2}/\left(2m_{Ca}\right)$, the momentum-dependent constraint on the integral vanishes since $\hat{k}_o \cdot \hat{p} = 0$. Under these circumstances, the restricted integral bounds are identical to the general Gaussian beam integral given by equation (2.5), and so the integration result of the generalized integral can be used to derive N_k.

[7] See Appendix B.2. Computing restricted Rabi rate magnitudes.

Approved for public release; distribution is unlimited

For a circular laser beam cross section, the general, un-restricted field integration of equation (2.5) evaluates to $4\pi/w_o^{\,2}$ at the peak intensity along the central axis of the laser. Setting this result equal to the analytic integral for the restricted Rabi rate given by equation (2.40) and applying $\hat{k}_o \cdot \hat{p} = 0$ results in the following relationship:

$$\frac{4\pi}{w_o^{\,2}} = N_k \left(k_o^{\,2} \frac{2\sqrt{\pi}}{w_o k_o} \right) \tag{2.42}$$

Equation (2.42) is readily solved for the scaling factor N_k:

$$N_k = \frac{2\sqrt{\pi}}{k_o w_o} \tag{2.43}$$

The units of the wave number $k_o = 2\pi/\lambda$ is m^{-1}, while the units of the circular beam waist radius w_o is m, resulting in N_k being dimensionless as required. With this scaling factor, a direct comparison can be conducted for restricted Rabi rates and other theoretical Rabi rates and atomic state probabilities after interaction with a laser beam can be calculated.

2.5.5. Comments regarding application to thermal and cold atoms

At the large atom velocities and momenta associated with a thermal atomic beam, the zeroth order description for interaction coupling as described by equation (2.32) is sufficient. When cold atoms are considered, however, the momentum space gradients involved in the first order distribution functions given by equations (2.35) involving the Rabi vector $\vec{\Omega}_{R,1}(\vec{p})$ provide a larger contribution and must be considered for an accurate description of the momentum-dependent, restricted wave vector interaction.

Approved for public release; distribution is unlimited

2.6. Restricted Rabi rate calculations

2.6.1. Evaluation of the restricted Rabi rate and a comparison to ideal coupling

Both the restricted Rabi rates and the standard definition for the Rabi rate involve the electric field magnitude E and the matrix coupling element $\langle e|\hat{\vec{r}}_{e-n}\cdot\hat{e}|g\rangle$ corresponding to the electric dipole transition between the ground and excited states. Recall that the standard definition for the Rabi rate for an ideal interaction is $\Omega \equiv eE\langle e|\hat{\vec{r}}_{e-n}\cdot\hat{e}|g\rangle/\hbar$. As described in section 2.2.1. Gaussian laser mode description, the electric field amplitude E can be expressed in terms of the total optical power of the laser beam P_o by equation (2.6), namely $E_o = \sqrt{16P_o/cw_1w_2}$. In order to derive a quantitative Rabi rate, the matrix coupling element must also be evaluated in terms of experimentally measured parameters.

Fermi's Golden Rule provides a mechanism to evaluate $\langle e|\hat{\vec{r}}_{e-n}\cdot\hat{e}|g\rangle$ using the natural linewidth of calcium's intercombination line $\Gamma = 2\pi\times 374\ \text{Hz}$ and the center frequency of the semi-forbidden transition given by $\omega_e - \omega_g = \omega_o = 2\pi\times 456\ \text{THz}$ according to:

$$\Gamma = \frac{4}{3}\frac{\omega_o{}^3 e^2}{\hbar c^3}\left|\langle \mathrm{g}|\hat{e}_L\cdot\hat{\vec{r}}_{e-n}|e\rangle\right|^2 \tag{2.44}$$

Solving for the matrix element yields:

$$\left|\langle \mathrm{g}|\hat{e}_L\cdot\hat{\vec{r}}_{e-n}|e\rangle\right| = \sqrt{\Gamma\frac{3c^2}{4\alpha\omega_o{}^3}} \tag{2.45}$$

Where $\alpha = e^2/\hbar c$ is the fine structure constant. Evaluating the coupling matrix element for the calcium intercombination line relevant to the clock transition results in $9.60\times10^{-11}\,\text{cm}$.

Approved for public release; distribution is unlimited

Using equations (2.6) and (2.45), it is possible to evaluate both the standard, bare Rabi rate $\Omega \equiv eE_o \left\langle e \left| \hat{\vec{r}}_{e-n} \cdot \hat{e} \right| g \right\rangle / \hbar$ as well as the restricted Rabi rates given by equations (2.25). For a laser with a circular cross section waist radius $w_0 = 0.5 \text{ mm}$ and total optical power $P_0 = 1.0 \text{ mW}$, the electric field at the Gaussian peak is given by:

$$\left| \vec{E}_L \right\|_{peak} = E_o = \sqrt{\frac{16P_o}{cw_o^{\,2}}}\Bigg|_{\substack{P_0=1 \text{ mW} \\ w_o=0.5 \text{ mm}}} = 0.04620 \ \frac{\text{statvolt}}{\text{cm}} \tag{2.46}$$

The elementary charge in CGS is equal to $e = 4.8032043 \times 10^{-10}$ statC, and the reduced Planck's constant $\hbar$ in CGS units is equal to 1.055×10^{-27} erg $\cdot$ s. Using these values, the bare Rabi rate is calculated to be:

$$\Omega \equiv \frac{eE_o}{\hbar} \left\langle e \left| \hat{\vec{r}}_{e-n} \cdot \hat{e}_L \right| g \right\rangle \Bigg|_{\substack{P_0=1 \text{ mW} \\ w_o=0.5 \text{ mm}}} = 2\pi \times 321 \text{ kHz} \tag{2.47}$$

Evaluation of the restricted Rabi rate requires a selection of atom-laser geometry and atom momenta. Assuming the ideal geometry in which the principal laser vector and the atom momentum vector are orthogonal, a velocity distribution for thermal calcium is considered for the calculation of $\Omega_{R,0}\left(\vec{p}\right)$. Figure 2-2 depicts in (a) a longitudinal velocity distribution for a calcium oven at 625°C using the Maxwellian distribution described in [Ramsey 1956] for effusive ovens. Plot (b) depicts $\left|\Omega_{R,0}\left(\vec{p}\right)\right|$ for $w_0 = 0.5 \text{ mm}$ and $P_0 = 1.0 \text{ mW}$ at several values of laser detuning from the Ca clock transition. At small detuning, the Rabi rate asymptotes at $\left|\Omega_{R,0}\left(\vec{p}\right)\right\|_{\substack{P_0=1 \text{ mW} \\ w_o=0.5 \text{ mm}}} = 2\pi \times 321 \text{ kHz}$, matching the standard ideal coupling rate in equation (2.47).

At a detuning equal to a single recoil frequency, i.e. at $\delta = \hbar \vec{k}_o^{\,2} / \left(2m_{Ca}\right) = 11.5 \text{ kHz}$, there is no momentum dependence in the Rabi rate as expected from the fact that this detuning corresponds to an unrestricted wave vector integration. The horizontal line in orange corresponds to this detuning and exhibits

Approved for public release; distribution is unlimited

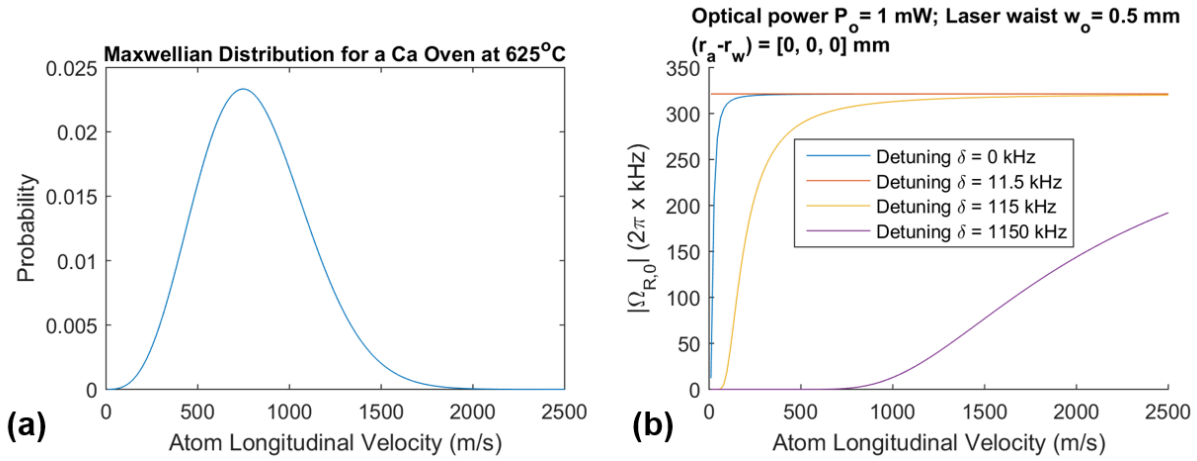

Figure 2-2. (a) Ca atom velocity distribution along the longitudinal direction of the atomic beam and (b) momentum-dependent restricted Rabi rates for various detuning when the atom passes through the center of a Gaussian monochromatic laser beam.

a Rabi rate of $2\pi \times 321\ \text{kHz}$. When $\delta = 0$ (blue line), atoms with longitudinal velocities $< 500\ \text{m/s}$ do not reach this maximum coupling, though the Rabi rate rapidly reaches the asymptote as atom velocities are increased. As detuning is further varied, fewer atoms at low velocities exhibit the maximum coupling strength. Detuning corresponding to 10 times the recoil frequency and 100 times the recoil frequency are depicted in yellow and purple, respectively.

The effect of the momentum dependence on the Rabi rate is most strongly exhibited when detuning is large. For instance, for the largest detuning plotted, negligible coupling exists for atoms traveling slower than 500 m/s, and even for the fastest moving atoms considered, which are well beyond the Maxwellian distribution envelope, the maximum Rabi rates calculated are still only about half as large as the ideal coupling frequency.

2.6.2. Restricted Rabi rate sensitivity to experimental parameters

2.6.2.1. Laser beam waist dependence on Rabi rate magnitude

The restricted Rabi rate $\Omega_{R,0}\left(\vec{p}\right)$ depends on experimental parameters that include atom momentum, atom-laser interaction geometry, detuning, and laser beam characteristics including total

Approved for public release; distribution is unlimited

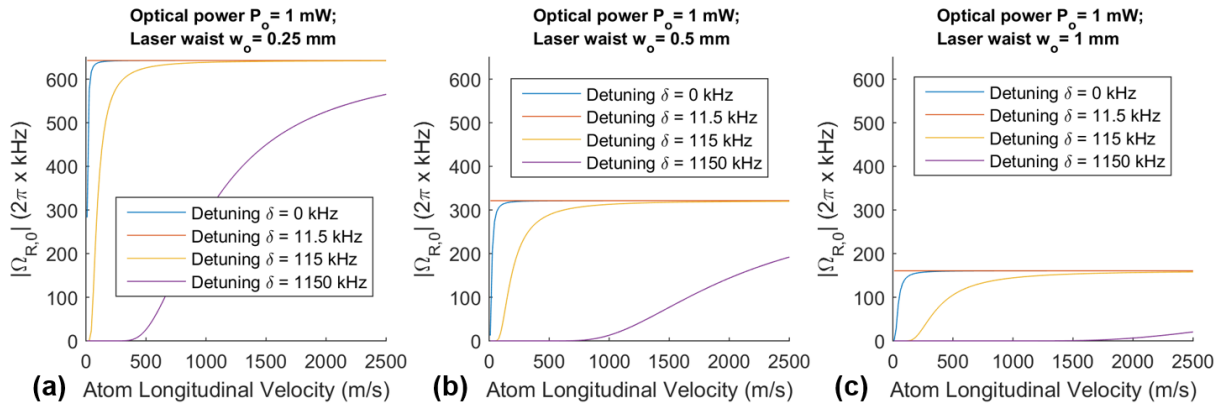

Figure 2-3. Restricted Rabi rate vs. atom longitudinal velocity for a Gaussian laser with a beam waist of (a) 0.25 mm, (b) 0.5 mm, and (c) 1.0 mm.

optical power and beam waist size. The dependence on momentum and detuning was introduced in the plots of Figure 2-2 in the context of ideally orthogonal atom-laser geometry for a single laser waist size and optical power. When maintaining the same optical beam power but varying the laser waist with the same atom-laser geometry, the effective Rabi rate magnitude $\left|\Omega_{R,0}\left(\vec{p}\right)\right|$ is scaled corresponding to the local electric field amplitude. This is illustrated in Figure 2-3. The figure depicts the same momentum-dependent Rabi rate calculation as in Figure 2-2, but for three different waist parameters. The plots in (a), (b), and (c) correspond to waist radii of $w_0 = 0.25$ mm, $w_0 = 0.5$ mm, and $w_0 = 1.0$ mm, respectively. Recall that the Rabi rate scales linearly with electric field strength, i.e. $\Omega_{R,0}\left(\vec{p}\right) \propto E_o$ and $E_o = \sqrt{16P_o/\left(cw_0^2\right)}$. When maintaining a fixed optical power of the laser beam P_o, the restricted Rabi rate magnitudes $\left|\Omega_{R,0}\left(\vec{p}\right)\right|$ scale inversely with the waist size w_0. This relationship is demonstrated in Figure 2-3. For a waist size of $w_0 = 0.25$ mm as depicted in (a), the maximum Rabi rate is $\left|\Omega_{R,0}\left(\vec{p}\right)\right| = 642$ kHz; when doubling the waist size to $w_0 = 0.5$ mm as plotted in (b), the Rabi rate is reduced by half to 321 kHz. Finally, by doubling the waist size once again to $w_0 = 1.0$ mm in (c), the Rabi rate is again reduced by a factor of two to 161 kHz.

Approved for public release; distribution is unlimited

2.6.2.2. Laser steering along Doppler and out-of-plane axes

For an optical atomic clock relying on optical spectroscopy, the tolerance for atom-laser steering uncertainty or errors must be known in order to optimize coupling strength and overall signal size. Figure 2-4 depicts restricted Rabi rate calculations as a function of atom-laser steering in two axes as compared with the nominal orthogonal interaction geometry for zero laser detuning $\delta = 0$.

The plots depict the relationship between the zeroth order restricted Rabi rate magnitude $\left|\Omega_{R,0}\left(\vec{p}\right)\right|$ with a waist radius of $w_0 = 0.5$ mm , an optical laser power of $P_0 = 1.0$ mW , and for an atom longitudinal speed of $\langle v \rangle = 748$ m/s corresponding to the most probable atomic velocity for a Ca oven temperature of $625\,^{\circ}\mathrm{C}$. For both the blue and red curves, a relative steering angle of 0 rad corresponds to a perfect alignment in which the atom momentum vector $\vec{p}$ intersects with an orthogonal laser principal vector $\vec{k}_o$ exactly at the waist of the laser beam (for a graphical depiction, see Figure 2-1). The initial atom position and laser waist position are separated by 9 cm , corresponding to the separation distance between the atom oven nozzle and the first R-B laser interaction site in the CaBOT frequency reference.

The broader blue curve in Figure 2-4 depicts the restricted Rabi rate $\left|\Omega_{R,0}\left(\vec{p}\right)\right|$ as the atom momentum vector is steered out of the interaction plane with an addition of a transverse velocity component $v_{\text{out-of-plane}}$ normal to both the principal atom and laser directions, i.e. along the cross section of the laser waist. The relative out-of-plane steering angle $\theta_{\text{out-of-plane}}$ is calculated as the ratio of the out-of-plane atom velocity $v_{\text{out-of-plane}}$ to the longitudinal atom velocity $v_{\text{long}} = \langle v \rangle = 748$ m/s . This longitudinal velocity and the atom collimator geometry for the CaBOT frequency reference are used to calculate the range of $v_{\text{out-of-plane}}$ that are sampled. Specifically, the atom collimator has a height of 6 mm in the out-of-plane direction and is separated from the atom source by 22 cm – for more information, see section 3.2.4.2. Atom source.

Approved for public release; distribution is unlimited

The $1/e$ full width of the blue curve in Figure 2-4 is $11\ \text{mrad}$ and exactly matches the angular size of the laser waist diameter, in this case equal to $1\ \text{mm}/90\ \text{mm} = 11\ \text{mrad}$. Recall that the beam waist radius is defined as the distance from the beam center to the point where the optical field power drops to $1/e^2$ of the peak value, or equivalently where the electric field amplitude drops to $1/e$ of the peak value. Since $\left|\Omega_{R,0}\left(\vec{p}\right)\right|$ scales with the electric field, a $1/e$ width is the proper comparison.

The narrower red curve in Figure 2-4 depicts the effect of steering the atom momentum vector with the addition of a velocity component along the principal laser propagation direction. This steering direction introduces a Doppler shift and the relative angle θ_{Dopp} from the nominal orthogonal geometry is calculated as the ratio of the transverse velocity in this direction v_{Dopp} with the longitudinal velocity v_{long}. As before, the CaBOT frequency reference geometry is used to set the limits for the transverse velocities selected, corresponding to an atom collimator width of $1.5\ \text{mm}$ and an atom-to-laser separation distance

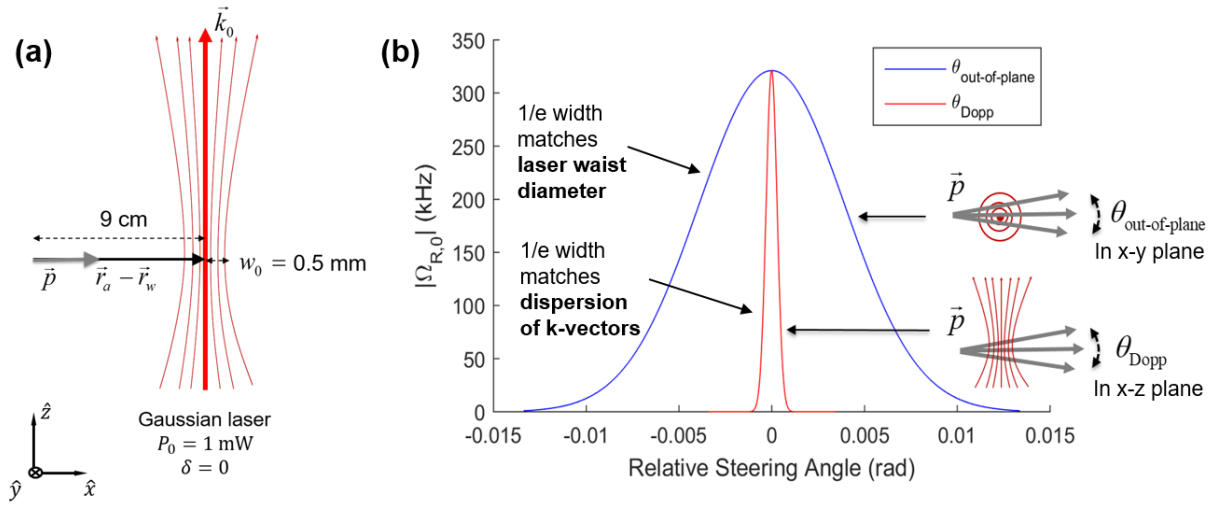

Figure 2-4. Restricted Rabi rates calculated for thermal Ca beam with a most probable velocity of 748 m/s as a function of atom momentum steering with respect to a fixed laser beam. (a) Model scenario geometry and experimental parameters; (b) Interaction strength as a function of atom Momentum Steering: the blue curve depicts steering out of plane in which the atom momentum vector traverses the laser cross-section, while the red curve depicts steering in plane in which the atom momentum is swept along the laser propagation direction; relative steering angle is calculated as the ratio of the transverse velocity to the longitudinal velocity for Doppler shift-inducing and out-of-plane directions.

Approved for public release; distribution is unlimited

of $22\ \text{cm}$. In this case, the $1/e$ full width of the red curve, $0.8\ \text{mrad}$, matches the angular spread of the wave vector distribution of the laser beam, or more specifically, the $1/e$ full width of the wavenumber distribution given by $4/(k_o w_o) = 0.8\ \text{mrad}$.

When taken together, the product of the full widths in the two scenarios will be independent of beam waist, since one width is beam-waist proportional, the other inversely proportional to beam waist. A useful property of the out-of-plane sweep shown in the blue plot is that expected changes to the curve are observed when altering the atom's initial position. For instance, wider widths are predicted when moving the atom's initial position closer to the laser field to the limit in which an infinite width is predicted for the case where the atom begins at the laser waist, i.e. $\vec{r}_a - \vec{r}_w = [0 \quad 0 \quad 0]$. In this way, the restricted Rabi rate theory as described in this thesis provides a mechanism to derive the interaction time between an atom the laser field given a beam waist size and an initial atom position and momentum vector. This interaction time may be used in evaluating expected transition rates and saturation profiles as in section 2.7.3. Doppler profiles and saturation study.

The effect of laser detuning is considered in Figure 2-5. The same exact configuration as modeled in Figure 2-4 is considered for detuning values of 11.5 kHz, 63.4 kHz, and 115 kHz. These detunings are plotted in solid, long dash, and short dash plots, respectively, and correspond to 1x, 5.5x, and 10x the single photon momentum recoil frequency given by $\delta_r = \hbar\vec{k}^2/(2m_{Ca}) = 11.5\ \text{kHz}$. As in Figure 2-4, blue plots correspond to varying out-of-plane angles $\theta_{\text{out-of-plane}}$ with a fixed Doppler-inducing angle of $\theta_{\text{Dopp}} = 0$, while red plots correspond to varying Doppler-inducing angles θ_{Dopp} with $\theta_{\text{out-of-plane}} = 0$.

As depicted in Figure 2-5, red curves for different detuning values do not change shape but instead are shifted relative to one another with respect to θ_{Dopp}, with the case of $\delta = \delta_r$ peaking at $\theta_{\text{Dopp}} = 0$.

Approved for public release; distribution is unlimited

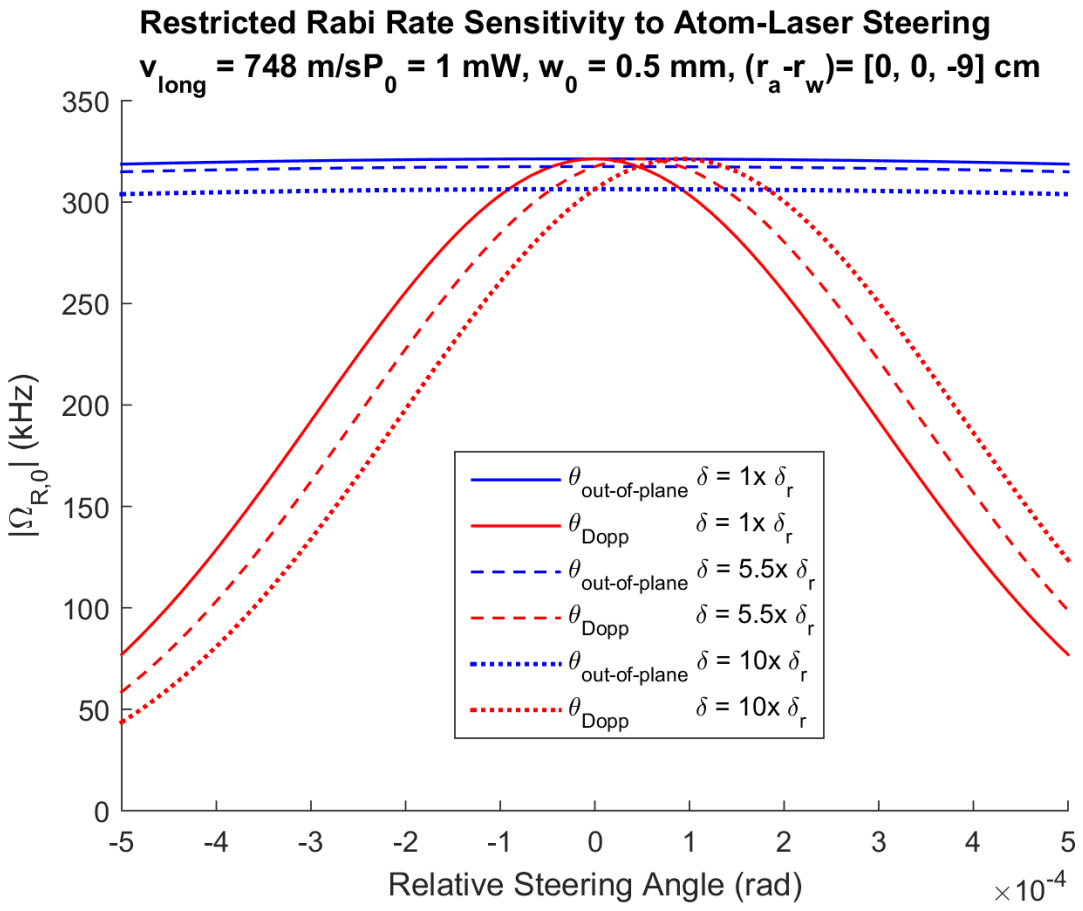

Figure 2-5. Restricted Rabi rates calculated for atomic beam steering for three different laser detunings. Blue curves correspond to atom momentum steering out-of-plane, across the laser waist cross section, and red curves correspond to atom momentum steering in the Doppler-inducing direction, along the principal laser direction.

Larger detunings feature red curves that are shifted to positive values of θ_{Dopp} such that the Doppler shift of the laser frequency as experienced by the atom is sufficient to produce an effective detuning in the atom rest frame equal to one photon recoil frequency. A consequence of this is that the observed shift in the red curves scale linearly with the detuning.

Blue curves associated with each detuning are relatively flat at the scale shown in Figure 2-5 and are not shifted in in the same way as the red curves. While all the red curves feature the same peak Rabi rate magnitude corresponding to the ideal restricted Rabi rate of $\left|\Omega_{R,0}\left(\vec{p}\right)\right|_{\substack{P_0=1\text{ mW}\\ w_o=0.5\text{ mm}}} = 2\pi\times 321\text{ kHz}$ and are shifted in the horizontal axis, the blue curves are scaled, with larger detunings associated with smaller

Approved for public release; distribution is unlimited

peak Rabi rates. Recall that the blue curves show the effect of varying the out-of-plane angle $\theta_{\text{out-of-plane}}$ for a fixed Doppler-inducing angle $\theta_{\text{Dopp}} = 0$. For all detunings $\delta \neq \delta_r$, a non-zero Doppler-inducing angle θ_{Dopp} is required to maximize the restricted Rabi rate. This implies that associated blue curves will never reach the ideal restricted Rabi rate for $\delta \neq \delta_r$ when the Doppler-inducing angle $\theta_{\text{Dopp}} = 0$. This effect is exaggerated for the short dotted blue line corresponding to $\delta = 10\delta_r$, where the Rabi rate peak reaches only $306\ \text{kHz}$ as compared with the global maximum of $321\ \text{kHz}$.

2.7. Excitation probability calculations

2.7.1. Excitation probability formulas for comparison with the literature

2.7.1.1. Atom state probabilities with formalism from Bordé et al. 1984

As described in section 1.4.1.2. Applied models for single pulse interactions: the Bordé et al. 1984 description, [Bordé *et al.* 1984] presents a theoretical treatment for a matter-wave interferometer involving the interaction of a molecule traveling predominantly along the $\hat{x}$ axis with several laser beams oriented along the $\hat{z}$ axis. This approach is now applied to the case of the Ca intercombination line and a single atom-laser interaction for comparison with the restricted Rabi rate introduced in this thesis.

In [Bordé *et al.* 1984], the electric field associated with each laser interaction is expressed in the atom rest frame as $\vec{E}(\vec{r},t) = \text{Re}\,\hat{e}^{\pm}E^{\pm}U^{\pm}\left(v_x\left(t-t_1\right)\right)\exp\left[i\left(\gamma\omega t \mp kv_z t \mp kz + \varphi^{\pm}\right)\right]$ where $\hat{e}$, E, U, k, and φ represent, respectively, the polarization vector, the amplitude, the transverse dependence, the wave number, and the phase of each laser. For the case where the electric field has no transverse dependence, i.e. for $U^{\pm} = 1$, the solution to the Schrödinger equation describing the relevant equations of

Approved for public release; distribution is unlimited

motion for an interaction between the atom and laser beginning at time t_0 and ending at time t is written as:

$$\begin{bmatrix} \tilde{e}(t) \\ \tilde{g}(t) \end{bmatrix} = \begin{bmatrix} A\exp\left[\frac{i}{2}\Omega_0(t-t_0)\right] & B\exp\left[-i\varphi^{\pm}\right] \\ C\exp\left[i\varphi^{\pm}\right] & D\exp\left[\frac{i}{2}\Omega_0(t-t_0)\right] \end{bmatrix} \begin{bmatrix} \tilde{e}(t_0) \\ \tilde{g}(t_0) \end{bmatrix}$$

$$A = \cos\left[\frac{\Omega_{Borde}(t-t_0)}{2}\right] + i\frac{\Omega_3}{\Omega_{Borde}}\sin\left[\frac{\Omega_{Borde}(t-t_0)}{2}\right] \tag{2.48}$$

$$B = C = i\frac{\Omega}{\Omega_{Borde}}\sin\left[\frac{\Omega_{Borde}(t-t_0)}{2}\right]$$

$$D = \cos\left[\frac{\Omega_{Borde}(t-t_0)}{2}\right] - i\frac{\Omega_3}{\Omega_{Borde}}\sin\left[\frac{\Omega_{Borde}(t-t_0)}{2}\right]$$

where $\tilde{g}$ and $\tilde{e}$ are spinors corresponding to the ground and excited states expressed in the rotating frame and where coupling rates governing the interaction strength are given by:

$$\vec{\Omega}_{Borde}\begin{cases} \Omega_1 = \Omega U^{\pm}\cos\varphi^{\pm} \\ \Omega_2 = \Omega U^{\pm}\sin\varphi^{\pm} \\ \Omega_3 = (\gamma\omega - \omega_0) \mp kv_z - \left[(m\pm 1)^2 - m^2\right]\delta_r + i(\gamma_e - \gamma_g)/2 \end{cases} \tag{2.49}$$

$$\Omega_0 = -\left[(m\pm 1)^2 + m^2\right]\delta_r - (2m\pm 1)kv_z + i(\gamma_e + \gamma_g)/2$$

In equation (2.49), m is the number of photon recoils corresponding to the interaction, where the initial ground state corresponds to $m = 0$ and an excited state after a single interaction corresponds to $m = 1$. Larger numbers of recoils correspond to multi-pulse interaction states. The recoil frequency is written as $\delta_r = \hbar k^2/(2m_{Ca})$, and relaxation constants for the excited and ground state are written as γ_e and γ_g, respectively. Positive or negative superscripts indicate interaction with a laser beam oriented along $\pm\hat{z}$ axis. As usual the standard bare Rabi is defined as $\Omega \equiv eE_o\langle e|\hat{\vec{r}}_{e-n}\cdot\hat{e}|g\rangle/\hbar$.

Approved for public release; distribution is unlimited

Equations (2.48)-(2.49) are used directly to calculate the observable ground and excitation probabilities, $P_{g,Borde}(t)$ and $P_{e,Borde}(t)$, for an atom beginning in a state given by $\begin{bmatrix}\tilde{e}(t_0)\\ \tilde{g}(t_0)\end{bmatrix}$ interacting with a laser beam for a duration of $(t-t_0)$ seconds. For an atom initially beginning in the ground state at $t_0 = 0$, i.e. for $\begin{bmatrix}\tilde{e}(t_0=0)\\ \tilde{g}(t_0=0)\end{bmatrix}=\begin{bmatrix}0\\1\end{bmatrix}$ interacting with a laser beam oriented in the $+\hat{z}$ axis, atomic internal state probabilities as a function of time are given by:

$$\begin{aligned} P_{g,Borde}(t) &= \tilde{g}_{m=0}(t)\,\tilde{g}_{m=0}(t)^* \\ P_{e,Borde}(t) &= \tilde{e}_{m=1}(t)\,\tilde{e}_{m=1}(t)^* \end{aligned} \tag{2.50}$$

In equation (2.50) subscripts explicitly identify the number of recoils *m* to be used when applying equations (2.48)-(2.49) to solve for internal state probabilities. Probability of conservation requires $P_{g,Borde}(t)+P_{e,Borde}(t)=1$, implying that only one or another of the probabilities need to be calculated to determine the atom population's internal state fraction. For the purposes of this discussion, spontaneous emission is not considered, and so $\gamma_e = 0$ and $\gamma_g = 0$.

2.7.1.2. Atom state probabilities with restricted Rabi rate formalism

As described in section 2.4.2. Normalization conditions for the general zeroth order solution, the restricted Rabi rate is given by equation (2.32). This expression is a function of momentum and time and it is reprinted here for reference:

Approved for public release; distribution is unlimited

$$P_{g,0}(t) = \int d^3\vec{p} \left(\begin{array}{l} |a(\vec{p})|^2 \cos^2\left(\frac{|\Omega_{R,0}(\vec{p})|}{2}t\right) \\ +|b(\vec{p})|^2 \sin^2\left(\frac{|\Omega_{R,0}(\vec{p})|}{2}t\right) \\ +\left(a(\vec{p})b(\vec{p})^* + a(\vec{p})^* b(\vec{p})\right)\cos\left(\frac{|\Omega_{R,0}(\vec{p})|}{2}t\right)\sin\left(\frac{|\Omega_{R,0}(\vec{p})|}{2}t\right) \end{array} \right)$$

$$P_{e,0}(t) = \int d^3\vec{p} \left(\begin{array}{l} |a(\vec{p})|^2 \sin^2\left(\frac{|\Omega_{R,0}(\vec{p})|}{2}t\right) \\ +|b(\vec{p})|^2 \cos^2\left(\frac{|\Omega_{R,0}(\vec{p})|}{2}t\right) \\ -\left(a(\vec{p})b(\vec{p})^* + a(\vec{p})^* b(\vec{p})\right)\cos\left(\frac{|\Omega_{R,0}(\vec{p})|}{2}t\right)\sin\left(\frac{|\Omega_{R,0}(\vec{p})|}{2}t\right) \end{array} \right)$$

For an atom beginning in the ground state in the restricted Rabi rate formalism, $b(\vec{p}) = 0$ for all momentum classes and the ground state probability reduces to:

$$P_{g,0}(t) = \int d^3\vec{p} \left|a(\vec{p})\right|^2 \cos^2\left(\left|\Omega_{R,0}(\vec{p})\right| t/2\right) \tag{2.51}$$

with a corresponding excitation probability given by $P_{e,0}(t) = 1 - P_{g,0}(t)$.

Given equations (2.50) and (2.51), all that remains is a description of the atom momentum distribution for a calculation of expected transition probabilities for a given simulation.

2.7.2. Atom source models and experimental parameters

2.7.2.1. Momentum distribution sampling

In [Bordé *et al*. 1984], calculations for excitation probabilities are presented corresponding to a single atom longitudinal velocity v_{long} along the principal atom beam direction and a flat distribution of transverse velocities v_{trans} along the principal laser axis in the $\hat{z}$ direction. While not explicitly stated, the bounds for transverse velocities are presumed to be selected according to the width of the atom beam collimator and the distance from the atom source to the collimator. Excitation probabilities are averaged

Approved for public release; distribution is unlimited

across this distribution, resulting in the final simulated states. While [Bordé *et al*. 1984] presents results for simulated excitation probabilities corresponding to four atom-laser interactions, the formalism presented in equations (2.48)-(2.50) provides a mechanism to calculate transition probabilities for a single pulse interaction with the same underlying theoretical framework.

In order to perform a comparison with the restricted Rabi theory and experimental data using a thermal atomic beam, this approach of averaging probability calculations across transverse momenta is extended to account for the Maxwellian distribution of longitudinal momenta as may be expected in a thermal atomic beam. The longitudinal velocity space is discretized with each velocity class assigned a weight according to the Maxwellian shown in Figure 2-6 (a). This particular Maxwellian corresponds to a thermal beam of calcium generated by an oven at $625^{\circ}\mathrm{C}$ with the cubic relationship to atom velocity given by [Ramsey 1956 p.20].

Each longitudinal momentum class in the discrete set will be treated in two ways: i) excited state amplitudes of the various momentum classes will be combined to compute an overall excited state amplitude; and ii) probabilities of the various momentum classes will be combined to compute overall excited state probability. The former corresponds to a thermal source model comprising atoms each of

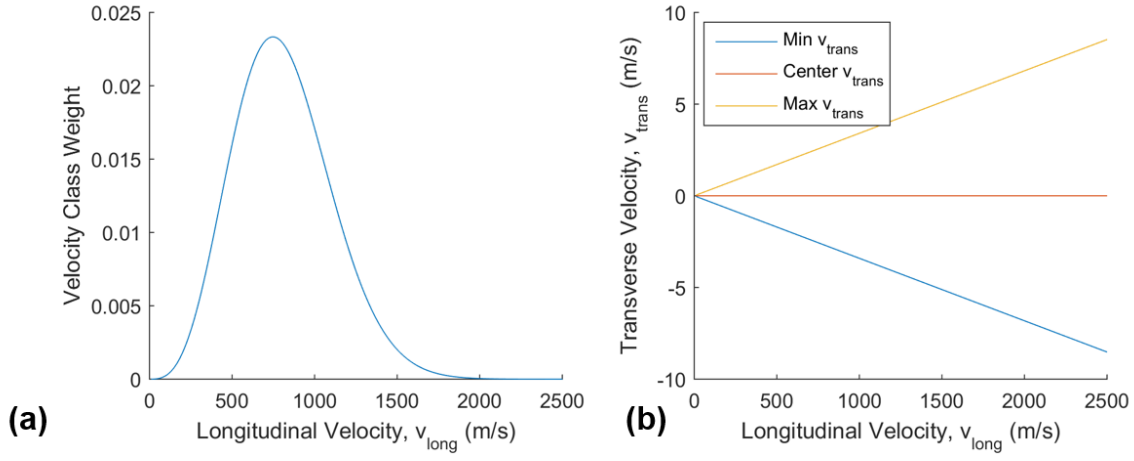

Figure 2-6. (a) Maxwellian Ca atom velocity distribution along the longitudinal direction of the atomic beam used to weight longitudinal atom velocity contributions to probability calculations and (b) range of transverse velocities allowed for each longitudinal velocity class in probability calculations corresponding to experimental apparatus geometry and longitudinal velocity; all transverse velocities are weighted equally.

Approved for public release; distribution is unlimited

which are a coherent superposition of thermal momenta (see "Case 2" in section 2.7.2.2. Cases for modeling probabilities: atom source description and transit time); the latter corresponds to a thermal source comprising atoms of thermally distributed energies (see "Case 3" in section 2.7.2.2. Cases for modeling probabilities: atom source description and transit time).

For each longitudinal velocity, a flat distribution of transverse velocities are allowed with minimum v_{trans} and maximum v_{trans} determined by the separation of the atom source to the laser beam and the atom beam collimating aperture dimensions. Minimum, mean, and maximum v_{trans} velocities that are included in the atom momentum distribution are depicted in Figure 2-6 (b) as a function of longitudinal atom velocity for an atom source-to-laser separation distance of 9 cm and an atom beam collimator width of 1.5 mm. Faster longitudinal velocities afford a greater spread of transverse velocities since the time in which the atom traverses the distance from the source to the collimator is shorter than the time for transit associated with smaller longitudinal velocities. As in [Bordé *et al.* 1984], the velocity in the out-of-plane ($\hat{y}$) axis is taken to be zero, i.e. $v_y = v_{\text{out-of-plnae}} = 0$ and so all velocities are assumed to lie in the plane defined by the atom and laser beams.

2.7.2.4. Laser intensity model for pulse interaction

For probability calculations with [Bordé *et al*. 1984] as with the restricted Rabi theory, interactions are assumed to be a square pulse featuring an intensity equal to the peak Gaussian laser intensity corresponding to the beam waist and overall optical power. This simple model matches the square pulse treatment explicitly employed in transition probability calculations presented in [Bordé *et al*. 1984] and also represents a good reference to compare with restricted Rabi rate probability calculation. The reason is that the lowest order perturbation of the restricted Rabi theory does not describe the position space motion of an atom through the laser beam. Effectively, the atom is modeled as illuminated by the peak Gaussian laser intensity for the duration of the interaction. For initial comparative studies, this simple model is

Approved for public release; distribution is unlimited

sufficient, though a more sophisticated treatment of the localization of the atom and laser beam in position space is desirable for more detailed theoretical investigations.

2.7.2.2. Cases for modeling probabilities: atom source description and transit time

For probability calculations, a $1/e^2$ beam waist radius w_0 and a laser waist position $\vec{r}_w$ are selected, assuming the initial atom position $\vec{r}_a$ is the origin. For each case, a probability of excitation is calculated corresponding to an interaction time determined by the geometry of the scenario and each of the atomic momentum points sampled in longitudinal and transverse space as described in section 2.7.2.1. Momentum distribution sampling. A weighted sum is then calculated in which each velocity class is assigned a weight corresponding to the longitudinal and transverse velocity. Longitudinal velocities are assigned weights corresponding to the Maxwellian distribution while transverse velocities are assigned equal weights. All contributions are normalized such that the weighted sum for the ground state population with no laser power results in a ground state probability of unity.

Case 1 corresponds to calculations with [Bordé *et al*. 1984]'s theoretical treatment. Cases 2-3 correspond to calculations using the restricted Rabi theory with two different approaches to modeling the atom source. Case 2 represents atoms leaving the source as each constituting a superposition of all possible momenta states leaving the oven, while Case 3 represents the description of atoms leaving the oven as a statistical mixture of atomic wavepackets with a range of most probable velocities associated with the atom beam distribution.

Case 1: For calculations with [Bordé *et al*. 1984], atom momenta are treated discretely, without a description for the momentum distribution of a given atom. An interaction time is determined uniquely for each longitudinal momentum class according to $t = 2w_{spot}/v_{long}$ where w_{spot} is the $1/e^2$ beam radius at the interaction site as determined by the waist location and Gaussian beam divergence.

Approved for public release; distribution is unlimited

Case 2: For calculations with the restricted Rabi rate theory one approach involves each atom being treated as a coherent superposition of all possible momentum classes exhibited in the atomic beam. In this case, a single interaction time should be used corresponding to the transit time of the most probable atom velocity of the thermal beam. For a thermal Ca beam at $T = 625^{\circ}\mathrm{C}$, the most probable longitudinal velocity is given by $\langle v_{long} \rangle = \sqrt{3/2}\sqrt{2k_B T/m_{Ca}} = 748$ m/s [Ramsey 1956]. For this case, a probability calculation is performed with an interaction time given by $t = 2w_{spot} / \langle v_{long} \rangle$.

Case 3: Alternatively, the atom beam can be modeled with the restricted Rabi theory as a statistical mixture of atom velocity classes, each of which corresponds to a different transit time corresponding to $t = 2w_{spot} / v_{long}$. In this picture, the statistical mixture consists of atoms with discrete energies according to the thermal momentum distribution of the atomic beam. Corresponding pulse times in this case match those used for the evaluation of probabilities with the [Bordé *et al*. 1984] treatment of Case 1.

It is interesting to compare Case 2 and Case 3 with experimental data, with an eye to assessing which better agrees with measurement.

2.7.2.3. Momentum distribution comment on atomic diffraction

The question of the significance of atomic diffraction through the collimator apertures can be addressed by considering the relative size of the collimator size and the coherence length of the atomic wavepackets. A thermal Ca beam with a temperature of $625^{\circ}\mathrm{C}$ has a momentum uncertainty of $\Delta p \approx m_{Ca} \times (700 \text{ m/s})$ corresponding to a coherence length of $L_{coh} \approx 14$ pm as calculated with $L_{coh} = h/\Delta p$ [Sterr *et al.* 1992]. The collimator aperture for CaBOT that is considered in this analysis measures 1.5 mm by 6 mm. Given this large discrepancy, diffraction is not a concern and need not figure into a discussion of atomic momentum distributions.

Approved for public release; distribution is unlimited

2.7.3. Doppler profiles and saturation study

2.7.3.1. Theory comparisons

For a given $1/e^2$ beam waist radius w_0 and laser optical power P_0, and waist position $\vec{r}_a - \vec{r}_w$ excitation probabilities are calculated as a function of laser detuning from the Ca clock transition resonance at $\omega_0 = 2\pi \times 456$ THz for the three cases introduced in section 2.7.2.2. Cases for modeling probabilities: atom source description and transit time: first, with [Bordé *et al*. 1984], second, with the restricted Rabi theory corresponding to an atom source modeled as a single atomic wavepacket composed of a superposition of all momentum classes present in the atomic beam , and third with the restricted Rabi theory corresponding to an atom source modeled as a statistical mixture of individual wavepackets.

Figure 2-7 depicts the resulting weighted sum of transition probabilities for ground state atoms as a function of laser detuning. For these calculations, the interaction geometry is assumed to be ideal in which the atom and laser beam principal axes are orthogonal and the laser waist size is $w_0 = 0.5$ mm . A geometry representative of the CaBOT frequency reference is selected in which $\vec{r}_a - \vec{r}_w = \left[36\hat{z} \quad 0\hat{y} \quad -14\hat{x}\right]$ cm where the atom initial position is taken to be the origin, i.e. where $\vec{r}_a = \vec{0}$. This scenario approximates the interaction geometry of the CaBOT frequency reference if there were no R-B optics to produce four parallel beams and instead if only a single laser were introduced to the vacuum chamber. In this scenario, the beam waist is located 36 cm away from the interaction region along the principal laser axis, and the interaction region itself is displaced 14 cm from the atom oven nozzle along the axis of atom propagation.

In Figure 2-7, a range of total laser optical powers P_0 are depicted for the same experimental parameters. At low optical powers, Cases 1-3 agree reasonably well. The “flat top” profile of the Doppler feature is an artefact of the flat transverse momentum distribution. As the optical power is increased, the Doppler feature for Case 1 (yellow) steadily grows until it is the largest Doppler profile by the last frame corresponding to $P_0 = 5.5$ mW . By contrast, the Doppler profiles corresponding to Case 3 (blue) do not

Approved for public release; distribution is unlimited

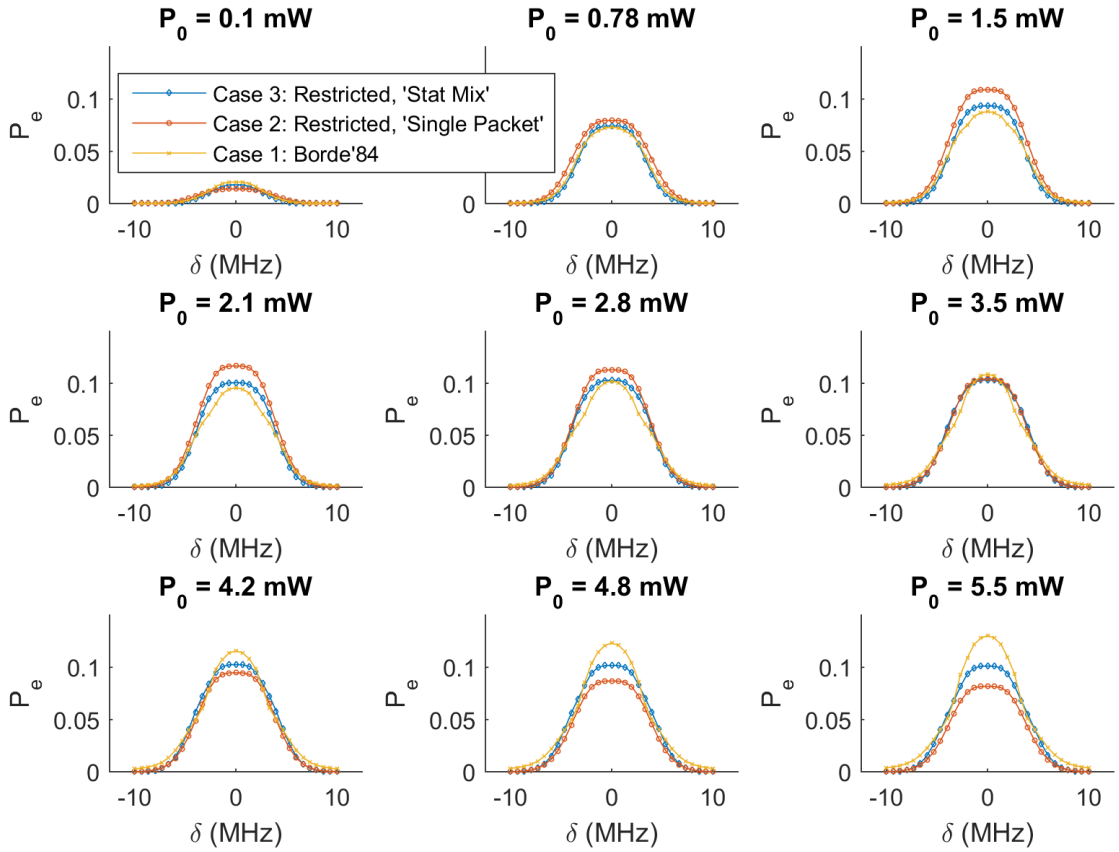

Figure 2-7. Doppler profiles for Cases 1-3 for optical laser powers between 0.1-5.5 mW.

perceptibly grow for powers exceeding 2-3 mW. Finally, the orange plots of Case 2 seem to exhibit Rabi flopping as the profile alternates between growing and shrinking with increased optical power.

By plotting the maximum Rabi rate values from Figure 2-7 in a single plot as a function of laser power, a saturation study can be considered directly. Figure 2-8 depicts the saturation characteristics associated with the same $w_0 = 0.5$ mm trials depicted in the series of Doppler profiles of Figure 2-7, plotted for a range of optical powers between $P_0 = \{0.1\text{ mW} - 50\text{ mW}\}$. Even at 50 mW, the excitation probability computed with the [Bordé *et al.* 1984] treatment in Case 1 (yellow) does not reach saturation. Interestingly, while the statistical mixture (Case 3, blue) reaches saturation near 3 mW and exhibits a

Approved for public release; distribution is unlimited

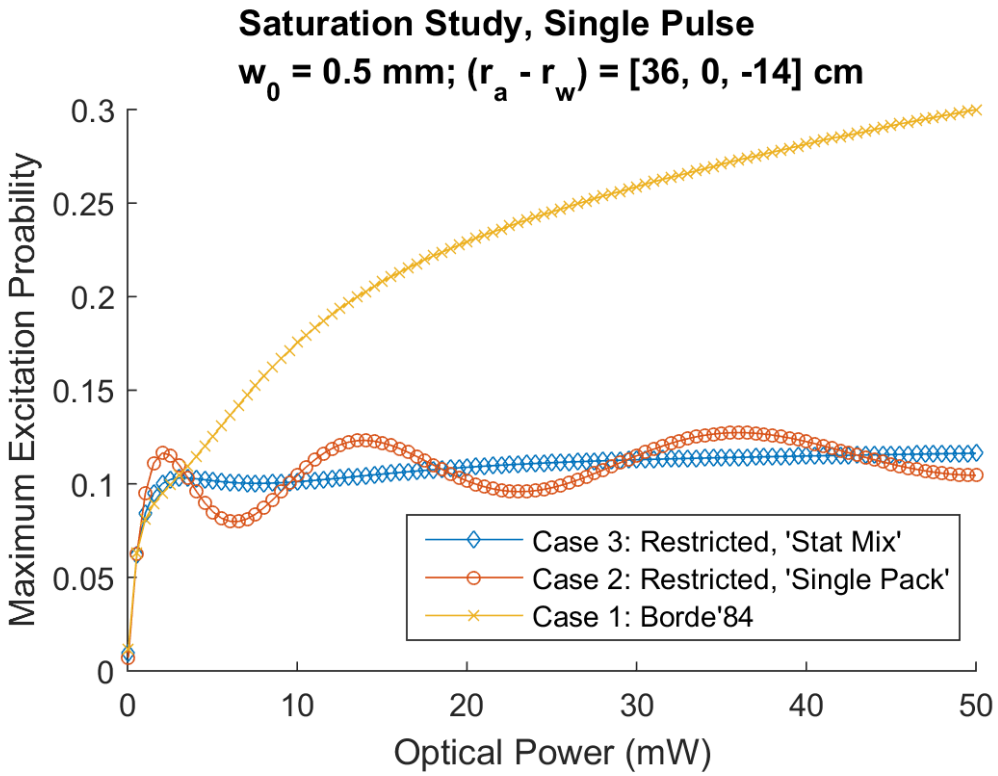

Figure 2-8. Saturation study for laser beam waist radius of 0.5mm.

roughly flat shape with higher powers, the superposition state (Case 2, orange) continues to exhibit Rabi flopping, notably with an average centered along the statistical mixture trace.

The saturation properties of Cases 1-3 vary as a function of waist size. Figure 2-9 shows two boundary cases for the same experimental scenario this time for optical powers between $P_0 = \{0.1\text{ mW} - 10\text{ mW}\}$ corresponding to waist sizes that may be achieved with common adjustable fiber collimators. (a) depicts the saturation characteristics predicted for a small waist radius of $w_0 = 0.1\text{ mm}$, while (b) corresponds to a large waist radius of $w_0 = 1.0\text{ mm}$. In both the small and large waist cases, the [Bordé *et al.* 1984] profile of Case 1 (yellow) does not saturate as readily as the restricted Rabi rate calculations of Case 2 and Case 3. While the predictions for Cases 1-3 agree for low powers in the wide waist scenario of (b), the [Bordé *et al.* 1984] and restricted Rabi predictions do not agree even at low powers for the small waist size depicted in (a). Another immediate observation may be made that the

Approved for public release; distribution is unlimited

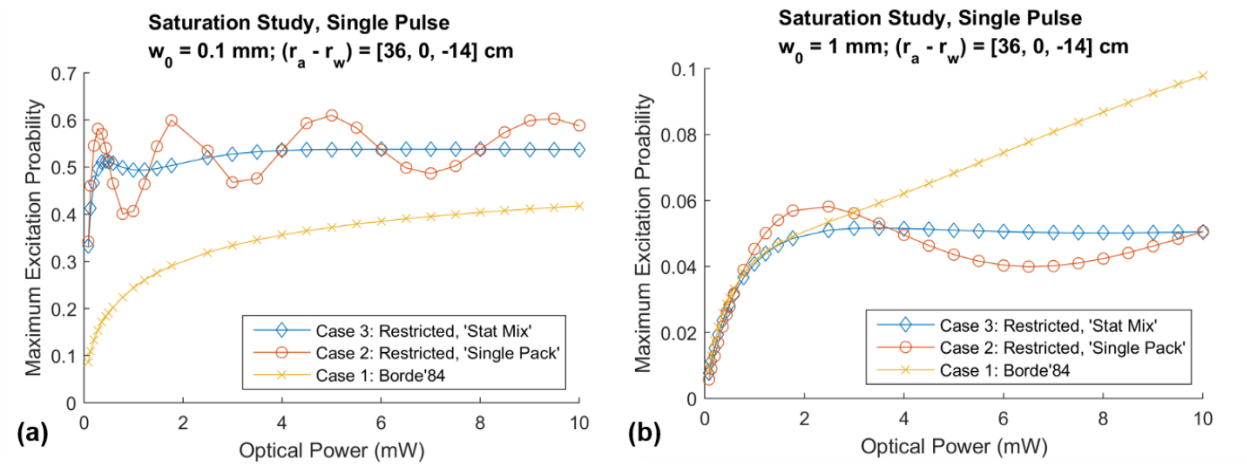

Figure 2-9. Saturation profiles for laser waist radius of: (a) 0.1 mm and (b) 1.0 mm.

[Bordé *et al.* 1984] plots for the small waist in (a) do not reach the excitation probabilities of the restricted Rabi Cases 2-3, while the [Bordé *et al.* 1984] plots rapidly exceed the excitation probabilities for Cases 2-3 at the larger waist size in (b).

Interestingly, Cases 1-3 all exhibit appreciably larger excitation probabilities in (a) as opposed to those in (b), indicating that the small waist produces a stronger coupling between the atoms and the laser field. In fact, for the restricted Rabi Cases 2-3 of (a), a maximum probability of $P_e = 0.5$ is reached. In other words, all three cases considered produce an effective $\pi/2$ pulse. This is particularly interesting given the fact that with such a small waist, the dispersion of laser wave vectors $\vec{k}$ is broad, indicating in the context of the restricted Rabi rate theory that a broad set of wave vector components are available for coupling with the atom. By contrast, Cases 2-3 saturate at a transition probability some 10x lower, around $P_e = 0.05$, for the larger waist size as depicted in (b), with fewer Rabi flops exhibited by Case 2 in (b) as compared to (a). As in the other saturation studies, the "single pack" Case 2 restricted Rabi plots for both (a) and (b) exhibit Rabi oscillations in the predicted transition probability with increased laser power with an average probability prediction centered on the statistical mixture Case 3.

Further theoretical investigations are needed to characterize the underlying mechanisms driving these observations. For instance, one hypothesis that may be proposed for higher coupling with narrower

Approved for public release; distribution is unlimited

waists may be that a narrow waist produces a higher laser intensity at the interaction region, leading to higher expected Rabi rates as a function of the local electric field amplitude. For the cases modeled in Figure 2-9, the spot size diameter for the $w_0 = 0.1$ mm waist of (a) is $2w_{spot}\big|_{(a)} = 1.5$ mm, while the spot size diameter for the $w_0 = 1.0$ mm is nearly identical to that at the waist: $2w_{spot}\big|_{(b)} = 2.0$ mm. These spot sizes are not appreciably different at the scale that the transition probabilities might otherwise indicate if electric field amplitude alone were the reason for a difference in saturation properties, and so an alternative hypothesis is warranted.

In these studies, the Maxwellian longitudinal and flat transverse distributions were discretized into various bin sizes to assess the effect of "granularity" of discretization. It may be noted that when discretization in the transverse direction for the most probable longitudinal velocities approached the single photon recoil velocity for calcium at 1.5 cm/s, little further variation was observed with further grid discretization.

2.7.3.2. Comparison to a measured saturation profile

During experimental efforts with the CaBOT system at NIST, a saturation study was performed for the four-beam R-B atom interferometry interaction sequence. The study was conducted to optimize the optical power to select a setting with a large R-B fringe contrast, a large overall signal as indicated by the height of the Doppler feature observed, and small relative background scattered light signal. One data set collected as part of this study was the base-to-peak size of the Doppler, which is used as a rough comparison for overall saturation characteristics (for more information about the saturation study performed for R-B optimization, see section 3.3.3. Optimization of R-B signal).

Figure 2-10 depicts this four-pulse saturation data alongside predictions corresponding to the [Bordé *et al.* 1984] treatment (Case 1: yellow), the restricted Rabi rate superposition state (Case 2: orange), and the restricted Rabi rate statistical mixture (Case 3: blue). To produce these predictions, the same experimental conditions are assumed as with the saturation studies depicted for the single pulse models of

Approved for public release; distribution is unlimited

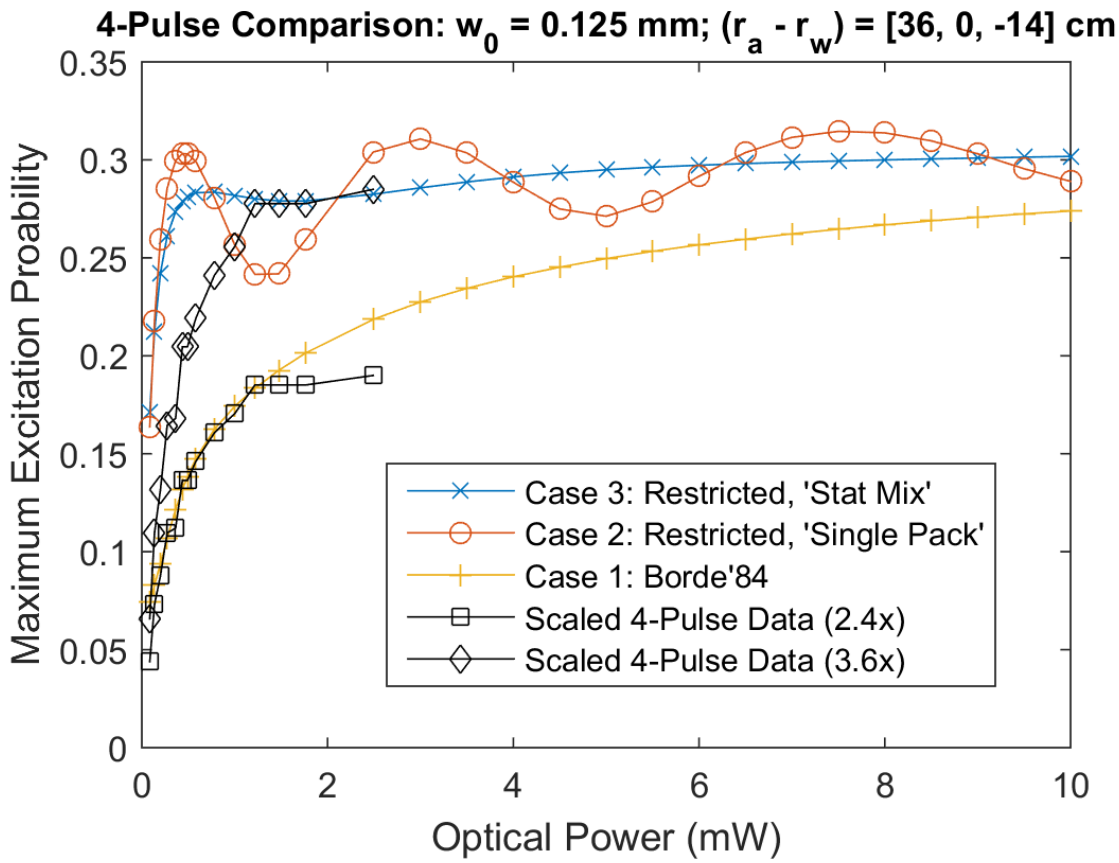

Figure 2-10. Saturation study extended to a four-pulse analogue for comparison with a related data set measured with the CaBOT frequency reference.

Figures 2-7–2-9, except that another three identical pulses are applied to the atoms such that the same excitation fraction results from each of four successive interactions. In order to produce the "Scaled 4-Pulse Data" from the experimentally measured saturation profile, a conversion (with substantial uncertainty) was determined between observed R-B signal power and the excitation probability for atoms in the Ca beam assuming all atoms begin in the ground state before interacting with the first laser beam.[8] In the CaBOT frequency reference, the laser beam is expanded by a factor of 5.5x in the vertical (out-of-plane) direction. To directly compare with the theoretical model constrained to the plane of atom and laser beams, the effective power of the laser along the plane is plotted. I.e. while the maximum laser power measured was 14.7 mW, because the beam was expanded by 5.5x in the vertical (out-of-plane) axis, the effective power

[8] See Appendix Appendix C On the comparison of theoretical predictions with a measured saturation profile.

Approved for public release; distribution is unlimited

of a circular beam with the same horizontal waist size is 5.5x lower, 2.7 mW. Finally, given the uncertainty of the scaling calculation, two multiplicative factors were selected to compare the experimental data set with theoretical predictions. These scalars are listed in the legend of Figure 2-10: a scalar of 2.4x is used to compare with [Bordé *et al.* 1984], and a scalar of 3.6x is used to compare with the restricted Rabi cases.

While the beam waist was not carefully measured for the data set collected, saturation was clearly observed at an optical power around 7 mW (or 1.3 mW adjusted for the beam expansion). A good-faith estimate of the beam waist based on observed beam expansion over the optical beam path was used to arrive at the waist radius selection of $w_0 = 0.125$ mm .

For laser waists near that which may have been used to generate the data depicted, both the [Bordé *et al.* 1984] and restricted Rabi rate predictions seem to match the data reasonably well, though measurements at higher optical powers are necessary to make further evaluative claims. Of course, further experiments involving different waist sizes and additional measurements for the purposes of a single pulse study are necessary to further investigate the predictive power of the restricted Rabi rate theory in its current state and to compare its predictions with existing theoretical frameworks.

2.8. Discussion and future work for restricted Rabi rate theory

The fact that the restricted Rabi rate theory as introduced predicts saturation at laser power levels easily accessible for experimental setups already in use provides a positive indication of the theory's relevance to realistic scenarios. A peculiar feature of the restricted Rabi rate theory as introduced is that the interaction between the atom and laser is exhibited with limited dependence on atom position. This arises from the fact that the lowest order perturbation theory does not contain time dependence of the atom-laser interaction strength. A more sophisticated treatment would more effectively account for the position space time history of a localized wavepacket passing through a localized Gaussian laser beam.

Future work may be separated into theoretical and experimental objectives. Among a broad range of theory improvements, an accounting of time dependence of the atom-laser interaction is desirable, as is

Approved for public release; distribution is unlimited

an extension of the theory to account for multi-pulse interactions and matter-wave interferometry for direct application to R-B modeling. An intermediate objective toward the goal of four-pulse interferometry is application to two-pulse saturation spectroscopy. Because saturation spectroscopy does not rely on atom interferometry, a careful description of the atomic phase is not necessary, allowing for a simple treatment of initial conditions similar to the approach taken for single pulse excitation probability calculations.

In addition to multi-pulse applications, a concentrated effort to apply the restricted Rabi theory to cold atom experiments would be highly valuable to the optical atomic physics community. In order to do so, the next order of the perturbation theory introduced must be investigated to account for larger gradients in the momentum distribution.

As for future work involving experimentation, it would be highly useful and potentially impactful for a set of single pulse experiments to be conducted with Hz-scale lasers and a thermal atomic beam or with a cold atom setup. The restricted Rabi rate theory produces a broad divergence in saturation characteristics as compared with extant theory, which would be readily tested with the proper experiment. As part of CaBOT and Ca-2 experimental work at NIST with a Hz-scale laser, it was routinely necessary to tighten the laser waist such that a wide beam divergence was afforded to the atom beam in order to optimize overall signal size. R-B interference signal and overall Doppler size were observed to drop when modifying the small waist size to a large waist size to collimate the laser light.

In experiments, higher coupling was observed for smaller waist sizes at fixed power levels, and specifically for very small waist sizes placed far away from the interaction region. The intensity of laser light in these interaction geometries is lower than for the case of highly collimated light with larger waist sizes. Absent another explanation, a lower optical intensity at the laser site would correspond to a weaker interaction strength. One hypothesis might be that the transit time was significantly longer for the narrow waist case, but this is unlikely given the high speeds of the atoms. The fact that the narrow waists regularly produced larger signals than wide waists may be readily explained by the momentum condition present for ultra-narrow linewidth lasers, a constraint that has begun to be explored with the restricted Rabi theory presented in this chapter.

Approved for public release; distribution is unlimited

Chapter 3

Frequency reference design and evaluation

3.1. Thermal Ca Ramsey-Bordé atom interferometry: application overview

3.1.1. Context

The Draper CaBOT and the NIST Ca-2 frequency references are based on Ramsey-Bordé atom interferometry with a thermal calcium beam. Neutral calcium's $4s^2\,{}^1S_0 \rightarrow 4s4p\,{}^3P_1$ transition, otherwise known as the Ca intercombination line, is an excellent candidate for an optical frequency reference, given the fact that the transition has a natural linewidth of just 374 Hz centered at 657 nm (456 THz) [Degenhardt *et al.* 2005]. However, despite the small natural linewidth of the Ca intercombination line, environmental and systematic effects lead to frequency shifts that broaden an observable spectroscopic signal. Atom cooling and trapping techniques are most commonly employed in optical atomic clock efforts to mitigate frequency shifts and broadening mechanisms (for a review, see Ludlow *et al.* 2015). Given the need for multiple lasers and complex procedures, these approaches involve large system SWaPs, posing formidable challenges to fielding optical atomic clocks based on cooling and trapping architectures.

CaBOT and Ca-2 rely on a different approach, using Ramsey-Bordé atom interferometry with a simple atomic beam to produce narrow spectroscopic signals. By foregoing laser atom cooling and instead using a thermal beam and R-B atom interferometry, significant SWaP reductions and large atom fluxes are possible. An added benefit to this approach is relaxed vacuum requirements $\left(<1\times10^{-6}\ \text{Torr}\right)$ as compared with that needed for the more delicate environments necessary for optical lattice clocks $\left(<1\times10^{-8}\ \text{Torr}\right)$ or ion traps $\left(<1\times10^{-9}\ \text{Torr}\right)$. Reduced vacuum requirements further reduce the complexity of the system.

Approved for public release; distribution is unlimited

With this approach, strengths of the standard cesium beam clock combine with an optical frequency transition to enable ultra-stable, deployable optical timekeeping technology for PNT in the near term.

3.1.2. Application of Ramsey-Bordé method

3.1.2.1. Method review

The CaBOT vacuum R-B atom interferometry with traveling waves, as introduced by Ch. Bordé and colleagues in Bordé *et al.* 1984, relies on separated oscillatory fields to generate Ramsey fringes with sub-Doppler resolution. When employed in a four-traveling-wave, counter-propagating geometry, the method is Doppler-free to first order. Figure 3-1a depicts an R-B atom interferometer of this type. At the left, a Ca atomic beam composed of atoms initially in the ground state moves from left to right, crossing four mutually-coherent laser beams. At each atom-laser interaction site, there is a probability that the atom will scatter with the laser light, undergoing a change in internal energy and momentum states via photon absorption or stimulated emission.

Figure 3-1a denotes internal states by color: green corresponds to the ground state and purple corresponds to the excited state. Momentum states separated by individual photon recoils are identified by the angle of atom trajectories traced through the interferometer. There are 2^4 possible final states for each atom passing through the interferometer, four of which are shown in Figure 3-1a. The atomic wavefunction recombines in the excited state in two distinct interferometer output ports indicated by $P_e(+)$ and $P_e(-)$ with signs indicating a positive (blue) or negative (red) recoil frequency shift, respectively.

The laser phase is imprinted on the atomic wavefunction at each interaction site such that the final atomic phase corresponds to the sum of the laser phase differences $-\varphi_1 + \varphi_2$ and $-\varphi_3 + \varphi_4$, where subscripts correspond to lasers 1-4 as labeled in Figure 3-1a. As a function of laser detuning from resonance δ, excitation after the fourth laser-beam interaction site scales as [Sterr *et al.* 1992]:

Approved for public release; distribution is unlimited

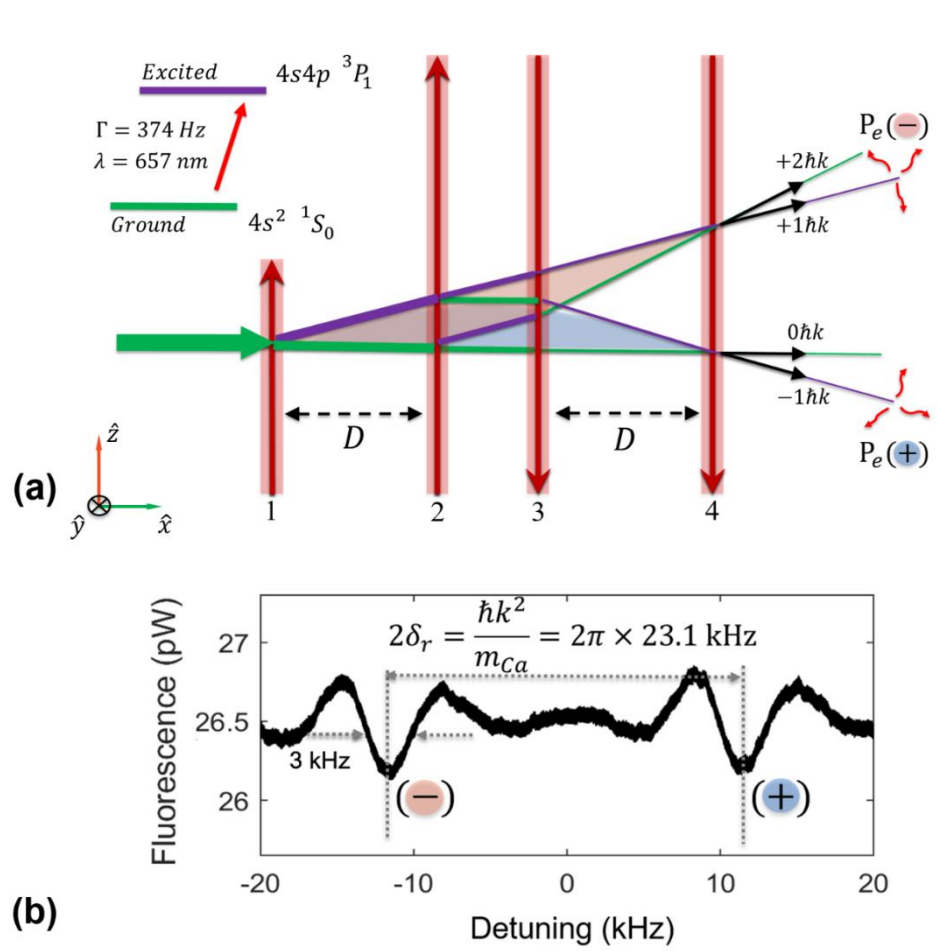

Figure 3-1. R-B atom interferometry with the Ca clock transition. (a) Four traveling wave, counter-propagating geometry with atom state labeling and interferometric output ports identified. (b) Fluorescence emission data with CaBOT frequency reference and a test laser at NIST.

$$P_e(\pm) \propto \cos\left[\frac{2D}{v_x}\left(\delta \mp \frac{\hbar k^2}{2m_{Ca}}\right) - \varphi_1 + \varphi_2 - \varphi_3 + \varphi_4\right] \tag{3.1}$$

In relation (3.1), v_x is the atom's speed from left to right in Figure 3-1a, D is the distance between lasers 1 and 2 and between lasers 3 and 4, and $\hbar k^2/2m_{Ca}$ is the single photon recoil frequency in angular units expressed in terms of the reduced Planck constant $\hbar$, the mass of the Ca atom m_{Ca}, and the laser wavenumber $k = 2\pi/\lambda$. As usual, the detuning is given by $\delta = \omega_L - \omega_0$ where ω_L is the laser frequency and $\omega_0 = 2\pi\nu_0$ is the clock transition frequency, both of which are also written in angular units.

At the interferometer exit ports, spontaneous emission of excited atoms is collected by fluorescence detectors viewing the atomic beam. By sweeping the laser frequency applied to the CaBOT frequency reference across the Ca resonance at 657 nm, fluorescence detection yielded Ramsey fringes as shown in Figure 3-1b. The width of an individual Ramsey fringe depends on atom times of flight between lasers 1 and 2 and between lasers 3 and 4, determined by the inter-laser spacing D and the atom mean speed, i.e. in terms of D/v_x . The R-B signal in Figure 3-1b, featuring a fringe width of 3 kHz, is generated with $D = 50$ mm and an oven temperature of 625°C, which corresponds to a most probable atomic velocity of $\langle v \rangle = \sqrt{3/2}\sqrt{2k_B T/m_{Ca}} = 748$ m/s as calculated by assuming a Maxwellian gas distribution collimated by an effusive oven nozzle [Ramsey 1956]. One of these fringes is used as a locking feature to stabilize the CaBOT laser and ultimately the outgoing timing signal. Separation between the centers of R-B fringe envelopes in the spectroscopic signal is determined by the two photon recoils separating the two ports, corresponding to 23 kHz.

3.1.2.2. Conditions for interferometry and design considerations

Equation (3.1) assumes an infinite coherence length for the atomic beam, i.e. an atomic beam composed of atoms with identical momenta and with a longitudinal velocity width $\Delta v_x = 0$ [Sterr *et al.* 1992]. An actual atomic beam has a finite coherence length in the longitudinal axis given by

$$L_{coh} = h/\left(m_{Ca}\Delta v_x\right) \tag{3.2}$$

For a calcium atomic beam with a temperature of 625°C, $\Delta v_x \approx 700$ m/s and $L_{coh} \approx 14$ pm. Interference fringes are visible only when the spatial displacement of the atomic wavefunction at the output port is smaller than the coherence length. For the R-B interferometer shown in Figure 3-1a, the final transverse displacement of each exit port is $\Delta z = 0$. In the longitudinal axis, the positive recoil port $P_e(+)$ and the negative recoil port $P_e(-)$ are displaced by [Sterr *et al.* 1992]:

Approved for public release; distribution is unlimited

$$\Delta x\left[P_e(+)\right] = \frac{2D\hbar}{v_x}\left(\delta - \frac{\hbar k^2}{2m_{Ca}}\right)\Big/\left(m_{Ca}v_x\right)$$
$$\Delta x\left[P_e(-)\right] = \frac{2D\hbar}{v_x}\left(\delta + \frac{\hbar k^2}{2m_{Ca}}\right)\Big/\left(m_{Ca}v_x\right) \tag{3.3}$$

Equation (3.3) is used to plot atomic wavepacket displacements as a function of laser detuning δ in Figure 3-2a. CaBOT's geometry is used, and the most probable longitudinal velocity $v_x = \langle v \rangle = 748\,\text{m/s}$ corresponding to an atom oven temperature of $625\,^{\circ}\text{C}$ is assumed. The atomic wavefunction displacement for the positive (blue) and negative (red) recoil components are shown along with the atom beam coherence length (black dotted horizontal lines) representing the maximum displacement allowed in either the positive or negative longitudinal $\hat{x}$ direction for fringes to be visible. Red and blue dotted vertical lines indicate the

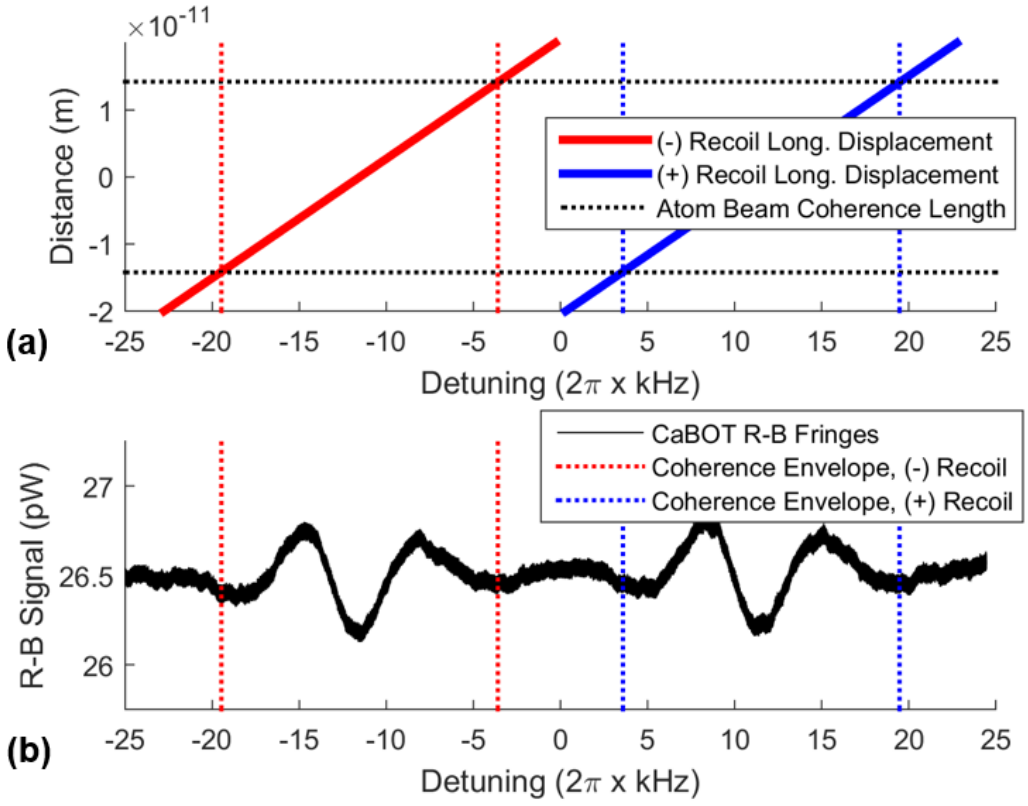

Figure 3-2. R-B atom interferometry with the Ca clock transition. (a) Four traveling wave, counter-propagating geometry with atom state labeling and interferometric output ports identified. (b) Fluorescence emission data with CaBOT frequency reference and a test laser at NIST.

Approved for public release; distribution is unlimited

boundaries at which fringes are expected to disappear when the displacement of atomic wavepackets exceeds the coherence length. Figure 3-2b plots the CaBOT R-B fringes measured at the same oven temperature and along the same detuning axis. As the calculation predicts, fringes disappear beyond detuning values corresponding to wavepacket displacements greater than the atomic beam coherence length.

Based on equation (3.1), a large inter-laser spacing D is desired to produce a narrow resonant locking feature with potential for better frequency instability performance. SWaP concerns drive a desire to limit the overall spacing to enable a small form-factor for the final clock. At the same time, equations (3.2)-(3.3) indicate that for a given oven temperature, increasing the spacing D also narrows the window in which fringes are visible. While a maximum fringe contrast of ¼ is possible in this configuration for each recoil component (with a total contrast of ½ achievable when the recoil components are allowed to overlap as with cold atom experiments) [Sterr *et al.* 1997], the actual fringe contrast that may be observed is limited by the window size determined by the atom oven temperature and the inter-laser spacing D. For a fixed source temperature, then, there are competing objectives: D must be large to produce narrow fringes, but short enough to preserve the coherence of the interferometer. A separation distance of 50 mm was selected for CaBOT following the successful operations of a 27 mm separation used in the Fox *et al.* 2012 design.

3.1.3. Time-Domain and other Ramsey-Bordé Interferometer Applications

Before discussing the CaBOT frequency reference implementation further, alternative R-B schemes and applications are introduced for context. R-B interferometry may also be conducted in the time domain: instead of passing an atom through four spatially separated laser fields, stationary atoms may be subjected to four laser pulses separated in time. The primary advantage of this approach is capacity to more readily modify interferometer characteristics and to work with cold atoms. Additionally, beam parallelism is guaranteed for the four pulses. Recently, the method has provided an exciting avenue for fundamental

Approved for public release; distribution is unlimited

physics research. With cold atom time-domain R-B interferometers, extremely large area atom interferometers may be achieved, involving many photon recoil exchanges separating atomic wavepackets before recombination at the interferometer output ports. Examples include recent measurements of the fine structure constant [Bouchendira *et al.* 2011, Muller 2008, Chiow *et al.* 2009, Cadoret *et al.* 2008, Bouchendira *et al.* 2013, Wicht *et al.* 2002, Weiss *et al.* 1994]; of local gravity measurement [Renee Charriere *et al.* 2012], and gravity wave detection [J. M. Hogan, *et al.* 2011]. For a further description of the state of the art in large area atom interferometry using time-domain R-B methods and their application to inertial sensing, fine structure constant measurement, and gravitational wave detection, see Chiow *et al.* 2011.

Time-domain R-B atom interferometry does not readily apply to thermal atoms, given requirements for interference. For atoms to contribute to the interferogram, they must be exposed to all laser pulses without being disturbed by collisions or other external influences, and they must remain within the interaction region for the duration of the pulse train. This implies the use of one of two approaches: either atoms must be cooled and trapped as previously discussed, which offers the advantage of interferometer flexibility and scientific application at the cost of large SWaP and high complexity; or pulse separation times must be exceedingly short, leading to broader Ramsey fringes that may not be adequate for experimental or operational purposes.

Because this effort has a focus of fielded timekeeping applications in which low SWaP is prioritized, the time domain is not selected for the CaBOT architecture. Instead, R-B interferometry in the spatial domain is selected. While low frequency instability timekeeping is the current focus, spatial R-B atom interferometers may more broadly be applied to applications ranging from space-time curvature investigations [Jurgen Audretsch and Karl-Peter Marzlin, 1994] to tests of the Sagnac effect [Riehle *et al.* 1991] and laser pre-stabilization for laboratory timekeeping and fundamental science objectives [Olson *et al.* 2017, Olson *et al.* 2019].

Approved for public release; distribution is unlimited

3.2. Calcium Beam Optical Timekeeping (CaBOT) frequency reference design

With a thermal beam, only one laser needed for interferometry, and with entirely passive fluorescence detection, CaBOT represents a simplified and potentially fieldable approach to optical timekeeping in contested environments. In order to realize the performance and SWaP made possible by a thermal calcium R-B atom interferometry architecture, CaBOT was designed to maintain a stable environment and geometry for atom-laser interactions. These efforts were addressed both with the design of the frequency reference itself, as well as the clock chassis.

3.2.1. CaBOT block diagram

A functional block diagram for the Calcium Beam Optical Timekeeping clock is depicted in Figure 3-3. The frequency reference, top left, maintains a four-traveling-wave, counter-propagating R-B geometry with 657 nm light from a frequency doubled, cavity stabilized 1314 nm laser. A Pound-Drever-Hall (PDH) feedback loop stabilizes the 1314 nm laser wavelength to an external cavity using an acousto-optical modulator (AOM 1 in Figure 3-3). A second AOM (AOM 2 in Figure 3-3), modulates the frequency-doubled light to lock to a single Ramsey fringe using feedback from fluorescence detectors viewing the atom beam at the output of the interferometer. The lock is achieved by modulating the laser frequency between two frequencies, one on each side of the R-B fringe peak (or trough) such that the two frequencies are separated by the FWHM of the fringe and have similar signal magnitude. The signal difference is the control input used for the lock: if the laser frequency drifts with respect to the R-B signal, the difference between these two frequencies grows, and control feedback modulates the 1314 nm laser frequency and the corresponding frequency doubled 657 nm frequency to reduce the signal difference. A fiber-based optical frequency comb is locked to the atom-stabilized 1314 nm light with heterodyne beating, and outputs an 80 MHz optical pulse train that is down-converted with digital division designed for low added noise to a final 10 MHz signal for distribution.

Approved for public release; distribution is unlimited

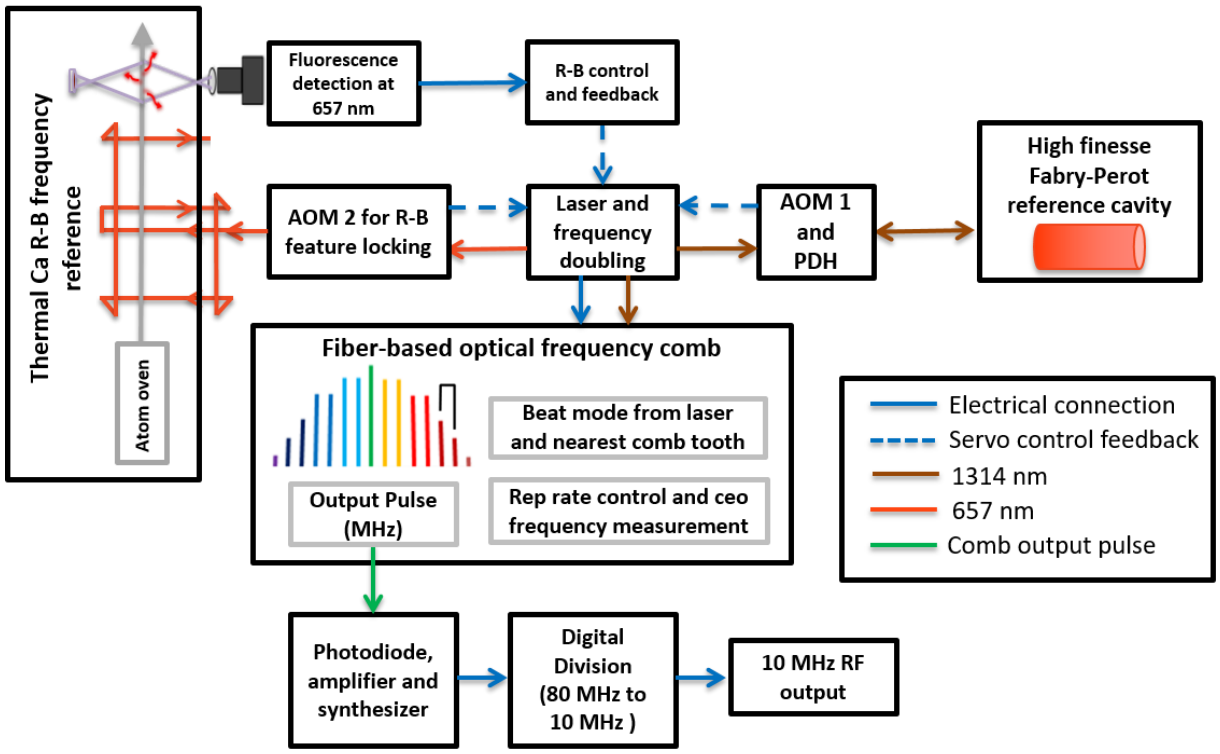

Figure 3-3. Block diagram for the Calcium Beam Optical Timekeeping clock.

The selection of a 1314 nm laser with frequency doubling and a fiber-based comb were intended as a compromise between reduced SWaP and performance reliability concerns. While chip-scale lasers and combs are available, these options suffer from relatively high instabilities making them unsuitable for application to CaBOT. The telecommunications and manufacturing industries are currently driving rapid advances in near-IR optical lasers in the 1000-1500nm range, which has driven down costs and SWaP of lasers in this region of the electromagnetic spectrum. In addition, laser performance at these wavelengths has also improved, making narrower linewidths and lower instabilities more readily available as compared with lasers at shorter wavelengths. Similarly, the rapid development of fiber-based optical frequency combs in recent years has enabled a reduction of optical comb SWaPs to those that are applicable to CaBOT and other fielded applications.

The thermal Ca R-B frequency reference and fluorescence detection system at the top left of the functional block diagram of Figure 3-3 are the focus of the remaining sections of this chapter. These critical subsystems provide the spectroscopic signal ultimately responsible for the final atom-based timing signal

Approved for public release; distribution is unlimited

and are the principal drivers of overall CaBOT performance and SWaP. The next chapter details investigations pertinent to clock chassis design and thermal control.

3.2.2. Frequency instability design error budget

Table 3-1 compiles a design error budget for the CaBOT frequency reference, including major sources of frequency error (uncertainty and instability) that were expected, as well as proposed mitigation strategies to ensure long term (up to and exceeding 10,000 second) fractional frequency instability in the 1×10^{-16} decade. Long term, low instability performance was emphasized in design objectives for CaBOT to support GPS-denied applications. Today, there are no fielded systems today that can achieve both excellent short and long term instability performance, an application area in which CaBOT would stand alone.

Table 3-1. Approximate CaBOT design error budget for frequency uncertainty and instability.

Effect	Shift magnitude	Long term instability	Proposed mitigation approach
First-order Doppler	< 20 mHz $< 4.4\times10^{-17}$	< 20 mHz $< 4.4\times10^{-17}$	Beam alignment: parallelism to < 1 μrad ; k-reversal: forward/reversed beam anti-parallelism to < 1 μrad
Second-order Doppler	750 Hz 1.6×10^{-12}	25 mHz 5.5×10^{-17}	0.1 K atom source temp control nested inside temp-controlled zone including atom source, interaction region, and optics; laser fractional power drift held to $< 2\times10^{-4}$ with active power control
Magnetic fields: Zeeman	2.4 Hz 5.3×10^{-15}	5 mHz 1.1×10^{-17}	$\sim 0.6\ \mathrm{Hz}/\mathrm{G}^2 = \sim 60\ \mathrm{Hz}/\mathrm{mT}^2$ shift; holding field of $2\ \mathrm{G} = 0.2\ \mathrm{mT}$ controlled to fractional variation $< 1\times10^{-3}$; magnetic shielding; possible field measurement and compensation
Electric fields: Stark	< 80 mHz $< 1.8\times10^{-16}$	< 5 mHz $< 1.1\times10^{-17}$	Place interaction region in metal case (same as magnetic shielding)
Blackbody Stark	1.0 Hz 2.2×10^{-15}	10 mHz 2.2×10^{-17}	0.7 K temperature variation in interaction region: temp control zone including atom source, interaction region, and optics
Technical	< 15 mHz $< 3.3\times10^{-17}$	< 15 mHz $< 3.3\times10^{-17}$	Low phase noise comb and digital division synthesizer electronics
Total		< 80 mHz $< 1.8\times10^{-16}$	

Approved for public release; distribution is unlimited

As listed in Table 3-1, the two largest contributors to instability are expected to be first- and second-order Doppler shifts. For a single atom-laser interaction, the first-order Doppler shift is given by $\vec{k} \cdot \vec{v}_{atom}$ where $\vec{k}$ is the wavevector of the laser and $\vec{v}_{atom}$ is the atom velocity vector. Unlike the first-order Doppler effect, the second-order Doppler does not depend on geometry but instead depends entirely on the atom velocity. The shift magnitude is given by $\gamma\omega_0 = 2\pi\nu_0\left(1 - {v_{atom}}^2/c^2\right)^{-1/2}$, where $\omega_0 = 2\pi\nu_0$ is the angular clock transition frequency, and γ is the usual relativistic term relating atom velocity $v_{atom} = \left|\vec{v}_{atom}\right|$ with the speed of light c. While the uncertainty associated with high atom velocities cannot be directly addressed (note the relatively large shift uncertainty of 750 Hz), instability corresponding to the second-order Doppler shift may be controlled with stable atom source temperatures. A target of 0.1 K temperature control for the atom oven was identified as a requirement for integration with CaBOT chassis temperature control to limit second-order Doppler shift instabilities to < 0.025 Hz as indicated in the table.

In addition to inhomogeneous shifts arising from individual atom velocities, homogeneous effects related to the presence of external magnetic and electric fields were also considered. Magnetic and electric fields modify the internal atom energy structure with Zeeman and Stark shifts, respectively, potentially affecting the energy splitting involved in the $4s^2\,{}^1S_0 \rightarrow 4s4p\,{}^3P_1$ clock transition. Because the clock transition couples the magnetic sublevel $m = 0$ of the ground state to the $m' = 0$ sublevel of the excited state, the transition is insensitive to magnetic fields to first order. A weak bias magnetic field of several Gauss (G) is sufficient to lift the degeneracy of the excited $m' = \{0, \pm 1\}$ states to ensure this insensitivity. In this manner, the usual Zeeman shift, which scales with the dot product of the atom's magnetic moment vector $\vec{\mu}$ with the magnetic field vector $\vec{B}$ according to $\vec{\mu} \cdot \vec{B}/\hbar$, is suppressed to some $0.6\ \text{Hz}/G^2$. A magnetic shield, i.e. a mu-metal case, is employed to protect the interaction region from any external magnetic fields.

Approved for public release; distribution is unlimited

Frequency shifts corresponding to static and varying electric fields (DC and AC fields, respectively) are mitigated with a Faraday cage (the same metal case used for magnetic shielding), as well as with amplitude control of the R-B laser light. In the atom-laser interaction region, light shifts corresponding to the AC Stark effect from the laser itself reduce the ground state energy and raise the excited state energy of the effective two level transition. The perturbation to the energy splitting scales with $\Omega_g{}^2 / \nu_0$ where $\Omega_g = \sqrt{\Omega^2 + \delta^2}$ is the generalized Rabi rate expressed in terms of the bare Rabi rate Ω and the laser detuning δ. Because the bare Rabi rate is orders of magnitude smaller than the transition frequency ν_0, this light shift is only appreciable with large detuning δ, which are not present given the need to keep the laser frequency near the transition frequency for R-B atom interferometry.

In addition to the DC and laser-induced AC Stark shifts, temperature changes alter blackbody radiation-induced Stark shifts. By maintaining the temperature variations within interaction zones to a range of 0.7 Kelvin, shifts limited to exceeding $0.010\ \text{Hz}$ may be expected. This analysis accounts only for temperature-induced frequency shifts in the internal atomic energy structure. More stringent control requirements arise from temperature variations in the physical apparatus of the frequency reference. Frequency shifts are mediated by beam steering resulting from thermal expansion of optical components or mounts exposed to thermal gradients and transients. Experimental assessment of thermal sensitivity is discussed in section 5.2 of this thesis.

Finally, technical noise associated with laser, optical comb, and synthesizer electronics constitutes the last item of the frequency instability design budget of Table 3-1. The target instability contribution from low noise components and low added noise digital division techniques was $0.015\ \text{Hz}$. When summing all expected contributions, $< 0.080\ \text{Hz}$ total frequency instability with a corresponding fractional frequency instability of 1.8×10^{-16} was proposed for the CaBOT clock.

Approved for public release; distribution is unlimited

3.2.3. Critical design overview

3.2.3.1. Principal design attributes

The CaBOT frequency reference was designed to operate in support of CaBOT clock performance targets indicated in the Table 3-1 for months at a time without supervision and subject to a broad range of environmental conditions including local temperatures between $0-50^{o}\mathrm{C}$. As such, standard laboratory optical fixtures and practices were avoided as these are usually intended for short duration operations and typically require constant supervision and manual adjustment. Components and interfaces are designed to accommodate the fundamental requirements to: maintain a stable atom-laser interaction geometry for extended periods of time; to mitigate sources of instability in the laser field shape, intensity, and phase and in the atom beam shape and intensity; to ensure low noise fluorescence detection and overall atom-based signal quality in the spectroscopic output of the frequency reference; and to mitigate external environmental perturbations including temperature, vibrations, and electrical and magnetic fields.

Critical design attributes selected to achieve instability performance goals include the use of monolith structures wherever possible among optical elements and vacuum system elements, the selection of coefficient of thermal expansion (CTE) matched materials, and a minimization of adjustment points to ensure atom beam and laser beam alignment and optical contrast maximization in fluorescence signals. A common reference datum was used for physical integration of optics, atom ovens, and atom collimator slits to ensure laser parallelism and consistent R-B geometry. Feedback control was employed to maintain stability in laser and atom beams. The same optics plate was designed to host optics both inside and outside of vacuum to mitigate alignment risk, and monolithic optics including penta-mirrors penta-prisms and a roof mirror produce a highly parallel R-B laser geometry even for a range of imperfect input steering angles.

The CaBOT frequency reference as a unit is composed of a vacuum system, atom source, an optics delivery system, and fluorescence detection system. An external view of the vacuum chamber integrated with the CaBOT optics baseplate is shown in Figure 3-4. Optical elements form and shape a single laser

Approved for public release; distribution is unlimited

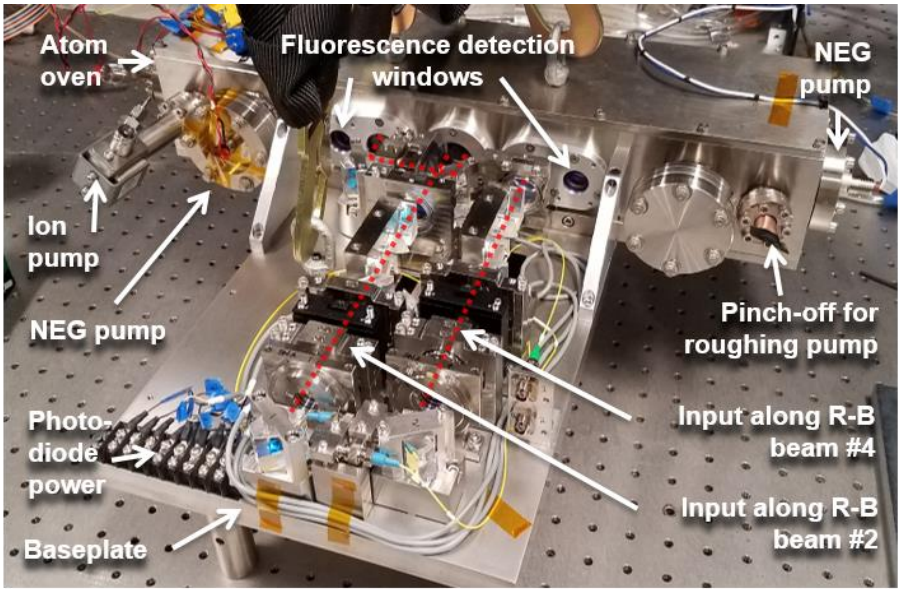

Figure 3-4. CaBOT frequency reference hardware: exterior view of vacuum chamber integrated with optics baseplate

input along one of two pathways indicated by dotted red lines. Monolithic optical elements inside and outside the vacuum chamber steer the laser into an R-B geometry to intersect with an atomic beam inside the vacuum chamber. The atom ovens were designed with a shroud for water cooling in order to limit the temperature gradients inside the vacuum chamber and along the optical path of the R-B laser.

Vacuum pumps include two non-evaporative getter (NEG) pumps, an ion pump, and a pinch-off tube leading to a roughing pump used in vacuum commissioning. Four photodiodes were integrated along the laser delivery pathways in order to pickoff laser light for laser intensity amplitude control, and their power supply terminal is indicated in the photograph. Not shown in the photo are fluorescence detectors that were integrated at the outermost vacuum chamber windows, as well as an optical switch to be used to alternate between the two laser input pathways.

The two laser input paths represent one of two mechanisms were employed to directly address the problem of residual first-order Doppler shifts for instability performance indicated in Table 3-1. At the outset of design, the R-B technique with opposing lasers was selected in part because this method is Doppler-free to first-order [Bordé *et al.* 1984, Sterr et al 1997]. Even so, residual first-order Doppler shifts

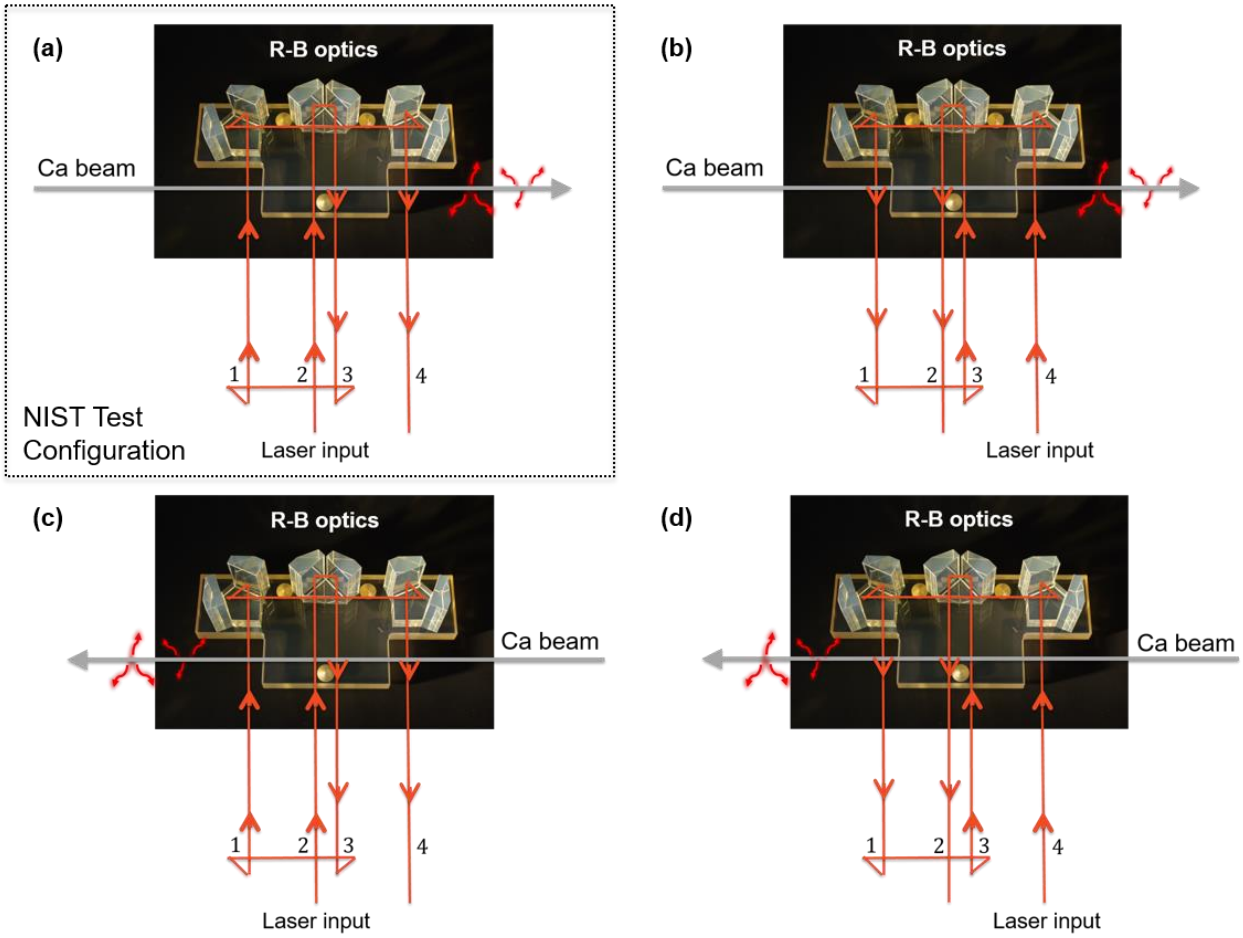

Figure 3-5. CaBOT operational modalities; (a) an atom beam traveling from left to right and with laser pathway 2 used as input; this mode, boxed, corresponds to the nominal configuration as tested at NIST and as pictured in the diagram of Figure 3-1a; (b) k-reversal of (a) with laser pathway 4 used as input; (c) same configuration as (a) but with opposing atom beam; (d) k-reversal of (c).

arising from imperfect atom-laser geometry would still be expected in a physical apparatus, and so additional means of reducing these shifts have been introduced.

Laser directionality switching, referred to as "k-reversal" after the reversing of laser wavevector $\vec{k}$ [Durfee, Shahan, and Kasevich 2006, Fox *et al.* 2012], allows for sequential R-B locks to be made to an atom-based signal derived from each laser direction. Asymmetries that lead to frequency shifts for one laser direction are canceled by equal and opposite shifts for the opposing laser direction with a sequential measurement of the frequency center of an R-B fringe generated with either directionality. The average of sequential locks produces an output frequency signal with laser directionality dependent shifts eliminated.

Approved for public release; distribution is unlimited

To accomplish laser directionality switching, equivalent optical pathways were populated on CaBOT baseplate, each of which produces an R-B laser geometry, but with opposite directionality. Figure 3-5a and Figure 3-5b show two such laser configurations that can be employed for R-B interferometry with a single atomic beam. With use of a 1x2 optical switch, laser light entering the vacuum chamber may begin at laser 2 as in Figure 3-5a, or at laser 4 as in Figure 3-5b, resulting in the opposing laser directionality shown in the images. In addition to mitigating residual first-order Doppler shifts, k-reversal also provides a means to discriminate against inertial effects, to be discussed further in section 3.2.3.2. Inertial effects.

The second mechanism introduced approaches the same problem of geometry dependent, residual first-order Doppler shifts and inertial effects with a reversal of atom direction as opposed to laser direction. To accommodate rapid, sequential R-B locking for oppositely-directed atomic beams, the CaBOT vacuum chamber was designed to host two opposing atom ovens, as well as two fluorescence detection zones. With atoms moving in both directions, and with fluorescence detection regions at either side of the four R-B laser interaction zones, leading residual Doppler and inertial shifts may be mitigated by the counteracting influence of signals produced by the opposing atom velocity. The use of opposing atom ovens in this manner was most recently demonstrated with Ca-2 at NIST [Olson *et al.* 2017, Olson *et al.* 2019].

With a dual atomic beam and k-reversal, four distinct configurations exist for R-B atom interferometry with CaBOT, all of which may be combined in a sequential R-B signal locking scheme to produce a single averaged frequency measurement to discipline the 1314 nm laser, the fiber comb, and the ultimate CaBOT timing signal. Figure 3-5 depicts each of these modalities in turn: (a) and (b) correspond to two different laser directionalities and an atom beam generated by an atom oven located at the left of the vacuum chamber, i.e. for atoms traveling from left to right; (c) and (d) show the complementary k-reversal options for the opposing atom oven, i.e. for atoms traveling from right to left.

Beyond the frequency reference, the chassis is designed to monitor the chassis environment as well as the external environment. A two-layered mu-metal magnetic shield structure was designed to encase the frequency reference to protect the atom-laser interaction zones from external electric and magnetic fields, and passive shock mounts between the frequency reference and the chassis provide vibrational isolation for

Approved for public release; distribution is unlimited

the frequency reference. A thermal fluid temperature control system was designed to both heat the frequency reference and chassis up to an operational temperature above the maximum expected environmental temperature, and then use the ambient air and a set of water-cooling loops to extract waste heat from electronics and active components in the chassis, but also to maintain mK-level temperature control for the frequency reference.

3.2.3.2. Inertial effects

Linear accelerations and angular rotations of the CaBOT frequency reference affect the final clock stability by imprinting phase shifts onto the R-B signal. To first order, the total phase shift $\Delta\varphi_{\text{inertial}}$ associated with these inertial effects is given by:

$$\Delta\varphi_{\text{inertial}} = \Delta\varphi_{\text{accel}} + \Delta\varphi_{\text{rot}} \tag{3.4}$$

where $\Delta\varphi_{\text{accel}}$ is the phase shift corresponding to linear accelerations and $\Delta\varphi_{\text{rot}}$ is the phase shift corresponding to rotation rates. The CaBOT frequency reference is most sensitive to inertial inputs acting along the direction of laser propagation, i.e. for linear accelerations along the principal laser axis and for angular rotations with a rate vector normal to the plane of the atom-laser interaction. Figure 3-6 depicts the coordinate frame of the CaBOT frequency reference and the associated orientations for linear accelerations and rotations which would produce the largest phase shift of the R-B fringes.

The magnitude of phase shifts for an acceleration a_z along the principal axis of laser propagation and for angular rates ω_y rotating about the out-of-plane axis are given by [Audretsch and Marzlin 1994]:

$$\begin{aligned} \Delta\varphi_{\text{accel}} &= -ka_zT\left(T+T'\right) \\ \Delta\varphi_{\text{rot}} &= 2kv_x\omega_yT\left(T+T'\right) \end{aligned} \tag{3.5}$$

where $k = 2\pi/\lambda$ is the wavenumber of the laser, v_x is the velocity of the atom along the principal atom beam direction, and $T = D/v_x$ is the transit time for an atom passing through beams 1-2 and between

Approved for public release; distribution is unlimited

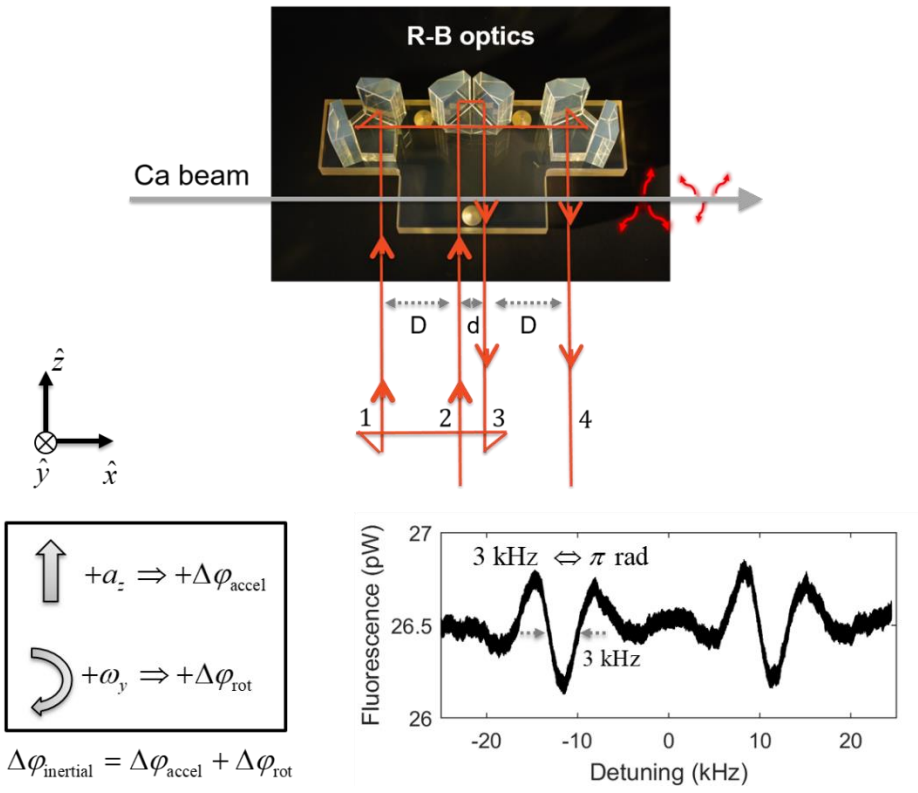

Figure 3-6. Coordinate frame and directionality for CaBOT sensitivity to inertial inputs.

beams 3-4. Finally, T' is the transit time for an atom passing through the central region of length d between beams 2-3. From an engineering perspective with thermal atomic beams, phase shifts approaching π radians for the most probable atom velocity may be considered as a threshold for significant contrast loss. The reason is that thermal beams exhibit a large range of atomic momenta: given the dependence of $\Delta\varphi_{\text{inertial}}$ on atomic velocity, a π radian phase shift for the most probable velocity would imply a range of phase shifts for the full momentum distribution spanning a large fraction of the full 2π phase space. The consequence of this would be diminished coherence that is necessary for interference.

To illustrate the magnitude of expected shifts with the CaBOT frequency reference, accelerations and rotations corresponding to Earth's gravity and rotation rate may be considered. A particularly illustrative scenario involves the operations of CaBOT at the equator with the frequency reference tilted such that the principal laser axis is oriented along the gravity vector. In this case, gravity acts along the

Approved for public release; distribution is unlimited

sensitive linear acceleration axis, i.e. the $\hat{z}$ axis, and Earth's rotation results in an angular rate about the sensitive rotation axis, i.e. the $\hat{y}$ axis. While CaBOT was designed to operate in Earth's gravity with the laser fields oriented orthogonally to the gravity vector, this hypothetical scenario is illuminating nonetheless to estimate the sensitivity of a stationary CaBOT to tipping and tilting, and also to determine the sensitivity of future versions of CaBOT that may be envisioned for space-based operations. With an oven temperature of $625\,^{\circ}\mathrm{C}$ the most probable atom velocity along the $\hat{x}$ axis is $\langle v \rangle = 748\ \mathrm{m/s}$. Given the inter-laser separations of $D = 5\ \mathrm{cm}$ and $d = 1.5\ \mathrm{cm}$ for CaBOT, corresponding transit times for use in equations (3.5) are $T = 67\ \mu\mathrm{s}$ and $T' = 20\ \mu\mathrm{s}$.

With these values and with the wavenumber corresponding to the Ca intercombination line at 657 nm, Earth's gravity at the equator (9.8 m/s^2) results in a phase shift of $\Delta\varphi_{\mathrm{accel}} = -0.54\ \mathrm{rad} \approx \pi/6$. For a nominal angular rate of one rotation per day (73 μrad/s), the resulting phase shift for this scenario is $\Delta\varphi_{\mathrm{rot}} = 6.0\ \mathrm{mrad} \approx \pi/500$. These phase shifts are converted to frequencies by noting that the CaBOT frequency reference produces fringes with a FWHM of 3 kHz, which corresponds to π radians of the interference signal. Using the conversion factor of $3\ \mathrm{kHz}/\pi\ \mathrm{rad}$, the expected frequency shifts for acceleration and rotation are given by $\Delta\nu_{\mathrm{accel}} = -0.52\ \mathrm{kHz}$ and $\Delta\nu_{\mathrm{rot}} = 5.8\ \mathrm{Hz}$, respectively. In fractional frequency terms, acceleration due to gravity produces a shift of $\Delta\nu_{\mathrm{accel}}/\nu_0 = -1.1\times10^{-12}$, while the Earth's rotation produces a shift of $\Delta\nu_{\mathrm{rot}}/\nu_0 = 1.3\times10^{-14}$ for the assumed scenario.

Given the GPS-denied objective for short-term fractional frequency instability of 1×10^{-14} and a long-term instability of 1×10^{-16}, the relatively large magnitude of shifts arising from linear accelerations and angular rates must be considered both in design and nominal operational configuration of CaBOT. As noted in section 3.2.3.1. Principal design attributes, the design of CaBOT includes the use of k-reversal and opposing ovens to produce a single averaged signal from sequential operations of the four modes depicted in Figure 3-5. Given the fact that equations (3.5) are derived with the atom beam and laser beam

Approved for public release; distribution is unlimited

directionality and geometry depicted in Figure 3-6 (and Figure 3-5a), either changing the direction of the lasers or changing the direction of the atom beam would flip the sign of both $\Delta\varphi_{\text{accel}}$ and $\Delta\varphi_{\text{rot}}$. By averaging the central frequency of the R-B signals observed for each of the four operational configurations depicted in Figure 3-5, leading shifts corresponding to inertial effects acting along the laser beam may be discriminated against.

The simple scenario considered for vertically-oriented CaBOT operations at the equator with a single operational mode may be used to estimate the sensitivity of the CaBOT frequency reference to tips or tilts before averaging across the four operational modes afforded by k-reveral and opposing oven operations. As described in the model scenario, tilting CaBOT about $\hat{x}$ axis such that the lasers propagate along the gravity vector would result in a fractional frequency shift of $\Delta\nu_{\text{accel}}/\nu_0 = -1.1\times10^{-12}$. In order to limit the fractional frequency shift to 1×10^{-16} for nominal operations with the laser fields oriented orthogonally to the gravity vector, the tilt angle of the CaBOT frequency refernece should be limited to less than or equal to $\sim 100\ \mu\text{rad}$. For the CaBOT chassis, which measures 63.5 cm (25”) in the axis along the laser propagation, a $100\ \mu\text{rad}$ tilt about $\hat{x}$ corresponds to a relative displacement of 63.5 μm (2.5 mils), which is a reasonable engineering objective for a static environment.

Given the inertial sensitivity of the CaBOT frequency reference, operational settings that minimize time-varying linear accelerations along the laser beam and rotations in the atom-laser plane are most favorable. For this reason, static environments are preferable to dynamic platforms. Even so, constant accelerations and constant angular rates in a static environment may not compromise high performance operations since GPS-denied operations as well as a broad range of other fielded applications envisioned for the CaBOT clock ultimately rely on timing stability as opposed to timing accuracy.

Approved for public release; distribution is unlimited

3.2.4. Frequency reference subsystems

3.2.4.1. Vacuum chamber

The CaBOT vacuum chamber contains the atom ovens and collimators, as well as optics necessary to steer an input laser into the required R-B geometry. In addition, the vacuum chamber accommodates two fluorescence detection zones that include parabolic reflectors in-vacuum and a light baffle tube that not only shields the fluorescence zone from background light by reducing overall scattered light inside the vacuum, but also prevents calcium deposition on optics or other structures within the vacuum chamber. Finally, permanent magnets with Gauss-scale magnetic strength are placed on top of the vacuum chamber over the atom-laser interaction zones to provide a bias field for the atomic beam to maximize coupling with the linearly polarized R-B laser fields.

The chamber was machined from a single block of 316 stainless steel and was designed for sealing via traditional flanges and O-rings to interface with flat stainless steel plates. Stainless steel was selected as a material for its low thermal conductance to help provide thermal isolation of the critical R-B optics needed to generate the highly parallel and stable laser geometry. In addition, 316 stainless steel is less magnetic than other alloys and so provides a level of magnetic isolation for the atom-beam interaction zones to supplement that provided by the double layered mu-metal magnetic shielding. To further address thermal radiation concerns, thermal baffles were machined as part of the primary structure to shield the interaction region in-vacuum optics from the atom ovens. A removable steel insert in the thermal baffle immediately in front of each oven was included to allow for quick removal and cleaning of residual calcium build-up if necessary between operational runs when calcium is reloaded into the crucibles. The windows of the vacuum chamber were designed with a pitch tilt of 3º to reduce the effect of back reflection.

Approved for public release; distribution is unlimited

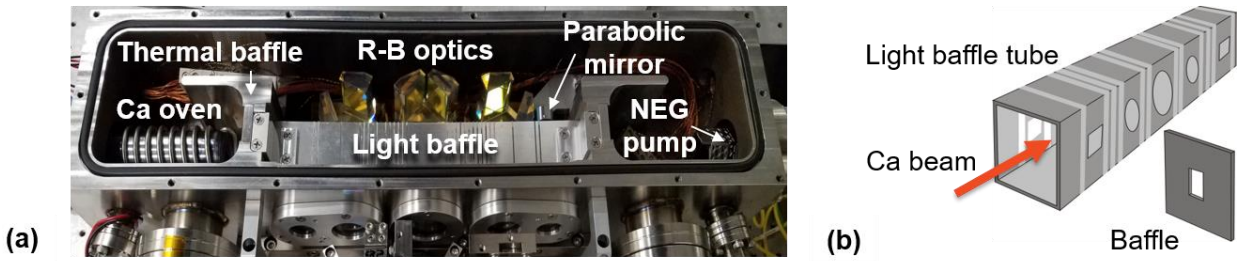

Figure 3-7. CaBOT vacuum chamber detail: (a) vacuum chamber interior, with single atom oven and parabolic mirror installed for NIST testing; (b) light baffle design graphic.

In the NIST experimental campaign, a roughing pump with a copper pinch-off was used for initial pump-down, while two 40 L/s NEG pumps performed primary pumping with an estimated pump rate near the R-B interaction region of 30 L/s, with a single 2 L/s ion pump placed outside the mu-metal magnetic shielding to avoid the strong magnetic field at the pump from interfering with the bias magnetic field at the interaction zones. Both the NEG pumps and ion pump were designed for continuous, low-noise operations while the frequency reference is in use.

Figure 3-7a shows an interior view of the vacuum chamber in the configuration used for experiments conducted at NIST. Operation of the Ca oven at left in the photograph results in an atom beam passing through the light baffle from left to right. A thermal baffle wraps around the atom oven, physically separating the oven from the rest of the vacuum chamber. While there is an identical space and thermal baffle at the right of the vacuum chamber to host dual, opposing atom beam operations, experiments at NIST were conducted with only the single oven installed. In place of a second atom oven, a NEG pump is placed opposite a single Ca oven in this configuration. For dual-oven use, this NEG pump would instead be placed at an alternate vacuum flange location to match the configuration at the other side of the vacuum chamber. The reason for the alternate NEG pump placement was a higher conductance for the pump when operated at this location, ensuring low vacuum pressures for operational testing even without actively cooling the atom oven.

Critical to the long-term operational success of the frequency reference is the maintenance of optics cleanliness as well as the mitigation of background laser light that might contribute to noise in the fluorescence readout. Figure 3-7b shows a graphic depicting the light baffle tube designed to address both

concerns. This rectangular structure is designed with several tens of removable baffles, separating zones in which laser light passes through and in which fluorescence detection occurs. In one sense, the tube serves as a traditional light dump, preventing background levels of light from reaching the fluorescence regions located at the ends of the light baffle tube. At the same time, the tube also collects stray calcium as the atomic beam passes through, mitigating unwanted deposition elsewhere in the vacuum chamber. Both the interior of the light baffling structure, as well as the interior of the vacuum chamber including the backs of the in-vacuum chamber R-B optics were coated with Aquadag, a blackening agent, to further reduce background scattered light.

Laser light entering the vacuum chamber from the windows at the bottom of the photograph in Figure 3-7a passes through holes in the light baffle and is steered with reflections off the R-B optics at the back of the vacuum chamber and several optics outside of the vacuum chamber (not pictured) for interaction with the atom beam. For further information regarding R-B laser optics design, see section 3.2.4.3. Optics, laser delivery, and alignment. In the fluorescence detection region, a parabolic mirror identified in Figure 3-7a allows for additional light collection than would otherwise be achieved with fluorescence detection optics located at the vacuum chamber window alone. For more information regarding the fluorescence capture system, see section 3.2.4.4. Fluorescence detection.

Over the course the experimental campaign at NIST, vacuum pressures between 1×10^{-6} Torr and 1×10^{-7} Torr as measured by ion pump current were common during operation with a single atom oven and no active shroud cooling of the atom oven as discussed further in the next section, 3.2.4.2. Atom source. The use of a thermal beam allowed for relaxed vacuum requirements ($\leq1\times10^{-6}$ Torr) as compared with optical lattice clocks, or ion traps, neither of which could be accomplished with relatively simple O-ring design used for CaBOT.

Approved for public release; distribution is unlimited

3.2.4.2. Atom source

On each side of the vacuum chamber, vacuum flanges for atom oven interfacing were welded to be precisely aligned with respect to a common vacuum chamber datum point. The same datum is used to reference the optics plate that serves as the base of the vacuum chamber and that hosts the R-B optics and atom collimator slits, enabling precise alignment of the atom and laser beams. Both ovens are identical and are composed of a heating element and an effusion cell that fits inside the heating element. They were designed with the objective of producing a high flux atomic beam with minimal thermal radiation so as to prevent localized heating of the R-B optics that lead to phase shifts in the laser light.

In order to mitigate thermal radiation, three Ta shielding layers and a water-cooled shroud were designed to surround the heating element of the ovens. The reason for selecting water over air for use as a thermal fluid in the shroud tubing is that water flow is less noisy than air flow, mitigating vibrational perturbations that may impact laser or atom beams. Even so, water cooling is not strictly required for operations, and was not employed during the NIST experimental campaign.

Figure 3-8a depicts effusion cell elements prior to assembly, and Figure 3-8b shows both atom ovens fully assembled, i.e. with Ca-filled effusion cells integrated with the oven body. Figure 3-8c and Figure 3-8d show a single atom oven from a side-view and from a head-on view, respectively. The ovens were designed to accommodate any number of nozzle designs featuring a channel with or without microtubules. The reason was to enable experimental trials with different nozzle geometries to provide different atomic beam fluxes to maximize observed R-B signal and contrast. All nozzle designs featured a narrow dimension along the axis of the laser beam propagation to limit Doppler shifts experienced by the atomic beam.

In addition to determining the flow rate of atoms from the crucible, the nozzle provides an initial degree of atom beam collimation. Nozzles with channel lengths between 1 cm and 3 cm were fabricated for use with the oven: while the 1 cm varieties allow for more Ca to be placed in the crucible, the shorter channel length results in higher atom fluxes and higher rates of Ca depletion. The molybdenum crucibles

Approved for public release; distribution is unlimited

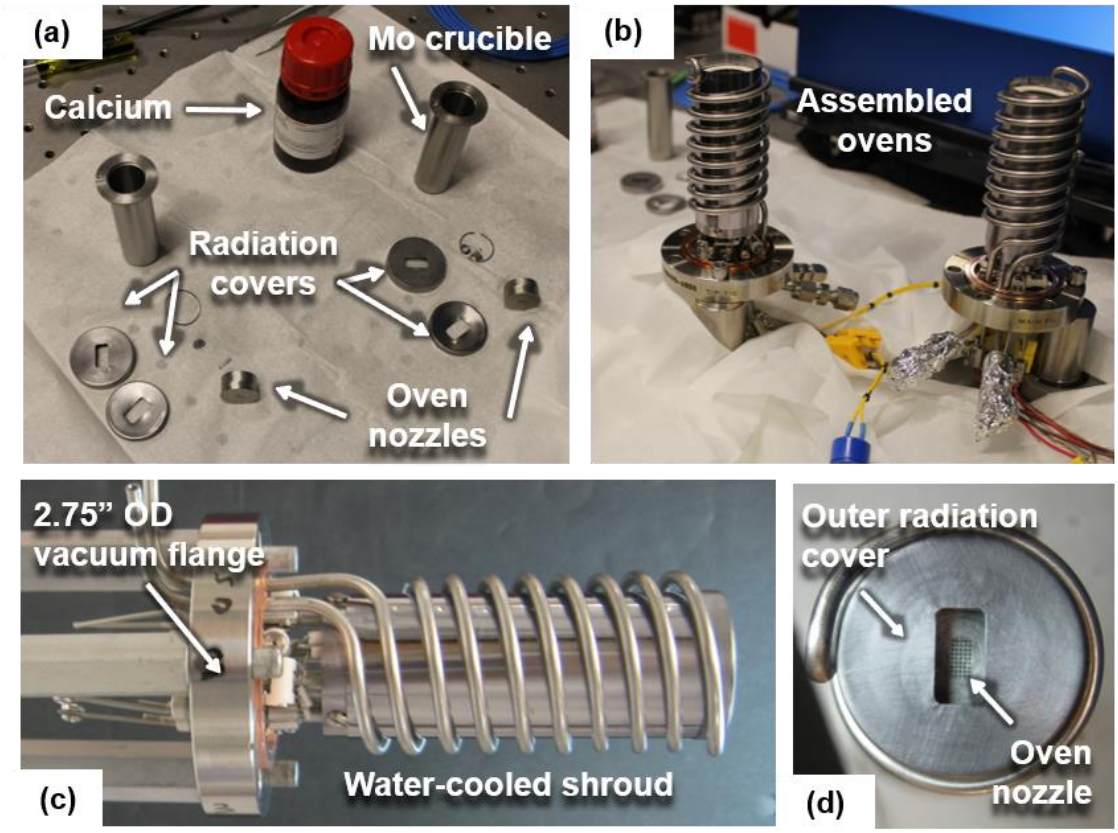

Figure 3-8. CaBOT atom source: (a) effusion cell components before assembly; (b) fully-assembled atom ovens; (c) side view of single atom oven with vacuum flange and water-cooled shroud labeled; (d) head-on view of single atom oven assembled with microtubule nozzle variant.

in Figure 3-8a were designed to have a capacity of 15 cubic centimeters and may be filled with high-purity $\geq 99\%$ calcium to be heated to an average temperature between $500^{\circ}\mathrm{C}$-$725^{\circ}\mathrm{C}$.

Figure 3-9 shows photographs of two different nozzle varieties. (a) and (b) depict a nozzle with microtubules with an inner radius of $r_{tube} = 190\ \mu\mathrm{m}$. (a) depicts the Mo crucible and nozzle alone, and (b) shows this assembly integrated into the rest of the atom oven, with a final Ta cover and the water shroud tubing seen head-on. (c) depicts an integrated atom oven with a nozzle that does not have microtubules but that instead features an open channel that was predominantly used during NIST frequency instability evaluations primarily because of the high atom fluxes and correspondingly large signals observed with this nozzle design.

Approved for public release; distribution is unlimited

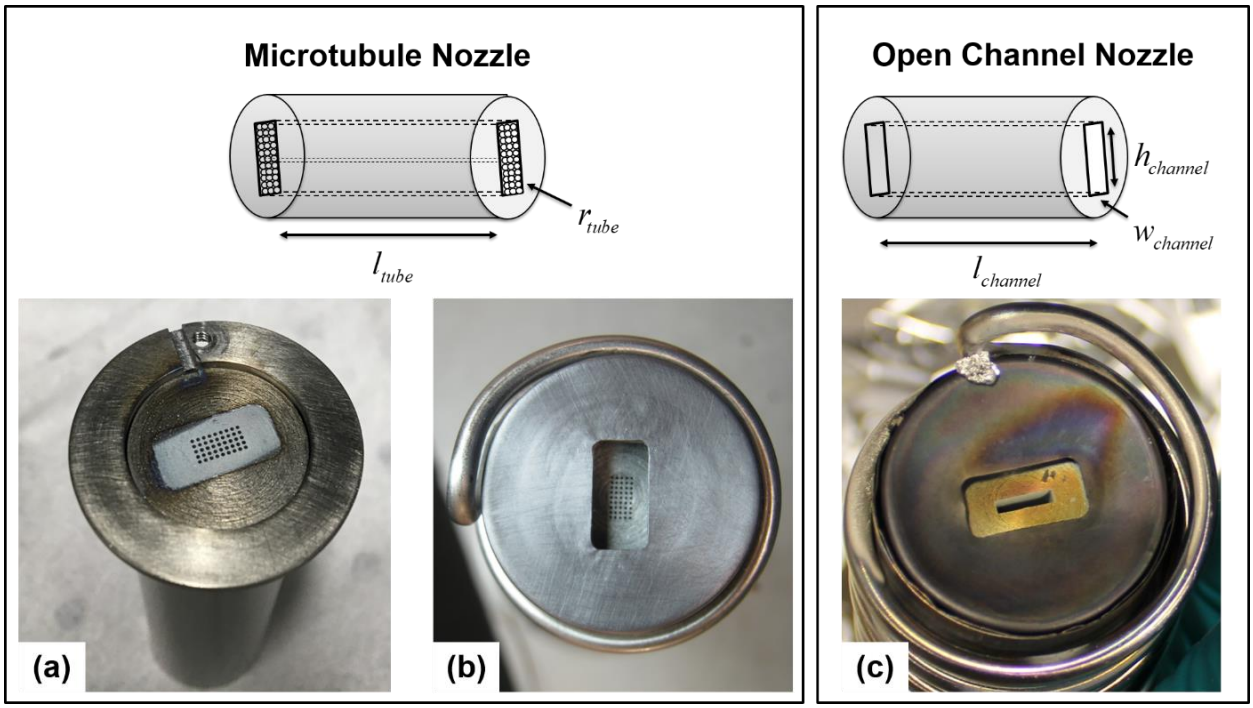

Figure 3-9. CaBOT nozzles with diagrams labeling principal dimensions for a microtubule nozzle (a) and (b) and an open channel nozzle (c). (a) microtubule nozzle resting within a Mo crucible; (b) the nozzle and crucible from (a) integrated into the atom oven with an outer Ta shield and water cooling shroud viewed head-on; (c) the same integrated oven as (b), but with an open channel nozzle.

Approximate calculations for atom flow rates corresponding to various nozzle designs may be used to estimate the lifetime of 15 cc of solid calcium loaded into the Mo crucible at the start of CaBOT oven commissioning. For the case of a nozzle with microtubules, the flow rate $\dot{N}_{tube}$ of each microtubule is expressed as [Loeb 1934]:

$$\dot{N}_{tube} = \frac{2\pi}{3}\frac{\rho v_{gas} r_{tube}^3}{l_{tube}} \tag{3.6}$$

where $\rho = P/(k_B T)$ is density in atoms/cm^3 calculated with the calcium vapor pressure P and temperature T at the high pressure end of the nozzle and where v_{gas} is the mean atomic speed inside the oven crucible in cm/s, r_{tube} is the microtubule radius in cm, and l_{tube} is the length of the tubule in cm. For

Approved for public release; distribution is unlimited

the case of a nozzle with an open channel, the flow rate of atoms through the channel $\dot{N}_{channel}$ is given by [Ramsey 1956 p. 14]:

$$\dot{N}_{channel} = (1/\kappa)\frac{1}{4}\rho v_{gas} A_{channel} \tag{3.7}$$

where $A_{channel}$ is the area of the channel opening and $(1/\kappa)$ is a constant that depends on the geometry of the channel opening. For a long rectangular slit opening with a channel length of $l_{channel}$, channel width of $w_{channel}$ and channel height of $h_{channel}$ in which the channel length far exceeds the channel height $l_{channel} \gg h_{channel}$ and channel width $l_{channel} \gg w_{channel}$, and where the channel height far exceeds the channel width $h_{channel} \gg w_{channel}$, this constant is given by [Ramsey 1956 p. 14]:

$$l \equiv l_{channel}, \quad w \equiv w_{channel}, \quad h \equiv h_{channel}$$

$$1/\kappa = \frac{1}{lwh}\left\{ w^2 h \ln\left[\frac{h}{w} + \sqrt{\left(1+\frac{h^2}{w^2}\right)}\right] + wh^2 \ln\left[\frac{w}{h} + \sqrt{\left(1+\frac{w^2}{h^2}\right)}\right] - \frac{\left(l^2+w^2\right)^{\frac{3}{2}}}{3} + \frac{l^3+w^3}{3}\right\} \tag{3.8}$$

For an oven temperature of $625^{\circ}\,\mathrm{C}$, equations (3.6)-(3.8) are used to populate Table 3-2. Among the nozzle designs considered for CaBOT, four versions are analyzed in the table: a microtubule nozzle design with tube lengths of $l_{tube} = 1.0$ cm and $l_{tube} = 3.0$ cm, and an open channel nozzle design with $l_{channel} = 1.0$ cm and $l_{channel} = 3.0$ cm. The microtubule design had $r_{tube} = 190$ μm with an array of 5x9 (45 total) microtubules, while the open channel design corresponded to $w_{channel} = 0.15$ cm and $h_{channel} = 0.60$ cm for channel width and height measurements, respectively. Mass flow rates are calculated assuming a calcium density of 1.55 g/cc for solid calcium pellets loaded into the molybdenum crucible.

The analysis shown in Table 3-2, quantifies a comparison between nozzle design options: open channels produce higher flow rates than nozzles with microtubules, and shorter nozzle tube and channel lengths produce higher flow rates. This may be understood from a geometric perspective: the solid viewing angle through a short channel is larger than that for a long channel. As the channel is lengthened, the solid

Approved for public release; distribution is unlimited

angle into which atoms are allowed to exit becomes smaller. In other words, longer channels collimate the beam to a greater extent and fewer atoms are able to exit the oven in much the same way that the microtubules collimate the atomic beam.

Table 3-2. Nozzle design flow rate and lifetime approximations.

	Atom flow rate (atoms/s)	Mass flow rate (g/s)	15 cc calcium lifetime (days)
Microtubules, $l_{tube} = 1$ cm	1.9×10^{16}	1.3×10^{-6}	210
Microtubules, $l_{tube} = 3$ cm	6.4×10^{15}	4.2×10^{-7}	640
Open channel, $l_{channel} = 1$ cm	2.3×10^{17}	1.5×10^{-5}	17
Open channel, $l_{channel} = 3$ cm	2.2×10^{16}	1.5×10^{-6}	180

The open channel $l_{channel} = 1.0$ cm design was selected for use in frequency reference evaluations at NIST given a priority to maximize atom flow rate and the corresponding atom interferometry signal. The width and height of the channel in this design were $w_{channel} = 0.15$ cm and $h_{channel} = 0.60$ cm respectively. Operations lasting longer than 17 days were possible, indicating that the open channel results included in Table 3-2 are conservative. For long term operations, a more efficient nozzle would be recommended.

Figure 3-10 depicts the atom source, collimation, and fluorescence detection geometry for one of the two CaBOT ovens. The CaBOT geometry is symmetric, so the geometry depicted is representative of both configurations. After exiting the nozzle at the left of the figure and traversing the interaction region, the atom beam is collimated by an aperture card 22 cm downstream from the oven nozzle. The collimating aperture is mounted to a three-point stand on the optics plate inside the vacuum chamber in a position referenced to the common vacuum chamber datum. The collimator mount was designed to accommodate replaceable aperture cards that may be screwed into place. During testing at NIST, an aperture with

Approved for public release; distribution is unlimited

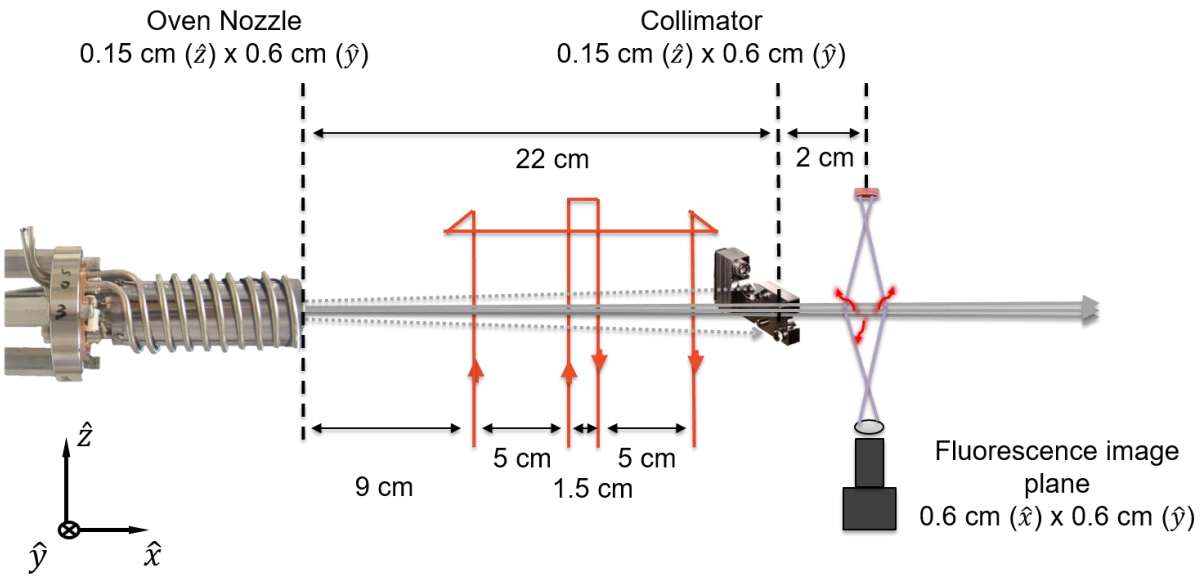

Figure 3-10. CaBOT atom source, collimation, and detection geometry.

dimensions 0.15 cm x 0.6 cm were selected to match the dimensions of the open nozzle channel width and height dimensions, respectively. Following collimation, atomic fluorescence is captured 2 cm further downstream with a 1-f imaging system capturing a 6 mm x 6 mm area of the fluorescent beam with a 6 mm x 6 mm imaging plane, described further in section 3.2.4.4. Fluorescence detection. With this design, a Doppler profile full-width half max (FWHM) of 5 MHz was observed for an atom oven temperature of $625^{\circ}\mathrm{C}$, as described further in section 3.3.2. Integration of R-B optics and test laser at NIST.

3.2.4.3. Optics, laser delivery, and alignment

Principal design objectives for the optics of CaBOT include preservation of beam parallelism and enforcement and preservation of atom and laser beam alignment. The first objective is addressed with the use of penta-mirrors, penta-prisms, and a roof-mirror, each of which steers the R-B laser beam precisely 90º or 180º for penta- and roof- optics, respectively. The use of these monolithic structures allows for beam parallelism across all four R-B lasers even with input steering angle deviations. The second objective is primarily addressed by means of construction of the entire optics train as well as the atom collimation apertures on a single, common baseplate, including both in-vacuum and out-of-vacuum components. By

Approved for public release; distribution is unlimited

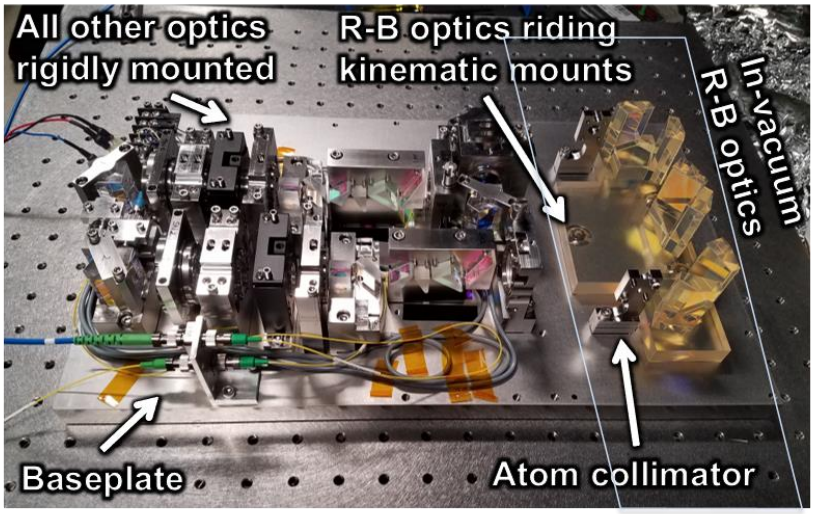

Figure 3-11. Populated CaBOT optics baseplate. All external optics are rigidly mounted while in-vacuum R-B optics are kinematically mounted; the approximate area of the vacuum chamber is identified with a narrow blue box.

using a common datum on the vacuum chamber structure to reference the placement and orientation of the atom ovens, the atom beam collimation apertures, and R-B optics, atom-laser beam geometry is enforced. The use of rigid, monolithic optics mounts with three contact points for all elements mounted on the common baseplate ensures the preservation of laser beam geometry, and to ensure the R-B optics inside the vacuum are not stressed with gravity, pressure, or thermal loads, the R-B optics are kinematically mounted to the baseplate at locations also referenced to the common vacuum chamber datum.

The floor of the vacuum chamber was designed as a flat plate that extends beyond the vacuum chamber, forming the baseplate of optical elements both inside and outside vacuum. This design choice minimized mechanical tolerance stack-up over the laser beam propagation distance, reducing misalignment risk. Figure 3-11 shows a photograph of the populated baseplate without the vacuum chamber sides or top. Diffractive optics external to the vacuum chamber were rigidly mounted, as opposed to traditional thumb-screw lens mounts. Optical mounts were designed with three points of contact and with sturdy construction to minimize drift in the optical beam path over continuous, long-duration operation of the frequency reference. Multiple locks for each mount aimed to reduce risk of long term drifts in alignment from mechanical slip arising from gravity or other environmental factors. Relative alignment of the atom beam

Approved for public release; distribution is unlimited

and the optical beams must be well-defined and highly stable. The atom beam geometry is constrained by atom collimators that were mounted also with three contact points on the same optics base plate on which the optical mounts are placed, ensuring mutually consistent datum referencing.

Unlike other thermal Ca R-B optical atomic clock efforts like [McFerran and Luiten 2010] and [Fox *et al.* 2012], both of which place all critical optics outside of vacuum, the CaBOT frequency reference was designed with some optics inside the vacuum chamber. This design was chosen for optical phase stability: reducing in-air propagation reduces optical frequency shifts corresponding to atmospheric disturbances. Additionally, reducing the number of air-to-vacuum interfaces reduced risk of misalignment of the parallel R-B traveling waves from index of refraction changes along the path of laser propagation.

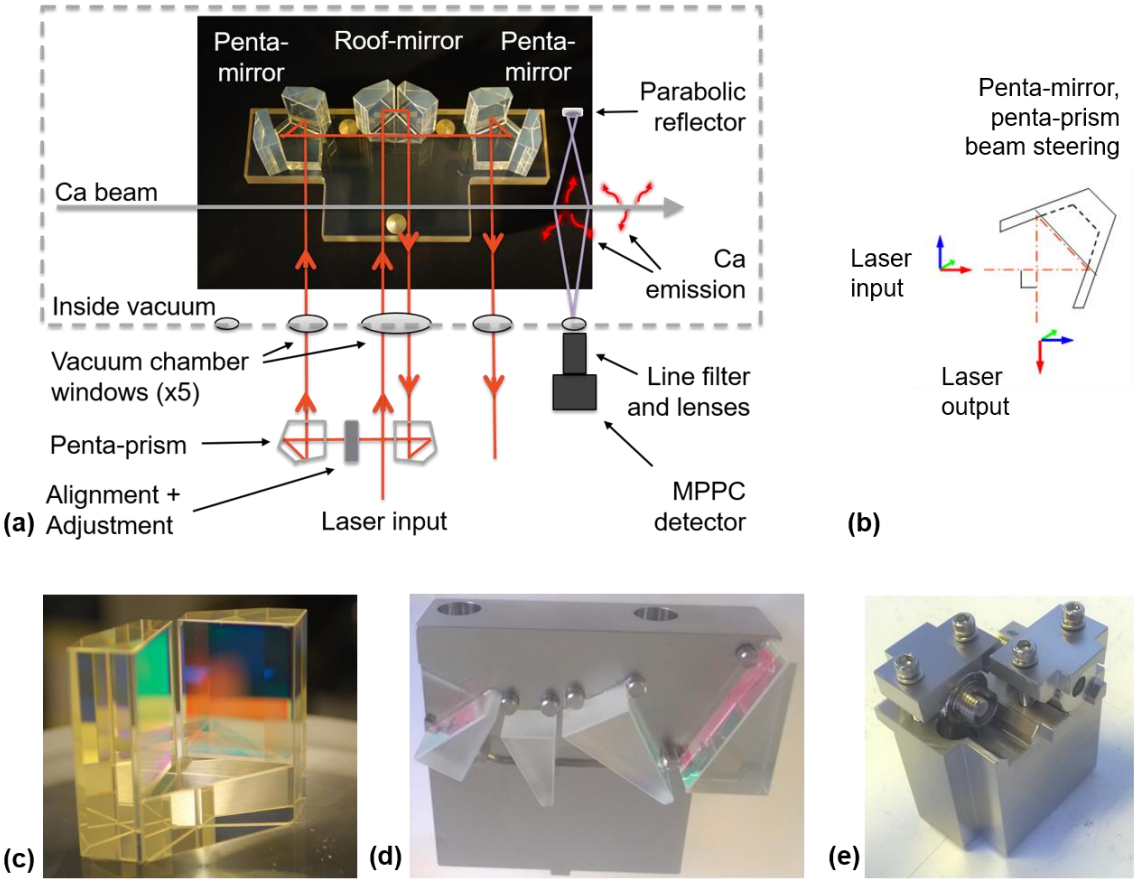

Figure 3-12. CaBOT optics. (a) in-vacuum R-B optics and diagram depicting R-B geometry; (b) diagram depicting penta-mirror and penta-prism steering; (c) detail of a penta-mirror; (d) detail of an athermalized anamorphic prism pair beam expander; (e) detail of a dual fiber collimator mount.

Approved for public release; distribution is unlimited

Figure 3-12 contains photographs and graphics depicting the CaBOT optics. (a) shows a photograph of the in-vacuum R-B optics with additional elements and the laser pathway labeled. The configuration shown matches the operational geometry employed in NIST experiments. (b) depicts the action of the penta-mirrors in-vacuum and the penta-prisms outside the vacuum, which steer the laser beam at a right angle while maintaining polarization, and (c) shows a photograph of a single penta-mirror for reference. At the beginning of the optical train, a dual fiber collimator mount, pictured in (e) provides an interface for laser light to be collimated into a beam for free space propagation. Like the optical mounts, this mount was designed for robustness and stability with three contact points for interfacing with the baseplate. The laser beam exiting these collimators is circular with a $1/e^2$ beam diameter of 1.5 mm, though an adjustable collimator may be employed to vary this waist size. Risley prisms and tip-tilt mounts are used to angle the laser beam along the input train, and an athermalized anamorphic prism pair beam expander, pictured in (d), expands the beam along the vertical axis by a factor of 5.5x to produce an elliptical beam shape. The anamorphic prism pairs provide mitigation against thermal expansion of the mount and low-CTE glass, further improving the design's robustness to environmental fluctuations.

The in-vacuum R-B optics were designed to ensure a high degree of parallelism involving discrete, monolithic optical elements like the penta-mirror shown in Figure 3-12c [Sinclair, Kelsey, and Stoner 2017]. Each individual element was optically bonded to a common, low coefficient of thermal expansion (CTE) glass. This carrier glass plate was then kinematically mounted to the common baseplate to account for differential thermal expansion and vacuum pressure- and gravity-induced loading. One of three kinematic mounts is labeled in Figure 3-11. The penta-mirrors and roof-mirror used in-vacuum were paired with two penta-prisms located just outside vacuum, which together with an optical mount placed for two degree-of-freedom adjustment, steer a single laser beam into the four R-B parallel lasers for atom interferometry. After the laser exits the vacuum chamber for the final time, the laser beam was designed to be picked off by a photodiode for power modulation through feedback control.

Approved for public release; distribution is unlimited

Penta-mirrors and penta-prisms are critical to achieving reliable, stable parallelism of the laser beams given their function of inducing a 90º deflection between incident and outgoing beams independent of the input beam's orientation with respect to the optic. This is graphically depicted in Figure 3-12b. This is the principal reason for their selection over a simple monolithic ULE mirror.

The difference between the penta-mirror and penta-prism concerns changes to the index of refraction in the optical pathway. For the penta-mirrors inside vacuum, the optical field does not pass through glass and is instead reflected between the mirrors while remaining in vacuum. Alternatively, steering with penta-prisms involves a change in the index of refraction from the air to the glass optic back to air as the light is steered within the penta-prism. These changes of index, as well as any remaining alignment problems between co-propagating laser pairs in the R-B geometry, may be addressed with a

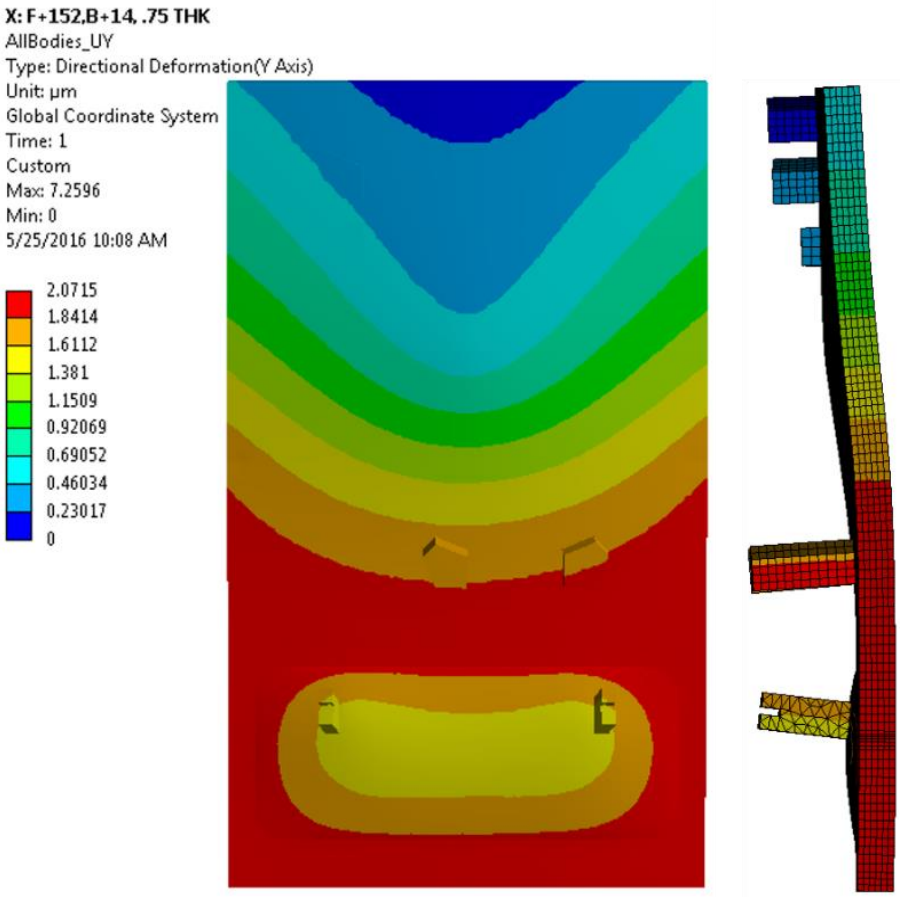

Figure 3-13. Finite element analysis for CaBOT optics plate for deflection under the influence of vacuum pressure and gravity.

Approved for public release; distribution is unlimited

Risley prism pair used for adjustment and alignment between the penta-prisms outside the vacuum as depicted in Figure 3-12a.

One implication of using the same stainless steel baseplate as an optics plate both outside and inside vacuum is pressure-induced deflection. To address this effect, finite-element analysis was conducted by Draper staff for proposed baseplate designs to determine the deflection of the baseplate and associated beam steering implications for the final CaBOT optics plate design assuming gravity and vacuum pressure loading. Figure 3-13 depicts the results of this analysis for 0.75" stainless steel optics plate. The maximum deflection calculated was just over $2\ \mu m$ with $< 7\ \mu rad$ pitch (rotation about $\hat{x}$) and yaw (rotation about $\hat{y}$) angular deviation of the laser beam from the designed optical path, indicating that atom-laser alignment and laser beam parallelism may be preserved with the existing baseplate design. In the figure, the baseplate is oriented with the vacuum chamber at the bottom, with plate deflection shown corresponding to vacuum forces acting on the center of the chamber floor to raise the plate as indicated. With this minimal deflection, the design with 0.75" optics plate thickness was determined to be sufficient.

3.2.4.4. Fluorescence detection

Figure 3-14 shows a photograph of three fluorescence detectors considered for CaBOT including a Thorlabs Photo-Multiplier Tube (PMT) and Hamamatsu's Multi-Pixel Photon Counter (MPPC) modules, one with an active detection area of 3mm x 3mm ("Hamamatsu MPPC 3x3"), and another with an active detection area of 6 mm x 6 mm ("Hamamatsu MPPC 6x6"). Aside from the advantage MPPCs provide with their small SWaP, the chip-based modules feature lower dark currents than PMTs at elevated temperatures and feature good detection sensitivity. Each MPPC module is hard-wired with a pre-selected gain setting and a mechanism to automatically disconnect power from the sensitive detector array if incident light exceeds a threshold.

Approved for public release; distribution is unlimited

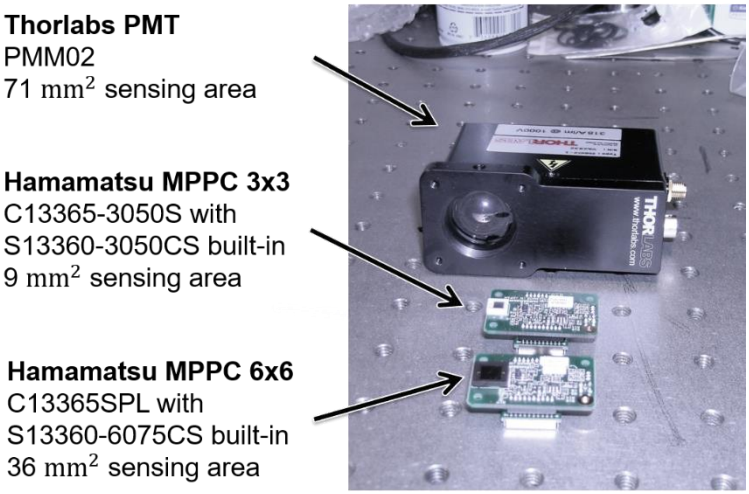

Figure 3-14. Fluorescence detectors considered for CaBOT; Hamamatsu MPPC 6x6 selected.

Even though the PMTs offer variable gain and higher detector sensitivity, and even though the detector collection area is larger for the PMT, the MPPCs are selected for their greater versatility and low dark currents at elevated operational temperatures. All experimental data discussed in section 3.4. CaBOT frequency measurements and instability analysis involve the use of the 6 mm x 6 mm MPPC depicted at the bottom of Figure 3-14.

Fluorescence capture occurs at either end of the vacuum apparatus at a location 35 mm downstream from the final atom-laser interaction site as depicted graphically in Figure 3-10. A lens tube mounted to each of the outermost vacuum chamber windows was designed to house a bandpass filter and a biconvex lens with a clear aperture of 24 mm. By spacing the biconvex lens two focal lengths both from the atom beam and the detector plane, a 6mm x 6mm area of the atomic beam is imaged on an equal area at the Hamamatsu MPPC pictured at the bottom of Figure 3-14 ("Hamamatsu MPPC 6x6").

The half-angle field of view for the imaging system is $\mathrm{FOV}_{1/2} = 45.9$ mrad , corresponding to a total solid angle of $\Theta = 2\pi\left[1-\cos\left(\mathrm{FOV}_{1/2}\right)\right] = 7.68\times10^{-3}$ sr . This accounts for approximately 0.06% of the total fluorescence emitted in 4π sr from the center of the fluorescence capture region. This is the proper figure of merit since the Ca optical clock transition's spontaneous emission profile is spatially

Approved for public release; distribution is unlimited

homogeneous. Inside the vacuum, a parabolic reflector was placed opposite the fluorescence capture lens tube, providing a two-fold improvement in collected light, yielding an estimated 0.12% collection fraction.

Sensitivity analyses were conducted at Draper for PMT and MPPC modules, using an unfocused laser source outputting 26 mW optical power at a throw distance of 40.6 cm (16”). For each detector tested, a lens tube forward of the detector contained a line filter and neutral density filters to reduce the incident light to pW scale incident power. This source of light was calibrated to have an intensity of $1.70\times10^{-7}\ \mathrm{W/m^2}$ using a Thorlabs digital handheld optical power and energy meter. The Hamamatsu MPPC modules output a signal with a bandwidth of 2 MHz. A chip-sized 20 kHz low-pass RC filter fabricated at Draper was used to filter MPPC output. The Thorlabs PMT has a bandwidth of 20 kHz and was not filtered further. A laboratory oscilloscope was used to measure detector signals.

The average sensitivity measured across five Hamamatsu MPPC 6x6 detectors was $2.6\times10^{9}\ \mathrm{V/W}$, with a variance of $0.0066\times10^{9}\ \mathrm{V/W}$. To compare gross noise between the MPPC and PMT, the PMT was set to a gain at which a sensitivity of $2.3\times10^{9}\ \mathrm{V/W}$ was measured. At these sensitivities, the fractional signal standard deviation (i.e. the signal standard deviation divided by the signal mean) was measured to be lower for the Hamamatsu MPPC 6x6 (0.09) than for the PMT (0.13), indicating the high level of performance available from the chip-based MPPC sensor.

3.3. CaBOT frequency reference integration

3.3.1. Vacuum chamber commissioning

3.3.1.1. Atom oven commissioning

A staged integration approach was employed to reduce risk leading to experimental operations of the frequency reference. Before integrating the in-vacuum R-B optics as described in section 3.2.4.3. Optics, laser delivery, and alignment, atom ovens were commissioned with an engineering model of the in-

Approved for public release; distribution is unlimited

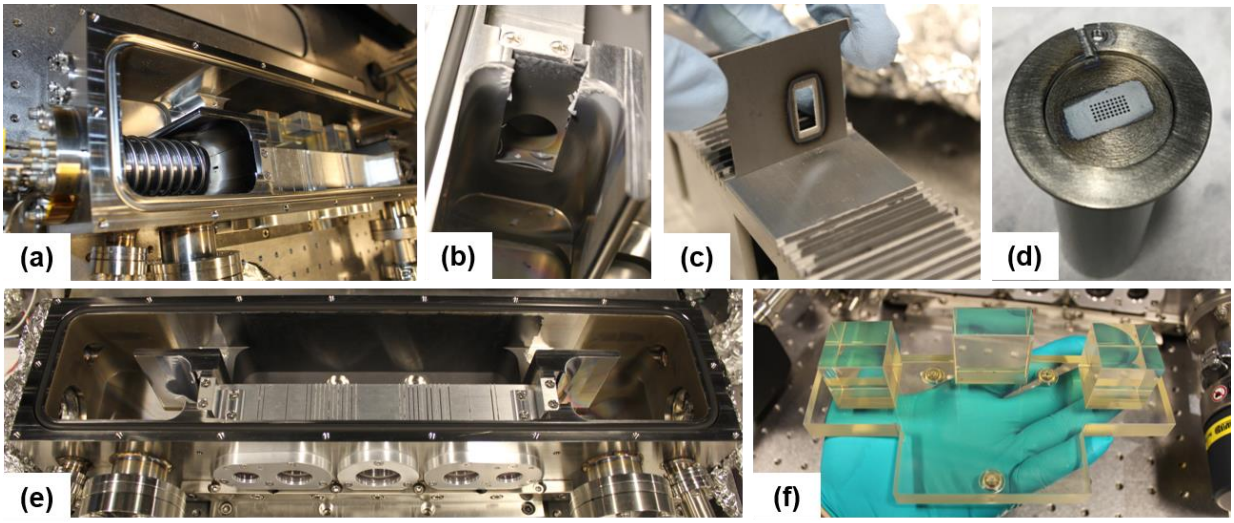

Figure 3-15. CaBOT vacuum operations for calcium oven commissioning. (a) interior view shortly after removing the vacuum chamber lid following operations (b) view of the thermal baffle with slot removed, showing atom beam passage to light baffle; (c) light baffle card showing ring of calcium deposition (d) opposing atom oven nozzle with calcium deposition; (e) interior view of vacuum chamber after operations with engineering optics model removed; (f) engineering optics model.

vacuum optics. One objective was to observe calcium deposition after sustained operations on the order of days with calcium oven mean temperatures between $500^{\circ}\mathrm{C}$-$700^{\circ}\mathrm{C}$, as well as to ensure that the R-B optics and the local region in the vacuum chamber near the optics would remain clear of deposition. A second objective was to ensure that the atom ovens were aligned so that the principal atom propagation vectors were anti-parallel.

Figure 3-15 shows a series of photographs taken after this initial oven commissioning phase for the oven used in the NIST test campaign. (a) shows a perspective of the interior of the vacuum chamber after removing the lid. The white area with a visible black slit just forward of the oven is oxidized calcium on the removable slot of the thermal baffle, with a slit for the passage of the atomic beam along the light baffle rectangular structure through the vacuum chamber. An image with the atom oven, thermal baffle slot removed to show the atom beam's entrance to the light baffle is shown in (b). After removing the engineering optics model shown in (f) and inspecting the local region around the optics as shown in (e) no visible trace of calcium deposition was found, indicating that the actual in-vacuum optics would also remain clean throughout nominal operations.

Approved for public release; distribution is unlimited

In order to assess the pointing of the atom beam, the optical baffle cards were individually inspected as shown in (c). The calcium deposition ring around the open slot in the card shown indicates that the slot was well aligned with the calcium beam. The best indication of atom beam steering within the vacuum chamber is evidence of calcium deposition on the opposite oven's nozzle, as pictured in (d). The angle between the nozzle orientation and the deposited calcium indicates a relative angular azimuthal difference between the orientation of the two ovens. Even so, the centroid of the deposited calcium overlaps with the nozzle center, indicating good alignment for the oven tested. Finally, (e) and (f) illustrate key observations regarding calcium deposition: neither the region around the engineering model R-B optics, nor the optics themselves indicated any visible trace of calcium, indicating that calcium containment was successfully achieved with the vacuum chamber design.

3.3.1.2. Uncollimated atom beam and single laser interactions

During initial vacuum operations without the final R-B optics, a 100-kHz linewidth Toptica 657 nm laser was used for frequency reference subsystem commissioning involving a single atom-laser interaction site. Figure 3-16 depicts the Doppler profile measured when sweeping the laser frequency across

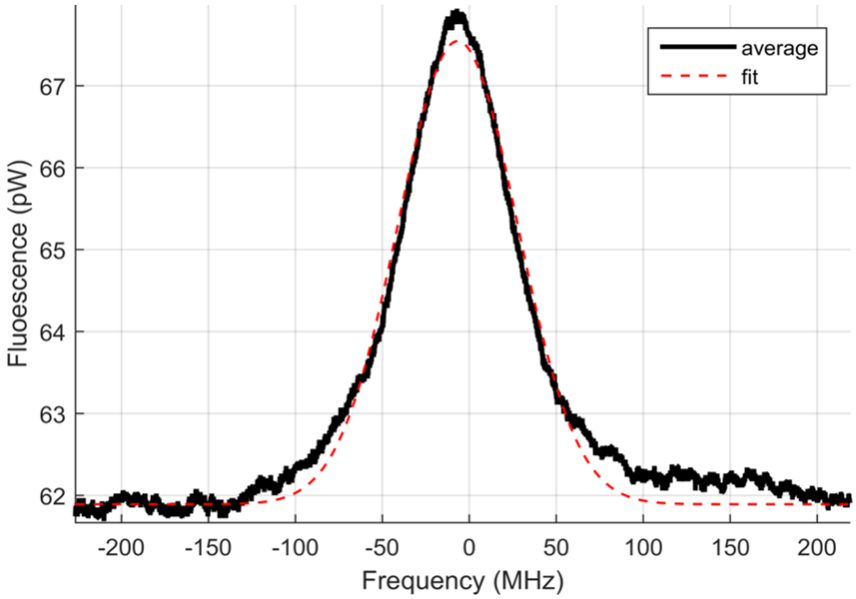

Figure 3-16. Doppler profile data and Gaussian fit with a single atom-laser interaction and no atom beam collimation.

Approved for public release; distribution is unlimited

the atomic resonance and when no atom beam collimation was used beyond the collimation that is derived simply from the nozzle and light baffle card slots. Data (black) is depicted along with a Gaussian fit (red dotted) in the figure. In this experiment, atoms from the right-hand side atom oven were utilized for interaction with a laser beam introduced along laser path #4 as numbered in Figure 3-5. Fluorescence was captured by the same system described in section 3.2.4.4. Fluorescence detection without the use of an in-vacuum parabolic reflector, i.e. with just the collection optics outside the vacuum chamber.

As a quick verification check that the fluorescence signal observed was indeed an atom-based Doppler profile, a correlation was probed between the beam steering angle and the central resonance frequency as indicated in the Toptica laser user interface. Figure 3-17 depicts this rapid verification study. (a) depicts a graphical representation of the experimental setup. In this instance, the right-hand atom oven

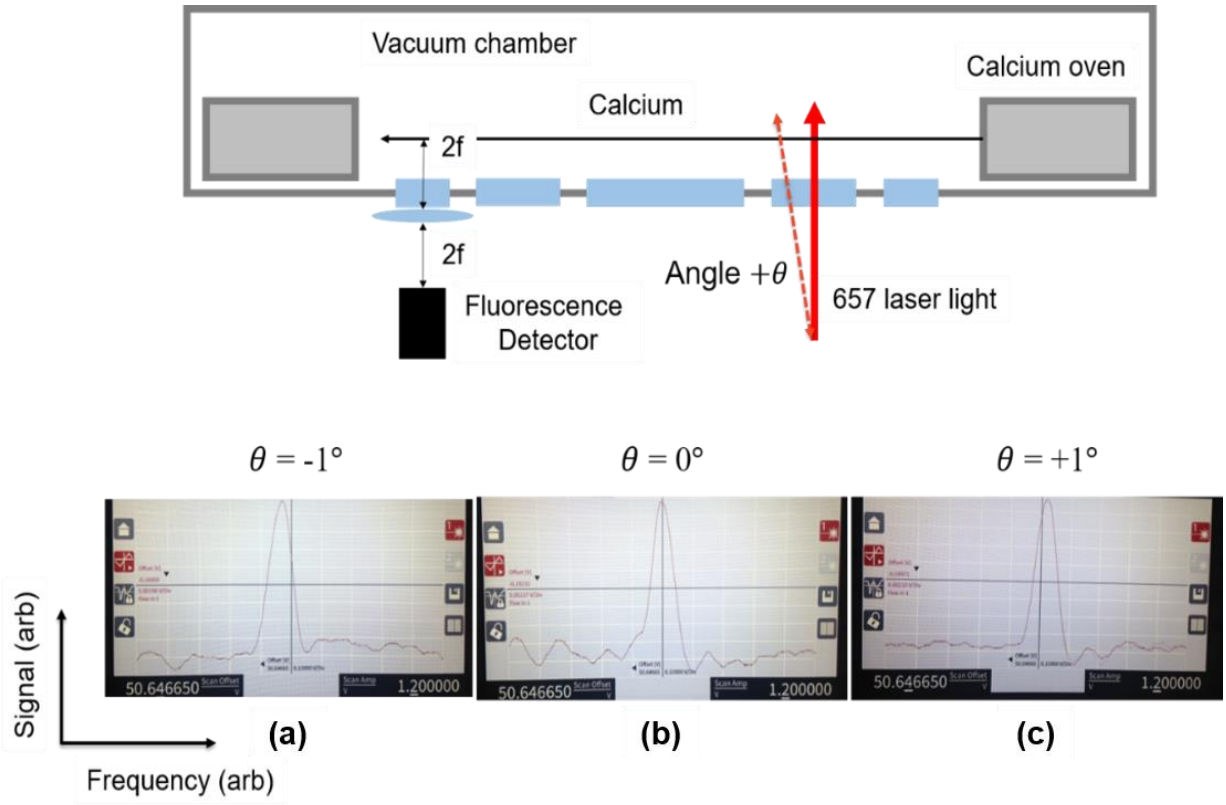

Figure 3-17. Verification of correlation between laser steering and fluorescence signal; (a) Doppler shift experimental set up; (b) Doppler profile measurement for laser input angle of $\theta \approx -1^{o}$, (c) $\theta \approx 0^{o}$, and (d) $\theta \approx +1^{o}$.

Approved for public release; distribution is unlimited

was used, and the laser input angle was changed by an angle θ in order to test to see if there were any corresponding movement of the peak as would be expected if the fluorescent signal was indeed a Doppler feature. (b)-(d) depict the observed fluorescence signal as a function of laser frequency at three laser angle settings. As can be seen, with a change in input laser angle, a Doppler shift in both directions can be observed, establishing without a doubt that the feature observed was indeed the atom-based Doppler resonance.

Returning to the data in Figure 3-16, it was observed that, when unmitigated, background laser light produces 62 pW of power at the fluorescence detector, while the Doppler feature rises above the background light another 5.7 pW. For these experiments, the average oven temperature was $725^{\circ}\mathrm{C}$, representing the hot extreme of oven operation and hence the highest atom flux that might be expected from the CaBOT system with microtubule nozzle design shown in Figure the nozzle utilized, in this case one with microtubules as shown in Figure 3-9a-b and 3-15d.

This experiment indicated that vacuum pressure was found to be sufficiently low, measured to be between 1×10^{-6} Torr and 1×10^{-5} Torr with ion pump current. Secondly, background light was found to be substantial, motivating efforts to mitigate the high intensity of scattered light.

3.3.1.3. Background light mitigation

Background light scatter was qualitatively assessed by introducing laser light to the fully-populated optics plate isolated from the vacuum chamber as depicted in Figure 3-11. A qualitative study of scatter

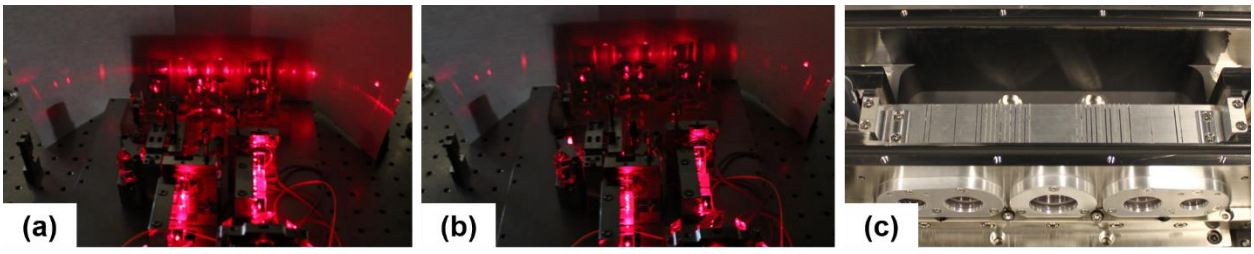

Figure 3-18. (a) Light scatter from optics without background mitigation; (b) light scatter from optics with three baffle cards placed in air-side locations; (c) blackening agent used inside vacuum chamber and also to coat the back surface of R-B optics in-vacuum to further reduce background light.

Approved for public release; distribution is unlimited

light is depicted in (a) and (b) of Figure 3-18. These photographs depict the background scatter present just behind the in-vacuum optics as indicated by the laser light that was visible on a piece of white paper. (b) shows the effect of placing three baffle cards at locations on the optics plate that are nominally out of vacuum. The baffle card placement resulted in a perceptible reduction in background scatter. To further reduce background scatter, the vacuum chamber back wall and floor were painted with Aquadag, a blackening agent as shown in (c). The same blackening agent was used on the back of the in-vacuum optics to further reduce transmitted light contributing to the background light scatter signal measured in initial Doppler feature measurements.

3.3.1.4. Typical vacuum chamber and temperature measurements

For each experimental run with an operational vacuum, commissioning activities included elevating the vacuum chamber and atom oven(s) in temperature ("bakeout") to allow the roughing pump to remove excess particles and to prepare for NEG pump activation. Following NEG pump activation, bakeout heaters were removed and the atom oven(s) were heated to operational temperature for experimental operations.

In order to assess the thermal response of the system at various locations to changes in oven temperature, we placed RTDs at various locations inside and outside the vacuum system and measured temperature vs. time subsequent to oven temperature adjustment. During one vacuum chamber commissioning effort, a single atom oven was prepared for experiments that involve a dry operation of the ovens, i.e. without water-cooling of the oven shroud. An RTD was placed inside the vacuum chamber near the active atom oven, taped to the inactive water cooling shroud with vacuum-compatible Kapton tape, and three more RTDs were taped to the R-B optics inside the vacuum chamber. Four additional RTDs were placed at various locations on the optics baseplate, with a final sensor was placed in a location to sense ambient laboratory temperatures.

Figure 3-19 depicts temperature data as well as the locations of each of the RTD sensors on photographs of the experimental hardware. The temperature data begins with initial commissioning of the

Approved for public release; distribution is unlimited

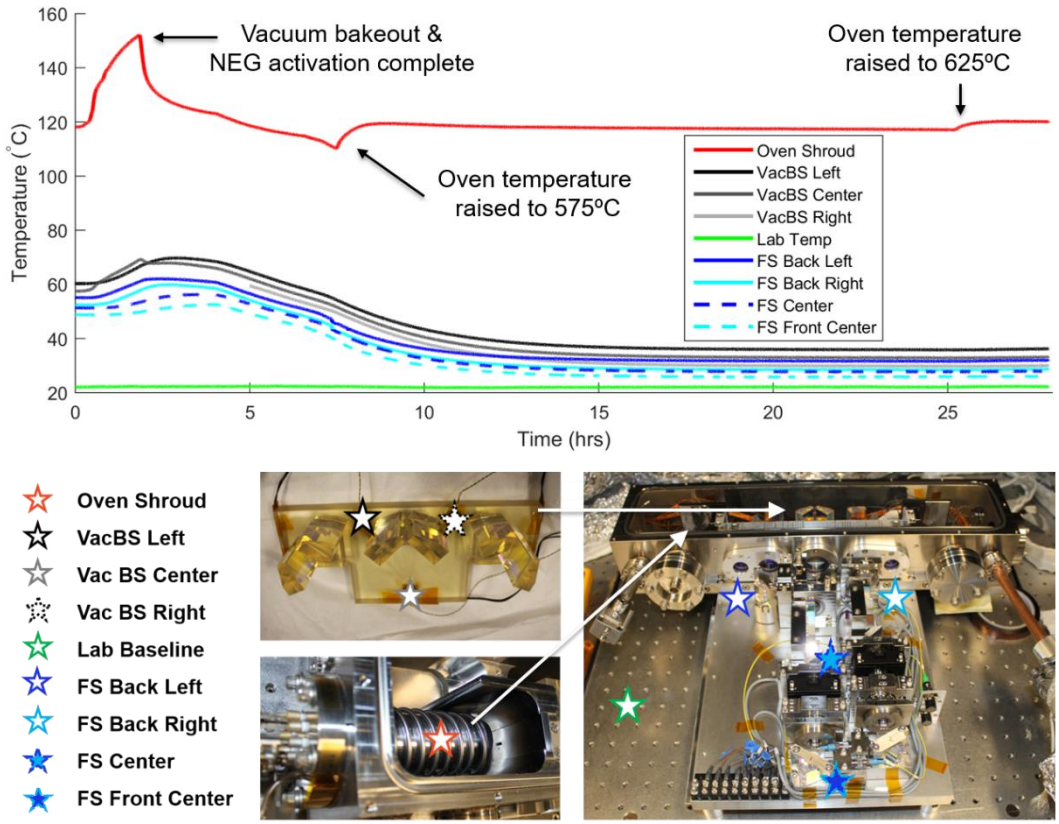

Figure 3-19. Thermal data corresponding to vacuum system commissioning with dry atom oven operations, and with temperature data referenced to the ambient laboratory temperature. Photographs indicate the locations of temperature sensors different temperatures.

vacuum chamber, just before NEG pump activation, when the vacuum chamber and entire frequency reference system is still wrapped in insulating material and heated by resistive Variac heaters. As indicated in the labeling of the plot, the temperature data extends beyond the end of bakeout operations when insulating material and Variac heaters are removed from the exterior of the apparatus, and into nominal experimental operations with the raising of atom oven temperatures.

An initial operational temperature of $575°C$ was selected for the atom oven and the system was allowed to cool down to nearly steady state. With a mean atom oven temperature of $575^{\circ}C$ and a laboratory (uncontrolled) temperature of $22^{\circ}C$, the outer shroud was measured at steady state to be $117^{\circ}C$. Following this, the atom oven temperature was raised once again to an average temperature of $625°C$. With a mean atom oven temperature of $625^{\circ}C$ in an uncontrolled laboratory environmental temperature

Approved for public release; distribution is unlimited

$\cong 22^{\circ}\mathrm{C}$, the outer shroud temperature was measured to be $120^{\circ}\mathrm{C}$. With the use of water cooling, the oven shroud temperature is expected to be a cooler $70^{\circ}\mathrm{C}$. Even without active temperature stabilization, the frequency reference physics package was observed to be insensitive to ambient laboratory temperature fluctuations on the order of $0.1°\mathrm{C}$.

Vacuum pressures varied between 1×10^{-6} Torr and 1×10^{-5} Torr when operating the NEG pumps in their nominal positions. In order to achieve low vacuum pressures for NIST testing, a re-configuration of the vacuum system to place a NEG pump at the location of one of the atom ovens yielded higher conductance for pumping and lower operational vacuum pressures.

3.3.2. Integration of R-B optics and test laser at NIST

The Draper CaBOT frequency reference performance evaluation at NIST involved integration of a test laser featuring a linewidth of several Hz at 657 nm to the optics train of the CaBOT system. A photograph of the integrated CaBOT frequency reference at NIST is shown in Figure 3-20.

Only one of the two laser delivery pathways was populated, as only one k-vector (one laser direction) was used for initial alignment and R-B signal optimization. NIST laser light was introduced to the system by means of the yellow and green pigtail at the bottom-right of the optics baseplate. The electrical terminals on the bottom-left of the baseplate provided power to operate photo-diodes in the optics train, which were illuminated by 1% pick-offs and used for optical power control with a NIST servo. Back-reflections from the flat pigtail (green connector) were utilized in another servo loop for phase stabilization of the red laser light. As experimentally confirmed, operations of the CaBOT system with NIST test laser light could only generate stable Ramsey-Bordé fringes with both amplitude and phase modulation servos active.

Approved for public release; distribution is unlimited

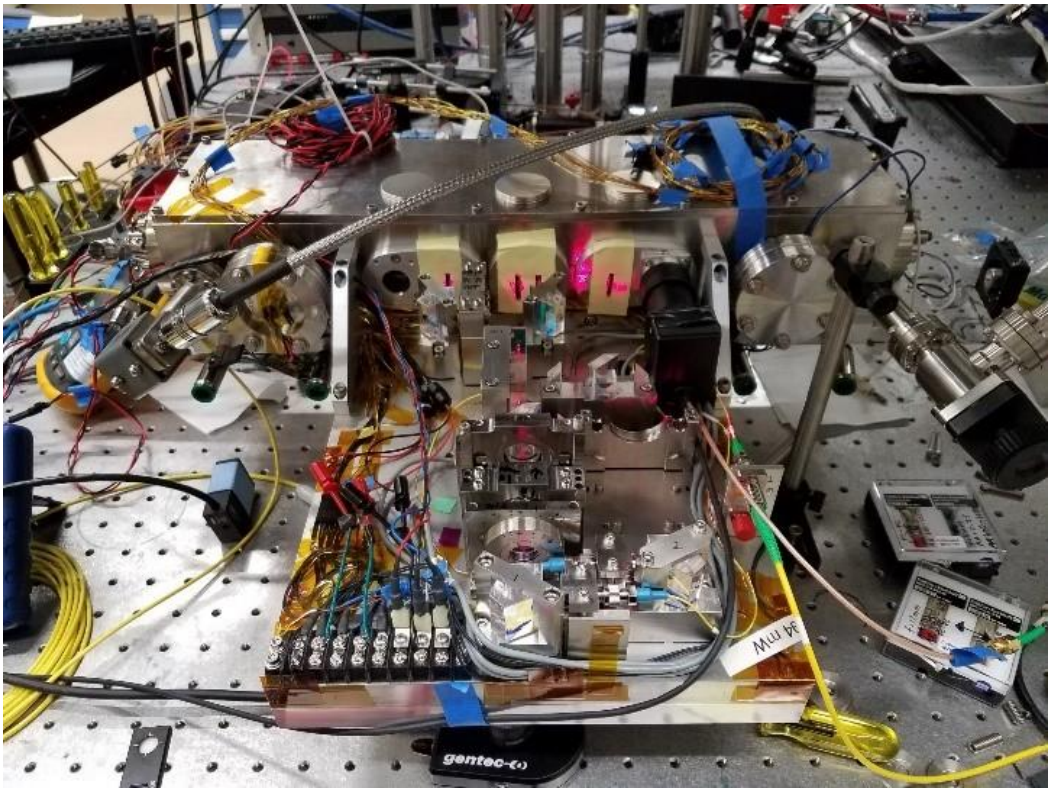

Figure 3-20. Draper CaBOT frequency reference integrated with NIST test laser.

With all vacuum chamber components installed for nominal operations with a single laser k-vector and atom beam, the optics were manually adjusted to produce R-B fringes in the fluorescence signal, and baffles were placed at the out-of-vacuum optics to block stray light contributing to background scatter. Figure 3-21a-b depicts the fluorescence signal across a detuning range to view the entire Doppler profile. The measured signal has a FWHM of 5.0 MHz. Based on the collimation geometry and operational temperature, the FWHM predicted for this interaction is given by equation (1.3) [equation 8-8 from Foot's *Atomic Physics* 2005] $\Delta\nu_{FWHM}\big|_{theory} \simeq \frac{1.2}{1.7}\frac{\alpha v_{atom}}{\lambda} = 5.5\ \text{MHz}$ where α is the collimation angle along the laser beam propagation axis, v_{atom} is the most probable atom velocity, and λ is the clock transition wavelength. A Gaussian shape scaled to the same magnitude with a FWHM corresponding to theoretical prediction is shown (dotted) along with the experimental data (gray) in Figure 3-21a.

Approved for public release; distribution is unlimited

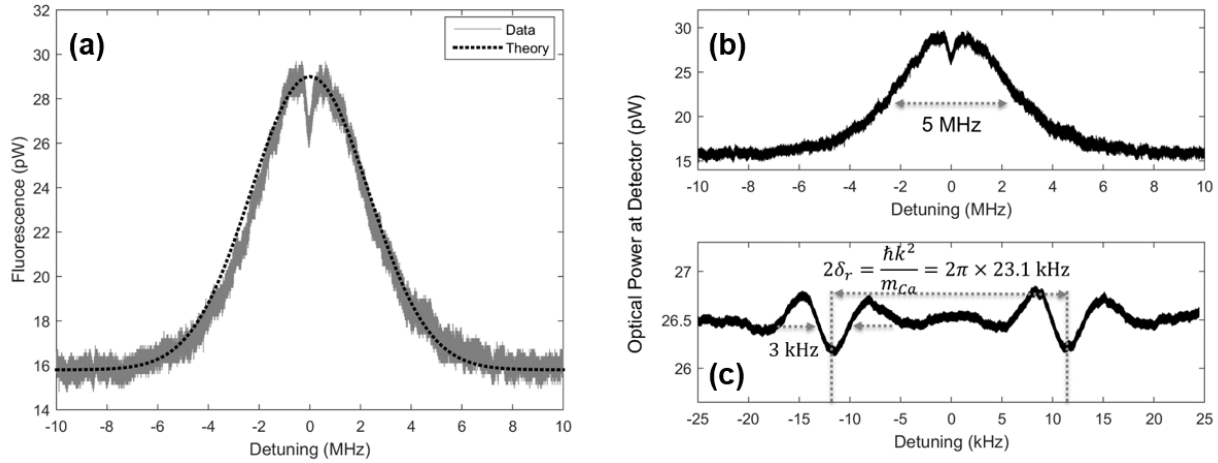

Figure 3-21. Atom fluorescence measurements as a function of laser detuning with the NIST test laser (a) measured and theoretical Doppler profiles; (b) Doppler-broadened resonance signal data with FWHM labeled; (c) kHz-scale frequency sweep data near resonance, depicting measured R-B fringes.

While the data indicates a FWHM of 5.0 MHz, some artificial narrowing of the measured data may be expected since large frequency modulations on the order of 10s MHz with the NIST laser had been previously observed to result in reduced AOM modulation efficiency at the extremes of the frequency sweep. This effect is small, but may explain the discrepancy between data and theory for the Doppler width.

With a mean oven temperature of $625^{\circ}\,\mathrm{C}$ and with a separation distance of $D = 50$ mm between laser beams 1-2 and between laser beams 3-4 as described in section 3.1.2. Application of Ramsey-Bordé method, Ramsey fringes with widths of roughly 3 kHz were measured with the CaBOT frequency reference as depicted in an oscilloscope average of 128 samples as shown in Figure 3-21c.

3.3.3. Optimization of R-B signal

Before measuring the instability of the CaBOT frequency reference, a saturation study was conducted to optimize the R-B signal. Objectives for the study were to identify an operational optical power resulting in large overall signal (large base-to-peak Doppler amplitude), high R-B fringe contrast (high ratio of R-B fringe amplitude to Doppler amplitude) and low background scatter (optical power measured at fluorescence detector at Doppler feature base). Figure 3-22a-c show measured values for each of these metrics as a function of optical laser power. The measured laser power indicated for all plots was not the

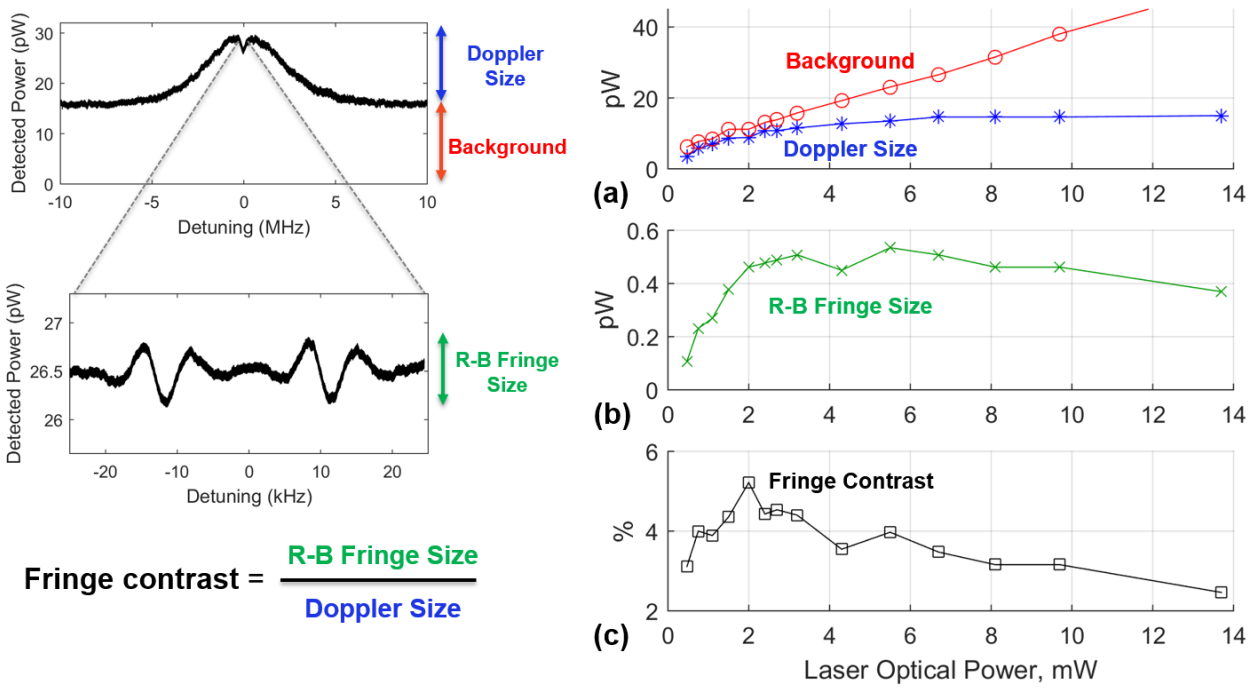

Figure 3-22. Saturation study to select laser optical power for CaBOT frequency reference performance evaluation; (a) Doppler signal and background signal vs. optical laser power; (b) R-B signal peak-to-peak vs. laser power; and (c) contrast of R-B signal over Doppler signal vs. laser power. Based on this study, an optical power of 2-3 mW was selected.

total laser power entering the vacuum chamber, but rather the total power measured with a slightly over-filled Thorlabs hand-held power meter just before the elongated, elliptical laser beam entered the vacuum chamber.

Experimental parameters for the saturation study include oven temperatures of 652.3 degrees Celsius and 597.7 degrees Celsius for the oven tip and oven crucible, respectively. This corresponds to an average source temperature of 625 degrees Celsius using the narrowest beam waist available for the Schafter + Kirchhoff 60FC-F-0-M12-33 adjustable collimator mated with an optical fiber with a nominal mode field diameter of $4.5\ \mu m$ and using an oscilloscope output of 512 trace averages for the fringe power measurements.

Ultimately, observed fringe contrast was limited to roughly 5%, as depicted in Figure 3-22c, most likely owing to imperfect alignment. Similar efforts with thermal beams have achieved 13-18% signal contrast, for example [Olson *et al.* 2019], and so this fringe contrast is expected to be improved in future

Approved for public release; distribution is unlimited

experiments. Based on the data depicted, an input power between 2-3 mW was selected for use in nominal CaBOT operations at NIST to maximize the R-B fringe signal while minimizing background light.

3.4. CaBOT frequency measurements and instability analysis

3.4.1. Fractional frequency instability measurement

Using an R-B signal with features equivalent to those depicted in Figure 3-21, the NIST test laser was locked to a single Ramsey fringe for frequency instability analysis with a measured optical power entering the chamber of 2.7 mW. The primary objective for the measurement campaign was to evaluate the CaBOT frequency reference with the simplest configuration and without environmental temperature control to assess baseline short term (1s) performance.

The frequency lock was achieved by modulating the laser frequency back and forth across a single 3 kHz fringe. The difference of the fluorescence signal measured at each side of the FWHM of the fringe was used as the control input for the lock: whenever the laser frequency drifted with respect to the atom-derived R-B feature, one of the measured fluorescence inputs would increase and the other would decrease as the center of modulation moved away from the center of the fringe. This difference between fluorescence measurements served as the control input, and the lock servo loop aimed to reduce the difference to zero to center the modulation center on the center of the R-B fringe. The dwell time utilized for the lock was 9.84 ms, corresponding to a locking bandwidth of 101.6 Hz.

Figure 3-23 shows the fractional frequency standard Allan deviation measured over a 37 minute run in which the oven temperature was measured to be 625.5 ºC. Frequency data collected corresponds to laser correction control inputs based on the R-B fringe signal lock, and a linear drift rate commensurate with drift rates historically observed for the same cavity was identified and removed from the data. As shown in the plot, a standard Allan deviation of 5.0×10^{-14} at one second was observed. This measured instability may be interpreted as the CaBOT frequency reference instability without need for another

Approved for public release; distribution is unlimited

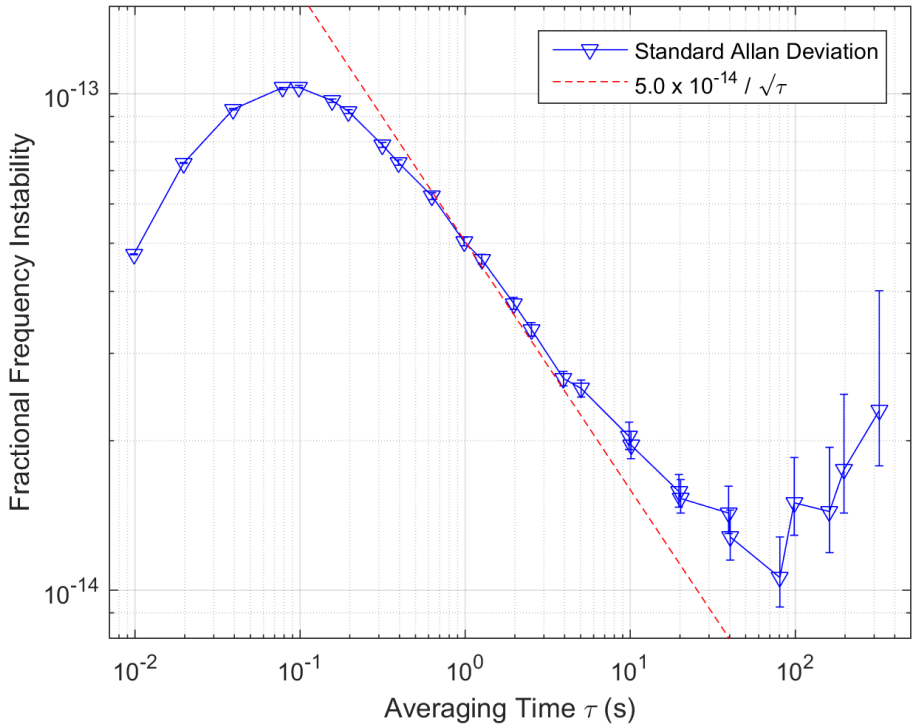

Figure 3-23. CaBOT frequency reference standard Allan deviation between 0.0098s – 322s of averaging time with linear cavity drift removed.

external reference given the fact that the laser alone is more than an order of magnitude more stable at these time scales. Specifically, the Fabry-Pérot cavity used to prestabilize the test laser used in the experiment has an Allan deviation of 2×10^{-15} at one second. The higher stability of the cavity also explains why at short time scales, the atom-referenced signal exibits worsening performance (and higher instabilities) with longer averaging times. At about 0.1s averaging time, the atom-referenced signal begins to improve in performance as indicated by reduced instabilities measured at still longer averaging times. Near the measurement interval of interest, namely near $\tau = 1\,\mathrm{s}$, the CaBOT frequency reference instability approximates the white noise asymptote (red dashed line) associated with a fractional frequency instability of 5.0×10^{-14} at one second.

To characterize the measured short-term (one second) CaBOT frequency reference performance in context with the experimental conditions and to identify leading instability drivers limiting CaBOT performance, an investigation of noise processes was conducted. First, the quantum limit to CaBOT

Approved for public release; distribution is unlimited

performance was calculated with an atom shot noise calculation. Next, technical and laser noise sources were investigated.

3.4.2. Atom shot noise

At atomic clock has a theoretical performance limited by atom shot noise given by [Fox *et al.* 2012]:

$$\sigma_{\text{atom shot}}(\tau) = \frac{\delta\nu}{\nu_0}\sqrt{\frac{1}{\dot{N}\tau}} \tag{3.9}$$

where $\delta\nu$ is the frequency width of the locking feature, ν_0 is the clock transition frequency, $\dot{N}$ is the number of atoms per second that contribute to the locking signal, and τ is the signal integration time.

For the CaBOT system as operated during the experiment shown in the Allan deviation of Figure 3-23, the locking feature measured $\delta\nu = 3\ \text{kHz}$, and the resonant clock transition frequency was $\nu_0 = 456\ \text{THz}$. The total number of atoms contributing per second to the Ramsey fringes in the fluorescence signal, $\dot{N}$ is given by:

$$\dot{N} = A_{\text{fringe}} / h\nu_0 \tag{3.10}$$

where A_{fringe} is the amplitude of the R-B fringes as detected with fluorescence optical power at the locking R-B fringe, and $h\nu_0$ is the single photon energy given by Planck's constant and the clock frequency. The R-B signal used had an R-B fringe optical power amplitude of $A_{\text{fringe}} = 0.55\ \text{pW}$. Using this value and the single photon energy, $\dot{N} = A_{\text{fringe}} / h\nu_0 = 1.8\times10^{6}$. The resulting root mean squared (RMS) quantum noise floor at one second is therefore $\sigma_{\text{atom shot}}(\tau) = 4.9\times10^{-15}$.

This atom-shot noise limited instability is an order of magnitude lower than the measured instability. Therefore, the Allan deviation measurement in Figure 3-23 was not atom shot-noise limited, but

Approved for public release; distribution is unlimited

instead limited by the measurement noise floor composed of technical noise derived from shot noise at the MPPC detector and noise on the laser light.

3.4.3. Detector and laser noise

3.4.3.1. Measured and calculated voltage fluctuations

The total measured voltage fluctuations $\delta V_{\text{detector+laser}}$ corresponding to the electrical noise floor of the detected light is the root sum square of the voltage fluctuations corresponding to the detector $\delta V_{\text{detector}}$ measured without laser light, and the voltage fluctuations corresponding to laser noise δV_{laser}. Measured voltage fluctuations related to laser noise are composed of fluctuations from optical, i.e. photon, shot noise δV_{opt} and relative intensity noise (RIN) δV_{RIN}. These relationships are captured by equation (3.11):

$$\begin{aligned} \delta V^2{}_{\text{detector+laser}} &= \delta V^2{}_{\text{detector}} + \delta V^2{}_{\text{laser}} \\ &= \delta V^2{}_{\text{detector}} + \delta V^2{}_{\text{opt}} + \delta V^2{}_{\text{RIN}} \end{aligned} \tag{3.11}$$

A Stanford Research Systems spectrum analyzer was used to assess the measurement noise of the signal from the Hamamatsu MPPC 6x6 fluorescence detector. Two measurements were conducted: first, measurements of the voltage fluctuations $\delta V_{\text{detector}}$ with no laser light input to the vacuum chamber; and second, measurements of $\delta V_{\text{detector+laser}}$ with laser light frequency shifted such that the detected fluorescence signal was just off the R-B fringes but still inside the saturation dip at the peak of the Doppler profile. The measured values were $\delta V_{\text{detector}} = 5\ \mu\text{V}/\sqrt{\text{Hz}}$ and $\delta V_{\text{detector+laser}} = 20\ \mu\text{V}/\sqrt{\text{Hz}}$ and the noise spectrum of the latter measurement with a 20x gain setting is shown in Figure 3-24. Using these measurements and equation (3.11), the corresponding laser noise was calculated to be $\delta V_{\text{laser}} = 19.4\ \mu\text{V}/\sqrt{\text{Hz}}$.

Approved for public release; distribution is unlimited

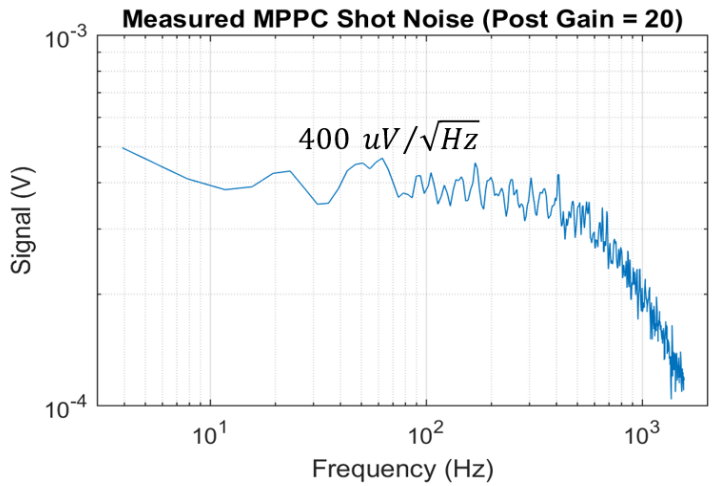

Figure 3-24. Spectral noise measurement of total detected signal. The average noise over the relevant bandwidth (101.6 Hz) is measured with a 20x gain setting to be $400\ \mu\text{V}/\sqrt{\text{Hz}}$, corresponding to $\delta V_{\text{detector+laser}} = 20\ \mu\text{V}/\sqrt{\text{Hz}}$.

Based on these results, the MPPC detector was found to produce only a small noise contribution to the measurement signal. Instead, the laser induced fluctuations dominate the total measurement floor noise budget. For improved performance then, the laser induced fluctuations need to be addressed. The components of laser induced voltage fluctuations are optical shot noise and relative intensity noise. The optical shot noise fluctuations can be expressed as:

$$\delta V_{\text{opt}} = \bar{V}\sqrt{\frac{2h\nu_0}{\bar{P}}} \tag{3.12}$$

where $\bar{V}$ is the average voltage measured at the R-B signal, and $\bar{P}$ is the average power measured at the R-B signal. This expression is the square root of the power spectral density (PSD) of the optical power at the clock frequency approximated by $2h\nu_0/\bar{P}$, which carries dimensions of $(\text{Hz})^{-1}$. Using relevant experimental parameters, i.e. $\bar{P} = 26.5\ \text{pW}$, $\bar{V} = 0.0655\ \text{V}$, voltage fluctuations corresponding to optical shot noise were approximated to be $\delta V_{\text{opt}} = 9.89\ \mu\text{V}/\sqrt{\text{Hz}}$. Equation (3.11) was used to calculate the approximate RIN induced fluctuations, resulting in $\delta V_{\text{RIN}} = 16.7\ \mu\text{V}/\sqrt{\text{Hz}}$.

Approved for public release; distribution is unlimited

3.4.3.2. Fractional frequency instability from voltage fluctuations

In order to derive the fractional frequency instability contribution of measurement noise sources, a conversion factor $\mu V/Hz$ was needed. This factor was determined by calculating the slope of the locking feature, i.e. the discriminator, of the R-B signal captured by the fluorescence detector. Analysis corresponding to this discriminator slope measurement is shown in Figure 3-25. The signal voltage of the R-B signal as measured by the MPPC detector is shown as a function of laser detuning. A zoomed perspective of the fringe used for frequency locking of the laser is shown on the right in Figure 3-25. Linear fits for each side of the locking feature were calculated as shown in the plot, and the absolute value of resulting slope calculations were averaged resulting in a discriminator of $m = 0.632\ \mu V/Hz$.

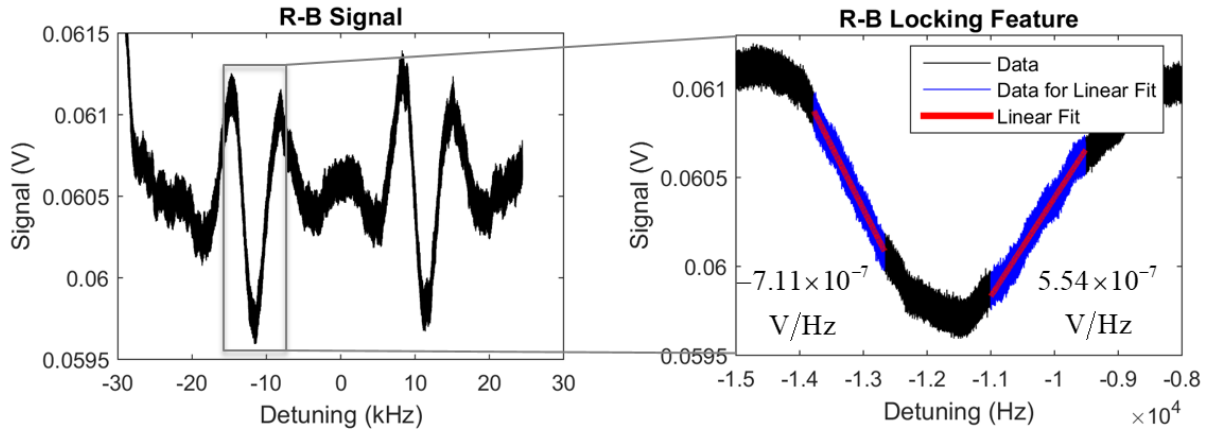

Figure 3-25. R-B signal discriminator measurement.

Fractional frequency instabilities σ corresponding to voltage fluctuations δV were calculated using this discriminator m according to:

$$\sigma = \frac{\delta V}{m}\frac{1}{\nu_0} \tag{3.13}$$

Approved for public release; distribution is unlimited

where the corresponding units are $[\sigma]=\frac{\mu V/\sqrt{Hz}}{\mu V/Hz}\frac{1}{Hz}=\left(\sqrt{Hz}\right)^{-1}$. Table 3-3 catalogues the voltage fluctuations (equation (3.11)) measured and calculated, as well as the fractional frequency instability corresponding to each noise source (equation (3.13)) with the measured discriminator $m = 0.632\ \mu V/Hz$.

The measurements contributing to the reported Allan deviation were performed with a bandwidth of $\Delta f = 101.6\ Hz$ corresponding to the $9.84\ ms$ dwell time of the frequency lock when modulating between each side of the R-B feature. Each measurement therefore had an RMS noise of $\delta V_{\text{detector+laser}}\sqrt{\Delta f} = 6.9\times10^{-14}/\sqrt{Hz}\times\sqrt{101.6\ Hz} = 7.0\times10^{-13}$ RMS. For the ideal case of zero dead time between measurements and no correlation between consecutive measurements, 101.6 independent measurements are made in one second. In this ideal case, the fractional frequency noise floor would be calculated to be $7.0\times10^{-13}/\sqrt{101.6\ Hz} = 6.9\times10^{-14}/\sqrt{Hz}$.

Table 3-3. CaBOT electrical measurement noise budget.

Measurement noise representation	Measured total electrical noise (with laser) $\delta V_{\text{detector+laser}}$ $\sigma_{\text{detector+laser}}$	Measured detector noise (without laser) $\delta V_{\text{detector}}$ σ_{detector}	Calculated laser induced noise δV_{laser} σ_{laser}	Calculated optical shot noise δV_{opt} σ_{opt}	Calculated RIN δV_{RIN} σ_{RIN}
Voltage noise δV $[\delta V]=\mu V\left(\sqrt{Hz}\right)^{-1}$	20	5.0	19.4	9.9	16.7
Fractional frequency noise σ $[\sigma]=\left(\sqrt{Hz}\right)^{-1}$ with $m = 0.632\ \mu V/Hz$	6.9×10^{-14}	1.7×10^{-14}	6.7×10^{-14}	3.4×10^{-14}	5.7×10^{-14}

Approved for public release; distribution is unlimited

The result for the measurement noise floor of 6.9×10^{-14} at one second matches closely to the actual measured Allan deviation of 5.0×10^{-14} at one second, indicating that measurement noise floor limited the CaBOT frequency reference instability. Based on the instability budget contained in Table 3-3, laser noise currently drives the system instability.

3.4.4. Prospects for reducing measurement noise

3.4.4.1. Qualitative description of noise reduction methods

Measured instability may be reduced by a combination of approaches including active RIN subtraction, background light mitigation, improved fluorescence collection efficiency, and R-B signal contrast improvements. Table 3-4 depicts the qualitative effect of each measurement noise reduction method in the context of discriminator slope, voltage fluctuations, and fractional frequency instabilities.

In RIN subtraction, a pickoff photodiode is used to directly measure the laser light, and the measured intensity fluctuations are removed from the fluorescence measurements. Because CaBOT already includes four photodiodes and 1% pickoffs in the optics baseplate design, the addition of RIN subtraction would not entail a large SWaP increase – instead, another small electronics board would be needed. The technique is commonly used in applications including optical gyroscopes and optical fibers, as reviewed for example in [NIST 1994]. Background light mitigation refers to objective of isolating the fluorescence detector such that the only light reaching the MPPC detector plane is atomic fluorescence. Improved fluorescence collection corresponds to increasing this atom signal by capturing a larger solid angle of atom fluorescence in the detection region. R-B signal contrast improvement corresponds to increasing the ratio of the R-B signal to the resonant Doppler feature by increasing the fraction of interfering atoms through an enforcement of precise atom-laser alignment.

Approved for public release; distribution is unlimited

Table 3-4. CaBOT electrical measurement noise budget.

Key: + performance boost – performance drop	R-B Signal discriminator slope *m*	Detector technical noise		Optical shot noise		Relative intensity noise	
Noise type	σ	$\delta V_{\text{detector}}$	σ_{detector}	δV_{opt}	σ_{opt}	δV_{RIN}	σ_{RIN}
RIN subtraction	0	0	0	0	0	+	+
Background scatter reduction	0	0	0	+	+	+	+
Collection efficiency improvement	+	0	+	–	+	–	+
Fringe contrast improvement	+	0	+	0	+	0	+

Considering once again the contributions to the signal noise given by equation (3.11), i.e. $\delta V^2_{\text{detector+laser}} = \delta V^2_{\text{detector}} + \delta V^2_{\text{opt}} + \delta V^2_{\text{RIN}}$, and the scaling to the final measured fractional frequency instability given by equation (3.13), i.e. $\sigma_{\text{detector+laser}} = \delta V_{\text{detector+laser}} / (m\nu_0)$, each noise reduction method can be described in terms of the effect on voltage fluctuations and fractional frequency instabilities of the reference.

Active RIN subtraction reduces δV_{RIN} without impacting other noise processes and without altering the R-B signal discriminator slope *m.* Background light mitigation without additional signal gain results in both a reduced RIN δV_{RIN} and reduced absolute optical shot noise δV_{opt} . While the fractional fluctuations scale with the square root of detected power as $\delta V_{\text{opt}} / \bar{V} \propto 1/\sqrt{\bar{P}}$ indicating a higher shot noise for a lower power, the measured voltage scales directly with power $\bar{V} \propto \bar{P}$. This implies $\delta V_{\text{opt}} \propto \sqrt{\bar{V}}$, resulting in a reduction of the absolute voltage fluctuations with reduced power collection

Approved for public release; distribution is unlimited

as would be the case with background scatter light reduction. Neither the detector voltage fluctuations nor the overall signal discriminator slope *m* are effected by reducing background light.

Improved fluorescence collection efficiency without added background noise increases both the measured RIN voltage fluctuations δV_{RIN} and optical shot noise fluctuations δV_{opt} given the larger signal voltage, but the increased signal size also directly increases the slope *m* of the R-B signal discriminator. This results in a reduction of all noise processes in the fractional frequency instability σ of the reference. Finally, improving R-B signal contrast does not directly affect voltage fluctuations since the average signal size remains the same as does the relative intensity noise on the signal. Rather, the action of improving R-B signal contrast is in an increase of the discriminator slope *m*, which as noted for the collection efficiency, directly improves the measurement noise floor fractional frequency instability.

3.4.4.2. Noise reduction recommendations and projected performance

As quantified in the measurement noise floor budget in Table 3-3, excess laser noise dominated by relative intensity noise was found to drive overall observed instability of the CaBOT frequency reference. Two methods to reduce detector voltage fluctuations corresponding to RIN that were qualitatively described in Table 3-4 include active RIN subtraction and background scatter light reduction. These would be the first approaches to consider to reduce measured instabilities. Reasonable objectives for the application of these methods as well as implementing increased fluorescence collection and R-B contrast improvements are considered quantitatively in Table 3-5.

In the table, different scenarios for reasonable experimental improvements are listed as rows, with associated improvement factors in terms of decibels of detected power for each scenario listed in the first column. These are designated as: RIN subtraction (RINs), background light reduction (BkRedux), fluorescence collection improvement (Coll), and R-B fringe contrast improvement (Fringe). Associated discriminator slopes m are listed along with the fractional frequency instabilities σ corresponding to detector shot noise, optical shot noise, and RIN are listed in the next four columns. The final two columns

Approved for public release; distribution is unlimited

list the total measurement noise floor $\sigma_{\text{detector+laser}}$ and the limiting performance as indicated by the atom shot noise $\sigma_{\text{atom shot}}$. A new atom shot noise is calculated according to the projected size of the R-B signal with equation (3.9) evaluated at $\tau = 1\ \text{s}$ using equation (3.10) and the projected amplitude of the R-B fringe signal. The first row of data in the table corresponds to CaBOT measurements.

Given precedents for active RIN subtraction, a modest objective for noise reduction would be a 10 dB improvement. This corresponds to a reduction of voltage fluctuation amplitudes by a factor of $\sqrt{10}$. Without any other noise reduction, a 10 dB reduction of RIN in detected power would result in a detector voltage fluctuation contribution from RIN of $16.7/\sqrt{10}\ \mu\text{V}\left(\sqrt{\text{Hz}}\right)^{-1} = 5.3\ \mu\text{V}\left(\sqrt{\text{Hz}}\right)^{-1}$. Using equations (3.11) and (3.13), and assuming no other improvements to the system are made, a corresponding total measurement noise floor of $4.3\times10^{-14}/\sqrt{\text{Hz}}$ would be expected. This scenario is presented in the second row of data in Table 3-5.

In addition to RIN subtraction, mitigation of background light would also help to reduce the measured RIN. This would be most readily achieved with further baffling and applying more blackening agent inside and outside the vacuum chamber. A 10 dB reduction of detected background light is a reasonable objective given the fact that nearly half the measured signal in the current CaBOT configuration is background scattered light (for more information, see the saturation study in Figure 3-22). Unlike RIN subtraction, which only reduces the RIN contribution to voltage fluctuations δV_{RIN}, background light scatter also reduces the absolute magnitude of optical shot noise derived fluctuations according to $\delta V_{\text{opt}} \propto \sqrt{\bar{V}}$ where $\bar{V}$ is the average voltage measured at the R-B signal. Using equations (3.11), (3.12) and (3.13) assuming the same signal size and detected background scattered light reduced by 10 dB (with a voltage amplitude reading reduced by a factor of $\sqrt{10}$), a total measurement noise floor of $3.4\times10^{-14}/\sqrt{\text{Hz}}$ would be expected. The third row of Table 3-5 depicts performance projections

Approved for public release; distribution is unlimited

corresponding to the scenario in which both a 10 dB of RIN subtraction and a 10 dB background light reduction are achieved.

Table 3-5. Projected fractional frequency instability assuming various combinations of noise reduction efforts including: RIN subtraction (RINs), background light reduction (BkRedux), fluorescence capture improvement (Coll), and fringe contrast improvement (Fringe).

Configuration	R-B Signal discriminator slope m $\mu V/Hz$	Detector technical noise σ_{detector} $\left(\sqrt{\text{Hz}}\right)^{-1}$	Optical shot noise σ_{opt} $\left(\sqrt{\text{Hz}}\right)^{-1}$	RIN σ_{RIN} $\left(\sqrt{\text{Hz}}\right)^{-1}$	Total meas. noise floor $\sigma_{\text{detector+laser}}$ $\left(\sqrt{\text{Hz}}\right)^{-1}$	Theoretical limit: Atom shot noise $\sigma_{\text{atom shot}}$ $\left(\sqrt{\text{Hz}}\right)^{-1}$
Current CaBOT	0.632	1.7×10^{-14}	3.4×10^{-14}	5.8×10^{-14}	6.9×10^{-14}	4.9×10^{-15}
10 dB RINs	0.632	1.7×10^{-14}	3.4×10^{-14}	1.8×10^{-14}	4.3×10^{-14}	4.9×10^{-15}
10 dB RINs 10 dB BkRedux	0.632	1.7×10^{-14}	2.6×10^{-14}	1.4×10^{-14}	3.4×10^{-14}	4.9×10^{-15}
10 dB RINs 10 dB BkRedux 10 dB Coll	1.999	5.5×10^{-15}	1.3×10^{-14}	6.9×10^{-15}	1.6×10^{-14}	1.5×10^{-15}
10 dB RINs 10 dB BkRedux 20 dB Coll	6.320	1.7×10^{-15}	7.0×10^{-15}	3.7×10^{-15}	8.1×10^{-15}	4.9×10^{-16}
10 dB RINs 10 dB BkRedux 20 dB Coll 6 dB Fringe	12.608	8.7×10^{-16}	3.5×10^{-15}	1.9×10^{-15}	4.1×10^{-15}	2.5×10^{-16}
10 dB RINs 10 dB BkRedux 20 dB Coll 10 dB Fringe	19.986	5.5×10^{-16}	2.2×10^{-15}	1.2×10^{-15}	2.6×10^{-15}	1.5×10^{-16}

In addition to approaches to reduce relative intensity noise, options exist to improve the signal strength of the R-B fringes. Increasing the detected atom fluorescence with an improved collection efficiency would produce increased optical shot noise related voltage fluctuations at the fluorescence detector, but also a steeper discriminator slope leading to an overall improvement in fractional frequency

Approved for public release; distribution is unlimited

noise. In the current CaBOT configuration, the collection efficiency was estimated to be only 0.12%. This fraction can be substantially improved with modifications to the fluorescence capture optics design involving a closer placement of the detector to the atom beam and the use of multiple detectors.

Scenarios in Table 3-5 involving collection improvements include options for a 10 dB and a 100 dB improvement in detected power. A 10 dB improvement would result in a discriminator slope improvement by a factor of $\sqrt{10}$, resulting in an atom shot noise projection of 1.5×10^{-15}, while a 100 dB improvement would correspond to a discriminator slope improvement by a factor of 10 with a projected atom shot noise of 4.9×10^{-16}. With a combination of 10 dB RIN subtraction, 10 dB background light reduction, and 10 dB collection fraction improvement, the resulting total measurement noise floor is projected to be 1.6×10^{-14}. With the same RIN subtraction and background light reduction targets, a more ambitious 100 dB collection improvement reduces the measurement shot noise into the 10^{-15} decade.

Finally, improving the fringe contrast provides a powerful mechanism by which the overall measurement instability can be reduced. Recall that the fringe contrast directly determines the discriminator slope *m*, which determines the overall fractional frequency instability from voltage fluctuations according to equation (3.13). Unlike collection efficiency improvements, fringe contrast improvements do not raise the average signal size, and so improving contrast does not involve an optical shot noise penalty like increasing the collection fraction of fluorescent light.

Two scenarios for fringe contrast improvements are considered in Table 3-5: a 6 dB and a 10 dB fringe improvement corresponding to a detected signal amplitude increase of ~2x and ~3x, respectively. These are reasonable targets for CaBOT given that a maximum fringe contrast of 5% has currently been measured with the CaBOT system. This may be compared with observed fringe contrasts between 13-18% in the Ca-2 system [Olson *et al.* 2019]. Of course, the two systems are not identical, and so there may be constraints on the maximum fringe size achievable with the CaBOT system. With a combination of 10 dB RIN subtraction, 10 dB background light reduction, 20 dB collection fraction improvement, and 6 dB fringe contrast improvement, the fractional frequency noise floor is projected to be 4.1×10^{-15}, while the same

Approved for public release; distribution is unlimited

configuration with a 10 dB fringe contrast improvement over the current CaBOT system would result in a measurement noise floor of 2.6×10^{-15}.

In general, improved fringe contrast can be achieved with better alignment of R-B lasers, though some concerns specific to CaBOT must be addressed. Challenges to alignment with CaBOT principally stem from the fact that two penta-prisms are placed outside the vacuum chamber to steer the R-B laser. This design choice was made to allow for an added degree of freedom to enable alignment corrections, but in practice, the decision resulted in two potential challenges: first, the vacuum chamber window pitch of 3º implies a corresponding pitch ($\hat{x}$) tilt of $15\ \mu\text{rad}$ from the air-to-vacuum transition, even assuming the window were perfectly flat (a wedge in the window would result in additional beam steering). Window induced tilts induce one co-propagating beam pair, while remaining parallel to each other, to be pitched up by $15\ \mu\text{rad}$, and the other pair to be pitched downward by $15\ \mu\text{rad}$. Thus, the two laser beam pairs are pitched $30\ \mu\text{rad}$ with respect to one another. A point of reference of the impact of pitch changes was provided by a sensitivity study conducted at NIST: this study revealed that a pitch (rotation about $\hat{x}$) change of $100\ \mu\text{rad}$ with their apparatus resulted in a fringe contrast reduction of 50%, while the same contrast reduction was observed for a yaw (rotation about $\hat{y}$) change of $1\ \text{mrad}$. While the NIST sensitivity study used a different apparatus, is it reasonable to expect that CaBOT would have sensitivity to laser beam pitch error.

Second, the separation of the R-B optics inside the vacuum and the penta-prisms outside the vacuum allow physical deformation of the optics baseplate with pressure and gravity loading to affect beam steering. While pitch (rotation about $\hat{x}$) and yaw (rotation about $\hat{y}$) were predicted to be $< 7\ \mu\text{rad}$ with finite element analysis of the structure in a temperature controlled environment, CaBOT was operated while exposed to laboratory temperature conditions and so actual pitch and yaw effects might have exceeded the $7\ \mu\text{rad}$ nominal value, thus reducing fringe contrast.

Approved for public release; distribution is unlimited

In order to address laser beam steering errors, an optical interferometer could be used to illuminate the evacuated R-B optics train with a large radius coherent wavefront. A six-inch commercial interferometer would be appropriate for this task. The interferometer would allow for an optimization of alignment as well as an assessment of the limitations to alignment. Even without a large aperture optical interferometer, more precise manual adjustment could result in improved signal contrast beyond the 5% contrast already observed.

3.5. Discussion and next steps

In addition to the methods already described to reduce the measurement noise floor including RIN subtraction, background scatter reduction, collection efficiency improvement, fringe contrast improvement, larger signal size and improved noise properties can also be achieved with increased atom fluxes. Higher flow rates with raised oven temperatures or nozzle designs would increase the number of atom oscillators that can contribute to the interference signal. Oven lifetime reduction with higher atom flow rates would need to be weighed against the performance gains possible with these modifications.

Future work beyond improving short-term instability performance through noise reduction and signal improvements involves the implementation of CaBOT frequency reference features to realize long-term instability design goals. This includes the application of k-reversal and dual oven operations, as well as the operation of water-cooling for atom ovens to reduce temperature gradients and the associated thermo-mechanical deformations, that would affect laser beam steering. Integration of the CaBOT frequency reference in the clock chassis with active temperature control is the final objective for the CaBOT system commissioning to enable unprecedented long-term instabilities for use in fielded applications.

Concerning recommendations for design improvements in future versions of the CaBOT frequency reference, it might be desirable in future versions for all R-B steering optics to be placed within the vacuum chamber on the same ULE monolithic structure. The NIST Ca-2 frequency reference placed all optics in-vacuum. The success of Ca-2 in producing high signal contrast indicated that the additional degree of

Approved for public release; distribution is unlimited

freedom CaBOT provides was probably not necessary. By eliminating this adjustment, the signal quality of CaBOT may be readily improved. Additionally, a fluorescence capture system that collects a larger fraction of emitted light would be helpful, and so a design in which multiple fluorescence detectors may be placed closer to the atom beam, potentially even from within the vacuum chamber, would be highly impactful.

Approved for public release; distribution is unlimited

Chapter 4

Thermal control with Ca-2 and CaBOT

4.1. Introduction to temperature control and chassis objectives

Thermal design plays a critical role in the performance of thermal Ca R-B optical atomic clocks. While the frequency instability budget described in section 4.2.2. includes a blackbody Stark contribution to fractional frequency instability of 2×10^{-17} with temperature excursions limited to a range of 0.7 K, this calculation disregards other effects of temperature on the system, most notably temperature-dependent expansion of the physical apparatus components. These changes may involve changes to optical surface orientation and placement, altering the R-B laser path and hence the R-B laser phase contributing to the interferometry signal. These sources of phase instability occur at timescales commensurate with the thermal time constant of the system.

In this chapter, a temperature control system and thermal enclosure designed and built for the NIST Ca-2 system are described that substantially improved measured Ca-2 frequency stability. With the active thermal enclosure operation, frequency instability was reduced by a factor of 5x at 2000 seconds when comparing against an experimental run without thermal control. A corresponding sensitivity study involving active heat application resulted in the determination of a demonstrative thermal control requirement of mK-level stability to enable clock instability at the 10^{-16} level. Also described in this thesis is the demonstration of a thermal fluid temperature control system for the compact, fieldable CaBOT clock that showed temperature stabilization to $\sim 56\ \mu K$ RMS in the presence of $0.5\,^{o}C$ full scale temperature

Approved for public release; distribution is unlimited

variation in ambient laboratory temperature. This performance level is appropriately matched to the thermal control requirements determined from the Ca-2 system.

In order to motivate the CaBOT thermal design discussion, Ca-2 thermal sensitivity and thermal control are discussed first. Section 4.2. Ca-2 temperature control and frequency instability analysis describes thermal design and experimental efforts with the Ca-2 system. Although the specific designs of the Ca-2 and CaBOT frequency references differ, both rely on the same underlying physical principles and both employ ultra-low expansion glass for R-B optical elements, so sensitivity analyses performed with Ca-2 are qualitatively representative for CaBOT and other thermal Ca R-B optical atomic clocks that involve a vacuum chamber housing ULE optics critical for R-B laser beam steering.

Next, section 4.3. CaBOT temperature control and chassis design describes thermal and chassis design and integration, in addition to experimental efforts related to the CaBOT system. Thermal design efforts with CaBOT focused on delivering a stable temperature environment for the thermal Ca R-B frequency reference, and chassis design efforts focused on integrating all required CaBOT clock components and electronics in a small volume while isolating the frequency reference to ensure quiet operational conditions despite local environmental conditions. An added challenge to the thermal design for CaBOT involved the need to remove heat loads on the order of 220 W from a small volume without use of convective cooling and with minimum mechanical vibration.

4.2. Ca-2 temperature control and frequency instability analysis

4.2.1. Ca-2 experimental setup

Like CaBOT's frequency reference, Ca-2 is also a frequency reference based on R-B atom interferometry using thermal calcium beams. Both systems were designed to operate with dual, counter-propagating atomic beams, though Ca-2 was not designed to accommodate laser directionality switching as demonstrated in the first generation NIST thermal Ca R-B frequency reference described in [Fox *et al.*

Approved for public release; distribution is unlimited

2012]. Aside from this, the principal difference between Ca-2 and CaBOT involved the detected signal: Ca-2 employs a blue light induced fluorescence (LIF) technique for SNR enhancement in which excited state electrons are rapidly cycled between the excited $\left(4s4p\right)^3P_1$ clock state to a shelving $\left(4p^2\right)^3P_0$ state through a strong coupling at 431 nm. The higher excited state accessible with 431nm has a natural linewidth of 40 MHz (as may be compared with the clock transitions natural linewidth of 374 Hz), enabling many excitations to occur while the atoms pass through the fluorescence detection region. Thus, many blue light photons can be produced by each excited state Ca, for each red photon produced in passive fluorescence collection.

The bias magnetic field in the Ca-2 system is generated with Helmholtz coils in Ca-2 as opposed to permanent magnets placed on the vacuum chamber as in CaBOT, and all R-B steering is performed inside the vacuum chamber with a single monolithic optical element composed of mirrored elements

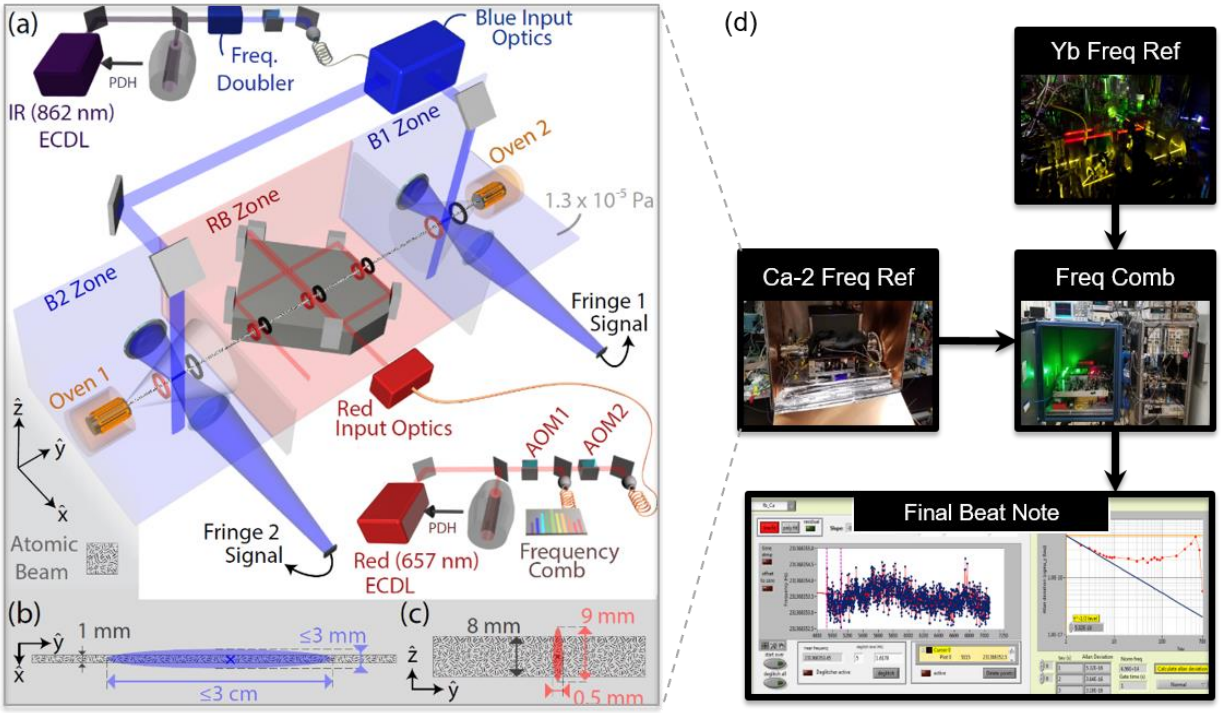

Figure 4-1. Ca-2 frequency reference experimental setup and measurement scheme. (a) Frequency reference graphical depiction; (b) approximate laser and atom beam geometry for blue LIF detection; (c) approximate laser and atom beam interaction geometry in R-B zone. (d) An optical comb is stabilized by an ytterbium optical lattice clock signal before beating with the Ca-2 reference for frequency instability measurements. Figure (a-c) credit: J. Olson *et al.* 2019.

Approved for public release; distribution is unlimited

optically bonded to an ultra-low expansion glass spacer. This ULE optic was designed with angular tolerances ~1 arcsecond and with characteristic separations between laser fields 1-2 and between fields 3-4 of 9 cm, generating R-B fringe FHHM widths of 1.6 kHz. This separation distance was selected to produce much narrower fringes than those observed in the previous, first generation NIST thermal Ca R-B atom interferometer described in [Fox *et al.* 2012], which featured a separation of 2.7 cm and fringe widths <5 kHz. As a point of comparison, the compact, fieldable CaBOT frequency reference was designed with optics that feature separations between these two values: in CaBOT, a 5 cm separation resulted in measured fringe widths of 3 kHz.

Figure 4-1 depicts the experimental setup for the Ca-2 system with a graphic of the apparatus from [Olson *et al.* 2019]. A graphical block diagram is shown in (a): both 657 nm and 862 nm (later frequency doubled to 431 nm) lasers are pre-stabilized by Fabry-Pérot cavities by means of a Pound-Drever-Hall feedback control loop as with the CaBOT system. Input optics for the blue and red lasers affixed to the vacuum chamber shape and deliver the light into the vacuum chamber. The vacuum chamber itself is partitioned into three zones: in the center, the R-B zone, and on either side of this central region, two blue detection zones (B1 and B2). Apertures placed between zones collimate the counter-propagating atomic beams, and a monolithic ULE optic in the R-B zone produces a four-beam R-B geometry from a single input red laser. Zones B1 and B2 are physically isolated from the R-B zone for isolation of focusing optics for blue LIF. Atoms originating in the oven labeled “Oven 1” pass through four red laser beam fields in the R-B zone, and continue to pass into the zone labeled “B1 Zone” where excited state atoms are rapidly cycled into the shelving state for LIF signal generation. (b) and (c) depict approximate shapes for laser and atom beam geometries in the blue LIF and R-B interaction zones, respectively.

Because the Ca-2 system achieves fractional frequency instabilities lower than that of the cavity-stabilized R-B laser, the R-B laser could not be used as a short term reference, as in the case of the CaBOT stability assessment. A measurement scheme involving a more stable reference was needed to evaluate the Ca-2 frequency reference instability performance: NIST’s ytterbium optical lattice clock [Hinkley et al. 2013] was used as an absolute frequency reference. Figure 4-1d depicts a block diagram for this

Approved for public release; distribution is unlimited

measurement scheme. The Ca-2 referenced signal was mixed with a Yb-stabilized optical frequency comb tooth to produce a final beat note with frequency deviations representative of the frequency instability of the Ca-2 reference.

Locking a laser to Ca-2 could offer a means to not only improve its long term stability, but its short term stability as well. Improvement in short term laser stability is an application under consideration for R-B based stabilization as described further in [Olson *et al.* 2019].

4.2.2. Ca-2 instability characterization without temperature control

In order to assess mid- to long-term (>100 s) instability drivers for the thermal Ca R-B approach, sustained operations lasting multiple hours in an uncontrolled laboratory environment were performed with sensors collecting environmental and experimental parameters at 0.1 Hz. Experimental and environmental parameters were recorded including temperatures, laboratory pressure, red and blue optical intensity, and bias magnetic field intensities. Correlations between this data and Ca-2 clock frequency measurements were sought in order to characterize and quantify instability drivers.

Over >100 s time scales, a strong dependence of measured Ca-2 frequency to system temperature was observed as evidenced by a correlation of temperature excursions and frequency drift. Figure 4-2 illustrates the correlation by depicting the Ca-2 frequency data and a scaled sum of resistive temperature detector (RTD) data collected over the same time period. These RTDs were located on the bottom side of the vacuum chamber exterior, with one near the back of the chamber, rear of the R-B ULE optics, and another near the front of the chamber, forward of the R-B ULE optics. (a) depicts the relative location of the RTDs with respect to the ULE optics and red input optics, and (b) depicts Ca-2 frequency drift over a 12,000 second period (black trace), along with combined and scaled temperature data. The red trace depicts the raw combined temperature data, while the blue trace depicts the Gaussian smoothed profile included to provide a clearer picture of the scaled temperature fluctuations in time.

Approved for public release; distribution is unlimited

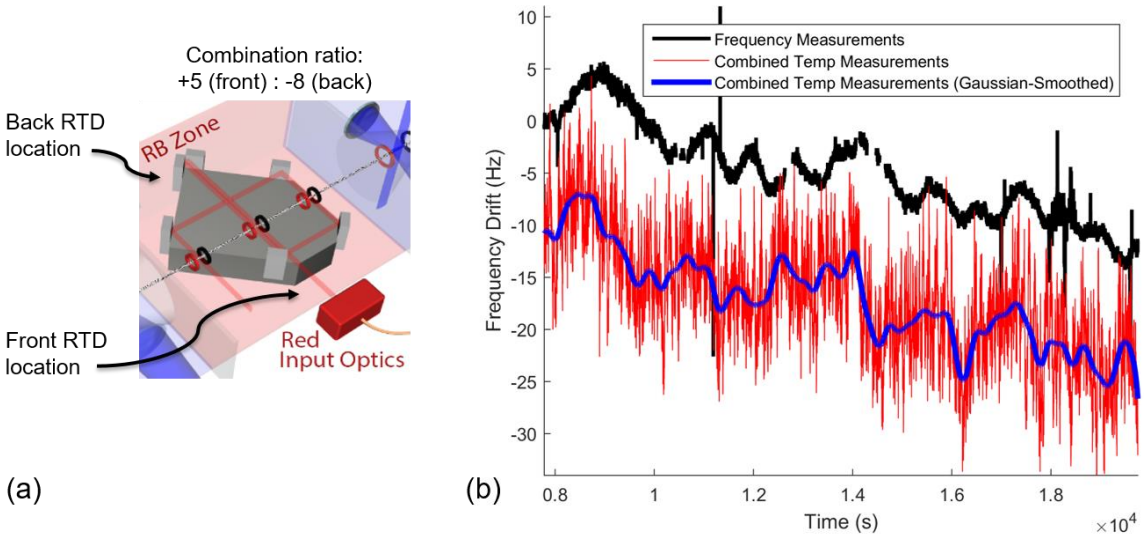

Figure 4-2. Ca-2 temperature-frequency correlation with uncontrolled temperatures: (a) two RTD readings are combined for comparison with frequency data; (b) frequency drift (black trace) shown with scaled and combined raw and Gaussian smoothed temperature data (red and blue traces, respectively).

Fluctuations in the frequency data depicted in Figure 4-2 indicated that temperature may be a leading instability driver at time scales >100 s. Absent a rigorous method to predict the thermal mechanical impact on Ca-2 frequency instability of temperature fluctuations at the specific RTD locations, relative weights were selected to produce a scaled sum of the temperature data to best match the observed frequency drift. The same scaling (+5x the forward RTD and -8x the rear RTD) was applied to temperature data in experiments where heat was applied to the system at the RTD locations, and again the scaled data correlated strongly with observed frequency drift. This latter investigation is discussed further in section 4.2.3. Ca-2 temperature sensitivity study.

4.2.3. Ca-2 temperature sensitivity study

The correlation observed between temperature and frequency measured with an uncontrolled environmental temperature as shown in Figure 4-2 motivated a more detailed investigation of Ca-2 frequency with temperature. In order to do so, thin-film heaters were placed at the two RTD locations described in Figure 4-2. The primary objective for these measurements was to establish causality as

Approved for public release; distribution is unlimited

opposed to mere correlation in system temperature and observed frequency drifts, and also to identify a representative figure of merit corresponding to the temperature stability that would be required to enable 10^{-16} level frequency instability at time scales >100 s.

To firmly establish a direction of causality, a 12.6 W heat load was applied to the base of the Ca-2 vacuum chamber near the rear temperature sensor indicated in Figure 4-2a., and subsequent evolution of system temperatures and Ca-2 reference frequency were measured. Temperatures at the front and back of the vacuum chamber base with the heater on and off were measured, while simultaneously measuring the frequency response of the Ca-2 system. The results of this study are shown in Figure 4-3.

Figure 4-3a depicts the rear and forward temperature profiles in red and pink respectively as measured before, during, and after heat load application. Figure 4-3b depicts a comparison between the measured Ca-2 frequency (black) and a combination of the rear and forward temperature sensor readings

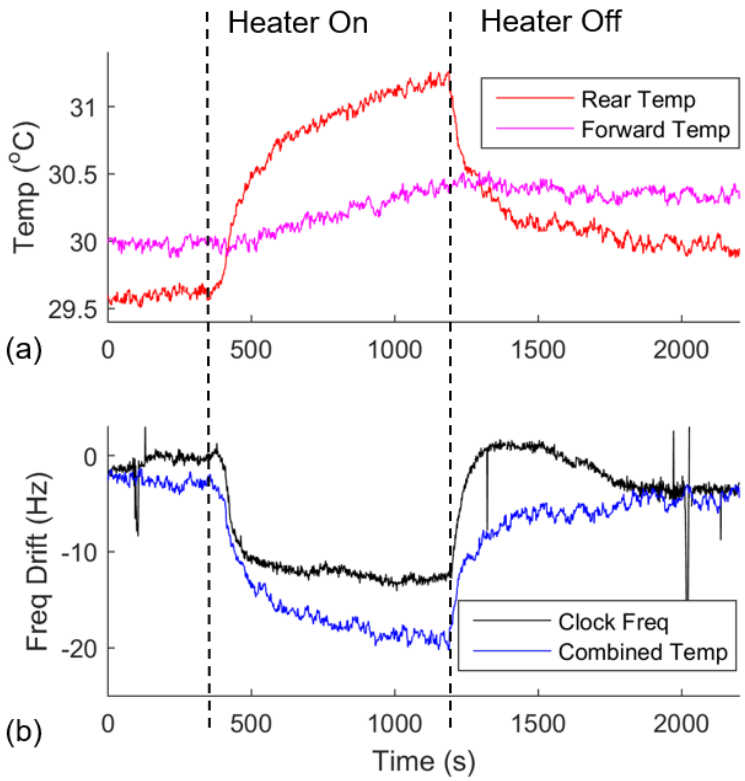

Figure 4-3. Temperature sensitivity: driven heat load. (a) Rear and forward temperature sensor data from the bottom of the Ca-2 vacuum chamber; (b) Frequency data (black) and a combination of the rear and forward temperature data (blue) over the same time period that the bottom plot's data is recorded.

Approved for public release; distribution is unlimited

(blue). The combination scaling used for this comparison was the same ratio identified in the uncontrolled temperature correlation depicted in Figure 4-2, i.e. a ratio of +5x to -8x corresponding to the forward and rear sensors, respectively. As with the uncontrolled case, the observed frequency response strongly correlated with the combined temperature profile over the same period of time.

Based on this study, a fractional frequency sensitivity of $6\ \mathrm{mK}/10^{-16}$ was measured for the Ca-2 frequency reference with respect to the temperature measured at the rear of the chamber near the heat load. 6 mK is a stringent, but feasible, temperature control requirement for achieving the desired long term Ca reference stability.

Regarding the applicability of this result to the CaBOT system, it should be emphasized that while Ca-2 vacuum chamber is physically larger than the CaBOT vacuum chamber, Ca-2 is constructed from aluminum as compared with CaBOT's steel design, and so the overall system masses are comparable. Comparing the thermal characteristics of the two systems is complicated by the fact that both the temperature coefficient of expansion and the thermal conductivity of aluminum are greater than that of 316 stainless steel: differential expansion from thermal gradients is larger in aluminum, but the higher thermal conductivity of aluminum suppresses formation of thermal gradients. On balance, thermomechanical properties of the two systems may be fairly comparable.

4.2.4. Ca-2 temperature control

Motivated by the assessment of Ca-2's frequency dependence on ambient temperature, an enclosure for the Ca-2 system was designed and implemented to reduce Ca-2's environmentally driven temperature variations. Temperature control of the enclosure was effected with a commercial off-the-shelf (COTS) controller (Wavelength Electronics RHM5K-CH). Figure 4-4 shows photographs of one of five identical walls prepared to enclose the Ca-2 system. Aluminum sheet metal was used for the wall structure, and four thin-film Kapton heaters were placed on the exterior of each, in addition to a single thermistor placed at the

Approved for public release; distribution is unlimited

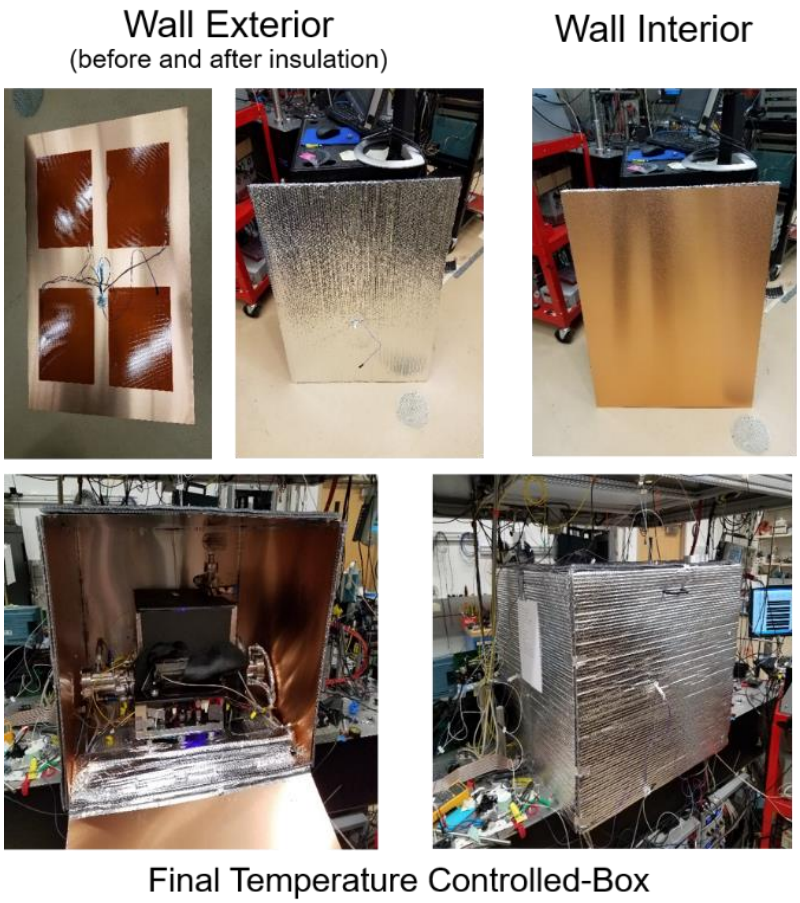

Figure 4-4. NIST Ca-2 enclosure for thermal insulation and active temperature control.

center of the panel. Two layers of aluminum-coated bubble wrap insulation were affixed over the heaters and thermistor as shown in the photographs.

Ca-2 was rigidly mounted to the optics bench and so instead of placing a sixth wall underneath the Ca-2 system, insulation material was used to cover the optics bench surface on the interior of the five walls to complete the box. Because the five walls extended some six inches beyond the surface of the optics bench, a strip of the aluminum sheet metal insulated identically to the five walls was used to complete the floor section of the enclosure. In addition to the thermistors placed at the center of each of the five walls, additional thermistors were thermally contacted to the Ca-2 vacuum chamber and the red laser input optics, and a final thermistor was placed outside of the enclosure to provide a laboratory temperature reference.

Approved for public release; distribution is unlimited

One of the thermistors placed in the interior of the thermal enclosure was used as the control input for the COTS controller.

Data were acquired with a Keithley 2000-20 multimeter with an installed scanner card. In addition to the thermistor voltages and the COTS controller outputs, additional experimental parameters including oscilloscope outputs corresponding to red and blue cavity transmission and reflection measurements and vacuum chamber pressures. All measurements logged were recorded at a 0.1 Hz rate. The COTS controller was set to a temperature above the maximum ambient laboratory temperature so that only heating was required for temperature control. The COTS proportional-integral-derivative (PID) feedback controller simultaneously commanded all Kapton heaters, and a thermistor placed inside the enclosure on the Ca-2 vacuum chamber served as the temperature control sensor.

Figure 4-5 shows a comparison of two data sets: grey data corresponds to the uncontrolled 12,000s run described in section 4.2.2. Ca-2 instability characterization without temperature control, while black data corresponds to a second run of equal duration conducted with temperature control. Figure 4-5a illustrates a relative comparison of frequency drifts over the duration of the 12,000s experimental run for each case, and Figure 4-5b depicts the measured temperature at the vacuum chamber base at the forward and rear temperature RTD sensor locations. In order to directly compare temperature profiles, the grey data

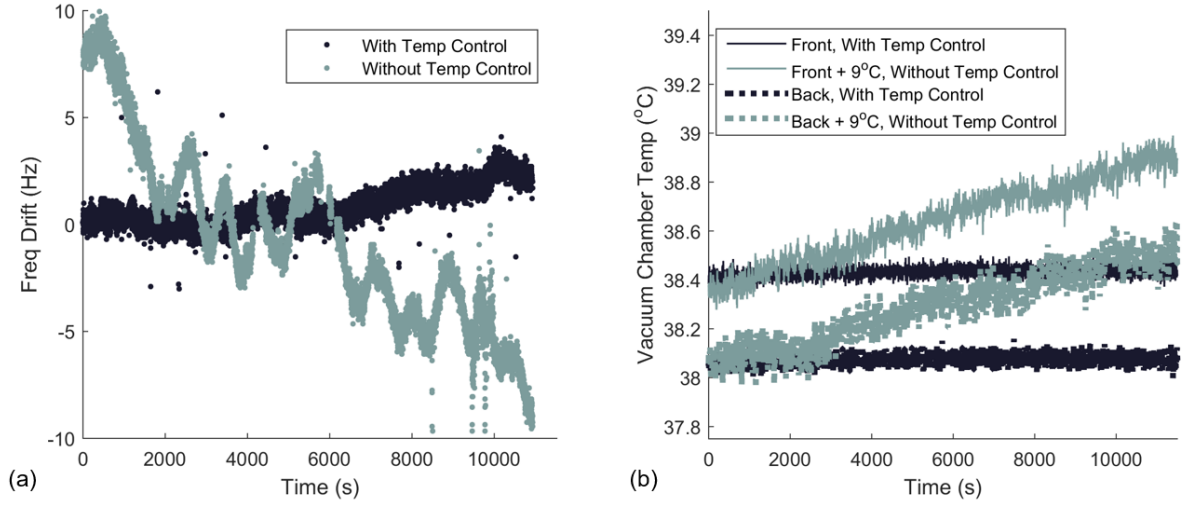

Figure 4-5. Results for temperature-controlled enclosure vs. no temperature control: (a) frequency drift comparison; (b) vacuum chamber temperature measurements for each experimental run.

Approved for public release; distribution is unlimited

corresponding to the uncontrolled case is shifted by $+9^{o}C$ as indicated in the legend, i.e. the laboratory environment on the day of the uncontrolled run depicted was $29^{o}C$.

The uncontrolled temperature case exhibited free drift of the vacuum chamber temperature over ~500 mK, with corresponding frequency drifts spanning ~18 Hz. In contrast, the controlled case involved temperature excursions < 25 mK at the vacuum chamber with frequency drifts limited to < 4 Hz.

Figure 4-6 depicts the standard Allan deviations, i.e. the fractional frequency instabilities, for the frequency data plotted in Figure 4-5a. While short term instabilities are comparable, the temperature controlled case (black) features instabilities ~70% lower after 10 seconds of averaging time. By 30 seconds, the instabilities are separated by an order of magnitude, and by 100 seconds, the difference in instability approaches 30x. While the temperature control achieved with the thermal enclosure described was not

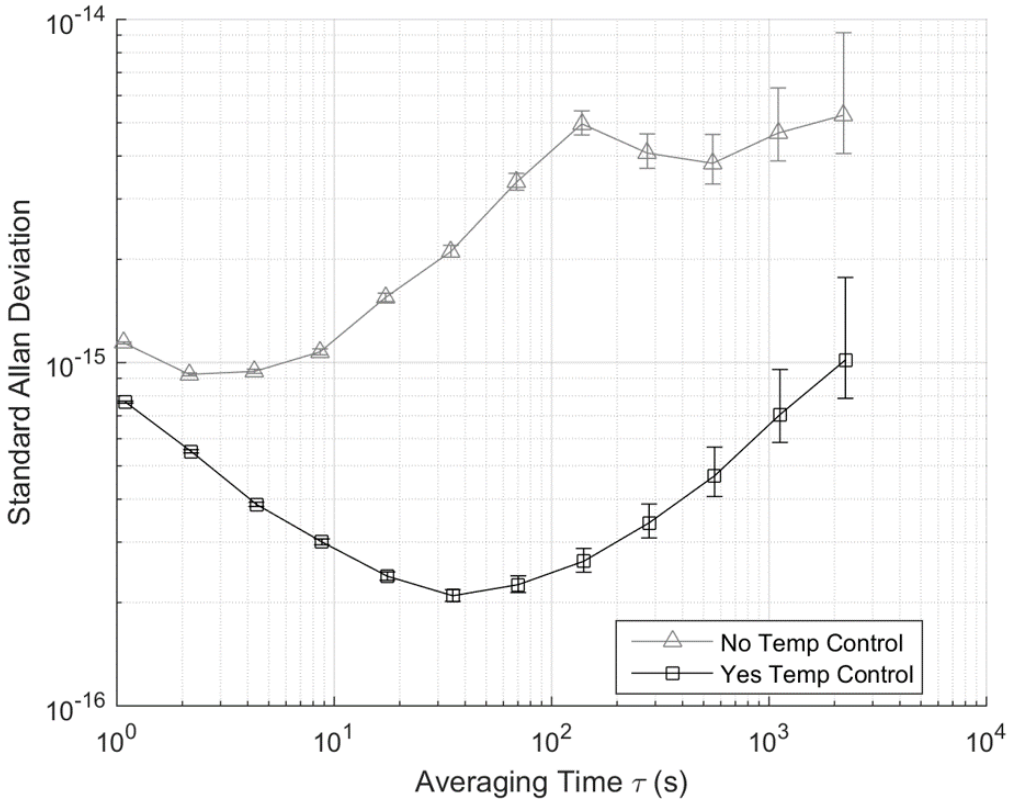

Figure 4-6. Fractional frequency instability comparison for 12,000s long experimental runs without temperature control (grey) and with temperature control (black); Allan deviations depicted do not include any drift removal and represent raw data characteristics for each experimental run.

Approved for public release; distribution is unlimited

perfect, allowing for temperature fluctuations at the vacuum chamber and the red input optics of < 25 mK and < 36 mK, respectively, the stark improvement in frequency response in the controlled case provides evidence for the importance of robust temperature control for mid- to long-term clock performance.

Finally, using the temperature enclosure and active temperature regulation, a long-duration, continuous run was conducted with the Ca-2 system and the measurement facilities at NIST. Figure 4-7 shows a 15-hour segment of this run depicting clock frequency variation (a) as well as an average of temperature data from thermistors placed in the enclosure (b). The last plot in the figure, (c), depicts a scaled sum of the same two vacuum chamber temperature sensors used for previous temperature studies is presented over the same time period. The same ratio of 5x to -8x corresponding to the forward and rear sensors, respectively, is employed once again.

A qualitative comparison indicates that temperature fluctuations still dominated the large scale structure of frequency instability variations. Nevertheless, the construction of a simple temperature-

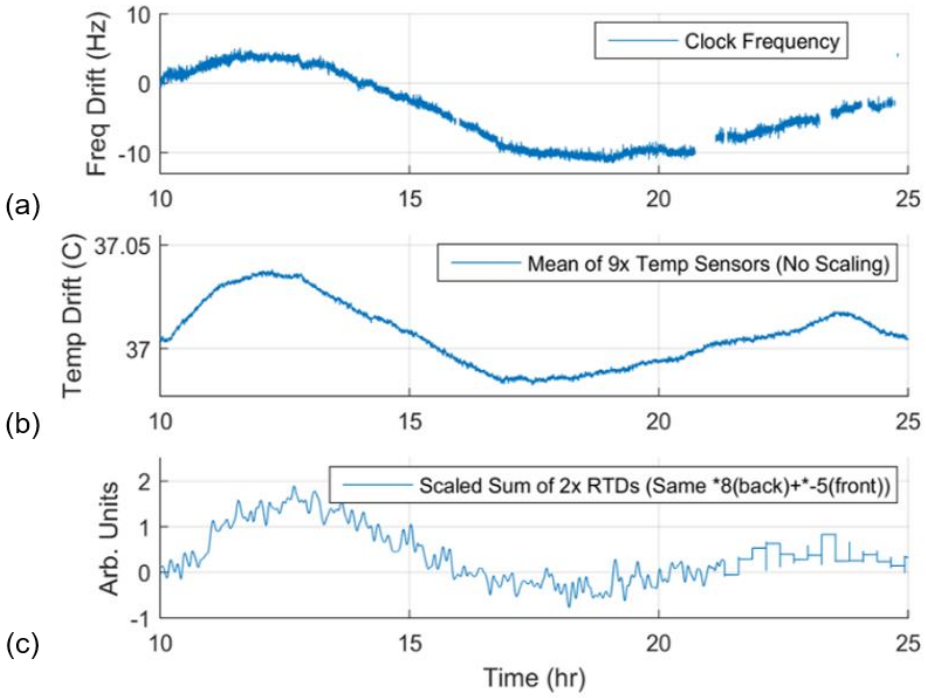

Figure 4-7. Measurements with Ca-2 for a 15-hr period: (a) frequency drift of the Ca-2 signal; (b) average of temperatures recorded by thermistors at enclosure walls and on Ca-2 frequency reference vacuum chamber and red input optics; (c) combined sum of temperature data from rear and forward RTDs.

Approved for public release; distribution is unlimited

controlled enclosure provided meaningful performance improvement: temperature and frequency excursions were strongly correlated at time scales longer than 10 seconds, and better temperature control would reduce drifts at these time scales for laboratory and fielded applications. According to the measurements reported here, a further reduction of temperature variations by ~8x would reduce temperature driven fractional frequency variations to below 1×10^{-16}. This is quite feasible given the relatively large temperature fluctuations (< 36 mK at the red input optics, < 25 mK at the vacuum chamber) allowed by the current thermal enclosure design. For more information regarding the frequency instability budget of Ca-2, the reader is referred to J. Olson's 2019 Ph.D. thesis [J. Olson 2019].

4.3. CaBOT temperature control and chassis design

4.3.1. Thermal fluid system

Liquid cooling was selected as a means to remove a large thermal load (~220 W) from a small volume without use of convective cooling. The reason to avoid convective cooling related to the need to maintain a quiet environment for free space optical propagation of the R-B laser inside the frequency reference and a desire to avoid unnecessary disturbances to the laser phase. The thermal fluid control system designed for CaBOT used a 70% water, 30% propylene glycol working fluid to remove waste heat from clock subsystems, by means of cold plates and externally mounted radiators. Ohmic heating elements are used to elevate the working fluid temperature for clock operation commissioning such that the internal CaBOT chassis temperature exceeded the maximum expected environmental temperature enabling feedback control involving only active cooling. Pulse width modulated fans, mounted to radiators in-line with the working fluid, provided a mechanism to control the chassis temperature. Figure 4-8 shows a schematic for the water cooling architecture employed.

The same cooling architecture is used in high-performance personal computer cooling systems, which provided a rich library of cheap, commercial off-the-shelf components. These cheap, quiet and

Approved for public release; distribution is unlimited

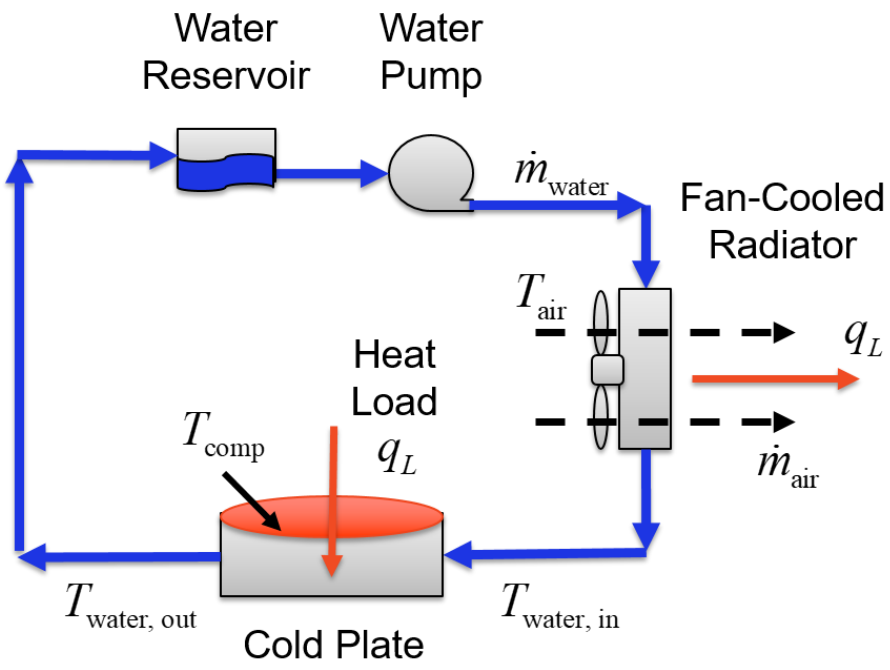

Figure 4-8. Thermal-fluid architecture for water cooling.

SWaP-compatible COTS components were exploited not only to solve the problem of removing a large thermal load (~220 W) from a small enclosure without convective cooling and with minimal vibration, but also to achieve temperature stabilization at the mK level.

Figure 4-8 depicts a simplified block flow circuit model of a liquid cooling system. It is identical in concept to an automotive cooling system in that it employs conductive coupling of waste heat to a flowing liquid coolant, which transports thermal energy via flow to a water-to-air heat exchanger. The system controls temperature by controlling the so-called thermal resistance, which is the coefficient relating the temperature difference between the air temperature T_{air} and the target component temperature T_{comp}, to the rate of thermal energy dissipation. In principle, this can be done by varying either the liquid coolant flow rate or the heat exchanger fan speed. However, in addition to gross heat extraction, the CaBOT cooling system must, as well as possible, minimize thermal gradients. Further, the CaBOT cooling system must minimize time variation of thermal gradients as well as measured temperature. These needs require that the coolant flow rate be held constant, at the highest value consistent with tolerable flow noise. This leaves fan

speed variation as the preferred modality to control thermal resistance, and the method chosen for CaBOT thermal control.

In Figure 4-8, the mass flow rate of water passing through the system is $\dot{m}_{\text{water}}$ while the mass flow rate of air passing through the radiator is $\dot{m}_{\text{air}}$. Water enters the cold-plate at temperature $T_{\text{water, in}}$, while the temperature of the component module to be cooled is at a temperature T_{comp}. A heat load q_L is transferred through the cold plate to the water, heating the water to a final temperature $T_{\text{water, out}}$. The water is then pumped through a radiator with a fan blowing air through the radiator; if the ambient air is cooler than the temperature of water entering the radiator, then heat is transferred from the water to the air, cooling the water so that it might return to the cold plate to execute another loop of cooling. In an actual system, the pump would also add heat to the water, though this is not included in the elementary thermal model depicted in the figure. It is common to place the pump as the last element downstream from the radiator so that added heat will not disturb components to be cooled.

The system thermal resistance, a function of the radiator model and fan speed, can be calculated in the following manner, as described for instance in [Incropera 1985, Kays 1984, or Simons 2002]. Given the heat to be dissipated through the cold plate q_L, the target temperature of the component to be cooled and the thermal resistance of the cold plate R_{cp}, the required inlet temperature of the cold plate $T_{\text{water, in}}$ is calculated as:

$$T_{\text{water, in}} = T_{\text{comp}} - q_L R_{cp} \tag{4.1}$$

Next, with the starting temperature of the water from equation (4.1), the outlet temperature of the cold plate $T_{\text{water, out}}$ is determined by:

$$T_{\text{water, out}} = T_{\text{water, in}} + \frac{q_L}{c_p \dot{m}_{\text{water}} \rho} \tag{4.2}$$

Approved for public release; distribution is unlimited

where $c_p = 4.183\ \mathrm{kJ/(kg \cdot K)}$ is the specific heat of water and ρ is the density of water at the working temperature and pressure. The outlet temperature of equation (4.2) is used to determine the required radiator thermal resistance R_{rad} to achieve the temperature change:

$$R_{rad} = \frac{T_{\text{water, out}} - T_{\text{air}}}{q_L} \tag{4.3}$$

In order to determine overall system flow rate and radiator size, the total heat load of the clock subsystems must be tabulated. However, in addition to accounting for heat removal, thermal circuit design must also prioritize system elements in terms of their respective thermal stability requirements. A series thermal circuit has the fundamental property that upstream variations in thermal load will perturb the temperature of downstream elements. System components with the most stringent thermal stability requirement must be the first elements in the thermal circuit. In addition, temperature sensors should be placed on the temperature-critical components. Less temperature-critical items or items generating large thermal loads should be downstream of more temperature-critical components. Figure 4-9 includes a table of power dissipation requirements (left) as well as the two cooling circuits required for the CaBOT system (right). Loop 1 first incorporates the R-B optics and the vacuum chamber adjacent to it, which we identified as having the most stringent temperature requirement (recalling the $6\ \mathrm{mK}/10^{-16}$ fractional frequency coefficient determined in measurements described in section 4.2.3. Ca-2 temperature sensitivity study). Less critical system elements are incorporated in a parallel network downstream of the R-B optics. Loop 2 components are less temperature sensitive, and are placed in order of increasing thermal load.

For each loop, equation (4.2) is applied to determine the rise in water temperature required to accommodate the loop's total heat load as $\Delta T_{\text{Cold Plate}} = q_L / (c_p \dot{m}_{\text{water}} \rho)$. As can be seen from Figure 4-9, by splitting up the total heat dissipation requirement into two loops of 100 W and 120 W, the total

Approved for public release; distribution is unlimited

Component	Power to Dissipate	Temp Rqmt
Optics	~1 W	57 C
Atom Chambers #1 & #2	~5 W + ~5 W	-
Comb Optics	15 W	57 C
Comb Electronics	50 W	< 60 C
Laser Optics	6 W	57 C
Laser Electronics	38 W	< 65 C
Draper Electronics	30 W	< 65 C
Oven Shrouds #1 & #2	35 W + 35 W	~70 C

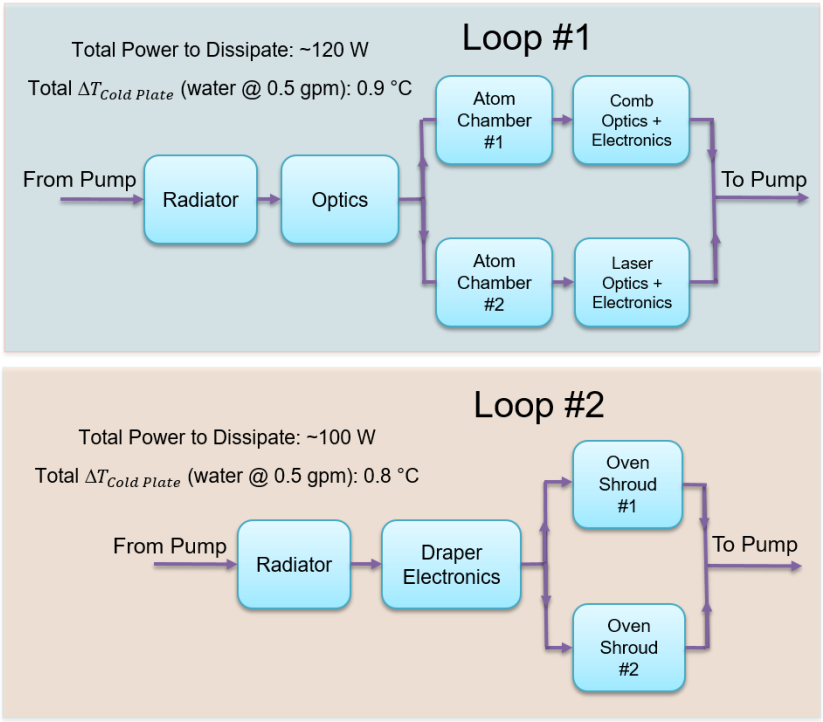

Figure 4-9. Thermal-fluid architecture. Approximate heat dissipation requirements for clock subsystems are listed on the left; both Loops #1 and #2 assume a flow rate of 0.5 gallons per minute and water as the working fluid. In Loop #1, 0.9 degrees change in the working fluid are necessary to dissipate 120 W, while only 0.8 degrees change in the working fluid are necessary for dissipation of 100 W in Loop #2. Components are ordered according to temperature sensitivity (most sensitive first) and thermal load (smaller loads first).

temperature rise of the working fluid is $<1^{o}\mathrm{C}$ in both loops. Minimizing the temperature increase of the coolant across the loops is advantageous, because it bounds possible temperature variations in downstream components.

In Figure 4-9, "Atom Chambers" correspond to cold plates placed beneath the vacuum chamber at the location of atom ovens. "Comb Optics" and "Comb Electronics" correspond to the optical frequency comb electronics and physics package; likewise, "Laser Optics" and "Laser Electronics" correspond to the cavity-stabilized laser and driving electronics. The atom ovens are outfitted with water-cooling shrouds, which are labeled "Oven Shroud"; finally, "Draper Electronics" correspond to the thermal board, laser lock board and other electronics necessary to drive chassis thermal control and monitoring functions. All components are listed with estimations for nominal power dissipation, selected to be conservative.

Approved for public release; distribution is unlimited

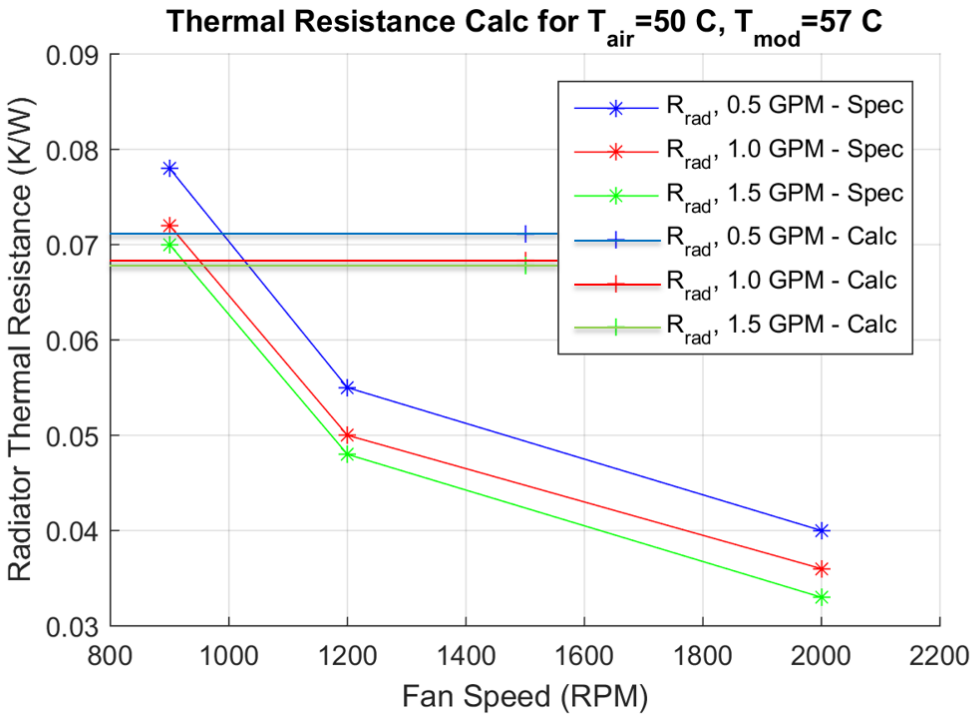

Figure 4-10. Swiftech MCR-220 thermal resistance curves for different water coolant flow rates. Horizontal lines correspond to upper limits for thermal resistance for design.

To assess thermal extraction achievable with this hardware suite, and the range of control provided by fan speed variation, we analyzed a lumped circuit in which a single cold plate represented the collective heat load of the clock chassis components. An MCR220 Swiftech radiator was modeled with manufacturer-provided operating parameters. Thermal resistance as a function of fan speed is shown in Figure 4-10 for water flow rates of 0.5 gallons per minute (gpm), 1.0 gpm and 1.5 gpm. By using equations (4.1)-(4.3) calculations for the maximum radiator thermal resistance permitted to dissipate thermal load for each of these flow rates are plotted as horizontal lines. Fan speeds were required that yielded thermal resistances below these limit lines, thus placing lower bounds on fan speeds for each flow rate considered. A worst-case condition was assumed, wherein the CaBOT system, with design internal temperature of $57^{\circ}\mathrm{C}$, was to operate in a maximum ambient temperature of $50^{\circ}\mathrm{C}$.

The performance plots in Figure 4-10 indicate that the radiator is calculated to provide better-than-required thermal resistance with fan speeds exceeding 1000 rpm. Figure 4-10 also shows that a change in the water flow rate beyond 0.5 gpm does not have a large impact in radiator performance. As earlier stated,

Approved for public release; distribution is unlimited

lower flow rates are favored since they produce less noise and vibration as compared with fast flow rates, as well as reducing the necessary pump power for operation.

Having specified a circuit order and series-parallel connectivity scheme based on control criteria, it was necessary to select the water pump and tube diameter for the system that could achieve the requisite 0.5 gpm flow rate. This selection was based on a system pressure analysis, the results of which are presented in Figure 4-11. The Innovatek HPPS+ pump was evaluated as a possible candidate. Blue, purple, and magenta curves with negative slopes correspond to the pump head available for the Innovatek pump in three modes of operation: "Silent," "Normal," and "Power." Pressure losses as a function of flow rate for cold plates, a radiator ("MCR220-QP") and tubes connecting system components are shown in orange, yellow and green, respectively and have positive slopes corresponding to increased resistance with increased flow rates. Two different flow circuits are considered: one in which all component cold plates are placed in series (plain yellow line), and one in which a parallel circuit is considered (starred yellow line). The sum of all pressure loss terms are plotted as black lines; the plain black line corresponds to a sum including the circuit

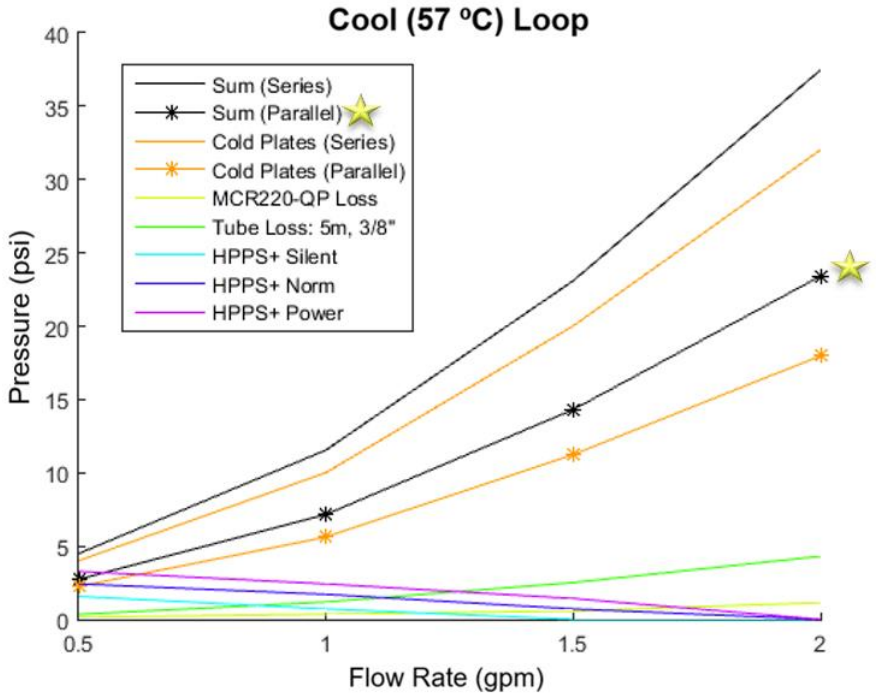

Figure 4-11. Pressure analysis for thermal fluid circuit design.

Approved for public release; distribution is unlimited

involving all cold plates in series, while the black line with stars includes loss terms from cold plates in a parallel circuit.

For a 5-meter length of tube, an inner diameter of 3/8” is selected with a simulation of multiple pipe diameters with flow rates between 0.5 – 2 gpm; calculations for pressure loss are performed with the use of the Darcy-Weisbach equation for pipe loss in the case of turbulent flow, and the Samee-Jain approximation of the Darcy friction factor is used given the roughness of the plastic tube interior and the Reynolds number of flow corresponding to the range of flow rates and tube diameter. In the bottom-left of the plot (at 0.5 gpm), the starred-black pressure loss curve intersects with the pump pressure curves. It is at these points that the pump head is sufficient to drive water through the system at 0.5 gpm. This simulation indicates that the HPPS+ is capable of pushing the desired 0.5 gpm flow through the system.

4.3.2. CaBOT temperature control design evaluation with demonstration circuit

In order to verify the results of the pressure and thermal analyses described above, a demonstration circuit was constructed. Figure 4-12 depicts a diagram (a), temperature sensor readings (b), and a photograph of the actual demonstration circuit used for testing (c). An Innovatek HPPS+ pump was used to propel water through a flow meter and fan-driven radiator before the water entered an insulation box (not shown in the photograph) housing a Lytron CP-30 cold plate. Riding the cold plate was a thin-film resistive heater that was used to output 100 W of power, simulating the heat load of one of two representative loops in the CaBOT thermal fluid system.

Temperature control was executed by a MicroZed board and carrier card with an ARM processor and an FPGA in conjunction with a custom thermal control board and a custom MATLAB Simulink controller program including a PID loop with temperature inputs indicated in Figure 4-12a,c). The thermal control board was developed by Draper and is described further in section 4.3.3. Electronics for chassis and clock control. It should be noted that: i) the card accommodated multiple temperature sensors and sensor

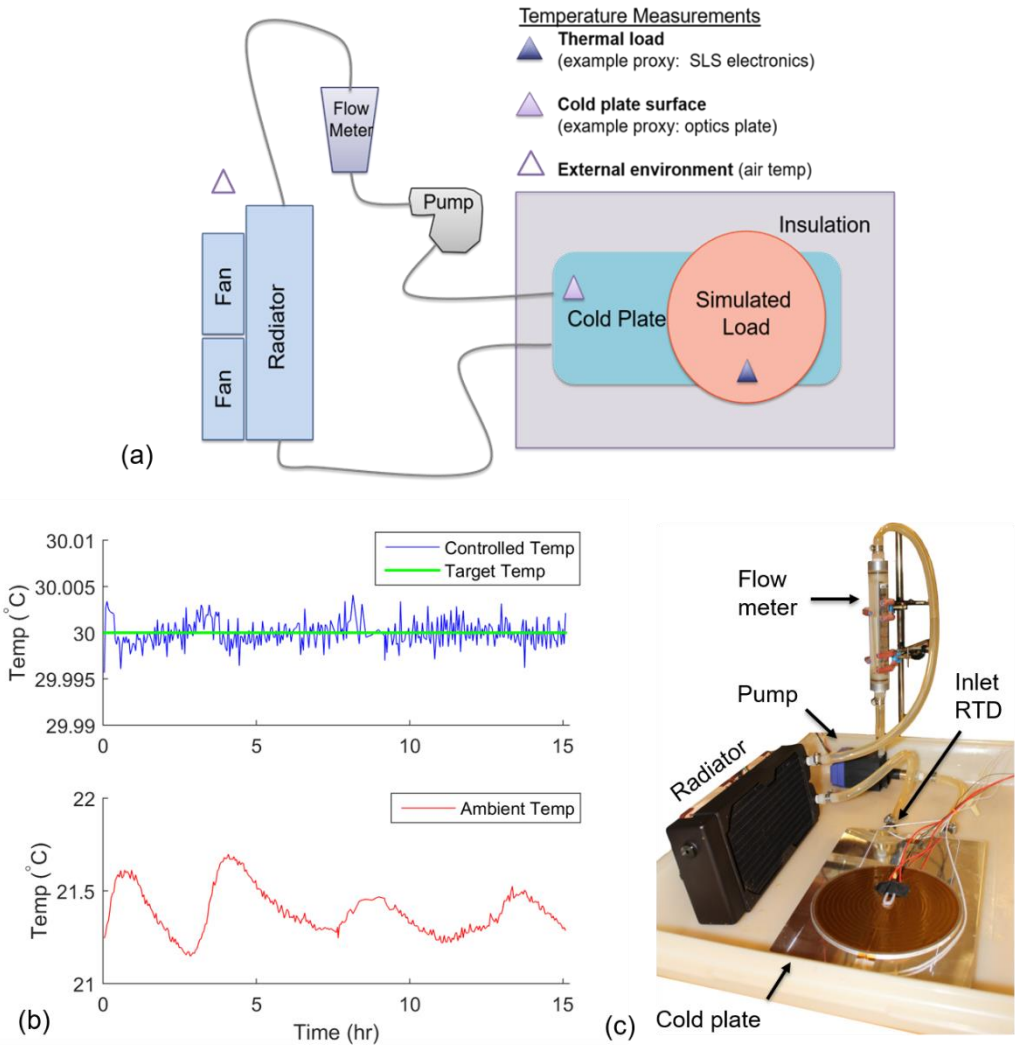

Figure 4-12. CaBOT thermal-fluid control demonstration circuit: (a) schematic of experimental setup; (b) measured temperatures presented as binned averages (160s bin size for 1 Hz data) corresponding to control point at the cold plate inlet (blue), control target (green), and ambient laboratory (red); (c) labeled photograph of thermal fluid components used for demonstration (driving electronics and insulation not shown).

types; supported Pulse Width Modulation (PWM) control of the radiator fans; provided current control for CaBOT Ca ovens; provided controlled current for multiple Watt-scale ohmic heaters; and provided a fully programmable custom thermal control capability. The controller used the cold plate inlet temperature as the primary input and control was exerted by varying the speed of the fans affixed to the radiator, dynamically tuning the thermal resistance of the heat exchanger.

Approved for public release; distribution is unlimited

The ambient lab temperature over the course of a 15-hour test is shown in red in Figure 4-12b, while the control temperature, i.e. the cold plate outlet temperature, over the course of the test is shown in blue; the green line indicates the target temperature that the controller is commanded to maintain. All temperature data was collected at a frequency of 1 Hz and binned into 160s windows for evaluation of performance. While the red plot of Figure 4-12b, the ambient laboratory temperature, exhibited excursions > 500 mK over the time period sampled, active temperature control limited cold plate temperature excursions shown in blue to < 8 mK, with an RMS error of $56\ \mu$K. This result strongly indicates that the fan speed temperature control modality was robust against exterior temperature variation. Given that the temperature sensitive components of the CaBOT system were designed to be enclosed within multiple layers of insulation, variations of less than a degree in their effective environmental temperature could reasonably be expected. Given these considerations, it is likely (but not proven, short of a full CaBOT demonstration) that the fan speed control modality is adequate to support excellent long term stability of the CaBOT frequency reference.

In addition to providing a stable temperature environment for the components within the CaBOT frequency reference, low vibrational noise was also prioritized for the thermal fluid control system. To assess mechanical vibrations, a frequency content analysis was performed for the Innovatek HPPS+ pump used for the demonstration circuit. Figure 4-13 depicts the results of this analysis.

An Axivity AX3 accelerometer was taped to the outer casing of the water pump with a coordinate frame orientation depicted in the figure. The pump was not attached to any structure and was only held in place by the inlet and outlet tubes connecting the other circuit components as shown in the photograph of Figure 4-12c. In this manner, any vibrational frequency content measured at the pump was ensured to reflect the mechanical properties of the pump itself and not of a larger rigid structure affixed to the pump. A fast Fourier transform of the accelerations measured during pump operations in the “normal” operational setting is plotted in Figure 4-13 in red blue and green corresponding to the three principal axes shown. These plots represent the frequency spectrum of pump-driven vibrations that may be presented to the CaBOT chassis

Approved for public release; distribution is unlimited

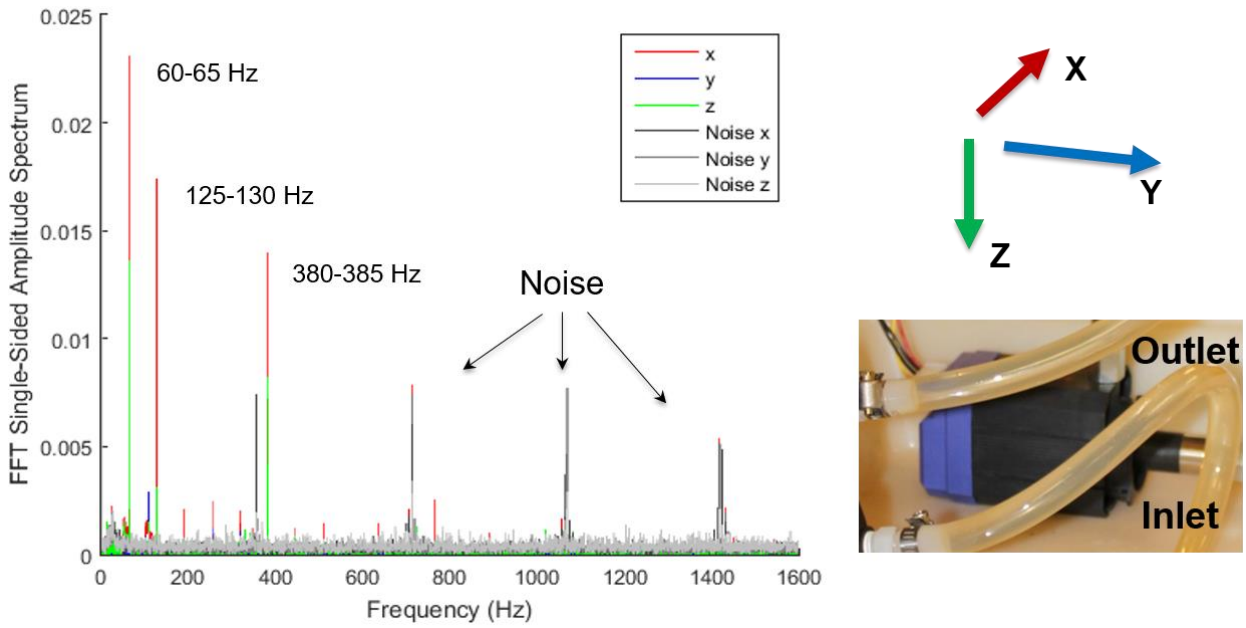

Figure 4-13. Innovatek HPPS+ pump vibration analysis.

during clock operations. By turning the pump off, accelerometer noise content is identified and plotted in grey.

From the analysis, 60-65 Hz, 125-130 Hz and 380-385 Hz were identified as principal pump-induced vibration frequencies of concern, with dominant vibrations measured in the plane normal to the pump inlet axis (the x and z axes labeled in red and green, respectively, in the figure). This frequency content analysis was used to specify dampening rubber mounts for use in isolating the thermal fluid pump and radiators from the CaBOT chassis body to ensure that the vibration frequencies driven by the pump are not allowed to propagate to the frequency reference from the pump.

4.3.3. Electronics for chassis and clock control

Draper thermal control electronics incorporated a MicroZed system-on-module 7Z020 board and input/output (I/O) carrier card and breakout board. The AVNet MicroZed development board is based on the Xilinx Zynq®-7000 All Programmable system-on-chip (SoC). A custom thermal control interface and

Approved for public release; distribution is unlimited

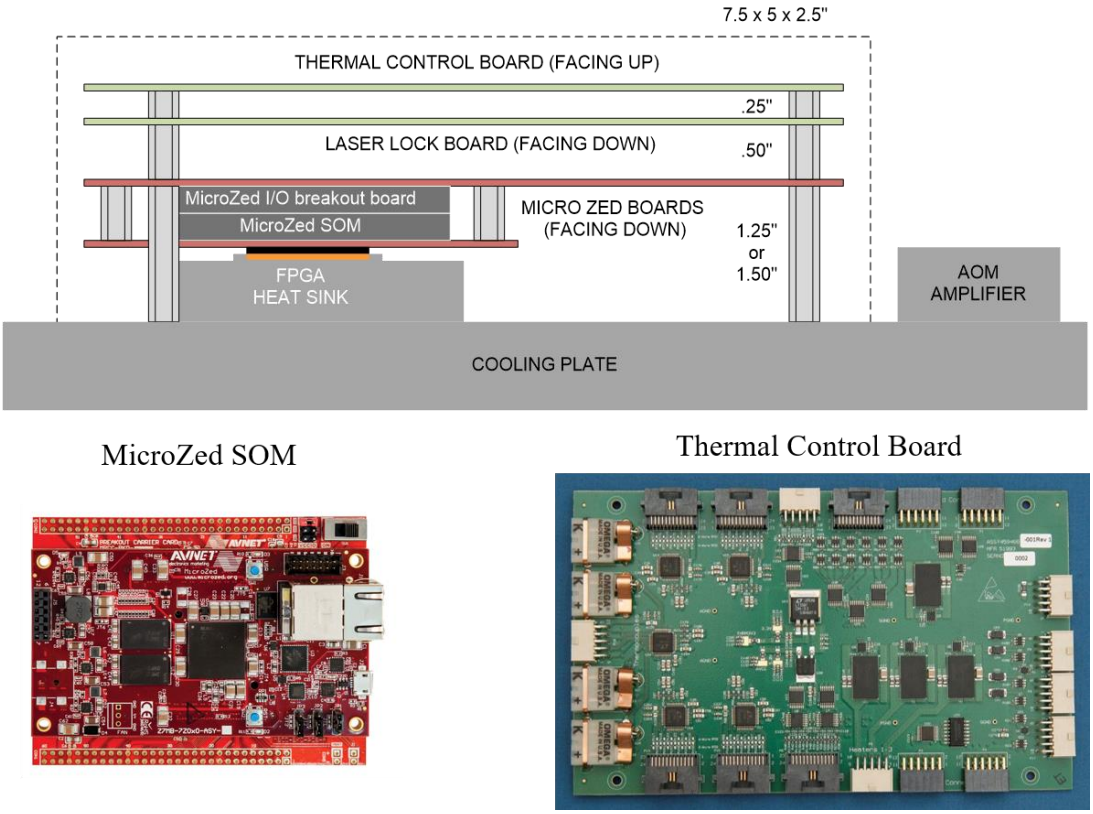

Figure 4-14. Integration concept for Draper electronics with photographs of MicroZed SOM and thermal control board.

sensor board were interfaced with the MicroZed, which itself contained an ARM processor and an FPGA. A MATLAB Simulink controller program in conjunction with Xilinx software was used to write firmware to perform control tasks such as the temperature control demonstration.

A concept for the integration of all boards including a laser lock board is shown in Figure 4-14, along with photographs of the MicroZed and thermal control boards. The laser lock board, intended to process fluorescence data and to apply various optical frequency modulation patterns for stabilization of the laser to the Ca resonance, was not designed or built. The MicroZed system-on-module board as well as its breakout board are depicted in red in the diagram, with the SOM board shown in the accompanying photograph.

Approved for public release; distribution is unlimited

4.4. Integration and next steps

The CaBOT chassis was designed to house all necessary subsystems of the clock, including the optical frequency reference, the cavity-stabilized laser, the optical frequency comb, all Draper electronics and thermal fluid system hardware. In addition to providing structural support for CaBOT components the chassis must isolate the sensitive CaBOT components including the frequency reference, laser, and comb from the local environment. Because the thermal fluid system included noisy mechanical components such as water pumps and fans, these components were housed in a structure physically removed from the rest of the chassis, mounted with rubber vibration-damping sandwich mounts. Figure 4-15 shows photographs of the CaBOT chassis without the thermal fluid attachment (a), a prototype of the thermal fluid plate (b), and the Draper electronics (c).

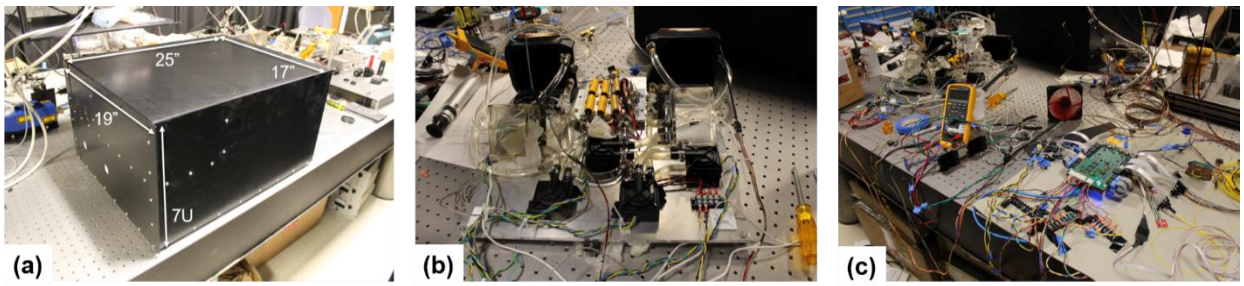

Figure 4-15. Photograph of CaBOT chassis.

Integration activities involved a fit-check and thermal fluid system check-out, a photograph of which is shown in Figure 4-16. The open chassis sitting on the optics bench was integrated with a loaded frequency reference, with the same vacuum, oven and optics configuration subsequently used in performance evaluation at NIST. In addition, all system cold plates and the bottom-half of magnetic shielding necessary for the final, fully integrated configuration were included. On a wheeled cart in the foreground, the top-shelf of the chassis can be seen with three cold plates carrying three dummy-load resistive heaters to stand in for Draper electronics, comb, and laser electronics. This top shelf also had temperature sensors integrated for temperature sensing and data acquisition commanded by the thermal control board.

Approved for public release; distribution is unlimited

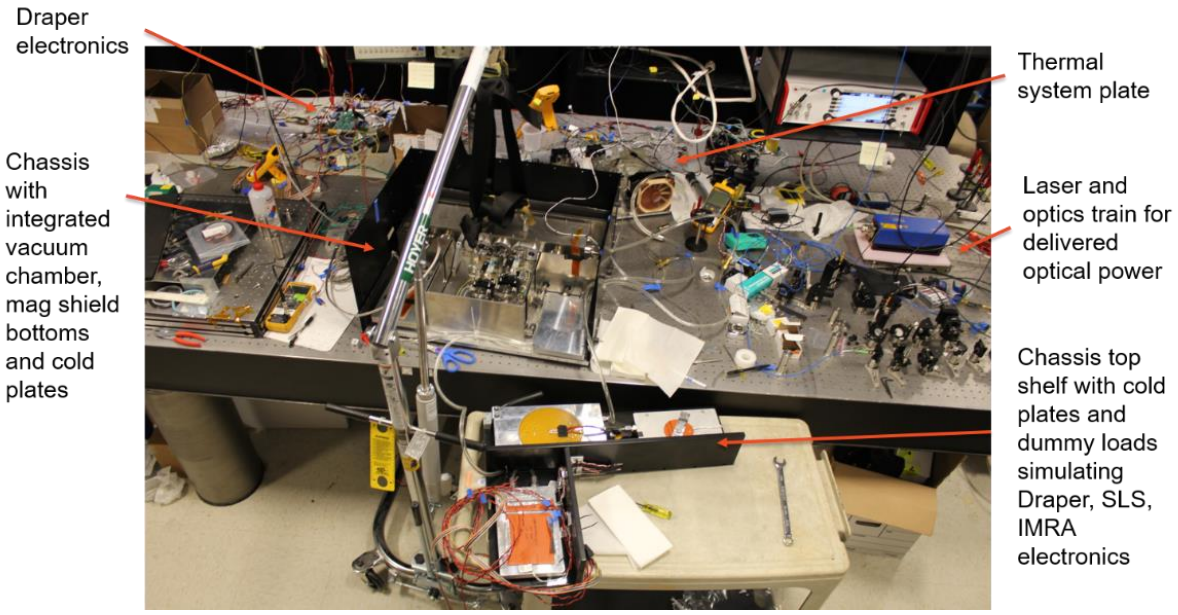

Figure 4-16. Frequency reference, chassis, and thermal control electronics integration at Draper.

The Draper electronics appear at the top left of the photograph, and the thermal fluid plate at the top center of the photograph. A 100 kHz linewidth Toptica laser and optics train are located at the right of the photograph. This laser was used for preliminary testing at Draper before the delivery of optics and before integration with the NIST test laser featuring a narrow (~1 Hz) linewidth for R-B atom interferometry and fractional frequency instability measurements.

Future work for the thermal control would include closed loop testing equivalent to that conducted for the demonstration circuit. The laser lock board would need to be designed, fabricated and integrated, and compact laser and optical comb elements would also require integration.

Chapter 5

Conclusion

5.1. Principal results and contributions review

Over the last several decades, the introduction of transformative laser technologies including ultra-narrow lasers [Salomon *et al.* 1988], ultra-fast lasers [Morgner *et al.* 1999, Sutter *et al.* 1999], and optical frequency combs [Eckstein *et al.* 1978, Cundiff and Ye 2003, Trabesinger 2005] have transformed the atomic molecular and optical physics community. Among other applications, these technologies have enabled the first optical atomic clocks that outperform existing microwave standards by orders of magnitude in laboratory demonstrations. While these rapid advances have opened new avenues of research and application, they have also introduced new challenges, both in the theoretical treatment of optical atomic interactions and in efforts to field technologies for broader application beyond the laboratory.

This thesis provided a description of a design and experimental evaluation of an optical atomic clock architecture relying on a thermal calcium Ramsey-Bordé matter-wave interferometer and relevant work toward realizing a first-of-its-kind compact, deployable optical atomic clock based on the same architecture. In addition to these efforts, a theoretical framework was introduced to explore the possible spectroscopic implications of using ultra-narrow linewidth lasers, like that used in the thermal calcium R-B optical atomic clocks considered in this thesis.

5.1.1. Theoretical contributions

The the ultra-narrow linewidth of modern lasers introduces a challenge to the application of traditional theoretical descriptions of optical atomic interactions. Because the narrowness of the laser line probing the optical clock transition drives the short term noise of the frequency reference, the use of this

Approved for public release; distribution is unlimited

kind of laser is critical to the performance of optical timekeeping devices. Spectroscopic approaches that probe absorption and stimulated emission events for atomic or molecular systems with quantized internal and momentum states involve the transfer of momentum from the laser to the atom not just in the laser propagation direction, but also in the (often orthogonal) atom propagation direction. This transverse momentum transfer compensates for the Doppler shift experienced by the atom [Sterr *et al.* 1992]. Quantitatively, the momentum and energy condition for a single photon absorption at the calcium clock transition frequency can be expressed as $\vec{k} \cdot \vec{v}_0 = \delta - \hbar\vec{k}^2/(2m_{Ca})$ where $\vec{k}$ is the laser wave vector, $\vec{v}_0$ is the principal atom velocity vector, δ is the laser detuning, and $\hbar\vec{k}^2/(2m_{Ca})$ is the single photon recoil frequency. Thus, the condition for absorption at detuning values $\delta \neq \hbar\vec{k}^2/(2m_{Ca})$ is that a laser momentum component along the atom propagation direction is transferred to the atom.

In standard theoretical treatments including that described in [Bordé *et al.* 1984], an implicit assumption is made that a sufficiently wide dispersion of laser wave vectors $\vec{k}$ exists to satisfy this momentum and energy conservation condition for each atomic velocity class. For a Gaussian laser with a fixed beam waist, the angular range of wave vectors $\vec{k}$ is fixed, and so this assumption is better stated as an assumption of a sufficiently wide frequency linewidth to allow for a range of wave vector magnitudes $\Delta|\vec{k}|$ to accommodate the Doppler shifts demanded by energy and momentum conservation. While this treatment provides a useful description of atom and molecule interactions with coherent radiation, the underlying assumption of a broad laser linewidth means that extant theory cannot explore the implications of using ultra-narrow, Hz-scale laser linewidths to drive optical atomic transitions.

In this thesis, a theory was presented in which an expression for a Gaussian laser electric field was introduced and an interaction Hamiltonian was derived for absorption and stimulated emission events that incorporates strict energy and momentum conservation assuming a monochromatic laser. Equations of motion were then derived by introducing the Schrödinger equation for a superposition of ground and excited

Approved for public release; distribution is unlimited

states of the atomic wavepacket. Solutions for ground and excited states were derived with a perturbation theory that introduced a new momentum- and laser-mode-dependent Rabi rate.

An investigation of basic implications of this restricted Rabi rate resulted in the prediction of a strong dependence of the interaction strength with laser steering along the plane of the atom-laser interaction, with a weaker dependence with steering out of the plane for the model scenarios considered. This result directly correlates to an intuitive qualitative understanding of the strong sensitivity of atom-laser interactions with Doppler shifts. When evaluating the restricted Rabi rate for a variety of momentum classes and laser beam waist sizes and optical powers, the peak restricted Rabi rate calculation matched the standard "bare" Rabi rate given by the classic relation $\Omega \equiv eE\left\langle e\left|\hat{\vec{r}}_{e-n}\cdot\hat{e}\right|g\right\rangle/\hbar$, lending further confidence in the viability of the theory.

In order to compare the momentum-dependent, restricted Rabi rate theory to the existing theoretical framework, atom source models were introduced to represent a thermal calcium beam configuration, and excitation probability calculations using both existing theory [Bordé *et al.* 1984] and the new theory are presented to investigate some basic spectroscopic signal predictions. Various beam waists were selected corresponding to common experimental parameters and for each a saturation study was performed in which excitation probabilities were calculated as a function of laser optical power. The momentum dependent, restricted Rabi rate theory exhibited saturation with properties that diverged from those predicted by [Bordé *et al.* 1984]. To the extent that a comparison with experimental data and extant theory could be made, it would appear that the restricted Rabi theory may offer new insights into spectroscopy with ultra-narrow lasers. Of course, this will need to be further investigated in experimental and theoretical work to come.

5.1.2. Experimental contributions

The Calcium Beam Optical Timekeeping clock is a first-of-its-kind design for a compact optical atomic clock based on a thermal Ca R-B matter-wave optical atomic frequency reference, designed to operate in environmental temperatures ranging from $0-50^{0}\mathrm{C}$ and within a full form factor measuring

Approved for public release; distribution is unlimited

$< 0.11\,\mathrm{m}^3$. CaBOT and similar optical atomic clocks including those that may be based on the NIST Ca-2 thermal Ca R-B frequency reference enable a broad range of positioning, navigation, and timing applications in fundamental science and defense, commercial, and civil sectors.

After describing motivation for design and specific subsystem integration efforts, this thesis described experimental and analytical evaluation of the CaBOT frequency reference. This was followed by the description of an investigation of noise processes that currently limit the technology's performance. A fractional frequency instability of $5.0\times10^{-14}/\sqrt{\mathrm{Hz}}$ was measured, and the observed R-B signal's atom shot noise was estimated to be $\sigma_{\text{atom shot}} = 4.9\times10^{-15}$ at one second. Excess laser noise was identified as the primary limitation to clock performance preventing atom shot noise limited instability. After distinguishing and identifying leading instability drivers, simple improvements to the CaBOT reference were proposed including the use of relative intensity noise subtraction, background scattered light reduction, fluorescence capture efficiency improvement, and R-B signal contrast improvement. While the first two methods address the relative intensity noise of the laser, the latter methods involve an improvement of the R-B signal size and hence involve not only a reduction of electrical shot noise of the measurement noise floor, but also a reduction of the theoretical limit to clock instability performance as represented by the atom shot noise. Projected performance calculations for a range of improvement options were presented that allow for reductions in measured instability well into the $1\times10^{-15}/\sqrt{\mathrm{Hz}}$ decade.

Experimental efforts with the NIST Ca-2 frequency reference supplemented CaBOT research and were also described in this thesis. Sensitivity studies with Ca-2 enabled an evaluation of the impact of experimental and environmental parameters on a clock signal derived form a thermal Ca R-B atom interferometer frequency reference. Characterizing the dependence of clock signal instability on local temperature was described in this thesis including a temperature-driven sensitivity study that identified mK-level temperature control as an indicative requirement to achieve instability at the 1×10^{-16} level. The design and operations of a thermal enclosure and temperature control system were also described that

Approved for public release; distribution is unlimited

regulated Ca-2 frequency reference temperatures to 10s-mK during experimental operations. With environmental isolation provided by the thermal enclosure, frequency measurements performed with the Ca-2 system resulted in regularly measured instabilities of $\leq 2\times10^{-16}$ between 10-1,000s, corresponding to more than an order of magnitude improvement over any previous thermal atomic architecture to date [Olson *et al.* 2019].

Finally, this thesis described a thermal control system for the compact, fieldable CaBOT clock addressing the engineering challenge of removing a large heat load (~220 W) from a small volume without the use of convective cooling, and to otherwise isolate the frequency reference from environmental or other perturbations. A demonstration thermal fluid cooling circuit was designed, constructed, and evaluated, successfully providing sub-mK temperature stability with the use of a water cooled cold plate system inside the physics package with radiators and a pulse-width modulated fan for control placed on the exterior of the CaBOT chassis. A full thermal fluid system based on the same operational principles was presented for the CaBOT chassis, providing a simple approach with relatively inexpensive components to achieve stable thermal control for the Draper CaBOT clock. The impact of the thermal fluid design extends beyond CaBOT: the same architecture may be applied to any fielded optical clock architecture that requires mK-level temperature stability and the removal of a large thermal load from a small volume without the use of convection cooling.

While CaBOT design efforts described in this thesis were supported by Draper and NIST staff, subsystem and CaBOT frequency reference integration and evaluation were led by the author of this thesis, as well as the design and demonstration of the thermal control system. Additionally, thermal sensitivity studies with NIST's Ca-2 and the design, construction, and operations of the Ca-2 thermal enclosure were also led by the author of this thesis.

5.2. CaBOT and Ca-2 in context

Figure 5-1 depicts the fractional frequency instability performance of the CaBOT and Ca-2 systems as they compare with current leading fielded timekeeping solutions as represented by data corresponding

Approved for public release; distribution is unlimited

to a commercially available cesium beam clock and active hydrogen maser. These experimental performance curves are accompanied in the plot by the GPS-denied objective identified by DARPA [DARPA 2014] and general performance characteristics of laboratory cavities and optical lattice clocks.

Measured CaBOT performance exceeds the performance of the Microsemi MHM 2010 Active Hydrogen Maser at short time scales, but exhibits increased instability at larger time scale. This may be expected since the CaBOT configuration tested did not include temperature control or environmental isolation, and did not employ k-reversal or dual oven operations, each of which were designed to be utilized in the CaBOT clock to mitigate mid to long term instability drivers. With minor and entirely feasible improvements to the CaBOT frequency reference, including relative intensity noise subtraction, scattered light induced noise reduction, fluorescence collection improvement, and increased signal contrast, CaBOT instability may approach $1\times10^{-15}/\sqrt{\text{Hz}}$ at short time scales, exceeding the GPS-denied objective and

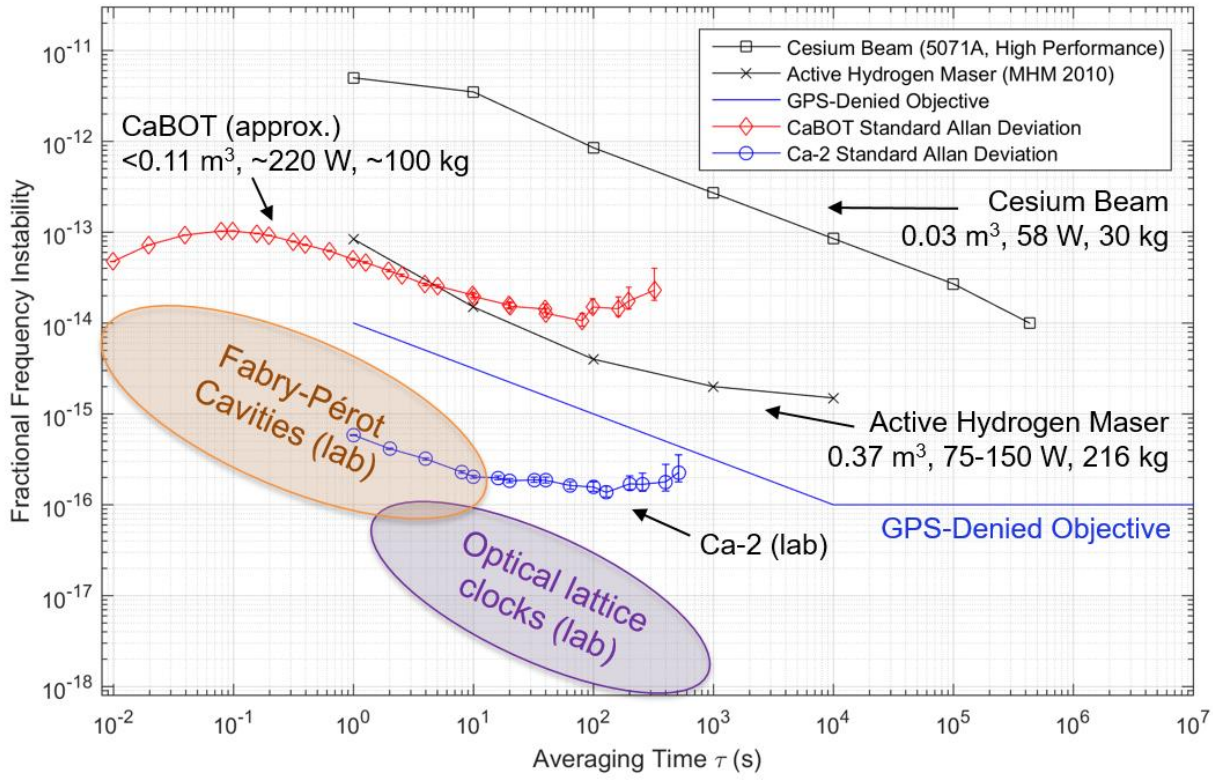

Figure 5-1. CaBOT and Ca-2 performance in context with current timekeeping leaders and the GPS-denied performance objective. Cesium beam and active hydrogen maser data from [Microsemi website, 5071A Cesium Clock Primary Frequency Standard and MHM 2010 Active Hydrogen Maser].

Approved for public release; distribution is unlimited

exceeding the performance of the leading fielded standard, the hydrogen maser, by nearly two orders of magnitude.

Even without these improvements, a CaBOT clock featuring performance equivalent to that already demonstrated would demonstrate a leap forward for fielded timekeeping, given the fact that this performance is commensurate with the hydrogen maser delivered by a device contained in a form factor comparable to the cesium beam clock. Given the near-term and reasonable performance improvements identified with the noise contribution study, prospects are promising for a CaBOT clock featuring performance exceeding the H-maser in a form factor comparable with the cesium beam clock.

The measured Ca-2 performance not only exceeds the GPS-denied objective, but also exceeds all previous thermal atomic timekeeping efforts by more than an order of magnitude [Olson *et al.* 2019]. While the Ca-2 clock is not designed for compactness or field deployment, and most notably includes the use of a secondary blue laser to improve signal strength with light induced fluorescence, the measured performance is representative of the ultimate performance of a thermal Ca R-B atom interferometer applied to optical timekeeping. As such, the same systematic and experimental sources of frequency instability that affect the Draper CaBOT system are also present in the NIST Ca-2 system, and so the performance of this system indicates the opportunity for extending the thermal Ca R-B architecture to applications that may accommodate larger size, weight and power. In addition, improvements are still possible for the Ca-2 system.

Together, the CaBOT and Ca-2 systems represent a potentially revolutionary approach to achieving practical optical timekeeping, demonstrating the applicability of a simple, thermal atomic beam based architecture to timekeeping solutions, and a means to transition optical timekeeping advances from the laboratory to the field in small SWaP packages.

Approved for public release; distribution is unlimited

5.3. Future work and concluding remarks

5.3.1. Future work relating to the restricted Rabi rate theory

The momentum dependent, restricted Rabi rate theory as presented depicts a single atom-laser interaction in a momentum space description with no inherent time dependence. As such, the theory is not readily applied to a position space description of an interaction of an atomic wavepacket moving through a laser field. One future improvement to the theoretical framework would be to include time dependence in the formulation.

Even in its current state, the utility of the theory may be readily investigated with single-pulse experiments involving saturation studies as a function of laser waist and total optical power. Such experiments may be conducted at any facility with a narrow linewidth laser involved in either thermal or cold atom experiments. This additional experimental data may be readily used to compare the restricted Rabi rate theory predictions with those that may be derived with existing interaction models and further elucidate implications and validity of the theory.

Finally, an extension of the theory to multiple atom-laser interactions would allow for the theory's application to saturation spectroscopy as well as matter-wave interferometers including the Ramsey-Bordé atom interferometer in CaBOT and Ca-2. As with the single-pulse theory, application of the theory to either thermal atomic beam or cold atom systems are possible and associated experimental efforts to accompany theoretical investigations are desirable for the broadest application of the theory to improve understanding of atom-laser interactions and to improving design and optimization efforts for experiments and fielded operational systems alike.

5.3.2. Future work related to CaBOT and Ca-2 clocks

Improvements to both the CaBOT and Ca-2 systems are possible that would reduce measured instability at short and long time scales. Laser noise reduction including relative intensity noise subtraction and background noise mitigation may be complemented by signal improvements possible with increased fluorescence capture and improved R-B signal contrast. In addition, the implementation of both k-reversal

Approved for public release; distribution is unlimited

and dual oven operations with CaBOT, as well as full integration within the CaBOT chassis with temperature control was not achieved. Integration of the full chassis including the compact 1314 nm laser and fiber optical comb as well as a laser lock board would realize the final CaBOT optical clock as designed. Regarding the Ca-2 system, improvements to the thermal enclosure are possible that would further isolate the Ca-2 frequency reference from temperature variations and that would improve long term instability performance.

Concerning the CaBOT system in particular, several design changes may be introduced to improve performance and to reduce SWaP. The most dramatic improvements to clock performance, as well as an overall SWaP reduction, may be achieved with a modest re-design of the frequency reference to afford significant improvement to fluorescence capture efficiency. A possible redesign would feature a frequency reference with only a single atom oven and a fluorescence capture region characterized by a small radius glass tube extending outside the vacuum chamber, separated by the rest of the vacuum chamber by a narrow aperture. With this updated design, background light would be significantly reduced, and collection efficiency could be improved by orders of magnitude since many fluorescence detectors could be placed very close and at multiple locations along the atom beam that enters the glass tube extending outside the main vacuum chamber body. While dual oven operations would not be possible, k-reversal could still be employed to eliminate residual first-order Doppler shifts to the clock frequency derived from atom-laser geometry imperfections.

In addition, another proposed design improvement for CaBOT is the expansion of the existing R-B optics in-vacuum to include elements that are currently outside the vacuum chamber. While the placement of penta-prisms outside of the vacuum chamber was included in the current CaBOT design to ensure a degree of freedom to improve R-B signal contrast, the separation of the R-B steering optics resulted in reduced R-B contrast and more difficult alignment processes. As demonstrated by the Ca-2 system, a single R-B steering element in-vacuum is possible and produces higher R-B signal contrast without significant alignment or steering effort (13-18% measured for Ca-2 as opposed to 5% measured for CaBOT).

Approved for public release; distribution is unlimited

5.3.3. Concluding remarks

Optical atomic clocks based on thermal Ca R-B matter-wave interferometry that were investigated in this thesis and with related research at Draper and NIST represent a unique and exciting avenue for thermal atomic beams to be employed in new optical atomic clock applications both in the laboratory and the field. The architecture investigated involves simple and compact technologies that provide a pathway to transferring optical atomic technology to the field for application across fundamental science, industry, civil, and defense sectors. Accompanying theoretical investigations for the interaction of narrow linewidth lasers and atoms as introduced in this thesis apply not only to optical atomic systems relying on thermal beam, but also to those employing cold atoms. As such, the new theoretical framework introduced may help to supplement current practices to deepen our understanding and to improve experimental design and implementation approaches across a large range of optical atomic physics experiments and future quantum-based systems and fielded experiments.

Taken together, the theoretical and experimental contributions contained in this thesis represent exciting progress toward transferring the latest optical atomic technologies from the laboratory to practical application in the field. In particular, thermal Ca Ramsey-Bordé atom interferometry has been shown to offer a promising path to realize optical atomic timekeeping in a simple, compact device capable of ensuring greater security for critical infrastructure across civil, commercial, and defense sectors, and also of enabling new science and engineering opportunities near and far from Earth.

Approved for public release; distribution is unlimited

Appendix A

Restricted Rabi rate theory derivations

A.1. The atom-laser interaction Hamiltonian

In the laboratory frame of reference, the atomic Hamiltonian for an atom interacting with an elliptical laser beam takes the form:

$$\hat{H}_{lab} = \frac{\hat{\vec{p}}^2}{2m} + \hat{H}_o + \hat{H}_1; \qquad \hat{H}_o = \hbar\left(\omega_g \left|\mathrm{g}\right\rangle\left\langle\mathrm{g}\right| + \omega_e \left|e\right\rangle\left\langle e\right|\right)$$

$$\hat{H}_1 = e\hat{\vec{r}}_{e-n}\cdot E\hat{e}_L = -\frac{eE_o}{2}\frac{w_1 w_2}{4\pi}\int_{\vec{k}\cdot\hat{k}_o\geq 0} d^3\vec{k}\left[\begin{array}{l}\delta\left(\left|\vec{k}\right|-k_o\right)\dfrac{\left(\vec{k}\cdot\hat{k}_o\right)}{k_o}\exp\left(-\dfrac{1}{4}\left(\begin{array}{l}w_1^{\,2}\left|\vec{k}\cdot\hat{e}_{w1}\right|^2\\ +w_2^{\,2}\left|\vec{k}\cdot\hat{e}_{w2}\right|^2\end{array}\right)\right)\\ \exp\left(i\vec{k}\cdot\left(\hat{\vec{r}}-\vec{r}_w\right)-ik_o ct\right)\end{array}\right]\hat{e}_L\cdot\hat{\vec{r}}_{e-n} + h.c.$$

(A1.1)

where the atom's kinetic energy contribution is given by the operator $\hat{\vec{p}}^2/\left(2m_{Ca}\right)$ and where the atomic internal energy operator is given by $\hat{H}_o$. The operators in equation (A1.1) are written in bra-ket notation in which the ground state is represented by $\left|\mathrm{g}\right\rangle$ and the excited state by $\left|e\right\rangle$, with their characteristic frequencies separated by the transition frequency $\omega_0 = \omega_e - \omega_g$. The position operator is written as $\hat{\vec{r}}$, and $\hat{\vec{r}}_{e-n}$ is the relative electron-nucleus position operator, and $\hat{e}_L$ is the polarization vector of the laser electric field. The field is a Gaussian mode propagating along $\vec{k}_o$ with the beam waist located at the origin. Note

Approved for public release; distribution is unlimited

that the interaction Hamiltonian H_1 is composed of the term shown, which includes time evolution of the Gaussian wave as $\exp\left(-ik_o ct\right)$, as well as the Hermitian conjugate term (*h.c.*) that includes $\exp\left(ik_o ct\right)$.

The lab-frame interaction Hamiltonian given by $\hat{H}_1$ in equation (A1.1) can be expressed in terms of the matrix coupling element $\left\langle e\left|\hat{e}_L\cdot\hat{\vec{r}}_{e-n}\right|\mathrm{g}\right\rangle$ and the coupled pair of states $\left\{\left|\mathrm{g}\right\rangle\left|\vec{p}\right\rangle,\left|\mathrm{e}\right\rangle\left|\vec{p}+\hbar\vec{k}\right\rangle\right\}$ by applying a product of internal and center-of-mass motion momentum space identity operators given by $\mathbf{1}_{\mathrm{int}}\equiv\left(\left|\mathrm{g}\right\rangle\left\langle\mathrm{g}\right|+\left|e\right\rangle\left\langle e\right|\right)$ and $\mathbf{1}_{c-m}\equiv\left(\int d^3\vec{p}\left|\vec{p}\right\rangle\left\langle\vec{p}\right|\right)$ respectively:

$$\hat{H}_1=\left(\left|\mathrm{g}\right\rangle\left\langle\mathrm{g}\right|+\left|e\right\rangle\left\langle e\right|\right)\begin{pmatrix}-\frac{eE_o}{2}\frac{w_1w_2}{4\pi}\left(\int d^3\vec{p}\left|\vec{p}\right\rangle\left\langle\vec{p}\right|\right)\int\limits_{\vec{k}\cdot\hat{k}_o\geq 0}d^3\vec{k}\left[\begin{matrix}\delta\left(\left|\vec{k}\right|-k_o\right)\frac{\left(\vec{k}\cdot\hat{k}_o\right)}{k_o}\exp\left(-\frac{1}{4}\left(\begin{matrix}w_1^{\,2}\left|\vec{k}\cdot\hat{e}_{w1}\right|^2\\+w_2^{\,2}\left|\vec{k}\cdot\hat{e}_{w2}\right|^2\end{matrix}\right)\right)\\ \exp\left(i\vec{k}\cdot\left(\hat{\vec{r}}-\vec{r}_w\right)-ik_o ct\right)\end{matrix}\right]\hat{e}_L\cdot\hat{\vec{r}}_{e-n}\left(\int d^3\vec{p}'\left|\vec{p}'\right\rangle\left\langle\vec{p}'\right|\right)\\ -\frac{eE_o}{2}\frac{w_1w_2}{4\pi}\left(\int d^3\vec{p}\left|\vec{p}\right\rangle\left\langle\vec{p}\right|\right)\int\limits_{\vec{k}\cdot\hat{k}_o\geq 0}d^3\vec{k}\left[\begin{matrix}\delta\left(\left|\vec{k}\right|-k_o\right)\frac{\left(\vec{k}\cdot\hat{k}_o\right)}{k_o}\exp\left(-\frac{1}{4}\left(\begin{matrix}w_1^{\,2}\left|\vec{k}\cdot\hat{e}_{w1}\right|^2\\+w_2^{\,2}\left|\vec{k}\cdot\hat{e}_{w2}\right|^2\end{matrix}\right)\right)\\ \exp\left(-i\vec{k}\cdot\left(\hat{\vec{r}}-\vec{r}_w\right)+ik_o ct\right)\end{matrix}\right]\hat{e}_L\cdot\hat{\vec{r}}_{e-n}\left(\int d^3\vec{p}'\left|\vec{p}'\right\rangle\left\langle\vec{p}'\right|\right)\end{pmatrix}\left(\left|\mathrm{g}\right\rangle\left\langle\mathrm{g}\right|+\left|e\right\rangle\left\langle e\right|\right)$$

$$=\left(\int d^3\vec{p}\left|\vec{p}\right\rangle\left\langle\vec{p}\right|\right)\begin{pmatrix}-\frac{eE_o}{2}\frac{w_1w_2}{4\pi}\int\limits_{\substack{\left|\vec{k}\right|^2=k_o^{\,2}\\ \vec{k}\cdot\hat{k}_o>0}}d^3\vec{k}\left[\begin{matrix}\delta\left(\left|\vec{k}\right|-k_o\right)\frac{\left(\vec{k}\cdot\hat{k}_o\right)}{k_o}\exp\left(-\frac{1}{4}\left(\begin{matrix}w_1^{\,2}\left|\vec{k}\cdot\hat{e}_{w1}\right|^2\\+w_2^{\,2}\left|\vec{k}\cdot\hat{e}_{w2}\right|^2\end{matrix}\right)\right)\\ \exp\left(i\vec{k}\cdot\left(\hat{\vec{r}}-\vec{r}_w\right)-ik_o ct\right)\end{matrix}\right]\left[\begin{matrix}\left|\mathrm{g}\right\rangle\left\langle\mathrm{g}\right|\hat{e}_L\cdot\hat{\vec{r}}_{e-n}\left|e\right\rangle\left\langle e\right|\\+\left|e\right\rangle\left\langle e\right|\hat{e}_L\cdot\hat{\vec{r}}_{e-n}\left|\mathrm{g}\right\rangle\left\langle\mathrm{g}\right|\end{matrix}\right]\\ -\frac{eE_o}{2}\frac{w_1w_2}{4\pi}\int\limits_{\substack{\left|\vec{k}\right|^2=k_o^{\,2}\\ \vec{k}\cdot\hat{k}_o>0}}d^3\vec{k}\left[\begin{matrix}\delta\left(\left|\vec{k}\right|-k_o\right)\frac{\left(\vec{k}\cdot\hat{k}_o\right)}{k_o}\exp\left(-\frac{1}{4}\left(\begin{matrix}w_1^{\,2}\left|\vec{k}\cdot\hat{e}_{w1}\right|^2\\+w_2^{\,2}\left|\vec{k}\cdot\hat{e}_{w2}\right|^2\end{matrix}\right)\right)\\ \exp\left(i\vec{k}\cdot\left(\hat{\vec{r}}-\vec{r}_w\right)+ik_o ct\right)\end{matrix}\right]\left[\begin{matrix}\left|\mathrm{g}\right\rangle\left\langle\mathrm{g}\right|\hat{e}_L\cdot\hat{\vec{r}}_{e-n}\left|e\right\rangle\left\langle e\right|\\+\left|e\right\rangle\left\langle e\right|\hat{e}_L\cdot\hat{\vec{r}}_{e-n}\left|\mathrm{g}\right\rangle\left\langle\mathrm{g}\right|\end{matrix}\right]\end{pmatrix}\left(\int d^3\vec{p}'\left|\vec{p}'\right\rangle\left\langle\vec{p}'\right|\right)$$

(A1.2)

To simplify the expression in equation (A1.2), the position operator $\hat{\vec{r}}$ acts on the momentum states:

Approved for public release; distribution is unlimited

$$\hat{H}_1 = \begin{bmatrix} |\mathrm{g}\rangle\langle \mathrm{g}|\hat{e}_L \cdot \hat{\vec{r}}_{e-n}|e\rangle\langle e| \\ +|e\rangle\langle e|\hat{e}_L \cdot \hat{\vec{r}}_{e-n}|\mathrm{g}\rangle\langle \mathrm{g}| \end{bmatrix} \begin{pmatrix} -\frac{eE_o}{2}\frac{w_1 w_2}{4\pi}\int d^3\vec{p} \int\limits_{\substack{|\vec{k}|^2=k_o^2 \\ \vec{k}\cdot\vec{k}_o>0}} d^3\vec{k} \begin{bmatrix} \delta\left(|\vec{k}|-k_o\right)\frac{\left(\vec{k}\cdot\hat{k}_o\right)}{k_o}\exp\left(-\frac{1}{4}\begin{pmatrix} w_1^2\left|\vec{k}\cdot\hat{e}_{w1}\right|^2 \\ +w_2^2\left|\vec{k}\cdot\hat{e}_{w2}\right|^2 \end{pmatrix}\right) \\ \exp\left(-\left(i\vec{k}\cdot\vec{r}_w + ik_o ct\right)\right) \end{bmatrix} |\vec{p}\rangle\langle \vec{p}-\hbar\vec{k}| \\ -\frac{eE_o}{2}\frac{w_1 w_2}{4\pi}\int d^3\vec{p} \int\limits_{\substack{|\vec{k}|^2=k_o^2 \\ \vec{k}\cdot\vec{k}_o>0}} d^3\vec{k} \begin{bmatrix} \delta\left(|\vec{k}|-k_o\right)\frac{\left(\vec{k}\cdot\hat{k}_o\right)}{k_o}\exp\left(-\frac{1}{4}\begin{pmatrix} w_1^2\left|\vec{k}\cdot\hat{e}_{w1}\right|^2 \\ +w_2^2\left|\vec{k}\cdot\hat{e}_{w2}\right|^2 \end{pmatrix}\right) \\ \exp\left(i\vec{k}\cdot\vec{r}_w + ik_o ct\right) \end{bmatrix} |\vec{p}\rangle\langle \vec{p}+\hbar\vec{k}| \end{pmatrix}$$

(A1.3)

The electric field adds momentum only when inducing transitions from the ground to the excited state, and removes momentum only when inducing transitions from excited to ground state. This implies that only two of the four terms in equation (A1.3) are physically allowed, resulting in:

$$\hat{H}_1 = \hbar \begin{pmatrix} -\frac{eE_o}{2\hbar}\langle e|\hat{e}_L \cdot \hat{\vec{r}}_{e-n}|\mathrm{g}\rangle\frac{w_1 w_2}{4\pi}\int d^3\vec{p} \int\limits_{\substack{|\vec{k}|^2=k_o^2 \\ \vec{k}\cdot\vec{k}_o>0}} d^3\vec{k} \begin{bmatrix} \delta\left(|\vec{k}|-k_o\right)\frac{\left(\vec{k}\cdot\hat{k}_o\right)}{k_o}\exp\left(-\frac{1}{4}\begin{pmatrix} w_1^2\left|\vec{k}\cdot\hat{e}_{w1}\right|^2 \\ +w_2^2\left|\vec{k}\cdot\hat{e}_{w2}\right|^2 \end{pmatrix}\right) \\ \exp\left(-\left(i\vec{k}\cdot\vec{r}_w + ik_o ct\right)\right) \end{bmatrix} |e\rangle|\vec{p}\rangle\langle \mathrm{g}|\langle \vec{p}-\hbar\vec{k}| \\ -\frac{eE_o}{2\hbar}\langle \mathrm{g}|\hat{e}_L \cdot \hat{\vec{r}}_{e-n}|e\rangle\frac{w_1 w_2}{4\pi}\int d^3\vec{p} \int\limits_{\substack{|\vec{k}|^2=k_o^2 \\ \vec{k}\cdot\vec{k}_o>0}} d^3\vec{k} \begin{bmatrix} \delta\left(|\vec{k}|-k_o\right)\frac{\left(\vec{k}\cdot\hat{k}_o\right)}{k_o}\exp\left(-\frac{1}{4}\begin{pmatrix} w_1^2\left|\vec{k}\cdot\hat{e}_{w1}\right|^2 \\ +w_2^2\left|\vec{k}\cdot\hat{e}_{w2}\right|^2 \end{pmatrix}\right) \\ \exp\left(i\vec{k}\cdot\vec{r}_w + ik_o ct\right) \end{bmatrix} |\mathrm{g}\rangle|\vec{p}\rangle\langle e|\langle \vec{p}+\hbar\vec{k}| \end{pmatrix}$$

(A1.4)

The first (top) term corresponds to a photon absorption event, while the second (bottom) term corresponds to a stimulated emission event. To arrive at the final form of the interaction Hamiltonian, it is necessary to restrict the action of the electromagnetic fields to the cases where the wave vector $\vec{k}$, atom momentum $\vec{p}$ and laser detuning δ are related according to the condition for conservation of energy and momentum. This condition is given by $\left(\vec{k}\cdot\vec{p}\right)/m_{Ca} = \delta - \hbar\vec{k}^2/\left(2m_{Ca}\right)$ and is applied as a restriction on the integration, resulting in the following form for the interaction Hamiltonian:

Approved for public release; distribution is unlimited

$$\hat{H}_1 = \hbar \begin{pmatrix} -\frac{eE_o}{2\hbar}\langle e|\hat{e}_L\cdot\hat{\vec{r}}_{e-n}|\mathrm{g}\rangle\frac{w_1 w_2}{4\pi}\int d^3\vec{p}\int\limits_{\substack{|\vec{k}|^2=k_o^2;\ \vec{k}\cdot\vec{k}_o>0 \\ \frac{\vec{k}\cdot\vec{p}}{m_{Ca}}=\left(\delta-\frac{\hbar\vec{k}_o^{\,2}}{2m_{Ca}}\right)}} d^3\vec{k}\left[\begin{array}{l}\delta\left(|\vec{k}|-k_o\right)\frac{\left(\vec{k}\cdot\hat{k}_o\right)}{k_o}\exp\left(-\frac{1}{4}\left(\begin{array}{l}w_1^{\,2}\left|\vec{k}\cdot\hat{e}_{w1}\right|^2 \\ +w_2^{\,2}\left|\vec{k}\cdot\hat{e}_{w2}\right|^2\end{array}\right)\right) \\ \exp\left(-\left(i\vec{k}\cdot\vec{r}_w+ik_o ct\right)\right)\end{array}\right]|e\rangle\left|\vec{p}+\hbar\vec{k}\right\rangle\langle\mathrm{g}|\langle\vec{p}| \\ -\frac{eE_o}{2\hbar}\langle\mathrm{g}|\hat{e}_L\cdot\hat{\vec{r}}_{e-n}|e\rangle\frac{w_1 w_2}{4\pi}\int d^3\vec{p}\int\limits_{\substack{|\vec{k}|^2=k_o^2;\ \vec{k}\cdot\vec{k}_o>0 \\ \frac{\vec{k}\cdot\vec{p}}{m_{Ca}}=\left(\delta-\frac{\hbar\vec{k}_o^{\,2}}{2m_{Ca}}\right)}} d^3\vec{k}\left[\begin{array}{l}\delta\left(|\vec{k}|-k_o\right)\frac{\left(\vec{k}\cdot\hat{k}_o\right)}{k_o}\exp\left(-\frac{1}{4}\left(\begin{array}{l}w_1^{\,2}\left|\vec{k}\cdot\hat{e}_{w1}\right|^2 \\ +w_2^{\,2}\left|\vec{k}\cdot\hat{e}_{w2}\right|^2\end{array}\right)\right) \\ \exp\left(i\vec{k}\cdot\vec{r}_w+ik_o ct\right)\end{array}\right]|\mathrm{g}\rangle|\vec{p}\rangle\langle e|\left\langle\vec{p}+\hbar\vec{k}\right| \end{pmatrix}$$

(A1.5)

Restriction of the integration is implemented by means of introducing delta functions appropriate to the selected coordinate representation.

A.2. Deriving equations of motion in the laboratory frame

The atomic Hamiltonian given by equation (A1.1) is used to develop equations of motion for an atomic wavepacket $\left|\Psi(t)\right\rangle = \left|\Psi_g(t)\right\rangle + \left|\Psi_e(t)\right\rangle$ composed of a superposition of ground and excited state wave functions given by $\left|\Psi_g(t)\right\rangle$ and $\left|\Psi_e(t)\right\rangle$ respectively. The time-dependent Schrödinger equation for this atomic system may be expressed in terms of the wavefunction $\left|\Psi(t)\right\rangle$ and the laboratory-frame atomic Hamiltonian $\hat{H}_{lab}$ given by equation (A1.1) as:

$$i\hbar\frac{d}{dt}\left|\Psi(t)\right\rangle = \hat{H}_{lab}\left|\Psi(t)\right\rangle \tag{A2.1}$$

The states $\left|\Psi(t)\right\rangle$ may be expressed as expansions in momentum states $\left|\vec{p}\right\rangle$ in anticipation of applying the electromagnetic Hamiltonian (A1.5). The following form is proposed for the atom state superposition coupled by the electromagnetic field:

Approved for public release; distribution is unlimited

$$
\begin{aligned}
&\left|\Psi\left(t\right)\right\rangle = \left|\Psi_g\left(t\right)\right\rangle + \left|\Psi_e\left(t\right)\right\rangle \\
&\left|\Psi_g\left(t\right)\right\rangle = \left|g\right\rangle \int d^3\vec{p}\cdot f_g\left(\vec{p},t\right)\exp\left(-i\omega_g t - i\frac{\vec{p}^2}{2m_{Ca}\hbar}t\right)\left|\vec{p}\right\rangle \\
&\left|\Psi_e\left(t\right)\right\rangle = \left|e\right\rangle \int d^3\vec{p}\, f_e\left(\vec{p},t\right)\exp\left(-i\omega_e t - i\frac{\vec{p}^2}{2m_{Ca}\hbar}t\right)\left|\vec{p}\right\rangle
\end{aligned}
\tag{A2.2}
$$

where the distribution functions $f_e\left(\vec{p},t\right)$ and $f_g\left(\vec{p},t\right)$ are yet to be determined, and the terms $\exp\left(-i\omega_e t - i\frac{\vec{p}^2}{2m_{Ca}\hbar}t\right)$ and $\exp\left(-i\omega_g t - i\frac{\vec{p}^2}{2m_{Ca}\hbar}t\right)$ are phase terms corresponding to freely propagating particles. The solution must be normalizable, i.e. $\left\langle\Psi\left(t\right)\middle|\Psi\left(t\right)\right\rangle = 1$. The forms for the atomic wavefunction in (A2.2) describe free space atom propagation, with an implicit assumption that the amplitude functions $f_e\left(\vec{p},t\right)$ and $f_g\left(\vec{p},t\right)$ are slowly varying as compared with the phase terms in the integrals over momentum.

Equations (A1.1) and (A2.2) are substituted into the right hand side of (A2.1) to express the Schrödinger equation as:

Approved for public release; distribution is unlimited

$$
\begin{aligned}
i\hbar\frac{d}{dt}\left|\Psi(t)\right\rangle &= \hat{H}_{lab}\left|\Psi(t)\right\rangle \\
&= \hbar\left[\begin{array}{l}
\left(\omega_g\left|\mathrm{g}\right\rangle\left\langle\mathrm{g}\right| + \omega_e\left|e\right\rangle\left\langle e\right|\right) + \dfrac{\hat{\vec{p}}^{\,2}}{2m\hbar} \\
+\left(\begin{array}{l}
-\dfrac{eE_o}{2\hbar}\left\langle e\left|\hat{e}_L\cdot\hat{\vec{r}}_{e-n}\right|\mathrm{g}\right\rangle\dfrac{w_1w_2}{4\pi}\int d^3\vec{p}\underset{\substack{\left|\vec{k}\right|^2=k_o^{\,2};\ \vec{k}\cdot\vec{k}_o>0\\ \frac{\vec{k}\cdot\vec{p}}{m_{Ca}}=\left(\delta-\frac{\hbar\vec{k}_o^{\,2}}{2m_{Ca}}\right)}}{\int} d^3\vec{k}\,\delta\left(\left|\vec{k}\right|-k_o\right)\dfrac{\left(\vec{k}\cdot\hat{k}_o\right)}{k_o}\left[\begin{array}{l}\exp\left(-\dfrac{1}{4}\left(\begin{array}{l}w_1^{\,2}\left|\vec{k}\cdot\hat{e}_{w1}\right|^2\\ +w_2^{\,2}\left|\vec{k}\cdot\hat{e}_{w2}\right|^2\end{array}\right)\right)\\ \times\exp\left(-\left(i\vec{k}\cdot\vec{r}_w+ik_oct\right)\right)\end{array}\right]\left|e\right\rangle\left|\vec{p}+\hbar\vec{k}\right\rangle\left\langle\mathrm{g}\right|\left\langle\vec{p}\right| \\
-\dfrac{eE_o}{2\hbar}\left\langle\mathrm{g}\left|\hat{e}_L\cdot\hat{\vec{r}}_{e-n}\right|e\right\rangle\dfrac{w_1w_2}{4\pi}\int d^3\vec{p}\underset{\substack{\left|\vec{k}\right|^2=k_o^{\,2};\ \vec{k}\cdot\vec{k}_o>0\\ \frac{\vec{k}\cdot\vec{p}}{m_{Ca}}=\left(\delta-\frac{\hbar\vec{k}_o^{\,2}}{2m_{Ca}}\right)}}{\int} d^3\vec{k}\,\delta\left(\left|\vec{k}\right|-k_o\right)\dfrac{\left(\vec{k}\cdot\hat{k}_o\right)}{k_o}\left[\begin{array}{l}\exp\left(-\dfrac{1}{4}\left(\begin{array}{l}w_1^{\,2}\left|\vec{k}\cdot\hat{e}_{w1}\right|^2\\ +w_2^{\,2}\left|\vec{k}\cdot\hat{e}_{w2}\right|^2\end{array}\right)\right)\\ \times\exp\left(i\vec{k}\cdot\vec{r}_w+ik_oct\right)\end{array}\right]\left|\mathrm{g}\right\rangle\left|\vec{p}\right\rangle\left\langle e\right|\left\langle\vec{p}+\hbar\vec{k}\right|
\end{array}\right)
\end{array}\right] \\
&\cdot\left[\begin{array}{l}
\left|e\right\rangle\int d^3\vec{p}\,'f_e\left(\vec{p}\,',t\right)\exp\left(-i\omega_et-i\dfrac{\vec{p}\,'^2}{2m\hbar}t\right)\left|\vec{p}\,'\right\rangle \\
+\left|g\right\rangle\int d^3\vec{p}\,'\cdot f_g\left(\vec{p}\,',t\right)\exp\left(-i\omega_gt-i\dfrac{\vec{p}\,'^2}{2m\hbar}t\right)\left|\vec{p}\,'\right\rangle
\end{array}\right]
\end{aligned}
$$

(A2.3)

In equation (A2.3), the momentum operator and the internal atomic Hamiltonian operators from equation (A1.1) are expressed in terms of the matrix coupling element $\left\langle e\left|\hat{e}_L\cdot\hat{\vec{r}}_{e-n}\right|\mathrm{g}\right\rangle$ and the coupled pair of states $\left\{\left|\mathrm{g}\right\rangle\left|\vec{p}\right\rangle,\left|\mathrm{e}\right\rangle\left|\vec{p}+\hbar\vec{k}\right\rangle\right\}$ by applying a product of internal and center-of-mass motion momentum space identity operators given by $\mathbf{1}_{\mathrm{int}}\equiv\left(\left|\mathrm{g}\right\rangle\left\langle\mathrm{g}\right|+\left|e\right\rangle\left\langle e\right|\right)$ and $\mathbf{1}_{c-m}\equiv\left(\int d^3\vec{p}\left|\vec{p}\right\rangle\left\langle\vec{p}\right|\right)$. This follows the same process employed to derive the expression for the interaction Hamiltonian, and results in the following expression for the sum of internal atomic state and momentum Hamiltonian operators:

$$
\begin{aligned}
\hat{H}_o+\frac{\hat{\vec{p}}^{\,2}}{2m} &= \mathbf{1}_{c-m}\mathbf{1}_{\mathrm{int}}\left(\hat{H}_o+\frac{\hat{\vec{p}}^{\,2}}{2m}\right)\mathbf{1}_{\mathrm{int}} \\
&= \frac{1}{\hbar}\left[\left(\omega_g\left|\mathrm{g}\right\rangle\left\langle\mathrm{g}\right|+\omega_e\left|e\right\rangle\left\langle e\right|\right)+\frac{\hat{\vec{p}}^{\,2}}{2m\hbar}\right]
\end{aligned}
\qquad \text{(A2.4)}
$$

Approved for public release; distribution is unlimited

The expression for $\left|\Psi(t)\right\rangle$ is distributed to the internal and momentum Hamiltonian operators and the Schrödinger equation (A2.3) becomes:

$$
\begin{aligned}
&\hat{H}_{lab}\left|\Psi(t)\right\rangle \\
&= \hbar\left[\begin{array}{l}
\left(\omega_g\left|\mathrm{g}\right\rangle\left\langle\mathrm{g}\right| + \omega_e\left|e\right\rangle\left\langle e\right|\right)\left[\begin{array}{l}\left|e\right\rangle\int d^3\vec{p}\,' f_e\left(\vec{p}\,',t\right)\exp\left(-i\omega_e t - i\dfrac{\vec{p}\,'^2}{2m\hbar}t\right)\left|\vec{p}\,'\right\rangle \\ \left|g\right\rangle\int d^3\vec{p}\,'\cdot f_g\left(\vec{p}\,',t\right)\exp\left(-i\omega_g t - i\dfrac{\vec{p}\,'^2}{2m\hbar}t\right)\left|\vec{p}\,'\right\rangle\end{array}\right] + \dfrac{\hat{\vec{p}}^2}{2m\hbar}\left[\begin{array}{l}\left|e\right\rangle\int d^3\vec{p}\,' f_e\left(\vec{p}\,',t\right)\exp\left(-i\omega_e t - i\dfrac{\vec{p}\,'^2}{2m\hbar}t\right)\left|\vec{p}\,'\right\rangle \\ \left|g\right\rangle\int d^3\vec{p}\,'\cdot f_g\left(\vec{p}\,',t\right)\exp\left(-i\omega_g t - i\dfrac{\vec{p}\,'^2}{2m\hbar}t\right)\left|\vec{p}\,'\right\rangle\end{array}\right] \\
+\left(\begin{array}{l}
-\dfrac{eE_o}{2\hbar}\left\langle e\right|\hat{e}_L\cdot\hat{\vec{r}}_{e-n}\left|\mathrm{g}\right\rangle\dfrac{w_1 w_2}{4\pi}\int d^3\vec{p}\left[\begin{array}{l}\displaystyle\int\limits_{\substack{\left|\vec{k}\right|^2=k_o^2;\ \vec{k}\cdot\vec{k}_o>0 \\ \frac{\vec{k}\cdot\vec{p}}{m_{Ca}}=\left(\delta-\frac{\hbar k_o^2}{2m_{Ca}}\right)}} d^3\vec{k}\,\delta\left(\left|\vec{k}\right|-k_o\right)\dfrac{\left(\vec{k}\cdot\hat{k}_o\right)}{k_o}\left[\begin{array}{l}\exp\left(-\dfrac{1}{4}\left(\begin{array}{l}w_1^2\left|\vec{k}\cdot\hat{e}_{w1}\right|^2 \\ +w_2^2\left|\vec{k}\cdot\hat{e}_{w2}\right|^2\end{array}\right)\right) \\ \times\exp\left(-\left(i\vec{k}\cdot\vec{r}_w + ik_o ct\right)\right)\end{array}\right]\left|e\right\rangle\left|\vec{p}+\hbar\vec{k}\right\rangle\left\langle\mathrm{g}\right|\left\langle\vec{p}\right| \\ \left(\begin{array}{l}\left|e\right\rangle\int d^3\vec{p}\,' f_e\left(\vec{p}\,',t\right)\exp\left(-i\omega_e t - i\dfrac{\vec{p}\,'^2}{2m\hbar}t\right)\left|\vec{p}\,'\right\rangle \\ +\left|g\right\rangle\int d^3\vec{p}\,'\cdot f_g\left(\vec{p}\,',t\right)\exp\left(-i\omega_g t - i\dfrac{\vec{p}\,'^2}{2m\hbar}t\right)\left|\vec{p}\,'\right\rangle\end{array}\right)\end{array}\right] \\
-\dfrac{eE_o}{2\hbar}\left\langle\mathrm{g}\right|\hat{e}_L\cdot\hat{\vec{r}}_{e-n}\left|e\right\rangle\dfrac{w_1 w_2}{4\pi}\int d^3\vec{p}\left[\begin{array}{l}\displaystyle\int\limits_{\substack{\left|\vec{k}\right|^2=k_o^2;\ \vec{k}\cdot\vec{k}_o>0 \\ \frac{\vec{k}\cdot\vec{p}}{m_{Ca}}=\left(\delta-\frac{\hbar k_o^2}{2m_{Ca}}\right)}} d^3\vec{k}\,\delta\left(\left|\vec{k}\right|-k_o\right)\dfrac{\left(\vec{k}\cdot\hat{k}_o\right)}{k_o}\left[\begin{array}{l}\exp\left(-\dfrac{1}{4}\left(\begin{array}{l}w_1^2\left|\vec{k}\cdot\hat{e}_{w1}\right|^2 \\ +w_2^2\left|\vec{k}\cdot\hat{e}_{w2}\right|^2\end{array}\right)\right) \\ \times\exp\left(i\vec{k}\cdot\vec{r}_w + ik_o ct\right)\end{array}\right]\left|\mathrm{g}\right\rangle\left|\vec{p}\right\rangle\left\langle e\right|\left\langle\vec{p}+\hbar\vec{k}\right| \\ \left(\begin{array}{l}\left|e\right\rangle\int d^3\vec{p}\,' f_e\left(\vec{p}\,',t\right)\exp\left(-i\omega_e t - i\dfrac{\vec{p}\,'^2}{2m\hbar}t\right)\left|\vec{p}\,'\right\rangle \\ +\left|g\right\rangle\int d^3\vec{p}\,'\cdot f_g\left(\vec{p}\,',t\right)\exp\left(-i\omega_g t - i\dfrac{\vec{p}\,'^2}{2m\hbar}t\right)\left|\vec{p}\,'\right\rangle\end{array}\right)\end{array}\right)
\end{array}\right]
\end{aligned}
$$

(A2.5)

Further distribution and applying inner products results, and carrying out integrations in momentum yields

Approved for public release; distribution is unlimited

$$
\begin{aligned}
&H_{lab}\left|\Psi(t)\right\rangle \\
&= \hbar\left[\begin{array}{l}
\left[\begin{array}{l}
|e\rangle\omega_e\int d^3\vec{p}\,' f_e(\vec{p}\,',t)\exp\left(-i\omega_e t - i\frac{\vec{p}\,'^2}{2m\hbar}t\right)\left|\vec{p}\,'\right\rangle \\
|g\rangle\omega_g\int d^3\vec{p}\,'\cdot f_g(\vec{p}\,',t)\exp\left(-i\omega_g t - i\frac{\vec{p}\,'^2}{2m\hbar}t\right)\left|\vec{p}\,'\right\rangle
\end{array}\right] + \left[\begin{array}{l}
|e\rangle\int d^3\vec{p}\,' f_e(\vec{p}\,',t)\frac{\vec{p}\,'^2}{2m\hbar}\exp\left(-i\omega_e t - i\frac{\vec{p}\,'^2}{2m\hbar}t\right)\left|\vec{p}\,'\right\rangle \\
|g\rangle\int d^3\vec{p}\,'\cdot f_g(\vec{p}\,',t)\frac{\vec{p}\,'^2}{2m\hbar}\exp\left(-i\omega_g t - i\frac{\vec{p}\,'^2}{2m\hbar}t\right)\left|\vec{p}\,'\right\rangle
\end{array}\right] \\
+\left[\begin{array}{l}
-\frac{eE_o}{2\hbar}\langle e|\hat{e}_L\cdot\hat{\vec{r}}_{e-n}|g\rangle\frac{w_1w_2}{4\pi}\int d^3\vec{p}\int\limits_{\substack{|\vec{k}|^2=k_o^2;\ \vec{k}\cdot\vec{k}_o>0\\ \frac{\vec{k}\cdot\vec{p}}{m_{Ca}}=\left(\delta-\frac{\hbar\vec{k}_o^{\,2}}{2m_{Ca}}\right)}} d^3\vec{k}\,\delta\left(|\vec{k}|-k_o\right)\frac{\left(\vec{k}\cdot\hat{k}_o\right)}{k_o}\left[\begin{array}{l}\exp\left(-\frac{1}{4}\left(\begin{array}{l}w_1^{\,2}\left|\vec{k}\cdot\hat{e}_{w1}\right|^2\\ +w_2^{\,2}\left|\vec{k}\cdot\hat{e}_{w2}\right|^2\end{array}\right)\right)\\ \times\exp\left(-\left(i\vec{k}\cdot\vec{r}_w+ik_o ct\right)\right)\end{array}\right]|e\rangle\left|\vec{p}+\hbar\vec{k}\right\rangle\left[\begin{array}{l}\int d^3\vec{p}\,'\left(\begin{array}{l}f_g(\vec{p}\,',t)\exp\left(-i\omega_g t - i\frac{\vec{p}\,'^2}{2m\hbar}t\right)\\ \delta\left(\vec{p}-\vec{p}\,'\right)\end{array}\right)\end{array}\right] \\
-\frac{eE_o}{2\hbar}\langle g|\hat{e}_L\cdot\hat{\vec{r}}_{e-n}|e\rangle\frac{w_1w_2}{4\pi}\int d^3\vec{p}\int\limits_{\substack{|\vec{k}|^2=k_o^2;\ \vec{k}\cdot\vec{k}_o>0\\ \frac{\vec{k}\cdot\vec{p}}{m_{Ca}}=\left(\delta-\frac{\hbar\vec{k}_o^{\,2}}{2m_{Ca}}\right)}} d^3\vec{k}\,\delta\left(|\vec{k}|-k_o\right)\frac{\left(\vec{k}\cdot\hat{k}_o\right)}{k_o}\left[\begin{array}{l}\exp\left(-\frac{1}{4}\left(\begin{array}{l}w_1^{\,2}\left|\vec{k}\cdot\hat{e}_{w1}\right|^2\\ +w_2^{\,2}\left|\vec{k}\cdot\hat{e}_{w2}\right|^2\end{array}\right)\right)\\ \times\exp\left(i\vec{k}\cdot\vec{r}_w+ik_o ct\right)\end{array}\right]|g\rangle\left|\vec{p}\right\rangle\left[\begin{array}{l}\int d^3\vec{p}\,'\left(\begin{array}{l}f_e(\vec{p}\,',t)\exp\left(-i\omega_e t - i\frac{\vec{p}\,'^2}{2m\hbar}t\right)\\ \delta\left(\left(\vec{p}+\hbar\vec{k}\right)-\vec{p}\,'\right)\end{array}\right)\end{array}\right]
\end{array}\right] \\
&= \hbar\left[\begin{array}{l}
\left[\begin{array}{l}
|e\rangle\omega_e\int d^3\vec{p}\,' f_e(\vec{p}\,',t)\exp\left(-i\omega_e t - i\frac{\vec{p}\,'^2}{2m\hbar}t\right)\left|\vec{p}\,'\right\rangle \\
|g\rangle\omega_g\int d^3\vec{p}\,'\cdot f_g(\vec{p}\,',t)\exp\left(-i\omega_g t - i\frac{\vec{p}\,'^2}{2m\hbar}t\right)\left|\vec{p}\,'\right\rangle
\end{array}\right] + \left[\begin{array}{l}
|e\rangle\int d^3\vec{p}\,' f_e(\vec{p}\,',t)\frac{\vec{p}\,'^2}{2m\hbar}\exp\left(-i\omega_e t - i\frac{\vec{p}\,'^2}{2m\hbar}t\right)\left|\vec{p}\,'\right\rangle \\
|g\rangle\int d^3\vec{p}\,'\cdot f_g(\vec{p}\,',t)\frac{\vec{p}\,'^2}{2m\hbar}\exp\left(-i\omega_g t - i\frac{\vec{p}\,'^2}{2m\hbar}t\right)\left|\vec{p}\,'\right\rangle
\end{array}\right] \\
+\left[\begin{array}{l}
-\frac{eE_o}{2\hbar}\langle e|\hat{e}_L\cdot\hat{\vec{r}}_{e-n}|g\rangle\frac{w_1w_2}{4\pi}\int d^3\vec{p}\left|\vec{p}+\hbar\vec{k}\right\rangle\int\limits_{\substack{|\vec{k}|^2=k_o^2;\ \vec{k}\cdot\vec{k}_o>0\\ \frac{\vec{k}\cdot\vec{p}}{m_{Ca}}=\left(\delta-\frac{\hbar\vec{k}_o^{\,2}}{2m_{Ca}}\right)}} d^3\vec{k}\,\delta\left(|\vec{k}|-k_o\right)\frac{\left(\vec{k}\cdot\hat{k}_o\right)}{k_o}\left[\begin{array}{l}\exp\left(-\frac{1}{4}\left(\begin{array}{l}w_1^{\,2}\left|\vec{k}\cdot\hat{e}_{w1}\right|^2\\ +w_2^{\,2}\left|\vec{k}\cdot\hat{e}_{w2}\right|^2\end{array}\right)\right)\\ \times\exp\left(-\left(i\vec{k}\cdot\vec{r}_w+ik_o ct\right)\right)\end{array}\right]|e\rangle\exp\left(-i\omega_g t - i\frac{\vec{p}^{\,2}}{2m\hbar}t\right)f_g(\vec{p},t) \\
-\frac{eE_o}{2\hbar}\langle g|\hat{e}_L\cdot\hat{\vec{r}}_{e-n}|e\rangle\frac{w_1w_2}{4\pi}\int d^3\vec{p}\left|\vec{p}\right\rangle\int\limits_{\substack{|\vec{k}|^2=k_o^2;\ \vec{k}\cdot\vec{k}_o>0\\ \frac{\vec{k}\cdot\vec{p}}{m_{Ca}}=\left(\delta-\frac{\hbar\vec{k}_o^{\,2}}{2m_{Ca}}\right)}} d^3\vec{k}\,\delta\left(|\vec{k}|-k_o\right)\frac{\left(\vec{k}\cdot\hat{k}_o\right)}{k_o}\left[\begin{array}{l}\exp\left(-\frac{1}{4}\left(\begin{array}{l}w_1^{\,2}\left|\vec{k}\cdot\hat{e}_{w1}\right|^2\\ +w_2^{\,2}\left|\vec{k}\cdot\hat{e}_{w2}\right|^2\end{array}\right)\right)\\ \times\exp\left(i\vec{k}\cdot\vec{r}_w+ik_o ct\right)\end{array}\right]|g\rangle\exp\left(-i\omega_e t - i\frac{\left(\vec{p}+\hbar\vec{k}\right)^2}{2m\hbar}t\right)f_e\left(\left(\vec{p}+\hbar\vec{k}\right),t\right)
\end{array}\right]
\end{aligned}
$$

(A2.6)

As per the Schrödinger equation, this expression is set to $i\hbar\frac{d}{dt}\left|\Psi(t)\right\rangle$, the time derivative of the wave function given by the left hand side of (A2.3). By substituting the form for the wave function given by equation (A2.2), the time derivative can be written as:

$$
\begin{aligned}
i\hbar\frac{d}{dt}\left|\Psi(t)\right\rangle &= ih\frac{d}{dt}\left[\begin{array}{l}\left|e\right\rangle\int d^3\vec{p}'\,f_e\left(\vec{p}',t\right)\exp\left(-i\omega_e t - i\frac{\vec{p}'^2}{2m\hbar}t\right)\left|\vec{p}'\right\rangle \\ +\left|g\right\rangle\int d^3\vec{p}'\cdot f_g\left(\vec{p}',t\right)\exp\left(-i\omega_g t - i\frac{\vec{p}'^2}{2m\hbar}t\right)\left|\vec{p}'\right\rangle\end{array}\right] \\
&= i\hbar\left[\begin{array}{l}\left|e\right\rangle\int d^3\vec{p}'\cdot\exp\left(-i\omega_e t - i\frac{\vec{p}'^2}{2m\hbar}t\right)\frac{d}{dt}f_e\left(\vec{p}',t\right)\left|\vec{p}'\right\rangle \\ +\left|e\right\rangle\int d^3\vec{p}'\cdot\left|\vec{p}'\right\rangle\exp\left(-i\omega_e t - i\frac{\vec{p}'^2}{2m\hbar}t\right)\left(-i\omega_e - i\frac{\vec{p}'^2}{2m\hbar}\right)f_e\left(\vec{p}',t\right) \\ +\left|g\right\rangle\int d^3\vec{p}'\cdot\exp\left(-i\omega_g t - i\frac{\vec{p}'^2}{2m\hbar}t\right)\frac{d}{dt}f_g\left(\vec{p}',t\right)\left|\vec{p}'\right\rangle \\ +\left|g\right\rangle\int d^3\vec{p}'\cdot\left|\vec{p}'\right\rangle\exp\left(-i\omega_g t - i\frac{\vec{p}'^2}{2m\hbar}t\right)\left(-i\omega_g - i\frac{\vec{p}'^2}{2m\hbar}\right)f_g\left(\vec{p}',t\right)\end{array}\right]
\end{aligned}
\tag{A2.7}
$$

Equating the left and right hand sides of the Schrödinger equation, i.e. equating (A2.6) and (A2.7), produces a set of coupled equations expressed as:

Approved for public release; distribution is unlimited

$$
i\hbar\left[\begin{array}{l}
|e\rangle\left(\begin{array}{l}
\int d^3\vec{p}'\cdot\exp\left(-i\omega_e t - i\dfrac{\vec{p}'^2}{2m\hbar}t\right)\dfrac{d}{dt}\,f_e\left(\vec{p}',t\right)|\vec{p}'\rangle \\
+\int d^3\vec{p}'\cdot|\vec{p}'\rangle\exp\left(-i\omega_e t - i\dfrac{\vec{p}'^2}{2m\hbar}t\right)\left(-i\omega_e - i\dfrac{\vec{p}'^2}{2m\hbar}\right)f_e\left(\vec{p}',t\right)
\end{array}\right) \\
+|g\rangle\left(\begin{array}{l}
\int d^3\vec{p}'\cdot\exp\left(-i\omega_g t - i\dfrac{\vec{p}'^2}{2m\hbar}t\right)\dfrac{d}{dt}\,f_g\left(\vec{p}',t\right)|\vec{p}'\rangle \\
+\int d^3\vec{p}'\cdot|\vec{p}'\rangle\exp\left(-i\omega_g t - i\dfrac{\vec{p}'^2}{2m\hbar}t\right)\left(-i\omega_g - i\dfrac{\vec{p}'^2}{2m\hbar}\right)f_g\left(\vec{p}',t\right)
\end{array}\right)
\end{array}\right]
$$

$$
=\hbar\left[\begin{array}{l}
|e\rangle\left[\begin{array}{l}
\omega_e\int d^3\vec{p}'\,f_e\left(\vec{p}',t\right)\exp\left(-i\omega_e t - i\dfrac{\vec{p}'^2}{2m\hbar}t\right)|\vec{p}'\rangle + \int d^3\vec{p}'\,f_e\left(\vec{p}',t\right)\dfrac{\vec{p}'^2}{2m\hbar}\exp\left(-i\omega_e t - i\dfrac{\vec{p}'^2}{2m\hbar}t\right)|\vec{p}'\rangle \\
-\dfrac{eE_o}{2\hbar}\langle e|\hat{e}_L\cdot\hat{\vec{r}}_{e-n}|\mathrm{g}\rangle\dfrac{w_1 w_2}{4\pi}\int d^3\vec{p}'\left|\vec{p}'+\hbar\vec{k}\right\rangle\underset{\substack{|\vec{k}|^2=k_o{}^2;\ \vec{k}\cdot\vec{k}_o>0 \\ \frac{\vec{k}\cdot\vec{p}'}{m_{Ca}}=\left(\delta-\frac{\hbar k_o{}^2}{2m_{Ca}}\right)}}{\int} d^3\vec{k}\left[\begin{array}{l}
\delta\left(|\vec{k}|-k_o\right)\dfrac{\left(\vec{k}\cdot\hat{k}_o\right)}{k_o}\left(\begin{array}{l}
\exp\left(-\dfrac{1}{4}\left(\begin{array}{l} w_1{}^2\left|\vec{k}\cdot\hat{e}_{w1}\right|^2 \\ +w_2{}^2\left|\vec{k}\cdot\hat{e}_{w2}\right|^2\end{array}\right)\right) \\
\exp\left(-\left(i\vec{k}\cdot\vec{r}_w + ik_o ct\right)\right) \\
\exp\left(-i\omega_g t - i\dfrac{\vec{p}'^2}{2m\hbar}t\right) \\
f_g\left(\vec{p}',t\right)
\end{array}\right)
\end{array}\right]
\end{array}\right] \\
+|g\rangle\left[\begin{array}{l}
\omega_g\int d^3\vec{p}'\cdot f_g\left(\vec{p}',t\right)\exp\left(-i\omega_g t - i\dfrac{\vec{p}'^2}{2m\hbar}t\right)|\vec{p}'\rangle + \int d^3\vec{p}'\cdot f_g\left(\vec{p}',t\right)\dfrac{\vec{p}'^2}{2m\hbar}\exp\left(-i\omega_g t - i\dfrac{\vec{p}'^2}{2m\hbar}t\right)|\vec{p}'\rangle \\
-\dfrac{eE_o}{2\hbar}\langle \mathrm{g}|\hat{e}_L\cdot\hat{\vec{r}}_{e-n}|e\rangle\dfrac{w_1 w_2}{4\pi}\int d^3\vec{p}'\left|\vec{p}'\right\rangle\underset{\substack{|\vec{k}|^2=k_o{}^2;\ \vec{k}\cdot\vec{k}_o>0 \\ \frac{\vec{k}\cdot\vec{p}'}{m_{Ca}}=\left(\delta-\frac{\hbar k_o{}^2}{2m_{Ca}}\right)}}{\int} d^3\vec{k}\left[\begin{array}{l}
\delta\left(|\vec{k}|-k_o\right)\dfrac{\left(\vec{k}\cdot\hat{k}_o\right)}{k_o}\left(\begin{array}{l}
\exp\left(-\dfrac{1}{4}\left(\begin{array}{l} w_1{}^2\left|\vec{k}\cdot\hat{e}_{w1}\right|^2 \\ +w_2{}^2\left|\vec{k}\cdot\hat{e}_{w2}\right|^2\end{array}\right)\right) \\
\exp\left(i\vec{k}\cdot\vec{r}_w + ik_o ct\right) \\
\exp\left(-i\omega_e t - i\dfrac{\left(\vec{p}'+\hbar\vec{k}\right)^2}{2m\hbar}t\right) \\
f_e\left(\left(\vec{p}'+\hbar\vec{k}\right),t\right)
\end{array}\right)
\end{array}\right]
\end{array}\right]
\end{array}\right].
$$

(A2.8)

Left-multiplying equation (A2.8) by the atomic states $|e\rangle$ and $|g\rangle$ projects the coupled equations into the internal atomic state space. Projection into the excited state $|e\rangle$ results in:

$$
\left(\begin{array}{l}
\int d^3\vec{p}' \cdot \exp\left(-i\omega_e t - i\dfrac{\vec{p}'^2}{2m\hbar}t\right) i\dfrac{d}{dt}\, f_e\left(\vec{p}',t\right)\left|\vec{p}'\right\rangle \\
+\int d^3\vec{p}' \cdot \left|\vec{p}'\right\rangle \exp\left(-i\omega_e t - i\dfrac{\vec{p}'^2}{2m\hbar}t\right)\left(\omega_e + \dfrac{\vec{p}'^2}{2m\hbar}\right) f_e\left(\vec{p}',t\right)
\end{array}\right)
$$

$$
= \left[\begin{array}{l}
\omega_e \int d^3\vec{p}' f_e\left(\vec{p}',t\right)\exp\left(-i\omega_e t - i\dfrac{\vec{p}'^2}{2m\hbar}t\right)\left|\vec{p}'\right\rangle + \int d^3\vec{p}' f_e\left(\vec{p}',t\right)\dfrac{\vec{p}'^2}{2m\hbar}\exp\left(-i\omega_e t - i\dfrac{\vec{p}'^2}{2m\hbar}t\right)\left|\vec{p}'\right\rangle \\
-\dfrac{eE_o}{2\hbar}\left\langle e\left|\hat{e}_L \cdot \hat{\vec{r}}_{e-n}\right|g\right\rangle \dfrac{w_1 w_2}{4\pi}\int d^3\vec{p}'\left|\vec{p}' + \hbar\vec{k}\right\rangle \underset{\substack{\left|\vec{k}\right|^2 = k_o^2;\ \vec{k}\cdot\vec{k}_o > 0 \\ \frac{\vec{k}\cdot\vec{p}'}{m_{Ca}} = \left(\delta - \frac{\hbar\vec{k}_o^{\,2}}{2m_{Ca}}\right)}}{\int} d^3\vec{k}\,\delta\left(\left|\vec{k}\right| - k_o\right)\dfrac{\left(\vec{k}\cdot\hat{k}_o\right)}{k_o}\left[\begin{array}{l}
\exp\left(-\dfrac{1}{4}\left(\begin{array}{l} w_1^{\,2}\left|\vec{k}\cdot\hat{e}_{w1}\right|^2 \\ +w_2^{\,2}\left|\vec{k}\cdot\hat{e}_{w2}\right|^2\end{array}\right)\right) \\
\exp\left(-\left(i\vec{k}\cdot\vec{r}_w + ik_o ct\right)\right) \\
\exp\left(-i\omega_g t - i\dfrac{\vec{p}'^2}{2m\hbar}t\right) \\
f_g\left(\vec{p}',t\right)
\end{array}\right]
\end{array}\right]
$$

(A2.9)

Complementary terms are selected when projecting (A2.8) into the ground state $\left|g\right\rangle$:

Approved for public release; distribution is unlimited

$$
\begin{pmatrix}
\int d^3\vec{p}' \cdot \exp\left(-i\omega_g t - i\frac{\vec{p}'^2}{2m\hbar}t\right) i\frac{d}{dt} f_g\left(\vec{p}', t\right) \left|\vec{p}'\right\rangle \\
+\int d^3\vec{p}' \cdot \left|\vec{p}'\right\rangle \exp\left(-i\omega_g t - i\frac{\vec{p}'^2}{2m\hbar}t\right)\left(\omega_g + \frac{\vec{p}'^2}{2m\hbar}\right) f_g\left(\vec{p}', t\right)
\end{pmatrix}
$$

$$
= \begin{bmatrix}
\omega_g \int d^3\vec{p}' \cdot f_g\left(\vec{p}', t\right) \exp\left(-i\omega_g t - i\frac{\vec{p}'^2}{2m\hbar}t\right) \left|\vec{p}'\right\rangle + \int d^3\vec{p}' \cdot f_g\left(\vec{p}', t\right) \frac{\vec{p}'^2}{2m\hbar} \exp\left(-i\omega_g t - i\frac{\vec{p}'^2}{2m\hbar}t\right) \left|\vec{p}'\right\rangle \\
-\frac{eE_o}{2\hbar} \left\langle \mathrm{g}\left|\hat{e}_L \cdot \hat{\vec{r}}_{e-n}\right|e\right\rangle \frac{w_1 w_2}{4\pi} \int d^3\vec{p}' \left|\vec{p}'\right\rangle \int\limits_{\substack{\left|\vec{k}\right|^2 = k_o^{\,2};\ \vec{k}\cdot\vec{k}_o > 0 \\ \frac{\vec{k}\cdot\vec{p}'}{m_{Ca}} = \left(\delta - \frac{\hbar\vec{k}_o^{\,2}}{2m_{Ca}}\right)}} d^3\vec{k}\,\delta\left(\left|\vec{k}\right| - k_o\right) \frac{\left(\vec{k}\cdot\hat{k}_o\right)}{k_o}
\begin{bmatrix}
\exp\left(-\frac{1}{4}\left(\begin{matrix} w_1^{\,2}\left|\vec{k}\cdot\hat{e}_{w1}\right|^2 \\ +w_2^{\,2}\left|\vec{k}\cdot\hat{e}_{w2}\right|^2 \end{matrix}\right)\right) \\
\exp\left(i\vec{k}\cdot\vec{r}_w + ik_o ct\right) \\
\exp\left(-i\omega_e t - i\frac{\left(\vec{p}' + \hbar\vec{k}\right)^2}{2m\hbar}t\right) \\
f_e\left(\left(\vec{p}' + \hbar\vec{k}\right), t\right)
\end{bmatrix}
\end{bmatrix}
$$

(A2.10)

Both equations (A2.9) and (A2.10) feature terms that can cancel, and so the equations simplify to:

Approved for public release; distribution is unlimited

$$\int d^3\vec{p}' \cdot \exp\left(-i\omega_e t - i\frac{\vec{p}'^2}{2m\hbar}t\right) i\frac{d}{dt} f_e\left(\vec{p}',t\right)\left|\vec{p}'\right\rangle$$

$$= -\frac{eE_o}{2\hbar}\left\langle e\left|\hat{e}_L \cdot \hat{\vec{r}}_{e-n}\right|\mathrm{g}\right\rangle \frac{w_1 w_2}{4\pi}\int d^3\vec{p}'\left|\vec{p}' + \hbar\vec{k}\right\rangle \int\limits_{\substack{|\vec{k}|^2 = {k_o}^2;\ \vec{k}\cdot\vec{k}_o > 0 \\ \frac{\vec{k}\cdot\vec{p}'}{m_{Ca}} = \left(\delta - \frac{\hbar {\vec{k}_o}^2}{2m_{Ca}}\right)}} d^3\vec{k}\,\delta\left(\left|\vec{k}\right| - k_o\right)\frac{\left(\vec{k}\cdot\hat{k}_o\right)}{k_o}\begin{bmatrix} \exp\left(-\frac{1}{4}\begin{pmatrix} {w_1}^2\left|\vec{k}\cdot\hat{e}_{w1}\right|^2 \\ +{w_2}^2\left|\vec{k}\cdot\hat{e}_{w2}\right|^2 \end{pmatrix}\right) \\ \exp\left(-\left(i\vec{k}\cdot\vec{r}_w + ik_o ct\right)\right) \\ \exp\left(-i\omega_g t - i\frac{\vec{p}'^2}{2m\hbar}t\right) \\ f_g\left(\vec{p}',t\right) \end{bmatrix}$$

$$\int d^3\vec{p}' \cdot \exp\left(-i\omega_g t - i\frac{\vec{p}'^2}{2m\hbar}t\right) i\frac{d}{dt} f_g\left(\vec{p}',t\right)\left|\vec{p}'\right\rangle$$

$$= -\frac{eE_o}{2\hbar}\left\langle \mathrm{g}\left|\hat{e}_L \cdot \hat{\vec{r}}_{e-n}\right|e\right\rangle \frac{w_1 w_2}{4\pi}\int d^3\vec{p}'\left|\vec{p}'\right\rangle \int\limits_{\substack{|\vec{k}|^2 = {k_o}^2;\ \vec{k}\cdot\vec{k}_o > 0 \\ \frac{\vec{k}\cdot\vec{p}'}{m_{Ca}} = \left(\delta - \frac{\hbar {\vec{k}_o}^2}{2m_{Ca}}\right)}} d^3\vec{k}\,\delta\left(\left|\vec{k}\right| - k_o\right)\frac{\left(\vec{k}\cdot\hat{k}_o\right)}{k_o}\begin{bmatrix} \exp\left(-\frac{1}{4}\begin{pmatrix} {w_1}^2\left|\vec{k}\cdot\hat{e}_{w1}\right|^2 \\ +{w_2}^2\left|\vec{k}\cdot\hat{e}_{w2}\right|^2 \end{pmatrix}\right) \\ \exp\left(i\vec{k}\cdot\vec{r}_w + ik_o ct\right) \\ \exp\left(-i\omega_e t - i\frac{\left(\vec{p}' + \hbar\vec{k}\right)^2}{2m\hbar}t\right) \\ f_e\left(\left(\vec{p}' + \hbar\vec{k}\right),t\right) \end{bmatrix}$$

(A2.11)

Equations of motion for the momentum distributions are derived with a projection onto the momentum state $\left|\vec{p}\right\rangle$ by left-multiplying equations (A2.11) by the bra $\left\langle\vec{p}\right|$. The first (top) equation from (A2.11) is considered first:

Approved for public release; distribution is unlimited

$$\exp\left(-i\omega_e t - i\frac{\vec{p}^{\,2}}{2m\hbar}t\right) i\frac{d}{dt} f_e(\vec{p},t) = \left(\begin{array}{l} -\frac{eE_o}{2\hbar}\langle e|\hat{e}_L\cdot\hat{\vec{r}}_{e-n}|\mathrm{g}\rangle\frac{w_1 w_2}{4\pi} \\ \int d^3\vec{p}\,'\left\langle \vec{p}\,\middle|\,\vec{p}\,'+\hbar\vec{k}\right\rangle \int\limits_{\substack{|\vec{k}|^2=k_o{}^2;\ \vec{k}\cdot\vec{k}_o>0 \\ \frac{\vec{k}\cdot\vec{p}\,'}{m_{Ca}}=\left(\delta-\frac{\hbar\vec{k}_o{}^2}{2m_{Ca}}\right)}} d^3\vec{k}\,\delta\left(|\vec{k}|-k_o\right)\frac{\left(\vec{k}\cdot\hat{k}_o\right)}{k_o} \end{array} \right. \left[\begin{array}{l} \exp\left(-\frac{1}{4}\left(\begin{array}{l} w_1{}^2\left|\vec{k}\cdot\hat{e}_{w1}\right|^2 \\ +w_2{}^2\left|\vec{k}\cdot\hat{e}_{w2}\right|^2 \end{array}\right)\right) \\ \exp\left(-\left(i\vec{k}\cdot\vec{r}_w + ik_o ct\right)\right) \\ \exp\left(-i\omega_g t - i\frac{\vec{p}\,'^2}{2m\hbar}t\right) \\ f_g(\vec{p}\,',t) \end{array} \right]$$

$$= -\frac{eE_o}{2\hbar}\langle e|\hat{e}_L\cdot\hat{\vec{r}}_{e-n}|\mathrm{g}\rangle\frac{w_1 w_2}{4\pi} \int\limits_{\substack{|\vec{k}|^2=k_o{}^2;\ \vec{k}\cdot\vec{k}_o>0 \\ \frac{\vec{k}\cdot\left(\vec{p}-\hbar\vec{k}\right)}{m_{Ca}}=\left(\delta-\frac{\hbar\vec{k}_o{}^2}{2m_{Ca}}\right)}} d^3\vec{k}\,\delta\left(|\vec{k}|-k_o\right)\frac{\left(\vec{k}\cdot\hat{k}_o\right)}{k_o} \left[\begin{array}{l} \exp\left(-\frac{1}{4}\left(\begin{array}{l} w_1{}^2\left|\vec{k}\cdot\hat{e}_{w1}\right|^2 \\ +w_2{}^2\left|\vec{k}\cdot\hat{e}_{w2}\right|^2 \end{array}\right)\right) \\ \times\exp\left(-\left(i\vec{k}\cdot\vec{r}_w + ik_o ct\right)\right) \\ \exp\left(-i\omega_g t - i\frac{\left(\vec{p}-\hbar\vec{k}\right)^2}{2m\hbar}t\right) \\ f_g\left(\left(\vec{p}-\hbar\vec{k}\right),t\right) \end{array} \right]$$

$$i\frac{d}{dt} f_e(\vec{p},t) = \left(\begin{array}{l} -\frac{eE_o}{2\hbar}\langle e|\hat{e}_L\cdot\hat{\vec{r}}_{e-n}|\mathrm{g}\rangle\frac{w_1 w_2}{4\pi} \\ \int\limits_{\substack{|\vec{k}|^2=k_o{}^2;\ \vec{k}\cdot\vec{k}_o>0 \\ \frac{\vec{k}\cdot\vec{p}}{m_{Ca}}=\left(\delta+\frac{\hbar\vec{k}_o{}^2}{2m_{Ca}}\right)}} d^3\vec{k}\,\delta\left(|\vec{k}|-k_o\right)\frac{\left(\vec{k}\cdot\hat{k}_o\right)}{k_o} \end{array} \right. \left[\begin{array}{l} \exp\left(-\frac{1}{4}\left(\begin{array}{l} w_1{}^2\left|\vec{k}\cdot\hat{e}_{w1}\right|^2 \\ +w_2{}^2\left|\vec{k}\cdot\hat{e}_{w2}\right|^2 \end{array}\right)\right) \\ \exp\left(-\left(i\vec{k}\cdot\vec{r}_w + ik_o ct\right)\right) \\ \exp\left(i\left(\omega_e-\omega_g\right)t + i\frac{2\vec{p}\cdot\hbar\vec{k}-\left(\hbar\vec{k}\right)^2}{2m\hbar}t\right) \\ f_g\left(\left(\vec{p}-\hbar\vec{k}\right),t\right) \end{array} \right]$$

(A2.12)

In equation (A2.12), the dot product $\left\langle \vec{p}\,\middle|\,\vec{p}\,'+\hbar\vec{k}\right\rangle$ picks out momentum states $\vec{p}\,' = \vec{p}-\hbar\vec{k}$ with a Delta function corresponding to $\delta\left(\vec{p}\,'-\left(\vec{p}-\hbar\vec{k}\right)\right)$. This is reflected both in the in the new integration restriction: $\frac{\vec{k}\cdot\left(\vec{p}-\hbar\vec{k}\right)}{m_{Ca}} = \left(\delta-\frac{\hbar\vec{k}_o{}^2}{2m_{Ca}}\right)$ and in the ground state population distribution argument:

Approved for public release; distribution is unlimited

$f_g\left(\vec{p}-\hbar\vec{k},t\right)$. The integration restriction is simplified to $\frac{\vec{k}\cdot\vec{p}}{m_{Ca}}=\left(\delta+\frac{\hbar\vec{k_o}^{\,2}}{2m_{Ca}}\right)$ by applying the identity $\left|\vec{k}\right|^2=\vec{k}\cdot\vec{k}={k_o}^2$. Projection of the second (bottom) equation of (A2.11) into momentum space $\left|\vec{p}\right\rangle$ results in:

$$\exp\left(-i\omega_g t-i\frac{\vec{p}^{\,2}}{2m\hbar}t\right)i\frac{d}{dt}f_g\left(\vec{p},t\right)=\left(\begin{array}{l}-\frac{eE_o}{2\hbar}\left\langle \mathrm{g}\left|\hat{e}_L\cdot\hat{\vec{r}}_{e-n}\right|e\right\rangle\frac{w_1w_2}{4\pi}\\ \int\limits_{\substack{\left|\vec{k}\right|^2={k_o}^2;\ \vec{k}\cdot\vec{k}_o>0\\ \frac{\vec{k}\cdot\vec{p}}{m_{Ca}}=\left(\delta-\frac{\hbar\vec{k_o}^{\,2}}{2m_{Ca}}\right)}} d^3\vec{k}\,\delta\left(\left|\vec{k}\right|-k_o\right)\frac{\left(\vec{k}\cdot\hat{k}_o\right)}{k_o}\left[\begin{array}{l}\exp\left(-\frac{1}{4}\left(\begin{array}{l}{w_1}^2\left|\vec{k}\cdot\hat{e}_{w1}\right|^2\\ +{w_2}^2\left|\vec{k}\cdot\hat{e}_{w2}\right|^2\end{array}\right)\right)\\ \exp\left(i\vec{k}\cdot\vec{r}_w+ik_oct\right)\\ \exp\left(-i\omega_e t-i\frac{\left(\vec{p}+\hbar\vec{k}\right)^2}{2m\hbar}t\right)\\ f_e\left(\left(\vec{p}+\hbar\vec{k}\right),t\right)\end{array}\right]\end{array}\right)$$

$$i\frac{d}{dt}f_g\left(\vec{p},t\right)=\left(\begin{array}{l}-\frac{eE_o}{2\hbar}\left\langle \mathrm{g}\left|\hat{e}_L\cdot\hat{\vec{r}}_{e-n}\right|e\right\rangle\frac{w_1w_2}{4\pi}\\ \int\limits_{\substack{\left|\vec{k}\right|^2={k_o}^2;\ \vec{k}\cdot\vec{k}_o>0\\ \frac{\vec{k}\cdot\vec{p}}{m_{Ca}}=\left(\delta-\frac{\hbar\vec{k_o}^{\,2}}{2m_{Ca}}\right)}} d^3\vec{k}\,\delta\left(\left|\vec{k}\right|-k_o\right)\frac{\left(\vec{k}\cdot\hat{k}_o\right)}{k_o}\left[\begin{array}{l}\exp\left(-\frac{1}{4}\left(\begin{array}{l}{w_1}^2\left|\vec{k}\cdot\hat{e}_{w1}\right|^2\\ +{w_2}^2\left|\vec{k}\cdot\hat{e}_{w2}\right|^2\end{array}\right)\right)\\ \exp\left(i\vec{k}\cdot\vec{r}_w+ik_oct\right)\\ \exp\left(-i\left(\omega_e-\omega_g\right)t-i\frac{2\vec{p}\cdot\hbar\vec{k}+\left(\hbar\vec{k}\right)^2}{2m\hbar}t\right)\\ f_e\left(\left(\vec{p}+\hbar\vec{k}\right),t\right)\end{array}\right]\end{array}\right)$$

(A2.13)

In this case, the dot product $\left\langle\vec{p}\,\middle|\,\vec{p}\,'\right\rangle$ picked out momentum states $\vec{p}\,'=\vec{p}$, and so the integration restriction corresponding to conservation of energy and momentum remains $\frac{\vec{k}\cdot\vec{p}}{m_{Ca}}=\left(\delta-\frac{\hbar\vec{k_o}^{\,2}}{2m_{Ca}}\right)$ and the excited

Approved for public release; distribution is unlimited

state population distribution argument remains as $f_e\left(\vec{p}+\hbar\vec{k},t\right)$. Rearranging the phase terms and applying the definitions $\delta=\omega_o-\left(\omega_e-\omega_g\right)$ and $\omega_o=k_o c$ results to equation (A2.12) results in:

$$
\begin{aligned}
i\frac{d}{dt}f_e\left(\vec{p},t\right) &= \left(-\frac{eE_o}{2\hbar}\left\langle e\left|\hat{e}_L\cdot\hat{\vec{r}}_{e-n}\right|g\right\rangle\frac{w_1 w_2}{4\pi}\int\limits_{\substack{|\vec{k}|^2=k_o{}^2;\ \vec{k}\cdot\vec{k}_o>0\\ \frac{\vec{k}\cdot\vec{p}}{m}=\left(\delta+\frac{\hbar\vec{k}_o{}^2}{2m}\right)}} d^3\vec{k}\left[\delta\left(\left|\vec{k}\right|-k_o\right)\frac{\left(\vec{k}\cdot\hat{k}_o\right)}{k_o}\left[\begin{array}{l}\exp\left(-\frac{1}{4}\left(\begin{array}{l}w_1{}^2\left|\vec{k}\cdot\hat{e}_{w1}\right|^2\\ +w_2{}^2\left|\vec{k}\cdot\hat{e}_{w2}\right|^2\end{array}\right)\right)\\ \exp\left(-i\vec{k}\cdot\vec{r}_w\right)\\ \exp\left(-i\omega_o t+i\left(\omega_e-\omega_g\right)t+i\frac{2\vec{p}\cdot\hbar\vec{k}-\left(\hbar\vec{k}\right)^2}{2m\hbar}t\right)\\ f_g\left(\left(\vec{p}-\hbar\vec{k}\right),t\right)\end{array}\right]\right]\right)\\
&= \left(-\frac{eE_o}{2\hbar}\left\langle e\left|\hat{e}_L\cdot\hat{\vec{r}}_{e-n}\right|g\right\rangle\frac{w_1 w_2}{4\pi}\int\limits_{\substack{|\vec{k}|^2=k_o{}^2;\ \vec{k}\cdot\vec{k}_o>0\\ \frac{\vec{k}\cdot\vec{p}}{m}=\left(\delta+\frac{\hbar\vec{k}_o{}^2}{2m}\right)}} d^3\vec{k}\left[\delta\left(\left|\vec{k}\right|-k_o\right)\frac{\left(\vec{k}\cdot\hat{k}_o\right)}{k_o}\left[\begin{array}{l}\exp\left(-\frac{1}{4}\left(\begin{array}{l}w_1{}^2\left|\vec{k}\cdot\hat{e}_{w1}\right|^2\\ +w_2{}^2\left|\vec{k}\cdot\hat{e}_{w2}\right|^2\end{array}\right)\right)\\ \exp\left(-i\vec{k}\cdot\vec{r}_w\right)\\ \exp\left(-it\left(\delta+\frac{\hbar\vec{k}_o{}^2}{2m}-\frac{\vec{p}\cdot\vec{k}}{m}\right)\right)\\ f_g\left(\left(\vec{p}-\hbar\vec{k}\right),t\right)\end{array}\right]\right]\right)
\end{aligned}
$$

(A2.14)

The time dependent phase term vanishes when applying the integration restriction corresponding to energy and momentum conservation since $\left(\delta+\frac{\hbar\vec{k}_o{}^2}{2m}-\frac{\vec{p}\cdot\vec{k}}{m}\right)=0$, resulting in:

Approved for public release; distribution is unlimited

$$i\frac{d}{dt}f_e(\vec{p},t)=\left(\begin{array}{l}-\frac{eE_o}{2\hbar}\langle e|\hat{e}_L\cdot\hat{\vec{r}}_{e-n}|\mathrm{g}\rangle\frac{w_1w_2}{4\pi}\\ \int\limits_{\substack{|\vec{k}|^2=k_o{}^2;\ \vec{k}\cdot\vec{k}_o>0\\ \frac{\vec{k}\cdot\vec{p}}{m}=\left(\delta+\frac{\hbar\vec{k}_o{}^2}{2m}\right)}} d^3\vec{k}\left[\delta\left(|\vec{k}|-k_o\right)\frac{\left(\vec{k}\cdot\hat{k}_o\right)}{k_o}\left[\exp\left(-\frac{1}{4}\left(\begin{array}{l}w_1{}^2\left|\vec{k}\cdot\hat{e}_{w1}\right|^2\\ +w_2{}^2\left|\vec{k}\cdot\hat{e}_{w2}\right|^2\end{array}\right)\right)\right]\right]f_g\left(\left(\vec{p}-\hbar\vec{k}\right),t\right)\\ \exp\left(-i\vec{k}\cdot\vec{r}_w\right)\end{array}\right)$$

(A2.15)

Turning to the second of the coupled equations, rearranging the phase terms and applying the definitions $\delta=\omega_o-\left(\omega_e-\omega_g\right)$ and $\omega_o=k_oc$ to equation (A2.13) results in:

Approved for public release; distribution is unlimited

$$
i\frac{d}{dt}f_g\left(\vec{p},t\right)=\left(\begin{array}{l}
-\frac{eE_o}{2\hbar}\left\langle \mathrm{g}\left|\hat{e}_L\cdot\hat{\vec{r}}_{e-n}\right|e\right\rangle\frac{w_1w_2}{4\pi} \\
\int\limits_{\substack{\left|\vec{k}\right|^2=k_o^{\,2};\ \vec{k}\cdot\vec{k}_o>0 \\ \frac{\vec{k}\cdot\vec{p}}{m}=\left(\delta-\frac{\hbar\vec{k}_o^{\,2}}{2m}\right)}} d^3\vec{k}\left[\delta\left(\left|\vec{k}\right|-k_o\right)\frac{\left(\vec{k}\cdot\hat{k}_o\right)}{k_o}\left[\begin{array}{l}
\exp\left(-\frac{1}{4}\left(\begin{array}{l} w_1^{\,2}\left|\vec{k}\cdot\hat{e}_{w1}\right|^2 \\ +w_2^{\,2}\left|\vec{k}\cdot\hat{e}_{w2}\right|^2\end{array}\right)\right) \\
\exp\left(i\vec{k}\cdot\vec{r}_w\right) \\
\exp\left(i\omega_o t-i\left(\omega_e-\omega_g\right)t-i\frac{2\vec{p}\cdot\hbar\vec{k}+\left(\hbar\vec{k}\right)^2}{2m\hbar}t\right) \\
f_e\left(\left(\vec{p}+\hbar\vec{k}\right),t\right)
\end{array}\right]\right]
\end{array}\right)
$$

$$
=\left(\begin{array}{l}
-\frac{eE_o}{2\hbar}\left\langle \mathrm{g}\left|\hat{e}_L\cdot\hat{\vec{r}}_{e-n}\right|e\right\rangle\frac{w_1w_2}{4\pi} \\
\int\limits_{\substack{\left|\vec{k}\right|^2=k_o^{\,2};\ \vec{k}\cdot\vec{k}_o>0 \\ \frac{\vec{k}\cdot\vec{p}}{m}=\left(\delta-\frac{\hbar\vec{k}_o^{\,2}}{2m}\right)}} d^3\vec{k}\left[\delta\left(\left|\vec{k}\right|-k_o\right)\frac{\left(\vec{k}\cdot\hat{k}_o\right)}{k_o}\left[\begin{array}{l}
\exp\left(-\frac{1}{4}\left(\begin{array}{l} w_1^{\,2}\left|\vec{k}\cdot\hat{e}_{w1}\right|^2 \\ +w_2^{\,2}\left|\vec{k}\cdot\hat{e}_{w2}\right|^2\end{array}\right)\right) \\
\exp\left(i\vec{k}\cdot\vec{r}_w\right) \\
\exp\left(it\left(\omega_o-\left(\left(\omega_e-\omega_g\right)+\frac{\hbar\vec{k}_o^{\,2}}{2m}\right)-\frac{\vec{k}\cdot\vec{p}}{m}\right)\right) \\
f_e\left(\left(\vec{p}+\hbar\vec{k}\right),t\right)
\end{array}\right]\right]
\end{array}\right)
$$

(A2.16)

Once again, the time dependent phase term vanishes when applying the integration restriction, this time corresponding to the relation $\left(\delta-\frac{\hbar\vec{k}_o^{\,2}}{2m}-\frac{\vec{p}\cdot\vec{k}}{m}\right)=0$, resulting in:

Approved for public release; distribution is unlimited

$$i\frac{d}{dt}f_g(\vec{p},t)=\left(\begin{array}{l} -\frac{eE_o}{2\hbar}\langle \mathrm{g}|\hat{e}_L\cdot\hat{\vec{r}}_{e-n}|e\rangle\frac{w_1w_2}{4\pi} \\ \int\limits_{\substack{|\vec{k}|^2=k_o{}^2;\ \vec{k}\cdot\vec{k}_o>0 \\ \frac{\vec{k}\cdot\vec{p}}{m}=\left(\delta-\frac{\hbar\vec{k}_o{}^2}{2m}\right)}} d^3\vec{k}\left[\delta\left(|\vec{k}|-k_o\right)\frac{\left(\vec{k}\cdot\hat{k}_o\right)}{k_o}\left[\begin{array}{l}\exp\left(-\frac{1}{4}\left(\begin{array}{l}w_1{}^2\left|\vec{k}\cdot\hat{e}_{w1}\right|^2 \\ +w_2{}^2\left|\vec{k}\cdot\hat{e}_{w2}\right|^2\end{array}\right)\right) \\ \exp\left(i\vec{k}\cdot\vec{r}_w\right)\end{array}\right]\right]f_e\left(\left(\vec{p}+\hbar\vec{k}\right),t\right)\end{array}\right)$$

(A2.17)

Equations (A2.15) and (A2.17) are exact coupled equations from which the rapid complex exponential time dependence has been removed. These equations of motion may be solved to derive time dependent atomic state amplitudes.

A.3. Green's function for a driven harmonic oscillator and solutions for atomic state amplitudes

A.3.1. Green's function application to the driven harmonic oscillator

Use of a time domain Green function provides a mechanism to derive a particular solution for the second order time differential equations derived for atom state amplitudes. The ground and excited state time evolution equations derived in the main text are repeated here for reference:

Approved for public release; distribution is unlimited

$$\frac{d^2}{dt^2} f'_{g,0}(\vec{p},t) + \frac{1}{4}\left|\Omega_{R,0}(\vec{p})\right|^2 f'_{g,0}(\vec{p},t) \cong 0$$

$$\frac{d^2}{dt^2} f'_{g,1}(\vec{p},t) + \frac{1}{4}\left|\Omega_{R,0}(\vec{p})\right|^2 f'_{g,1}(\vec{p},t) \cong \frac{1}{4}\begin{bmatrix} 2i\hbar k_o\left(\nabla_p f'_{g,0}(\vec{p},t)\right)\cdot \mathrm{Im}\left(\Omega_{R,0}(\vec{p})^* \vec{\Omega}_{R,1}(\vec{p})\right) \\ -\hbar k_0 f'_{g,0}(\vec{p},t)\vec{\Omega}_{R,1}(\vec{p})^* \cdot\left(\nabla_p \Omega_{R,0}(\vec{p})\right) \end{bmatrix}$$

$$\frac{d^2}{dt^2} f'_{e,0}\left(\vec{p}+\hbar\vec{k}_0,t\right) + \frac{1}{4}\left|\Omega_{R,0}(\vec{p})\right|^2 f'_{e,0}\left(\vec{p}+\hbar\vec{k}_0,t\right) \cong 0$$

$$\frac{d^2}{dt^2} f'_{e,1}\left(\vec{p}+\hbar\vec{k}_0,t\right) + \frac{1}{4}\left|\Omega_{R,0}(\vec{p})\right|^2 f'_{e,1}\left(\vec{p}+\hbar\vec{k}_0,t\right) \cong \frac{1}{4}\begin{bmatrix} 2i\hbar k_o\left(\nabla_p\left(f'_{e,0}\left(\vec{p}+\hbar\vec{k}_0,t\right)\right)\right)\cdot \mathrm{Im}\left(\Omega_{R,0}(\vec{p})^* \vec{\Omega}_{R,1}(\vec{p})\right) \\ +\hbar k_o f'_{e,0}\left(\vec{p}+\hbar\vec{k}_0,t\right)\vec{\Omega}_{R,1}(\vec{p})\cdot\nabla_p\left(\Omega_{R,0}(\vec{p})^*\right) \end{bmatrix}$$

(A3.1)

Equations (A3.1) can be compared to the standard driven harmonic oscillator equation given by:

$$\left[\frac{d^2}{dt^2} + 2\gamma\frac{d}{dt} + {\omega_{osc}}^2\right] x(t) = \frac{f(t)}{m_{osc}} \tag{A3.2}$$

where $x(t)$ is the position of the oscillator, ω_{osc} is the oscillation frequency, γ is the damping factor, $f(t)$ is the driving force and m_{osc} is the oscillator mass. When comparing equations (A3.1) and (A3.2), the damping term is $\gamma = 0$ and the oscillator frequency is given by $\omega_{osc} = \left|\Omega_{R,0}(\vec{p})\right|/2$. The time history of the oscillator position $x(t)$ is given by the distribution functions themselves and the driving force $f(t)/m_{osc}$ is given by the right hand side of equations (A3.1). A Green's function equation for the harmonic oscillator can be expressed as:

$$\left[\frac{d^2}{dt^2} + 2\gamma\frac{d}{dt} + {\omega_{osc}}^2\right] G(t,t') = \delta(t-t') \tag{A3.3}$$

where the delta function $\delta(t-t') = f(t')/m_{osc}$ corresponds to a discrete pulse acceleration for an arbitrary driving force. Using this Green's function, a solution for the oscillator's position time history $x(t)$ can be derived according to:

Approved for public release; distribution is unlimited

$$x(t) = \int_{-\infty}^{\infty} dt' G(t,t') \frac{f(t')}{m_{osc}} \tag{A3.4}$$

The solution for the Green's function for the driven harmonic oscillator is evaluated with the following analytical expression:

$$G(t,t') = \Theta(t-t')\exp\left[-\gamma(t-t')\right] \times \left\{ \begin{array}{ll} \frac{1}{\sqrt{\omega_{osc}{}^2 - \gamma^2}} \sin\left[\sqrt{\omega_{osc}{}^2 - \gamma^2}\,(t-t')\right], & \gamma < \omega_{osc} \\ \frac{1}{\sqrt{\gamma^2 - \omega_{osc}{}^2}} \sinh\left[\sqrt{\gamma^2 - \omega_{osc}{}^2}\,(t-t')\right], & \gamma > \omega_{osc} \end{array} \right\}$$

$$\Theta(\tau) = \left\{ \begin{array}{ll} 1, & \tau \geq 0 \\ 0, & \text{otherwise} \end{array} \right\}$$

(A3.5)

where $\Theta(\tau)$ is the Heaviside step function. For the leading order perturbation expansion, the Green's function given by equation (A3.5) becomes:

$$G(t,t') = \Theta(t-t') \frac{2}{\left|\Omega_{R,0}(\vec{p})\right|} \sin\left(\frac{\left|\Omega_{R,0}(\vec{p})\right|}{2} (t-t') \right) \tag{A3.6}$$

A.3.2. Use of Green's function to derive state amplitude solutions

The general solutions for the coupled homogeneous equations of (A3.1) are readily found to share the form of the standard harmonic oscillator:

$$\begin{aligned} f'_{g,0}(\vec{p},t)\big|_{general} &= a(\vec{p}) \cos\left(\frac{\left|\Omega_{R,0}(\vec{p})\right|}{2} t \right) + b(\vec{p}) \sin\left(\frac{\left|\Omega_{R,0}(\vec{p})\right|}{2} t \right) \\ f'_{e,0}(\vec{p},t)\big|_{general} &= b(\vec{p}) \cos\left(\frac{\left|\Omega_{R,0}(\vec{p})\right|}{2} t \right) + a(\vec{p}) \sin\left(\frac{\left|\Omega_{R,0}(\vec{p})\right|}{2} t \right) \end{aligned} \tag{A3.7}$$

Approved for public release; distribution is unlimited

These zeroth order solutions (A3.7) are used to derive particular solutions for the inhomogeneous equations of (A3.1). The ground state particular solution is considered first, given by the second equation in (A3.1), i.e. for

$$\frac{d^2}{dt^2} f'_{g,1}(\vec{p},t) + \frac{1}{4}\left|\Omega_{R,0}(\vec{p})\right|^2 f'_{g,1}(\vec{p},t) \cong \frac{1}{4}\begin{bmatrix} 2i\hbar k_o \left(\nabla_p f'_{g,0}(\vec{p},t)\right)\cdot \mathrm{Im}\left(\Omega_{R,0}(\vec{p})^* \vec{\Omega}_{R,1}(\vec{p})\right) \\ -\hbar k_0 f'_{g,0}(\vec{p},t)\vec{\Omega}_{R,1}(\vec{p})^* \cdot \left(\nabla_p \Omega_{R,0}(\vec{p})\right) \end{bmatrix}$$

Equations (A3.4) and (A3.5) are expressed with the following substitutions corresponding to the ground state particular solution:

$$\begin{aligned} x(t) &= f'_{g,1}(\vec{p},t) \\ \gamma &= 0 \\ \omega_0 &= \frac{\left|\Omega_{R,0}(\vec{p})\right|}{2} \\ \frac{f(t)}{m} &= \frac{1}{4}\begin{bmatrix} 2i\hbar k_o \left(\nabla_p f'_{g,0}(\vec{p},t)\right)\cdot \mathrm{Im}\left(\Omega_{R,0}(\vec{p})^* \vec{\Omega}_{R,1}(\vec{p})\right) \\ -\hbar k_0 f'_{g,0}(\vec{p},t)\vec{\Omega}_{R,1}(\vec{p})^* \cdot \left(\nabla_p \Omega_{R,0}(\vec{p})\right) \end{bmatrix} \end{aligned} \tag{A3.8}$$

Applying the substitutions in equation (A3.8) to (A3.4) and (A3.5) results in:

$$f'_{g,1}(\vec{p},t)\Big|_{particular} = \int_{-\infty}^{\infty} dt'\Theta(t-t')\frac{2}{\left|\Omega_{R,0}(\vec{p})\right|}\sin\left[\frac{\left|\Omega_{R,0}(\vec{p})\right|}{2}(t-t')\right]\frac{1}{4}\begin{bmatrix} 2i\hbar k_o \left(\nabla_p f'_{g,0}(\vec{p},t')\right)\cdot \mathrm{Im}\left(\Omega_{R,0}(\vec{p})^* \vec{\Omega}_{R,1}(\vec{p})\right) \\ -\hbar k_0 f'_{g,0}(\vec{p},t')\vec{\Omega}_{R,1}(\vec{p})^* \cdot \left(\nabla_p \Omega_{R,0}(\vec{p})\right) \end{bmatrix}$$

(A3.9)

Making the notation substitution $t' \to u$, a particular solution for the first order equation, in terms of a zeroth order solution, may be written directly:

Approved for public release; distribution is unlimited

$$f'_{g,1}(\vec{p},t)\Big|_{particular} = \int_{-\infty}^{\infty} dt'\Theta(t-t')\frac{2}{\left|\Omega_{R,0}(\vec{p})\right|}\sin\left[\frac{\left|\Omega_{R,0}(\vec{p})\right|}{2}(t-t')\right]\frac{1}{4}\begin{bmatrix} 2i\hbar k_o\left(\nabla_p f'_{g,0}(\vec{p},t')\right)\cdot \mathrm{Im}\left(\Omega_{R,0}(\vec{p})^*\vec{\Omega}_{R,1}(\vec{p})\right) \\ -\hbar k_0 f'_{g,0}(\vec{p},t')\vec{\Omega}_{R,1}(\vec{p})^*\cdot\left(\nabla_p\Omega_{R,0}(\vec{p})\right)\end{bmatrix}$$

$$= \int_0^t du\frac{1}{2\left|\Omega_{R,0}(\vec{p})\right|}\sin\left[\frac{\left|\Omega_{R,0}(\vec{p})\right|}{2}(t-u)\right]\begin{bmatrix} 2i\hbar k_o\left(\nabla_p f'_{g,0}(\vec{p},u)\right)\cdot \mathrm{Im}\left(\Omega_{R,0}(\vec{p})^*\vec{\Omega}_{R,1}(\vec{p})\right) \\ -\hbar k_0 f'_{g,0}(\vec{p},u)\vec{\Omega}_{R,1}(\vec{p})^*\cdot\left(\nabla_p\Omega_{R,0}(\vec{p})\right)\end{bmatrix}$$

$$= \begin{bmatrix} 2i\hbar k_o\dfrac{\mathrm{Im}\left(\Omega_{R,0}(\vec{p})^*\vec{\Omega}_{R,1}(\vec{p})\right)}{2\left|\Omega_{R,0}(\vec{p})\right|}\cdot\displaystyle\int_0^t du\sin\left(\frac{\left|\Omega_{R,0}(\vec{p})\right|}{2}(t-u)\right)\left(\nabla_p f'_{g,0}(\vec{p},u)\right) \\ -\hbar k_0\dfrac{\vec{\Omega}_{R,1}(\vec{p})^*\cdot\left(\nabla_p\Omega_{R,0}(\vec{p})\right)}{2\left|\Omega_{R,0}(\vec{p})\right|}\displaystyle\int_0^t du\sin\left(\frac{\left|\Omega_{R,0}(\vec{p})\right|}{2}(t-u)\right)f'_{g,0}(\vec{p},u)\end{bmatrix}$$

(A3.10)

In equation (A3.10) the integration bounds $\int_{-\infty}^{\infty} du\Theta(t-u)$ become $\int_0^t du$ when applying the Heaviside step function and the initial condition corresponding to times $t \le 0$, i.e. the first order perturbation of the ground and excited states vanish. With this expression, integrations may be performed using the generalized solution to the homogeneous equation for the ground state in (A3.7). Specifically, the following general and particular solutions describe the ground state distribution amplitude in this perturbation theory:

$$f'_{g,0}(\vec{p},t)\Big|_{general} = a(\vec{p})\cos\left(\frac{\left|\Omega_{R,0}(\vec{p})\right|}{2}t\right)+b(\vec{p})\sin\left(\frac{\left|\Omega_{R,0}(\vec{p})\right|}{2}t\right)$$

$$f'_{g,1}(\vec{p},t)\Big|_{particular} = \begin{bmatrix} 2i\hbar k_o\dfrac{\mathrm{Im}\left(\Omega_{R,0}(\vec{p})^*\vec{\Omega}_{R,1}(\vec{p})\right)}{2\left|\Omega_{R,0}(\vec{p})\right|}\cdot\displaystyle\int_0^t du\sin\left(\frac{\left|\Omega_{R,0}(\vec{p})\right|}{2}(t-u)\right)\left(\nabla_p\ f'_{g,0}(\vec{p},u)\Big|_{general}\right) \\ -\hbar k_0\dfrac{\vec{\Omega}_{R,1}(\vec{p})^*\cdot\left(\nabla_p\Omega_{R,0}(\vec{p})\right)}{2\left|\Omega_{R,0}(\vec{p})\right|}\displaystyle\int_0^t du\sin\left(\frac{\left|\Omega_{R,0}(\vec{p})\right|}{2}(t-u)\right)f'_{g,0}(\vec{p},u)\Big|_{general}\end{bmatrix}$$

(A3.11)

Before evaluating these integrals, an expression for the excited state distribution particular solution may be found in the same way. This process begins with an application of the Green's function formalism to the

Approved for public release; distribution is unlimited

excited state particular solution. The excited state particular solution is given by the fourth equation in (A3.1) and reprinted here for reference:

$$\frac{d^2}{dt^2} f'_{e,1}\left(\vec{p}+\hbar\vec{k}_0,t\right)+\frac{1}{4}\left|\Omega_{R,0}\left(\vec{p}\right)\right|^2 f'_{e,1}\left(\vec{p}+\hbar\vec{k}_0,t\right)\cong\frac{1}{4}\left[\begin{array}{l}2i\hbar k_o\left(\nabla_p\left(f'_{e,0}\left(\vec{p}+\hbar\vec{k}_0,t\right)\right)\right)\cdot\mathrm{Im}\left(\Omega_{R,0}\left(\vec{p}\right)^*\vec{\Omega}_{R,1}\left(\vec{p}\right)\right)\\+\hbar k_o f'_{e,0}\left(\vec{p}+\hbar\vec{k}_0,t\right)\vec{\Omega}_{R,1}\left(\vec{p}\right)\cdot\nabla_p\left(\Omega_{R,0}\left(\vec{p}\right)^*\right)\end{array}\right]$$

Equations (A3.4) and (A3.5) are expressed with the following substitutions corresponding to the ground state particular solution:

$$\begin{aligned}x(t)&=f'_{e,1}\left(\vec{p}+\hbar\vec{k}_0,t\right)\\\gamma&=0\\\omega_0&=\frac{\left|\Omega_{R,0}\left(\vec{p}\right)\right|}{2}\\\frac{f(t)}{m}&=\frac{1}{4}\left[\begin{array}{l}2i\hbar k_o\left(\nabla_p\left(f'_{e,0}\left(\vec{p}+\hbar\vec{k}_0,t\right)\right)\right)\cdot\mathrm{Im}\left(\Omega_{R,0}\left(\vec{p}\right)^*\vec{\Omega}_{R,1}\left(\vec{p}\right)\right)\\+\hbar k_o f'_{e,0}\left(\vec{p}+\hbar\vec{k}_0,t\right)\vec{\Omega}_{R,1}\left(\vec{p}\right)\cdot\nabla_p\left(\Omega_{R,0}\left(\vec{p}\right)^*\right)\end{array}\right]\end{aligned}\qquad\text{(A3.12)}$$

Applying the substitutions in equation (A3.8) to (A3.4) and (A3.5) results in:

$$f'_{e,1}\left(\vec{p}+\hbar\vec{k}_0,t\right)\Big|_{particular}=\int_{-\infty}^{\infty}dt'\Theta\left(t-t'\right)\frac{2}{\left|\Omega_{R,0}\left(\vec{p}\right)\right|}\sin\left[\frac{\left|\Omega_{R,0}\left(\vec{p}\right)\right|}{2}\left(t-t'\right)\right]\frac{1}{4}\left[\begin{array}{l}2i\hbar k_o\left(\nabla_p\left(f'_{e,0}\left(\vec{p}+\hbar\vec{k}_0,t'\right)\right)\right)\cdot\mathrm{Im}\left(\Omega_{R,0}\left(\vec{p}\right)^*\vec{\Omega}_{R,1}\left(\vec{p}\right)\right)\\+\hbar k_o f'_{e,0}\left(\vec{p}+\hbar\vec{k}_0,t'\right)\vec{\Omega}_{R,1}\left(\vec{p}\right)\cdot\nabla_p\left(\Omega_{R,0}\left(\vec{p}\right)^*\right)\end{array}\right]$$

(A3.13)

As with the ground state particular solution, the notation substitution $t'\to u$ is made and a particular solution in terms of a zeroth order solution, assuming the zeroth and first order solutions vanishes at all times $t\le 0$, is written as:

Approved for public release; distribution is unlimited

$$
\begin{aligned}
f'_{e,1}\left(\vec{p}+\hbar\vec{k}_0,t\right)\Big|_{particular} &= \int_{-\infty}^{\infty} dt'\Theta\left(t-t'\right)\frac{2}{\left|\Omega_{R,0}\left(\vec{p}\right)\right|}\sin\left[\frac{\left|\Omega_{R,0}\left(\vec{p}\right)\right|}{2}\left(t-t'\right)\right]\frac{1}{4}\begin{bmatrix} 2i\hbar k_o\left(\nabla_p\left(f'_{e,0}\left(\vec{p}+\hbar\vec{k}_0,t'\right)\right)\right)\cdot\mathrm{Im}\left(\Omega_{R,0}\left(\vec{p}\right)^*\vec{\Omega}_{R,1}\left(\vec{p}\right)\right) \\ +\hbar k_o f'_{e,0}\left(\vec{p}+\hbar\vec{k}_0,t'\right)\vec{\Omega}_{R,1}\left(\vec{p}\right)\cdot\nabla_p\left(\Omega_{R,0}\left(\vec{p}\right)^*\right)\end{bmatrix} \\
&= \int_{-\infty}^{\infty} dt'\Theta\left(t-t'\right)\frac{1}{2\left|\Omega_{R,0}\left(\vec{p}\right)\right|}\sin\left[\frac{\left|\Omega_{R,0}\left(\vec{p}\right)\right|}{2}\left(t-t'\right)\right]\begin{bmatrix} 2i\hbar k_o\left(\nabla_p\left(f'_{e,0}\left(\vec{p}+\hbar\vec{k}_0,t'\right)\right)\right)\cdot\mathrm{Im}\left(\Omega_{R,0}\left(\vec{p}\right)^*\vec{\Omega}_{R,1}\left(\vec{p}\right)\right) \\ +\hbar k_o f'_{e,0}\left(\vec{p}+\hbar\vec{k}_0,t'\right)\vec{\Omega}_{R,1}\left(\vec{p}\right)\cdot\nabla_p\left(\Omega_{R,0}\left(\vec{p}\right)^*\right)\end{bmatrix} \\
&= \int_0^t du\frac{\sin\left[\frac{\left|\Omega_{R,0}\left(\vec{p}\right)\right|}{2}\left(t-u\right)\right]}{2\left|\Omega_{R,0}\left(\vec{p}\right)\right|}\begin{bmatrix} 2i\hbar k_o\left(\nabla_p\left(f'_{e,0}\left(\vec{p}+\hbar\vec{k}_0,u\right)\right)\right)\cdot\mathrm{Im}\left(\Omega_{R,0}\left(\vec{p}\right)^*\vec{\Omega}_{R,1}\left(\vec{p}\right)\right) \\ +\hbar k_o f'_{e,0}\left(\vec{p}+\hbar\vec{k}_0,u\right)\vec{\Omega}_{R,1}\left(\vec{p}\right)\cdot\nabla_p\left(\Omega_{R,0}\left(\vec{p}\right)^*\right)\end{bmatrix} \\
&= \begin{bmatrix} 2i\hbar k_o\frac{\mathrm{Im}\left(\Omega_{R,0}\left(\vec{p}\right)^*\vec{\Omega}_{R,1}\left(\vec{p}\right)\right)}{2\left|\Omega_{R,0}\left(\vec{p}\right)\right|}\cdot\int_0^t du\sin\left(\frac{\left|\Omega_{R,0}\left(\vec{p}\right)\right|}{2}\left(t-u\right)\right)\left(\nabla_p\left(f'_{e,0}\left(\vec{p}+\hbar\vec{k}_0,u\right)\right)\right) \\ +\hbar k_o\frac{\vec{\Omega}_{R,1}\left(\vec{p}\right)\cdot\nabla_p\left(\Omega_{R,0}\left(\vec{p}\right)^*\right)}{2\left|\Omega_{R,0}\left(\vec{p}\right)\right|}\int_0^t du\sin\left(\frac{\left|\Omega_{R,0}\left(\vec{p}\right)\right|}{2}\left(t-u\right)\right)f'_{e,0}\left(\vec{p}+\hbar\vec{k}_0,u\right)\end{bmatrix}
\end{aligned}
$$

(A3.14)

With this expression, integrations may be performed using the generalized solution to the homogeneous equation for the excited state from (A3.7), resulting in the following expression for the general and particular solutions of the excited state distribution amplitude:

$$
\begin{aligned}
f'_{e,0}\left(\vec{p}+\hbar\vec{k}_0,t\right)\Big|_{general} &= b\left(\vec{p}\right)\cos\left(\frac{\left|\Omega_{R,0}\left(\vec{p}\right)\right|}{2}t\right)+a\left(\vec{p}\right)\sin\left(\frac{\left|\Omega_{R,0}\left(\vec{p}\right)\right|}{2}t\right) \\
f'_{e,1}\left(\vec{p}+\hbar\vec{k}_0,t\right)\Big|_{particular} &= \begin{bmatrix} 2i\hbar k_o\frac{\mathrm{Im}\left(\Omega_{R,0}\left(\vec{p}\right)^*\vec{\Omega}_{R,1}\left(\vec{p}\right)\right)}{2\left|\Omega_{R,0}\left(\vec{p}\right)\right|}\cdot\int_0^t du\sin\left(\frac{\left|\Omega_{R,0}\left(\vec{p}\right)\right|}{2}\left(t-u\right)\right)\left(\nabla_p\left(f'_{e,0}\left(\vec{p}+\hbar\vec{k}_0,u\right)\Big|_{general}\right)\right) \\ +\hbar k_o\frac{\vec{\Omega}_{R,1}\left(\vec{p}\right)\cdot\nabla_p\left(\Omega_{R,0}\left(\vec{p}\right)^*\right)}{2\left|\Omega_{R,0}\left(\vec{p}\right)\right|}\int_0^t du\sin\left(\frac{\left|\Omega_{R,0}\left(\vec{p}\right)\right|}{2}\left(t-u\right)\right)f'_{e,0}\left(\vec{p}+\hbar\vec{k}_0,u\right)\Big|_{general}\end{bmatrix}
\end{aligned}
$$

(A3.15)

Comparing (A3.15) with the ground state solutions given by (A3.11), it is clear that both share the same form including the integrals to be evaluated with a difference only in variables that depend on momentum alone (no time dependence) and the name of variables. Therefore, time dependent integrals must only be

Approved for public release; distribution is unlimited

evaluated once. Integration proceeds by considering the particular solution to the ground state from equation (A3.11), reprinted here for clarity:

$$f'_{g,1}(\vec{p},t)\Big|_{particular} = \begin{bmatrix} 2i\hbar k_o \dfrac{\mathrm{Im}\left(\Omega_{R,0}(\vec{p})^* \vec{\Omega}_{R,1}(\vec{p})\right)}{2\left|\Omega_{R,0}(\vec{p})\right|} \cdot \int_0^t du \sin\left(\dfrac{\left|\Omega_{R,0}(\vec{p})\right|}{2}(t-u)\right)\left(\nabla_p\ f'_{g,0}(\vec{p},u)\Big|_{general}\right) \\ -\hbar k_0 \dfrac{\vec{\Omega}_{R,1}(\vec{p})^* \cdot\left(\nabla_p \Omega_{R,0}(\vec{p})\right)}{2\left|\Omega_{R,0}(\vec{p})\right|} \int_0^t du \sin\left(\dfrac{\left|\Omega_{R,0}(\vec{p})\right|}{2}(t-u)\right) f'_{g,0}(\vec{p},u)\Big|_{general} \end{bmatrix}$$

Each integral is calculated in turn, beginning with $\int_0^t du \sin\left(\dfrac{\left|\Omega_{R,0}(\vec{p})\right|}{2}(t-u)\right)\left(\nabla_p\ f'_{g,0}(\vec{p},u)\Big|_{general}\right)$:

Approved for public release; distribution is unlimited

$$
\begin{aligned}
& f'_{g,0}(\vec{p},t)\big|_{general} = a(\vec{p})\cos\left(\frac{\left|\Omega_{R,0}(\vec{p})\right|}{2}t\right) + b(\vec{p})\sin\left(\frac{\left|\Omega_{R,0}(\vec{p})\right|}{2}t\right) \\
& \int_0^t du \sin\left(\frac{\left|\Omega_{R,0}(\vec{p})\right|}{2}(t-u)\right)\left(\nabla_p\ f'_{g,0}(\vec{p},u)\big|_{general}\right) \\
& = \int_0^t du \sin\left(\frac{\left|\Omega_{R,0}(\vec{p})\right|}{2}(t-u)\right)\left(\nabla_p\left[a(\vec{p})\cos\left(\frac{\left|\Omega_{R,0}(\vec{p})\right|}{2}u\right) + b(\vec{p})\sin\left(\frac{\left|\Omega_{R,0}(\vec{p})\right|}{2}u\right)\right]\right) \\
& = \int_0^t du \sin\left(\frac{\left|\Omega_{R,0}(\vec{p})\right|}{2}(t-u)\right)\left(\begin{array}{l}\nabla_p\left[a(\vec{p})\cos\left(\frac{\left|\Omega_{R,0}(\vec{p})\right|}{2}u\right)\right] \\ +\nabla_p\left[b(\vec{p})\sin\left(\frac{\left|\Omega_{R,0}(\vec{p})\right|}{2}u\right)\right]\end{array}\right) \\
& = \int_0^t du \sin\left(\frac{\left|\Omega_{R,0}(\vec{p})\right|}{2}(t-u)\right)\left(\begin{array}{l}a(\vec{p})\nabla_p\cos\left(\frac{\left|\Omega_{R,0}(\vec{p})\right|}{2}u\right) + \cos\left(\frac{\left|\Omega_{R,0}(\vec{p})\right|}{2}u\right)\nabla_p a(\vec{p}) \\ +b(\vec{p})\nabla_p\sin\left(\frac{\left|\Omega_{R,0}(\vec{p})\right|}{2}u\right) + \sin\left(\frac{\left|\Omega_{R,0}(\vec{p})\right|}{2}u\right)\nabla_p b(\vec{p})\end{array}\right) \\
& = \int_0^t du \sin\left(\frac{\left|\Omega_{R,0}(\vec{p})\right|}{2}(t-u)\right)\left(\begin{array}{l}a(\vec{p})\left(-\nabla_p\left(\frac{\left|\Omega_{R,0}(\vec{p})\right|}{2}u\right)\sin\left(\frac{\left|\Omega_{R,0}(\vec{p})\right|}{2}u\right)\right) \\ +\cos\left(\frac{\left|\Omega_{R,0}(\vec{p})\right|}{2}u\right)\nabla_p a(\vec{p}) \\ +b(\vec{p})\left(\nabla_p\left(\frac{\left|\Omega_{R,0}(\vec{p})\right|}{2}u\right)\cos\left(\frac{\left|\Omega_{R,0}(\vec{p})\right|}{2}u\right)\right) \\ +\sin\left(\frac{\left|\Omega_{R,0}(\vec{p})\right|}{2}u\right)\nabla_p b(\vec{p})\end{array}\right)
\end{aligned}
\tag{A3.16}
$$

The trigonometric identity $\sin(x-y) = \sin(x)\cos(y) - \cos(x)\sin(y)$ is used to expand the term $\sin\left(\frac{\left|\Omega_{R,0}(\vec{p})\right|}{2}(t-u)\right)$. For convenience, the following substitution is made:

$$
\left|\Omega'_{R,0}(\vec{p})\right| \equiv \frac{\left|\Omega_{R,0}(\vec{p})\right|}{2} \tag{A3.17}
$$

and equation (A3.16) becomes:

Approved for public release; distribution is unlimited

$$
\begin{aligned}
&\int_0^t du \sin\left(\frac{\left|\Omega_{R,0}(\vec{p})\right|}{2}(t-u)\right)\left(\nabla_p\ f'_{g,0}(\vec{p},u)\Big|_{general}\right)\\
&=\int_0^t du \sin\left(\left|\Omega'_{R,0}(\vec{p})\right|(t-u)\right)\left(\nabla_p\ f'_{g,0}(\vec{p},u)\Big|_{general}\right)\\
&=\int_0^t du \sin\left(\left|\Omega'_{R,0}(\vec{p})\right|(t-u)\right)\begin{pmatrix} a(\vec{p})\left(-\nabla_p\left(\left|\Omega'_{R,0}(\vec{p})\right|\right)u\sin\left(\left|\Omega_{R,0}(\vec{p})\right|u\right)\right)\\ +\cos\left(\left|\Omega'_{R,0}(\vec{p})\right|u\right)\nabla_p\left(a(\vec{p})\right)\\ +b(\vec{p})\left(\nabla_p\left(\left|\Omega'_{R,0}(\vec{p})\right|\right)u\cos\left(\left|\Omega'_{R,0}(\vec{p})\right|u\right)\right)\\ +\sin\left(\left|\Omega'_{R,0}(\vec{p})\right|u\right)\nabla_p\left(b(\vec{p})\right)\end{pmatrix}\\
&=\begin{bmatrix}\sin\left(\left|\Omega'_{R,0}(\vec{p})\right|t\right)\int_0^t du\cos\left(\left|\Omega'_{R,0}(\vec{p})\right|u\right)\begin{pmatrix} a(\vec{p})\left(-\nabla_p\left(\left|\Omega'_{R,0}(\vec{p})\right|\right)u\sin\left(\left|\Omega'_{R,0}(\vec{p})\right|u\right)\right)\\ +\cos\left(\left|\Omega'_{R,0}(\vec{p})\right|u\right)\nabla_p\left(a(\vec{p})\right)\\ +b(\vec{p})\left(\nabla_p\left(\left|\Omega'_{R,0}(\vec{p})\right|\right)u\cos\left(\left|\Omega'_{R,0}(\vec{p})\right|u\right)\right)\\ +\sin\left(\left|\Omega'_{R,0}(\vec{p})\right|u\right)\nabla_p\left(b(\vec{p})\right)\end{pmatrix}\\ -\cos\left(\left|\Omega'_{R,0}(\vec{p})\right|t\right)\int_0^t du\sin\left(\left|\Omega_{R,0}(\vec{p})\right|u\right)\begin{pmatrix} a(\vec{p})\left(-\nabla_p\left(\left|\Omega'_{R,0}(\vec{p})\right|\right)u\sin\left(\left|\Omega'_{R,0}(\vec{p})\right|u\right)\right)\\ +\cos\left(\left|\Omega'_{R,0}(\vec{p})\right|u\right)\nabla_p\left(a(\vec{p})\right)\\ +b(\vec{p})\left(\nabla_p\left(\left|\Omega'_{R,0}(\vec{p})\right|\right)u\cos\left(\left|\Omega'_{R,0}(\vec{p})\right|u\right)\right)\\ +\sin\left(\left|\Omega'_{R,0}(\vec{p})\right|u\right)\nabla_p\left(b(\vec{p})\right)\end{pmatrix}\end{bmatrix}\\
&=\begin{bmatrix}\begin{pmatrix} -a(\vec{p})\nabla_p\left(\left|\Omega'_{R,0}(\vec{p})\right|\right)\sin\left(\left|\Omega'_{R,0}(\vec{p})\right|t\right)\int_0^t du\cos\left(\left|\Omega'_{R,0}(\vec{p})\right|u\right)\sin\left(\left|\Omega'_{R,0}(\vec{p})\right|u\right)u\\ +\nabla_p\left(a(\vec{p})\right)\sin\left(\left|\Omega'_{R,0}(\vec{p})\right|t\right)\int_0^t du\cos\left(\left|\Omega'_{R,0}(\vec{p})\right|u\right)\cos\left(\left|\Omega'_{R,0}(\vec{p})\right|u\right)\\ +b(\vec{p})\nabla_p\left(\left|\Omega'_{R,0}(\vec{p})\right|\right)\sin\left(\left|\Omega'_{R,0}(\vec{p})\right|t\right)\int_0^t du\cos\left(\left|\Omega'_{R,0}(\vec{p})\right|u\right)\cos\left(\left|\Omega'_{R,0}(\vec{p})\right|u\right)u\\ +\nabla_p\left(b(\vec{p})\right)\sin\left(\left|\Omega'_{R,0}(\vec{p})\right|t\right)\int_0^t du\cos\left(\left|\Omega'_{R,0}(\vec{p})\right|u\right)\sin\left(\left|\Omega'_{R,0}(\vec{p})\right|u\right)\end{pmatrix}\\ -\begin{pmatrix} -a(\vec{p})\nabla_p\left(\left|\Omega'_{R,0}(\vec{p})\right|\right)\cos\left(\left|\Omega'_{R,0}(\vec{p})\right|t\right)\int_0^t du\sin\left(\left|\Omega'_{R,0}(\vec{p})\right|u\right)\sin\left(\left|\Omega'_{R,0}(\vec{p})\right|u\right)u\\ +\nabla_p\left(a(\vec{p})\right)\cos\left(\left|\Omega'_{R,0}(\vec{p})\right|t\right)\int_0^t du\sin\left(\left|\Omega'_{R,0}(\vec{p})\right|u\right)\cos\left(\left|\Omega'_{R,0}(\vec{p})\right|u\right)\\ +b(\vec{p})\nabla_p\left(\left|\Omega'_{R,0}(\vec{p})\right|\right)\cos\left(\left|\Omega'_{R,0}(\vec{p})\right|t\right)\int_0^t du\sin\left(\left|\Omega'_{R,0}(\vec{p})\right|u\right)\cos\left(\left|\Omega'_{R,0}(\vec{p})\right|u\right)u\\ +\nabla_p\left(b(\vec{p})\right)\cos\left(\left|\Omega'_{R,0}(\vec{p})\right|t\right)\int_0^t du\sin\left(\left|\Omega'_{R,0}(\vec{p})\right|u\right)\sin\left(\left|\Omega'_{R,0}(\vec{p})\right|u\right)\end{pmatrix}\end{bmatrix}
\end{aligned}
\tag{A3.18}
$$

Equation (A3.18) includes several integrals that may be solved by hand or with the aid of computational tools like those provided by Wolfram Alpha, for instance. The relevant integrals of (A3.18) and their solutions are:

$$\int_0^t du \cos\left(\left|\Omega'_{R,0}(\vec{p})\right|u\right)\sin\left(\left|\Omega'_{R,0}(\vec{p})\right|u\right)u = \frac{\sin\left(2\left|\Omega'_{R,0}(\vec{p})\right|t\right) - 2\left|\Omega'_{R,0}(\vec{p})\right|t\cos\left(2\left|\Omega'_{R,0}(\vec{p})\right|t\right)}{8\left|\Omega_{R,0}(\vec{p})\right|^2}$$

$$\int_0^t du \cos\left(\left|\Omega'_{R,0}(\vec{p})\right|u\right)\cos\left(\left|\Omega'_{R,0}(\vec{p})\right|u\right) = \frac{2\left|\Omega'_{R,0}(\vec{p})\right|t + \sin\left(2\left|\Omega'_{R,0}(\vec{p})\right|t\right)}{4\left|\Omega'_{R,0}(\vec{p})\right|}$$

$$\int_0^t du \cos\left(\left|\Omega'_{R,0}(\vec{p})\right|u\right)\cos\left(\left|\Omega'_{R,0}(\vec{p})\right|u\right)u = \frac{2\left|\Omega'_{R,0}(\vec{p})\right|^2 t^2 + 2\left|\Omega'_{R,0}(\vec{p})\right|t\sin\left(2\left|\Omega'_{R,0}(\vec{p})\right|t\right) + \cos\left(2\left|\Omega'_{R,0}(\vec{p})\right|t\right) - 1}{8\left|\Omega'_{R,0}(\vec{p})\right|^2}$$

$$\int_0^t du \cos\left(\left|\Omega'_{R,0}(\vec{p})\right|u\right)\sin\left(\left|\Omega'_{R,0}(\vec{p})\right|u\right) = \frac{\sin^2\left(\left|\Omega'_{R,0}(\vec{p})\right|t\right)}{2\left|\Omega'_{R,0}(\vec{p})\right|}$$

$$\int_0^t du \sin\left(\left|\Omega'_{R,0}(\vec{p})\right|u\right)\sin\left(\left|\Omega'_{R,0}(\vec{p})\right|u\right)u = \frac{2\left|\Omega'_{R,0}(\vec{p})\right|^2 t^2 - 2\left|\Omega'_{R,0}(\vec{p})\right|t\sin\left(2\left|\Omega'_{R,0}(\vec{p})\right|t\right) - \cos\left(2\left|\Omega'_{R,0}(\vec{p})\right|t\right) + 1}{8\left|\Omega'_{R,0}(\vec{p})\right|^2}$$

$$\int_0^t du \sin\left(\left|\Omega'_{R,0}(\vec{p})\right|u\right)\cos\left(\left|\Omega'_{R,0}(\vec{p})\right|u\right) = \frac{\sin^2\left(\left|\Omega'_{R,0}(\vec{p})\right|t\right)}{2\left|\Omega'_{R,0}(\vec{p})\right|}$$

$$\int_0^t du \sin\left(\left|\Omega'_{R,0}(\vec{p})\right|u\right)\cos\left(\left|\Omega'_{R,0}(\vec{p})\right|u\right)u = \frac{\sin\left(2\left|\Omega'_{R,0}(\vec{p})\right|t\right) - 2\left|\Omega'_{R,0}(\vec{p})\right|t\cos\left(2\left|\Omega'_{R,0}(\vec{p})\right|t\right)}{8\left|\Omega'_{R,0}(\vec{p})\right|^2}$$

$$\int_0^t du \sin\left(\left|\Omega'_{R,0}(\vec{p})\right|u\right)\sin\left(\left|\Omega'_{R,0}(\vec{p})\right|u\right) = \frac{2\left|\Omega'_{R,0}(\vec{p})\right|t - \sin\left(2\left|\Omega'_{R,0}(\vec{p})\right|t\right)}{4\left|\Omega'_{R,0}(\vec{p})\right|}$$

(A3.19)

Substitution of these integrals in (A3.18) results in:

Approved for public release; distribution is unlimited

$$\int_0^t du \sin\left(\left|\Omega'_{R,0}(\vec{p})\right|(t-u)\right)\left(\nabla_p f'_{g,0}(\vec{p},u)\Big|_{general}\right)$$

$$= \left[\begin{array}{l}
\left(\begin{array}{l}
-a(\vec{p})\nabla_p\left(\left|\Omega'_{R,0}(\vec{p})\right|\right)\sin\left(\left|\Omega'_{R,0}(\vec{p})\right|t\right)\dfrac{\sin\left(2\left|\Omega'_{R,0}(\vec{p})\right|t\right)-2\left|\Omega'_{R,0}(\vec{p})\right|t\cos\left(2\left|\Omega'_{R,0}(\vec{p})\right|t\right)}{8\left|\Omega'_{R,0}(\vec{p})\right|^2} \\
+\nabla_p\left(a(\vec{p})\right)\sin\left(\left|\Omega'_{R,0}(\vec{p})\right|t\right)\dfrac{2\left|\Omega'_{R,0}(\vec{p})\right|t+\sin\left(2\left|\Omega'_{R,0}(\vec{p})\right|t\right)}{4\left|\Omega'_{R,0}(\vec{p})\right|} \\
+b(\vec{p})\nabla_p\left(\left|\Omega'_{R,0}(\vec{p})\right|\right)\sin\left(\left|\Omega'_{R,0}(\vec{p})\right|t\right)\dfrac{2\left|\Omega'_{R,0}(\vec{p})\right|^2t^2+2\left|\Omega'_{R,0}(\vec{p})\right|t\sin\left(2\left|\Omega'_{R,0}(\vec{p})\right|t\right)+\cos\left(2\left|\Omega'_{R,0}(\vec{p})\right|t\right)-1}{8\left|\Omega'_{R,0}(\vec{p})\right|^2} \\
+\nabla_p\left(b(\vec{p})\right)\sin\left(\left|\Omega'_{R,0}(\vec{p})\right|t\right)\dfrac{\sin^2\left(\left|\Omega'_{R,0}(\vec{p})\right|t\right)}{2\left|\Omega'_{R,0}(\vec{p})\right|}
\end{array}\right) \\
-\left(\begin{array}{l}
-a(\vec{p})\nabla_p\left(\left|\Omega'_{R,0}(\vec{p})\right|\right)\cos\left(\left|\Omega'_{R,0}(\vec{p})\right|t\right)\dfrac{2\left|\Omega'_{R,0}(\vec{p})\right|^2t^2-2\left|\Omega'_{R,0}(\vec{p})\right|t\sin\left(2\left|\Omega'_{R,0}(\vec{p})\right|t\right)-\cos\left(2\left|\Omega'_{R,0}(\vec{p})\right|t\right)+1}{8\left|\Omega'_{R,0}(\vec{p})\right|^2} \\
+\nabla_p\left(a(\vec{p})\right)\cos\left(\left|\Omega'_{R,0}(\vec{p})\right|t\right)\dfrac{\sin^2\left(\left|\Omega'_{R,0}(\vec{p})\right|t\right)}{2\left|\Omega'_{R,0}(\vec{p})\right|} \\
+b(\vec{p})\nabla_p\left(\left|\Omega'_{R,0}(\vec{p})\right|\right)\cos\left(\left|\Omega'_{R,0}(\vec{p})\right|t\right)\dfrac{\sin\left(2\left|\Omega'_{R,0}(\vec{p})\right|t\right)-2\left|\Omega'_{R,0}(\vec{p})\right|t\cos\left(2\left|\Omega'_{R,0}(\vec{p})\right|t\right)}{8\left|\Omega'_{R,0}(\vec{p})\right|^2} \\
+\nabla_p\left(b(\vec{p})\right)\cos\left(\left|\Omega'_{R,0}(\vec{p})\right|t\right)\dfrac{2\left|\Omega'_{R,0}(\vec{p})\right|t-\sin\left(2\left|\Omega'_{R,0}(\vec{p})\right|t\right)}{4\left|\Omega'_{R,0}(\vec{p})\right|}
\end{array}\right)
\end{array}\right]$$

(A3.20)

Collecting like terms, equation (A3.20) becomes:

$$\int_0^t du \sin\left(\left|\Omega'_{R,0}(\vec{p})\right|(t-u)\right)\left(\nabla_p f'_{g,0}(\vec{p},u)\Big|_{general}\right)$$

$$= \left[\begin{array}{l} a(\vec{p})\nabla_p\left(\left|\Omega'_{R,0}(\vec{p})\right|\right)\left(\begin{array}{l} -\sin\left(\left|\Omega'_{R,0}(\vec{p})\right|t\right)\dfrac{\sin\left(2\left|\Omega'_{R,0}(\vec{p})\right|t\right)-2\left|\Omega'_{R,0}(\vec{p})\right|t\cos\left(2\left|\Omega'_{R,0}(\vec{p})\right|t\right)}{8\left|\Omega'_{R,0}(\vec{p})\right|^2} \\ +\cos\left(\left|\Omega'_{R,0}(\vec{p})\right|t\right)\dfrac{2\left|\Omega'_{R,0}(\vec{p})\right|^2 t^2-2\left|\Omega'_{R,0}(\vec{p})\right|t\sin\left(2\left|\Omega'_{R,0}(\vec{p})\right|t\right)-\cos\left(2\left|\Omega'_{R,0}(\vec{p})\right|t\right)+1}{8\left|\Omega'_{R,0}(\vec{p})\right|^2} \end{array} \right) \\ +\nabla_p\left(a(\vec{p})\right)\left(\begin{array}{l} \sin\left(\left|\Omega'_{R,0}(\vec{p})\right|t\right)\dfrac{2\left|\Omega'_{R,0}(\vec{p})\right|t+\sin\left(2\left|\Omega'_{R,0}(\vec{p})\right|t\right)}{4\left|\Omega'_{R,0}(\vec{p})\right|} \\ -\cos\left(\left|\Omega'_{R,0}(\vec{p})\right|t\right)\dfrac{\sin^2\left(\left|\Omega'_{R,0}(\vec{p})\right|t\right)}{2\left|\Omega'_{R,0}(\vec{p})\right|} \end{array} \right) \\ +b(\vec{p})\nabla_p\left(\left|\Omega'_{R,0}(\vec{p})\right|\right)\left(\begin{array}{l} \sin\left(\left|\Omega'_{R,0}(\vec{p})\right|t\right)\dfrac{2\left|\Omega'_{R,0}(\vec{p})\right|^2 t^2+2\left|\Omega'_{R,0}(\vec{p})\right|t\sin\left(2\left|\Omega'_{R,0}(\vec{p})\right|t\right)+\cos\left(2\left|\Omega'_{R,0}(\vec{p})\right|t\right)-1}{8\left|\Omega'_{R,0}(\vec{p})\right|^2} \\ -\cos\left(\left|\Omega'_{R,0}(\vec{p})\right|t\right)\dfrac{\sin\left(2\left|\Omega'_{R,0}(\vec{p})\right|t\right)-2\left|\Omega'_{R,0}(\vec{p})\right|t\cos\left(2\left|\Omega'_{R,0}(\vec{p})\right|t\right)}{8\left|\Omega'_{R,0}(\vec{p})\right|^2} \end{array} \right) \\ +\nabla_p\left(b(\vec{p})\right)\left(\begin{array}{l} \sin\left(\left|\Omega'_{R,0}(\vec{p})\right|t\right)\dfrac{\sin^2\left(\left|\Omega'_{R,0}(\vec{p})\right|t\right)}{2\left|\Omega'_{R,0}(\vec{p})\right|} \\ -\cos\left(\left|\Omega'_{R,0}(\vec{p})\right|t\right)\dfrac{2\left|\Omega'_{R,0}(\vec{p})\right|t-\sin\left(2\left|\Omega'_{R,0}(\vec{p})\right|t\right)}{4\left|\Omega'_{R,0}(\vec{p})\right|} \end{array} \right) \end{array} \right]$$

(A3.21)

Using trigonometric identities, terms may be eliminated to yield a simpler result. Each line from Equation (A3.21) is considered in turn:

$$
\begin{aligned}
&\left(\begin{array}{l}
-\sin\left(\left|\Omega'_{R,0}(\vec{p})\right|t\right)\dfrac{\sin\left(2\left|\Omega'_{R,0}(\vec{p})\right|t\right)-2\left|\Omega'_{R,0}(\vec{p})\right|t\cos\left(2\left|\Omega'_{R,0}(\vec{p})\right|t\right)}{8\left|\Omega'_{R,0}(\vec{p})\right|^2} \\
+\cos\left(\left|\Omega'_{R,0}(\vec{p})\right|t\right)\dfrac{2\left|\Omega'_{R,0}(\vec{p})\right|^2t^2-2\left|\Omega'_{R,0}(\vec{p})\right|t\sin\left(2\left|\Omega'_{R,0}(\vec{p})\right|t\right)-\cos\left(2\left|\Omega'_{R,0}(\vec{p})\right|t\right)+1}{8\left|\Omega'_{R,0}(\vec{p})\right|^2}
\end{array}\right) \\
&=\left(\begin{array}{l}
\dfrac{-\sin\left(2\left|\Omega'_{R,0}(\vec{p})\right|t\right)\sin\left(\left|\Omega'_{R,0}(\vec{p})\right|t\right)+2\left|\Omega'_{R,0}(\vec{p})\right|t\cos\left(2\left|\Omega'_{R,0}(\vec{p})\right|t\right)\sin\left(\left|\Omega'_{R,0}(\vec{p})\right|t\right)}{8\left|\Omega'_{R,0}(\vec{p})\right|^2} \\
+\dfrac{2\left|\Omega'_{R,0}(\vec{p})\right|^2t^2\cos\left(\left|\Omega'_{R,0}(\vec{p})\right|t\right)-2\left|\Omega'_{R,0}(\vec{p})\right|t\sin\left(2\left|\Omega'_{R,0}(\vec{p})\right|t\right)\cos\left(\left|\Omega'_{R,0}(\vec{p})\right|t\right)-\cos\left(2\left|\Omega'_{R,0}(\vec{p})\right|t\right)\cos\left(\left|\Omega'_{R,0}(\vec{p})\right|t\right)+\cos\left(\left|\Omega'_{R,0}(\vec{p})\right|t\right)}{8\left|\Omega'_{R,0}(\vec{p})\right|^2}
\end{array}\right) \\
&=\left(\begin{array}{l}
\dfrac{-2\cos\left(\left|\Omega'_{R,0}(\vec{p})\right|t\right)\sin^2\left(\left|\Omega'_{R,0}(\vec{p})\right|t\right)+2\left|\Omega'_{R,0}(\vec{p})\right|t\sin\left(\left|\Omega'_{R,0}(\vec{p})\right|t\right)\left(2\cos^2\left(\left|\Omega'_{R,0}(\vec{p})\right|t\right)-1\right)}{8\left|\Omega'_{R,0}(\vec{p})\right|^2} \\
+\dfrac{2\left|\Omega'_{R,0}(\vec{p})\right|^2t^2\cos\left(\left|\Omega'_{R,0}(\vec{p})\right|t\right)-4\left|\Omega'_{R,0}(\vec{p})\right|t\sin\left(\left|\Omega'_{R,0}(\vec{p})\right|t\right)\cos^2\left(\left|\Omega'_{R,0}(\vec{p})\right|t\right)+\left(-\cos\left(\left|\Omega'_{R,0}(\vec{p})\right|t\right)+2\sin^2\left(\left|\Omega'_{R,0}(\vec{p})\right|t\right)\cos\left(\left|\Omega'_{R,0}(\vec{p})\right|t\right)\right)+\cos\left(\left|\Omega'_{R,0}(\vec{p})\right|t\right)}{8\left|\Omega'_{R,0}(\vec{p})\right|^2}
\end{array}\right) \\
&=\left(\begin{array}{l}
\dfrac{-2\cos\left(\left|\Omega'_{R,0}(\vec{p})\right|t\right)\sin^2\left(\left|\Omega'_{R,0}(\vec{p})\right|t\right)+\left(4\left|\Omega'_{R,0}(\vec{p})\right|t\sin\left(\left|\Omega'_{R,0}(\vec{p})\right|t\right)\cos^2\left(\left|\Omega'_{R,0}(\vec{p})\right|t\right)-2\left|\Omega'_{R,0}(\vec{p})\right|t\sin\left(\left|\Omega'_{R,0}(\vec{p})\right|t\right)\right)}{8\left|\Omega'_{R,0}(\vec{p})\right|^2} \\
+\dfrac{2\left|\Omega'_{R,0}(\vec{p})\right|^2t^2\cos\left(\left|\Omega'_{R,0}(\vec{p})\right|t\right)-4\left|\Omega'_{R,0}(\vec{p})\right|t\sin\left(\left|\Omega'_{R,0}(\vec{p})\right|t\right)\cos^2\left(\left|\Omega'_{R,0}(\vec{p})\right|t\right)+2\sin^2\left(\left|\Omega'_{R,0}(\vec{p})\right|t\right)\cos\left(\left|\Omega'_{R,0}(\vec{p})\right|t\right)}{8\left|\Omega'_{R,0}(\vec{p})\right|^2}
\end{array}\right) \\
&=\left(\frac{-2\left|\Omega'_{R,0}(\vec{p})\right|t\sin\left(\left|\Omega'_{R,0}(\vec{p})\right|t\right)}{8\left|\Omega'_{R,0}(\vec{p})\right|^2}+\frac{2\left|\Omega'_{R,0}(\vec{p})\right|^2t^2\cos\left(\left|\Omega'_{R,0}(\vec{p})\right|t\right)}{8\left|\Omega'_{R,0}(\vec{p})\right|^2}\right)
\end{aligned}
$$

(A3.22)

$$\left(\sin\left(\left|\Omega'_{R,0}(\vec{p})\right|t\right)\frac{2\left|\Omega'_{R,0}(\vec{p})\right|t+\sin\left(2\left|\Omega'_{R,0}(\vec{p})\right|t\right)}{4\left|\Omega'_{R,0}(\vec{p})\right|}-\cos\left(\left|\Omega'_{R,0}(\vec{p})\right|t\right)\frac{\sin^2\left(\left|\Omega'_{R,0}(\vec{p})\right|t\right)}{2\left|\Omega'_{R,0}(\vec{p})\right|}\right)$$

$$=\left(\frac{2\left|\Omega'_{R,0}(\vec{p})\right|t\sin\left(\left|\Omega'_{R,0}(\vec{p})\right|t\right)+\sin\left(2\left|\Omega'_{R,0}(\vec{p})\right|t\right)\sin\left(\left|\Omega'_{R,0}(\vec{p})\right|t\right)}{4\left|\Omega'_{R,0}(\vec{p})\right|}-\frac{\sin^2\left(\left|\Omega'_{R,0}(\vec{p})\right|t\right)\cos\left(\left|\Omega'_{R,0}(\vec{p})\right|t\right)}{2\left|\Omega'_{R,0}(\vec{p})\right|}\right)$$

$$=\left(\frac{2\left|\Omega'_{R,0}(\vec{p})\right|t\sin\left(\left|\Omega'_{R,0}(\vec{p})\right|t\right)+2\sin^2\left(\left|\Omega'_{R,0}(\vec{p})\right|t\right)\cos\left(\left|\Omega'_{R,0}(\vec{p})\right|t\right)}{4\left|\Omega'_{R,0}(\vec{p})\right|}-\frac{2\sin^2\left(\left|\Omega'_{R,0}(\vec{p})\right|t\right)\cos\left(\left|\Omega'_{R,0}(\vec{p})\right|t\right)}{4\left|\Omega'_{R,0}(\vec{p})\right|}\right)$$

$$=\left(\frac{\left|\Omega'_{R,0}(\vec{p})\right|t\sin\left(\left|\Omega'_{R,0}(\vec{p})\right|t\right)}{2\left|\Omega'_{R,0}(\vec{p})\right|}\right)$$

(A3.23)

Approved for public release; distribution is unlimited

$$
\begin{pmatrix}
\sin\left(\left|\Omega'_{R,0}(\vec{p})\right|t\right)\dfrac{2\left|\Omega'_{R,0}(\vec{p})\right|^2 t^2+2\left|\Omega'_{R,0}(\vec{p})\right|t\sin\left(2\left|\Omega'_{R,0}(\vec{p})\right|t\right)+\cos\left(2\left|\Omega'_{R,0}(\vec{p})\right|t\right)-1}{8\left|\Omega'_{R,0}(\vec{p})\right|^2} \\
-\cos\left(\left|\Omega'_{R,0}(\vec{p})\right|t\right)\dfrac{\sin\left(2\left|\Omega'_{R,0}(\vec{p})\right|t\right)-2\left|\Omega'_{R,0}(\vec{p})\right|t\cos\left(2\left|\Omega'_{R,0}(\vec{p})\right|t\right)}{8\left|\Omega'_{R,0}(\vec{p})\right|^2}
\end{pmatrix}
$$

$$
=\begin{pmatrix}
\dfrac{2\left|\Omega'_{R,0}(\vec{p})\right|^2 t^2\sin\left(\left|\Omega'_{R,0}(\vec{p})\right|t\right)+2\left|\Omega'_{R,0}(\vec{p})\right|t\sin\left(2\left|\Omega'_{R,0}(\vec{p})\right|t\right)\sin\left(\left|\Omega'_{R,0}(\vec{p})\right|t\right)+\cos\left(2\left|\Omega'_{R,0}(\vec{p})\right|t\right)\sin\left(\left|\Omega'_{R,0}(\vec{p})\right|t\right)-\sin\left(\left|\Omega'_{R,0}(\vec{p})\right|t\right)}{8\left|\Omega'_{R,0}(\vec{p})\right|^2} \\
-\dfrac{\sin\left(2\left|\Omega'_{R,0}(\vec{p})\right|t\right)\cos\left(\left|\Omega'_{R,0}(\vec{p})\right|t\right)-2\left|\Omega'_{R,0}(\vec{p})\right|t\cos\left(2\left|\Omega'_{R,0}(\vec{p})\right|t\right)\cos\left(\left|\Omega'_{R,0}(\vec{p})\right|t\right)}{8\left|\Omega'_{R,0}(\vec{p})\right|^2}
\end{pmatrix}
$$

$$
=\begin{pmatrix}
\dfrac{2\left|\Omega'_{R,0}(\vec{p})\right|^2 t^2\sin\left(\left|\Omega'_{R,0}(\vec{p})\right|t\right)+4\left|\Omega'_{R,0}(\vec{p})\right|t\cos\left(\left|\Omega'_{R,0}(\vec{p})\right|t\right)\sin^2\left(\left|\Omega'_{R,0}(\vec{p})\right|t\right)+\left(-2\sin\left(\left|\Omega'_{R,0}(\vec{p})\right|t\right)\sin^2\left(\left|\Omega'_{R,0}(\vec{p})\right|t\right)\right)}{8\left|\Omega'_{R,0}(\vec{p})\right|^2} \\
-\dfrac{2\sin\left(\left|\Omega'_{R,0}(\vec{p})\right|t\right)\cos^2\left(\left|\Omega'_{R,0}(\vec{p})\right|t\right)-2\left|\Omega'_{R,0}(\vec{p})\right|t\left(\cos\left(\left|\Omega'_{R,0}(\vec{p})\right|t\right)-2\sin^2\left(\left|\Omega'_{R,0}(\vec{p})\right|t\right)\cos\left(\left|\Omega'_{R,0}(\vec{p})\right|t\right)\right)}{8\left|\Omega'_{R,0}(\vec{p})\right|^2}
\end{pmatrix}
$$

$$
=\begin{pmatrix}
\dfrac{2\left|\Omega'_{R,0}(\vec{p})\right|^2 t^2\sin\left(\left|\Omega'_{R,0}(\vec{p})\right|t\right)+4\left|\Omega'_{R,0}(\vec{p})\right|t\cos\left(\left|\Omega'_{R,0}(\vec{p})\right|t\right)\sin^2\left(\left|\Omega'_{R,0}(\vec{p})\right|t\right)+\left(-2\sin\left(\left|\Omega'_{R,0}(\vec{p})\right|t\right)\sin^2\left(\left|\Omega'_{R,0}(\vec{p})\right|t\right)\right)}{8\left|\Omega'_{R,0}(\vec{p})\right|^2} \\
-\dfrac{2\sin\left(\left|\Omega'_{R,0}(\vec{p})\right|t\right)\cos^2\left(\left|\Omega'_{R,0}(\vec{p})\right|t\right)-2\left|\Omega'_{R,0}(\vec{p})\right|t\cos\left(\left|\Omega'_{R,0}(\vec{p})\right|t\right)+4\left|\Omega'_{R,0}(\vec{p})\right|t\sin^2\left(\left|\Omega'_{R,0}(\vec{p})\right|t\right)\cos\left(\left|\Omega'_{R,0}(\vec{p})\right|t\right)}{8\left|\Omega'_{R,0}(\vec{p})\right|^2}
\end{pmatrix}
$$

$$
=\begin{pmatrix}
\dfrac{2\left|\Omega'_{R,0}(\vec{p})\right|^2 t^2\sin\left(\left|\Omega'_{R,0}(\vec{p})\right|t\right)-2\sin\left(\left|\Omega'_{R,0}(\vec{p})\right|t\right)\sin^2\left(\left|\Omega'_{R,0}(\vec{p})\right|t\right)}{8\left|\Omega'_{R,0}(\vec{p})\right|^2} \\
+\dfrac{-2\sin\left(\left|\Omega'_{R,0}(\vec{p})\right|t\right)\cos^2\left(\left|\Omega'_{R,0}(\vec{p})\right|t\right)+2\left|\Omega'_{R,0}(\vec{p})\right|t\cos\left(\left|\Omega'_{R,0}(\vec{p})\right|t\right)}{8\left|\Omega'_{R,0}(\vec{p})\right|^2}
\end{pmatrix}
$$

$$
=\begin{pmatrix}
\dfrac{2\left|\Omega'_{R,0}(\vec{p})\right|^2 t^2\sin\left(\left|\Omega'_{R,0}(\vec{p})\right|t\right)-2\sin\left(\left|\Omega'_{R,0}(\vec{p})\right|t\right)+2\sin\left(\left|\Omega'_{R,0}(\vec{p})\right|t\right)\cos^2\left(\left|\Omega'_{R,0}(\vec{p})\right|t\right)}{8\left|\Omega'_{R,0}(\vec{p})\right|^2} \\
+\dfrac{-2\sin\left(\left|\Omega'_{R,0}(\vec{p})\right|t\right)\cos^2\left(\left|\Omega'_{R,0}(\vec{p})\right|t\right)+2\left|\Omega'_{R,0}(\vec{p})\right|t\cos\left(\left|\Omega'_{R,0}(\vec{p})\right|t\right)}{8\left|\Omega'_{R,0}(\vec{p})\right|^2}
\end{pmatrix}
$$

$$
=\begin{pmatrix}
\dfrac{2\left|\Omega'_{R,0}(\vec{p})\right|^2 t^2\sin\left(\left|\Omega'_{R,0}(\vec{p})\right|t\right)+2\left|\Omega'_{R,0}(\vec{p})\right|t\cos\left(\left|\Omega'_{R,0}(\vec{p})\right|t\right)-2\sin\left(\left|\Omega'_{R,0}(\vec{p})\right|t\right)}{8\left|\Omega'_{R,0}(\vec{p})\right|^2}
\end{pmatrix}
$$

(A3.24)

$$\left(\sin\left(\left|\Omega'_{R,0}\left(\vec{p}\right)\right|t\right)\frac{\sin^2\left(\left|\Omega'_{R,0}\left(\vec{p}\right)\right|t\right)}{2\left|\Omega'_{R,0}\left(\vec{p}\right)\right|}-\cos\left(\left|\Omega'_{R,0}\left(\vec{p}\right)\right|t\right)\frac{2\left|\Omega'_{R,0}\left(\vec{p}\right)\right|t-\sin\left(2\left|\Omega'_{R,0}\left(\vec{p}\right)\right|t\right)}{4\left|\Omega'_{R,0}\left(\vec{p}\right)\right|}\right)$$

$$=\left(\begin{array}{c}\dfrac{\sin\left(\left|\Omega'_{R,0}\left(\vec{p}\right)\right|t\right)\left(1-\cos^2\left(\left|\Omega'_{R,0}\left(\vec{p}\right)\right|t\right)\right)}{2\left|\Omega'_{R,0}\left(\vec{p}\right)\right|}\\ -\dfrac{2\left|\Omega'_{R,0}\left(\vec{p}\right)\right|t\cos\left(\left|\Omega'_{R,0}\left(\vec{p}\right)\right|t\right)-2\sin\left(\left|\Omega'_{R,0}\left(\vec{p}\right)\right|t\right)\cos^2\left(\left|\Omega'_{R,0}\left(\vec{p}\right)\right|t\right)}{4\left|\Omega'_{R,0}\left(\vec{p}\right)\right|}\end{array}\right)$$

$$=\left(\begin{array}{c}\dfrac{2\sin\left(\left|\Omega'_{R,0}\left(\vec{p}\right)\right|t\right)-2\sin\left(\left|\Omega'_{R,0}\left(\vec{p}\right)\right|t\right)\cos^2\left(\left|\Omega'_{R,0}\left(\vec{p}\right)\right|t\right)}{4\left|\Omega'_{R,0}\left(\vec{p}\right)\right|}\\ +\dfrac{-2\left|\Omega'_{R,0}\left(\vec{p}\right)\right|t\cos\left(\left|\Omega'_{R,0}\left(\vec{p}\right)\right|t\right)+2\sin\left(\left|\Omega'_{R,0}\left(\vec{p}\right)\right|t\right)\cos^2\left(\left|\Omega'_{R,0}\left(\vec{p}\right)\right|t\right)}{4\left|\Omega'_{R,0}\left(\vec{p}\right)\right|}\end{array}\right)$$

$$=\left(\frac{\sin\left(\left|\Omega'_{R,0}\left(\vec{p}\right)\right|t\right)}{2\left|\Omega'_{R,0}\left(\vec{p}\right)\right|}+\frac{-\left|\Omega'_{R,0}\left(\vec{p}\right)\right|t\cos\left(\left|\Omega'_{R,0}\left(\vec{p}\right)\right|t\right)}{2\left|\Omega'_{R,0}\left(\vec{p}\right)\right|}\right)$$

(A3.25)

Substituting equations (A3.22)-(A3.25) into equation (A3.21) yields:

Approved for public release; distribution is unlimited

$$\int_0^t du \sin\left(\left|\Omega'_{R,0}(\vec{p})\right|(t-u)\right)\left(\nabla_p\, f'_{g,0}(\vec{p},u)\Big|_{general}\right)$$

$$= \left[\begin{array}{l} a(\vec{p})\nabla_p\left(\left|\Omega'_{R,0}(\vec{p})\right|\right)\left(\dfrac{-2\left|\Omega'_{R,0}(\vec{p})\right| t\sin\left(\left|\Omega'_{R,0}(\vec{p})\right| t\right)}{8\left|\Omega'_{R,0}(\vec{p})\right|^2} + \dfrac{2\left|\Omega'_{R,0}(\vec{p})\right|^2 t^2\cos\left(\left|\Omega'_{R,0}(\vec{p})\right| t\right)}{8\left|\Omega'_{R,0}(\vec{p})\right|^2}\right) \\ +\nabla_p\left(a(\vec{p})\right)\left(\dfrac{\left|\Omega'_{R,0}(\vec{p})\right| t\sin\left(\left|\Omega'_{R,0}(\vec{p})\right| t\right)}{2\left|\Omega'_{R,0}(\vec{p})\right|}\right) \\ +b(\vec{p})\nabla_p\left(\left|\Omega'_{R,0}(\vec{p})\right|\right)\left(\dfrac{2\left|\Omega'_{R,0}(\vec{p})\right|^2 t^2\sin\left(\left|\Omega'_{R,0}(\vec{p})\right| t\right) + 2\left|\Omega'_{R,0}(\vec{p})\right| t\cos\left(\left|\Omega'_{R,0}(\vec{p})\right| t\right) - 2\sin\left(\left|\Omega'_{R,0}(\vec{p})\right| t\right)}{8\left|\Omega'_{R,0}(\vec{p})\right|^2}\right) \\ +\nabla_p\left(b(\vec{p})\right)\left(\dfrac{\sin\left(\left|\Omega'_{R,0}(\vec{p})\right| t\right)}{2\left|\Omega'_{R,0}(\vec{p})\right|} + \dfrac{-\left|\Omega'_{R,0}(\vec{p})\right| t\cos\left(\left|\Omega'_{R,0}(\vec{p})\right| t\right)}{2\left|\Omega'_{R,0}(\vec{p})\right|}\right) \end{array}\right]$$

(A3.26)

Next, the second integral from the particular solution (A3.11), reprinted here, is considered:

$$f'_{g,1}(\vec{p},t)\Big|_{particular} = \left[\begin{array}{l} 2i\hbar k_o \dfrac{\mathrm{Im}\left(\Omega_{R,0}(\vec{p})^*\,\vec{\Omega}_{R,1}(\vec{p})\right)}{2\left|\Omega_{R,0}(\vec{p})\right|}\cdot\displaystyle\int_0^t du\sin\left(\frac{\left|\Omega_{R,0}(\vec{p})\right|}{2}(t-u)\right)\left(\nabla_p\, f'_{g,0}(\vec{p},u)\Big|_{general}\right) \\ -\hbar k_0 \dfrac{\vec{\Omega}_{R,1}(\vec{p})^*\cdot\left(\nabla_p\Omega_{R,0}(\vec{p})\right)}{2\left|\Omega_{R,0}(\vec{p})\right|}\displaystyle\int_0^t du\sin\left(\frac{\left|\Omega_{R,0}(\vec{p})\right|}{2}(t-u)\right) f'_{g,0}(\vec{p},u)\Big|_{general} \end{array}\right]$$

When written with the substitution $\left|\Omega'_{R,0}(\vec{p})\right| \equiv \dfrac{\left|\Omega_{R,0}(\vec{p})\right|}{2}$ (A3.17) applied to the cosine and sine arguments, this particular solution is written as:

Approved for public release; distribution is unlimited

$$f'_{g,0}(\vec{p},t)\Big|_{general} = a(\vec{p})\cos\left(\left|\Omega'_{R,0}(\vec{p})\right|t\right) + b(\vec{p})\sin\left(\left|\Omega'_{R,0}(\vec{p})\right|t\right)$$

$$f'_{g,1}(\vec{p},t)\Big|_{particular} = \begin{bmatrix} 2i\hbar k_o \dfrac{\mathrm{Im}\left(\Omega_{R,0}(\vec{p})^* \vec{\Omega}_{R,1}(\vec{p})\right)}{\left|\Omega_{R,0}(\vec{p})\right|} \cdot \int_0^t du \sin\left(\left|\Omega'_{R,0}(\vec{p})\right|(t-u)\right)\left(\nabla_p f'_{g,0}(\vec{p},u)\Big|_{general}\right) \\ -\hbar k_0 \dfrac{\vec{\Omega}_{R,1}(\vec{p})^* \cdot \left(\nabla_p \Omega_{R,0}(\vec{p})\right)}{\left|\Omega_{R,0}(\vec{p})\right|} \int_0^t du \sin\left(\left|\Omega'_{R,0}(\vec{p})\right|(t-u)\right) f'_{g,0}(\vec{p},u)\Big|_{general} \end{bmatrix}$$

(A3.27)

The second integral may be evaluated as:

$$\int_0^t du \sin\left(\left|\Omega'_{R,0}(\vec{p})\right|(t-u)\right) f'_{g,0}(\vec{p},u)\Big|_{general}$$

$$= \int_0^t du \sin\left(\left|\Omega'_{R,0}(\vec{p})\right|(t-u)\right)\left(a(\vec{p})\cos\left(\left|\Omega'_{R,0}(\vec{p})\right|u\right) + b(\vec{p})\sin\left(\left|\Omega'_{R,0}(\vec{p})\right|u\right)\right)$$

$$= \begin{bmatrix} \sin\left(\left|\Omega'_{R,0}(\vec{p})\right|t\right)\int_0^t du \cos\left(\left|\Omega'_{R,0}(\vec{p})\right|u\right)\left(a(\vec{p})\cos\left(\left|\Omega'_{R,0}(\vec{p})\right|u\right) + b(\vec{p})\sin\left(\left|\Omega'_{R,0}(\vec{p})\right|u\right)\right) \\ -\cos\left(\left|\Omega'_{R,0}(\vec{p})\right|t\right)\int_0^t du \sin\left(\left|\Omega'_{R,0}(\vec{p})\right|u\right)\left(a(\vec{p})\cos\left(\left|\Omega'_{R,0}(\vec{p})\right|u\right) + b(\vec{p})\sin\left(\left|\Omega'_{R,0}(\vec{p})\right|u\right)\right) \end{bmatrix}$$

$$= \begin{bmatrix} a(\vec{p})\sin\left(\left|\Omega'_{R,0}(\vec{p})\right|t\right)\int_0^t du \cos^2\left(\left|\Omega'_{R,0}(\vec{p})\right|u\right) \\ +b(\vec{p})\sin\left(\left|\Omega'_{R,0}(\vec{p})\right|t\right)\int_0^t du \cos\left(\left|\Omega'_{R,0}(\vec{p})\right|u\right)\sin\left(\left|\Omega'_{R,0}(\vec{p})\right|u\right) \\ -a(\vec{p})\cos\left(\left|\Omega'_{R,0}(\vec{p})\right|t\right)\int_0^t du \sin\left(\left|\Omega'_{R,0}(\vec{p})\right|u\right)\cos\left(\left|\Omega'_{R,0}(\vec{p})\right|u\right) \\ -b(\vec{p})\cos\left(\left|\Omega'_{R,0}(\vec{p})\right|t\right)\int_0^t du \sin^2\left(\left|\Omega'_{R,0}(\vec{p})\right|u\right) \end{bmatrix}$$

(A3.28)

Approved for public release; distribution is unlimited

Referring to the integrals previously evaluated in (A3.19), relevant integral solutions are identified including:

$$\begin{aligned}
&\int_0^t du \cos\left(\left|\Omega'_{R,0}\left(\vec{p}\right)\right|u\right)\cos\left(\left|\Omega'_{R,0}\left(\vec{p}\right)\right|u\right) = \frac{2\left|\Omega'_{R,0}\left(\vec{p}\right)\right|t + \sin\left(2\left|\Omega'_{R,0}\left(\vec{p}\right)\right|t\right)}{4\left|\Omega'_{R,0}\left(\vec{p}\right)\right|} \\
&\int_0^t du \cos\left(\left|\Omega'_{R,0}\left(\vec{p}\right)\right|u\right)\sin\left(\left|\Omega'_{R,0}\left(\vec{p}\right)\right|u\right) = \frac{\sin^2\left(\left|\Omega'_{R,0}\left(\vec{p}\right)\right|t\right)}{2\left|\Omega'_{R,0}\left(\vec{p}\right)\right|} \\
&\int_0^t du \sin\left(\left|\Omega'_{R,0}\left(\vec{p}\right)\right|u\right)\cos\left(\left|\Omega'_{R,0}\left(\vec{p}\right)\right|u\right) = \frac{\sin^2\left(\left|\Omega'_{R,0}\left(\vec{p}\right)\right|t\right)}{2\left|\Omega'_{R,0}\left(\vec{p}\right)\right|} \\
&\int_0^t du \sin\left(\left|\Omega'_{R,0}\left(\vec{p}\right)\right|u\right)\sin\left(\left|\Omega'_{R,0}\left(\vec{p}\right)\right|u\right) = \frac{2\left|\Omega'_{R,0}\left(\vec{p}\right)\right|t - \sin\left(2\left|\Omega'_{R,0}\left(\vec{p}\right)\right|t\right)}{4\left|\Omega'_{R,0}\left(\vec{p}\right)\right|}
\end{aligned} \tag{A3.29}$$

Substituting integrals from (A3.29) into equation (A3.28) yields:

Approved for public release; distribution is unlimited

$$
\begin{aligned}
&\int_0^t du \sin\left(\left|\Omega'_{R,0}(\vec{p})\right|(t-u)\right) f'_{g,0}(\vec{p},u)\Big|_{general} \\
&= \begin{bmatrix}
a(\vec{p})\sin\left(\left|\Omega'_{R,0}(\vec{p})\right|t\right)\int_0^t du \cos^2\left(\left|\Omega'_{R,0}(\vec{p})\right|u\right) \\
+b(\vec{p})\sin\left(\left|\Omega'_{R,0}(\vec{p})\right|t\right)\int_0^t du \cos\left(\left|\Omega'_{R,0}(\vec{p})\right|u\right)\sin\left(\left|\Omega'_{R,0}(\vec{p})\right|u\right) \\
-a(\vec{p})\cos\left(\left|\Omega'_{R,0}(\vec{p})\right|t\right)\int_0^t du \sin\left(\left|\Omega'_{R,0}(\vec{p})\right|u\right)\cos\left(\left|\Omega'_{R,0}(\vec{p})\right|u\right) \\
-b(\vec{p})\cos\left(\left|\Omega'_{R,0}(\vec{p})\right|t\right)\int_0^t du \sin^2\left(\left|\Omega'_{R,0}(\vec{p})\right|u\right)
\end{bmatrix} \\
&= \begin{bmatrix}
a(\vec{p})\sin\left(\left|\Omega'_{R,0}(\vec{p})\right|t\right)\dfrac{2\left|\Omega'_{R,0}(\vec{p})\right|t+\sin\left(2\left|\Omega'_{R,0}(\vec{p})\right|t\right)}{4\left|\Omega'_{R,0}(\vec{p})\right|} \\
+b(\vec{p})\sin\left(\left|\Omega'_{R,0}(\vec{p})\right|t\right)\dfrac{\sin^2\left(\left|\Omega'_{R,0}(\vec{p})\right|t\right)}{2\left|\Omega'_{R,0}(\vec{p})\right|} \\
-a(\vec{p})\cos\left(\left|\Omega'_{R,0}(\vec{p})\right|t\right)\dfrac{\sin^2\left(\left|\Omega'_{R,0}(\vec{p})\right|t\right)}{2\left|\Omega'_{R,0}(\vec{p})\right|} \\
-b(\vec{p})\cos\left(\left|\Omega'_{R,0}(\vec{p})\right|t\right)\dfrac{2\left|\Omega'_{R,0}(\vec{p})\right|t-\sin\left(2\left|\Omega'_{R,0}(\vec{p})\right|t\right)}{4\left|\Omega'_{R,0}(\vec{p})\right|}
\end{bmatrix}
\end{aligned}
\tag{A3.30}
$$

Like terms are combined and simplified as:

Approved for public release; distribution is unlimited

$$\int_0^t du \sin\left(\left|\Omega'_{R,0}(\vec{p})\right|(t-u)\right) f'_{g,0}(\vec{p},u)\Big|_{general}$$

$$= \begin{bmatrix} a(\vec{p})\sin\left(\left|\Omega'_{R,0}(\vec{p})\right|t\right)\dfrac{2\left|\Omega'_{R,0}(\vec{p})\right|t+\sin\left(2\left|\Omega'_{R,0}(\vec{p})\right|t\right)}{4\left|\Omega'_{R,0}(\vec{p})\right|}+b(\vec{p})\sin\left(\left|\Omega'_{R,0}(\vec{p})\right|t\right)\dfrac{\sin^2\left(\left|\Omega'_{R,0}(\vec{p})\right|t\right)}{2\left|\Omega'_{R,0}(\vec{p})\right|} \\ -a(\vec{p})\cos\left(\left|\Omega'_{R,0}(\vec{p})\right|t\right)\dfrac{\sin^2\left(\left|\Omega'_{R,0}(\vec{p})\right|t\right)}{2\left|\Omega'_{R,0}(\vec{p})\right|}-b(\vec{p})\cos\left(\left|\Omega'_{R,0}(\vec{p})\right|t\right)\dfrac{2\left|\Omega'_{R,0}(\vec{p})\right|t-\sin\left(2\left|\Omega'_{R,0}(\vec{p})\right|t\right)}{4\left|\Omega'_{R,0}(\vec{p})\right|} \end{bmatrix}$$

$$= \begin{bmatrix} a(\vec{p})\left(\sin\left(\left|\Omega'_{R,0}(\vec{p})\right|t\right)\dfrac{2\left|\Omega'_{R,0}(\vec{p})\right|t+\sin\left(2\left|\Omega'_{R,0}(\vec{p})\right|t\right)}{4\left|\Omega'_{R,0}(\vec{p})\right|}-\cos\left(\left|\Omega'_{R,0}(\vec{p})\right|t\right)\dfrac{\sin^2\left(\left|\Omega'_{R,0}(\vec{p})\right|t\right)}{2\left|\Omega'_{R,0}(\vec{p})\right|}\right) \\ +b(\vec{p})\left(\sin\left(\left|\Omega'_{R,0}(\vec{p})\right|t\right)\dfrac{\sin^2\left(\left|\Omega'_{R,0}(\vec{p})\right|t\right)}{2\left|\Omega'_{R,0}(\vec{p})\right|}-\cos\left(\left|\Omega'_{R,0}(\vec{p})\right|t\right)\dfrac{2\left|\Omega'_{R,0}(\vec{p})\right|t-\sin\left(2\left|\Omega'_{R,0}(\vec{p})\right|t\right)}{4\left|\Omega'_{R,0}(\vec{p})\right|}\right) \end{bmatrix}$$

$$= \begin{bmatrix} a(\vec{p})\left(\sin\left(\left|\Omega'_{R,0}(\vec{p})\right|t\right)\dfrac{2\left|\Omega'_{R,0}(\vec{p})\right|t+\sin\left(2\left|\Omega'_{R,0}(\vec{p})\right|t\right)}{4\left|\Omega'_{R,0}(\vec{p})\right|}-\cos\left(\left|\Omega'_{R,0}(\vec{p})\right|t\right)\dfrac{\sin^2\left(\left|\Omega'_{R,0}(\vec{p})\right|t\right)}{2\left|\Omega'_{R,0}(\vec{p})\right|}\right) \\ +b(\vec{p})\left(\sin\left(\left|\Omega'_{R,0}(\vec{p})\right|t\right)\dfrac{\sin^2\left(\left|\Omega'_{R,0}(\vec{p})\right|t\right)}{2\left|\Omega'_{R,0}(\vec{p})\right|}-\cos\left(\left|\Omega'_{R,0}(\vec{p})\right|t\right)\dfrac{2\left|\Omega'_{R,0}(\vec{p})\right|t-\sin\left(2\left|\Omega'_{R,0}(\vec{p})\right|t\right)}{4\left|\Omega'_{R,0}(\vec{p})\right|}\right) \end{bmatrix}$$

(A3.31)

Each line of the last equation in (A3.31) is simplified in turn:

Approved for public release; distribution is unlimited

$$\left(\sin\left(\left|\Omega'_{R,0}(\vec{p})\right|t\right)\frac{2\left|\Omega'_{R,0}(\vec{p})\right|t+\sin\left(2\left|\Omega'_{R,0}(\vec{p})\right|t\right)}{4\left|\Omega'_{R,0}(\vec{p})\right|}-\cos\left(\left|\Omega'_{R,0}(\vec{p})\right|t\right)\frac{\sin^2\left(\left|\Omega'_{R,0}(\vec{p})\right|t\right)}{2\left|\Omega'_{R,0}(\vec{p})\right|}\right)$$

$$=\left(\frac{2\left|\Omega'_{R,0}(\vec{p})\right|t\sin\left(\left|\Omega'_{R,0}(\vec{p})\right|t\right)+\sin\left(2\left|\Omega'_{R,0}(\vec{p})\right|t\right)\sin\left(\left|\Omega'_{R,0}(\vec{p})\right|t\right)}{4\left|\Omega'_{R,0}(\vec{p})\right|}-\frac{\sin^2\left(\left|\Omega'_{R,0}(\vec{p})\right|t\right)\cos\left(\left|\Omega'_{R,0}(\vec{p})\right|t\right)}{2\left|\Omega'_{R,0}(\vec{p})\right|}\right)$$

$$=\left(\frac{2\left|\Omega'_{R,0}(\vec{p})\right|t\sin\left(\left|\Omega'_{R,0}(\vec{p})\right|t\right)+2\cos\left(\left|\Omega'_{R,0}(\vec{p})\right|t\right)\sin^2\left(\left|\Omega'_{R,0}(\vec{p})\right|t\right)}{4\left|\Omega'_{R,0}(\vec{p})\right|}-\frac{2\sin^2\left(\left|\Omega'_{R,0}(\vec{p})\right|t\right)\cos\left(\left|\Omega'_{R,0}(\vec{p})\right|t\right)}{4\left|\Omega'_{R,0}(\vec{p})\right|}\right)$$

$$=\left(\frac{\left|\Omega'_{R,0}(\vec{p})\right|t\sin\left(\left|\Omega'_{R,0}(\vec{p})\right|t\right)}{2\left|\Omega'_{R,0}(\vec{p})\right|}\right)$$

(A3.32)

$$\left(\sin\left(\left|\Omega'_{R,0}(\vec{p})\right|t\right)\frac{\sin^2\left(\left|\Omega'_{R,0}(\vec{p})\right|t\right)}{2\left|\Omega'_{R,0}(\vec{p})\right|}-\cos\left(\left|\Omega'_{R,0}(\vec{p})\right|t\right)\frac{2\left|\Omega'_{R,0}(\vec{p})\right|t-\sin\left(2\left|\Omega'_{R,0}(\vec{p})\right|t\right)}{4\left|\Omega'_{R,0}(\vec{p})\right|}\right)$$

$$=\left(\frac{\sin^2\left(\left|\Omega'_{R,0}(\vec{p})\right|t\right)\sin\left(\left|\Omega'_{R,0}(\vec{p})\right|t\right)}{2\left|\Omega'_{R,0}(\vec{p})\right|}-\frac{2\left|\Omega'_{R,0}(\vec{p})\right|t\cos\left(\left|\Omega'_{R,0}(\vec{p})\right|t\right)-\sin\left(2\left|\Omega'_{R,0}(\vec{p})\right|t\right)\cos\left(\left|\Omega'_{R,0}(\vec{p})\right|t\right)}{4\left|\Omega'_{R,0}(\vec{p})\right|}\right)$$

$$=\left(\frac{\left(1-\cos^2\left(\left|\Omega'_{R,0}(\vec{p})\right|t\right)\right)\sin\left(\left|\Omega'_{R,0}(\vec{p})\right|t\right)}{2\left|\Omega'_{R,0}(\vec{p})\right|}-\frac{2\left|\Omega_{R,0}(\vec{p})\right|t\cos\left(\left|\Omega'_{R,0}(\vec{p})\right|t\right)-2\sin\left(\left|\Omega'_{R,0}(\vec{p})\right|t\right)\cos^2\left(\left|\Omega'_{R,0}(\vec{p})\right|t\right)}{4\left|\Omega'_{R,0}(\vec{p})\right|}\right)$$

$$=\left(\begin{array}{l}\dfrac{2\sin\left(\left|\Omega'_{R,0}(\vec{p})\right|t\right)-2\cos^2\left(\left|\Omega'_{R,0}(\vec{p})\right|t\right)\sin\left(\left|\Omega'_{R,0}(\vec{p})\right|t\right)}{4\left|\Omega'_{R,0}(\vec{p})\right|}\\ +\dfrac{-2\left|\Omega'_{R,0}(\vec{p})\right|t\cos\left(\left|\Omega'_{R,0}(\vec{p})\right|t\right)+2\sin\left(\left|\Omega'_{R,0}(\vec{p})\right|t\right)\cos^2\left(\left|\Omega'_{R,0}(\vec{p})\right|t\right)}{4\left|\Omega'_{R,0}(\vec{p})\right|}\end{array}\right)$$

$$=\left(\frac{\sin\left(\left|\Omega'_{R,0}(\vec{p})\right|t\right)}{2\left|\Omega'_{R,0}(\vec{p})\right|}+\frac{-\left|\Omega'_{R,0}(\vec{p})\right|t\cos\left(\left|\Omega'_{R,0}(\vec{p})\right|t\right)}{2\left|\Omega'_{R,0}(\vec{p})\right|}\right)$$

(A3.33)

Approved for public release; distribution is unlimited

Substituting equations (A3.32)-(A3.33) into equation (A3.31) results in:

$$\int_0^t du \sin\left(\left|\Omega'_{R,0}(\vec{p})\right|(t-u)\right) f'_{g,0}(\vec{p},u)\Big|_{general}$$

$$= \left[\begin{array}{l} a(\vec{p}) \left(\sin\left(\left|\Omega'_{R,0}(\vec{p})\right|t\right) \dfrac{2\left|\Omega'_{R,0}(\vec{p})\right|t + \sin\left(2\left|\Omega'_{R,0}(\vec{p})\right|t\right)}{4\left|\Omega'_{R,0}(\vec{p})\right|} - \cos\left(\left|\Omega'_{R,0}(\vec{p})\right|t\right) \dfrac{\sin^2\left(\left|\Omega'_{R,0}(\vec{p})\right|t\right)}{2\left|\Omega'_{R,0}(\vec{p})\right|} \right) \\ +b(\vec{p}) \left(\sin\left(\left|\Omega'_{R,0}(\vec{p})\right|t\right) \dfrac{\sin^2\left(\left|\Omega'_{R,0}(\vec{p})\right|t\right)}{2\left|\Omega'_{R,0}(\vec{p})\right|} - \cos\left(\left|\Omega'_{R,0}(\vec{p})\right|t\right) \dfrac{2\left|\Omega'_{R,0}(\vec{p})\right|t - \sin\left(2\left|\Omega'_{R,0}(\vec{p})\right|t\right)}{4\left|\Omega'_{R,0}(\vec{p})\right|} \right) \end{array} \right]$$

$$= \left[\begin{array}{l} a(\vec{p}) \left(\dfrac{\left|\Omega'_{R,0}(\vec{p})\right|t \sin\left(\left|\Omega'_{R,0}(\vec{p})\right|t\right)}{2\left|\Omega'_{R,0}(\vec{p})\right|} \right) \\ +b(\vec{p}) \left(\dfrac{\sin\left(\left|\Omega'_{R,0}(\vec{p})\right|t\right)}{2\left|\Omega'_{R,0}(\vec{p})\right|} + \dfrac{-\left|\Omega'_{R,0}(\vec{p})\right|t \cos\left(\left|\Omega'_{R,0}(\vec{p})\right|t\right)}{2\left|\Omega'_{R,0}(\vec{p})\right|} \right) \end{array} \right]$$

(A3.34)

To summarize, the two integrals from equation (A3.27) are evaluated to be:

Approved for public release; distribution is unlimited

$$\int_0^t du \sin\left(\left|\Omega'_{R,0}(\vec{p})\right|(t-u)\right)\left(\nabla_p f'_{g,0}(\vec{p},u)\Big|_{general}\right) = \begin{bmatrix} a(\vec{p})\nabla_p\left(\left|\Omega'_{R,0}(\vec{p})\right|\right)\left(\dfrac{-2\left|\Omega'_{R,0}(\vec{p})\right| t\sin\left(\left|\Omega'_{R,0}(\vec{p})\right| t\right)}{8\left|\Omega'_{R,0}(\vec{p})\right|^2} + \dfrac{2\left|\Omega'_{R,0}(\vec{p})\right|^2 t^2\cos\left(\left|\Omega'_{R,0}(\vec{p})\right| t\right)}{8\left|\Omega'_{R,0}(\vec{p})\right|^2}\right) \\ +\nabla_p\left(a(\vec{p})\right)\left(\dfrac{\left|\Omega'_{R,0}(\vec{p})\right| t\sin\left(\left|\Omega'_{R,0}(\vec{p})\right| t\right)}{2\left|\Omega'_{R,0}(\vec{p})\right|}\right) \\ +b(\vec{p})\nabla_p\left(\left|\Omega'_{R,0}(\vec{p})\right|\right)\left(\dfrac{2\left|\Omega'_{R,0}(\vec{p})\right|^2 t^2\sin\left(\left|\Omega'_{R,0}(\vec{p})\right| t\right) + 2\left|\Omega'_{R,0}(\vec{p})\right| t\cos\left(\left|\Omega'_{R,0}(\vec{p})\right| t\right) - 2\sin\left(\left|\Omega'_{R,0}(\vec{p})\right| t\right)}{8\left|\Omega'_{R,0}(\vec{p})\right|^2}\right) \\ +\nabla_p\left(b(\vec{p})\right)\left(\dfrac{\sin\left(\left|\Omega'_{R,0}(\vec{p})\right| t\right)}{2\left|\Omega'_{R,0}(\vec{p})\right|} + \dfrac{-\left|\Omega'_{R,0}(\vec{p})\right| t\cos\left(\left|\Omega'_{R,0}(\vec{p})\right| t\right)}{2\left|\Omega'_{R,0}(\vec{p})\right|}\right) \end{bmatrix}$$

$$\int_0^t du \sin\left(\left|\Omega'_{R,0}(\vec{p})\right|(t-u)\right) f'_{g,0}(\vec{p},u)\Big|_{general} = \begin{bmatrix} a(\vec{p})\left(\dfrac{\left|\Omega'_{R,0}(\vec{p})\right| t\sin\left(\left|\Omega'_{R,0}(\vec{p})\right| t\right)}{2\left|\Omega'_{R,0}(\vec{p})\right|}\right) \\ +b(\vec{p})\left(\dfrac{\sin\left(\left|\Omega'_{R,0}(\vec{p})\right| t\right)}{2\left|\Omega'_{R,0}(\vec{p})\right|} + \dfrac{-\left|\Omega'_{R,0}(\vec{p})\right| t\cos\left(\left|\Omega'_{R,0}(\vec{p})\right| t\right)}{2\left|\Omega'_{R,0}(\vec{p})\right|}\right) \end{bmatrix}$$

(A3.35)

Rearranging terms for clarity, equation (A3.35) becomes:

$$\int_0^t du \sin\left(\left|\Omega'_{R,0}(\vec{p})\right|(t-u)\right)\left(\nabla_p f'_{g,0}(\vec{p},u)\Big|_{general}\right) = \begin{bmatrix} a(\vec{p})\nabla_p\left(\left|\Omega'_{R,0}(\vec{p})\right|\right)\left(\dfrac{t^2}{4}\cos\left(\left|\Omega'_{R,0}(\vec{p})\right| t\right) - \dfrac{t}{4\left|\Omega_{R,0}(\vec{p})\right|}\sin\left(\left|\Omega'_{R,0}(\vec{p})\right| t\right)\right) \\ +\nabla_p\left(a(\vec{p})\right)\left(\dfrac{t}{2}\sin\left(\left|\Omega'_{R,0}(\vec{p})\right| t\right)\right) \\ +b(\vec{p})\nabla_p\left(\left|\Omega'_{R,0}(\vec{p})\right|\right)\left(\begin{array}{l}\dfrac{t^2}{4}\sin\left(\left|\Omega'_{R,0}(\vec{p})\right| t\right) + \dfrac{t}{4\left|\Omega'_{R,0}(\vec{p})\right|}\cos\left(\left|\Omega'_{R,0}(\vec{p})\right| t\right) \\ -\dfrac{1}{4\left|\Omega'_{R,0}(\vec{p})\right|^2}\sin\left(\left|\Omega'_{R,0}(\vec{p})\right| t\right)\end{array}\right) \\ +\nabla_p\left(b(\vec{p})\right)\left(\dfrac{-t}{2}\cos\left(\left|\Omega'_{R,0}(\vec{p})\right| t\right) + \dfrac{1}{2\left|\Omega'_{R,0}(\vec{p})\right|}\sin\left(\left|\Omega'_{R,0}(\vec{p})\right| t\right)\right) \end{bmatrix}$$

$$\int_0^t du \sin\left(\left|\Omega_{R,0}(\vec{p})\right|(t-u)\right) f'_{g,0}(\vec{p},u)\Big|_{general} = \begin{bmatrix} a(\vec{p})\left(\dfrac{t}{2}\sin\left(\left|\Omega'_{R,0}(\vec{p})\right| t\right)\right) \\ +b(\vec{p})\left(\dfrac{-t}{2}\cos\left(\left|\Omega'_{R,0}(\vec{p})\right| t\right) + \dfrac{1}{2\left|\Omega'_{R,0}(\vec{p})\right|}\sin\left(\left|\Omega'_{R,0}(\vec{p})\right| t\right)\right) \end{bmatrix}$$

(A3.36)

Approved for public release; distribution is unlimited

The integrals of equation (A3.36) are substituted into the particular solution $f'_{g,1}(\vec{p},t)\big|_{particular}$ corresponding to the first order ground state amplitude in the perturbation theory. When converting back to $\left|\Omega'_{R,0}(\vec{p})\right| \equiv \left|\Omega_{R,0}(\vec{p})\right|/2$ with (A3.17), the expression for $f'_{g,1}(\vec{p},t)\big|_{particular}$ becomes:

$$f'_{g,1}(\vec{p},t)\big|_{particular} = \begin{bmatrix} 2i\hbar k_o \dfrac{\mathrm{Im}\left(\Omega_{R,0}(\vec{p})^* \vec{\Omega}_{R,1}(\vec{p})\right)}{2\left|\Omega_{R,0}(\vec{p})\right|} \cdot \displaystyle\int_0^t du \sin\left(\frac{\left|\Omega_{R,0}(\vec{p})\right|}{2}(t-u)\right)\left(\nabla_p\, f'_{g,0}(\vec{p},u)\big|_{general}\right) \\ -\hbar k_0 \dfrac{\vec{\Omega}_{R,1}(\vec{p})^* \cdot \left(\nabla_p \Omega_{R,0}(\vec{p})\right)}{2\left|\Omega_{R,0}(\vec{p})\right|} \displaystyle\int_0^t du \sin\left(\frac{\left|\Omega_{R,0}(\vec{p})\right|}{2}(t-u)\right) f'_{g,0}(\vec{p},u)\big|_{general} \end{bmatrix}$$

$$= \begin{bmatrix} 2i\hbar k_o \dfrac{\mathrm{Im}\left(\Omega_{R,0}(\vec{p})^* \vec{\Omega}_{R,1}(\vec{p})\right)}{2\left|\Omega_{R,0}(\vec{p})\right|} \cdot \begin{bmatrix} a(\vec{p})\nabla_p\left(\dfrac{\left|\Omega_{R,0}(\vec{p})\right|}{2}\right)\left(\dfrac{t^2}{4}\cos\left(\dfrac{\left|\Omega_{R,0}(\vec{p})\right|}{2}t\right) - \dfrac{t}{2\left|\Omega_{R,0}(\vec{p})\right|}\sin\left(\dfrac{\left|\Omega_{R,0}(\vec{p})\right|}{2}t\right)\right) \\ +\nabla_p\left(a(\vec{p})\right)\left(\dfrac{t}{2}\sin\left(\dfrac{\left|\Omega_{R,0}(\vec{p})\right|}{2}t\right)\right) \\ +b(\vec{p})\nabla_p\left(\dfrac{\left|\Omega_{R,0}(\vec{p})\right|}{2}\right)\left(\dfrac{t^2}{4}\sin\left(\dfrac{\left|\Omega_{R,0}(\vec{p})\right|}{2}t\right) + \dfrac{t}{2\left|\Omega_{R,0}(\vec{p})\right|}\cos\left(\dfrac{\left|\Omega_{R,0}(\vec{p})\right|}{2}t\right) - \dfrac{1}{\left|\Omega_{R,0}(\vec{p})\right|^2}\sin\left(\dfrac{\left|\Omega_{R,0}(\vec{p})\right|}{2}t\right)\right) \\ +\nabla_p\left(b(\vec{p})\right)\left(\dfrac{-t}{2}\cos\left(\dfrac{\left|\Omega_{R,0}(\vec{p})\right|}{2}t\right) + \dfrac{1}{\left|\Omega_{R,0}(\vec{p})\right|}\sin\left(\dfrac{\left|\Omega_{R,0}(\vec{p})\right|}{2}t\right)\right) \end{bmatrix} \\ -\hbar k_0 \dfrac{\vec{\Omega}_{R,1}(\vec{p})^* \cdot \left(\nabla_p \Omega_{R,0}(\vec{p})\right)}{2\left|\Omega_{R,0}(\vec{p})\right|} \begin{bmatrix} a(\vec{p})\left(\dfrac{t}{2}\sin\left(\dfrac{\left|\Omega_{R,0}(\vec{p})\right|}{2}t\right)\right) \\ +b(\vec{p})\left(\dfrac{-t}{2}\cos\left(\dfrac{\left|\Omega_{R,0}(\vec{p})\right|}{2}t\right) + \dfrac{1}{\left|\Omega_{R,0}(\vec{p})\right|}\sin\left(\dfrac{\left|\Omega_{R,0}(\vec{p})\right|}{2}t\right)\right) \end{bmatrix} \end{bmatrix}$$

(A3.37)

This result may be directly applied to the evaluation of the excited state distributions in the perturbation theory. Recall the expressions before integration given by equations (A3.11) and (A3.15), repeated here for clarity:

Approved for public release; distribution is unlimited

$$f'_{g,1}(\vec{p},t)\Big|_{particular} = \begin{bmatrix} 2i\hbar k_o \dfrac{\mathrm{Im}\left(\Omega_{R,0}(\vec{p})^* \vec{\Omega}_{R,1}(\vec{p})\right)}{2\left|\Omega_{R,0}(\vec{p})\right|} \cdot \int_0^t du \sin\left(\dfrac{\left|\Omega_{R,0}(\vec{p})\right|}{2}(t-u)\right)\left(\nabla_p\, f'_{g,0}(\vec{p},u)\Big|_{general}\right) \\ -\hbar k_0 \dfrac{\vec{\Omega}_{R,1}(\vec{p})^* \cdot\left(\nabla_p \Omega_{R,0}(\vec{p})\right)}{2\left|\Omega_{R,0}(\vec{p})\right|} \int_0^t du \sin\left(\dfrac{\left|\Omega_{R,0}(\vec{p})\right|}{2}(t-u)\right) f'_{g,0}(\vec{p},u)\Big|_{general} \end{bmatrix}$$

$$f'_{e,1}\left(\vec{p}+\hbar\vec{k}_0,t\right)\Big|_{particular} = \begin{bmatrix} 2i\hbar k_o \dfrac{\mathrm{Im}\left(\Omega_{R,0}(\vec{p})^* \vec{\Omega}_{R,1}(\vec{p})\right)}{2\left|\Omega_{R,0}(\vec{p})\right|} \cdot \int_0^t du \sin\left(\dfrac{\left|\Omega_{R,0}(\vec{p})\right|}{2}(t-u)\right)\left(\nabla_p\left(f'_{e,0}\left(\vec{p}+\hbar\vec{k}_0,u\right)\Big|_{general}\right)\right) \\ +\hbar k_o \dfrac{\vec{\Omega}_{R,1}(\vec{p})\cdot\nabla_p\left(\Omega_{R,0}(\vec{p})^*\right)}{2\left|\Omega_{R,0}(\vec{p})\right|} \int_0^t du \sin\left(\dfrac{\left|\Omega_{R,0}(\vec{p})\right|}{2}(t-u)\right) f'_{e,0}\left(\vec{p}+\hbar\vec{k}_0,u\right)\Big|_{general} \end{bmatrix}$$

To derive the solutions for the first order excited state distribution $f'_{e,1}\left(\vec{p}+\hbar\vec{k}_0,t\right)\Big|_{particular}$ the following substitutions are made:

$$\begin{gathered} f'_g(\vec{p},t) \rightarrow f'_e\left(\vec{p}+\hbar\vec{k}_0,t\right) \\ a(\vec{p}) \rightarrow b(\vec{p}) \\ b(\vec{p}) \rightarrow a(\vec{p}) \\ -\hbar k_0 \frac{\vec{\Omega}_{R,1}(\vec{p})^* \cdot\left(\nabla_p \Omega_{R,0}(\vec{p})\right)}{\left|\Omega_{R,0}(\vec{p})\right|} \rightarrow +\hbar k_o \frac{\vec{\Omega}_{R,1}(\vec{p})\cdot\nabla_p\left(\Omega_{R,0}(\vec{p})^*\right)}{\left|\Omega_{R,0}(\vec{p})\right|} \end{gathered} \tag{A3.38}$$

Applying the substitutions from (A3.38) to equation (A3.37) results in the following expression for the first order excited state solution:

Approved for public release; distribution is unlimited

$$f'_{e,1}\left(\vec{p}+\hbar\vec{k}_0,t\right)\Big|_{particular}=\left[\begin{array}{l} 2i\hbar k_o\dfrac{\mathrm{Im}\left(\Omega_{R,0}\left(\vec{p}\right)^*\vec{\Omega}_{R,1}\left(\vec{p}\right)\right)}{2\left|\Omega_{R,0}\left(\vec{p}\right)\right|}\cdot\left[\begin{array}{l} b\left(\vec{p}\right)\nabla_p\left(\dfrac{\left|\Omega_{R,0}\left(\vec{p}\right)\right|}{2}\right)\left(\dfrac{t^2}{4}\cos\left(\dfrac{\left|\Omega_{R,0}\left(\vec{p}\right)\right|}{2}t\right)-\dfrac{t}{2\left|\Omega_{R,0}\left(\vec{p}\right)\right|}\sin\left(\dfrac{\left|\Omega_{R,0}\left(\vec{p}\right)\right|}{2}t\right)\right) \\ +\nabla_p\left(b\left(\vec{p}\right)\right)\left(\dfrac{t}{2}\sin\left(\dfrac{\left|\Omega_{R,0}\left(\vec{p}\right)\right|}{2}t\right)\right) \\ +a\left(\vec{p}\right)\nabla_p\left(\dfrac{\left|\Omega_{R,0}\left(\vec{p}\right)\right|}{2}\right)\left(\dfrac{t^2}{4}\sin\left(\dfrac{\left|\Omega_{R,0}\left(\vec{p}\right)\right|}{2}t\right)+\dfrac{t}{2\left|\Omega_{R,0}\left(\vec{p}\right)\right|}\cos\left(\dfrac{\left|\Omega_{R,0}\left(\vec{p}\right)\right|}{2}t\right)-\dfrac{1}{\left|\Omega_{R,0}\left(\vec{p}\right)\right|^2}\sin\left(\dfrac{\left|\Omega_{R,0}\left(\vec{p}\right)\right|}{2}t\right)\right) \\ +\nabla_p\left(a\left(\vec{p}\right)\right)\left(\dfrac{-t}{2}\cos\left(\dfrac{\left|\Omega_{R,0}\left(\vec{p}\right)\right|}{2}t\right)+\dfrac{1}{\left|\Omega_{R,0}\left(\vec{p}\right)\right|}\sin\left(\dfrac{\left|\Omega_{R,0}\left(\vec{p}\right)\right|}{2}t\right)\right) \end{array}\right] \\ +\hbar k_o\dfrac{\vec{\Omega}_{R,1}\left(\vec{p}\right)\cdot\nabla_p\left(\Omega_{R,0}\left(\vec{p}\right)^*\right)}{\left|\Omega_{R,0}\left(\vec{p}\right)\right|}\left[\begin{array}{l} b\left(\vec{p}\right)\left(\dfrac{t}{2}\sin\left(\dfrac{\left|\Omega_{R,0}\left(\vec{p}\right)\right|}{2}t\right)\right) \\ +a\left(\vec{p}\right)\left(\dfrac{-t}{2}\cos\left(\dfrac{\left|\Omega_{R,0}\left(\vec{p}\right)\right|}{2}t\right)+\dfrac{1}{\left|\Omega_{R,0}\left(\vec{p}\right)\right|}\sin\left(\dfrac{\left|\Omega_{R,0}\left(\vec{p}\right)\right|}{2}t\right)\right) \end{array}\right] \end{array}\right]$$

(A3.39)

Note that the distribution functions $a\left(\vec{p}\right)$ and $b\left(\vec{p}\right)$ correspond to initial momentum distributions for ground and excited state atoms, respectively. Equations (A3.37) and (A3.39) are solutions for the first order perturbation of the atomic state amplitudes in the perturbation theory. Time dependence and phase information are captured by the sine and cosine terms governed by the frequencies $\Omega_{R,0}\left(\vec{p}\right)$ and $\vec{\Omega}_{R,1}\left(\vec{p}\right)$ in the zeroth order and first order expressions for the ground and excited atomic state amplitudes.

Approved for public release; distribution is unlimited

Appendix B

Evaluation of restricted Rabi rates

B.1. Integrating restricted Rabi rate integrals for evaluation

B.1.1. Restricted Rabi expressions and coordinate frame definition

The restricted Rabi rates derived in the main text are reprinted here for clarity. In terms corresponding to the interaction involving a Gaussian laser beam with an elliptical cross-section with a $1/e^2$ semi-major radius of w_1 oriented along $\hat{e}_{w1}$ and a semi-minor radius of w_2 oriented along $\hat{e}_{w2}$, the restricted Rabi rates are expressed as:

$$\Omega_{R,0}\left(\vec{p}\right) \equiv \left[\begin{array}{l} \frac{eE_o}{\hbar}\left\langle e\left|\hat{e}_L\cdot\hat{\vec{r}}_{e-n}\right|\mathrm{g}\right\rangle \frac{w_1 w_2}{4\pi}\cdot \\ \int\limits_{\substack{|\vec{k}|^2=k_o{}^2;\ \vec{k}\cdot\vec{k}_o>0 \\ \frac{\vec{k}\cdot\vec{p}}{m_{Ca}}=\left(\delta-\frac{\hbar\vec{k}_o{}^2}{2m_{Ca}}\right)}} d^3\vec{k}\,\delta\left(\left|\vec{k}\right|-k_o\right)\frac{\left(\vec{k}\cdot\hat{k}_o\right)}{k_o}\exp\left(-\frac{1}{4}\left(\begin{array}{l} w_1{}^2\left|\vec{k}\cdot\hat{e}_{w1}\right|^2 \\ +w_2{}^2\left|\vec{k}\cdot\hat{e}_{w2}\right|^2 \end{array}\right)\right)\exp\left(i\vec{k}\cdot\left(\vec{r}_a-\vec{r}_w\right)\right) \end{array}\right] \tag{B1.1}$$

$$\vec{\Omega}_{R,1}\left(\vec{p}\right) \equiv \left[\begin{array}{l} \frac{eE_o}{\hbar}\left\langle e\left|\hat{e}_L\cdot\hat{\vec{r}}_{e-n}\right|\mathrm{g}\right\rangle \frac{w_1 w_2}{4\pi}\cdot \\ \int\limits_{\substack{|\vec{k}|^2=k_o{}^2;\ \vec{k}\cdot\vec{k}_o>0 \\ \frac{\vec{k}\cdot\vec{p}}{m_{Ca}}=\left(\delta-\frac{\hbar\vec{k}_o{}^2}{2m_{Ca}}\right)}} d^3\vec{k}\,\delta\left(\left|\vec{k}\right|-k_o\right)\frac{\left(\vec{k}\cdot\hat{k}_o\right)}{k_o}\exp\left(-\frac{1}{4}\left(\begin{array}{l} w_1{}^2\left|\vec{k}\cdot\hat{e}_{w1}\right|^2 \\ +w_2{}^2\left|\vec{k}\cdot\hat{e}_{w2}\right|^2 \end{array}\right)\right)\exp\left(i\vec{k}\cdot\left(\vec{r}_a-\vec{r}_w\right)\right)\frac{\left(\vec{k}-\vec{k}_0\right)}{k_o} \end{array}\right]$$

For a Gaussian laser beam with a circular cross-section characterized by a $1/e^2$ waist radius w_o, equation (B1.1) is written as:

Approved for public release; distribution is unlimited

$$\Omega_{R,0}\left(\vec{p}\right) \equiv \left[\begin{array}{l} \frac{eE_o}{\hbar}\left\langle e\left|\hat{e}_L \cdot \hat{\vec{r}}_{e-n}\right|g\right\rangle \frac{{w_o}^2}{4\pi} \cdot \\ \int\limits_{\substack{|\vec{k}|^2={k_o}^2;\ \vec{k}\cdot\vec{k}_o>0 \\ \frac{\vec{k}\cdot\vec{p}}{m_{Ca}}=\left(\delta-\frac{\hbar{k_o}^2}{2m_{Ca}}\right)}} d^3\vec{k}\,\delta\left(\left|\vec{k}\right|-k_o\right)\frac{\left(\vec{k}\cdot\hat{k}_o\right)}{k_o}\exp\left(-{w_o}^2\frac{\left|\vec{k}\times\vec{k}_o\right|^2}{4{k_o}^2}\right)\exp\left(i\vec{k}\cdot\left(\vec{r}_a-\vec{r}_w\right)\right) \end{array} \right] \tag{B1.2}$$

$$\vec{\Omega}_{R,1}\left(\vec{p}\right) \equiv \left[\begin{array}{l} \frac{eE_o}{\hbar}\left\langle e\left|\hat{e}_L \cdot \hat{\vec{r}}_{e-n}\right|g\right\rangle \frac{{w_o}^2}{4\pi} \cdot \\ \int\limits_{\substack{|\vec{k}|^2={k_o}^2;\ \vec{k}\cdot\vec{k}_o>0 \\ \frac{\vec{k}\cdot\vec{p}}{m_{Ca}}=\left(\delta-\frac{\hbar{k_o}^2}{2m_{Ca}}\right)}} d^3\vec{k}\,\delta\left(\left|\vec{k}\right|-k_o\right)\frac{\left(\vec{k}\cdot\hat{k}_o\right)}{k_o}\exp\left(-{w_o}^2\frac{\left|\vec{k}\times\vec{k}_o\right|^2}{4{k_o}^2}\right)\exp\left(i\vec{k}\cdot\left(\vec{r}_a-\vec{r}_w\right)\right)\frac{\left(\vec{k}-\vec{k}_0\right)}{k_o} \end{array} \right]$$

The integrals of equation (B1.1) and (B1.2) are evaluated by defining a spherical coordinate frame and expressing each integrand in terms of those coordinates. As described in the main text, a coordinate frame spanned by the basis vectors $\hat{e}_1$, $\hat{e}_2$, and $\hat{e}_3$ may be defined in terms of the atom momentum vector $\vec{p}$ and principal laser wave vector $\vec{k}_o$ according to:

$$\begin{aligned} \hat{e}_1 = \hat{e}_z &\equiv \frac{\hat{k}_o - \left(\hat{k}_o \cdot \hat{p}\right)\hat{p}}{\sqrt{1-\left(\hat{k}_o \cdot \hat{p}\right)^2}} \\ \hat{e}_2 = \hat{e}_y &\equiv \hat{e}_3 \times \hat{e}_1 = \frac{\hat{p} \times \hat{k}_o}{\sqrt{1-\left(\hat{k}_o \cdot \hat{p}\right)^2}} \\ \hat{e}_3 = \hat{e}_x &\equiv \frac{\vec{p}}{\left|\vec{p}\right|} = \hat{p} \end{aligned} \tag{B1.3}$$

In this notation, the principal laser propagation direction $\hat{k}_o$ and the atom momentum direction $\hat{p}$ may be freely assigned in the laboratory frame of reference. With the coordinate frame of (B1.3), an arbitrary wave vector $\vec{k}$ can be described in spherical coordinates as:

$$\vec{k} = k_o\left(\hat{e}_1 \sin\theta_k \cos\phi_k + \hat{e}_2 \sin\theta_k \sin\phi_k + \hat{e}_3 \cos\theta_k\right) \tag{B1.4}$$

Approved for public release; distribution is unlimited

where θ_k is the polar angle and ϕ_k is the azimuthal angle describing the orientation of the $\vec{k}$ vector. An elliptical laser beam in this coordinate frame has an $1/e^2$ semi-major radius of w_1 and a semi-minor radius of w_2 in the plane orthogonal to $\hat{k}_o$. While the rotation of the beam is possible along this axis, the semi-major and semi-minor axes are taken to be oriented such that for an orthogonal $\hat{k}_o$ and $\hat{p}$, w_1 is oriented along the atom momentum vector $\hat{p}$ and w_2 is oriented vertical to the interaction plane, i.e. along $\hat{e}_2$.

The integrand terms of the restricted Rabi rates are expressed in terms of the Cartesian coordinate frame defined by (B1.3) transformed into this spherical frame for integration. The arbitrary wave vector $\vec{k}$ and the principal wave vector $\vec{k}_o$ are expressed as:

$$\begin{aligned}
\vec{k} &= k_o\left(\hat{e}_1 \sin\theta_k \cos\phi_k + \hat{e}_2 \sin\theta_k \sin\phi_k + \hat{e}_3 \cos\theta_k\right) \\
&= k_o\left(\frac{\hat{k}_o - \left(\hat{k}_o \cdot \hat{p}\right)\hat{p}}{\sqrt{1-\left(\hat{k}_o \cdot \hat{p}\right)^2}} \sin\theta_k \cos\phi_k + \frac{\hat{p} \times \hat{k}_o}{\sqrt{1-\left(\hat{k}_o \cdot \hat{p}\right)^2}} \sin\theta_k \sin\phi_k + \hat{p}\cos\theta_k\right) \\
\vec{k}_o &= k_o\left(\hat{e}_1\left(\hat{k}_o \cdot \hat{e}_1\right) + \hat{e}_2\left(\hat{k}_o \cdot \hat{e}_2\right) + \hat{e}_3\left(\hat{k}_o \cdot \hat{e}_3\right)\right) \\
&= k_o\left(\frac{\hat{k}_o - \left(\hat{k}_o \cdot \hat{p}\right)\hat{p}}{\sqrt{1-\left(\hat{k}_o \cdot \hat{p}\right)^2}} \sqrt{1-\left(\hat{k}_o \cdot \hat{p}\right)^2} + \hat{p}\left(\hat{k}_o \cdot \hat{p}\right)\right)
\end{aligned} \tag{B1.5}$$

The difference vector $\left(\vec{k} - \vec{k}_o\right)/k_o$ involved in the restricted Rabi vector $\vec{\Omega}_{R,1}\left(\vec{p}\right)$ is given by:

$$\frac{\left(\vec{k} - \vec{k}_o\right)}{k_o} = \left(\frac{\hat{k}_o - \left(\hat{k}_o \cdot \hat{p}\right)\hat{p}}{\sqrt{1-\left(\hat{k}_o \cdot \hat{p}\right)^2}}\left(\sin\theta_k \cos\phi_k - \sqrt{1-\left(\hat{k}_o \cdot \hat{p}\right)^2}\right) + \frac{\hat{p} \times \hat{k}_o}{\sqrt{1-\left(\hat{k}_o \cdot \hat{p}\right)^2}} \sin\theta_k \sin\phi_k + \hat{p}\left(\cos\theta_k - \hat{k}_o \cdot \hat{p}\right)\right) \tag{B1.6}$$

Approved for public release; distribution is unlimited

Remaining integrand terms common to $\Omega_{R,0}\left(\vec{p}\right)$ and $\vec{\Omega}_{R,1}\left(\vec{p}\right)$ are considered each in turn. First, the dot products $\hat{k}_o \cdot \hat{e}_1$, $\hat{k}_o \cdot \hat{e}_2$, and $\hat{k}_o \cdot \hat{e}_3$ are expressed as:

$$\begin{aligned}
\hat{k}_o \cdot \hat{e}_1 &= \frac{1-\left(\hat{k}_o \cdot \hat{p}\right)^2}{\sqrt{1-\left(\hat{k}_o \cdot \hat{p}\right)^2}} = \sqrt{1-\left(\hat{k}_o \cdot \hat{p}\right)^2} \\
\hat{k}_o \cdot \hat{e}_2 &= \frac{\hat{k}_o \cdot \left(\hat{p} \times \hat{k}_o\right)}{\sqrt{1-\left(\hat{k}_o \cdot \hat{p}\right)^2}} = 0 \\
\hat{k}_o \cdot \hat{e}_3 &= \hat{k}_o \cdot \hat{p}
\end{aligned} \tag{B1.7}$$

Next, $\hat{k} \cdot \hat{k}_o$ is expressed as:

$$\begin{aligned}
\hat{k} \cdot \hat{k}_o &= \left(\hat{e}_1 \sin\theta_k \cos\phi_k + \hat{e}_2 \sin\theta_k \sin\phi_k + \hat{e}_3 \cos\theta_k\right) \cdot \hat{k}_o \\
&= \left(\frac{\hat{k}_o - \left(\hat{k}_o \cdot \hat{p}\right)\hat{p}}{\sqrt{1-\left(\hat{k}_o \cdot \hat{p}\right)^2}} \sin\theta_k \cos\phi_k + \frac{\hat{p} \times \hat{k}_o}{\sqrt{1-\left(\hat{k}_o \cdot \hat{p}\right)^2}} \sin\theta_k \sin\phi_k + \hat{p}\cos\theta_k \right) \cdot \hat{k}_o \\
&= \sqrt{1-\left(\hat{k}_o \cdot \hat{p}\right)^2} \sin\theta_k \cos\phi_k + \left(\hat{k}_o \cdot \hat{p}\right)\cos\theta_k
\end{aligned} \tag{B1.8}$$

For the elliptical beam case (B1.1), the dot products $\vec{k} \cdot \hat{e}_{w1}$ and $\vec{k} \cdot \hat{e}_{w2}$ are considered next, beginning with $\vec{k} \cdot \hat{e}_{w1}$:

Approved for public release; distribution is unlimited

$$
\begin{aligned}
\vec{k}\cdot\hat{e}_{w1} &= k_o\left(\hat{e}_1\sin\theta_k\cos\phi_k+\hat{e}_2\sin\theta_k\sin\phi_k+\hat{e}_3\cos\theta_k\right)\cdot\hat{e}_{w1}\\
&= k_o\left(\frac{\hat{k}_o-\left(\hat{k}_o\cdot\hat{p}\right)\hat{p}}{\sqrt{1-\left(\hat{k}_o\cdot\hat{p}\right)^2}}\sin\theta_k\cos\phi_k+\frac{\hat{p}\times\hat{k}_o}{\sqrt{1-\left(\hat{k}_o\cdot\hat{p}\right)^2}}\sin\theta_k\sin\phi_k+\frac{\vec{p}}{|\vec{p}|}\cos\theta_k\right)\cdot\hat{e}_{w1}\\
&= k_o\left(\frac{-\left(\hat{k}_o\cdot\hat{p}\right)\hat{p}\cdot\hat{e}_{w1}}{\sqrt{1-\left(\hat{k}_o\cdot\hat{p}\right)^2}}\sin\theta_k\cos\phi_k+\frac{\left(\hat{p}\times\hat{k}_o\right)\cdot\hat{e}_{w1}}{\sqrt{1-\left(\hat{k}_o\cdot\hat{p}\right)^2}}\sin\theta_k\sin\phi_k+\frac{\vec{p}\cdot\hat{e}_{w1}}{|\vec{p}|}\cos\theta_k\right)\\
&= k_o\left(\hat{p}\cdot\hat{e}_{w1}\left[\frac{-\left(\hat{k}_o\cdot\hat{p}\right)}{\sqrt{1-\left(\hat{k}_o\cdot\hat{p}\right)^2}}\sin\theta_k\cos\phi_k+\cos\theta_k\right]+\frac{\hat{p}\cdot\hat{e}_{w2}}{\sqrt{1-\left(\hat{k}_o\cdot\hat{p}\right)^2}}\sin\theta_k\sin\phi_k\right)
\end{aligned}
\tag{B1.9}
$$

where $\hat{e}_{w2}=\hat{k}_o\times\hat{e}_{w1}$ is used in the final line of equation (B1.9). Next, $\vec{k}\cdot\hat{e}_{w2}$ is considered:

$$
\begin{aligned}
\vec{k}\cdot\hat{e}_{w2} &= k_o\left(\hat{e}_1\sin\theta_k\cos\phi_k+\hat{e}_2\sin\theta_k\sin\phi_k+\hat{e}_3\cos\theta_k\right)\cdot\hat{e}_{w2}\\
&= k_o\left(\frac{\hat{k}_o-\left(\hat{k}_o\cdot\hat{p}\right)\hat{p}}{\sqrt{1-\left(\hat{k}_o\cdot\hat{p}\right)^2}}\sin\theta_k\cos\phi_k+\frac{\hat{p}\times\hat{k}_o}{\sqrt{1-\left(\hat{k}_o\cdot\hat{p}\right)^2}}\sin\theta_k\sin\phi_k+\frac{\vec{p}}{|\vec{p}|}\cos\theta_k\right)\cdot\hat{e}_{w2}\\
&= k_o\left(\frac{-\left(\hat{k}_o\cdot\hat{p}\right)\hat{p}\cdot\hat{e}_{w2}}{\sqrt{1-\left(\hat{k}_o\cdot\hat{p}\right)^2}}\sin\theta_k\cos\phi_k+\frac{\left(\hat{k}_o\times\hat{e}_{w2}\right)\cdot\hat{p}}{\sqrt{1-\left(\hat{k}_o\cdot\hat{p}\right)^2}}\sin\theta_k\sin\phi_k+\frac{\vec{p}\cdot\hat{e}_{w2}}{|\vec{p}|}\cos\theta_k\right)\\
&= k_o\left(\hat{p}\cdot\hat{e}_{w2}\left[\frac{-\left(\hat{k}_o\cdot\hat{p}\right)}{\sqrt{1-\left(\hat{k}_o\cdot\hat{p}\right)^2}}\sin\theta_k\cos\phi_k+\cos\theta_k\right]-\frac{\hat{p}\cdot\hat{e}_{w1}}{\sqrt{1-\left(\hat{k}_o\cdot\hat{p}\right)^2}}\sin\theta_k\sin\phi_k\right)
\end{aligned}
$$

(B1.10)

Together, (B1.9) and (B1.10) are combined to express $\left(w_1^{\,2}\left|\vec{k}\cdot\hat{e}_{w1}\right|^2+w_2^{\,2}\left|\vec{k}\cdot\hat{e}_{w2}\right|^2\right)$, the full exponential argument, in the prescribed coordinate frame:

Approved for public release; distribution is unlimited

$$\left(w_1^{\,2}\left|\vec{k}\cdot\hat{e}_{w1}\right|^2+w_2^{\,2}\left|\vec{k}\cdot\hat{e}_{w2}\right|^2\right)=\left(\begin{array}{l} w_1^{\,2}\left|k_o\left(\hat{p}\cdot\hat{e}_{w1}\left[\begin{array}{l}\dfrac{-\left(\hat{k}_o\cdot\hat{p}\right)}{\sqrt{1-\left(\hat{k}_o\cdot\hat{p}\right)^2}}\sin\theta_k\cos\phi_k\\ +\cos\theta_k\end{array}\right]+\dfrac{\hat{p}\cdot\hat{e}_{w2}}{\sqrt{1-\left(\hat{k}_o\cdot\hat{p}\right)^2}}\sin\theta_k\sin\phi_k\right)\right|^2 \\ +w_2^{\,2}\left|k_o\left(\hat{p}\cdot\hat{e}_{w2}\left[\begin{array}{l}\dfrac{-\left(\hat{k}_o\cdot\hat{p}\right)}{\sqrt{1-\left(\hat{k}_o\cdot\hat{p}\right)^2}}\sin\theta_k\cos\phi_k\\ +\cos\theta_k\end{array}\right]-\dfrac{\hat{p}\cdot\hat{e}_{w1}}{\sqrt{1-\left(\hat{k}_o\cdot\hat{p}\right)^2}}\sin\theta_k\sin\phi_k\right)\right|^2 \end{array}\right)$$

$$=k_o^{\,2}\left(\begin{array}{l}\left(\begin{array}{l}\dfrac{-\left(\hat{k}_o\cdot\hat{p}\right)}{\sqrt{1-\left(\hat{k}_o\cdot\hat{p}\right)^2}}\sin\theta_k\cos\phi_k\\ +\cos\theta_k\end{array}\right)^2\left(w_1^{\,2}\left(\hat{p}\cdot\hat{e}_{w1}\right)^2+w_2^{\,2}\left(\hat{p}\cdot\hat{e}_{w2}\right)^2\right)\\ +\left(\dfrac{\sin\theta_k\sin\phi_k}{\sqrt{1-\left(\hat{k}_o\cdot\hat{p}\right)^2}}\right)^2\left(w_2^{\,2}\left(\hat{p}\cdot\hat{e}_{w1}\right)^2+w_1^{\,2}\left(\hat{p}\cdot\hat{e}_{w2}\right)^2\right)\\ +2\left[\begin{array}{l}\dfrac{-\left(\hat{k}_o\cdot\hat{p}\right)}{\sqrt{1-\left(\hat{k}_o\cdot\hat{p}\right)^2}}\sin\theta_k\cos\phi_k\\ +\cos\theta_k\end{array}\right]\left(\dfrac{\sin\theta_k\sin\phi_k}{\sqrt{1-\left(\hat{k}_o\cdot\hat{p}\right)^2}}\right)\left(\hat{p}\cdot\hat{e}_{w1}\right)\left(\hat{p}\cdot\hat{e}_{w2}\right)\left(w_1^{\,2}-w_2^{\,2}\right)\end{array}\right)$$

(B1.11)

The following definitions are proposed to simplify notation for equation (B1.11):

$$\begin{aligned}\Sigma w^2 &\equiv \frac{w_1^{\,2}}{2}+\frac{w_2^{\,2}}{2}\\ \Delta w^2 &\equiv \frac{w_1^{\,2}}{2}-\frac{w_2^{\,2}}{2}\\ \Rightarrow \Sigma w^2+\Delta w^2 &= w_1^{\,2}\\ \Rightarrow \Sigma w^2-\Delta w^2 &= w_2^{\,2}\end{aligned} \qquad \text{(B1.12)}$$

Substituting (B1.12) into equation (B1.11) and combining terms results in the following expression for $\left(w_1^{\,2}\left|\vec{k}\cdot\hat{e}_{w1}\right|^2+w_2^{\,2}\left|\vec{k}\cdot\hat{e}_{w2}\right|^2\right)$:

Approved for public release; distribution is unlimited

$$\left(w_1^{\,2} \left| \vec{k} \cdot \hat{e}_{w1} \right|^2 + w_2^{\,2} \left| \vec{k} \cdot \hat{e}_{w2} \right|^2 \right)$$

$$= k_o^{\,2} \left(\begin{array}{l} \Sigma w^2 \left(\begin{array}{l} \left| \hat{p} \times \hat{k}_o \right|^2 \left(\begin{array}{l} \dfrac{-\left(\hat{k}_o \cdot \hat{p} \right)}{\sqrt{1-\left(\hat{k}_o \cdot \hat{p} \right)^2}} \sin\theta_k \cos\phi_k \\ +\cos\theta_k \end{array} \right)^2 \\ +\left(\sin\theta_k \sin\phi_k \right)^2 \end{array} \right) + \dfrac{\Delta w^2 \left(\begin{array}{l} \left(\hat{p} \cdot \hat{e}_{w1} \right)^2 \\ -\left(\hat{p} \cdot \hat{e}_{w2} \right)^2 \end{array} \right)}{\left| \hat{p} \times \hat{k}_o \right|^2} \left(\begin{array}{l} \left| \hat{p} \times \hat{k}_o \right|^2 \left(\begin{array}{l} \dfrac{-\left(\hat{k}_o \cdot \hat{p} \right)}{\sqrt{1-\left(\hat{k}_o \cdot \hat{p} \right)^2}} \sin\theta_k \cos\phi_k \\ +\cos\theta_k \end{array} \right)^2 \\ -\left(\sin\theta_k \sin\phi_k \right)^2 \end{array} \right) \\ +4 \left[\begin{array}{l} \dfrac{-\left(\hat{k}_o \cdot \hat{p} \right)}{\sqrt{1-\left(\hat{k}_o \cdot \hat{p} \right)^2}} \sin\theta_k \cos\phi_k \\ +\cos\theta_k \end{array} \right] \left(\dfrac{\sin\theta_k \sin\phi_k}{\sqrt{1-\left(\hat{k}_o \cdot \hat{p} \right)^2}} \right) \left(\hat{p} \cdot \hat{e}_{w1} \right) \left(\hat{p} \cdot \hat{e}_{w2} \right) \Delta w^2 \end{array} \right)$$

$$= k_o^{\,2} \Sigma w^2 \left(\begin{array}{l} \left| \hat{p} \times \hat{k}_o \right|^2 \left(\begin{array}{l} \dfrac{-\left(\hat{k}_o \cdot \hat{p} \right)}{\sqrt{1-\left(\hat{k}_o \cdot \hat{p} \right)^2}} \sin\theta_k \cos\phi_k \\ +\cos\theta_k \end{array} \right)^2 \left(1 + \dfrac{\Delta w^2 \left(\begin{array}{l} \left(\hat{p} \cdot \hat{e}_{w1} \right)^2 \\ -\left(\hat{p} \cdot \hat{e}_{w2} \right)^2 \end{array} \right)}{\Sigma w^2 \left| \hat{p} \times \hat{k}_o \right|^2} \right) \\ +\left(\sin\theta_k \sin\phi_k \right)^2 \left(1 - \dfrac{\Delta w^2 \left(\begin{array}{l} \left(\hat{p} \cdot \hat{e}_{w1} \right)^2 \\ -\left(\hat{p} \cdot \hat{e}_{w2} \right)^2 \end{array} \right)}{\Sigma w^2 \left| \hat{p} \times \hat{k}_o \right|^2} \right) \\ +4 \dfrac{\Delta w^2}{\Sigma w^2} \left[\begin{array}{l} \dfrac{-\left(\hat{k}_o \cdot \hat{p} \right)}{\sqrt{1-\left(\hat{k}_o \cdot \hat{p} \right)^2}} \sin\theta_k \cos\phi_k \\ +\cos\theta_k \end{array} \right] \left(\dfrac{\sin\theta_k \sin\phi_k}{\sqrt{1-\left(\hat{k}_o \cdot \hat{p} \right)^2}} \right) \left(\hat{p} \cdot \hat{e}_{w1} \right) \left(\hat{p} \cdot \hat{e}_{w2} \right) \end{array} \right)$$

(B1.13)

For the case of a Gaussian beam with a circular cross section and waist radius w_o, $\Delta w^2 = 0$ and $\Sigma w^2 = w_o$, and the exponential term $\exp\left(-\dfrac{1}{4} \left(\begin{array}{l} w_1^{\,2} \left| \vec{k} \cdot \hat{e}_{w1} \right|^2 \\ +w_2^{\,2} \left| \vec{k} \cdot \hat{e}_{w2} \right|^2 \end{array} \right) \right)$ is written as $\exp\left(-w_o^{\,2} \dfrac{\left| \vec{k} \times \vec{k}_o \right|^2}{4 k_o^{\,2}} \right)$. For an evaluation of the integral for the circular beam case, then, $\left| \vec{k} \times \vec{k}_o \right|^2$ must also be written in the integration coordinate frame:

Approved for public release; distribution is unlimited

$$
\begin{aligned}
\vec{k}\times\vec{k}_o &= {k_o}^2\left(\left(\hat{e}_1\sin\theta_k\cos\phi_k+\hat{e}_2\sin\theta_k\sin\phi_k+\hat{e}_3\cos\theta_k\right)\times\hat{k}_o\right)\\
&= {k_o}^2\left(\left(\hat{e}_1\times\hat{k}_o\right)\sin\theta_k\cos\phi_k+\left(\hat{e}_2\times\hat{k}_o\right)\sin\theta_k\sin\phi_k+\left(\hat{e}_3\times\hat{k}_o\right)\cos\theta_k\right)\\
&= {k_o}^2\left(\left(-\frac{\left(\hat{k}_o\cdot\hat{p}\right)\hat{p}\times\hat{k}_o}{\sqrt{1-\left(\hat{k}_o\cdot\hat{p}\right)^2}}\right)\sin\theta_k\cos\phi_k+\left(\frac{\hat{p}\times\hat{k}_o}{\sqrt{1-\left(\hat{k}_o\cdot\hat{p}\right)^2}}\times\hat{k}_o\right)\sin\theta_k\sin\phi_k+\left(\hat{p}\times\hat{k}_o\right)\cos\theta_k\right)\\
&= {k_o}^2\left(\hat{p}\times\hat{k}_o\left(-\left(\frac{\left(\hat{k}_o\cdot\hat{p}\right)}{\sqrt{1-\left(\hat{k}_o\cdot\hat{p}\right)^2}}\right)\sin\theta_k\cos\phi_k+\cos\theta_k\right)+\left(\frac{\hat{k}_o\left(\hat{k}_o\cdot\hat{p}\right)-\hat{p}}{\sqrt{1-\left(\hat{k}_o\cdot\hat{p}\right)^2}}\right)\sin\theta_k\sin\phi_k\right)\\
\left|\vec{k}\times\vec{k}_o\right|^2 &= {k_o}^4\left(\left|\hat{p}\times\hat{k}_o\right|^2\left(-\left(\frac{\left(\hat{k}_o\cdot\hat{p}\right)}{\sqrt{1-\left(\hat{k}_o\cdot\hat{p}\right)^2}}\right)\sin\theta_k\cos\phi_k+\cos\theta_k\right)^2+\left(\sin\theta_k\sin\phi_k\right)^2\right)
\end{aligned}
$$

(B1.14)

As expected, the last line of equation (B1.14) is seen to match the result of applying $\Delta w^2 = 0$ to equation (B1.13).

All integrand terms, both for $\Omega_{R,0}\left(\vec{p}\right)$ and $\vec{\Omega}_{R,1}\left(\vec{p}\right)$ in equations (B1.1) and (B1.2) have now been accounted for and converted into the appropriate spherical coordinates for integration. Before performing the required integration, though, the integral constraints must be converted into appropriate integrands to ensure the constraints are enforced. These constraints are reprinted here for reference:

$$
\begin{aligned}
\left|\vec{k}\right|^2 &= {k_o}^2\\
\vec{k}\cdot\vec{k}_o &> 0\\
\frac{\vec{k}\cdot\vec{p}}{m_{Ca}} &= \left(\delta-\frac{\hbar{\vec{k}_o}^2}{2m_{Ca}}\right)
\end{aligned}
\qquad \text{(B1.15)}
$$

Approved for public release; distribution is unlimited

The first constraint as described by the first line of (B1.15), $\left|\vec{k}\right|^2 = k_o{}^2$, is already embedded in the definitions for restricted Rabi rates in the form of the delta function integrand $\delta\left(\left|\vec{k}\right| - k_o\right)$. The second condition $\vec{k}\cdot\vec{k}_o > 0$ be represented as a Heaviside step function $\Theta\left(\vec{k}\cdot\vec{k}_o\right)$ according to:

$$\Theta\left(\vec{k}\cdot\vec{k}_o\right) = \begin{cases} 0, & \vec{k}\cdot\vec{k}_o < 0 \\ 1, & \vec{k}\cdot\vec{k}_o \geq 0 \end{cases} \tag{B1.16}$$

The energy and momentum conservation condition given by the last of equations (B1.15) can be reduced to a restriction of the polar spherical angle θ_k by expressing the dot product between the wave vector $\vec{k}$ and the atom momentum $\vec{p}$ in spherical coordinates according to:

$$\begin{aligned} &\vec{k} = k_o\left(\hat{e}_1 \sin\theta_k \cos\phi_k + \hat{e}_2 \sin\theta_k \sin\phi_k + \hat{e}_3 \cos\theta_k\right) \\ &\vec{p} = \left|\vec{p}\right|\hat{e}_3 \\ &\Rightarrow \vec{k}\cdot\vec{p} = k_o\left|\vec{p}\right|\cos\theta_k \\ &\Rightarrow \frac{\vec{k}\cdot\vec{p}}{m_{Ca}} = \left(\delta - \frac{\hbar\vec{k}_o{}^2}{2m_{Ca}}\right) = \frac{k_o\left|\vec{p}\right|\cos\theta_k}{m_{Ca}} \\ &\Rightarrow \cos\theta_k = \frac{m_{Ca}}{k_o\left|\vec{p}\right|}\left(\delta - \frac{\hbar\vec{k}_o{}^2}{2m_{Ca}}\right) \end{aligned} \tag{B1.17}$$

The application of this condition can be installed into the integration by including a delta function in the integrand of the form:

$$\delta\left(\cos\theta_k - \frac{m}{k_o\left|\vec{p}\right|}\left(\delta - \frac{\hbar\vec{k}_o{}^2}{2m_{Ca}}\right)\right) \tag{B1.18}$$

As described in the main text, when expressing the full integrand in spherical coordinates, the definition $u_p \equiv \cos\theta_k$, or equivalently, $u_p \equiv \frac{m}{k_o\left|\vec{p}\right|}\left(\delta - \frac{\hbar\vec{k}_o{}^2}{2m_{Ca}}\right)$ is used along with the Heaviside step function $\Theta_H\left(1 - \left|u_p\right|\right)$ enforcing the requirement that the absolute magnitude $\left|u_p\right| = \left|\cos\theta_k\right|$ cannot exceed unity.

Approved for public release; distribution is unlimited

Because the delta function of (B1.18) concerns a dimensionless variable, this constraint is effectively only a constraint in direction and not in magnitude. To account for this, a dimensionless scaling factor N_k must also be included in the integrand. The main text describes how this value is derived: the basic process involves integrating the restricted integral for a detuning $\delta = \hbar\vec{k}_o^{\,2} / \left(2m_{Ca}\right)$ in which the momentum and energy constraint vanishes and the value of the integration can be directly equated to the standard Gaussian electric field integral presented for instance in [Enderlein and Pamploni 2004]. With all integrand terms accounted for, the zeroth and first order restricted Rabi integrals can be evaluated.

B.1.2. Evaluating the zeroth order restricted Rabi integral

Applying the spherical coordinate expressions described in section B.1.1. Restricted Rabi expressions and coordinate frame definition, the integral corresponding to the leading (zeroth) order restricted Rabi rate for an elliptical Gaussian beam is expressed as:

Approved for public release; distribution is unlimited

$$\int_{\substack{|\vec{k}|^2=k_o^2;\ \vec{k}\cdot\vec{k}_o>0 \\ \frac{\vec{k}\cdot\vec{p}}{m_{Ca}}=\left(\delta\sim\frac{\hbar k_o^2}{2m_{Ca}}\right)}} d^3\vec{k}\left[\begin{array}{l}\delta\left(|\vec{k}|-k_o\right)\dfrac{\left(\vec{k}\cdot\hat{k}_o\right)}{k_o}\exp\left(-\dfrac{1}{4}\left(\begin{array}{l}w_1^{\,2}\left|\vec{k}\cdot\hat{e}_{w1}\right|^2 \\ +w_2^{\,2}\left|\vec{k}\cdot\hat{e}_{w2}\right|^2\end{array}\right)\right) \\ \exp\left(-i\vec{k}\cdot\vec{r}_w\right)\end{array}\right]$$

$$= N_k\left(\begin{array}{l}\Theta_H\left(1-|u_p|\right)k_o^{\,2} \\ \exp\left(-ik_o u_p\vec{r}_w\cdot\hat{e}_3\right)\end{array}\right)\int_0^{2\pi} d\phi_k\left(\begin{array}{l}\sqrt{1-\left(\hat{k}_o\cdot\hat{p}\right)^2}\sqrt{1-u_p^{\,2}}\cos\phi_k \\ +\left(\hat{k}_o\cdot\hat{p}\right)u_p\end{array}\right)\left[\begin{array}{l}\exp\left(-\dfrac{k_o^{\,2}\Sigma w^2}{4}\left(\begin{array}{l}\left|\hat{p}\times\hat{k}_o\right|^2\left(\dfrac{-\left(\hat{k}_o\cdot\hat{p}\right)}{\sqrt{1-\left(\hat{k}_o\cdot\hat{p}\right)^2}}\sqrt{1-u_p^{\,2}}\cos\phi_k\right)^2\left(1+\dfrac{\Delta w^2\left(\begin{array}{l}\left(\hat{p}\cdot\hat{e}_{w1}\right)^2 \\ -\left(\hat{p}\cdot\hat{e}_{w2}\right)^2\end{array}\right)}{\Sigma w^2\left|\hat{p}\times\hat{k}_o\right|^2}\right) \\ +\left(\sqrt{1-u_p^{\,2}}\sin\phi_k\right)^2\left(1-\dfrac{\Delta w^2\left(\begin{array}{l}\left(\hat{p}\cdot\hat{e}_{w1}\right)^2 \\ -\left(\hat{p}\cdot\hat{e}_{w2}\right)^2\end{array}\right)}{\Sigma w^2\left|\hat{p}\times\hat{k}_o\right|^2}\right) \\ +4\dfrac{\Delta w^2}{\Sigma w^2}\left[\dfrac{-\left(\hat{k}_o\cdot\hat{p}\right)}{\sqrt{1-\left(\hat{k}_o\cdot\hat{p}\right)^2}}\sqrt{1-u_p^{\,2}}\cos\phi_k\right]\left(\dfrac{\sqrt{1-u_p^{\,2}}\sin\phi_k}{\sqrt{1-\left(\hat{k}_o\cdot\hat{p}\right)^2}}\right)\left(\hat{p}\cdot\hat{e}_{w1}\right)\left(\hat{p}\cdot\hat{e}_{w2}\right)\end{array}\right)\right) \\ \exp\left(-ik_o\left(\begin{array}{l}\sqrt{1-u_p^{\,2}}\cos\phi_k\vec{r}_w\cdot\hat{e}_1 \\ +\sqrt{1-u_p^{\,2}}\sin\phi_k\vec{r}_w\cdot\hat{e}_2\end{array}\right)\right) \\ \Theta\left(\begin{array}{l}\sqrt{1-u_p^{\,2}}\cos\phi_k\sqrt{1-\left(\hat{k}_o\cdot\hat{p}\right)^2} \\ +u_p\left(\hat{p}\cdot\hat{k}_o\right)\end{array}\right)\end{array}\right]$$

(B1.19)

In equation (B1.19), the definition $u_p \equiv \cos\theta_k$ is employed to convert all instances of $\cos\theta_k$ and $\sin\theta_k$ to expressions of u_p. For a circular beam cross-section, $\Sigma w^2 = w_o^{\,2}$ and $\Delta w^2 = 0$, and the integration can be written as:

$$\int_{\substack{|\vec{k}|^2=k_o^2;\ \vec{k}\cdot\vec{k}_o>0 \\ \frac{\vec{k}\cdot\vec{p}}{m_{Ca}}=\left(\delta-\frac{\hbar\vec{k}_o^2}{2m_{Ca}}\right)}} d^3\vec{k}\left[\begin{array}{l}\delta\left(|\vec{k}|-k_o\right)\dfrac{\left(\vec{k}\cdot\hat{k}_o\right)}{k_o}\exp\left(-w_o{}^2\dfrac{\left|\vec{k}\times\vec{k}_o\right|^2}{4k_o{}^2}\right) \\ \exp\left(-i\vec{k}\cdot\vec{r}_w\right)\end{array}\right]$$

$$= N_k\begin{pmatrix}\Theta_H\left(1-|u_p|\right)k_o{}^2 \\ \exp\left(-ik_o u_p\vec{r}_w\cdot\hat{e}_3\right)\end{pmatrix}\int_0^{2\pi} d\phi_k\begin{pmatrix}\sqrt{1-\left(\hat{k}_o\cdot\hat{p}\right)^2}\sqrt{1-u_p{}^2}\cos\phi_k \\ +\left(\hat{k}_o\cdot\hat{p}\right)u_p\end{pmatrix}\left[\begin{array}{l}\exp\left(-\dfrac{w_o{}^2k_o{}^2}{4}\left(\begin{array}{l}\left|\hat{p}\times\hat{k}_o\right|^2\left(-\dfrac{\left(\hat{k}_o\cdot\hat{p}\right)}{\sqrt{1-\left(\hat{k}_o\cdot\hat{p}\right)^2}}\right)\sqrt{1-u_p{}^2}\cos\phi_k \\ +u_p \\ +\left(\sqrt{1-u_p{}^2}\sin\phi_k\right)^2\end{array}\right)^2\right)\right) \\ \exp\left(-ik_o\begin{pmatrix}\sqrt{1-u_p{}^2}\cos\phi_k\vec{r}_w\cdot\hat{e}_1 \\ +\sqrt{1-u_p{}^2}\sin\phi_k\vec{r}_w\cdot\hat{e}_2\end{pmatrix}\right) \\ \Theta_H\begin{pmatrix}\sqrt{1-u_p{}^2}\cos\phi_k\sqrt{1-\left(\hat{k}_o\cdot\hat{p}\right)^2} \\ +u_p\left(\hat{k}_o\cdot\hat{p}\right)\end{pmatrix}\end{array}\right]$$

(B1.20)

Expressions (B1.19) and (B1.20) are integrals with one degree of freedom, completely defined in terms of dot products of relevant system orientation and position vectors. Both are expressed for the case that $\vec{r}_a = 0$ but of course these expressions can be expressed for the more general case with the following substitution: $-\vec{r}_w \to \left(\vec{r}_a - \vec{r}_w\right)$. While these integrals can be readily integrated numerically, an analytical solution to these integrals may be derived by expanding the integrand about the points where the exponential function can have appreciable value, i.e. near $\phi_k = 0, 2\pi$ corresponding to the case where the wavevector is nearly orthogonal to the atom momentum vector.

For demonstrative purposes, the circular beam case (B1.20) is considered in depth. The integrand of the real exponential is considered first:

Approved for public release; distribution is unlimited

$$\left|\hat{p}\times\hat{k}_o\right|^2\left(\left(\frac{-\left(\hat{k}_o\cdot\hat{p}\right)}{\sqrt{1-\left(\hat{k}_o\cdot\hat{p}\right)^2}}\right)\sqrt{1-u_p{}^2}\cos\phi_k+u_p\right)^2+\left(\sqrt{1-u_p{}^2}\sin\phi_k\right)^2=\left|\hat{p}\times\hat{k}_o\right|^2\left(\begin{array}{l}\dfrac{\left(\hat{k}_o\cdot\hat{p}\right)^2}{1-\left(\hat{k}_o\cdot\hat{p}\right)^2}\left(1-u_p{}^2\right)\cos^2\phi_k\\ -2\left(\dfrac{\left(\hat{k}_o\cdot\hat{p}\right)}{\sqrt{1-\left(\hat{k}_o\cdot\hat{p}\right)^2}}\right)u_p\sqrt{1-u_p{}^2}\cos\phi_k\\ +u_p{}^2\end{array}\right)+\left(1-u_p{}^2\right)\sin^2\phi_k$$

(B1.21)

Cosine and sine terms are expressed as Taylor series in the following manner:

$$
\begin{aligned}
&= \left|\hat{p}\times\hat{k}_o\right|^2 \left(\begin{array}{l} \dfrac{\left(\hat{k}_o\cdot\hat{p}\right)^2}{1-\left(\hat{k}_o\cdot\hat{p}\right)^2}\left(1-u_p{}^2\right)\left(1-\phi_k{}^2+\cdots\right) \\ -2\left(\dfrac{\left(\hat{k}_o\cdot\hat{p}\right)}{\sqrt{1-\left(\hat{k}_o\cdot\hat{p}\right)^2}}\right)u_p\sqrt{1-u_p{}^2}\left(1-\dfrac{\phi_k{}^2}{2}+\cdots\right)+\left(1-u_p{}^2\right)\left(\phi_k{}^2+\cdots\right) \\ +u_p{}^2 \end{array} \right) \\
&\cong \left(\begin{array}{l} \left|\hat{p}\times\hat{k}_o\right|^2\left(\dfrac{\left(\hat{k}_o\cdot\hat{p}\right)^2}{1-\left(\hat{k}_o\cdot\hat{p}\right)^2}\left(1-u_p{}^2\right)-2\left(\dfrac{\left(\hat{k}_o\cdot\hat{p}\right)}{\sqrt{1-\left(\hat{k}_o\cdot\hat{p}\right)^2}}\right)u_p\sqrt{1-u_p{}^2}+u_p{}^2\right) \\ +\phi_k{}^2\left(\left(1-u_p{}^2\right)-\left|\hat{p}\times\hat{k}_o\right|^2\dfrac{\left(\hat{k}_o\cdot\hat{p}\right)\sqrt{1-u_p{}^2}}{\sqrt{1-\left(\hat{k}_o\cdot\hat{p}\right)^2}}\left(\dfrac{\left(\hat{k}_o\cdot\hat{p}\right)}{\sqrt{1-\left(\hat{k}_o\cdot\hat{p}\right)^2}}\sqrt{1-u_p{}^2}-u_p\right)\right) \end{array} \right) \\
&\cong \left(\begin{array}{l} \left|\hat{p}\times\hat{k}_o\right|^2\left(\left(\dfrac{\left(\hat{k}_o\cdot\hat{p}\right)}{\sqrt{1-\left(\hat{k}_o\cdot\hat{p}\right)^2}}\right)\sqrt{1-u_p{}^2}-u_p\right)^2 \\ +\phi_k{}^2\left(\left(1-u_p{}^2\right)-\left|\hat{p}\times\hat{k}_o\right|^2\dfrac{\left(\hat{k}_o\cdot\hat{p}\right)\sqrt{1-u_p{}^2}}{\sqrt{1-\left(\hat{k}_o\cdot\hat{p}\right)^2}}\left(\dfrac{\left(\hat{k}_o\cdot\hat{p}\right)}{\sqrt{1-\left(\hat{k}_o\cdot\hat{p}\right)^2}}\sqrt{1-u_p{}^2}-u_p\right)\right) \end{array} \right)
\end{aligned}
\tag{B1.22}
$$

The argument of the complex exponential is

$$
\begin{aligned}
k_o\begin{pmatrix}\sqrt{1-u_p{}^2}\cos\phi_k\left(\vec{r}_w\cdot\hat{e}_1\right)\\ +\sqrt{1-u_p{}^2}\sin\phi_k\left(\vec{r}_w\cdot\hat{e}_2\right)\end{pmatrix} &= k_o\begin{pmatrix}\sqrt{1-u_p{}^2}\left(1-\dfrac{\phi_k{}^2}{2}+\cdots\right)\left(\vec{r}_w\cdot\hat{e}_1\right)\\ +\sqrt{1-u_p{}^2}\left(\phi_k-\dfrac{\phi_k{}^3}{6}+\cdots\right)\left(\vec{r}_w\cdot\hat{e}_2\right)\end{pmatrix} \\
&\cong k_o\left(\sqrt{1-u_p{}^2}\left(\vec{r}_w\cdot\hat{e}_1\right)+\left(\sqrt{1-u_p{}^2}\left(\vec{r}_w\cdot\hat{e}_2\right)\right)\phi_k-\left(\frac{1}{2}\sqrt{1-u_p{}^2}\left(\vec{r}_w\cdot\hat{e}_1\right)\right)\phi_k{}^2\right)
\end{aligned}
\tag{B1.23}
$$

(B1.24)

Approved for public release; distribution is unlimited

Exactly analogous results are obtained for the expansion about $\phi_k = 2\pi$. The integration is broken into separate pieces near $\phi_k = 0$ and $\phi_k = 2\pi$:

Approved for public release; distribution is unlimited

$$\int_{\substack{|\vec{k}|^2=k_o^2;\ \vec{k}\cdot\vec{k}_o>0 \\ \frac{\vec{k}\cdot\vec{p}}{m_{Ca}}=\left(\delta-\frac{\hbar\vec{k}_o^2}{2m_{Ca}}\right)}} d^3\vec{k}\begin{bmatrix}\delta\left(|\vec{k}|-k_o\right)\dfrac{\left(\vec{k}\cdot\hat{k}_o\right)}{k_o}\exp\left(-w_o^2\dfrac{\left|\vec{k}\times\vec{k}_o\right|^2}{4k_o^2}\right)\\ \exp\left(-i\vec{k}\cdot\vec{r}_w\right)\end{bmatrix}$$

$$\cong\begin{pmatrix}N_k\Theta_H\left(1-|u_p|\right)k_o^2\\ \times\exp\left(-ik_o u_p\left(\vec{r}_w\cdot\hat{e}_3\right)\right)\end{pmatrix}\left[\begin{array}{l}\displaystyle\int_0^{\infty}d\phi_k\begin{pmatrix}\sqrt{1-\left(\hat{k}_o\cdot\hat{p}\right)^2}\sqrt{1-u_p^2}\\ +\left(\hat{k}_o\cdot\hat{p}\right)u_p\\ -\sqrt{1-\left(\hat{k}_o\cdot\hat{p}\right)^2}\sqrt{1-u_p^2}\dfrac{\phi_k^2}{2}\end{pmatrix}\begin{bmatrix}\exp\left(-\dfrac{w_o^2k_o^2}{4}\begin{pmatrix}\left|\hat{p}\times\hat{k}_o\right|^2\left(\left(\dfrac{\left(\hat{k}_o\cdot\hat{p}\right)}{\sqrt{1-\left(\hat{k}_o\cdot\hat{p}\right)^2}}\right)\sqrt{1-u_p^2}-u_p\right)^2\\ +\phi_k^2\left(\left(1-u_p^2\right)-\left[\begin{array}{l}\left|\hat{p}\times\hat{k}_o\right|^2\dfrac{\left(\hat{k}_o\cdot\hat{p}\right)\sqrt{1-u_p^2}}{\sqrt{1-\left(\hat{k}_o\cdot\hat{p}\right)^2}}\\ \times\left(\dfrac{\left(\hat{k}_o\cdot\hat{p}\right)}{\sqrt{1-\left(\hat{k}_o\cdot\hat{p}\right)^2}}\sqrt{1-u_p^2}-u_p\right)\end{array}\right]\right)\end{pmatrix}\right)\\ \exp\left(-ik_o\begin{pmatrix}\sqrt{1-u_p^2}\left(\vec{r}_w\cdot\hat{e}_1\right)\\ +\left(\sqrt{1-u_p^2}\left(\vec{r}_w\cdot\hat{e}_2\right)\right)\phi_k\\ -\left(\frac{1}{2}\sqrt{1-u_p^2}\left(\vec{r}_w\cdot\hat{e}_1\right)\right)\phi_k^2\end{pmatrix}\right)\\ \Theta_H\begin{pmatrix}\sqrt{1-\left(\hat{k}_o\cdot\hat{p}\right)^2}\sqrt{1-u_p^2}\\ +\left(\hat{k}_o\cdot\hat{p}\right)u_p\\ -\sqrt{1-\left(\hat{k}_o\cdot\hat{p}\right)^2}\sqrt{1-u_p^2}\dfrac{\phi_k^2}{2}\end{pmatrix}\end{bmatrix}\\ +\displaystyle\int_{-\infty}^{2\pi}d\phi_k\begin{pmatrix}\sqrt{1-\left(\hat{k}_o\cdot\hat{p}\right)^2}\sqrt{1-u_p^2}\\ +\left(\hat{k}_o\cdot\hat{p}\right)u_p\\ -\sqrt{1-\left(\hat{k}_o\cdot\hat{p}\right)^2}\sqrt{1-u_p^2}\dfrac{\left(\phi_k-2\pi\right)^2}{2}\end{pmatrix}\begin{bmatrix}\exp\left(-\dfrac{w_o^2k_o^2}{4}\begin{pmatrix}\left|\hat{p}\times\hat{k}_o\right|^2\left(\left(\dfrac{\left(\hat{k}_o\cdot\hat{p}\right)}{\sqrt{1-\left(\hat{k}_o\cdot\hat{p}\right)^2}}\right)\sqrt{1-u_p^2}-u_p\right)^2\\ +\left(\phi_k-2\pi\right)^2\left(\left(1-u_p^2\right)-\left[\begin{array}{l}\left|\hat{p}\times\hat{k}_o\right|^2\dfrac{\left(\hat{k}_o\cdot\hat{p}\right)\sqrt{1-u_p^2}}{\sqrt{1-\left(\hat{k}_o\cdot\hat{p}\right)^2}}\\ \times\left(\dfrac{\left(\hat{k}_o\cdot\hat{p}\right)}{\sqrt{1-\left(\hat{k}_o\cdot\hat{p}\right)^2}}\sqrt{1-u_p^2}-u_p\right)\end{array}\right]\right)\end{pmatrix}\right)\\ \exp\left(-ik_o\begin{pmatrix}\sqrt{1-u_p^2}\left(\vec{r}_w\cdot\hat{e}_1\right)\\ +\left(\sqrt{1-u_p^2}\left(\vec{r}_w\cdot\hat{e}_2\right)\right)\left(\phi_k-2\pi\right)\\ -\left(\frac{1}{2}\sqrt{1-u_p^2}\left(\vec{r}_w\cdot\hat{e}_1\right)\right)\left(\phi_k-2\pi\right)^2\end{pmatrix}\right)\\ \Theta_H\begin{pmatrix}\sqrt{1-\left(\hat{k}_o\cdot\hat{p}\right)^2}\sqrt{1-u_p^2}\\ +\left(\hat{k}_o\cdot\hat{p}\right)u_p\\ -\sqrt{1-\left(\hat{k}_o\cdot\hat{p}\right)^2}\sqrt{1-u_p^2}\dfrac{\left(\phi_k-2\pi\right)^2}{2}\end{pmatrix}\end{bmatrix}\end{array}\right]$$

(B1.25)

Approved for public release; distribution is unlimited

The second integral can be transformed using a variable of integration $\phi_k' = \phi_k - 2\pi$; the integrals can then be combined to yield:

$$\int\limits_{\substack{|\vec{k}|^2=k_o^2;\ \vec{k}\cdot\vec{k}_o>0 \\ \frac{\vec{k}\cdot\vec{p}}{m_{Ca}}=\left(\delta-\frac{\hbar k_o^2}{2m_{Ca}}\right)}} d^3\vec{k}\left[\begin{array}{l}\delta\left(|\vec{k}|-k_o\right)\dfrac{\left(\vec{k}\cdot\hat{k}_o\right)}{k_o}\exp\left(-w_o{}^2\dfrac{\left|\vec{k}\times\vec{k}_o\right|^2}{4k_o{}^2}\right) \\ \exp\left(-i\vec{k}\cdot\vec{r}_w\right)\end{array}\right]$$

$$\cong\left(\begin{array}{l}N_k\Theta_H\left(1-|u_p|\right)k_o{}^2 \\ \times\exp\left(-ik_o u_p\left(\vec{r}_w\cdot\hat{e}_3\right)\right) \\ \times\Theta_H\left(\begin{array}{l}\sqrt{1-\left(\hat{k}_o\cdot\hat{p}\right)^2}\sqrt{1-u_p{}^2} \\ +\left(\hat{k}_o\cdot\hat{p}\right)u_p\end{array}\right)\end{array}\right)\int_{-\infty}^{\infty}d\phi_k\left(\begin{array}{l}\sqrt{1-\left(\hat{k}_o\cdot\hat{p}\right)^2}\sqrt{1-u_p{}^2} \\ +\left(\hat{k}_o\cdot\hat{p}\right)u_p\end{array}\right)\left[\begin{array}{l}\exp\left(-\dfrac{w_o{}^2k_o{}^2}{4}\left(\begin{array}{l}\left|\hat{p}\times\hat{k}_o\right|^2\left(\left(\dfrac{\left(\hat{k}_o\cdot\hat{p}\right)}{\sqrt{1-\left(\hat{k}_o\cdot\hat{p}\right)^2}}\right)\sqrt{1-u_p{}^2}-u_p\right)^2 \\ +\phi_k{}^2\left(\left(1-u_p{}^2\right)-\left[\begin{array}{l}\left|\hat{p}\times\hat{k}_o\right|^2\dfrac{\left(\hat{k}_o\cdot\hat{p}\right)\sqrt{1-u_p{}^2}}{\sqrt{1-\left(\hat{k}_o\cdot\hat{p}\right)^2}} \\ \times\left(\dfrac{\left(\hat{k}_o\cdot\hat{p}\right)}{\sqrt{1-\left(\hat{k}_o\cdot\hat{p}\right)^2}}\sqrt{1-u_p{}^2}-u_p\right)\end{array}\right]\right)\end{array}\right)\right) \\ \times\exp\left(-ik_o\left(\begin{array}{l}\sqrt{1-u_p{}^2}\left(\vec{r}_w\cdot\hat{e}_1\right) \\ +\left(\sqrt{1-u_p{}^2}\left(\vec{r}_w\cdot\hat{e}_2\right)\right)\phi_k \\ -\left(\frac{1}{2}\sqrt{1-u_p{}^2}\left(\vec{r}_w\cdot\hat{e}_1\right)\right)\phi_k{}^2\end{array}\right)\right)\end{array}\right]$$

(B1.26)

This form can be integrated analytically. Note that the ϕ_k dependence of the Heaviside step function is ignored in the integrand, as is the $\phi_k{}^2$ proportional integrand term. By collecting terms, equation (B1.26) becomes:

Approved for public release; distribution is unlimited

$$\int\limits_{\substack{|\vec{k}|^2=k_o^2;\ \vec{k}\cdot\vec{k}_o>0 \\ \frac{\vec{k}\cdot\vec{p}}{m_{Ca}}=\left(\delta-\frac{\hbar\vec{k}_o^{\,2}}{2m_{Ca}}\right)}} d^3\vec{k}\begin{bmatrix}\delta\left(\left|\vec{k}\right|-k_o\right)\dfrac{\left(\vec{k}\cdot\hat{k}_o\right)}{k_o}\exp\left(-w_o{}^2\dfrac{\left|\vec{k}\times\vec{k}_o\right|^2}{4k_o{}^2}\right)\\ \exp\left(-i\vec{k}\cdot\vec{r}_w\right)\end{bmatrix}$$

$$\cong\begin{pmatrix}N_k\Theta_H\left(1-\left|u_p\right|\right)k_o{}^2\\ \times\exp\left(-ik_o u_p\left(\vec{r}_w\cdot\hat{e}_3\right)\right)\\ \times\exp\left(-ik_o\sqrt{1-u_p{}^2}\left(\vec{r}_w\cdot\hat{e}_1\right)\right)\\ \times\begin{pmatrix}\sqrt{1-\left(\hat{k}_o\cdot\hat{p}\right)^2}\sqrt{1-u_p{}^2}\\ +\left(\hat{k}_o\cdot\hat{p}\right)u_p\end{pmatrix}\\ \times\Theta_H\begin{pmatrix}\sqrt{1-\left(\hat{k}_o\cdot\hat{p}\right)^2}\sqrt{1-u_p{}^2}\\ +\left(\hat{k}_o\cdot\hat{p}\right)u_p\end{pmatrix}\\ \times\exp\left(-\dfrac{w_o{}^2k_o{}^2}{4}\left(\left|\hat{p}\times\hat{k}_o\right|^2\left(\left(\dfrac{\left(\hat{k}_o\cdot\hat{p}\right)}{\sqrt{1-\left(\hat{k}_o\cdot\hat{p}\right)^2}}\right)\sqrt{1-u_p{}^2}-u_p\right)^2\right)\right)\end{pmatrix}\int\limits_{-\infty}^{\infty}d\phi_k\begin{bmatrix}\exp\left(-\phi_k{}^2\begin{bmatrix}\dfrac{w_o{}^2k_o{}^2}{4}\left(1-u_p{}^2\right)\\ -\left[\left|\hat{p}\times\hat{k}_o\right|^2\dfrac{\left(\hat{k}_o\cdot\hat{p}\right)\sqrt{1-u_p{}^2}}{\sqrt{1-\left(\hat{k}_o\cdot\hat{p}\right)^2}}\right.\\ \left.\times\left(\dfrac{\left(\hat{k}_o\cdot\hat{p}\right)}{\sqrt{1-\left(\hat{k}_o\cdot\hat{p}\right)^2}}\sqrt{1-u_p{}^2}-u_p\right)\right]\\ -ik_o\left(\dfrac{1}{2}\sqrt{1-u_p{}^2}\left(\vec{r}_w\cdot\hat{e}_1\right)\right)\end{bmatrix}\right)\\ \times\exp\left(-ik_o\left(\sqrt{1-u_p{}^2}\left(\vec{r}_w\cdot\hat{e}_2\right)\right)\phi_k\right)\end{bmatrix}$$

(B1.27)

The integral can be immediately evaluated using Gradshteyn and Ryzhik integral 3.323 [Gradshteyn and Ryzhik 1980]:

$$\int\limits_{-\infty}^{\infty}dx\exp\left(-p^2x^2\pm qx\right)=\frac{\sqrt{\pi}}{p}\exp\left(\frac{q^2}{4p^2}\right)\tag{B1.28}$$

Comparing (B1.27) with (B1.28) yields the following substitutions:

$$p^2=\left[\frac{w_o{}^2k_o{}^2}{4}\left(\left(1-u_p{}^2\right)-\left[\left|\hat{p}\times\hat{k}_o\right|^2\frac{\left(\hat{k}_o\cdot\hat{p}\right)\sqrt{1-u_p{}^2}}{\sqrt{1-\left(\hat{k}_o\cdot\hat{p}\right)^2}}\times\left(\frac{\left(\hat{k}_o\cdot\hat{p}\right)}{\sqrt{1-\left(\hat{k}_o\cdot\hat{p}\right)^2}}\sqrt{1-u_p{}^2}-u_p\right)\right]\right)-ik_o\left(\frac{1}{2}\sqrt{1-u_p{}^2}\left(\vec{r}_w\cdot\hat{e}_1\right)\right)\right]$$

$$q=-ik_o\left(\sqrt{1-u_p{}^2}\left(\vec{r}_w\cdot\hat{e}_2\right)\right)$$

(B1.29)

Approved for public release; distribution is unlimited

Substituting (B1.29) into the integral result as expressed by (B1.28) yields the following analytic expression for the full integral:

$$\int\limits_{\substack{|\vec{k}|^2=k_o^{\,2};\ \vec{k}\cdot\vec{k}_0>0 \\ \frac{\hat{k}\cdot\hat{p}}{m_{Ca}}=\left(\delta-\frac{\hbar\vec{k}_o^{\,2}}{2m_{Ca}}\right)}} d^3\vec{k}\begin{bmatrix}\delta\left(|\vec{k}|-k_o\right)\dfrac{\left(\vec{k}\cdot\hat{k}_o\right)}{k_o}\exp\left(-w_o^{\,2}\dfrac{\left|\vec{k}\times\vec{k}_o\right|^2}{4k_o^{\,2}}\right)\\ \exp\left(i\vec{k}\cdot\left(-\vec{r}_w\right)\right)\end{bmatrix}$$

$$\cong\begin{pmatrix}N_k\Theta_H\left(1-|u_p|\right)k_o^{\,2}\\ \exp\left(ik_o u_p\left(-\vec{r}_w\right)\cdot\hat{e}_3\right)\\ \exp\left(ik_o\sqrt{1-u_p^{\,2}}\left(-\vec{r}_w\right)\cdot\hat{e}_1\right)\\ \begin{pmatrix}\sqrt{1-\left(\hat{k}_o\cdot\hat{p}\right)^2}\sqrt{1-u_p^{\,2}}\\ +\left(\hat{k}_o\cdot\hat{p}\right)u_p\end{pmatrix}\\ \Theta_H\begin{pmatrix}\sqrt{1-\left(\hat{k}_o\cdot\hat{p}\right)^2}\sqrt{1-u_p^{\,2}}\\ +\left(\hat{k}_o\cdot\hat{p}\right)u_p\end{pmatrix}\\ \exp\left(-\dfrac{w_o^{\,2}k_o^{\,2}}{4}\left(\left|\hat{p}\times\hat{k}_o\right|^2\left(\left(\dfrac{\left(\hat{k}_o\cdot\hat{p}\right)}{\sqrt{1-\left(\hat{k}_o\cdot\hat{p}\right)^2}}\right)\sqrt{1-u_p^{\,2}}-u_p\right)^2\right)\right)\end{pmatrix}\begin{bmatrix}\dfrac{\sqrt{\pi}}{\sqrt{\dfrac{w_o^{\,2}k_o^{\,2}}{4}\left(\left(1-u_p^{\,2}\right)-\left[\left|\hat{p}\times\hat{k}_o\right|^2\dfrac{\left(\hat{k}_o\cdot\hat{p}\right)\sqrt{1-u_p^{\,2}}}{\sqrt{1-\left(\hat{k}_o\cdot\hat{p}\right)^2}}\right]\right)}+ik_o\left(\dfrac{1}{2}\sqrt{1-u_p^{\,2}}\left(-\vec{r}_w\right)\cdot\hat{e}_1\right)}\\ \exp\left(-\dfrac{\left(k_o\sqrt{1-u_p^{\,2}}\left(-\vec{r}_w\right)\cdot\hat{e}_2\right)^2\left[w_o^{\,2}k_o^{\,2}\left(\left(1-u_p^{\,2}\right)-\left[\left|\hat{p}\times\hat{k}_o\right|^2\dfrac{\left(\hat{k}_o\cdot\hat{p}\right)\sqrt{1-u_p^{\,2}}}{\sqrt{1-\left(\hat{k}_o\cdot\hat{p}\right)^2}}\right]\right)\right]}{\left[w_o^{\,2}k_o^{\,2}\left(\left(1-u_p^{\,2}\right)-\left[\left|\hat{p}\times\hat{k}_o\right|^2\dfrac{\left(\hat{k}_o\cdot\hat{p}\right)\sqrt{1-u_p^{\,2}}}{\sqrt{1-\left(\hat{k}_o\cdot\hat{p}\right)^2}}\right]\right)\right]^2+\left(2k_o\sqrt{1-u_p^{\,2}}\left(-\vec{r}_w\right)\cdot\hat{e}_1\right)^2}\end{bmatrix}$$

(B1.30)

B.1.3. Evaluating the first order restricted Rabi integral

The only difference between the zeroth order restricted Rabi scalar $\Omega_{R,0}\left(\vec{p}\right)$ and the first order restricted Rabi vector $\vec{\Omega}_{R,1}\left(\vec{p}\right)$ is the inclusion of $\left(\vec{k}-\vec{k}_0\right)/k_o$ in the integrand of $\vec{\Omega}_{R,1}\left(\vec{p}\right)$. This vector is expressed in the integration spherical coordinates by equation (B1.6), reprinted here for reference:

$$\frac{\left(\vec{k}-\vec{k}_o\right)}{k_o}=\left(\frac{\hat{k}_o-\left(\hat{k}_o\cdot\hat{p}\right)\hat{p}}{\sqrt{1-\left(\hat{k}_o\cdot\hat{p}\right)^2}}\left(\sin\theta_k\cos\phi_k-\sqrt{1-\left(\hat{k}_o\cdot\hat{p}\right)^2}\right)+\frac{\hat{p}\times\hat{k}_o}{\sqrt{1-\left(\hat{k}_o\cdot\hat{p}\right)^2}}\sin\theta_k\sin\phi_k+\hat{p}\left(\cos\theta_k-\hat{k}_o\cdot\hat{p}\right)\right)$$

Applying the definition $u_p\equiv\cos\theta_k$, this expression is written as:

$$\begin{aligned}\frac{\left(\vec{k}-\vec{k}_o\right)}{k_o}&=\left(\frac{\hat{k}_o-\left(\hat{k}_o\cdot\hat{p}\right)\hat{p}}{\sqrt{1-\left(\hat{k}_o\cdot\hat{p}\right)^2}}\left(\sqrt{1-u_p{}^2}\cos\phi_k-\sqrt{1-\left(\hat{k}_o\cdot\hat{p}\right)^2}\right)+\frac{\hat{p}\times\hat{k}_o}{\sqrt{1-\left(\hat{k}_o\cdot\hat{p}\right)^2}}\sqrt{1-u_p{}^2}\sin\phi_k+\hat{p}\left(u_p-\hat{k}_o\cdot\hat{p}\right)\right)\\&=\left(\frac{\hat{k}_o-\left(\hat{k}_o\cdot\hat{p}\right)\hat{p}}{\sqrt{1-\left(\hat{k}_o\cdot\hat{p}\right)^2}}\sqrt{1-u_p{}^2}\cos\phi_k+\frac{\hat{p}\times\hat{k}_o}{\sqrt{1-\left(\hat{k}_o\cdot\hat{p}\right)^2}}\sqrt{1-u_p{}^2}\sin\phi_k-\left(\hat{k}_o-\left(\hat{k}_o\cdot\hat{p}\right)\hat{p}\right)+\hat{p}u_p-\hat{p}\left(\hat{k}_o\cdot\hat{p}\right)\right)\end{aligned}$$

(B1.31)

The second line of (B1.31) separates the expression into five terms, two of which that depend on ϕ_k, and three that do not. In order to make use of the integration already performed for the zeroth order Rabi rate $\Omega_{R,0}\left(\vec{p}\right)$, an expression for the integration of $\Omega_{R,0}\left(\vec{p}\right)$ before integrating over ϕ_k, (B1.20) is revisited for consideration:

$$\int\limits_{\substack{\left|\vec{k}\right|^2=k_o{}^2;\ \vec{k}\cdot\vec{k}_o>0\\ \frac{\vec{k}\cdot\vec{p}}{m_{Ca}}=\left(\delta-\frac{\hbar\vec{k}_o{}^2}{2m_{Ca}}\right)}} d^3\vec{k}\left[\begin{array}{l}\delta\left(\left|\vec{k}\right|-k_o\right)\dfrac{\left(\vec{k}\cdot\hat{k}_o\right)}{k_o}\exp\left(-w_o{}^2\dfrac{\left|\vec{k}\times\vec{k}_o\right|^2}{4k_o{}^2}\right)\\ \exp\left(-i\vec{k}\cdot\vec{r}_w\right)\end{array}\right]=N_k\left(\begin{array}{l}\Theta_H\left(1-\left|u_p\right|\right)k_o{}^2\\ \exp\left(-ik_ou_p\vec{r}_w\cdot\hat{e}_3\right)\end{array}\right)\int_0^{2\pi}d\phi_k Z\left(\phi_k\right)$$

(B1.32)

where the following definition is introduced:

Approved for public release; distribution is unlimited

$$Z(\phi_k) \equiv \begin{pmatrix} \sqrt{1-\left(\hat{k}_o \cdot \hat{p}\right)^2}\sqrt{1-u_p^{\,2}}\cos\phi_k \\ +\left(\hat{k}_o \cdot \hat{p}\right)u_p \end{pmatrix} \left[\begin{array}{l} \exp\left(-\frac{w_o^{\,2}k_o^{\,2}}{4} \left(\begin{array}{l} \left|\hat{p}\times\hat{k}_o\right|^2 \left(-\left(\frac{\left(\hat{k}_o \cdot \hat{p}\right)}{\sqrt{1-\left(\hat{k}_o \cdot \hat{p}\right)^2}} \right)\sqrt{1-u_p^{\,2}}\cos\phi_k \right)^2 \\ +u_p \\ +\left(\sqrt{1-u_p^{\,2}}\sin\phi_k\right)^2 \end{array} \right) \right) \\ \exp\left(-ik_o \left(\begin{array}{l} \sqrt{1-u_p^{\,2}}\cos\phi_k \vec{r}_w \cdot \hat{e}_1 \\ +\sqrt{1-u_p^{\,2}}\sin\phi_k \vec{r}_w \cdot \hat{e}_2 \end{array} \right) \right) \\ \Theta_H \left(\begin{array}{l} \sqrt{1-u_p^{\,2}}\cos\phi_k\sqrt{1-\left(\hat{k}_o \cdot \hat{p}\right)^2} \\ +u_p\left(\hat{k}_o \cdot \hat{p}\right) \end{array} \right) \end{array} \right] \tag{B1.33}$$

In order to convert this integral into that relevant to $\vec{\Omega}_{R,1}\left(\vec{p}\right)$, the expression for $\left(\vec{k}-\vec{k}_0\right)\big/k_o$, i.e. equation (B1.31), must be included in the integrand, yielding:

$$\int\limits_{\substack{|\vec{k}|^2=k_o^2;\ \vec{k}\cdot\vec{k}_o>0 \\ \frac{\vec{k}\cdot\vec{p}}{m_{Ca}}=\left(\delta-\frac{\hbar\vec{k}_o^{\,2}}{2m_{Ca}}\right)}} d^3\vec{k}\begin{bmatrix}\delta\left(|\vec{k}|-k_o\right)\dfrac{\left(\vec{k}\cdot\hat{k}_o\right)}{k_o}\exp\left(-w_o{}^2\dfrac{\left|\vec{k}\times\vec{k}_o\right|^2}{4k_o{}^2}\right)\\ \exp\left(-i\vec{k}\cdot\vec{r}_w\right)\end{bmatrix}\frac{\left(\vec{k}-\vec{k}_0\right)}{k_0}$$

$$= N_k\begin{pmatrix}\Theta_H\left(1-|u_p|\right)k_o{}^2\\ \exp\left(-ik_o u_p\vec{r}_w\cdot\hat{e}_3\right)\end{pmatrix}\int_0^{2\pi} d\phi_k\begin{pmatrix}\sqrt{1-\left(\hat{k}_o\cdot\hat{p}\right)^2}\sqrt{1-u_p{}^2}\cos\phi_k\\ +\left(\hat{k}_o\cdot\hat{p}\right)u_p\end{pmatrix}\begin{bmatrix}\exp\left(-\dfrac{w_o{}^2k_o{}^2}{4}\begin{pmatrix}\left|\hat{p}\times\hat{k}_o\right|^2\\ +u_p\\ +\left(\sqrt{1-u_p{}^2}\sin\phi_k\right)^2\end{pmatrix}\right)\\ \exp\left(-ik_o\begin{pmatrix}\sqrt{1-u_p{}^2}\cos\phi_k\vec{r}_w\cdot\hat{e}_1\\ +\sqrt{1-u_p{}^2}\sin\phi_k\vec{r}_w\cdot\hat{e}_2\end{pmatrix}\right)\\ \Theta_H\begin{pmatrix}\sqrt{1-u_p{}^2}\cos\phi_k\sqrt{1-\left(\hat{k}_o\cdot\hat{p}\right)^2}\\ +u_p\left(\hat{k}_o\cdot\hat{p}\right)\end{pmatrix}\\ \begin{pmatrix}\dfrac{\hat{k}_o-\left(\hat{k}_o\cdot\hat{p}\right)\hat{p}}{\sqrt{1-\left(\hat{k}_o\cdot\hat{p}\right)^2}}\left(\sqrt{1-u_p{}^2}\cos\phi_k-\sqrt{1-\left(\hat{k}_o\cdot\hat{p}\right)^2}\right)\\ +\dfrac{\hat{p}\times\hat{k}_o}{\sqrt{1-\left(\hat{k}_o\cdot\hat{p}\right)^2}}\sqrt{1-u_p{}^2}\sin\phi_k+\hat{p}\left(u_p-\hat{k}_o\cdot\hat{p}\right)\end{pmatrix}\\ \begin{pmatrix}\dfrac{\hat{k}_o-\left(\hat{k}_o\cdot\hat{p}\right)\hat{p}}{\sqrt{1-\left(\hat{k}_o\cdot\hat{p}\right)^2}}\sqrt{1-u_p{}^2}\cos\phi_k+\dfrac{\hat{p}\times\hat{k}_o}{\sqrt{1-\left(\hat{k}_o\cdot\hat{p}\right)^2}}\sqrt{1-u_p{}^2}\sin\phi_k\\ -\left(\hat{k}_o-\left(\hat{k}_o\cdot\hat{p}\right)\hat{p}\right)+\hat{p}u_p-\hat{p}\left(\hat{k}_o\cdot\hat{p}\right)\end{pmatrix}\end{bmatrix}$$

(B1.34)

Or, in terms of $Z\left(\phi_k\right)$, (B1.34) is written as:

$$\int_{\substack{|\vec{k}|^2=k_o^2;\ \vec{k}\cdot\vec{k}_o>0 \\ \frac{\vec{k}\cdot\vec{p}}{m_{Ca}}=\left(\delta-\frac{\hbar\vec{k}_o^{\,2}}{2m_{Ca}}\right)}} d^3\vec{k}\left[\begin{array}{l}\delta\left(|\vec{k}|-k_o\right)\dfrac{\left(\vec{k}\cdot\hat{k}_o\right)}{k_o}\exp\left(-w_o{}^2\dfrac{\left|\vec{k}\times\vec{k}_o\right|^2}{4k_o{}^2}\right) \\ \exp\left(-i\vec{k}\cdot\vec{r}_w\right)\end{array}\right]\frac{\left(\vec{k}-\vec{k}_0\right)}{k_0}$$

$$=\left[\begin{array}{l}\left(N_k\Theta_H\left(1-|u_p|\right)k_o{}^2\right) \\ \exp\left(-ik_o u_p\vec{r}_w\cdot\hat{e}_3\right)\end{array}\right]\int_0^{2\pi}d\phi_k\left(Z(\phi_k)\left[\begin{array}{l}\dfrac{\hat{k}_o-\left(\hat{k}_o\cdot\hat{p}\right)\hat{p}}{\sqrt{1-\left(\hat{k}_o\cdot\hat{p}\right)^2}}\sqrt{1-u_p{}^2}\cos\phi_k+\dfrac{\hat{p}\times\hat{k}_o}{\sqrt{1-\left(\hat{k}_o\cdot\hat{p}\right)^2}}\sqrt{1-u_p{}^2}\sin\phi_k \\ -\left(\hat{k}_o-\left(\hat{k}_o\cdot\hat{p}\right)\hat{p}\right)+\hat{p}u_p-\hat{p}\left(\hat{k}_o\cdot\hat{p}\right)\end{array}\right]\right)$$

$$=\left[\begin{array}{l}\left(N_k\Theta_H\left(1-|u_p|\right)k_o{}^2\right) \\ \exp\left(-ik_o u_p\vec{r}_w\cdot\hat{e}_3\right)\end{array}\right]\left[\begin{array}{l}\left(\hat{p}u_p-\hat{p}\left(\hat{k}_o\cdot\hat{p}\right)-\left(\hat{k}_o-\left(\hat{k}_o\cdot\hat{p}\right)\hat{p}\right)\right)\int_0^{2\pi}d\phi_k Z(\phi_k) \\ +\left(\dfrac{\hat{k}_o-\left(\hat{k}_o\cdot\hat{p}\right)\hat{p}}{\sqrt{1-\left(\hat{k}_o\cdot\hat{p}\right)^2}}\sqrt{1-u_p{}^2}\right)\int_0^{2\pi}d\phi_k\cos\phi_k Z(\phi_k) \\ +\left(\dfrac{\hat{p}\times\hat{k}_o}{\sqrt{1-\left(\hat{k}_o\cdot\hat{p}\right)^2}}\sqrt{1-u_p{}^2}\right)\int_0^{2\pi}d\phi_k\sin\phi_k Z(\phi_k)\end{array}\right]$$

(B1.35)

The integral $\int_0^{2\pi}d\phi_k Z(\phi_k)$ has already been evaluated with the analytic result (B1.30). The expression (B1.35) may either be numerically evaluated or analytically evaluated by expanding the expressions for $\int_0^{2\pi}d\phi_k Z(\phi_k)\cos\phi_k$ and $\int_0^{2\pi}d\phi_k Z(\phi_k)\sin\phi_k$ according to the method described in section B.1.2. Evaluating the zeroth order restricted Rabi integral.

B.1.4. Isolating phase terms in the zeroth order restricted Rabi integral

It is desirable to express the restricted Rabi rate in terms of a magnitude and phase, especially for future investigations involving theoretical descriptions of the R-B atom interferometer with multi-pulse interactions. Toward this end, equation (B1.30) is revisited for isolation of phase terms, reprinted here for reference:

$$\int_{\substack{|\vec{k}|^2=k_o^{\,2};\ \vec{k}\cdot\vec{k}_o>0 \\ \frac{\vec{k}\cdot\vec{p}}{m_{Cs}}=\left(\delta-\frac{\hbar\vec{k}_o^{\,2}}{2m_{Cs}}\right)}} d^3\vec{k}\begin{bmatrix}\delta\left(|\vec{k}|-k_o\right)\dfrac{\left(\vec{k}\cdot\hat{k}_o\right)}{k_o}\exp\left(-w_o^{\,2}\dfrac{\left|\vec{k}\times\vec{k}_o\right|^2}{4k_o^{\,2}}\right)\\ \exp\left(i\vec{k}\cdot\left(-\vec{r}_w\right)\right)\end{bmatrix}$$

$$\cong\begin{pmatrix}N_k\Theta_H\left(1-|u_p|\right)k_o^{\,2}\\ \exp\left(ik_ou_p\left(-\vec{r}_w\right)\cdot\hat{e}_3\right)\\ \exp\left(ik_o\sqrt{1-u_p^{\,2}}\left(-\vec{r}_w\right)\cdot\hat{e}_1\right)\\ \begin{pmatrix}\sqrt{1-\left(\hat{k}_o\cdot\hat{p}\right)^2}\sqrt{1-u_p^{\,2}}\\ +\left(\hat{k}_o\cdot\hat{p}\right)u_p\end{pmatrix}\\ \Theta_H\begin{pmatrix}\sqrt{1-\left(\hat{k}_o\cdot\hat{p}\right)^2}\sqrt{1-u_p^{\,2}}\\ +\left(\hat{k}_o\cdot\hat{p}\right)u_p\end{pmatrix}\\ \exp\left(-\dfrac{w_o^{\,2}k_o^{\,2}}{4}\left(\left|\hat{p}\times\hat{k}_o\right|^2\left(\left(\dfrac{\left(\hat{k}_o\cdot\hat{p}\right)}{\sqrt{1-\left(\hat{k}_o\cdot\hat{p}\right)^2}}\right)\sqrt{1-u_p^{\,2}}-u_p\right)^2\right)\right)\end{pmatrix}\begin{bmatrix}\dfrac{\sqrt{\pi}}{\sqrt{\dfrac{w_o^{\,2}k_o^{\,2}}{4}\left(\left(1-u_p^{\,2}\right)-\left[\left|\hat{p}\times\hat{k}_o\right|^2\dfrac{\left(\hat{k}_o\cdot\hat{p}\right)\sqrt{1-u_p^{\,2}}}{\sqrt{1-\left(\hat{k}_o\cdot\hat{p}\right)^2}}\right]\right)}}\\ +ik_o\left(\dfrac{1}{2}\sqrt{1-u_p^{\,2}}\left(-\vec{r}_w\right)\cdot\hat{e}_1\right)\end{bmatrix}$$

$$\exp\left(-\frac{\left(k_o\sqrt{1-u_p^{\,2}}\left(-\vec{r}_w\right)\cdot\hat{e}_2\right)^2\left[w_o^{\,2}k_o^{\,2}\left(\left(1-u_p^{\,2}\right)-\left[\left|\hat{p}\times\hat{k}_o\right|^2\dfrac{\left(\hat{k}_o\cdot\hat{p}\right)\sqrt{1-u_p^{\,2}}}{\sqrt{1-\left(\hat{k}_o\cdot\hat{p}\right)^2}}\right]\right)\right]-2ik_o\sqrt{1-u_p^{\,2}}\left(-\vec{r}_w\right)\cdot\hat{e}_1}{\left[\left[w_o^{\,2}k_o^{\,2}\left(\left(1-u_p^{\,2}\right)-\left[\left|\hat{p}\times\hat{k}_o\right|^2\dfrac{\left(\hat{k}_o\cdot\hat{p}\right)\sqrt{1-u_p^{\,2}}}{\sqrt{1-\left(\hat{k}_o\cdot\hat{p}\right)^2}}\right]\right)\right]\right]^2+\left(2k_o\sqrt{1-u_p^{\,2}}\left(-\vec{r}_w\right)\cdot\hat{e}_1\right)^2}\right)$$

The complex exponential is considered first, and separated into real and imaginary components simply by noting:

$$\exp\left(-\frac{\left(k_o\sqrt{1-u_p^2}\left(-\vec{r}_w\right)\cdot\hat{e}_2\right)^2\left[w_o^2k_o^2\left(\left(1-u_p^2\right)-\left[\left|\hat{p}\times\hat{k}_o\right|^2\frac{\left(\hat{k}_o\cdot\hat{p}\right)\sqrt{1-u_p^2}}{\sqrt{1-\left(\hat{k}_o\cdot\hat{p}\right)^2}}\right]\right)\right]-2ik_o\sqrt{1-u_p^2}\left(-\vec{r}_w\right)\cdot\hat{e}_1}{\left[\left(w_o^2k_o^2\left(\left(1-u_p^2\right)-\left[\left|\hat{p}\times\hat{k}_o\right|^2\frac{\left(\hat{k}_o\cdot\hat{p}\right)\sqrt{1-u_p^2}}{\sqrt{1-\left(\hat{k}_o\cdot\hat{p}\right)^2}}\right]\right)\right)^2+\left(2k_o\sqrt{1-u_p^2}\left(-\vec{r}_w\right)\cdot\hat{e}_1\right)^2\right]}\right)=$$

$$\left[\exp\left(\frac{2ik_o\left(k_o\sqrt{1-u_p^2}\left(-\vec{r}_w\right)\cdot\hat{e}_2\right)^2\left(\sqrt{1-u_p^2}\left(-\vec{r}_w\right)\cdot\hat{e}_1\right)}{\left[\left(w_o^2k_o^2\left(\left(1-u_p^2\right)-\left[\left|\hat{p}\times\hat{k}_o\right|^2\frac{\left(\hat{k}_o\cdot\hat{p}\right)\sqrt{1-u_p^2}}{\sqrt{1-\left(\hat{k}_o\cdot\hat{p}\right)^2}}\right]\right)\right)^2+\left(2k_o\sqrt{1-u_p^2}\left(-\vec{r}_w\right)\cdot\hat{e}_1\right)^2\right]}\right)\right.$$

$$\left.\exp\left(-\frac{\left(k_o\sqrt{1-u_p^2}\left(-\vec{r}_w\right)\cdot\hat{e}_2\right)^2\left[w_o^2k_o^2\left(\left(1-u_p^2\right)-\left[\left|\hat{p}\times\hat{k}_o\right|^2\frac{\left(\hat{k}_o\cdot\hat{p}\right)\sqrt{1-u_p^2}}{\sqrt{1-\left(\hat{k}_o\cdot\hat{p}\right)^2}}\right]\right)\right]}{\left[\left(w_o^2k_o^2\left(\left(1-u_p^2\right)-\left[\left|\hat{p}\times\hat{k}_o\right|^2\frac{\left(\hat{k}_o\cdot\hat{p}\right)\sqrt{1-u_p^2}}{\sqrt{1-\left(\hat{k}_o\cdot\hat{p}\right)^2}}\right]\right)\right)^2+\left(2k_o\sqrt{1-u_p^2}\left(-\vec{r}_w\right)\cdot\hat{e}_1\right)^2\right]}\right)\right]$$

(B1.36)

The square root term can be isolated and considered alone to isolate its phase contribution:

Approved for public release; distribution is unlimited

$$\frac{\sqrt{\pi}}{\sqrt{\frac{w_o^2 k_o^2}{4}\left(1-u_p^2\right)-\left[\left|\hat{p}\times\hat{k}_o\right|^2\frac{\left(\hat{k}_o\cdot\hat{p}\right)\sqrt{1-u_p^2}}{\sqrt{1-\left(\hat{k}_o\cdot\hat{p}\right)^2}}\times\left(\frac{\left(\hat{k}_o\cdot\hat{p}\right)}{\sqrt{1-\left(\hat{k}_o\cdot\hat{p}\right)^2}}\sqrt{1-u_p^2}-u_p\right)\right]}+ik_o\left(\frac{1}{2}\sqrt{1-u_p^2}\left(-\vec{r}_w\right)\cdot\hat{e}_1\right)}=\frac{\sqrt{\pi}}{\sqrt{\frac{w_o^2 k_o^2}{4}\left(1-u_p^2\right)-\left[\left|\hat{p}\times\hat{k}_o\right|^2\frac{\left(\hat{k}_o\cdot\hat{p}\right)\sqrt{1-u_p^2}}{\sqrt{1-\left(\hat{k}_o\cdot\hat{p}\right)^2}}\times\left(\frac{\left(\hat{k}_o\cdot\hat{p}\right)}{\sqrt{1-\left(\hat{k}_o\cdot\hat{p}\right)^2}}\sqrt{1-u_p^2}-u_p\right)\right]}+ik_o\left(\frac{1}{2}\sqrt{1-u_p^2}\left(-\vec{r}_w\right)\cdot\hat{e}_1\right)}\frac{\sqrt{\pi}}{\sqrt{\frac{w_o^2 k_o^2}{4}\left(1-u_p^2\right)-\left[\left|\hat{p}\times\hat{k}_o\right|^2\frac{\left(\hat{k}_o\cdot\hat{p}\right)\sqrt{1-u_p^2}}{\sqrt{1-\left(\hat{k}_o\cdot\hat{p}\right)^2}}\times\left(\frac{\left(\hat{k}_o\cdot\hat{p}\right)}{\sqrt{1-\left(\hat{k}_o\cdot\hat{p}\right)^2}}\sqrt{1-u_p^2}-u_p\right)\right]}-ik_o\left(\frac{1}{2}\sqrt{1-u_p^2}\left(-\vec{r}_w\right)\cdot\hat{e}_1\right)}$$

$$=\frac{\sqrt{\frac{w_o^2 k_o^2}{4}\left(1-u_p^2\right)-\left[\left|\hat{p}\times\hat{k}_o\right|^2\frac{\left(\hat{k}_o\cdot\hat{p}\right)\sqrt{1-u_p^2}}{\sqrt{1-\left(\hat{k}_o\cdot\hat{p}\right)^2}}\times\left(\frac{\left(\hat{k}_o\cdot\hat{p}\right)}{\sqrt{1-\left(\hat{k}_o\cdot\hat{p}\right)^2}}\sqrt{1-u_p^2}-u_p\right)\right]}\sqrt{\pi}}{\sqrt{\frac{w_o^2 k_o^2}{4}\left(1-u_p^2\right)-\left[\left|\hat{p}\times\hat{k}_o\right|^2\frac{\left(\hat{k}_o\cdot\hat{p}\right)\sqrt{1-u_p^2}}{\sqrt{1-\left(\hat{k}_o\cdot\hat{p}\right)^2}}\times\left(\frac{\left(\hat{k}_o\cdot\hat{p}\right)}{\sqrt{1-\left(\hat{k}_o\cdot\hat{p}\right)^2}}\sqrt{1-u_p^2}-u_p\right)\right]}-ik_o\left(\frac{1}{2}\sqrt{1-u_p^2}\left(-\vec{r}_w\right)\cdot\hat{e}_1\right)}$$

$$=\frac{\sqrt{\pi}}{\sqrt{\frac{w_o^2 k_o^2}{4}\left(1-u_p^2\right)-\left[\left|\hat{p}\times\hat{k}_o\right|^2\frac{\left(\hat{k}_o\cdot\hat{p}\right)\sqrt{1-u_p^2}}{\sqrt{1-\left(\hat{k}_o\cdot\hat{p}\right)^2}}\times\left(\frac{\left(\hat{k}_o\cdot\hat{p}\right)}{\sqrt{1-\left(\hat{k}_o\cdot\hat{p}\right)^2}}\sqrt{1-u_p^2}-u_p\right)\right]}+ik_o\left(\frac{1}{2}\sqrt{1-u_p^2}\left(-\vec{r}_w\right)\cdot\hat{e}_1\right)}$$

(B1.37)

Equation (B1.37) is simplified as:

Approved for public release; distribution is unlimited

$$\frac{\sqrt{\pi}}{\sqrt{\frac{w_o^{\,2}k_o^{\,2}}{4}\left(\left(1-u_p^{\,2}\right)-\left[\begin{array}{l}\left|\hat{p}\times\hat{k}_o\right|^2\dfrac{\left(\hat{k}_o\cdot\hat{p}\right)\sqrt{1-u_p^{\,2}}}{\sqrt{1-\left(\hat{k}_o\cdot\hat{p}\right)^2}}\\ \times\left(\dfrac{\left(\hat{k}_o\cdot\hat{p}\right)}{\sqrt{1-\left(\hat{k}_o\cdot\hat{p}\right)^2}}\sqrt{1-u_p^{\,2}}-u_p\right)\end{array}\right]\right)+ik_o\left(\frac{1}{2}\sqrt{1-u_p^{\,2}}\left(-\vec{r}_w\right)\cdot\hat{e}_1\right)}}=\sqrt{\pi}\frac{\sqrt{\frac{w_o^{\,2}k_o^{\,2}}{4}\left(\left(1-u_p^{\,2}\right)-\left[\begin{array}{l}\left|\hat{p}\times\hat{k}_o\right|^2\dfrac{\left(\hat{k}_o\cdot\hat{p}\right)\sqrt{1-u_p^{\,2}}}{\sqrt{1-\left(\hat{k}_o\cdot\hat{p}\right)^2}}\\ \times\left(\dfrac{\left(\hat{k}_o\cdot\hat{p}\right)}{\sqrt{1-\left(\hat{k}_o\cdot\hat{p}\right)^2}}\sqrt{1-u_p^{\,2}}-u_p\right)\end{array}\right]\right)-ik_o\left(\frac{1}{2}\sqrt{1-u_p^{\,2}}\left(-\vec{r}_w\right)\cdot\hat{e}_1\right)}}{\sqrt{\left[\frac{w_o^{\,2}k_o^{\,2}}{4}\left(\left(1-u_p^{\,2}\right)-\left[\begin{array}{l}\left|\hat{p}\times\hat{k}_o\right|^2\dfrac{\left(\hat{k}_o\cdot\hat{p}\right)\sqrt{1-u_p^{\,2}}}{\sqrt{1-\left(\hat{k}_o\cdot\hat{p}\right)^2}}\\ \times\left(\dfrac{\left(\hat{k}_o\cdot\hat{p}\right)}{\sqrt{1-\left(\hat{k}_o\cdot\hat{p}\right)^2}}\sqrt{1-u_p^{\,2}}-u_p\right)\end{array}\right]\right)\right]^2+\left[k_o\left(\frac{1}{2}\sqrt{1-u_p^{\,2}}\left(-\vec{r}_w\right)\cdot\hat{e}_1\right)\right]^2}}$$

(B1.38)

The complex argument of the square root in the numerator of (B1.38) is:

$$\frac{w_o^{\,2}k_o^{\,2}}{4}\left(\left(1-u_p^{\,2}\right)-\left[\begin{array}{l}\left|\hat{p}\times\hat{k}_o\right|^2\dfrac{\left(\hat{k}_o\cdot\hat{p}\right)\sqrt{1-u_p^{\,2}}}{\sqrt{1-\left(\hat{k}_o\cdot\hat{p}\right)^2}}\\ \times\left(\dfrac{\left(\hat{k}_o\cdot\hat{p}\right)}{\sqrt{1-\left(\hat{k}_o\cdot\hat{p}\right)^2}}\sqrt{1-u_p^{\,2}}-u_p\right)\end{array}\right]\right)-ik_o\left(\frac{1}{2}\sqrt{1-u_p^{\,2}}\left(-\vec{r}_w\right)\cdot\hat{e}_1\right)$$

$$=\left(\left[\frac{w_o^{\,2}k_o^{\,2}}{4}\left(\left(1-u_p^{\,2}\right)-\left[\begin{array}{l}\left|\hat{p}\times\hat{k}_o\right|^2\dfrac{\left(\hat{k}_o\cdot\hat{p}\right)\sqrt{1-u_p^{\,2}}}{\sqrt{1-\left(\hat{k}_o\cdot\hat{p}\right)^2}}\\ \times\left(\dfrac{\left(\hat{k}_o\cdot\hat{p}\right)}{\sqrt{1-\left(\hat{k}_o\cdot\hat{p}\right)^2}}\sqrt{1-u_p^{\,2}}-u_p\right)\end{array}\right]\right)\right]^2+\left[k_o\left(\frac{1}{2}\sqrt{1-u_p^{\,2}}\left(-\vec{r}_w\right)\cdot\hat{e}_1\right)\right]^2\right)^{\frac{1}{2}}\times\exp\left(i\cdot\arctan\left(\frac{-k_o\left(\frac{1}{2}\sqrt{1-u_p^{\,2}}\left(-\vec{r}_w\right)\cdot\hat{e}_1\right)}{\frac{w_o^{\,2}k_o^{\,2}}{4}\left(\left(1-u_p^{\,2}\right)-\left[\begin{array}{l}\left|\hat{p}\times\hat{k}_o\right|^2\dfrac{\left(\hat{k}_o\cdot\hat{p}\right)\sqrt{1-u_p^{\,2}}}{\sqrt{1-\left(\hat{k}_o\cdot\hat{p}\right)^2}}\\ \times\left(\dfrac{\left(\hat{k}_o\cdot\hat{p}\right)}{\sqrt{1-\left(\hat{k}_o\cdot\hat{p}\right)^2}}\sqrt{1-u_p^{\,2}}-u_p\right)\end{array}\right]\right)}\right)\right)$$

(B1.39)

Taking the square root of (B1.39) results in:

Approved for public release; distribution is unlimited

$$\sqrt{\frac{w_o^2 k_o^2}{4}\left(\left(1-u_p^2\right)-\left[\left|\hat{p}\times\hat{k}_o\right|^2\frac{\left(\hat{k}_o\cdot\hat{p}\right)\sqrt{1-u_p^2}}{\sqrt{1-\left(\hat{k}_o\cdot\hat{p}\right)^2}}\right.\right.}$$
$$\left.\left.\times\left(\frac{\left(\hat{k}_o\cdot\hat{p}\right)}{\sqrt{1-\left(\hat{k}_o\cdot\hat{p}\right)^2}}\sqrt{1-u_p^2}-u_p\right)\right]\right)-ik_o\left(\frac{1}{2}\sqrt{1-u_p^2}\left(-\vec{r}_w\right)\cdot\hat{e}_1\right)$$
$$=\left(\left[\frac{w_o^2 k_o^2}{4}\left(\left(1-u_p^2\right)-\left[\left|\hat{p}\times\hat{k}_o\right|^2\frac{\left(\hat{k}_o\cdot\hat{p}\right)\sqrt{1-u_p^2}}{\sqrt{1-\left(\hat{k}_o\cdot\hat{p}\right)^2}}\right.\right.\right.\right.$$
$$\left.\left.\left.\left.\times\left(\frac{\left(\hat{k}_o\cdot\hat{p}\right)}{\sqrt{1-\left(\hat{k}_o\cdot\hat{p}\right)^2}}\sqrt{1-u_p^2}-u_p\right)\right]\right)\right]^2+\left[k_o\left(\frac{1}{2}\sqrt{1-u_p^2}\left(-\vec{r}_w\right)\cdot\hat{e}_1\right)\right]^2\right)^{\frac{1}{4}}\times\exp\left(\frac{i}{2}\cdot\arctan\left(\frac{-k_o\left(\frac{1}{2}\sqrt{1-u_p^2}\left(-\vec{r}_w\right)\cdot\hat{e}_1\right)}{\frac{w_o^2 k_o^2}{4}\left(\left(1-u_p^2\right)-\left[\left|\hat{p}\times\hat{k}_o\right|^2\frac{\left(\hat{k}_o\cdot\hat{p}\right)\sqrt{1-u_p^2}}{\sqrt{1-\left(\hat{k}_o\cdot\hat{p}\right)^2}}\right.\right.\right.\right.\right.$$
$$\left.\left.\left.\left.\left.\times\left(\frac{\left(\hat{k}_o\cdot\hat{p}\right)}{\sqrt{1-\left(\hat{k}_o\cdot\hat{p}\right)^2}}\sqrt{1-u_p^2}-u_p\right)\right]\right)\right)\right)$$

(B1.40)

The following definitions are introduced to simplify notation:

$$\alpha_1\equiv\frac{1}{2}k_o\sqrt{1-u_p^2}\left(-\vec{r}_w\right)\cdot\hat{e}_1$$
$$\beta\equiv\frac{w_o^2 k_o^2}{4}\left(\left(1-u_p^2\right)-\left[\left|\hat{p}\times\hat{k}_o\right|^2\frac{\left(\hat{k}_o\cdot\hat{p}\right)\sqrt{1-u_p^2}}{\sqrt{1-\left(\hat{k}_o\cdot\hat{p}\right)^2}}\right.\right.$$
$$\left.\left.\times\left(\frac{\left(\hat{k}_o\cdot\hat{p}\right)}{\sqrt{1-\left(\hat{k}_o\cdot\hat{p}\right)^2}}\sqrt{1-u_p^2}-u_p\right)\right]\right)\qquad\text{(B1.41)}$$

With the substitutions proposed in (B1.41), equation (B1.40) is written more simply as:

Approved for public release; distribution is unlimited

$$\int_{\substack{|\vec{k}|^2=k_o^2;\ \vec{k}\cdot\vec{k}_o>0 \\ \frac{\vec{k}\cdot\vec{p}}{m_{ca}}=\left(\delta-\frac{\hbar\vec{k}_o^{\,2}}{2m_{ca}}\right)}} d^3\vec{k}\left[\begin{matrix}\delta\left(\left|\vec{k}\right|-k_o\right)\frac{\left(\vec{k}\cdot\hat{k}_o\right)}{k_o}\exp\left(-w_o^{\,2}\frac{\left|\vec{k}\times\vec{k}_o\right|^2}{4k_o^{\,2}}\right) \\ \exp\left(i\vec{k}\cdot\left(-\vec{r}_w\right)\right)\end{matrix}\right]$$

$$\equiv\left(\begin{matrix}\Theta_H\left(1-\left|u_p\right|\right)k_o^{\,2} \\ \times\exp\left(ik_o u_p\left(-\vec{r}_w\right)\cdot\hat{e}_3\right) \\ \times\exp\left(ik_o\sqrt{1-u_p^{\,2}}\left(-\vec{r}_w\right)\cdot\hat{e}_1\right) \\ \times\exp\left(\frac{2ik_o\left(k_o\sqrt{1-u_p^{\,2}}\left(-\vec{r}_w\right)\cdot\hat{e}_2\right)^2\left(\sqrt{1-u_p^{\,2}}\left(-\vec{r}_w\right)\cdot\hat{e}_1\right)}{\left[\left[\left[w_o^{\,2}k_o^{\,2}\left(\left(1-u_p^{\,2}\right)-\left[\begin{matrix}\left|\hat{p}\times\hat{k}_o\right|^2\frac{\left(\hat{k}_o\cdot\hat{p}\right)\sqrt{1-u_p^{\,2}}}{\sqrt{1-\left(\hat{k}_o\cdot\hat{p}\right)^2}} \\ \times\left(\frac{\left(\hat{k}_o\cdot\hat{p}\right)}{\sqrt{1-\left(\hat{k}_o\cdot\hat{p}\right)^2}}\sqrt{1-u_p^{\,2}}-u_p\right)\end{matrix}\right]\right)\right]\right]^2+\left(2k_o\sqrt{1-u_p^{\,2}}\left(-\vec{r}_w\right)\cdot\hat{e}_1\right)^2}\right) \\ \times\left(\begin{matrix}\sqrt{1-\left(\hat{k}_o\cdot\hat{p}\right)^2}\sqrt{1-u_p^{\,2}} \\ +\left(\hat{k}_o\cdot\hat{p}\right)u_p\end{matrix}\right) \\ \times\Theta_H\left(\begin{matrix}\sqrt{1-\left(\hat{k}_o\cdot\hat{p}\right)^2}\sqrt{1-u_p^{\,2}} \\ +\left(\hat{k}_o\cdot\hat{p}\right)u_p\end{matrix}\right) \\ \times\exp\left(-\frac{w_o^{\,2}k_o^{\,2}}{4}\left|\hat{p}\times\hat{k}_o\right|^2\left(\left(\frac{\left(\hat{k}_o\cdot\hat{p}\right)}{\sqrt{1-\left(\hat{k}_o\cdot\hat{p}\right)^2}}\right)\sqrt{1-u_p^{\,2}}-u_p\right)^2\right)\end{matrix}\right)$$

$$=\sqrt{\pi}\left[\begin{matrix}\frac{\left(\beta^2+\alpha_1^{\,2}\right)^{\frac{1}{4}}\times\exp\left(i\cdot\frac{1}{2}\arccos\left(\frac{\beta}{\sqrt{\alpha_1^{\,2}+\beta^2}}\right)\right)}{\sqrt{\left[\left[\frac{w_o^{\,2}k_o^{\,2}}{4}\left(\left(1-u_p^{\,2}\right)-\left[\begin{matrix}\left|\hat{p}\times\hat{k}_o\right|^2\frac{\left(\hat{k}_o\cdot\hat{p}\right)\sqrt{1-u_p^{\,2}}}{\sqrt{1-\left(\hat{k}_o\cdot\hat{p}\right)^2}} \\ \times\left(\frac{\left(\hat{k}_o\cdot\hat{p}\right)}{\sqrt{1-\left(\hat{k}_o\cdot\hat{p}\right)^2}}\sqrt{1-u_p^{\,2}}-u_p\right)\end{matrix}\right]\right)\right]^2+\left[k_o\left(\frac{1}{2}\sqrt{1-u_p^{\,2}}\left(\vec{r}_a-\vec{r}_w\right)\cdot\hat{e}_1\right)\right]^2}} \\ \times\exp\left(-\frac{\left(k_o\sqrt{1-u_p^{\,2}}\left(-\vec{r}_w\right)\cdot\hat{e}_2\right)^2\left[w_o^{\,2}k_o^{\,2}\left(\left(1-u_p^{\,2}\right)-\left[\begin{matrix}\left|\hat{p}\times\hat{k}_o\right|^2\frac{\left(\hat{k}_o\cdot\hat{p}\right)\sqrt{1-u_p^{\,2}}}{\sqrt{1-\left(\hat{k}_o\cdot\hat{p}\right)^2}} \\ \times\left(\frac{\left(\hat{k}_o\cdot\hat{p}\right)}{\sqrt{1-\left(\hat{k}_o\cdot\hat{p}\right)^2}}\sqrt{1-u_p^{\,2}}-u_p\right)\end{matrix}\right]\right)\right]}{\left[\left[\left[w_o^{\,2}k_o^{\,2}\left(\left(1-u_p^{\,2}\right)-\left[\begin{matrix}\left|\hat{p}\times\hat{k}_o\right|^2\frac{\left(\hat{k}_o\cdot\hat{p}\right)\sqrt{1-u_p^{\,2}}}{\sqrt{1-\left(\hat{k}_o\cdot\hat{p}\right)^2}} \\ \times\left(\frac{\left(\hat{k}_o\cdot\hat{p}\right)}{\sqrt{1-\left(\hat{k}_o\cdot\hat{p}\right)^2}}\sqrt{1-u_p^{\,2}}-u_p\right)\end{matrix}\right]\right)\right]^2+\left(2k_o\sqrt{1-u_p^{\,2}}\left(-\vec{r}_w\right)\cdot\hat{e}_1\right)^2}\right)\end{matrix}\right]$$

(B1.42)

The substitutions proposed in (B1.41) may be more widely applied in the expression, resulting in:

Approved for public release; distribution is unlimited

$$\int\limits_{\substack{|\vec{k}|^2=k_o^{\,2};\ \vec{k}\cdot\vec{k}_o>0 \\ \frac{\vec{k}\cdot\vec{p}}{m_{Ca}}=\left(\delta-\frac{\hbar\vec{k}_o^{\,2}}{2m_{Ca}}\right)}} d^3\vec{k}\left[\begin{array}{l}\delta\left(\left|\vec{k}\right|-k_o\right)\dfrac{\left(\vec{k}\cdot\hat{k}_o\right)}{k_o}\exp\left(-w_o^{\,2}\dfrac{\left|\vec{k}\times\vec{k}_o\right|^2}{4k_o^{\,2}}\right) \\ \exp\left(i\vec{k}\cdot\left(-\vec{r}_w\right)\right)\end{array}\right]$$

$$\cong\left(\begin{array}{l}\Theta_H\left(1-\left|u_p\right|\right)k_o^{\,2} \\ \times\exp\left(ik_o u_p\left(-\vec{r}_w\right)\cdot\hat{e}_3\right) \\ \times\exp\left(ik_o\sqrt{1-u_p^{\,2}}\left(-\vec{r}_w\right)\cdot\hat{e}_1\right) \\ \times\exp\left(i\dfrac{\left(k_o\sqrt{1-u_p^{\,2}}\left(-\vec{r}_w\right)\cdot\hat{e}_2\right)^2\left(4\alpha_1\right)}{\left[\left(4\beta\right)^2+\left(4\alpha_1\right)^2\right]}\right) \\ \times\left(\begin{array}{l}\sqrt{1-\left(\hat{k}_o\cdot\hat{p}\right)^2}\sqrt{1-u_p^{\,2}} \\ +\left(\hat{k}_o\cdot\hat{p}\right)u_p\end{array}\right) \\ \times\Theta_H\left(\begin{array}{l}\sqrt{1-\left(\hat{k}_o\cdot\hat{p}\right)^2}\sqrt{1-u_p^{\,2}} \\ +\left(\hat{k}_o\cdot\hat{p}\right)u_p\end{array}\right) \\ \times\exp\left(-\dfrac{w_o^{\,2}k_o^{\,2}}{4}\left|\hat{p}\times\hat{k}_o\right|^2\left(\left(\dfrac{\left(\hat{k}_o\cdot\hat{p}\right)}{\sqrt{1-\left(\hat{k}_o\cdot\hat{p}\right)^2}}\right)\sqrt{1-u_p^{\,2}}-u_p\right)^2\right)\end{array}\right)\left[\begin{array}{l}\sqrt{\pi}\dfrac{\left(\beta^2+\alpha_1^{\,2}\right)^{\frac{1}{4}}\times\exp\left(i\cdot\dfrac{1}{2}\arccos\left(\dfrac{\beta}{\sqrt{\alpha_1^{\,2}+\beta^2}}\right)\right)}{\sqrt{\left(\beta^2+\alpha_1^{\,2}\right)}} \\ \times\exp\left(-\dfrac{\left(k_o\sqrt{1-u_p^{\,2}}\left(-\vec{r}_w\right)\cdot\hat{e}_2\right)^2 4\beta}{\left[\left(4\beta\right)^2+\left(4\alpha_1\right)^2\right]}\right)\end{array}\right]$$

(B1.43)

Re-arranging terms, equation (B1.43) is written as:

$$\int\limits_{\substack{|\vec{k}|^2=k_o{}^2;\ \vec{k}\cdot\vec{k}_o>0 \\ \frac{\vec{k}\cdot\vec{p}}{m_{Ca}}=\left(\delta-\frac{\hbar k_o{}^2}{2m_{Ca}}\right)}} d^3\vec{k}\left[\begin{array}{l}\delta\left(|\vec{k}|-k_o\right)\dfrac{\left(\vec{k}\cdot\hat{k}_o\right)}{k_o}\exp\left(-w_o{}^2\dfrac{\left|\vec{k}\times\vec{k}_o\right|^2}{4k_o{}^2}\right) \\ \exp\left(i\vec{k}\cdot\left(-\vec{r}_w\right)\right)\end{array}\right]$$

$$\cong\left[\begin{array}{l}\left(\begin{array}{l}N_k\Theta_H\left(1-|u_p|\right)k_o{}^2 \\ \Theta_H\left(\begin{array}{l}\sqrt{1-\left(\hat{k}_o\cdot\hat{p}\right)^2}\sqrt{1-u_p{}^2} \\ +\left(\hat{k}_o\cdot\hat{p}\right)u_p\end{array}\right) \\ \left(\begin{array}{l}\sqrt{1-\left(\hat{k}_o\cdot\hat{p}\right)^2}\sqrt{1-u_p{}^2} \\ +\left(\hat{k}_o\cdot\hat{p}\right)u_p\end{array}\right) \\ \dfrac{\sqrt{\pi}}{\left(\beta^2+\alpha_1{}^2\right)^{\frac{1}{4}}}\end{array}\right)\left(\begin{array}{l}\exp\left(-\dfrac{w_o{}^2k_o{}^2}{4}\left|\hat{p}\times\hat{k}_o\right|^2\left(\left(\dfrac{\left(\hat{k}_o\cdot\hat{p}\right)}{\sqrt{1-\left(\hat{k}_o\cdot\hat{p}\right)^2}}\right)\sqrt{1-u_p{}^2}-u_p\right)^2\right) \\ \exp\left(-\dfrac{\beta\left(k_o\sqrt{1-u_p{}^2}\left(-\vec{r}_w\right)\cdot\hat{e}_2\right)^2}{4\left(\beta^2+\alpha_1{}^2\right)}\right)\end{array}\right) \\ \exp\left(i\left[\left(k_o u_p\left(-\vec{r}_w\right)\cdot\hat{e}_3\right)+\left(2\alpha_1\right)+\left(\dfrac{\alpha_1\left(k_o\sqrt{1-u_p{}^2}\left(-\vec{r}_w\right)\cdot\hat{e}_2\right)^2}{4\left(\beta^2+\alpha_1{}^2\right)}\right)+\left(\dfrac{1}{2}\arccos\left(\dfrac{\beta}{\sqrt{\alpha_1{}^2+\beta^2}}\right)\right)\right]\right)\end{array}\right]$$

(B1.44)

Finally, extending the definition of α to include the effect of $\left(-\vec{r}_w\right)\cdot\hat{e}_2$ and $\left(-\vec{r}_w\right)\cdot\hat{e}_3$, i.e. $\alpha_i\equiv\frac{1}{2}k_o\sqrt{1-u_p{}^2}\left(-\vec{r}_w\right)\cdot\hat{e}_i\quad\forall i=\{1,2,3\}$, the expression can be further simplified:

$$\int_{\substack{|\vec{k}|^2=k_o{}^2;\ \vec{k}\cdot\vec{k}_o>0 \\ \frac{\vec{k}\cdot\vec{p}}{m_{Ca}}=\left(\delta-\frac{\hbar k_o{}^2}{2m_{Ca}}\right)}} d^3\vec{k}\left[\begin{array}{l}\delta\left(\left|\vec{k}\right|-k_o\right)\dfrac{\left(\vec{k}\cdot\hat{k}_o\right)}{k_o}\exp\left(-w_o{}^2\dfrac{\left|\vec{k}\times\vec{k}_o\right|^2}{4k_o{}^2}\right) \\ \exp\left(i\vec{k}\cdot\left(-\vec{r}_w\right)\right)\end{array}\right]$$

$$\cong\left[\begin{array}{l}\left(\begin{array}{l}N_k\Theta_H\left(1-\left|u_p\right|\right)k_o{}^2 \\ \Theta_H\left(\begin{array}{l}\sqrt{1-\left(\hat{k}_o\cdot\hat{p}\right)^2}\sqrt{1-u_p{}^2} \\ +\left(\hat{k}_o\cdot\hat{p}\right)u_p\end{array}\right)\end{array}\right)\left(\exp\left(-\dfrac{w_o{}^2k_o{}^2}{4}\left(\left|\hat{p}\times\hat{k}_o\right|^2\left(\left(\dfrac{\left(\hat{k}_o\cdot\hat{p}\right)}{\sqrt{1-\left(\hat{k}_o\cdot\hat{p}\right)^2}}\right)\sqrt{1-u_p{}^2}-u_p\right)^2\right)\right)\right) \\ \left(\begin{array}{l}\sqrt{1-\left(\hat{k}_o\cdot\hat{p}\right)^2}\sqrt{1-u_p{}^2} \\ +\left(\hat{k}_o\cdot\hat{p}\right)u_p\end{array}\right)\left(\exp\left(-\dfrac{\beta\alpha_2{}^2}{\beta^2+\alpha_1{}^2}\right)\right) \\ \dfrac{\sqrt{\pi}}{\left(\beta^2+\alpha_1{}^2\right)^{\frac{1}{4}}} \\ \exp\left(i\left[\dfrac{2u_p}{\sqrt{1-u_p{}^2}}\alpha_3+2\alpha_1+\dfrac{\alpha_1\alpha_2{}^2}{\left(\beta^2+\alpha_1{}^2\right)}+\dfrac{1}{2}\arccos\left(\dfrac{\beta}{\sqrt{\alpha_1{}^2+\beta^2}}\right)\right]\right)\end{array}\right]$$

(B1.45)

B.2. Computing restricted Rabi rate magnitudes

B.2.1. Verifying the analytical integration result for the restricted Rabi scalar

To verify the form of the analytical solutions to the leading (zeroth) order restricted Rabi rate integrals as given by equation (B1.44), a comparison is performed with a numerical integration computed with equation (B1.20). These integrations are scaled by the appropriate factors corresponding to the restricted Rabi rate $\Omega_{R,0}\left(\vec{p}\right)$ definition given by equation (B1.2), reprinted here for reference:

Approved for public release; distribution is unlimited

$$\Omega_{R,0}\left(\vec{p}\right) \equiv \left[\begin{array}{l} \dfrac{eE_o}{\hbar}\left\langle e\left|\hat{e}_L \cdot \hat{\vec{r}}_{e-n}\right|\mathrm{g}\right\rangle \dfrac{{w_o}^2}{4\pi} \cdot \\ \displaystyle\int_{\substack{|\vec{k}|^2={k_o}^2;\ \vec{k}\cdot\vec{k}_o>0 \\ \frac{\vec{k}\cdot\vec{p}}{m_{Ca}}=\left(\delta-\frac{\hbar{k_o}^2}{2m_{Ca}}\right)}} d^3\vec{k}\,\delta\left(\left|\vec{k}\right|-k_o\right)\dfrac{\left(\vec{k}\cdot\hat{k}_o\right)}{k_o}\exp\left(-{w_o}^2\dfrac{\left|\vec{k}\times\vec{k}_o\right|^2}{4{k_o}^2}\right)\exp\left(i\vec{k}\cdot\left(\vec{r}_a-\vec{r}_w\right)\right) \end{array} \right]$$

As described in the main text, the coupling element $\left\langle e\left|\hat{\vec{r}}_{e-n}\cdot\hat{e}\right|g\right\rangle$ for the Ca intercombination line is equal to $9.60\times10^{-11}\mathrm{cm}$ in CGS units. For a laser beam with a waist radius $w_0 = 0.5\ \mathrm{mm}$ and total optical power $P_0 = 1.0\ \mathrm{mW}$, the electric field magnitude is equal to $E_o = \sqrt{16P_o/c{w_o}^2}$, or in CGS units, $E_o = 0.04620\ \mathrm{statvolt/cm}$, and the elementary charge is equal to $e = 4.8032043\times10^{-10}\ \mathrm{statC}$. The dimensionless scaling factor is given by $N_k = 2\sqrt{\pi}/\left(k_o w_o\right) = 7.4135\times10^{-4}$.

For evaluation of the restricted Rabi rate $\Omega_{R,0}\left(\vec{p}\right)$ with the analytical integration (B1.20) and numerical integration (B1.44), a range of discrete atom momenta relevant to a thermal Ca beam at $625^{\circ}\mathrm{C}$ with the CaBOT system were used. Specifically, longitudinal atom velocities along the principal atom beam propagation direction were sampled between $v_{long} = \left\{10\ \mathrm{m/s},\ 2618\ \mathrm{m/s}\right\}$. Atom velocities along the axis that contributes most to Doppler shifts, i.e. along the principal laser beam propagation direction and along the narrow width dimension of the atomic beam collimator, were sampled between $v_{\mathrm{Dopp}} = \left\{\text{-}5.2\ \mathrm{m/s},\ 5.2\ \mathrm{m/s}\right\}$. Finally, atom velocities out of the plane described by the principal atom beam vector and the principal laser beam direction were sampled between $v_{\text{out-of-plane}} = \left\{\text{-}20.8\ \mathrm{m/s},\ 20.8\ \mathrm{m/s}\right\}$. The out-of-plane direction corresponds to the vertical height dimension of the atomic beam collimator. Zero laser detuning $\delta = 0$ was assumed. Furthermore, for the numerical integrations (B1.44), ϕ_k space was discretized in a non-uniform grid with 208 points, localized almost exclusively around $\phi_k = \left\{0, 2\pi\right\}$.

Approved for public release; distribution is unlimited

Figure B-1 depicts the calculated Rabi rate magnitude $\left|\Omega_{R,0}\left(\vec{p}\right)\right|$ for both the analytical integration (a) and the numerical integration (b) as a function of the longitudinal and Doppler-inducing atom velocities. An out-of-plane velocity of $v_{\text{out-of-plane}} = 0$ m/s was assumed for these plots. For all plots, the color bar indicating the third dimension represents the magnitude of $\left|\Omega_{R,0}\left(\vec{p}\right)\right|$ in units of $2\pi \times \text{kHz}$. Inspecting the magnitudes of calculated rates $\left|\Omega_{R,0}\left(\vec{p}\right)\right|$ revealed that the analytical and numerical solutions agree to 99.9%. (c) confirms this result with a plot of the difference at each grid point between the restricted Rabi rates calculated with analytical and numerical integrations: the largest discrepancy was < 0.15 kHz.

Figure B-2 depicts the same calculations for the restricted Rabi rate $\left|\Omega_{R,0}\left(\vec{p}\right)\right|$, but for $v_{\text{Dopp}} = 0$ m/s and with varying out-of-plane velocities $v_{\text{out-of-plane}}$. In this case, once again the calculations were observed to match as indicated by the equivalence of (a) and (b). The largest discrepancy between analytical and numerical integrations for this case was two orders of magnitude larger at < 19 kHz, but these differences are restricted to regions of the computational space that were sparsely sampled and that feature negligible Rabi rates. This is depicted in the three-dimensional view of (c). Because the discrepancies were restricted to regions of momentum space in which the restricted Rabi rates are near zero, errors were deemed to be acceptable for further studies.

The good agreement between numerical and analytical Rabi rate calculations provided confidence both in the analytical integration implemented in (B1.44) and in the grid size used for momentum and ϕ_k discretization in future investigations including the numerical integration of the integral corresponding to the first order perturbation to the Rabi rate $\vec{\Omega}_{R,1}\left(\vec{p}\right)$.

Approved for public release; distribution is unlimited

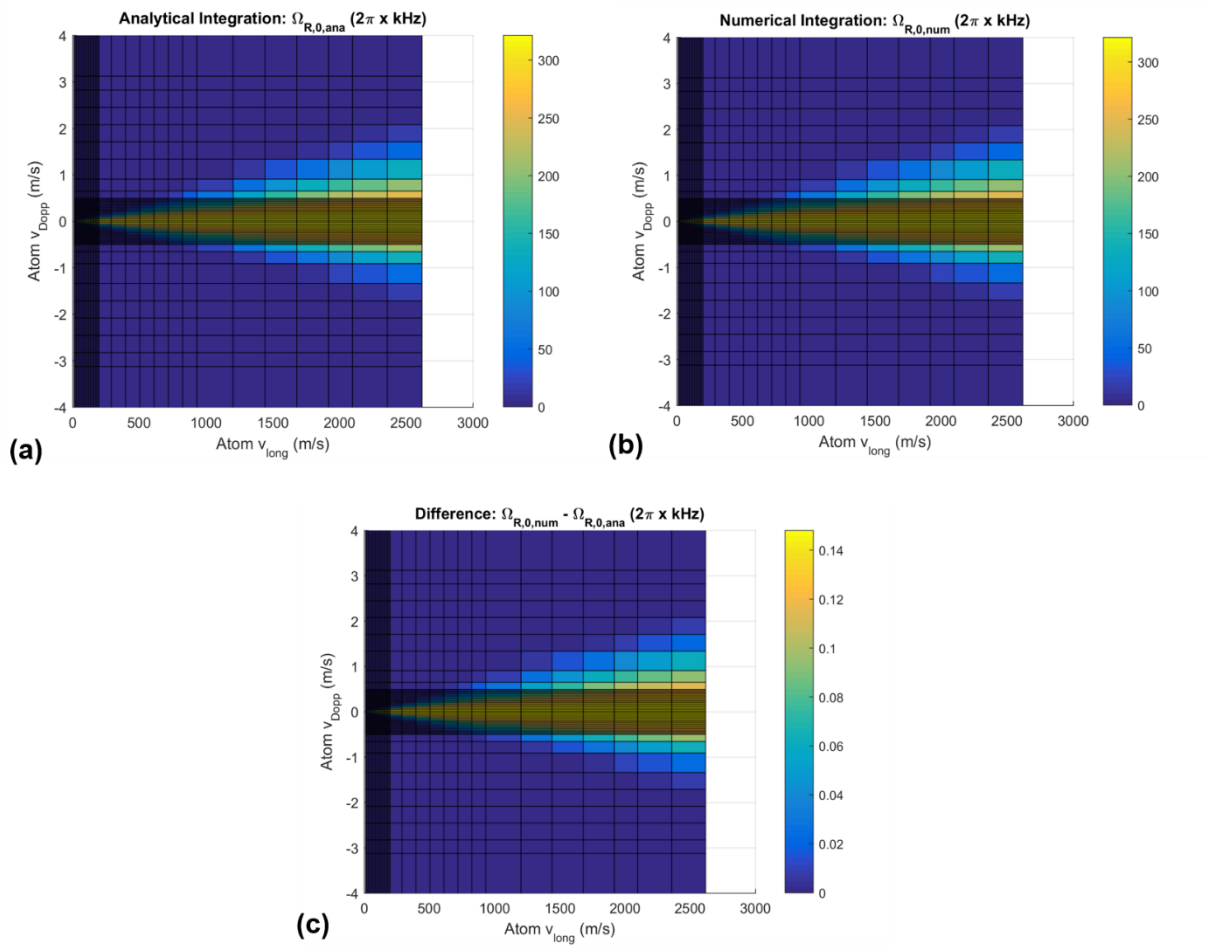

Figure B-1. Evaluations for $\left|\Omega_{R,0}\left(\vec{p}\right)\right|$ with $v_{\text{out-of-plane}} = 0$ m/s, with analytical (a) and numerical (b) integrations of the restricted wave vector integral. (c) depicts the difference between numerical and analytical results. All color bars are in units of $2\pi \times \text{kHz}$ as indicated in the plot titles.

Approved for public release; distribution is unlimited

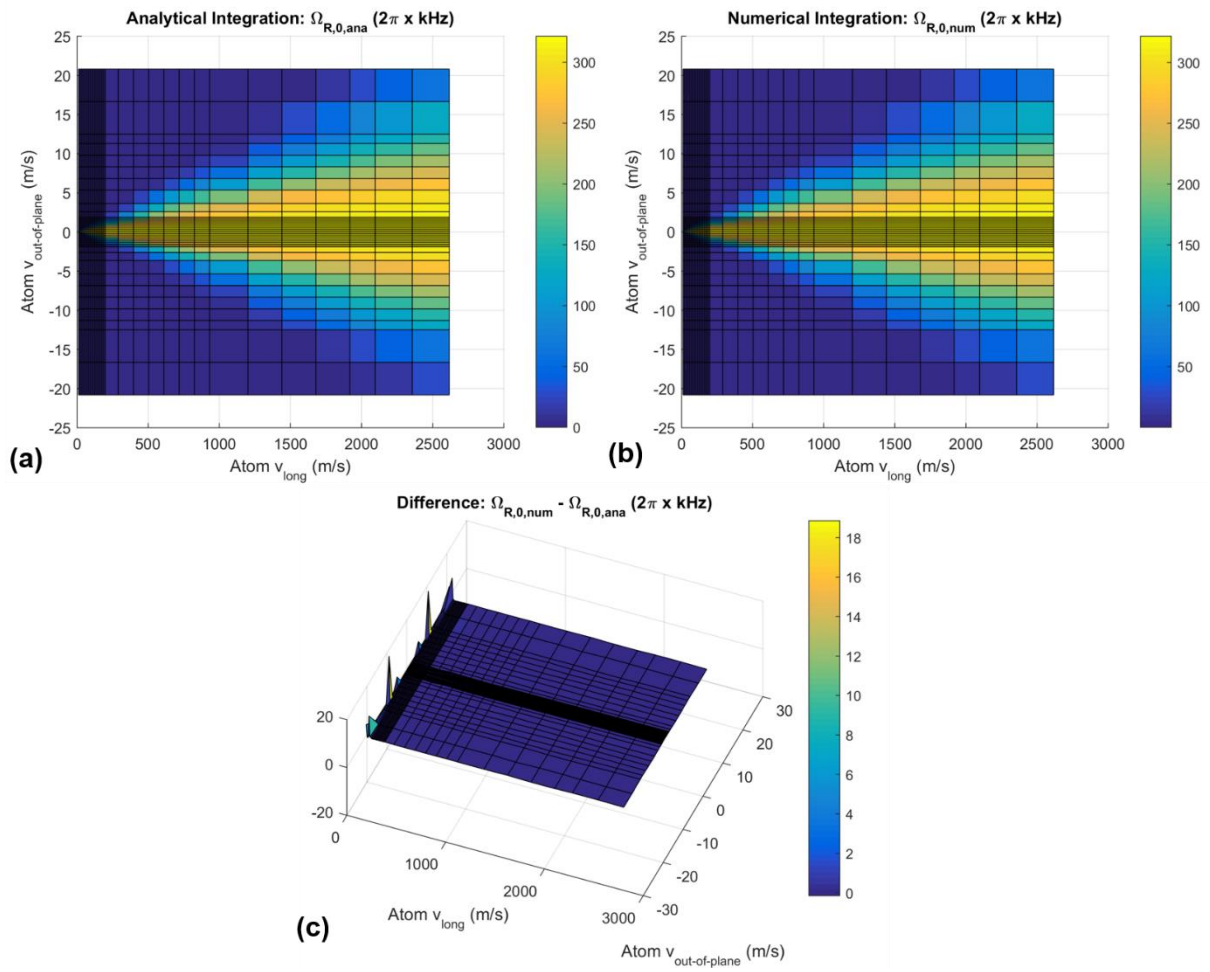

Figure B-2. Evaluations for $\left|\Omega_{R,0}\left(\vec{p}\right)\right|$ with $v_{\mathrm{Dopp}} = 0$ m/s, with analytical (a) and numerical (b) integrations of the restricted wave vector integral. (c) depicts the difference between numerical and analytical results. All color bars are in units of $2\pi \times \mathrm{kHz}$ as indicated in the plot titles.

B.2.2. Comparing the leading (zeroth) and first order restricted Rabi rates

An assumption of the perturbation theory introduced in the main text is that the leading (zeroth) order atom state amplitudes $f'_{g,0}\left(\vec{p},t\right)\Big|_{general}$ and $f'_{e,0}\left(\vec{p}+\hbar\vec{k}_0,t\right)\Big|_{general}$ are much larger than the first order perturbative expressions $f'_{g,1}\left(\vec{p},t\right)\Big|_{particular}$ and $f'_{e,1}\left(\vec{p}+\hbar\vec{k}_0,t\right)\Big|_{particular}$, i.e.:

Approved for public release; distribution is unlimited

$$
\begin{aligned}
f'_{g,0}\left(\vec{p},t\right)\Big|_{general} &\gg f'_{g,1}\left(\vec{p},t\right)\Big|_{particular} \\
f'_{e,0}\left(\vec{p}+\hbar\vec{k}_0,t\right)\Big|_{general} &\gg f'_{e,1}\left(\vec{p}+\hbar\vec{k}_0,t\right)\Big|_{particular}
\end{aligned}
\tag{B2.1}
$$

Recall that the zeroth order (general solution) amplitudes are expressed as:

$$
\begin{aligned}
f'_{g,0}\left(\vec{p},t\right)\Big|_{general} &= a\left(\vec{p}\right)\cos\left(\frac{\left|\Omega_{R,0}\left(\vec{p}\right)\right|}{2}t\right)+b\left(\vec{p}\right)\sin\left(\frac{\left|\Omega_{R,0}\left(\vec{p}\right)\right|}{2}t\right) \\
f'_{e,0}\left(\vec{p}+\hbar\vec{k}_0,t\right)\Big|_{general} &= b\left(\vec{p}\right)\cos\left(\frac{\left|\Omega_{R,0}\left(\vec{p}\right)\right|}{2}t\right)+a\left(\vec{p}\right)\sin\left(\frac{\left|\Omega_{R,0}\left(\vec{p}\right)\right|}{2}t\right)
\end{aligned}
$$

The first order (particular solution) amplitudes are given by:

$$
\begin{aligned}
f'_{g,1}\left(\vec{p},t\right)\Big|_{particular} = &\left[\begin{array}{l}
2i\hbar k_o\dfrac{\mathrm{Im}\left(\Omega_{R,0}\left(\vec{p}\right)^*\vec{\Omega}_{R,1}\left(\vec{p}\right)\right)}{2\left|\Omega_{R,0}\left(\vec{p}\right)\right|}\cdot \\
\left[\begin{array}{l}
a\left(\vec{p}\right)\nabla_p\left(\dfrac{\left|\Omega_{R,0}\left(\vec{p}\right)\right|}{2}\right)\left(\dfrac{t^2}{4}\cos\left(\dfrac{\left|\Omega_{R,0}\left(\vec{p}\right)\right|}{2}t\right)-\dfrac{t}{2\left|\Omega_{R,0}\left(\vec{p}\right)\right|}\sin\left(\dfrac{\left|\Omega_{R,0}\left(\vec{p}\right)\right|}{2}t\right)\right) \\
+\nabla_p\left(a\left(\vec{p}\right)\right)\left(\dfrac{t}{2}\sin\left(\dfrac{\left|\Omega_{R,0}\left(\vec{p}\right)\right|}{2}t\right)\right) \\
+b\left(\vec{p}\right)\nabla_p\left(\dfrac{\left|\Omega_{R,0}\left(\vec{p}\right)\right|}{2}\right)\left(\dfrac{t^2}{4}\sin\left(\dfrac{\left|\Omega_{R,0}\left(\vec{p}\right)\right|}{2}t\right)+\dfrac{t}{2\left|\Omega_{R,0}\left(\vec{p}\right)\right|}\cos\left(\dfrac{\left|\Omega_{R,0}\left(\vec{p}\right)\right|}{2}t\right)-\dfrac{1}{\left|\Omega_{R,0}\left(\vec{p}\right)\right|^2}\sin\left(\dfrac{\left|\Omega_{R,0}\left(\vec{p}\right)\right|}{2}t\right)\right) \\
+\nabla_p\left(b\left(\vec{p}\right)\right)\left(\dfrac{-t}{2}\cos\left(\dfrac{\left|\Omega_{R,0}\left(\vec{p}\right)\right|}{2}t\right)+\dfrac{1}{\left|\Omega_{R,0}\left(\vec{p}\right)\right|}\sin\left(\dfrac{\left|\Omega_{R,0}\left(\vec{p}\right)\right|}{2}t\right)\right)
\end{array}\right] \\
-\hbar k_0\dfrac{\vec{\Omega}_{R,1}\left(\vec{p}\right)^*\cdot\left(\nabla_p\Omega_{R,0}\left(\vec{p}\right)\right)}{2\left|\Omega_{R,0}\left(\vec{p}\right)\right|}\left[\begin{array}{l}
a\left(\vec{p}\right)\left(\dfrac{t}{2}\sin\left(\dfrac{\left|\Omega_{R,0}\left(\vec{p}\right)\right|}{2}t\right)\right) \\
+b\left(\vec{p}\right)\left(\dfrac{-t}{2}\cos\left(\dfrac{\left|\Omega_{R,0}\left(\vec{p}\right)\right|}{2}t\right)+\dfrac{1}{\left|\Omega_{R,0}\left(\vec{p}\right)\right|}\sin\left(\dfrac{\left|\Omega_{R,0}\left(\vec{p}\right)\right|}{2}t\right)\right)
\end{array}\right]
\end{array}\right] \\
f'_{e,1}\left(\vec{p}+\hbar\vec{k}_0,t\right)\Big|_{particular} = &\left[\begin{array}{l}
2i\hbar k_o\dfrac{\mathrm{Im}\left(\Omega_{R,0}\left(\vec{p}\right)^*\vec{\Omega}_{R,1}\left(\vec{p}\right)\right)}{2\left|\Omega_{R,0}\left(\vec{p}\right)\right|}\cdot \\
\left[\begin{array}{l}
c\left(\vec{p}\right)\nabla_p\left(\dfrac{\left|\Omega_{R,0}\left(\vec{p}\right)\right|}{2}\right)\left(\dfrac{t^2}{4}\cos\left(\dfrac{\left|\Omega_{R,0}\left(\vec{p}\right)\right|}{2}t\right)-\dfrac{t}{2\left|\Omega_{R,0}\left(\vec{p}\right)\right|}\sin\left(\dfrac{\left|\Omega_{R,0}\left(\vec{p}\right)\right|}{2}t\right)\right) \\
+\nabla_p\left(c\left(\vec{p}\right)\right)\left(\dfrac{t}{2}\sin\left(\dfrac{\left|\Omega_{R,0}\left(\vec{p}\right)\right|}{2}t\right)\right) \\
+d\left(\vec{p}\right)\nabla_p\left(\dfrac{\left|\Omega_{R,0}\left(\vec{p}\right)\right|}{2}\right)\left(\dfrac{t^2}{4}\sin\left(\dfrac{\left|\Omega_{R,0}\left(\vec{p}\right)\right|}{2}t\right)+\dfrac{t}{2\left|\Omega_{R,0}\left(\vec{p}\right)\right|}\cos\left(\dfrac{\left|\Omega_{R,0}\left(\vec{p}\right)\right|}{2}t\right)-\dfrac{1}{\left|\Omega_{R,0}\left(\vec{p}\right)\right|^2}\sin\left(\dfrac{\left|\Omega_{R,0}\left(\vec{p}\right)\right|}{2}t\right)\right) \\
+\nabla_p\left(d\left(\vec{p}\right)\right)\left(\dfrac{-t}{2}\cos\left(\dfrac{\left|\Omega_{R,0}\left(\vec{p}\right)\right|}{2}t\right)+\dfrac{1}{\left|\Omega_{R,0}\left(\vec{p}\right)\right|}\sin\left(\dfrac{\left|\Omega_{R,0}\left(\vec{p}\right)\right|}{2}t\right)\right)
\end{array}\right] \\
+\hbar k_o\dfrac{\vec{\Omega}_{R,1}\left(\vec{p}\right)\cdot\nabla_p\left(\Omega_{R,0}\left(\vec{p}\right)^*\right)}{\left|\Omega_{R,0}\left(\vec{p}\right)\right|}\left[\begin{array}{l}
c\left(\vec{p}\right)\left(\dfrac{t}{2}\sin\left(\dfrac{\left|\Omega_{R,0}\left(\vec{p}\right)\right|}{2}t\right)\right) \\
+d\left(\vec{p}\right)\left(\dfrac{-t}{2}\cos\left(\dfrac{\left|\Omega_{R,0}\left(\vec{p}\right)\right|}{2}t\right)+\dfrac{1}{\left|\Omega_{R,0}\left(\vec{p}\right)\right|}\sin\left(\dfrac{\left|\Omega_{R,0}\left(\vec{p}\right)\right|}{2}t\right)\right)
\end{array}\right]
\end{array}\right]
\end{aligned}
$$

Based on these expressions, the underlying assumption that the zeroth order approximation is much larger than the first order approximation as described by (B2.1), can also be expressed as an assumption that the magnitude of the first order Rabi rate is much smaller than that of the zeroth order Rabi rate, i.e. $\left|\vec{\Omega}_{R,1}\left(\vec{p}\right)\right| \ll \left|\Omega_{R,0}\left(\vec{p}\right)\right|$. Additionally, the dot product of the gradient $\nabla_p \Omega_{R,0}\left(\vec{p}\right)$ with the vector $\vec{\Omega}_{R,1}\left(\vec{p}\right)$ contributes the overall scaling for the particular (first order) solutions for atomic state amplitudes, and so the rate $\left|\hbar k_0 \nabla_p \Omega_{R,0}\left(\vec{p}\right)\right|$ must not far exceed $\left|\Omega_{R,0}\left(\vec{p}\right)\right|$ for the perturbation theory to be valid. In summary, the assumptions that need to be verified to ensure the validity of the perturbation theory are given by:

$$\begin{aligned} \left|\vec{\Omega}_{R,1}\left(\vec{p}\right)\right| &\ll \left|\Omega_{R,0}\left(\vec{p}\right)\right| \\ \left|\hbar k_0 \nabla_p \Omega_{R,0}\left(\vec{p}\right)\right| &\lesssim \left|\Omega_{R,0}\left(\vec{p}\right)\right| \end{aligned} \tag{B2.2}$$

These relationships were explored with the same computational scheme as described in section B.2.1. Verifying the analytical integration result for the restricted Rabi scalar. Equation (B1.35) is used to numerically evaluate $\left|\vec{\Omega}_{R,1}\left(\vec{p}\right)\right|$ over the atom momentum space, and an evaluation of $\left|\Omega_{R,0}\left(\vec{p}\right)\right|$ for points separated in momentum space by $\hbar k_0/10$ is used to compute gradients $\left|\hbar k_0 \nabla_p \Omega_{R,0}\left(\vec{p}\right)\right|$. comparison was also conducted for the comparison of $\left|\Omega_{R,0}\left(\vec{p}\right)\right|$ with $\left|\vec{\Omega}_{R,1}\left(\vec{p}\right)\right|$.

Figure B-3 and Figure B-4 depict $\left|\vec{\Omega}_{R,1}\left(\vec{p}\right)\right|$ and $\hbar k_0 \nabla_p \Omega_{R,0}\left(\vec{p}\right)$ as a function of atomic momenta with $v_{\text{out-of-plane}} = 0$ m/s in Figure B-3 and with $v_{\text{Dopp}} = 0$ m/s in Figure B-4. For all plots, the color bar legend is in units of $2\pi \times \text{kHz}$. As can be seen, the magnitude of the restricted Rabi vector $\left|\vec{\Omega}_{R,1}\left(\vec{p}\right)\right|$ was computed to be many orders of magnitude smaller than $\Omega_{R,0}\left(\vec{p}\right)$, with a peak rate of $\max\left(\left|\vec{\Omega}_{R,1}\left(\vec{p}\right)\right|\right) = 2\pi \times 0.0577$ kHz as compared with $\max\left(\left|\Omega_{R,0}\left(\vec{p}\right)\right|\right) = 2\pi \times 321$ kHz. For both $v_{\text{out-of-plane}} = 0$ m/s and $v_{\text{Dopp}} = 0$ m/s, the gradients $\left|\hbar k_0 \nabla_p \Omega_{R,0}\left(\vec{p}\right)\right|$ were observed to be roughly

Approved for public release; distribution is unlimited

commensurate with peak rates for $\Omega_{R,0}\left(\vec{p}\right)$, but localized for small momenta corresponding to longitudinal atom velocities much smaller than the most probable velocity (748 m/s) for a Ca beam at $625^{\circ}\mathrm{C}$.

These analyses satisfy (B2.2) and validate the perturbation theory assumption that for a thermal atomic Ca beam, calculations are dominated by the leading order rate $\Omega_{R,0}\left(\vec{p}\right)$ and associated atomic state amplitudes $f'_{g,0}\left(\vec{p},t\right)\Big|_{general}$ and $f'_{e,0}\left(\vec{p}+\hbar\vec{k}_0,t\right)\Big|_{general}$.

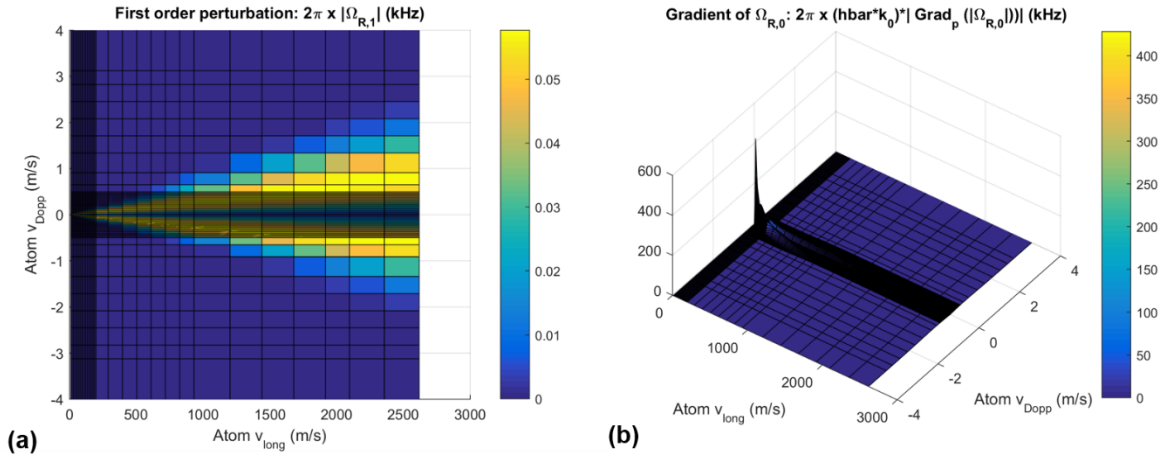

Figure B-3. Evaluations for (a) $\left|\vec{\Omega}_{R,1}\left(\vec{p}\right)\right|$ and (b) $\hbar k_0 \nabla_p \Omega_{R,0}\left(\vec{p}\right)$ with $v_{\text{out-of-plane}} = 0$ m/s.

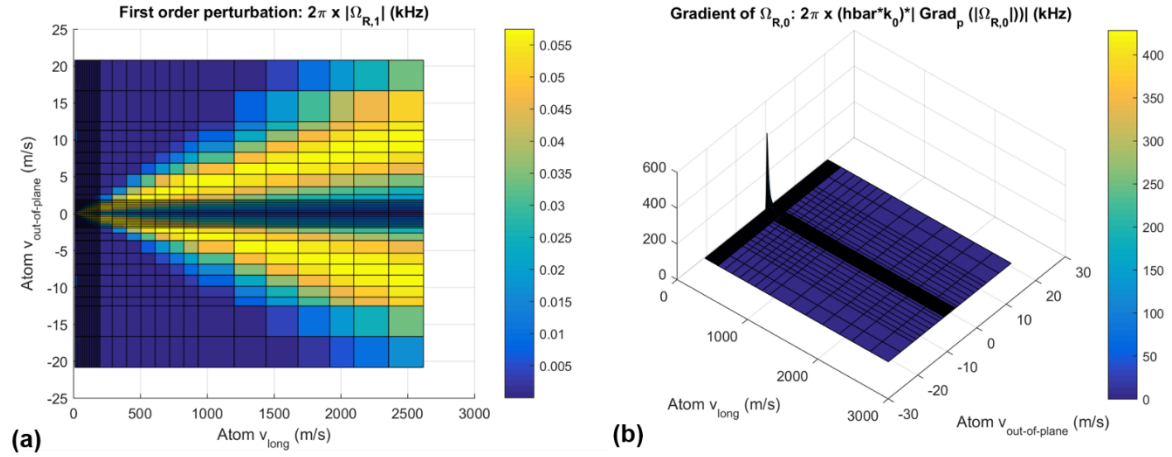

Figure B-4. Evaluations for (a) $\left|\vec{\Omega}_{R,1}\left(\vec{p}\right)\right|$ and (b) $\hbar k_0 \nabla_p \Omega_{R,0}\left(\vec{p}\right)$ with $v_{\text{Dopp}} = 0$ m/s,

Appendix C

On the comparison of theoretical predictions with a measured saturation profile

A scaling metric was devised to convert R-B fluorescence power measurements from the CaBOT frequency reference into an estimate for excitation probability after interaction with all four beams given by $P_e^{(4)}$. This metric is given by:

$$N_{RB} = N_{coll} P_e^{(4)} \eta_\gamma \eta_{coll} \eta_{fringe} \tag{C.1}$$

In relation (C.1), $N_{RB} = W_{RB} / h\nu_0$ is in units of atoms/s and represents the participation rate of atoms in the R-B signal derived by dividing the measured R-B signal amplitude power W_{RB} by the single photon energy. N_{coll} is also in units of atoms/s and corresponds to an estimate for the number of atoms passing through the collimator according to a relationship for an open channel given by [Ramsey 1956, p. 16] as applied to experimental parameters associated with CaBOT. η_γ is the fraction of atoms that are expected to fluoresce in the detection window, η_{coll} is the fluorescence collection efficiency (calculated from measurements to be 0.12%), and η_{fringe} is the R-B fringe contrast measured as the ratio of the R-B fringe size to the Doppler feature size. For each data point in the saturation study, unique values for N_{RB} and η_{fringe} are measured, allowing unique $P_e^{(4)}$ values to be calculated for each measured data point.

A summary of the process to calculate each $P_e^{(4)}$ is described in equation (C.2) in which the value for η_γ is calculated assuming a most probable atom velocity of 748 m/s corresponding to a Ca oven at $625^\circ\mathrm{C}$ across a detection region measuring 6 mm across.

Approved for public release; distribution is unlimited

$$N_{RB} = N_{coll} P_e^{(4)} \eta_\gamma \eta_{coll} \eta_{fringe}$$

$$N_{RB} = W_{RB} / h\nu_0 \quad \text{[measured vs. power]}$$
$$\eta_{fringe} = W_{RB} / W_{Dopp} \quad \text{[measured vs. power]}$$
$$N_{coll} = 1.118 \times 10^{22} \frac{p' A_s A_{coll}}{l_{cd}{}^2 \sqrt{MT}}$$
$$= 1.118 \times 10^{22} \frac{(0.045 \text{ mm Hg})(0.09 \text{ cm}^2)(0.09 \text{ cm}^2)}{(22 \text{ cm})^2 \sqrt{(40.078 \text{ amu})(898.15 \text{ K})}} = 4.4378 \times 10^{13} \text{ atoms/s}$$
$$\eta_\gamma = \exp[-\Gamma t_{start}] - \exp[-\Gamma t_{end}] = 0.0169$$
$$\eta_{coll} = 0.0012$$

$$\Rightarrow$$

$$P_e^{(4)} = \frac{N_{RB}}{N_{coll}} \left(\eta_\gamma \eta_{coll} \eta_{fringe} \right)^{-1} \tag{C.2}$$

Given the uncertainties introduced by the process of (C.2), particularly in the calculation of N_{coll}, it is interesting that this scaling of the saturation data results in a saturation profile that closely matches predictions for $P_e^{(4)}$ calculated with the restricted Rabi rate theory and the [Bordé *et al.* 1984] theory up to a factor <10x.

Approved for public release; distribution is unlimited

References

B. P. Abbott, R. Abbott, T. D. Abbott, M. R. Abernathy, F. Acernese, K. Ackley, C. Adams, T. Adams, P. Addesso, Adhikari, et al. (LIGO Scientific Collaboration and Virgo Collaboration), *Phys. Rev. Lett*. 116, 061102 (2016).

F. Acernese, M. Agathos, K. Agatsuma, D. Aisa, N. Allemandou, A. Allocca, J. Amarni, P. Astone, G. Balestri, G. Ballardin, et al., *Classical and Quantum Gravity* 32, 024001 (2014).

D. Allan, "Statistics of Atomic Frequency Standards." *Proceedings of the IEEE*, Vol 54, No 2, (Feb 1966).

D. Allan, N. Ashby, C. Hodge, "The Science of Timekeeping." Hewlett Packard Application Note 1289 (1997).

N. Ashby, T. E. Parker, and B. R. Patla, *Nature Physics*, 1 (2018).

J. Audretsch and K.P. Marzlin, "Ramsey fringes in atomic interferometry: Measurability of the influence of space-time curvature" *Physical Review A*, Vol. 50, No. 3. (1994).

R. Barger, J. Bergquist, T. English, and D. Glaze, "Resolution of photon-recoil structure of the 6573-angstrom calcium line in an atomic beam with optical Ramsey fringes." *Applied Physics Letters*, Vol 34, 850 (1979).

K. Bongs, et al. "Development of a strontium lattice clock for the SOC mission on the ISS." arXiv preprint: arXiv:1503.08457v1 (2015).

Ch.J. Bordé, Ch. Salomon, S. Avrillier, A. Van Lerberghe, Ch. Br´eant, D. Bassi, G. Scoles, "Optical Ramsey fringes with traveling waves," *Phys. Rev. A* 30, 1836 (1984).

Ch.J. Bordé, "Atomic interferometry with internal state labelling." *Phys. Lett A* Vol 140 (1989).

R. Bouchendira, P. Clade, S. Guellati-Khelifa, and F. N. N. Biraben, Physical Review Letters 106, 080801(4) (2011).

R. Bouchendira, P. Clade, S. Guellati-Khelifa, and F. N. N. Biraben, Annalen der Adp Physik 525, 484 (2013).

S. Brewer, J. Chen, D. Leibrandt, C. Chou, D. Wineland, J. Bergquist, and T. Rosenband, "A high-accuracy mobile Al+ optical clock." IEEE conference abstract 2014.

J. Cao, P. Zhang, J. Shang, K. Cui, J. Yuan, S. Chao, S. Wang, H. Shu, and X. Huang, "A transportable 40Ca+ single-ion clock with 7.7e-17 systematic uncertainty." arXiv preprint: https://arxiv.org/pdf/1607.03731 (2016).

Approved for public release; distribution is unlimited

M. Cadoret, E. de Mirandes, P. Clade, S. Guellati-Khelifa, C. Schwob, F. Nez, L. Julien, and F. Biraben, Physical Review Letters 101, 230801(4) (2008).

J. Carroll and K. Montgomery, "Global Positioning System timing criticality assessment – preliminary performance results," *40th Annual Precise Time and Time Interval (PTTI) Meeting*, (2008).

R. Charriere, M. Cadoret, N. Zahzam, Y. Bidel, and A. Bresson, "Local gravity measurement with the combination of atom interferometry and Bloch oscillations," *Physical Review A* 85, 013639 (2012).

S. Chiow, S. Hermann, and S. C. C. Muller, Physical Review Letters 103, 050402(4) (2009).

S. Chiow, T. Kovachy, H.C. Chien, and M. A. Kasevich, "102hk Large Area Atom Interferometers" Phys. Rev. Lett. 107, 130403 (2011).

C. W. Chou, D. Hume, T. Rosenband, and D. Wineland, *Science* 329, 1630 (2010).

S. Cook, T. Rosenband, and D. R. Leibrandt, "Laser-Frequency Stabilization Based on Steady-State Spectral-Hole Burning in Eu3+:Y2SiO5," *Phys. Rev. Lett. 114*, 253902 (2015).

A. Corney, *Atomic and laser spectroscopy*. Oxford University Press (2000).

A. Cronin, J. Schmeidmayer and D. Pritchard, "Optics and interferometry with atoms and molecules." *Reviews of Modern Physics*, Volume 81, Jul-Sep 2009.

S. T. Cundiff and J. Ye, "*Colloquium:* Femtosecond optical frequency combs," *Reviews of Modern Physics*, Vo. 75 (2003).

DARPA Defense Advanced Research Projects Agency Broad Agency Announcement: "Spatial, Temporal and Orientation Information in Contested Environments (STOIC)," Strategic Technology Office, DARPA-BAA-14-41. (June 3, 2014).

C. Degenhardt, H. Stoehr, Ch. Lisdat, G. Wilpers, H. Schnatz, B. Lipphardt, T. Nazarova, P. Pottie, U. Sterr, J. Helmcke, and F. Riehle, "Calcium optical frequency standard with ultracold atoms: Approaching 1e-15 relative uncertainty" *Phys Rev A* Vol 72, 062111 (2005).

W. Demtröder, *Laser spectroscopy*, 2nd ed. Berlin: Springer (1996).

A. Derevianko and M. Pospelov, *Nature Physics* 10, 933 (2014).

European GNSS Agency, "GNSS Market Report: Issue 4" Publications Office of the European Union, ISSN 2443-5236 DOI:10.2878/251572 (2015).

D. S. Durfee, Y. K. Shaham, and M. A. Kasevich, *Phys. Rev. Lett.* 97, 240801. (2006).

C. Foot, *Atomic Physics*, Oxford University Press (2005).

R. Fox, J. Sherman, W. Douglas, J. Olson, A. Ludlow, and C. Oates, "A high stability optical frequency reference based on thermal calcium atoms." *Frequency Control Symposium, IEEE International* (2012).

Approved for public release; distribution is unlimited

I. Georgescu, *Nature Physics* 13, 529 (2017).

I. S. Gradshteyn and I.M. Ryzhik, *Table of Integrals, Series, and Products, Corrected and Enlarged Edition*, Ed. by Alan Jeffrey, incorporating the 4th Ed. prepared by Yu. V. Geronimus and M. Yu. Tseytlin, translated from the Russian by Scripta Technica, Inc. Academic Press, Inc., 1965, 1980.

P. W. Graham, J. M. Hogan, M. A. Kasevich, and S. Rajendran, *Physical Review D* 94, 104022 (2016).

T. P. Heavner, E. A. Donley, F. Levi, G. Costanzo, T. E. Parker, J. H. Shirley, N. Ashby, S. Barlow, and S. R. Jefferts, "First accuracy evaluation of NIST-F2" *Metrologia* Vol. 51. No. 3. (2014).

B. Hemingway, J. Taylor, T. B. Swanson, and S. Peil, "Preliminary investigation of a calcium thermal beam in order to build an operational optical clock," *2018 IEEE International Frequency Control Symposium* (2018).

N. Hinkley, J.A. Sherman, N.B. Phillips, M. Schioppo, N.D. Lemke, K. Beloy, M. Pizzocaro, C.W. Oates, A.D. Ludlow, "An atomic clock with 10-18 stability", *Science* 341,1215-1218. 2013.

L. Hollberg, S. Diddams, A. Bartels, T. Fortier and K. Kim, "The measurement of optical frequencies." *Metrologia* Volume 42, S105-S124 (2005).

J. Holloway, W. Mainberger, F. Reder, G. Winkler, L. Essen, and J. Parry, "Comparison and Evaluation of Cesium Atomic Beam Frequency Standards." *Proceedings of the IRE*, Vol 47, Issue 10, (Oct 1959).

F. P. Incropera and D. P. DeWitt, *Fundamentals of Heat and Mass Transfer*, John Wiley and Sons, New York, NY (1985).

W. M. Kays and A. L. London, *Compact Heat Exchanger*, 3rd ed., McGraw-Hill, New York, NY, (1984).

P. Kersten, F. Mensing, U. Sterr, and F. Riehle, "A transportable optical calcium frequency standard." *Appl Phys B*, Vol 68 Issue 1 (1999).

Th. Kisters, K. Zeiske, F. Riehle, J. Helmcke, "High-resolution spectroscopy with laser-cooled and trapped calcium atoms." *App Phys B*, Vol 59, Issue 2, pp 89-98 (1994)

S. Koller, J. Grotti, St. Vogt, A. Al-Masoudi, S. Dorscher, S. Hafner, U. Sterr, and Ch. Lisdat, "Transportable Optical Lattice Clock with 7e-17 Uncertainty." *Physical Review Letters*, Vol 118, 073601 (2017).

H. Leopardi, J. Davila-Rodriguez, F. Quinlan, J. Olson, J. A. Sherman, S. A. Diddams, and T. M. Fortier, *Optica* 4, 879 (2017).

V. Letokhov and V. Chebotaev, *Nonlinear laser spectroscopy*. Berlin: Springer (1977).

I. Leveson "GPS Civilian Economic Value to the U.S., Interim Report," Prepared for the National Executive Committee for Space-Based Positioning, Navigation, and Timing, Version 3 (2015).

L. B. Loeb, *The Kinetic Theory of Gases* (McGraw-Hill Book Company, Inc., New York, 1934), 2nd edition, p. 294.

Approved for public release; distribution is unlimited

M. A. Lombardi, L. M. Nelson, and A. N. Novick, “Time and frequency measurements using the global positioning system,” *Cal Lab: The International Journal of Metrology*, pp. 21–33, July–Sept. 2001. [Online]. Available: http://tf.nist.gov/general/pdf/1424.pdf

A. Ludlow, M. Boyd, J. Ye, E. Peik and P. Schmidt, “Optical Atomic Clocks.” *Reviews of Modern Physics*, Volume 87 (Apr-Jun 2015).

J. McFerran and A. Luiten “Fractional frequency instability in the 1e-14 range with a thermal beam optical frequency reference.” *J. Opt. Soc. Am. B*, Vol 27, No 2 (2010).

D. Meschede, *Optics, light and lasers: an introduction to the modern aspects of laser physics, optics and photonics*. New York: Wiley-VCH (2004).

Microsemi website: Cs beam clock and H-maser commercial model performance data available at www.microsemi.com

Morgner, U., F. X. Ka¨ rtner, S. H. Cho, Y. Chen, H. A. Haus, J. G. Fujimoto, E. P. Ippen, V. Scheuer, G. Angelow, and T. Tschudi, 1999, ‘‘Sub-two-cycle pulses from a Kerr-lens mode-locked Ti:sapphire laser,’’ *Opt. Lett.* 24, 411.

H. Muller, Physical Review Letters 100, 180405(4) (2008).

NIST Special Publication 864, Ed. G. W. Day, D. L. Franzen, and R. K. Hinkernell, “Technical Digest – Symposium on Optical Fiber Measurements, 1994” *Digest of a symposium sponsored by the National Institute of Standards and Technology in cooperation with the IEEE Lasers and Electro-Optics Society and the Optical Society of America*, NIST Boulder, CO. (1994).

C.W. Oates, E. Curtis, and L. Hollberg, “Improved short-term stability of optical frequency standards; approaching 1 Hz in 1 s with the Ca standard at 657 nm.” Optics Letters, Vol 25, No 21 (2000).

J. Olson, R. Fox, R. Brown, T. Fortier, T. F. Sheerin, C. W. Oates, and A. D. Ludlow, “High-stability laser using Ramsey-Borde Interferometry,” *Joint Conference of the European Frequency and Time Forum and IEEE International Frequency Control Symposium (EFTF/IFC)*, Besançon, France. July 2017.

J. Olson, R. W. Fox, T. M. Fortier, T. F. Sheerin, R. C. Brown, H. Leopardi, R. E. Stoner, C. W. Oates, and A. D. Ludlow, “Ramsey-Borde matter-wave interferometry for laser stabilization at 10^-16 frequency instability and below,” currently in review (2019).

J. Olson, Ph.D. Thesis, University of Colorado Boulder (2019).

N. Poli, M. Schioppo, S. Vogt, St. Falke, U. Sterr, Ch. Lisdat and G. Tino, “A transportable strontium optical lattice clock.” arXiv preprint: arXiv:1409.4572v2 (2014).

N. Poli, C. Oates, P. Gill, and G. Tino, “Optical atomic clocks,” arXiv preprint arXiv:1401.2378 (2014).

J. D. Prestage and G. L. Weaver, “Atomic Clocks and Oscillators for Deep-Space Navigation and Radio Science” *Proc. of the IEEE* Vol 95, No. 11. (2007).

I. Rabi, J. Zacharias, S. Millman and P. Kusch, “The molecular beam resonance method for measuring nuclear magnetic moments.” *Phys. Rev*. (1939).

N. Ramsey, *Molecular Beams,* Clarendon Press (1956).

F. Riehle, Th. Kisters, A. Witte, J. Helmcke, and Ch. Bordé, “Optical Ramsey Spectroscopy in a Rotating Frame: Sagnac Effect in a Matter-Wave Interferometer” *Phys Rev Letters*, Vol 67, No 2 (1991).

M. Safronova, D. Budker, D. DeMille, D. F. J. Kimball, A. Derevianko, and C. W. Clark, *Reviews of Modern Physics* 90, 025008 (2018).

Ch. Salomon, D. Hils, and J. L. Hall, “Laser stabilization at the millihertz level,” *J. Opt. Soc. Am. B.* Vol. 5, No. 8. (1988).

F. Schmidt-Kaler, H. Haffner, M. Riebe, S. Gulde, G. P. Lancaster, T. Deuschle, C. Becher, C. F. Roos, J. Eschner, and R. Blatt, *Nature* 422, 408 (2003).

H. Shang, X. Zhang, S. Zhang, D. Pan, H. Chen, and J. Chen, “Miniaturized calcium beam optical frequency standard using fully-sealed vacuum tube with 10-15 instability,” *Optics Express* Vol. 25, No. 24. (2017).

R. Simons, “Estimating Temperatures in a Water-to-Air Hybrid Cooling System,” *Electronics Cooling*, May 2002.

M. A. Sinclair, A. Kelsey, R. E. Stoner, “Separated Parallel Beam Generation for Atom Interferometry,” US Patent US20170370840A1 (US9952154B2), filed by Charles Stark Draper Laboratory, Inc. (2017).

L. C. Sinclair, H. Bergeron, W. C. Swann, E. Baumann, J.-D. Desch^enes, and N. R. Newbury, *Physical Review Letters* 120, 050801 (2018).

Y. Stadnik and V. Flambaum, *Physical Review A* 93, 063630 (2016).

U. Sterr, K. Sengstock, J. H. Muller, D. Bettermann, and W. Ertmer, “The Magnesium Ramsey Interferometer: Applications and Prospects,” *Appl. Phys. B.* 54, 341-346 (1992).

U. Sterr, K. Sengstock, W. Ertmer, F. Riehle, J. Helmcke, “Atom Interferometry”, ed. by P.R. Berman, Academic Press, San Diego (1997).

R. Stoner, K. Kotru, J. Hamilton, J. Durant, A. Kelsey, M. Sinclair, V. Lowe, A. Ludlow, R. Fox, T. Fortier, J. Olson, C. Oates, and T. F. Sheerin, “A Compact Ca Atomic Reference for Optical Timekeeping,” *Institute of Navigation Joint Navigation Conference*, Dayton, OH. June 2017.

Sutter, D. H., G. Steinmeyer, L. Gallmann, N. Matuschek, F. Morier-Genoud, U. Keller, V. Scheuer, G. Angelow, and T. Tschudi, 1999, ‘‘Semiconductor saturable-absorber mirrorassisted Kerr-lens mode-locked Ti:sapphire laser producing pulses in the two-cycle regime,’’ *Opt. Lett.* 24, 631.

M. Thorpe, L. Rippe, T. Fortier, M. Kirchner, and T. Rosenband, “Frequency stabilization to 6× 10−16 via spectral-hole burning,” *Nat. Photonics* 5, 688–693 (2011).

Approved for public release; distribution is unlimited

A. Trabesinger, “Nobel Prize 2005: Glauber, Hall and Hansch,” *Nature Physics* Vol 1, No. 930. (2005).

D. S. Weiss, B. C. Young, and S. Chu, Appl. Phys. B 59, 217 (1994).

A. Wicht, J. M. Hensley, E. Sarajilic, and S. Chu, Physica Scripta 102, 82 (2002).

X. Zhang, M. Bishof, S. L. Bromley, C. V. Kraus, M. S. Safronova, P. Zoller, A. M. Rey, and J. Ye, *Science* 345, 1467 (2014).

X. Zhang, et al. “A transportable calcium atomic beam optical clock.” *Frequency Control Symposium*, IEEE (2016).

Approved for public release; distribution is unlimited